THÈSE DE DOCTORAT
DE L'UNIVERSITÉ PIERRE ET MARIE CURIE

présentée par

Matej Pavin

Pour obtenir le grade de

DOCTEUR ÈS SCIENCES
DE L'UNIVERSITÉ PIERRE ET MARIE CURIE

Spécialité : Physique de l'Univers (ED 560)

Measurements of hadron yields from the T2K replica target in the NA61/SHINE experiment for neutrino flux prediction in T2K

Soutenue le 27 Septembre 2017 devant le jury compose de:

Mme	Delphine	HARDIN	Présidente
	Fabienne	KUNNE	Rapporteuse
MM	Alfons	WEBER	Rapporteur
	Boris	POPOV	Directeur de thèse
	Alain	BLONDEL	Examinateur

PhD THESIS
OF THE UNIVERSITÉ PIERRE ET MARIE CURIE

presented by

Matej Pavin

Submitted in fulfillment of the recquirements for the degree of

DOCTEUR ÈS SCIENCES
DE L'UNIVERSITÉ PIERRE ET MARIE CURIE

Specialty : Physique de l'Univers (ED 560)

Measurements of hadron yields from the T2K replica target in the NA61/SHINE experiment for neutrino flux prediction in T2K

Defended on September 27th in front of the comittee :

Mme	Delphine	HARDIN	President
	Fabienne	KUNNE	Referee
Mr	Alfons	WEBER	Referee
	Boris	POPOV	Supervisor
	Alain	BLONDEL	Examiner

Acknowledgements

First, I would like to thank my thesis supervisor Boris Popov who recognized my work during my stay at CERN as a summer student. He invited me to apply for a Ph.D. position at LPNHE, and this thesis would not exist without him. Whenever I needed to discuss my results or if I simply got stuck, he was just one office away and always provided me with very valuable pieces of advice. Also, these discussions played a pivotal role in my professional development as a member of NA61/SHINE and T2K. For this, I will be forever grateful.

Many thanks to other members of the LPNHE neutrino group: Jacques Dumarchez, Jean-Michel Levy, Claudio Giganti, Pierre Bartet-Friburg and Simon Bienstock for providing a friendly and supportive work environment.

In the end, I would like to thank my family back in Croatia, without their support over the years, I would not be here. Thanks to my friends, mostly in Croatia and Germany for encouragement and support. Long Skype conversations over beer helped me to keep my sanity intact when I was working long hours.

Summary

T2K is an accelerator-based long-baseline neutrino experiment in Japan. The main goal of the T2K experiment is a search for CP violation in the lepton sector by measuring electron (anti)neutrino appearance in a muon (anti)neutrino beam. Initial (anti)neutrino flux is produced in decays of hadrons which originate from the interactions and the re-interactions of a 30 GeV proton beam with a 90 cm long graphite target. Knowledge of the T2K neutrino flux is limited due to large hadron production uncertainties. A series of hadron production measurements were done to solve this problem, in the NA61/SHINE experiment at CERN. Measurements were performed with a proton beam and two target types: a thin graphite target and a replica of the T2K target. Work presented in this thesis concentrates on the T2K replica target data taken in 2010 and the development of the analysis and calibration software. The aim of these measurements is to fully constrain production of π^+, π^-, K^+, K^- and p coming from the target surface by measuring differential hadron yields in the bins of outgoing particle momentum (p), polar angle (θ) and longitudinal position on the target surface (z). This will allow reduction of the T2K neutrino flux uncertainties from around 10% to below 5%. Predictions of FLUKA2011.2c.5 Monte Carlo, NUBEAM and QGSP_BERT physics lists from GEANT4.10.03 have been compared to the data, and it has been found that FLUKA2011.2c.5 gives the best prediction.

Keywords: T2K, NA61/SHINE, neutrino, hadron production, neutrino flux, replica target

Contents

Chapter 1

Neutrinos

Contents

1.1 Introduction

During the last 70 years, physicists have developed and extensively tested a remarkable theory called the Standard Model of particle physics. The Standard Model gives a very precise description of the particle composition of the known matter and the particle interactions based on quantum field theory. However, there are some observations which cannot be predicted by the Standard Model itself. For example, an existence of the particle masses was explained with the Englert–Brout–Higgs mechanism [1, 2] within the framework of the Standard Model and proven by the discovery of the Higgs boson [3, 4]. The same mechanism does not predict values of the masses which must be taken from different measurements. Also, measurements of the anisotropies of the cosmic microwave background (for example, the latest measurements of the Planck space observatory [5]) strongly suggest that 95% of the energy-matter content of the visible universe is not made of the particles predicted by the Standard Model. Furthermore, an asymmetry between matter and antimatter quantity in the universe which we observe today, cannot be explained by any of the measured processes within the Standard Model (see, for example the strong CP problem). These are just a few hints showing that there must exist a better theory of nature. The limitations of the Standard Model do not only arise from the disagreements with the previously described observations, but they are also engraved in its base. It is important to note that a quantum description of gravity was never achieved and therefore, gravity is not one of the interactions described by the Standard Model. The theory which will explain all the problematic observations must also include the quantum description of gravity.

It is natural to think that the Standard Model can be extended by adding new particles and interactions which would at least solve some of the discrepancies between the theory and experiments. Since we haven't observed any new particle so far, the hypothetical particle masses are usually bounded from below, and the strength of their interactions with ordinary matter is bounded from above. New theories or models can be (dis)proved by searching for new particles and by looking for rare interactions of the hypothetical dark matter particles in a detector. Both approaches have their strengths and limitations. However, it is nearly impossible to discriminate between the theories on the market, since it is often possible to modify a disproved model and change the phase space of the model's parameters. While this is not an explicit topic for this thesis, it illustrates that it is necessary to approach the physics beyond the Standard Model from a different perspective.

An opportunity to do this has arisen after the discovery that the weakly interacting Standard Model particles called neutrinos can oscillate between the flavors - electron, muon and tau neutrino (ν_e, ν_μ, ν_τ). The discovery was made by two independent groups: *Super-Kamiokande* [6] and SNO [7], and it was awarded a Nobel prize in 2015. Neutrino oscillations, as it will be shown later, imply that neutrinos have non-zero masses. This requires modification of the Standard Model since initially, neutrinos in the Standard Model were considered to be the massless particles. The structure of the neutrino mass matrix which is not yet fully understood could potentially point to the existence of a sterile neutrino which in turn may solve the dark matter puzzle. Also, depending on the properties of the neutrino oscillations, this can potentially address some of the discrepancies presented above (for example asymmetry between the matter and the antimatter). All of the possibilities will be tackled later in this chapter. It is clear that neutrinos can be considered as a window on the physics beyond the Standard Model. However, there are many experimental challenges when measuring neutrino properties, since they interact only via the weak nuclear force.

The aim of this thesis is to solve some of the experimental challenges which limit the precision of the neutrino oscillation measurements in a particular type of neutrino experiment - an accelerator-based long-baseline neutrino experiment. Although the results presented in this thesis will be mostly used for a specific neutrino experiment called T2K (Tokai to Kamioka, see chapter 2), the principles behind the results can be applied to similar experiments in the future.

This chapter serves as an introduction to the field of neutrino physics, and it is divided as follows. First, a brief history of the neutrino discoveries is presented. Afterwards, neutrinos are described within the framework of the Standard Model. And finally, a concept of neutrino oscillations is introduced alongside with the all relevant experimental results.

1.2 A brief history of neutrinos

1.2.1 From the proposition to the discovery of the neutrinos

In the beginning of the 20th century, after the discovery of the atomic nucleus by Rutherford it was not clear how to explain processes such as beta decay which was observed as a decay of a nucleus with charge z to a nucleus with charge $z+1$ and a beta particle (electron):

$$A_z \to A_{z+1} + e^-. \tag{1.1}$$

Since beta decay was considered to be a two-body decay, energies of the outgoing nucleus and the electron should be unambiguously defined by the conservation laws. However, in 1914. James Chadwick measured the energy spectrum of the beta particles by using a magnetic spectrometer and discovered that the spectrum was continuous. A problem was also observed in some cases with the angular momentum of the outgoing nuclei. One possibility was that conservation laws were violated, but unsatisfied with this, Wolfgang Pauli in 1930 proposed a solution to this puzzle in his letter to the Federal Institute of Technology in Zürich. He proposed a new neutral particle which at that time he called neutron. This particle is emitted from the nucleus alongside with the electron, thus allowing a continuous energy spectrum for the electron and accounting for the missing angular momentum. After Chadwick discovered what is known today as a neutron, this mysterious particle was renamed by Enrico Fermi to an Italian word for "a little neutral one" - a neutrino. It became clear that the process shown in Eq. 1.1 is a decay of the neutron in the nucleus:

$$n \to p^+ + e^- + \bar{\nu}. \tag{1.2}$$

The neutron decays to a proton, an electron and an antineutrino. The neutrino is defined as a particle appearing with the positron if the number of electrons(positrons) is zero in the initial state. On the other hand, a particle which appears with the electron in the final state is defined as the antineutrino. Fermi invented the first effective field theory of the beta decay. The theory can be found in any undergraduate textbook such as Introduction to elementary particles by D. Griffiths [8] and will not be explained here. The strength of the weak interactions in this theory is given by the Fermi constant (G_F, which has a value of 1.6674×10^{-5} GeV $^{-2}$). Although neutrinos resolved the puzzle of beta decay, there was one difficulty left: how to observe neutrinos, since they are neutral and the Fermi constant is extremely small. One possibility to detect neutrinos was to measure the inverse beta decay by putting a large water tank near a high-intensity neutrino source:

$$\bar{\nu} + p \to n + e^+. \tag{1.3}$$

In July of 1956., a few decades after Pauli's letter, Frederick Reines and Clyde Cowan published their observation of anti-neutrinos coming from the nuclear reactor [9]. They placed a tank filled with aqueous solution of cadmium chloride ($CdCl_2$) near the nuclear reactor. Positrons created in inverse beta decays annihilated with an electrons in the solution and created two gamma rays, while neutrons were captured by cadmium which released an additional gamma ray according to:

$$n + {}^{108}Cd \to {}^{109m}Cd \to {}^{109}Cd + \gamma. \tag{1.4}$$

These gamma rays were detected by a scintillator array sandwiching the tank. For his work, Reines was awarded the Nobel prize in 1995. The discovered (anti)neutrino should be actually called electron (anti)neutrino (ν_e) since it always comes in pair with electron(positron). However, today we know that electron has two more massive partners - muon and tau lepton which in turn come with their own neutrinos - muon and tau neutrinos (ν_μ, ν_τ). The muon neutrino was discovered in 1962 by Leon M. Lederman, Melvin Schwartz, and Jack Steinberger at BNL [10] where they produced neutrinos through the interactions of a 15 GeV proton beam with a beryllium target and then observed their interactions in a spark chamber after other particles were stopped by a steel wall. In 1988, they were awarded the Nobel prize for their work. The discovery of ν_τ was made in the DONUT experiment at Fermilab [11] by producing tau neutrinos through decays of charmed mesons and observing their interactions in the nuclear emulsion layers, again after stopping all other particles.

1.2.2 Solar neutrino puzzle and atmospheric neutrino problem

In parallel to the beta decay puzzle, there was an ongoing discussion about what is the energy source in the Sun. An English astronomer and physicist Arthur Eddington realized that four hydrogen nuclei (protons) are a bit heavier than one helium nucleus. This meant that nuclear fusion of hydrogen to helium, if possible, would release enormous amounts of energy. This was especially convenient since the Sun is mostly made of hydrogen. After the discovery of the neutron and the development of the Fermi theory, all necessary tools were available to calculate which processes contribute to the production of energy in the solar core. The calculations were done by Hans Bethe in 1938 and it was realized that the underlying processes in the stars depend on their masses. In the lower mass stars like the Sun, fusion processes are dominated by the so-called *pp* cycle. There are several possible branches of the *pp* cycle which depend on the temperature of the star's core. The schematic overview of the first branch which dominates in the Sun is shown in Fig. 1.1. There are two additional branches of the *pp* cycle which include a production of beryllium, lithium and boron. However, these are more significant for hotter stars whose temperature of the core is closer to 20×10^6 K. It is clear from Fig. 1.1 that the Sun should produce a considerable flux of neutrinos, measurable on the Earth.

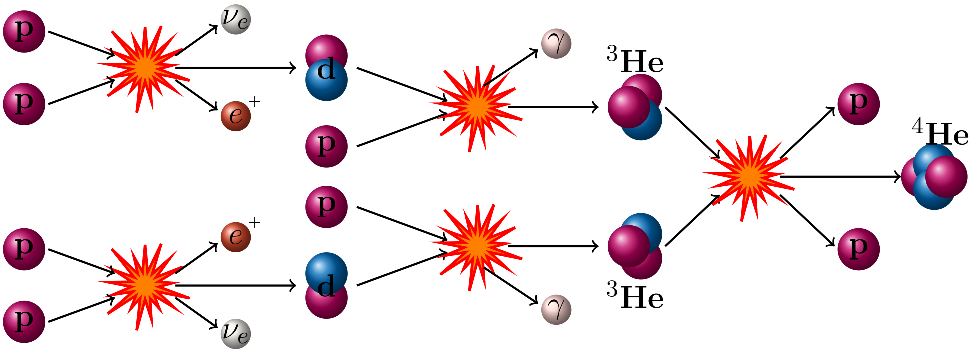

Figure 1.1: First branch of the *pp* fusion cycle in the Sun.

Contributions to the solar neutrino flux on the Earth from all processes is shown in Fig. 1.2 and it was taken from the calculation done by J. Bahcall et al. [12]. The dominant contribution for low neutrino energies comes from the first branch of the *pp* cycle. However, the high energy contribution comes from boron decays on two beryllium nuclei. Ray Davis measured the solar neutrino flux in 1968. by putting a tank of chlorine deep into the Homestake mine in South Dakota. If the Sun produces electron neutrinos, they would be able to convert chlorine into argon:

$$\nu_e + {}^{37}Cl \rightarrow {}^{37}Ar + e^- . \tag{1.5}$$

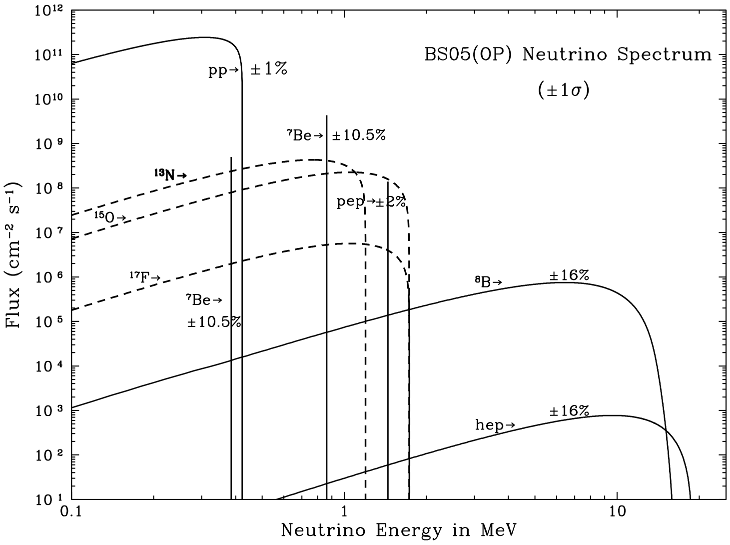

Figure 1.2: Contribution of the all relevant process in the Sun to the solar neutrino flux on Earth. Taken from Ref. [12].

Davis devised a method for counting argon atoms and he measured only a third of what was expected [13]. Resolution of the Solar neutrino problem is closely tied to the phenomenon of neutrino oscillations during which neutrinos change their flavor (for example, ν_μ becomes ν_τ while traveling from the source to the detector). Apart for the solar neutrinos, another natural source of neutrinos is interactions of cosmic rays with upper layers of the atmosphere. These neutrinos are produced in decays of hadrons, mostly pions and the expected ratio of the ν_μ flux and the ν_e flux is:

$$R\left(\frac{\nu_\mu}{\nu_e}\right) = \frac{2}{1}. \tag{1.6}$$

However, the measured number of atmospheric neutrinos by the Kamiokande-II collaboration [14] revealed that there some muon neutrinos are missing (i.e., $R < 2$). This effect is known as the atmospheric neutrino problem. In 1998, the *Super-Kamiokande* collaboration measured the ν_μ and ν_e energy spectra as a function of the zenith angle [6]. Since the typical height in the atmosphere where neutrinos are created is known and neutrino energy spectra and zenith angle are measured, it is possible to calculate the ratio of the neutrino flight path length to its energy L/E. As it will be shown later in section 1.4, the probability of neutrino oscillations changes as a function of L/E. Measurement performed in *Super-Kamiokande* are shown in Fig. 1.3. Missing muon neutrinos for higher L/E are created on the opposite side of the Earth. It is important to note that these measurements are only consistent with the neutrino oscillations, while other, more exotic models like neutrino decays are disfavored.

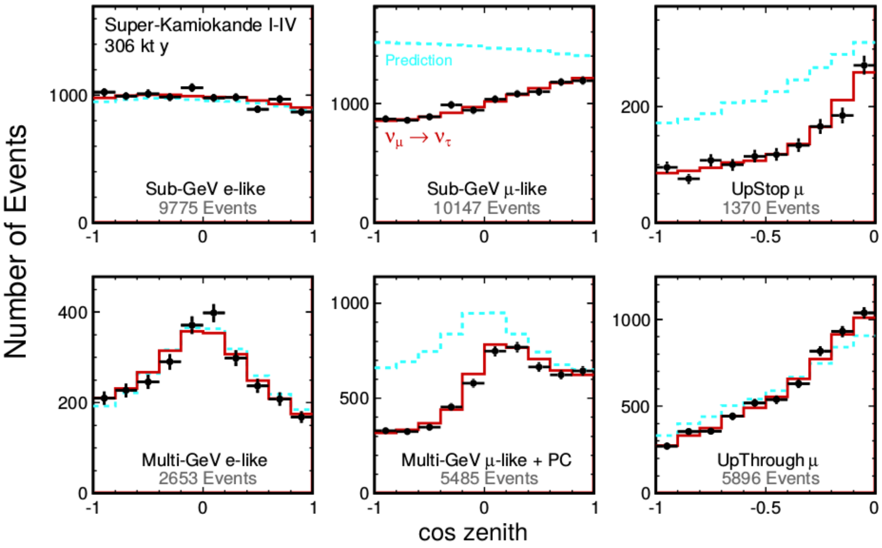

Figure 1.3: The zenith angle distributions for fully contained 1-ring e-like and μ-like events with visible energy $< 1.33\,\text{GeV}$ (sub-GeV) and $> 1.33\,\text{GeV}$ (multi-GeV). For multi-GeV μ-like events, a combined distribution with partially contained (PC) events is shown. The dotted histograms show the non-oscillated Monte Carlo events, and the solid histograms show the best-fit expectations for $\nu_\mu \to \nu_\tau$ oscillations. Taken from Ref. [15].

After the discovery of the neutrino oscillations by *Super-Kamiokande*, Sudbury Neutrino Observatory (SNO) started measuring neutrino flux from the Sun. They measured three independent interactions in heavy water:

$$\nu + {}^2H \to p + p + e^-, \tag{1.7a}$$
$$\nu + e^- \to \nu + e^-, \tag{1.7b}$$
$$\nu + {}^2H \to \nu + p + n. \tag{1.7c}$$

The first interaction (so-called charged current interaction - CC) is sensitive only to ν_e, the second one (elastic scattering - ES) is sensitive to all three neutrino flavors. However, ν_e contribution is the largest one. And the third interaction (neutral current interaction - NC) is sensitive to all flavors equally. This allowed SNO collaboration to measure the total solar neutrino flux and compare it to the solar ν_e neutrino flux and prediction of the Standard Solar Model (SSM) [12]. The final results from the SNO collaboration are shown in Fig. 1.4 and can be found in Ref. [16]. The ratio of the ν_e flux to the total flux is:

$$\frac{\Phi_{\nu_e}}{\Phi_{all}} = 0.340 \pm 0.023\,(\text{stat})^{+0.029}_{-0.031}\,(\text{syst}), \tag{1.8}$$

The measurement of the NC flux is:

$$\phi^{NC} = (4.94 \pm 0.21\,(\text{stat})^{+0.38}_{-0.34}\,(\text{syst})) \times 10^6 \text{cm}^{-2}\text{s}^{-1}, \tag{1.9}$$

while the lower and the upper bound for the ϕ^{NC} prediction from the standard solar model is:

$$\phi^{NC}_{SSM,low} = 4.34^{+0.71}_{-0.61} \times 10^6 \mathrm{cm}^{-2}\mathrm{s}^{-1}, \tag{1.10a}$$

$$\phi^{NC}_{SSM,high} = 5.49^{+0.95}_{-0.81} \times 10^6 \mathrm{cm}^{-2}\mathrm{s}^{-1}. \tag{1.10b}$$

The result is consistent with the SSM prediction and with neutrino oscillations - i.e. only one-third of the ν_e flux arrives to the Earth. Although neutrino oscillations solved the solar neutrino puzzle and the atmospheric neutrino problem, its consequences are far-reaching and to understand them properly one must understand underlying theory of particles and interactions - the Standard Model (SM) of particle physics.

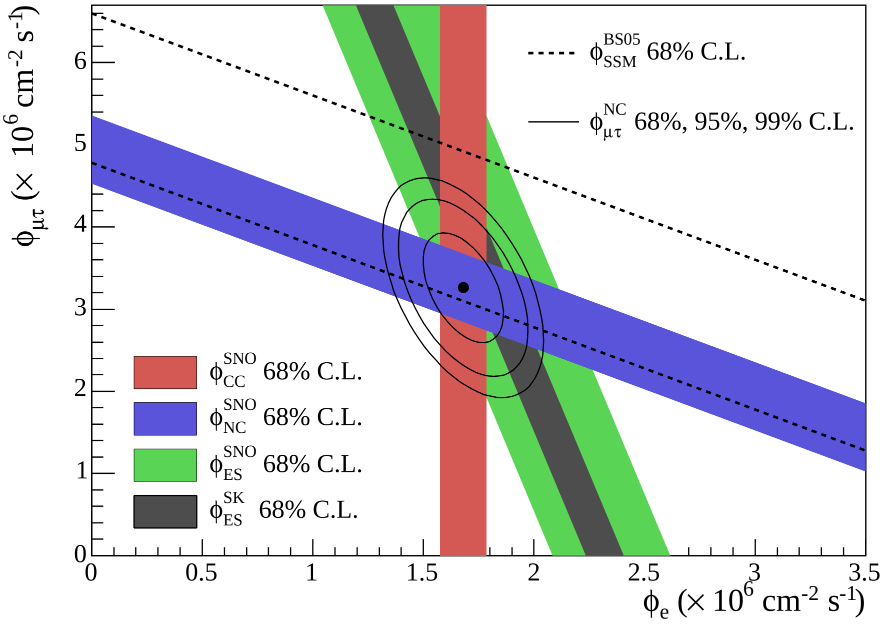

Figure 1.4: Flux of $\mu + \tau$ neutrinos versus flux of electron neutrinos. CC, NC and ES flux measurements are indicated by the filled bands. The total ^8B solar neutrino flux predicted by the Standard Solar Model [12] is shown as dashed lines, and that measured with the NC channel is shown as the solid band parallel to the model prediction. The narrow band parallel to the SNO ES result correponds to the Super-Kamiokande result in [17]. The intercepts of these bands with the axes represent the $\pm 1\sigma$ uncertainties. The non-zero value of $\phi_{\mu\tau}$ provides strong evidence for neutrino flavor transformation. The point represents ϕ_e from the CC flux and $\phi_{\mu\tau}$ from the NC-CC difference with 68%, 95%, and 99% C.L. contours included. Taken from Ref. [16].

1.3 Neutrinos in the Standard Model of particle physics

1.3.1 Standard Model

The Standard Model of particle physics divides the elementary particle content of the universe into spin one-half fermions and spin one bosons. Fermions interact by exchanging the bosons and each fermion has its antiparticle - a particle with the same mass but opposite additive quantum numbers. Depending on the type of its interactions, the fermion can be either a quark or a lepton. Quarks interact via all fundamental interactions: strong, weak, electromagnetic and gravity. Leptons do not interact via the strong interaction, and some of them (neutrinos) are without electrical charge so they can interact only via the weak nuclear force and gravity. Fermions are further divided into three families. In each family, fermions with the same fundamental quantum numbers can be found. The only difference is in their masses, fermions in the first family being lightest ones and in the third family, the heaviest ones. Although all fermions can interact via gravity, the gravity itself is not included in the Standard Model, in particular, because it is notoriously difficult to construct a quantum theory of gravity. In addition, this interaction is 29 orders of magnitude weaker than the weak nuclear force at the proton scale and therefore can be neglected for single particles in the energy domains that we are studying. The Standard Model contains four spin one bosons which carry three fundamental interactions between the fermions: photons (γ) for the electromagnetic interaction $W^{\pm}$ bosons and Z^0 bosons for the weak interaction and gluons (g) for the strong interaction. The particle content of the Standard Model is further completed with the already mentioned discovery of the SM Higgs boson, which has spin zero and whose importance lies in the $SU(2) \times U(1)$ symmetry breaking mechanism resulting in the weak bosons becoming massive. The Higgs also gives their masses to the fermions. The particle content of the Standard Model is depicted in Fig. 1.5.

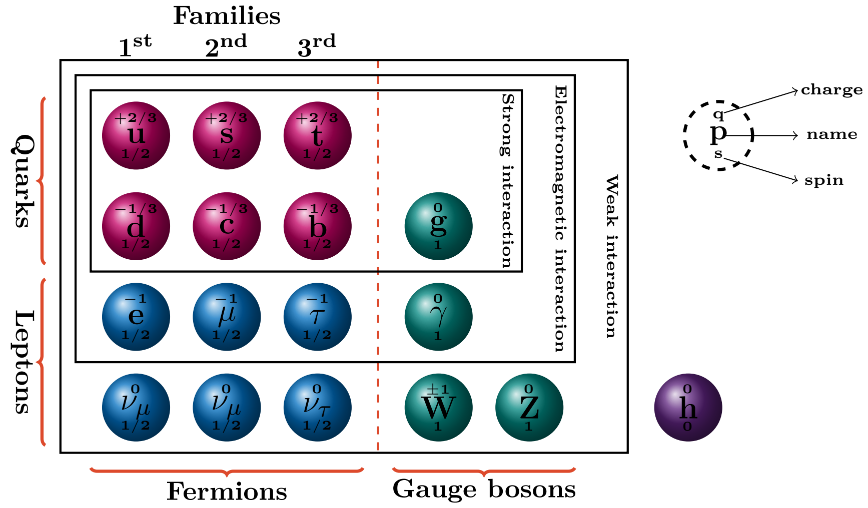

Figure 1.5: Standard Model of particle physics.

1.3.1.1 Gauge invariance in the Standard Model

The notion of symmetry has always been important in physics. From the Noether's theorem, we know that to every continuous symmetry of the action corresponds a conserved quantity. Well known examples are energy, momentum, and angular momentum conservation. The Standard Model was built to be invariant to the Poincaré group of transformations which include Lorentz boosts, space-time translations and spatial rotations. The Standard Model is also invariant under the transformation of the so-called internal gauge symmetry group. This can be best illustrated through the example of quantum electrodynamics. In the 1930s, Paul Dirac tried to include the special theory of relativity into quantum mechanics, since the standard formulation of quantum mechanics is not invariant under the Lorentz transformations. He ended up with a linearized equation which bears his name:

$$(i\gamma^{\mu}\partial_{\mu} - m)\psi = 0, \tag{1.11}$$

where γ^{μ} are 4×4 matrices, ∂_{μ} is the energy-momentum operator, m the mass of the particle and ψ a four-component wave function of the particle, the so-called Dirac spinor. Two degrees of freedom of the spinor describe particle with projections of the spin $+1/2$ and $-1/2$ and the other two describe the antiparticle. The mere inclusion of special relativity into quantum mechanics and the requirement that the obtained equation is the first order, lead naturally Dirac to find the spin of the particle and to predict the existence of the antiparticles. Gamma matrices can be written in many different representations of the Dirac basic anti-commutation rule:

$$\{\gamma^{\mu}, \gamma^{\nu}\} = -2\eta^{\mu\nu} I_4, \tag{1.12}$$

where $\eta^{\mu\nu}$ represents the Minkovski metric and I_4 is a 4×4 unit matrix. For the sake of brevity, a derivation of the Dirac equation and all consequences will not be described here. Instead they can be found in textbooks, for example those of Walter Greiner [18, 19]. Dirac equation is valid for all particles in vacuum. It is useful to write a Dirac Lagrangian:

$$\mathcal{L} = \bar{\psi}(\gamma^{\mu}\partial_{\mu} - m)\psi, \tag{1.13}$$

where $\bar{\psi} = \psi^{\dagger}\gamma^{0}$. The Lagrangian is invariant under a global phase transformation:

$$\psi \rightarrow e^{i\alpha}\psi. \tag{1.14}$$

The transformations are representations of the unitary group $U(1)$. We can imagine that the Lagrangian should be invariant to the different but simultaneous phase transformation in each point of the space-time. In other words, we want to be able to choose different phases for different electrons in the universe and the Lagrangian should be invariant to the transformations:

$$\psi \rightarrow e^{i\alpha(x^{\mu})}\psi, \tag{1.15}$$

where now $\alpha(x^{\mu})$ is a function of the space-time coordinates. It turns out that Lagrangian defined in Eq. 1.13 is not invariant under the local $U(1)$ transformations. Nevertheless, if we add a new vector field A^{μ} to the Lagrangian which transforms under the $U(1)$ transformations like:

$$A_{\mu} \rightarrow A_{\mu} + \frac{1}{e}\partial_{\mu}\alpha, \tag{1.16}$$

it is possible to get Lagrangian which is invariant under the local gauge transformations:

$$\mathcal{L} = \bar{\psi}(\gamma^{\mu}\partial_{\mu} - m)\psi + e\bar{\psi}\gamma^{\mu}\psi A^{\mu}. \tag{1.17}$$

A new term in the Lagrangian represents the interaction between the electron and the new vector field. If the vector field is a real physical field, it should also have a kinetic energy term, which can be built from the field tensor:

$$F_{\mu\nu} = \partial_{\mu}A_{\nu} - \partial_{\nu}A_{\mu}. \tag{1.18}$$

Furthermore, if we define a covariant derivative:

$$D_\mu = \partial_\mu - ieA_\mu, \tag{1.19}$$

it is possible to write Lagrangian in the same form as in Eq. 1.13:

$$\mathcal{L} = \bar{\psi}(\gamma^\mu D_\mu - m)\psi - \frac{1}{4}F_{\mu\nu}F^{\mu\nu}. \tag{1.20}$$

One may be tempted to introduce a mass term of the vector field $\frac{1}{2}mA^\mu A_\mu$. However, this is excluded because this term is not invariant under the local gauge transformations. This new Lagrangian is the same as the Lagrangian of the quantum electrodynamics, and the introduced massless vector field is a photon field. Therefore, the mere demand of local gauge invariance under $U(1)$ leads to the charged particle-photon coupled dynamics. This is a compelling idea and it is possible to follow the same argument and obtain the Lagrangian for the strong interactions. In order to follow experimental observations, one would need to require the local invariance under the $SU(3)$ transformations. Quarks carry a charge which is called the color and comes in three different forms (called red, green and blue). Strong interactions are propagated by eight massless vector bosons called gluons which also carry color and therefore, can self-interact. However, this discussion is out of the scope of this chapter which is orientated towards weak interactions and neutrinos. More details about the gauge invariance in the quantum chromodynamics can be found in the book by F. Halzen and A. Martin [20].

1.3.2 Electroweak interactions

1.3.2.1 Weak interactions

Understanding weak interactions is of crucial importance for understanding neutrinos. It was already shown that it is possible to get the interaction Lagrangian for quantum electrodynamics and chromodynamics by applying a local gauge invariance principle. However, the weak force is several magnitudes weaker compared to the strong and the electromagnetic forces. This could potentially be explained if weak interactions are mediated by massive vector bosons ($W^\pm$). Furthermore, in an experiment done in 1956, Chien-Shiung Wu studied beta decays of polarized ^{60}Co nuclei and showed that parity (symmetry under reflections) was violated in the measured weak interactions (see Ref. [21]). In particular, Wu observed that electrons are preferentially emitted in the direction opposite to the nuclear spin. The amplitude of any process (for example scattering of two particles) can be written as a product of the currents:

$$\mathscr{M} \propto J_\mu J^\mu \tag{1.21}$$

If we examine an electromagnetic scattering of two electrons we expect the current to be proportional to:

$$J_\mu \propto \bar{u}_1\gamma_\mu u_2, \tag{1.22}$$

where u_1 and u_2 are spinors of the outgoing particles. In order to accommodate parity violation and other experimental results, current for the weak scattering or decay (let's say $\nu_e + e^- \rightarrow e^- + \nu_e$) must be written in the vector minus axial vector (V-A) form:

$$J_\mu \propto \bar{e}\gamma_\mu\frac{1}{2}(1-\gamma_5)\nu_e, \tag{1.23}$$

where $\gamma_5 = i\gamma^0\gamma^1\gamma^2\gamma^3$. This current is called the charged current since it transfers a unit of charge. For example, an electron can become ν_e and the excess charge is transferred by the emitted W^- boson to some other fermion. The same principle is valid for the positron and $\overline{\nu}_e$ as can be seen in Fig. 1.6. Later on, Glashow proposed the existence of a weak neutral current.

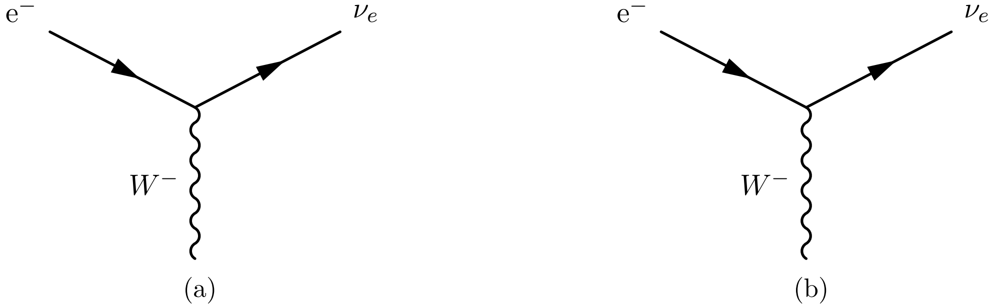

Figure 1.6: Charged weak currents: positive (a) and negative (b).

These interactions should be mediated by a massive neutral boson (Z^0). The existence of neutral weak interactions was proved by the measurement of the $\overline{\nu}_\mu + e^-$ scattering. The form of the weak neutral current is:

$$J_\mu \propto \bar{e}\gamma_\mu(c_V - c_A\gamma_5)\nu_\mu, \tag{1.24}$$

where c_V and c_A are constants which depend on the interacting particles. While in charged current interactions (CC) parity violation is maximal, this is not the case in neutral current interactions (NC) because of the c_V and c_A factors. In the previous subsections, electromagnetic and strong interactions were derived from the principle of the local gauge invariance. In contrast to these interactions which are mediated by massless bosons, weak interactions seem to be mediated by the massive bosons. The mass term for the vector field is not invariant under local gauge transformations, therefore we cannot directly apply the same principles to weak interactions.

1.3.2.2 Electroweak unification

In 1961, Glashow attempted to unify the electromagnetic and the weak interactions under the electroweak interaction. From the first glance, both of these interactions have a totally different form: the electromagnetic interaction has vector form, while weak interactions have V-A form. A useful concept to define are chirality operators $\hat{P}_L$ and $\hat{P}_R$ such that:

$$\begin{aligned} \hat{P}_L\psi &= \frac{1}{2}(1-\gamma_5)\psi = \psi_L, \quad & \hat{P}_R\psi &= \frac{1}{2}(1+\gamma_5)\psi = \psi_R \\ \hat{P}_L\bar{\psi} &= \frac{1}{2}(1-\gamma_5)\bar{\psi} = \bar{\psi}_R \quad & \hat{P}_R\bar{\psi} &= \frac{1}{2}(1+\gamma_5)\bar{\psi} = \bar{\psi}_L, \end{aligned} \tag{1.25}$$

where ψ_L and $\bar{\psi}_L$ are the particle and the antiparticle left-handed chiral states respectively, while ψ_R and $\bar{\psi}_R$ are the particle and the antiparticle right-handed chiral states. Chiral states are equal to the helicity states (projection of the spin on the momentum) if the fermion is massless. From Eq. 1.23, it follows that the CC interactions only include the left particle and the right antiparticle states. From all experiments so far, we have only observed left-handed neutrinos. The chiral states allow us to rewrite the electromagnetic interactions as a sum of the interaction between the left-handed and the interaction between the right-handed states:

$$J_\mu^{em} \propto \bar{u}_L\gamma_\mu u_L + \bar{u}_R\gamma_\mu u_R. \tag{1.26}$$

The same principle can be applied to the measured NC interactions, however, in this case, we have additional c_V and c_A factors. From the experimental measurements, we know that the specific flavor of neutrinos, for example, ν_e ($\overline{\nu}_e$), always comes with the same charged lepton flavor, in this case, $e^{\pm}$. It is possible to construct a left-handed doublet states:

$$\chi_L = \begin{pmatrix} \nu_e \\ e \end{pmatrix}_L, \begin{pmatrix} \nu_\mu \\ \mu \end{pmatrix}_L, \begin{pmatrix} \nu_\tau \\ \tau \end{pmatrix}_L, \begin{pmatrix} u \\ d' \end{pmatrix}_L, \begin{pmatrix} c \\ s' \end{pmatrix}_L, \begin{pmatrix} t \\ b' \end{pmatrix}_L \tag{1.27}$$

and right-handed singlet states:

$$\chi_R = e_R, \mu_R, \tau_R, u_R, d'_R, c_R, s'_R, t_R, b'_R. \tag{1.28}$$

These states are singlets and doublets under the $SU(2)$ symmetry group. Doublet states are constructed from the lepton-neutrino pair or the quark pair and can undergo CC interactions, while this is not the case for the right-handed singlet states. Quark eigenstates of the weak interaction are not equal to the quark eigenstates of the strong interaction and therefore we have quark mixing. For this reason, left-handed quark doublets are constructed, for example, from u and d' quarks where the latter one is a linear combination of the d, s, and b quarks. The mixing of the quarks is represented by the Cabibbo-Kobayashi-Maskawa (CKM) matrix and for the sake of brevity will not be explained here. More details can be found in Ref. [20]. Since the symmetry group is $SU(2)$, this allows as to define a quantum number called weak isospin, which should not be confused with the regular spin. By using the doublets we can write the charged currents in a more compact form:

$$J^{\pm}_\mu = \bar{\chi}_L \gamma_\mu \sigma^{\pm} \chi_L, \tag{1.29}$$

where $\sigma^{\pm}$ are isospin raising and lowering operators defined as a combination of the Pauli matrices. So, for the charged current we also expect to observe two charged vector bosons ($W^{\pm}$). There are three generators of the symmetry group $SU(2)$ which are represented by the Pauli matrices or some linear combination of them (in our case $\sigma^{\pm} = \frac{1}{2}(\sigma_1 + i\sigma_2)$). For the charged current two operators are being used ($\sigma^{\pm}$), while we are missing the third operator (third Pauli matrix) and respective neutral vector field (W^3) which can be used for the neutral current:

$$J^3_\mu = \bar{\chi}_L \gamma_\mu \sigma^3 \chi_L. \tag{1.30}$$

The obtained neutral current, just from the symmetry considerations, has pure V-A form, while this is not the case in the experiments. This proves that $SU(2)$ symmetry group does not give a complete description of weak interactions. The idea of Glashow was to introduce another $U(1)$ gauge symmetry similar to the electromagnetic $U(1)$ symmetry and a neutral vector field B_μ. An equivalent of the electromagnetic charge is called a weak hypercharge (Y). A superposition of the two neutral vector fields (W^3_μ and B_μ) can explain the observed NC weak interactions and the physical neutral vector field Z_μ. In addition, a second independent superposition gives rise of the photon field A_μ:

$$A_\mu = B_\mu \cos\theta_w + W^3_\mu \sin\theta_w, \tag{1.31a}$$

$$Z_\mu = -B_\mu \sin\theta_w + W^3_\mu \cos\theta_w, \tag{1.31b}$$

where θ_w is a weak mixing angle. Because of the relation 1.31b, it is possible to write a relation connecting the charge, the hypercharge and the third component of the weak isospin:

$$Q = I^3 + \frac{1}{2}Y. \tag{1.32}$$

In order for this theory to work, the couplings of the CC interactions (g_w), the NC interactions (g_z) and the electromagnetic interactions (g_e) should be related as:

$$g_w \sin\theta_w = g_z \cos\theta_w \sin\theta_w = g_e. \tag{1.33}$$

By including the gauge symmetry $SU(3)_L \times U(1)_Y$ and two charged and two neutral vector fields, we obtain the theory of the electroweak interactions. However, there are a few problems left. To explain the effective weakness of weak interactions at low energy, we need massive $W^\pm$ and Z bosons. The mass terms violate the local gauge invariance. The bosons were discovered in 1983 in the UA1 [22, 23] and UA2 [24, 25] experiments at CERN, thus confirming the hypothesis of the massive weak bosons. Furthermore, the fermion mass terms which were always included ad hoc in the Lagrangian without a deep understanding of the origin of these terms, also violate the local gauge invariance of weak interactions. The problem comes from the fact that the mass term can be written as:

$$\mathcal{L}_m = -m\bar{\psi}\psi = -m(\bar{\psi}_L\psi_R + \bar{\psi}_R\psi_L). \tag{1.34}$$

The diagonal terms are equal to zero, while cross terms have only single left field, so any $SU(2)_L$ transformation will change these terms.

1.3.3 Spontaneus symmetry breaking

In order to allow for the massive bosons, weak gauge symmetry of the Lagrangian must be broken as seen in nature:

$$SU(2)_L \times U(1)_Y \rightarrow U(1)_{em}, \tag{1.35}$$

so that only electromagnetic $U(1)$ symmetry with a massless photon field remains. The mechanism of the symmetry breaking will be illustrated on the example of the $U(1)$ symmetry and the extension of this principle to the real world problem in the Eq. 1.35 can be found in Ref. [20]. First, we introduce a complex scalar field ϕ which can be parametrized by two real fields ($\phi = \phi_1 + i\phi_2$) so that Lagrangian becomes:

$$\mathcal{L} = \frac{1}{2}(\partial_\mu\phi_1)^2 + \frac{1}{2}(\partial_\mu\phi_2)^2 - \underbrace{\left(\frac{1}{2}\mu^2(\phi_1^2+\phi_2^2) - \frac{1}{4}\lambda(\phi_1^2+\phi_2^2)^2\right)}_{V}. \tag{1.36}$$

The Lagrangian has a global $U(1)$ symmetry and includes a potential with two parameters: μ^2 and λ. The potential has a quadratic term which is a mass term for the field if $\mu^2 > 0$ and a quartic term which describes possible self-interactions of ϕ. If we select only potentials for which $\lambda > 0$ and $\mu^2 < 0$, the potential will have minima for nonzero fields which can be seen in Fig. 1.7. In fact, minima of the potential can be easily calculated:

$$\phi_1^2 + \phi_2^2 = v^2 = -\frac{\mu^2}{\lambda}. \tag{1.37}$$

We can choose a point where the potential is minimal and expand the scalar field around this point. It is convenient to choose the point $(v,0)$. The field becomes:

$$\phi(x) = \sqrt{\frac{1}{2}}\left(v + \eta(x) + i\xi(x)\right), \tag{1.38}$$

where η and ξ are excitations around the minimum. The Lagrangian becomes:

$$\mathcal{L}' = \frac{1}{2}\left(\partial_\mu \xi\right)^2 + \frac{1}{2}\left(\partial_\mu \eta\right)^2 + \mu^2\eta^2 + \text{const.} + \text{self. int.} \tag{1.39}$$

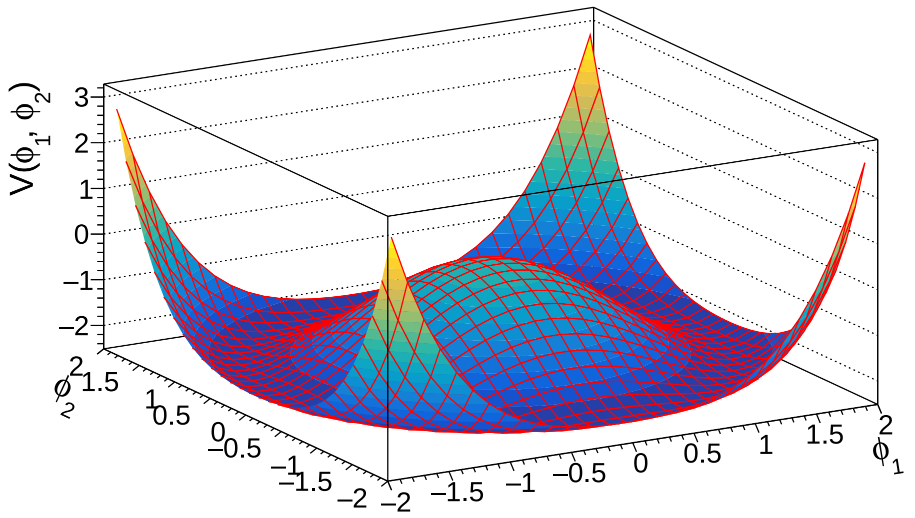

Figure 1.7: Scalar field potential with parameters $\mu^2 < 0$ and $\lambda > 0$.

The new Lagrangian does not display $U(1)$ symmetry, but it represents the same physics as the Lagrangian in Eq. 1.36 with one difference. The choice of the ground state which is not invariant under the $U(1)$ transformations brakes the explicit global $U(1)$ symmetry. This breaking by an unsymmetrical ground state, rather than by non-invariant terms in the Lagrangian, is spontaneous symmetry breaking. The nonsymmetrical choice is necessary because we can only use the perturbation theory around the minimum. Along the way, two fields are generated, one (η) with the mass term $\mu^2\eta^2$ and other massless (ξ). If we imagine the potential in Fig. 1.7 in a cylindrical coordinate system, the massive field represents excitations in the radial direction, while the massless field (called Goldstone boson) represents excitations in the tangential direction where the potential is flat. If we try to impose the local gauge $U(1)$ invariance on the Lagrangian, we need to repeat the same procedure as previously done for the fermions. In other words, it is necessary to replace the derivative ∂_μ with the covariant derivative D_μ and introduce the massless vector field A_μ. The Lagrangian 1.36 becomes invariant under local gauge transformations:

$$\mathcal{L} = \left(\partial^\mu + ieA^\mu\right)\phi^*\left(\partial_\mu - ieA_\mu\right)\phi - \mu^2\phi^*\phi - \lambda(\phi^*\phi)^2 - \frac{1}{4}F_{\mu\nu}F^{\mu\nu}. \tag{1.40}$$

Now, if the field ϕ is again expanded around the minimum, the Lagrangian loses explicit local gauge invariance:

$$\mathcal{L}' = \frac{1}{2}(\partial_\mu\xi)^2 + \frac{1}{2}(\partial_\mu\eta)^2 - v^2\lambda\eta^2 + \frac{1}{2}e^2v^2A_\mu A^\mu - evA_\mu\partial\xi - \frac{1}{4}F_{\mu\nu}F^{\mu\nu}. \tag{1.41}$$

It is seen that after the spontaneous symmetry breaking. The vector boson A_μ acquires a mass ev. However, we are left with the two scalar fields. In particular, the massless field is a problem, since no such massless scalar has been observed in nature. Nevertheless, the expansion of the field ϕ around the minimum can be written in the form:

$$\phi = \sqrt{\frac{1}{2}}(v + \eta(x))\, e^{i\xi/v} \tag{1.42}$$

and we can get rid of the exponential factor by a local gauge transformation. If we choose a particular gauge transformation so that we gauge away the phase of the ϕ field:

$$\phi \to \sqrt{\frac{1}{2}}(v + h(x)), \tag{1.43}$$

the Lagrangian becomes:

$$\begin{aligned}\mathcal{L}'' = \frac{1}{2}(\partial_\mu h)^2 - \lambda v^2 h^2 + \frac{1}{2}e^2v^2A_\mu A^\mu - \lambda v h^3 \\ - \frac{1}{4}\lambda h^4 + \frac{1}{2}e^2A_\mu A^\mu h^2 + ve^2A_\mu A^\mu h - \frac{1}{4}F_{\mu\nu}F^{\mu\nu}.\end{aligned} \tag{1.44}$$

The Goldstone boson is absorbed into the field A_μ. Before the symmetry is broken, A_μ is massless and has only two polarizations. After the spontaneous symmetry breaking, A_μ becomes massive and must have three polarizations. Therefore, one degree of freedom (Goldstone boson) is taken from the scalar field and used as a third component of the polarization. This mechanism is called Englert–Brout–Higgs mechanism and the remaining massive scalar boson h is called the Higgs boson. In the case of the $SU(2)_L \times U(1)_Y$ symmetry breaking, we need to introduce scalar $SU(2)$ doublet

$$\Phi = \begin{pmatrix} \phi^+ \\ \phi^0 \end{pmatrix}_L, \tag{1.45}$$

but the principle is the same, bosons ($W^\pm$ and Z) acquire mass and the single massive scalar field remains (check Ref. [20]). As it was already mentioned in the introduction, the existence of the Higgs boson has been confirmed by CMS and ATLAS collaborations [3, 4].

1.3.3.1 Fermion masses

After the introduction of the scalar field, it is possible to construct $SU(2)_L \times U(1)_Y$ invariant terms:

$$\mathcal{L} = -G\left(\bar{\chi}_L\Phi\chi_R + \bar{\chi}_R\bar{\Phi}\chi_L\right), \tag{1.46}$$

where G is arbitrary constant, χ_L and χ_R are one of the doublets and singlets defined in Eq. 1.27 and Eq. 1.28 respectively, for example (ν_e, e) and e_R. After the spontaneous symmetry breaking, the previously defined term becomes:

$$\mathcal{L} = -\frac{Gv}{\sqrt{2}}\bar{e}e - \frac{G}{\sqrt{2}}\bar{e}eh. \tag{1.47}$$

The constant coming with the first term can be recognized as a mass of the electron ($m_e = \frac{Gv}{\sqrt{2}}$). Therefore, introducing the scalar field and the spontaneous symmetry breaking resolves both of our problems, it generates mass terms for the weak bosons and fermions. Since both coupling G and Higgs vacuum expectation value v are not predicted by the theory, we cannot predict masses of the fermions. Instead, they must be measured.

1.3.4 Neutrino masses

From the theory of weak interactions presented in the last several subsections, it is clear that neutrinos in the Standard Model should be massless particles. All (anti)neutrinos produced in the SM weak interactions are left particles and right antiparticles. However, fermion mass terms coming from the coupling with the Higgs field only exist if both chiral states are realized in nature. Right neutrino states in the Standard Model are not strictly forbidden, and they are not necessary for the explanation of the weak interaction. After the discovery of neutrino oscillations which will be explained in more details in the next chapter, it was clear that neutrinos have tiny but nonzero mass. Neutrino oscillations from one flavor to another are a consequence of the neutrino eigenstates in the vacuum not being equal to the flavor states (ν_e, ν_μ, ν_τ). The mechanism behind the neutrino mass is not yet understood. The constraint on the antineutrino mass can be measured from the electron energy spectra in the beta decay. World-leading measurements of the electron antineutrino mass were performed in the Troitsk experiment [26] by measuring tritium decays. A measured constraint is:

$$m_{eff}(\overline{\nu}_e) < 2\,\mathrm{eV}\,(95\%\,\mathrm{CL}). \tag{1.48}$$

It is important to note that this is the measurement of the effective mass since $\overline{\nu}_e$ is not the mass eigenstate. In contrast to the $\overline{\nu}_e$ mass measurement, measurements of the effective ν_e mass were done by measuring the X-ray spectra of the electron capture in holmium atoms [27]. However, these measurements are two orders of magnitude less precise than the measurements for $\overline{\nu}_e$. An additional constraint to the neutrino masses was obtained from the cosmological measurements. The best constraint was obtained from the measurements of the fluctuations in the cosmic microwave background combined with the galaxy clustering measurements and the measurements of the baryon acoustic oscillations (see Ref. [28]):

$$m_{tot} < 0.0926\,\mathrm{eV}(90\%\,\mathrm{CL}). \tag{1.49}$$

These measurements include all stable neutrinos which contribute to the energy density of the universe. Planck experiment also measured the effective number of these neutrinos which is equal to:

$$n_\nu = 3.3 \pm 0.5, \tag{1.50}$$

as can be found in the Ref. [5]. However, similar measurements of the number of the neutrinos which couple to the Z boson were done in the LEP (Large Electron-Positron) collider at CERN [29]. These measurements take into consideration only neutrinos lighter than $m_Z/2$. The existence of more than three neutrino flavors would decrease cross-section of the Z boson decay into the hadrons by providing an additional channel for Z decay. The measurement is shown in Fig. 1.8 and it is equal to:

$$n_{\nu,\mathrm{light}} = 2.9840 \pm 0.0082 \tag{1.51}$$

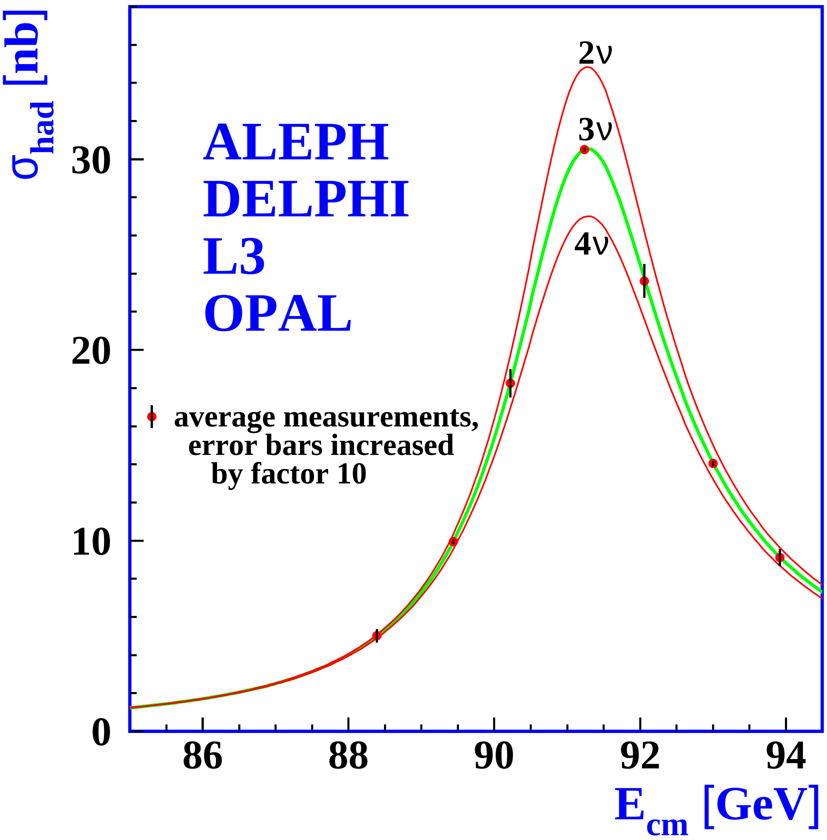

Figure 1.8: Measurements of the $Z \to$ hadrons cross section at LEP (green) and predicted change of the cross section if the number of light neutrinos is two and four (see Ref. [29]).

1.3.4.1 Dirac or Majorana neutrinos?

Although, the mechanism behind neutrinos masses is not known, there are some hints that it is not the same as the mechanism which gives masses to other fermions. If we compare previously mentioned constraints to the neutrino mass with the masses of other fermions, neutrinos are lighter at least six orders of magnitude compared to the next lightest fermion (electron). Such difference shows that if the right neutrino states exist, a coupling of the neutrinos with the Higgs field would be extremely small. If we assume an existence of the right-handed neutrino field, on top of the Dirac mass term which comes from the coupling with the Higgs field, we can construct a Majorana mass term:

$$\mathcal{L}_{m_\nu} = -\frac{1}{2} m_R \overline{(\nu_R)^C} \nu_R + h.c., \tag{1.52}$$

where C denotes a charge conjugation. In other words, the Majorana mass term turns neutrino to antineutrino. For all other fermions including the left-handed neutrinos, such term is not possible since it will require the violation of the charge conservations (electromagnetic charge and weak isospin). In a simplified picture with only one neutrino flavor, a total neutrino mass

Lagrangian can be written as:

$$\begin{aligned}\mathcal{L}_{m_\nu} &= -m_D\bar{\nu}_R\nu_L - \frac{1}{2}m_R\overline{(\nu_R)^C}\nu_R + h.c.\\ &= -\frac{1}{2}\left(\overline{(\nu_L)^C}, \bar{\nu}_R\right)\begin{pmatrix} 0 & m_D \\ m_D & m_R \end{pmatrix}\begin{pmatrix} \bar{\nu}_L \\ (\nu_R)^C \end{pmatrix} + h.c.,\end{aligned} \tag{1.53}$$

where m_D is the Dirac mass and m_R is the Majorana mass. The mass eigenstates can be obtained after matrix M_ν:

$$M_\nu = \begin{pmatrix} 0 & m_D \\ m_D & m_R \end{pmatrix} \tag{1.54}$$

is diagonalized. The obtained eigenvalues are:

$$M'_\nu = \begin{pmatrix} m_D^2/m_R & 0 \\ 0 & m_R \end{pmatrix} \tag{1.55}$$

and it is easy to show that the mass eigenstates are Majorana particles (for example, see Ref. [30]). If the mass of the second Majorana neutrino is large, we can get an arbitrarily small mass for the first eigenstate which can explain our observations. A heavy neutrino can be a possible candidate for the dark matter. Furthermore, if neutrinos are Majorana particles (neutrino is its own antiparticle), a process called the neutrinoless double beta decay would be possible:

$$^A_Z X \rightarrow {}^A_{Z+2}X + 2e^-. \tag{1.56}$$

Several experiments are trying to find the neutrinoless double beta decay in various materials, but up to now, this process stays unconfirmed. One of the examples is the COURE experiment which measures double beta decays of ^{130}Te (see Ref. [31]) and sets a limit on the half-life of this decay $t_{1/2} > 4000 \times 10^{21}\,\mathrm{y}\,(90\%\mathrm{CL})$.

1.4 Neutrino oscillations

The first prediction of the neutrino oscillations between ν and $\bar{\nu}$ was given in 1957 by Bruno Pontecorvo [32]. After the discovery of ν_μ and a possibility of the existence of ν_τ, neutrino oscillations were reformulated, and it was assumed that weak eigenstates (ν_e, ν_μ, ν_τ) are not eigenstates of the free Hamiltonian. This means that a produced neutrino is a superposition of the mass eigenstates:

$$\nu_\alpha = \sum_i U^*_{\alpha i}\nu_i, \tag{1.57}$$

where ν_α is a neutrino of defined flavor, ν_i are eigenstates of the free Hamiltonian with a defined masses m_i and the parameters $U^*_{\alpha i}$ are elements of the neutrino mixing matrix. A square of the absolute value of each parameter gives the probability that the neutrino ν_α is ν_i. The previous relation can be inverted to show the mass states as a superposition of the flavor states:

$$\nu_i = \sum_\alpha U_{\alpha i}\nu_\alpha. \tag{1.58}$$

The scheme, showing the neutrino oscillations is presented in Fig. 1.9. First, a neutrino of the flavor α is created together with an antilepton of the same flavor in the CC interactions.

The neutrino travels freely through space, and after some distance L, it interacts with matter in a detector and produces a lepton of the flavor β.

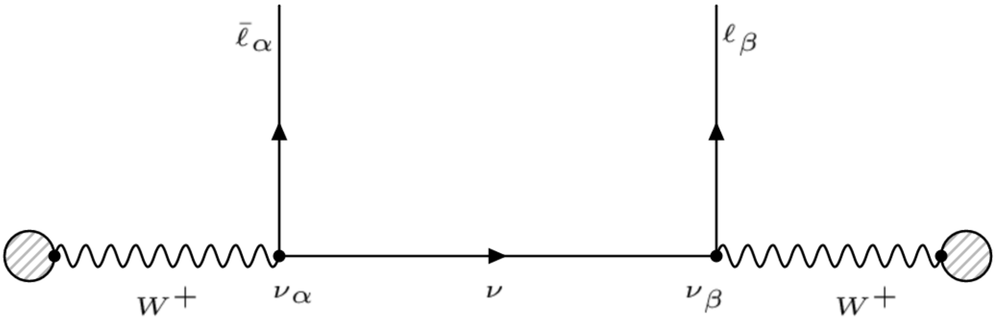

Figure 1.9: Scheme of the neutrino oscilations.

The amplitude of such process can be written as:

$$A(\nu_\alpha \to \nu_\beta) = \sum_i U^*_{\alpha i} e^{-i m_i \tau_i} U_{\beta i}, \tag{1.59}$$

where an exponential factor is a propagator, m_i is a mass of the neutrino and τ_i is a proper time needed for the neutrino to travel from its source to the detector. Since we assume that the neutrino has mass, we can boost the neutrino in the center of mass frame. In this case, the neutrino is not a relativistic particle, and we can solve Schroedinger equation in the vacuum. After some time t, the neutrino will only gain a phase because it is an eigenstate of the Hamiltonian. The propagator must be transformed to the lab reference frame:

$$m_i \tau_i = E_i t - p_i L = E_i t - \sqrt{E_i^2 - m_i^2} L \approx E(t-L) + \frac{m_i^2}{2E} L. \tag{1.60}$$

It is assumed that all mass states must have the same energy to contribute coherently to the oscillations and therefore $E_i \to E$. In addition, the neutrino mass is expected to be much smaller compared to the total energy, and because of this, we can use an ultra-relativistic approximation for the momentum term $\sqrt{E_i^2 - m_i^2} L \approx EL - \frac{m_i^2}{2E}$. The constant value $E(t-L)$ can be ignored since it gives rise to a global phase which is the same for all mass states. The probability of the oscillation from ν_α to ν_β is just a square of the absolute value of the amplitude, and after using the propagator in the lab reference frame, we get:

$$\begin{aligned} P(\nu_\alpha \to \nu_\beta) = |A|^2 = \delta_{\alpha\beta} - 4 \sum_{i>j} \Re\left(U^*_{\alpha i} U_{\beta i} U_{\alpha j} U^*_{\beta j}\right) \sin^2\left(\Delta m^2_{ij} \frac{L}{4E}\right) \\ + 2 \sum_{i>j} \Im\left(U^*_{\alpha i} U_{\beta i} U_{\alpha j} U^*_{\beta j}\right) \sin^2\left(\Delta m^2_{ij} \frac{L}{2E}\right), \end{aligned} \tag{1.61}$$

where $\delta_{\alpha\beta}$ is a Kronecker delta and Δm^2_{ij} is defined as:

$$\Delta m^2_{ij} = m_i^2 - m_j^2. \tag{1.62}$$

If we assume that $P(\bar{\nu}_\alpha \to \bar{\nu_\beta}) = P(\nu_\beta \to \nu_\alpha)$, in other words, that CPT invariance is valid and observe a feature of Eq. 1.61:

$$P(\nu_\beta \to \nu_\alpha, U) = P(\nu_\alpha \to \nu_\beta, U^*), \tag{1.63}$$

it is straightforward to obtain the oscillation probability of the antineutrinos:

$$\begin{aligned} P(\bar{\nu}_\alpha \to \bar{\nu}_\beta) = |A|^2 = \delta_{\alpha\beta} - 4\sum_{i>j} \Re\left(U^*_{\alpha i} U_{\beta i} U_{\alpha j} U^*_{\beta j}\right) \sin^2\left(\Delta m^2_{ij} \frac{L}{4E}\right) \\ - 2\sum_{i>j} \Im\left(U^*_{\alpha i} U_{\beta i} U_{\alpha j} U^*_{\beta j}\right) \sin^2\left(\Delta m^2_{ij} \frac{L}{2E}\right). \end{aligned} \tag{1.64}$$

The main difference between the neutrino and antineutrino oscillation probabilities comes from the third term which is only nonzero if the mixing matrix is complex. If this is the case, it will cause a CP violation in the lepton sector, which is not yet confirmed experimentally. However, some indications of the CP violation have been observed by the T2K collaboration [33]. Both, oscillation probabilities for neutrinos and antineutrinos depend on the squared mass splittings. Therefore, the oscillation probability would be:

$$P(\nu_\alpha \to \nu_\beta) = \delta_{\alpha\beta} \tag{1.65}$$

if all masses are zero or degenerate. Because of this, the absolute values of the neutrino masses cannot be measured in the oscillation experiments. Furthermore, since squared mass splittings appear only as arguments of the sine squared, signs of these splittings cannot be directly determined. This is a so-called problem of the neutrino mass hierarchy and it will be explained later. Although we know that there are three light neutrino flavors, sometimes it is useful to use an approximation of two neutrinos (for example, ν_e and ν_μ). If there is a clear difference between the splittings (one is much smaller than the other), we will be sensitive to a specific type of neutrino oscillations depending on the experiment (neutrino energy and distance from the source). In the case when we have only two neutrinos, the oscillation probability is the same for both, the neutrinos and antineutrinos (CP violation is not possible):

$$P(\overset{(-)}{\nu}_\alpha \to \overset{(-)}{\nu}_\beta) = \sin^2 2\theta \sin^2\left(\Delta m^2 \frac{L}{4E}\right), \alpha \neq \beta. \tag{1.66}$$

The mixing matrix U, in this case, can be parametrized only by one parameter - a mixing angle θ:

$$U = \begin{bmatrix} U_{e1} & U_{e2} \\ U_{\mu 1} & U_{\mu 2} \end{bmatrix} = \begin{bmatrix} \cos\theta & \sin\theta \\ -\sin\theta & \cos\theta \end{bmatrix}. \tag{1.67}$$

The neutrino oscillations can be measured in two ways by placing the detector at some distance from the neutrino source: a measurement of the neutrino disappearance ($P(\nu_\alpha \to \nu_\alpha)$) and a measurement of the neutrino appearance ($P(\nu_\alpha \to \nu_\beta)$, $\alpha \neq \beta$). In most cases, it is useful to rewrite oscillation probability in units which represent typical values of the distance and the neutrino energy in experiments. In addition, we already know that neutrino masses have values in the sub-eV range. Therefore, Eq. 1.66 becomes:

$$P(\overset{(-)}{\nu}_\alpha \to \overset{(-)}{\nu}_\beta) = \sin^2 2\theta \sin^2\left(1.27\Delta m^2[\text{eV}^2] \frac{L[\text{km}]}{E[\text{GeV}]}\right), \alpha \neq \beta \tag{1.68}$$

and the similar thing can be done for Eq. 1.61 and Eq. 1.64.

1.4.1 PMNS mixing matrix

A general mixing matrix for three light neutrino flavors can be parametrized by three mixing angles: θ_{12}, θ_{13}, θ_{23}, by a CP violating phase δ_{CP} and by two Majorana phases α_1 and α_2. This parametrization is called Pontecorvo-Maki-Nakagawa-Sakata (PMNS) matrix:

$$
\begin{aligned}
U_{\text{PMNS}} &= \begin{bmatrix} U_{e1} & U_{e2} & U_{e3} \\ U_{\mu 1} & U_{\mu 2} & U_{\mu 3} \\ U_{\tau 1} & U_{\tau 2} & U_{\tau 3} \end{bmatrix} \\
&= \begin{bmatrix} c_{12}c_{13} & s_{12}c_{13} & s_{13}e^{-i\delta} \\ -s_{12}c_{23}-c_{12}s_{23}s_{13}e^{i\delta} & c_{12}c_{23}-s_{12}s_{23}s_{13}e^{i\delta} & s_{23}c_{13} \\ s_{12}s_{23}-c_{12}c_{23}s_{13}e^{i\delta} & -c_{12}s_{23}-s_{12}c_{23}s_{13}e^{i\delta} & c_{23}c_{13} \end{bmatrix} \begin{bmatrix} e^{\frac{i}{2}\alpha_1} & 0 & 0 \\ 0 & e^{\frac{i}{2}\alpha_2} & 0 \\ 0 & 0 & 1 \end{bmatrix} \\
&= \underbrace{\begin{bmatrix} 1 & 0 & 0 \\ 0 & c_{23} & s_{23} \\ 0 & -s_{23} & c_{23} \end{bmatrix}}_{atmospheric} \begin{bmatrix} c_{13} & 0 & s_{13}e^{-i\delta} \\ 0 & 1 & 0 \\ -s_{13}e^{i\delta} & 0 & c_{13} \end{bmatrix} \underbrace{\begin{bmatrix} c_{12} & s_{12} & 0 \\ -s_{12} & c_{12} & 0 \\ 0 & 0 & 1 \end{bmatrix}}_{solar} \begin{bmatrix} e^{\frac{i}{2}\alpha_1} & 0 & 0 \\ 0 & e^{\frac{i}{2}\alpha_2} & 0 \\ 0 & 0 & 1 \end{bmatrix},
\end{aligned}
\tag{1.69}
$$

where $s_{ij} = \sin\theta_{ij}$ and $c_{ij} = \cos\theta_{ij}$. The PMNS matrix is often decomposed to a product of the four different matrices. The first three matrices are of special interest since they govern the oscillations, while the fourth one contains only Majorana phases. Historically, neutrino oscillations were first measured for the atmospheric neutrinos by the *Super-Kamiokande* collaboration [6] and for the solar neutrinos by the SNO collaboration [7]. Solar neutrinos of interest come from the boron decays and have typical energies around 10 MeV, while atmospheric neutrinos created in the collisions of the cosmic rays with the atmosphere have very broad spectra up to several GeV. As a consequence of this difference in the energy scale, experiments measuring solar and atmospheric neutrino oscillations are sensitive to different squared mass splittings. Atmospheric neutrino oscillations are mostly oscillations from ν_μ to ν_τ, and they are governed by a mass splitting

$$\Delta m^2_{atm} \approx \Delta m_{23} \approx 2.4 \times 10^{-3}\,\text{eV}^2. \tag{1.70}$$

In this case, we can use two neutrino approximation, and the corresponding mixing matrix is the first matrix in the decomposition shown in Eq. 1.69. The mixing angle is θ_{23} and it is close to 45°. On the other hand, solar neutrino oscillations are governed by about two orders of magnitude smaller squared mass splitting

$$\Delta m^2_{sol} \approx \Delta m^2_{12} \approx 8.0 \times 10^{-5}\,\text{eV}^2. \tag{1.71}$$

Fusion processes in the Sun produce only ν_e, and solar neutrino oscillations are oscillations of ν_e to ν_μ and ν_τ. It may seem that atmospheric and solar neutrino oscillations are for any purpose the same and the only difference is in the mass splittings and mixing angles. However, the process of solar neutrino oscillations is a strongly dependent on neutrino interactions with the matter in the Sun. This will be explained in more details in the next subsection. The third matrix in the decomposition of the PMNS matrix in Eq. 1.69 and the corresponding mixing angle θ_{12} is a good approximation for the observed solar neutrino oscillations. The matter effect in the Sun also allows us to measure the sign of the solar mass squared splitting, while this is not the case for the atmospheric neutrino oscillations measurements. Consequently, today we do not know if $m_3 > m_2 > m_1$ or $m_2 > m_1 > m_3$ which is portrayed in Fig. 1.10. The second matrix in the PMNS decomposition cannot be studied with solar or atmospheric neutrinos. However, experiments measuring reactor neutrinos and the accelerator-based neutrino experiments have access to this oscillation sector. The former ones are usually measuring the oscillation parameters by comparing the neutrino flux coming from the nuclear reactors placed at different distances from the detector. The latter ones produce a neutrino beam from decays of pions and measure the beam composition near to the source and after some distance L. Both of these experiment types can measure the mixing angle θ_{13}. This is of special interest since only recently it was shown that θ_{13} has a nonzero value (see subsection 1.4.3. The necessary condition for the observation of the CP violation in the lepton sector is that all three mixing angles have nonzero values.

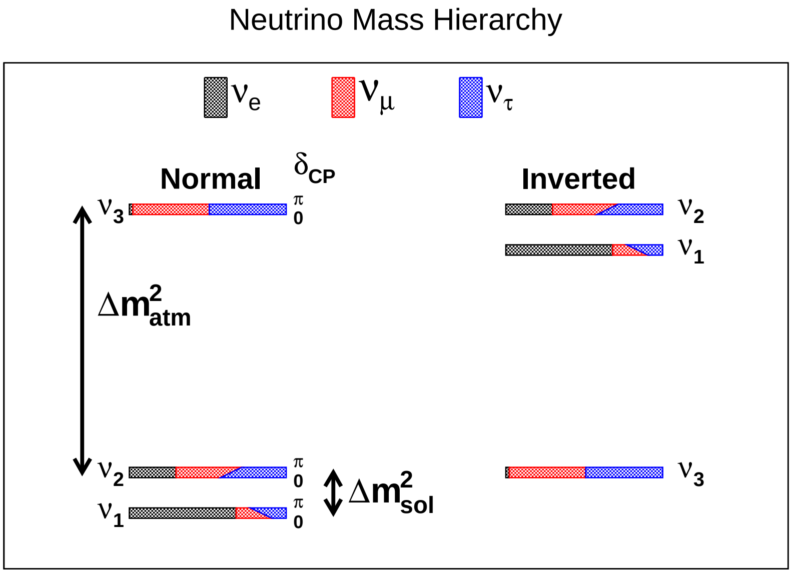

Figure 1.10: Fractions of the ν_e, ν_μ, ν_τ in the neutrino mass eigenstates ν_1, ν_2 and ν_3 for the normal and inverted hierarchy (see Ref. [34]).

1.4.2 The matter effect

In different neutrino experiments, neutrinos rarely pass through the vacuum. If we take, for example, neutrinos in a long-baseline neutrino experiment, they pass through the Earth's crust. Neutrinos can interact with electrons in the matter via CC interactions. The Standard Model interactions are flavor conserving, and therefore, only ν_e or $\overline{\nu}_e$ can interact with electrons. This gives rise to an effective potential:

$$V_W = \pm\sqrt{2} G_F N_e, \tag{1.72}$$

where + is for ν_e and − is for $\overline{\nu}_e$. Parameter G_F is the already mentioned Fermi constant, and N_e is a number of electrons per unit volume. The second contribution to the neutrino interaction with matter is coming from the elastic scattering by exchanging Z boson. This type of interactions can happen for any neutrino flavor, but for zero momentum transfer has an opposite sign for electrons and protons. Consequently, only interactions with neutrons are important on average. Similarly, they give rise to the effective potential:

$$V_Z = -\frac{\sqrt{2}}{2} G_F N_n, \tag{1.73}$$

where N_n is a number of neutrons per unit volume. If we imagine a two neutrino case, where we have ν_e and ν_μ, it is possible to write a Hamiltonian for the free neutrinos in the vacuum (see Ref. [35]):

$$\mathcal{H}_0 = \frac{\Delta m^2}{4E} \begin{bmatrix} \cos 2\theta & \sin 2\theta \\ -\sin 2\theta & \cos 2\theta \end{bmatrix}. \tag{1.74}$$

Hamiltonian for two neutrino flavors in the matter is obtained easily by adding previously defined potentials:

$$\mathcal{H}_{mat} = \frac{\Delta m^2}{4E} \begin{bmatrix} \cos 2\theta & \sin 2\theta \\ -\sin 2\theta & \cos 2\theta \end{bmatrix} + V_W \begin{bmatrix} 1 & 0 \\ 0 & 0 \end{bmatrix} + V_Z \begin{bmatrix} 1 & 0 \\ 0 & 1 \end{bmatrix}. \tag{1.75}$$

Added potentials reflect the fact that ν_e can interact by exchanging W and Z bosons, while ν_μ can only interact by exchanging Z bosons. Terms which are proportional to the unit matrix can be neglected because they just add constant to the energies of both flavors. After taking this into consideration, the Hamiltonian can be rewritten as:

$$\mathcal{H}_{mat} = \frac{\Delta m^2}{4E} \begin{bmatrix} \cos 2\theta & \sin 2\theta \\ -\sin 2\theta & \cos 2\theta \end{bmatrix} + \frac{V_W}{2} \begin{bmatrix} 1 & 0 \\ 0 & -1 \end{bmatrix}. \tag{1.76}$$

It is useful to define following quantities:

$$x \equiv \frac{2\sqrt{2} G_F N_e E}{\Delta m^2}, \tag{1.77a}$$

$$\Delta m_M^2 \equiv \Delta m^2 \sqrt{\sin^2 2\theta + (\cos 2\theta - x)^2}, \tag{1.77b}$$

$$\sin^2 2\theta_M \equiv \frac{\sin^2 2\theta}{\sin^2 2\theta + (\cos 2\theta - x)^2}, \tag{1.77c}$$

where the parameter x is a measure of the competition between the two effects: the neutrino oscillations with the mass squared splitting Δm^2 and the matter effect. The Hamiltonian can be transformed to be a function of Δm_M^2 and $\sin^2 2\theta_M$:

$$\mathcal{H}_{mat} = \frac{\Delta m_M^2}{4E} \begin{bmatrix} \cos 2\theta_M & \sin 2\theta_M \\ -\sin 2\theta_M & \cos 2\theta_M \end{bmatrix}. \tag{1.78}$$

The form of the matter Hamiltonian is the same as the form of the Vacuum Hamiltonian, the only differences being $\theta \to \theta_M$ and $\Delta m^2 \to \Delta m_M^2$. It is straightforward to conclude that matter effect modifies the neutrino oscillations. This effect is often called the Mikheyev-Smirnov-Wolfenstein effect, and it increases with the neutrino energy, as can be seen in Eq. 1.77a. For neutrino energies at the GeV scale, neutrino oscillations are governed by the atmospheric mass squared splitting. The parameter x is:

$$x \approx \frac{E}{12\,\mathrm{GeV}}. \tag{1.79}$$

The matter effect becomes important for neutrino energies above 10 GeV. The Hamiltonian in Eq. 1.78 also holds for the antineutrinos if we change the sign of the V_W constant. This difference between the neutrinos and the antineutrinos creates a false signal of the CP violation and must be always taken into account. Additionally, the Hamiltonian is also sensitive to the mass hierarchy, i.e., change of the sign in the mass squared splitting. If the $\cos_{2\theta}$ is known, one can determine the sign of the mass squared splitting. A good example of this effect can be found in solar neutrino oscillations. If we take only solar neutrinos produced in the boron decays which have higher energies, it becomes clear that the matter effect gives a dominant contribution to the Hamiltonian because:

$$\sqrt{2}G_F N_e \approx 0.75 \times 10^{-5}\,\mathrm{eV}^2/\mathrm{MeV} \tag{1.80}$$

which is three times larger than:

$$\frac{\Delta m^2_{sol}}{4E} = 0.25 \times 10^{-5}\,\mathrm{eV}^2/\mathrm{MeV}. \tag{1.81}$$

Neutrinos in the Sun are born as ν_e, and if we ignore the oscillation part of the Hamiltonian, they are always the eigenstates of the Hamiltonian with higher energy $\sqrt{2}G_F N_e$. If we assume that the electron density adiabatically changes from the core to the surface, we can solve the Schroedinger equation for different regions and patch the wave functions. Neutrinos reaching the Sun surface will still be the eigenstate with the higher energy. Once they enter the vacuum, the electron density drops to zero and the eigenstate with higher energy becomes the mass state with higher mass. Since neutrinos coming from the surface of the Sun are mostly in the more massive mass eigenstate, they don't oscillate while traveling to the Earth. We only measure a flavor composition of the mass eigenstate. As it happens, $m_2 > m_1$, so we measure the flavor content of ν_2 and the ν_e flux is around 1/3 of the total flux coming from the Sun. This is illustrated in Fig. 1.10.

1.4.3 Current knowledge of the oscillation parameters

It was previously shown that atmospheric and solar neutrino oscillations are fundamentally governed by different squared mass splittings. Since these neutrinos are coming from the natural sources, it is impossible to control neutrino energies or distances of the sources. Consequently, it is beneficial to build detectors at some distance from nuclear reactors which are artificial sources of the $\overline{\nu}_e$. In reactor neutrino experiments, the energy of antineutrinos is defined by the nuclear reactions and cannot be changed. However, the distance can be tuned by carefully choosing a position of the detector. For example, if we aim to get sensitivity to the solar squared mass splitting and according to Eq. 1.68, the position should be chosen so that:

$$1.27\Delta m^2_{\mathrm{sol.}}[\mathrm{eV}^2]\frac{L[\mathrm{km}]}{E[\mathrm{GeV}]} = \frac{\pi}{2}. \tag{1.82}$$

Neutrino oscillations in the solar regime were measured by the KamLAND experiment [36]. The experiment was built in the Japanese Alps and it was measuring neutrino flux coming from the 53 nuclear reactors. In contrast to the solar experiments like SNO or *Super-Kamiokande*, KamLAND gives the best sensitivity to the squared mass splitting, while measurements of the mixing angle θ_{12} are less precise. In that sense, KamLAND is the complementary experiment to the solar neutrino experiments. Comparison of the KamLAND best-fit contours for $\Delta m^2_{\mathrm{sol.}}$ and $\sin^2\theta_{12}$ with the *Super-Kamiokande* solar neutrino measurements is shown in Fig. 1.11. Values of the parameters are overlaid on top of the figure. There is a 2σ tension between the *Super-Kamiokande* results and the KamLAND results, which is not yet understood.

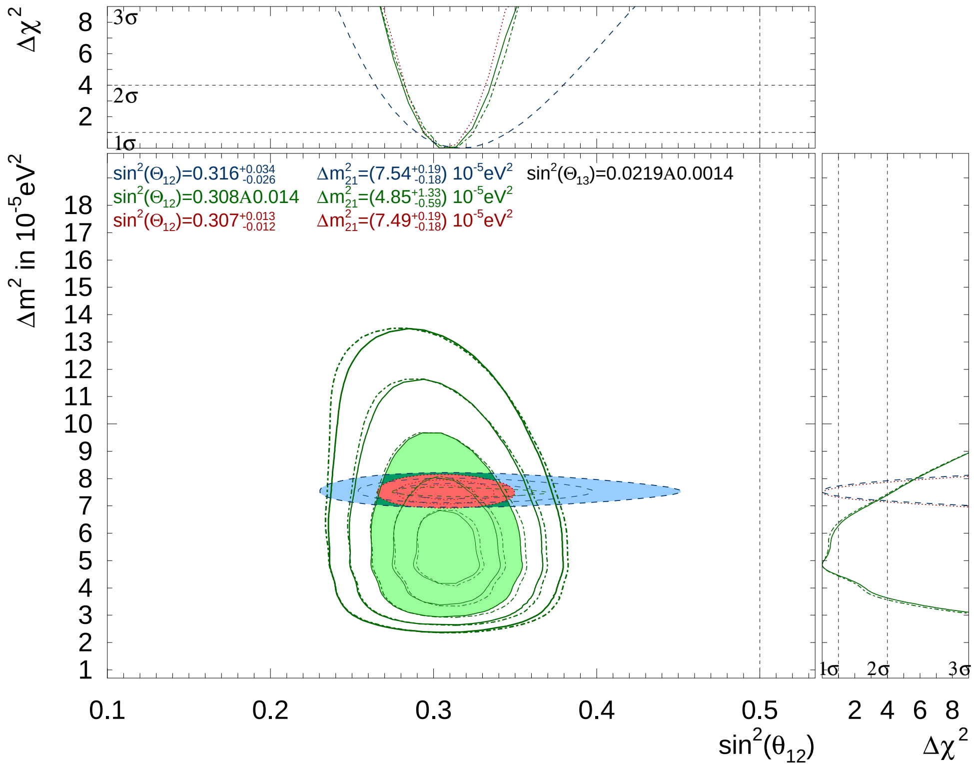

Figure 1.11: Allowed contours of Δm^2_{21} vs. $\sin^2\theta_{12}$ from *Super-Kamiokande* solar neutrino data (green), KamLAND data (blue), and the combined result (red). For comparison, the almost identical result of the SK+SNO combined fit is shown by the dashed dotted lines. The filled regions give the 3 σ confidence level results, the other contours shown are at the 1 and 2 σ confidence level (for the solar analyses, 4 and 5 σ confidence level contours are also displayed). θ_{13} is constrained by $\left(\frac{\sin^2\theta_{13}-0.0219}{0.0014}\right)^2$ [37].

Measurements of the neutrino oscillations in the atmospheric regime are possible in a controlled manner with accelerator-based long-baseline neutrino experiments. In this case, neutrinos are produced from decays of hadrons which are coming from the proton beam interactions with a target. Hadrons are focused by a magnetic field, and as a consequence, it is possible to obtain narrow, a high-intensity neutrino beam. Usually, two detectors are built: one near the target for measuring the unoscillated neutrino flux and other far away to measure the oscillated neutrino flux. In principle, neutrino energy can be tuned by changing the energy of the proton beam or by placing the detector at some angle with respect to the neutrino beam direction. While distances of the detectors from the target can be optimized before the experiment is built, ratio L/E, for this kind of experiments is usually tunned for the atmospheric squared mass splitting $\Delta m^2_{\mathrm{atm.}}$. On top of that, it is possible to control the composition of the neutrino beam, by changing the polarity of the focusing magnetic field. Depending on the polarity, positively or negatively charged hadrons are focused and they, in turn, produce a ν_μ or $\overline{\nu}_\mu$ enhanced beam. Measurements of θ_{23} and Δm^2_{23} were performed by several accelerator-based long-baseline neutrino experiments: K2K [38], MINOS [39], T2K [33] and NOvA [40]. These measurements were obtained by measuring the ν_μ disappearance. Currently, the most precise measurements are provided by the T2K collaboration which combines measurements with the ν_μ and the $\overline{\nu}_\mu$ beam. Confidence regions of this measurement are presented in Fig. 1.12 and compared to other relevant measurements.

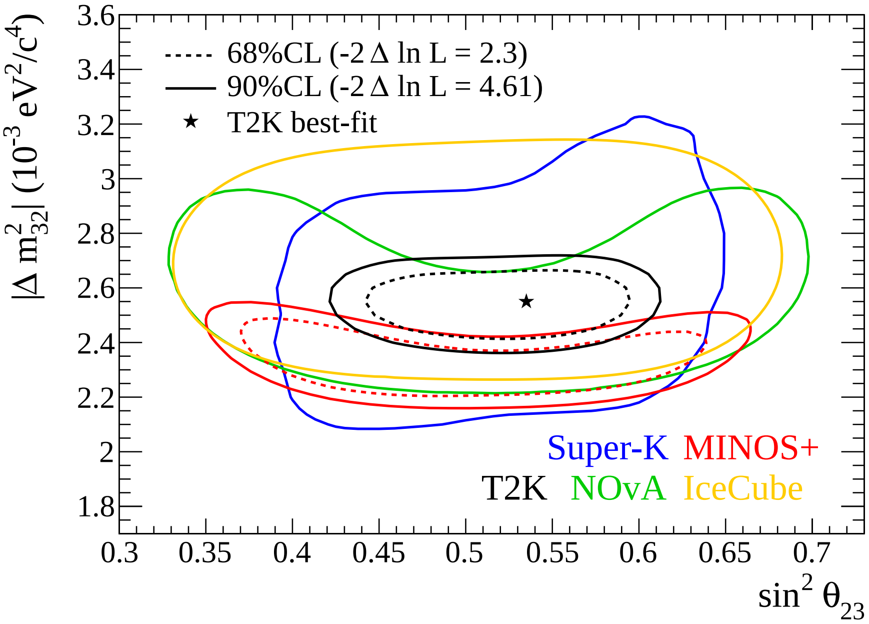

Figure 1.12: The 68% (90%) constant $-2\Delta \ln L$ confidence regions for the $\sin^2\theta_{23} - |\Delta m^2_{32}|$ plane assuming normal hierarchy, alongside NOvA[40], MINOS+[39], SK[41], and IceCube[42] confidence regions. Taken from Ref. [33].

Apart from the solar and the atmospheric neutrino sectors, in recent years the most interesting progress was achieved in the so-called θ_{13} sector. The mixing angle θ_{13} was the only unmeasured mixing angle. Reactor neutrino experiments are sensitive to the θ_{13} mixing angle in $\overline{\nu}_e \to \overline{\nu}_e$ channel. The most precise measurement of the θ_{13} mixing angle was performed by the Daya Bay experiment [43] in China. The obtained result is $sin^2\theta_{13} = 0.084 \pm 0.005$ and it is shown in Fig. 1.13. Several other reactor experiments like RENO [44] or Double Chooz [45] also measured the mixing angle θ_{13}. Results from Double Chooz are in 2σ tension with the results from Daya Bay. Long-baseline accelerator experiments are also sensitive to the θ_{13} mixing angle, by measuring the ν_e ($\overline{\nu}_e$) appearance in a ν_μ ($\overline{\nu}_\mu$) beam (see, for example, T2K results [46] and MINOS [47]).

Discovery of the $\theta_{13} \neq 0$ fulfilled the necessary condition that all mixing angles have nonzero values in order to have a possibility for studying the CP violation in the lepton sector. A value of the CP phase δ_{CP} is not yet constrained, but there are some indications from the T2K experiment which favors maximal CP violation $\delta_{CP} = \frac{3\pi}{2}$ as can be seen in Fig. 1.14.

Although three-flavor neutrino oscillations are well established, there are experiments searching for sterile neutrinos and oscillations between them and the Standard Model neutrinos. Usually, these are short-baseline neutrino experiments which are constructed so that the probability of already established neutrino oscillations is negligible. Instead, L/E ratio is tunned to be sensitive to the squared mass splittings around $1\,\mathrm{eV}^2$. Observation of the $\overline{\nu}_\mu \to \overline{\nu}_e$ oscillations for large mass squared splitting has been reported by the LSND collaboration [49]. The proposed hypothesis was a so-called (3+1) scheme with one additional sterile neutrino flavor so that $\overline{\nu}_\mu$

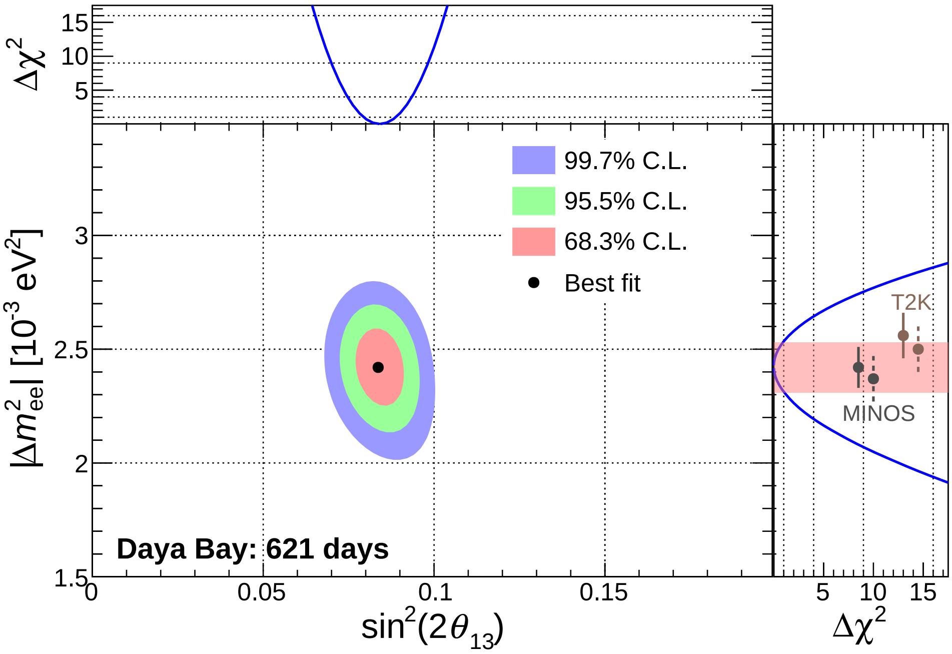

Figure 1.13: Regions of 68.3%, 95.5% and 99.7% confidence levels in the $|\Delta m^2_{\rm ee}|$-$\sin^2 2\theta_{13}$ parameter space. The adjoining panels show the dependence of $\Delta\chi^2$ on $\sin^2 2\theta_{13}$ (top) and $|\Delta m^2_{\rm ee}|$ (right). The $|\Delta m^2_{\rm ee}|$ allowed region (shaded band, 68.3% C.L.) was consistent with measurements of $|\Delta m^2_{32}|$ using muon neutrino disappearance by the MINOS [47] and T2K [48] experiments, converted to $|\Delta m^2_{\rm ee}|$ assuming the normal (solid) and inverted (dashed) mass hierarchy. Taken from Ref. [43].

oscillate to sterile neutrinos and afterward sterile neutrinos oscillate to $\overline{\nu}_e$. This anomaly was later refuted by measurements from the MiniBoone experiment [50]. However, if one assumes the existence of two sterile neutrino flavors, this induces possibility of the additional CP violation, and since the LSND measured antineutrino oscillations and MiniBoone measured neutrino oscillations, their results become consistent.

1.4.3.1 Global fit

One of the global fits of the neutrino oscillation parameters was performed by Esteban et al. [51] while using all relevant experimental data. The fit was done in six-dimensional parameter space which includes: three oscillation angles (θ_{12}, θ_{13}, θ_{23}), one CP phase (δ_{CP}) and two squared mass splittings (Δm^2_{12} and $\Delta m^2_{3\ell}$). The second mass squared splitting $\Delta m^2_{3\ell}$ depends on the mass hierarchy: in the normal hierarchy, it becomes Δm^2_{32}, while in the inverted hierarchy it is Δm^2_{13}. Best fit parameters are obtained for the normal hierarchy(ordering), and they are summarized in Tab. 1.1 alongside with the results for the assumption that the mass hierarchy is inverted. In addition, allowed two-dimensional regions after the marginalization over other parameters are shown in Fig. 1.15. The list of all experiments used in the global fit can also be found in Ref. [51].

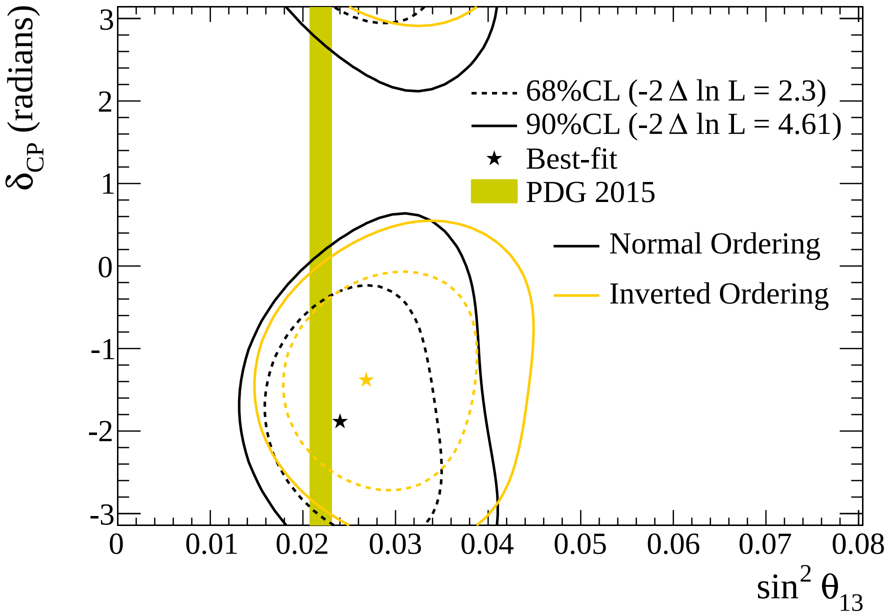

Figure 1.14: The 68% (90%) constant $-2\Delta\ln L$ confidence regions in the $\delta_{CP} - \sin^2\theta_{13}$ plane are shown by the dashed (continuous) lines, computed independently for the normal (black) and inverted (red) mass ordering. The best-fit point is shown by a star for each mass ordering hypothesis. The 68% confidence region from reactor experiments on $\sin^2\theta_{13}$ is shown by the yellow vertical band. Taken from Ref. [33].

	Normal Ordering (best fit)		Inverted Ordering ($\Delta\chi^2 = 0.83$)		Any Ordering
	bfp $\pm 1\sigma$	3σ range	bfp $\pm 1\sigma$	3σ range	3σ range
$\sin^2\theta_{12}$	$0.306^{+0.012}_{-0.012}$	$0.271 \to 0.345$	$0.306^{+0.012}_{-0.012}$	$0.271 \to 0.345$	$0.271 \to 0.345$
$\theta_{12}/^\circ$	$33.56^{+0.77}_{-0.75}$	$31.38 \to 35.99$	$33.56^{+0.77}_{-0.75}$	$31.38 \to 35.99$	$31.38 \to 35.99$
$\sin^2\theta_{23}$	$0.441^{+0.027}_{-0.021}$	$0.385 \to 0.635$	$0.587^{+0.020}_{-0.024}$	$0.393 \to 0.640$	$0.385 \to 0.638$
$\theta_{23}/^\circ$	$41.6^{+1.5}_{-1.2}$	$38.4 \to 52.8$	$50.0^{+1.1}_{-1.4}$	$38.8 \to 53.1$	$38.4 \to 53.0$
$\sin^2\theta_{13}$	$0.02166^{+0.00075}_{-0.00075}$	$0.01934 \to 0.02392$	$0.02179^{+0.00076}_{-0.00076}$	$0.01953 \to 0.02408$	$0.01934 \to 0.02397$
$\theta_{13}/^\circ$	$8.46^{+0.15}_{-0.15}$	$7.99 \to 8.90$	$8.49^{+0.15}_{-0.15}$	$8.03 \to 8.93$	$7.99 \to 8.91$
$\delta_{\mathrm{CP}}/^\circ$	261^{+51}_{-59}	$0 \to 360$	277^{+40}_{-46}	$145 \to 391$	$0 \to 360$
$\dfrac{\Delta m^2_{12}}{10^{-5}\ \mathrm{eV}^2}$	$7.50^{+0.19}_{-0.17}$	$7.03 \to 8.09$	$7.50^{+0.19}_{-0.17}$	$7.03 \to 8.09$	$7.03 \to 8.09$
$\dfrac{\Delta m^2_{3\ell}}{10^{-3}\ \mathrm{eV}^2}$	$+2.524^{+0.039}_{-0.040}$	$+2.407 \to +2.643$	$-2.514^{+0.038}_{-0.041}$	$-2.635 \to -2.399$	$\begin{bmatrix} +2.407 \to +2.643 \\ -2.629 \to -2.405 \end{bmatrix}$

Table 1.1: Three-neutrino oscillation parameters after the fit to the global data. Taken from Ref. [51].

1.4.4 Open questions

Among many open questions in the neutrino physics, neutrino oscillations experiments are directed toward answering the following questions:

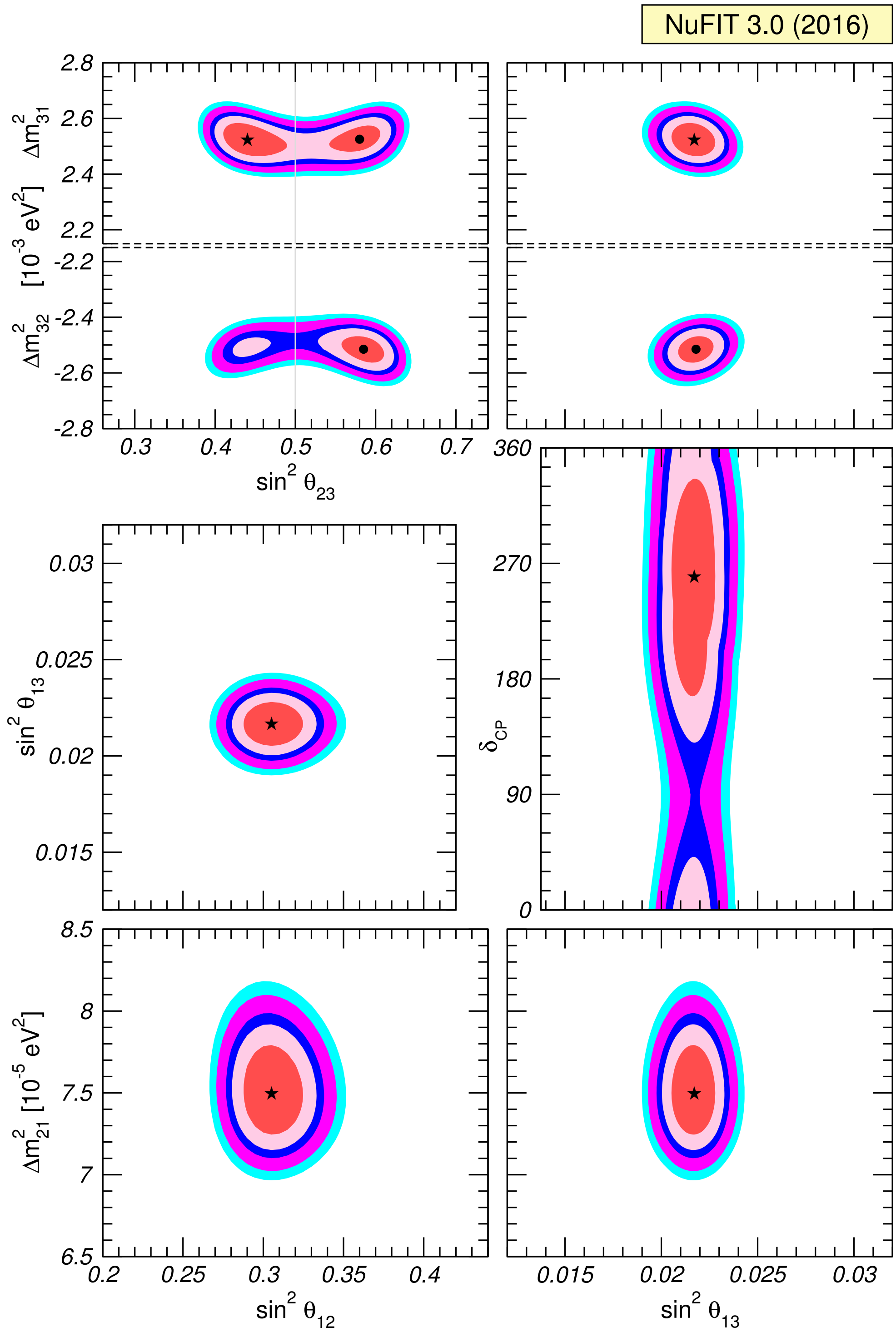

Figure 1.15: Global 3ν oscillation analysis. Each panel shows the two-dimensional projection of the allowed six-dimensional region after marginalization with respect to the undisplayed parameters. The different contours correspond to 1σ, 90%, 2σ, 99%, 3σ CL (2 dof). The regions in the four lower panels are obtained from $\Delta\chi^2$ minimized with respect to the mass ordering. Taken from Ref. [51].

1. is there a CP violation in the lepton sector,
2. what is the neutrino mass hierarchy and
3. in which octant is the mixing angle θ_{23} located.

Measurement of the CP violation in the lepton sector could potentially help constrain models which predict the matter-antimatter asymmetry created in the early universe. The CP violation can be measured in the accelerator-based long-baseline neutrino experiments, by comparing the appearance of ν_e in a ν_μ beam and the appearance of $\overline{\nu}_e$ in a $\overline{\nu}_\mu$ beam. From these measurements, one can obtain a CP asymmetry factor:

$$A_{CP} = \frac{P(\nu_\mu \to \nu_e) - P(\overline{\nu}_\mu \to \overline{\nu}_e)}{P(\nu_\mu \to \nu_e) + P(\overline{\nu}_\mu \to \overline{\nu}_e)} \approx \frac{\Delta m^2_{12} L}{4E} \cdot \frac{\sin 3\theta_{12}}{\sin \theta_{13}} \cdot \sin \delta_{CP} \tag{1.83}$$

and consequently measure δ_{CP}. The knowledge of the neutrino mass hierarchy is important for testing the neutrino mass models. In addition some of the cosmological constraints on the sum of the neutrino masses depend on the neutrino mass hierarchy. To measure the neutrino mass hierarchy, one needs large matter effect, in other words, long distance between the neutrino source and the detector. The probability of neutrino appearance (for example $\nu_\mu \to \nu_e$) depends on the $\sin^2\theta_{23}$. Such dependence creates ambiguity in the true value of the θ_{23} since we cannot determine in which octant θ_{23} is located. As a consequence, this ambiguity propagates when we try to measure the mass hierarchy or the CP violation. All of these questions will be tackled by the new generation of the neutrino experiments such as DUNE [52] or Hyper-K [53, 54], but they will be ready to take data in ten years. In the meantime, a good candidate for getting an indication of the CP violation in the lepton sector is the T2K experiment in Japan. After the planned upgrade in 2020 expected sensitivity to the δ_{CP} if it is maximal is larger than 3σ [55] as can be seen in Fig. 1.16.

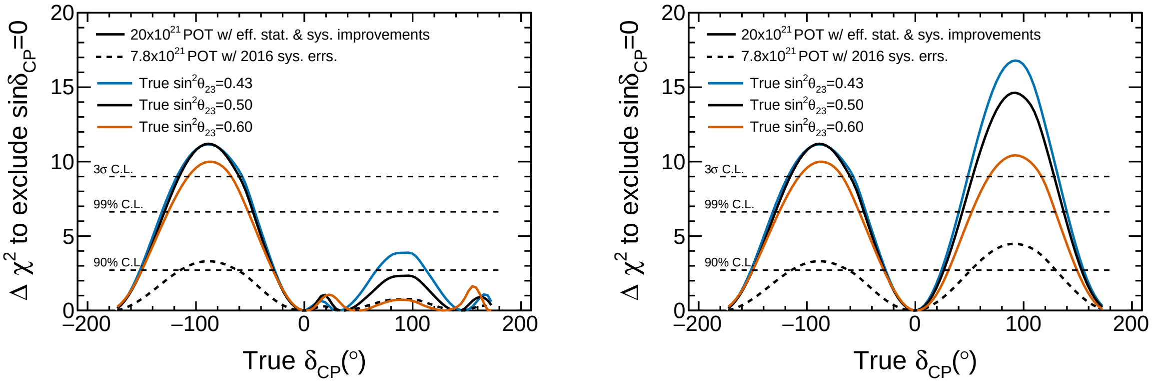

(a) (b)

Figure 1.16: T2K phase II sensitivity to δ_{CP} [55] if the mass hierarchy is unknown a) and if it is measured by other experiment b).

Chapter 2

The T2K experiment

Contents

The T2K (Tokai to Kamioka) experiment is an accelerator long-baseline neutrino experiment. It has been designed to use a muon (anti-)neutrino beam and to measure:

1. muon (anti-)neutrino disappearance,
2. electron (anti-)neutrino appearance,
3. a CP violation in the lepton sector,
4. neutrino-nucleus cross sections and
5. to search for sterile neutrinos.

The T2K neutrino beam is produced in the T2K neutrino beam facility which is located at the J-PARC [56] accelerator complex in Tokai on the east cost of Japan. It is produced as follows: first, a proton beam with the kinetic energy of 30 GeV is directed towards a graphite target where hadrons (mostly pions) are produced in the proton-carbon interactions. Afterwards, positively charged hadrons are focused by a set of three focusing elements (called magnetic horns) and directed to the decay volume where they undergo decays. This way we obtain muon neutrino enhanced beam. The polarity of the horns can be reversed to focus negatively charged hadrons and therefore produce a muon antineutrino enhanced beam. Positive and negative focusings are also denoted as a forward horn current (FHC) and reverse horn current (RHC) mode. Produced (anti-)neutrino beam passes through two near detectors the *ND280* and *INGRID*, located 280 m from the target, which measure the non-oscillated (anti-)neutrino flux. The measurement of the oscillated (anti-)neutrino beam is performed 295 km away at *Super-Kamiokande*. A schematic display of the T2K experiment is shown in Fig. 2.1.

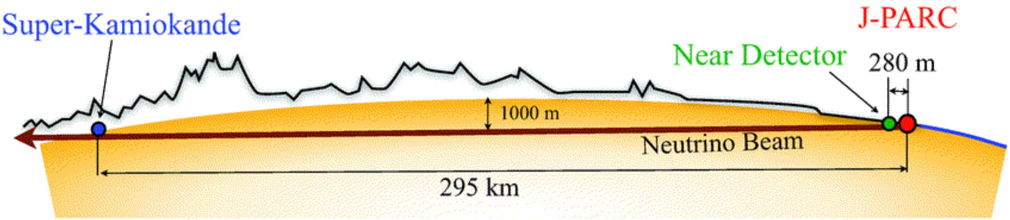

Figure 2.1: Shematic display of the T2K baseline from J-PARC to the *Super-Kamiokande*.

It is important to note that the T2K experiment is the first experiment to employ a so-called off-axis method. The (anti-)neutrino beam has been directed at 2.5° angle to the baseline between the *ND280* and *Super-Kamiokande*. Consequently, the neutrino beam passing through *Super-Kamiokande* has a narrow energy spectrum with a maximum at 0.6 GeV. At this energy, the effect of neutrino oscillations at *Super-Kamiokande* is maximized (see Fig. 2.2). The off-axis method will be described in more details in subsection 2.4.1. The advantages of off-axis (anti-)neutrino beams produced in an accelerator neutrino experiment are obvious: it is possible to get well-controlled, high-intensity, highly collimated beam with the narrow energy spectrum. It is impossible to achieve all of these requirements with the neutrinos from any other source.

The oscillation measurements in the T2K experiment are done by comparing the number and energy spectrum of the predicted neutrino interactions (without oscillations) in *Super-Kamiokande* with the number and energy spectra of measured neutrino interactions. The prediction is constrained by the measurements of the neutrino interaction rates from the *ND280* and the hadron production measurements which reduce the (anti-)neutrino flux uncertainty. The most significant measurement from the T2K experiment shows the first indication and later confirmation of the ν_e appearance in the ν_μ beam [57, 58]. This is a ground-breaking discovery since ν_e appearance proves that the mixing angle θ_{13} is nonzero. This is a necessary requirement for the possible experimental detection of the CP violation in the lepton sector as explained in

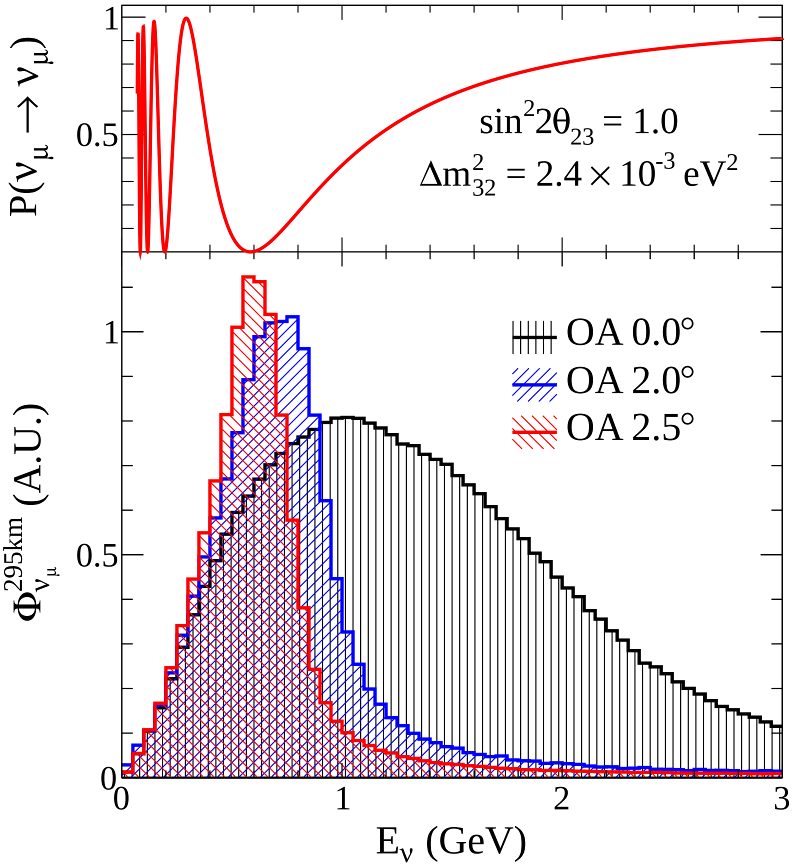

Figure 2.2: Neutrino off-axis flux and approximate probability of the ν_μ disapearance in *Super-Kamiokande*.

section 1.4. Recently, a new measurement from T2K [33] indicates the existence of the CP violation. The hypothesis of CP conservation is excluded at 90% confidence level for both, normal and inverted mass hierarchies (see Fig. 2.3). Measurements planed for the T2K phase II will try to improve this significance [55].

The T2K data-taking started in 2010 with the muon neutrino beam (so-called positive focusing mode in which ν_μ enhanced beam is created) and continued with several large interruptions (due to the earthquake in 2011 and the hadron hall accident at J-PARC in 2013) till the spring of 2014 when we switched to the muon anti-neutrino beam (negative focusing mode of the horns). During the summer of 2016, we switched again to the positive focusing mode. A total number of protons on target (POT) collected is equal to 22.5×10^{20}, and it is shown in Fig. 2.4 with approximately one third taken in the negative focusing mode. The proton beam power was rising steadily during the data-taking and reached a maximum of 470 kW. The goal is to achieve the proton beam power of 750 kW during the T2K-I phase (before 2020). During the T2K-II extension (2020-2025), the beam power increase to 1.3 MW is planned.

This section is organized as follows: first, the most important measurements of the T2K experiment will be discussed. Then, a brief overview of the near (*ND280* and *INGRID*) and the far (*Super-Kamiokande*) detectors will be presented. Towards the end of the section, the neutrino beam-line with all of its elements will be described in great detail. Additionally, a

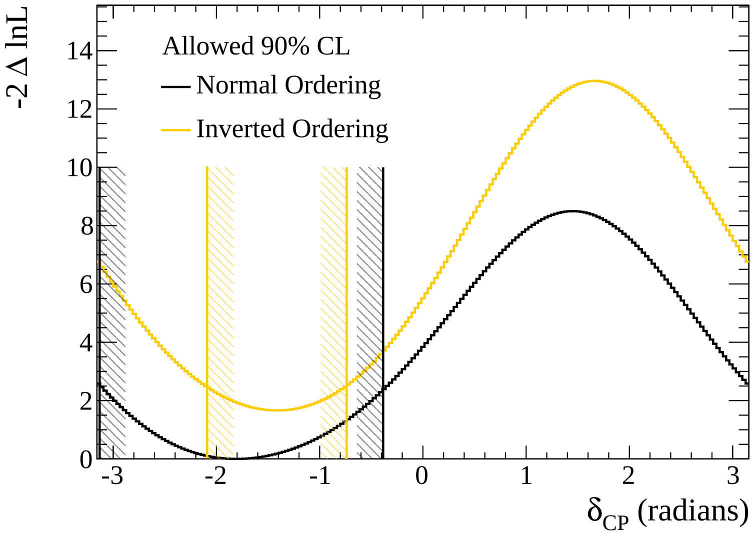

Figure 2.3: Log likelihood ratio vs. δ_{CP} after the oscillation fit. Black and yellow curves are for normal and inverted mass hierachy respectively. Vertical lines show 90% confidence interval.

neutrino beam simulation alongside with a neutrino flux prediction and its uncertainties will be presented. This will illustrate the main motivation for the measurements presented in this thesis.

2.1 Near detector complex

The near detector complex is located 280 m away from the target. It consists of two separate detectors: an off-axis near detector (*ND280*) and an on-axis detector called Interactive Neutrino Grid (*INGRID*).

2.1.1 Near detector (*ND280*)

In principle, a near detector would not be the necessary part of the long-baseline neutrino experiments if the neutrino flux and the neutrino interaction rates are entirely known. However, this is not the case and for this reason, *ND280* was constructed for T2K. In particular, it is used for the measurements of the neutrino flux, ν_e ($\overline{\nu}_e$) contamination of the ν_μ ($\overline{\nu}_\mu$) neutrino beam and the neutrino interaction rates. These measurements considerably decrease systematic uncertainties of the ν_μ ($\overline{\nu}_\mu$) disappearance and the ν_e ($\overline{\nu}_e$) appearance measurements in *Super-Kamiokande*. Above all, it is necessary to constrain ν_e ($\overline{\nu}_e$) contamination of the neutrino beam with respect to the neutrino energy. In addition, ν_μ neutral current interactions in which single π^0 is created are of special interest, since they represent a dominant background in the ν_e appearance measurements in *Super-Kamiokande*.

To perform all necessary measurements, the *ND280* consists of several different sub-detector systems. The sub-detectors are placed in the magnetic field of the dipole UA1/NOMAD magnet from CERN (see Fig. 2.5a). The magnetic field strength is 0.2 T. The magnet is cooled with the water cooling. A pi-zero detector (PØD) is placed at the upstream part of the detector followed by the tracker which consists of three time projection chambers (TPC) and two fine-grained

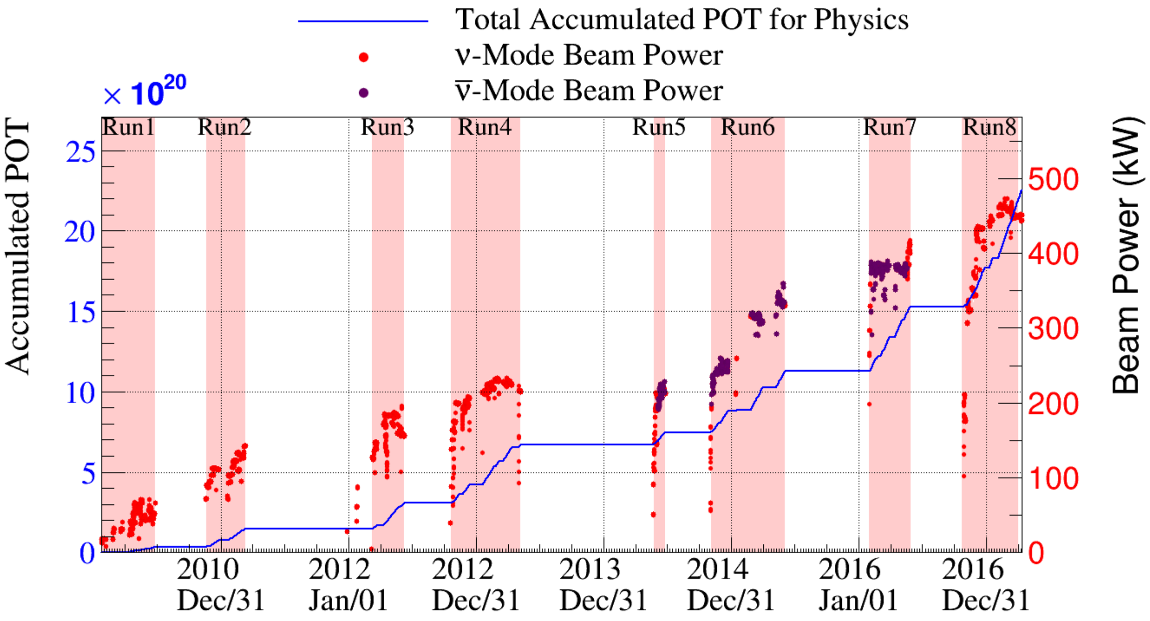

Figure 2.4: The total POT collected from the start of the data-taking till June 2017, both in positive and negative focusing mode. Beam power is shown on the right side of the plot.

detectors (FGD). The tracker and the PØD are surrounded by an electromagnetic calorimeter which captures most of the outgoing particles. Also, the magnet yoke is instrumented with the side muon range detector (SMRD) made of scintillators, to measure the range of the exiting muons. A schematic overview of the whole setup can be seen in Fig. 2.5b.

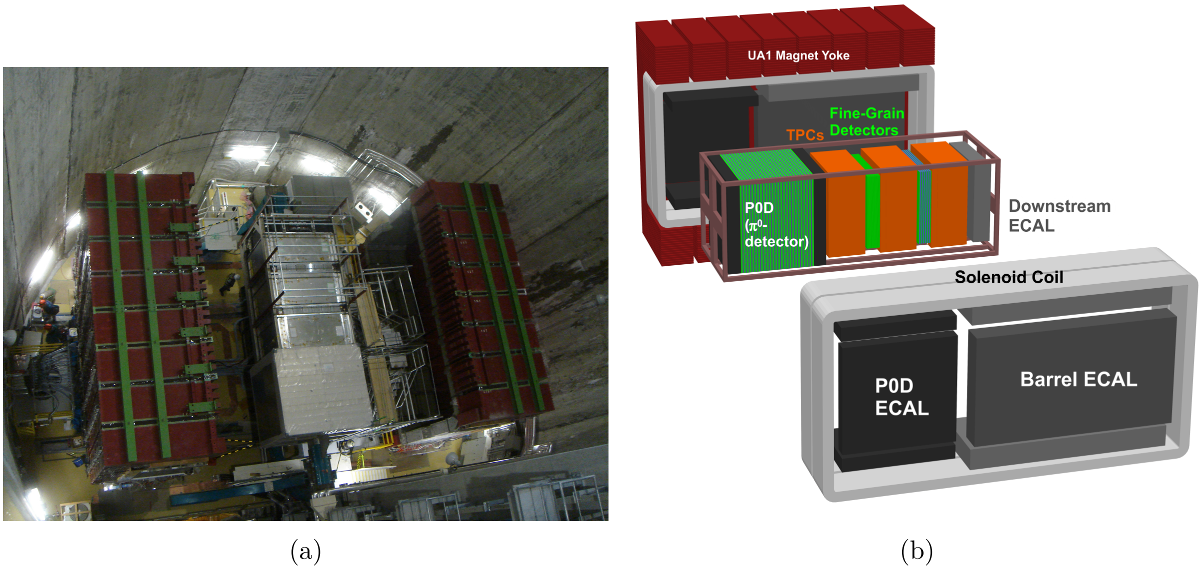

(a)

(b)

Figure 2.5: A top view of the magnet and ND280 between the yokes (a). A schematic overview of the ND280 (b).

Pi-zero detector

The purpose of the PØD is to measure already mentioned ν_μ neutral current interactions in water where single π^0 is created:

$$\nu_\mu + N \rightarrow \nu_\mu + N + \pi^0 + X. \tag{2.1}$$

The detector is made of x and y scintillator planes of scintillator bars. All bars are extruded so that light guide can be inserted into them. The light from each bar is guided through the wavelength shifting (WLS) fibers and transported to a multi-pixel photon counter (MPPC) which is essentially a multi-pixel avalanche photo-diode operating as a multiple of small Geiger counters. The *ND280* uses extensively the MPPC technology since MPPCs can operate inside the magnetic field. The space between the scintillator planes is filled with water bags, lead and brass sheets. The material is used as a neutrino target. Water can be filled or emptied so that a contribution to the measurements from other materials can be subtracted. More details about the PØD design can be found in Ref. [59].

Time projection chambers

The TPCs are detectors which can reconstruct a trajectory of a particle in 3D. The particle ionizes a medium which is usually, some gas and then electrons drift towards the sense plane in the high electric field. The position in two dimensions is measured by a segmented sense plane, while the third coordinate is obtained from the measurement of drift time which is needed for electrons to reach the sense plane. Energy loss in the gas can be used as a method for particle identification. On top of that, if a TPC is placed in the magnetic field as in T2K, it is possible to measure particle momentum and charge. The three TPCs in the *ND280* are using Ar:CF_4:iC_4H_10 ($95:3:2$) mixture as a drift gas. The box containing the mixture is placed in the outer box filled with CO_2 which is used as an insulator. For the sense planes, the TPCs employ in total 72 micromegas detectors [60]. The position resolution of the TPCs is around 0.7 mm, the momentum resolution is around 10%, while the energy loss resolution is around 7.8%. More details about the construction of the TPCs alongside with their characteristics can be found in Ref. [61].

Fine grained detectors

The fine-grained detectors which were placed between the three previously described TPCs (see Fig. 2.5b), provide a target for the neutrinos. First FGD consists of 30 scintillator layers. Each layer has x and y plane made of 192 extruded scintillator bars. The scintillator is polystyrene (like in the PØD), and it is used as a target and a tracking system. The light signal is again transported via the inserted WLS fibers and read out with the MPPCs. While first FGD contains only scintillator bars, this is not the case for the second FGD. It has seven scintillator layers, and the space between them is filled with water which is again used as a target for the neutrinos. Despite the differences between the two FGDs, their outside dimensions are the same. The FGD paper [62] provides more details about the construction and performance of the FGDs.

Electromagnetic calorimeter

It was already described that electromagnetic calorimeter (ECal) surrounds the PØD and the tracker (TPCs + FGDs). The purpose of the ECal is two-fold: it stops all outgoing particles, and it reconstructs photons produced from the π^0 decays. The ECal has 13 independent modules, and each module is made of the active scintillator and lead absorber layers. First six modules surround the PØD from four sides parallel to the neutrino beam and form the PØD ECal. Next six modules encompass the tracker in a similar manner and make the barrel ECal. One additional module is placed at the downstream side. Again, light from the scintillator bars is read out by the MPPCs. More details about the ECal can be found in one of the T2K instrumentation papers [63].

Side muon range detector

High angle escaping muons are measured by 440 scintillator modules inserted in the air gaps between the steel plates of the magnet yoke. In addition, these scintillators forming side muon range detector (SMRD), are used to trigger on cosmic ray muons passing through the *ND280*. Also, the SMRD can identify neutrino interactions in the cavity walls and the magnet yoke. Again, readout system employs MPPCs for the light detection. Additional information about the SMRD can be found in Ref. [64].

2.1.2 *INGRID*

The purpose of *INGRID* is to measure the neutrino beam intensity and direction on a daily basis. This is done by measuring a neutrino interaction rate in iron. The detector consists of 14 modules arranged in a cross pattern centered on the beam axis. Two additional modules are placed off-axis as shown in Fig. 2.6a, for checking the axial symmetry of the beam. Each module is made of 11 scintillator planes and nine iron plates with a total mass of iron exceeding 7 tons per module (Fig. 2.6b). The scintillator planes consist of two layers which are made of 24 horizontal and 24 vertical scintillator bars. On the outside faces of the detector and between the modules, an additional segmented scintillator layer is placed to discard particles created outside of the detector. The light created in the scintillator bars is transported by the WLS fibers and read out by the already mentioned MPPCs. The precision of the measured beam center is around 10 cm which corresponds to the neutrino beam direction precision of 0.4 mrad (see Ref. [65]).

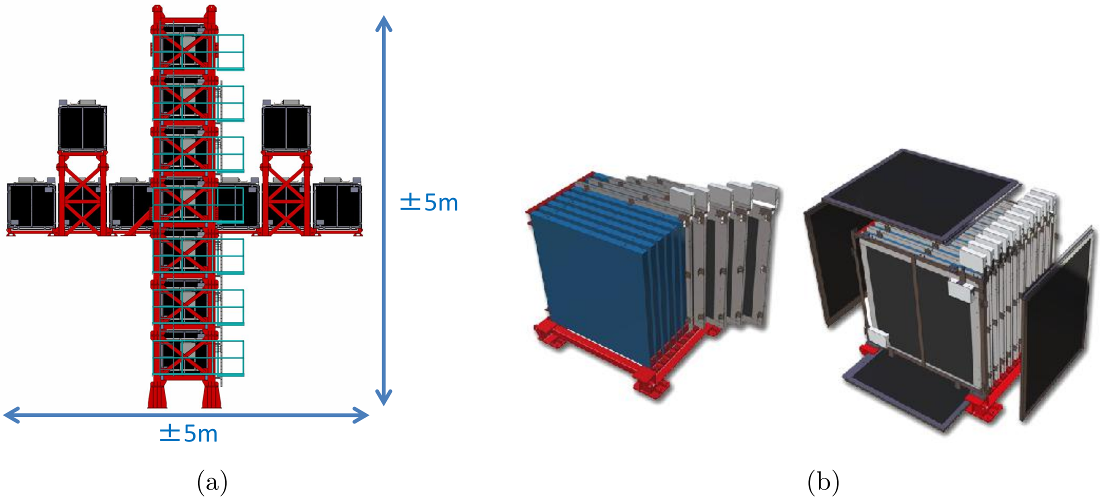

(a) (b)

Figure 2.6: An overview of INGRID (a) with 14 modules in the cross pattern and two off-axis modules. The composition of one module (b). Blue planes are tracking scintillator planes, while veto planes are black. The iron planes are grey.

2.2 *Super-Kamiokande*

Super-Kamiokande is a far detector of the T2K experiment which measures neutrino interaction rate after oscillations. On top of that, *Super-Kamiokande* functions as the independent detector and also measures atmospheric neutrinos [17, 66]. In fact, neutrino oscillations were discovered by the measurement of the atmospheric neutrinos done with *Super-Kamiokande* [6]. Additionally, *Super-Kamiokande* was an integral part of the previous accelerator experiment K2K [38]. Furthermore, measurements of the proton lifetime [67] have also been performed at *Super-Kamiokande*.

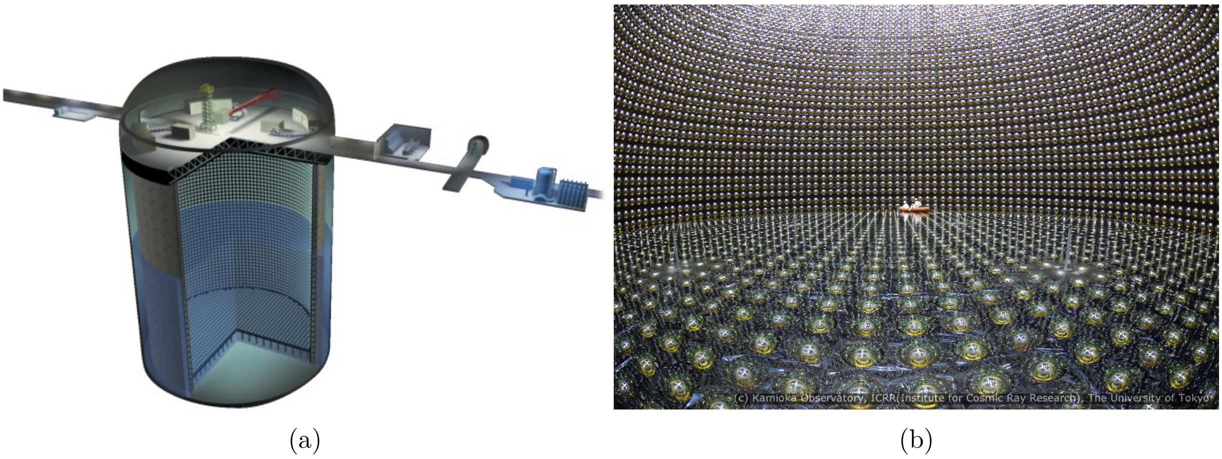

(a) (b)

Figure 2.7: An overview of *Super-Kamiokande* with surrounding facilities (a) and a look inside of the detector during the service work.

Super-Kamiokande is a large water Cherenkov detector located 1 km under Mt. Ikenoyama, near Kamioka on the west coast of Japan. The detector is a large cylinder filled with 50 kton of water and divided into an inner detector (ID) and an outer detector (OD). The inner wall of the ID is instrumented with 11129 PMTs, which cover 40% of the surface. The wall is also covered with the special coating to prevent light reflecting back to the ID volume. The OD, on the other hand, is only sparsely instrumented and it is covered with 1885 outward facing PMTs. The purpose of the ID is to count a number of ν_μ and ν_e interactions to determine neutrino beam flavor composition and compare the results with the prediction from the *ND280* and flux simulation. The primary task of the OD is to remove cosmic muons with ~100% efficiency. However, neutrino events coming from the T2K neutrino beam can be separated from the background, and the information from the OD can be used to a limited degree since the OD is not well instrumented. More details about the hardware can be found in the *Super-Kamiokande* detector paper [68].

Super-Kamiokande detects neutrino charged current quasi-elastic interactions (CCQE) in which a lepton is produced with the same flavor as the incoming neutrino. The produced lepton is either a muon (coming from the ν_μ) or an electron (coming from the ν_e). Their speed in the detector is usually larger than the speed of light in the water. Hence, they produce a cone of Cherenkov radiation which is then detected by the PMTs on the detector walls. However, while the leptons pass through water, they experience multiple Coulomb scattering. Since they have the same charge and muons are around 210 times more massive, electrons will be much more affected by the scattering. For this reason, detected Cherenkov ring on the wall is sharp for muons and diffuse for electrons. In this way, it is possible to distinguish between electrons and muons. An example of the muon-like and electron-like event in *Super-Kamiokande* can be seen in Fig. 2.8.

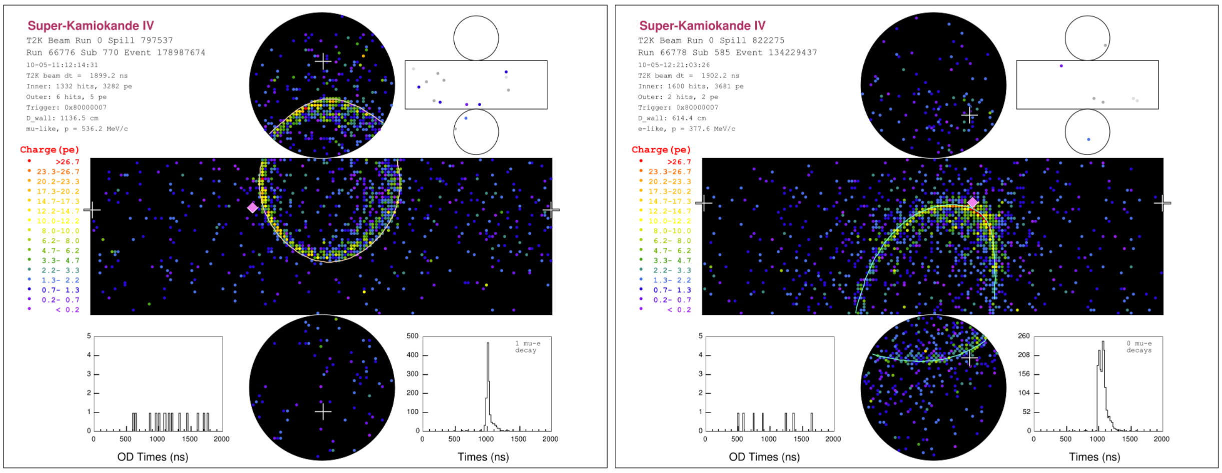

(a)

(b)

Figure 2.8: An example of the muon-like (a) and the electron-like events in *Super-Kamiokande*.

2.3 The T2K neutrino beam facility

The advantage of the accelerator-based neutrino experiments is a much higher degree of control over its neutrino source, which is not the case for other types of the neutrino experiments. The T2K neutrino beam is produced at the T2K neutrino beam facility in Tokai, Japan. The facility includes the J-PARC accelerator complex in which protons are accelerated, a primary beam-line which is used for the transportation of the 30 GeV protons and a secondary beam-line where protons interact and produce hadrons. Also, the hadrons then decay to neutrinos in the secondary beam-line.

2.3.1 J-PARC accelerator complex

The J-PARC accelerator complex consists of three accelerators working as a part of a single chain (Fig. 2.9): a linear accelerator (LINAC), a rapid-cycling synchrotron (RCS) and a main ring (MR). The accelerating chain works as follows: first, H^- ions are accelerated by LINAC to the kinetic energy up to 400 MeV. Then, H^- ions are stripped of their electrons and injected to the RCS, where they are accelerated to the kinetic energy of 3 GeV. After the RCS, protons are injected to the MR and accelerated to the kinetic energy of 30 GeV in eight bunches. The protons are then extracted and guided towards the experiment. There are two modes of the proton extraction from the main ring: a fast extraction mode and a slow extraction mode. In the fast extraction mode which is used for the T2K experiment, all eight bunches are extracted in one step. This mode can be used only with the targets which are located underground because of the high beam power and therefore high radiation risks. On the other hand, slow extraction mode which gives lower beam power is used for other experimental facilities which are above ground (see Fig. 2.9). The designed beam power with fast extraction mode is 750 kW, and proton beam intensity is 3×10^{14} p/spill [69]. However, this power was never achieved because main ring power supplies are not fully upgraded. So far, beam power peaked around 470 kW.

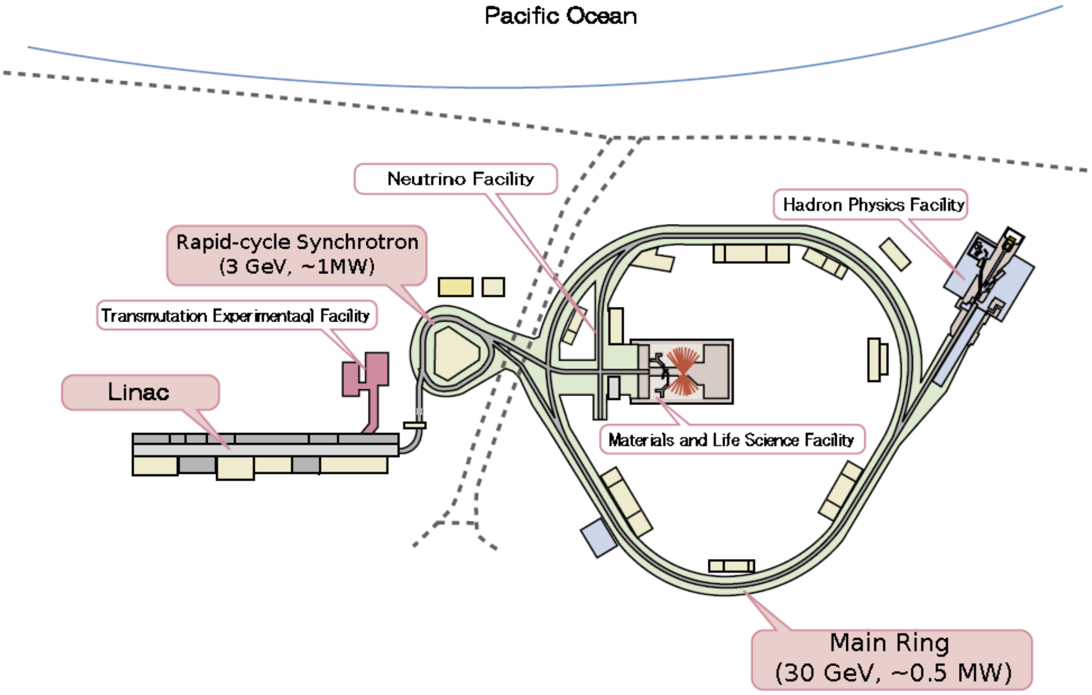

Figure 2.9: A schematic overview of the J-PARC accelerator chain.

2.3.2 Primary beam-line

The extracted proton beam needs to be safely transported towards the target. This is done by the primary beam-line. Along the way, measurements of the proton beam profile, position, beam loss and beam intensity are performed. These are important for accurately predicting the flux, since a number of protons on target and width of the beam influence hadron production and in turn the neutrino flux. Also, if large beam loss is detected, an abort signal is sent to the MR to protect the beam-line. The primary beam-line consists of three main parts: a preparation section, an arc section, and a final focusing section. The preparation section and the final focusing section contain normal conducting magnets, while the arc section which is used for bending the beam towards the secondary beam-line, contains superconducting magnets. An overview of the primary and secondary beamline is shown in Fig. 2.10. More details about the primary section and the magnet configuration used can be found in Ref. [69]. Inside all three sections, there are several types of beam monitors which are used for already mentioned measurements.

Beam monitors

Different types of beam monitors are used for each measurement. The intensity of the beam is measured by five current transformers (CT) which are essentially toroidal coils wrapped around the specially designed ferromagnetic core. Each CT measures absolute beam intensity with a precision of around 2% and a beam timing with an accuracy of 10 ns. Position of the beam is measured by 15 electrostatic monitors (ESM), which have four segmented cylindrical electrodes. By measuring asymmetry of the signals between top-bottom and left-right electrodes, it is possible to determine the proton beam center. The precision of the measurements is estimated to be 450 μm.

It is important to note that the CT and ESM measurements are nondestructive measurements, i.e., there is no beam loss because of the measurements. On the contrary, measurements of the beam profile done by 19 segmented secondary emission monitors (SSEM) are destructive. The estimated beam loss is around 0.005% per SSEM. For this reason, only a couple of SSEMs are kept inside the beam-line during the data-taking, while others are only used during the beam tuning. Each SSEM has two sets of titanium strips with the anode foil between them. When the beam hits the strips, secondary electrons are emitted and they begin to drift towards the anode. In turn, they induce a signal in the strips. The precision of the beam profile measurements is around 200 μm.

The beam loss measurement is done by 50 beam loss monitors (BLM) which are proportional wire counters. They can measure beam loses up to 16 mW. Previously mentioned loss caused by SSEM is estimated by the BLMs. All of these measurements are of utmost importance since a bias in the understanding of the proton beam will bias the calculated neutrino flux. For this reason, there is ongoing research and development to replace and improve some of these detectors. In particular, SSEM will be replaced by similar design which uses titanium wires instead of strips.

2.3.3 Secondary beam-line

The secondary beam-line is the volume where hadrons are produced and decay to the neutrinos. The volume is around 1500 m ^{3} and it is filled with helium at atmospheric pressure to reduce the pion absorption and the production of tritium. The secondary beam-line consists of the three main sections: a target station, a decay volume, and a beam dump.

Target station

The target station is located immediately after the primary beam-line. It consists of the target and the set of three magnetic focusing horns. The target itself is located inside the first horn. In front of the target, there is an optical transition radiation monitor (OTR) and a graphite

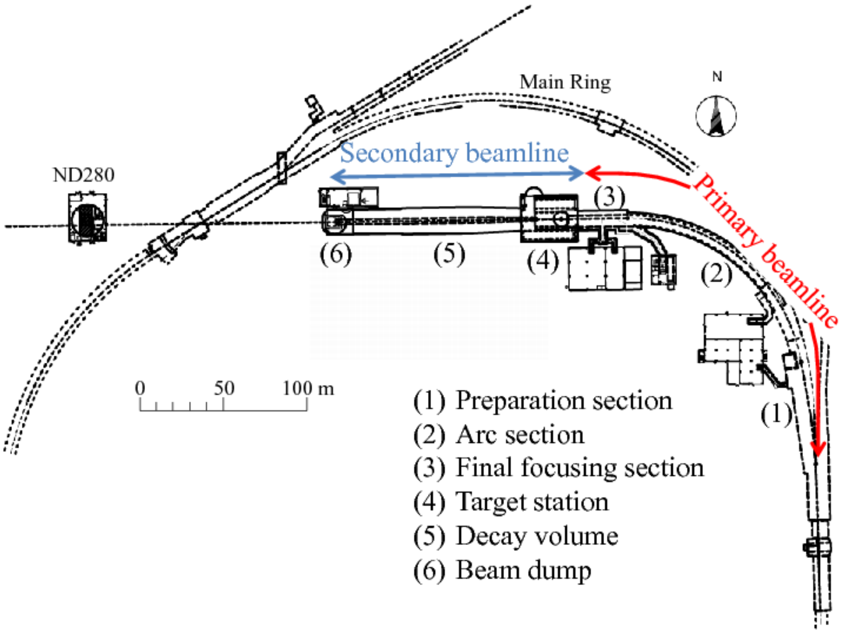

Figure 2.10: A schematic overview of the T2K primary and secondary beam-lines.

baffle which serves as a beam collimator and protects the horns from the excess radiation. An overview of the target station area is shown in Fig. 2.11. The OTR uses thin titanium foils tilted by 45° with respect to the proton beam. When the beam hits the foil, the transition radiation is created at the surface of the foil. After reflecting on several parabolic mirrors, the light is then collected by a charge injection device camera which produces an image of the beam. The OTR has a carousel with eight positions, similar to the revolver. Each position can contain a different type of foil or an empty slot.

The target is a 91.4 cm long graphite rod, with the radius of 1.3 cm and density of $1.8\,\mathrm{g/cm^3}$. The material was selected to maximize the neutrino flux and to withstand the heat transfer from the beam. The rod has been enclosed in the graphite tube and on top of that, in the thin titanium case. The cooling is provided by helium flowing between the tube, the rod, and the case. The whole structure is attached to the flange made of aluminum and titanium. In addition, two titanium pipes are installed onto the flange, and they are used for transporting helium in and out from the target. The whole assembly is inserted into the first horn.

Each of the three magnetic horns consists of two coaxial aluminum conductors which give rise to the toroidal field in the space between them ($B \propto \frac{1}{r}$). An example of the working principle is shown in Fig. 2.12, alongside with the preview of the horn 1. The thickness of the conductors is 3 mm. This value was chosen to minimize the pion absorption while withstanding 750 kW beam power and the Lorentz force created by 320 kA current. The shape of the horns which can be seen in Fig. 2.11, is optimized to focus pions. Typical transverse momenta of pions in the T2K experiment is around $0.4\,\mathrm{GeV}/c$ and for this reason, it is necessary to have bending power of 1.3 Tm. This could be done by one large horn however, because of the cooling and radiation, a present design with three separate horns was adopted. Although the horns were designed to operate with a pulse current of 320 kA, they have been operated with a current of 250 kA up to now. More details about the horn operation and design can be found in Ref. [70, 71]

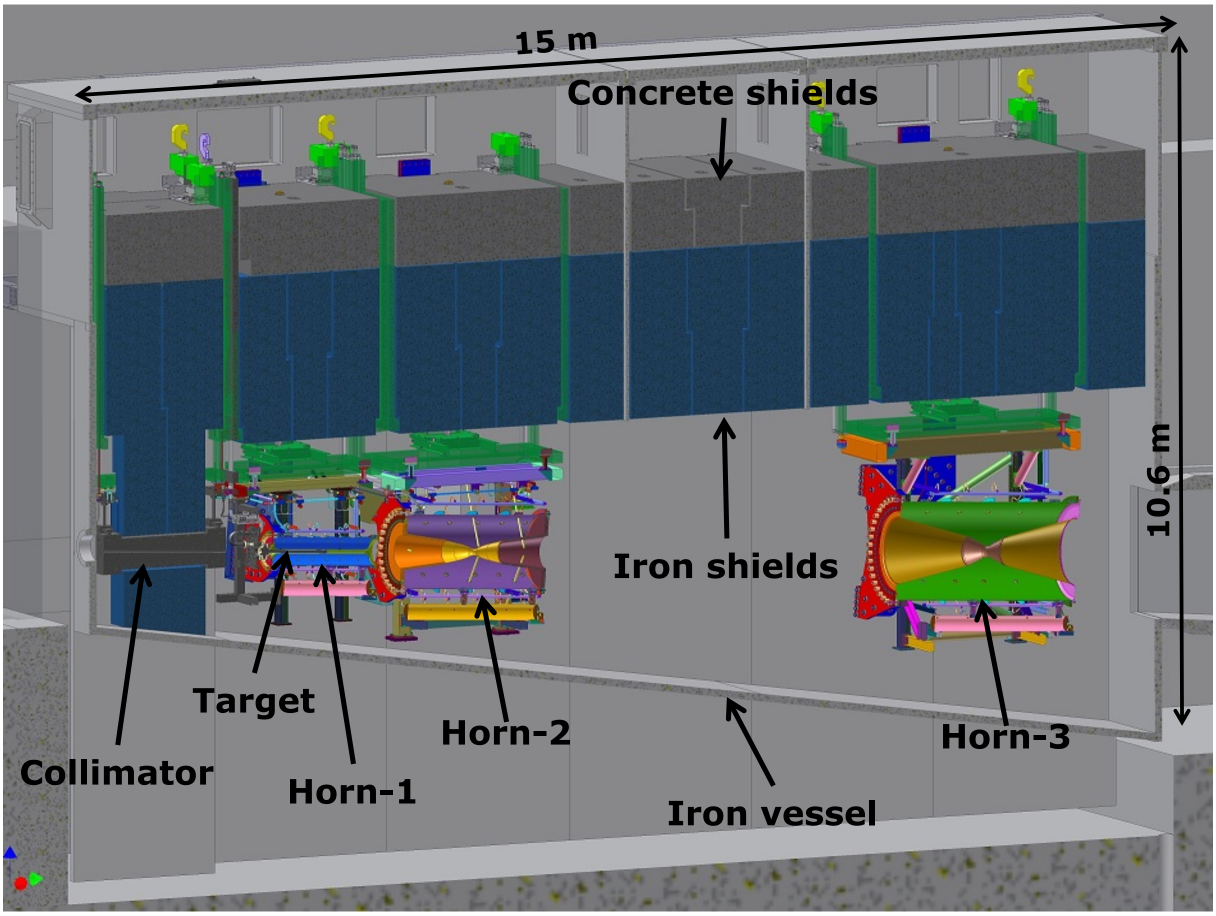

Figure 2.11: A schematic overview the target station [70].

Decay volume and beam dump

After passing through the horns, hadrons enter the decay volume which is a 96 m long steel tunnel. At the end of the tunnel, a beam dump is placed to contain all non-decayed hadrons. It is made of graphite core with the thickness of 3.2 m and fifteen iron plates with a total thickness of 2.4 m. This stops all particles except muons with energy above 5 GeV. The flux of these muons is measured by the muon monitor [72, 73], behind the beam dump. Muons are produced in the same decays with the neutrinos, so their direction is correlated with the direction of the neutrino beam. The muon monitor consists of two types of the detectors: ionization chambers and silicone PIN photo-diodes. It is designed to monitor neutrino beam direction with a precision of 0.25 mrad and the intensity with a precision better than 3%.

2.4 Neutrino beam

Knowledge of the neutrino flux is of the utmost importance for the T2K experiment since it is one of the limiting factors for the precise measurement of the neutrino oscillation parameters and the neutrino-nucleus cross sections. In this section, the off-axis method will be presented, followed by the description of the neutrino beam simulation and uncertainties of the neutrino flux.

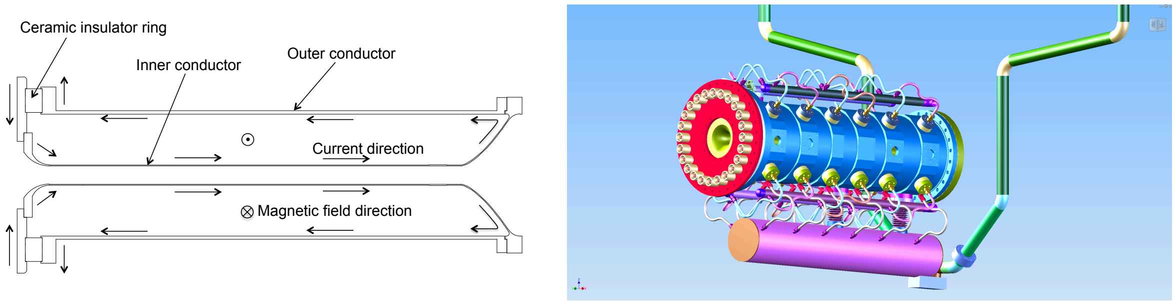

(a) (b)

Figure 2.12: Working principle of the horns (a) and model of the horn 1 [70].

2.4.1 Off-axis technique

The off-axis method in T2K is used for achieving two things:

1. tune neutrino energy, so that the oscillation probability at *Super-Kamiokande* is maximal and
2. reduce the high energy tail of the neutrino energy spectrum.

Here, only a brief review of the off-axis method will be presented, while the more detailed explanation can be found in the work of J.M. Levy [74] which has been used as a base of this subsection. Neutrinos in the T2K experiment, depending on which horn focusing mode is used, are mostly muon (anti-)neutrinos produced in decays of pions:

$$\pi^+ \rightarrow \mu^+ + \nu_\mu, \tag{2.2a}$$

$$\pi^- \rightarrow \mu^- + \overline{\nu}_\mu. \tag{2.2b}$$

Therefore, their energy spectra are limited by the energy spectra of the pions and in turn, the energy of the proton beam. In the lab reference frame, maximum neutrino energy for a given pion energy can be achieved only for the neutrinos created with momenta parallel to the pion momenta. This can be easily understood since no additional momentum is transferred to the muons for balancing out transverse momentum of the neutrinos. It is useful to look at the pion decays in the pion center of mass reference frame and then obtain values in the lab frame by applying Lorentz boost to the four-momenta of the neutrinos. Quantities in the center of mass frame will be presented with the star, for example, neutrino energy in the center of mass frame is E^*_ν, while in the lab system, they will be denoted without a star (for example E_ν). It is also assumed that the lab frame and the center of mass frame have aligned axes, i.e. they are parallel to each other. Energy of the neutrino in the pion center of mass frame is constant and it is equal to:

$$E^*_\nu = \frac{m^2_\pi - m^2_\mu}{2m_\pi}, \tag{2.3}$$

where m_π and m_μ are pion and muon masses respectively, while the neutrino mass is considered to be 0. Consequently, longitudinal ($p^*_{\nu,l}$) and transverse momenta ($p^*_{\nu,t}$) of the neutrinos are equal to:

$$p^*_{\nu,l} = \frac{m_\pi^2 - m_\mu^2}{2m_\pi}\cos\theta^*_\nu, \tag{2.4a}$$

$$p^*_{\nu,t} = \frac{m_\pi^2 - m_\mu^2}{2m_\pi}\sin\theta^*_\nu, \tag{2.4b}$$

where θ^* is an angle of the neutrinos with respect to the axis which is parallel to the pion momenta in the lab system. The angular distribution in the center of mass system is uniform. Now, it is possible to introduce Lorentz transformations to get previously defined quantities in the lab reference frame. These transformations are:

$$E_\nu = \gamma E^*_\nu(1+\beta\cos\theta^*_\nu), \tag{2.5a}$$

$$p_{\nu,l} = \gamma E^*_\nu(\beta+\cos\theta^*_\nu), \tag{2.5b}$$

$$p_{\nu,t} = E^*_\nu\sin\theta^*_\nu. \tag{2.5c}$$

It is easy to rewrite the neutrino energy only as a function of the variables in the lab system:

$$E_\nu = \frac{m_\pi^2 - m_\mu^2}{2E_\pi}\frac{1}{1-\cos\theta_\nu\sqrt{1-m_\pi^2/E_\pi^2}}, \tag{2.6}$$

where E_π is a pion energy and θ_ν is a neutrino angle which can be written as a function of the center of mass angle and pion velocity β:

$$\tan\frac{\theta_\nu}{2} = \sqrt{\frac{1-\beta}{1+\beta}}\tan\frac{\theta^*_\nu}{2}. \tag{2.7}$$

Depending on the pion energy, a small interval in the angle θ_ν is represented by a large angle interval in the center of mass frame. In the ultra-relativistic limit ($E_\pi >> m_\pi$), for 0° angle, the neutrino energy becomes a linear function of the pion energy:

$$E_\nu = \frac{m_\pi^2 - m_\mu^2}{m_\pi^2}E_\pi. \tag{2.8}$$

It is clear that for 0° angle, neutrino energy is the unbounded function of the pion energy. However, this is not the case for non-zero angle, it rises with pion energy and it reaches a maximum value of:

$$E_{\nu,max} = \frac{m_\pi^2 - m_\mu^2}{2m_\pi}\frac{1}{\sin\theta_\nu} = \frac{E^*_\nu}{\sin\theta_\nu}. \tag{2.9}$$

It is equal to the neutrino energy in the pion center of mass frame (E^*_ν) divided by $\sin\theta_\nu$. This can be understood differently: the neutrino energy E_ν can be found only for the angles which are equal or smaller than:

$$\theta_\nu \leq \arcsin\left(\frac{E^*_\nu}{E_\nu}\right). \tag{2.10}$$

The maximum neutrino energy for a given angle is achieved for:

$$E_\pi = \frac{m_\pi}{\sin\theta_\nu}. \tag{2.11}$$

Now, let's imagine that we want neutrinos with a certain value of the angle θ_ν, for example, 2.5°. The neutrino energy in the lab frame is a product of two competing factors: γ and $(1+\beta\cos\theta_\nu^*)$. The first one, γ, increases with the pion energy in the lab frame, while the second one decreases with the pion energy for relativistic pions ($\beta \approx 1$). To keep neutrino angle θ_ν constant while increasing pion energy, it is necessary to increase neutrino angle in the center of mass frame, like it was shown in Eq. 2.7. After we cross pion energy defined in 2.11, we start to select backward neutrinos in the center of mass frame. Consequently, $\cos\theta_\nu^*$ becomes negative and term $(1+\beta\cos\theta_\nu^*)$ in the neutrino energy (equation 2.5a) starts to dominate. Neutrino energy is shown as a function of the pion energy in Fig. 2.13a for the six neutrino angles ($\theta = 0°, 0.5°, ..., 2.5°$).

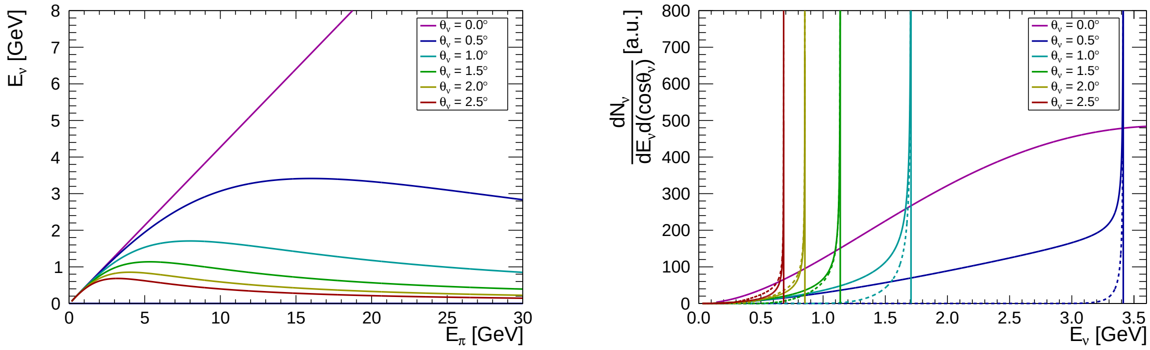

(a) (b)

Figure 2.13: Neutrino energy vs. pion energy for six angles (a) and neutrino probability density vs. neutrino energy (b). The full line is the contribution of the forward neutrinos, while the dashed line is the contribution of the backward neutrinos.

It is useful to introduce neutrino probability density distribution ($\frac{d^2P}{dE_\nu d\Omega}$) in terms of the neutrino energy E_ν and the neutrino angle θ_ν. This distribution represents a probability that we will get a neutrino (in this case from the pion decay) in the energy interval $E_\nu + dE_\nu$ and solid angle interval $\Omega + d\Omega$. Furthermore, the distribution can be multiplied with the pion energy spectra from the proton-carbon interactions and integrated over the possible energies and the angle coverage of the detectors to obtain neutrino flux. For the pion decays in the center of mass frame, it is straightforward to write the neutrino probability distribution:

$$\frac{dP}{dE_\nu^* d\Omega^*} = \frac{1}{4\pi}\delta\left(E_\nu^* - \frac{m_\pi^2 - m_\mu^2}{2\mathrm{m}_\pi}\right), \tag{2.12}$$

where δ represents Dirac delta distribution. For the neutrino flux calculation we assume the following pion energy spectra:

$$g(E_\pi) \propto (E_p - E_\pi)^5 H(E_p - E_\pi), \tag{2.13}$$

where $H(E_p - E_\pi)$ is the Heaviside step function, and E_p is the energy of the proton beam. It is implicitly assumed that the pion energy spectra does not depend on the angle with respect to the proton beam since all pions are focused by the magnetic horns. In reality, divergence of the pions is nonzero and changes with energy, but for the sake of this exercise, it is assumed to be negligible. The probability distribution shown in Eq. 2.12, must be transformed from the variables $(E_\nu^*, \cos\theta_\nu^*)$ to the $(E_\pi, \cos\theta_\nu^*)$. After the transformation, the probability distribution can be multiplied by the pion energy spectra from Eq. 2.13. Now, an additional transformation is introduced: $(E_\pi, \cos\theta_\nu^*) \to (E_\pi, \cos\theta_\nu)$. This yields a new probability density distribution: $\frac{dN_\nu}{dE_\nu d\Omega_\nu}$ which if multiplied by the energy and the solid angle interval (dE_ν and $d\Omega$) gives a fraction of the neutrino flux in the defined interval. The distribution is:

$$\frac{dN_\nu}{dE_\nu d\Omega_\nu} = \frac{m_\pi}{4\pi E^* \sin^2\theta_\nu \sqrt{1 - r^2 \sin^2\theta_\nu}} \sum_{k=1,2} g(E_k)\,|\cos\theta_\nu + (-1)^k \sqrt{1 - r^2 \sin^2\theta_\nu}|, \qquad (2.14)$$

where $r = \frac{E_\nu}{E_\nu^*}$ and E_k are pion energies:

$$E_k = m_\pi \frac{1 + (-1)^k \cos\theta_\nu \sqrt{1 - r^2 \sin^2\theta_\nu}}{r \sin^2\theta_\nu}, \quad k = 1, 2. \qquad (2.15)$$

The first term in Eq. 2.14 (for $k = 1$) is to be kept only for $r \geq 1$. Apart from that, the first term represents contributions of the forward neutrinos. Similarly, the second term is the contribution of the backward neutrinos which is possible only if the pion energy spectra has a non-vanishing contribution for the energies larger than the energy defined in the relation 2.11. Both contributions have been plotted in Fig. 2.13b for several angles θ_ν. The peaks in the probability distributions are produced by the bound on the neutrino energy for a given angle (equation 2.9). It is also important to note that the backward neutrinos tend to group close to the maximum energy and therefore reinforce the peaks. This also could be seen in Fig. 2.13a, where backward neutrinos are represented by a very long tail after the maximum.

2.4.2 T2K neutrino beam simulation

It was shown in the previous subsection that it is possible to calculate neutrino flux analytically if the produced pions are perfectly collimated and if the pion production is known. In fact, it is possible to repeat all calculations if the neutrinos are created from the decays of charged kaons. However, in reality, none of these assumptions are true. The target is a 90 cm long graphite rod inserted in the first magnetic horn, and because of that, not all hadrons are produced in the same position along the target. Therefore, length of the trajectory inside the focusing volume of the horns is not the same for all hadrons with the same momentum. Additionally, hadrons are produced with different polar angles and momenta, which also reduces the efficiency of the focusing. Some of the hadrons will be created nearly parallel to the beam-line. In this case, they will never enter region between the conductors in the horns and some of the π^- (in the positive focusing mode) which would otherwise be defocused, will contribute to the wrong sign neutrino flux ($\overline{\nu}_\mu$ instead of ν_μ). Focusing and geometry of the experiment are not the only problems. Hadron production is not well understood at the energies used in T2K, and there exists only a handful of measurements which can be used to constrain the hadron production. This will be explained in great detail in the next subsection.

A Monte Carlo simulation was developed to properly estimate neutrino flux at the *ND280* and *Super-Kamiokande*. The simulation consists of two main parts. First part uses FLUKA2011 Monte Carlo model for generating beam protons at the upstream part of the baffle, transporting them to the target and simulating interactions inside the target. Once the produced particles or non-interacted protons exit the target, tracking with FLUKA2011 is stopped, and the tracking is continued with GEANT3 based simulation called J-PARC neutrino beam (JNUBEAM) simulation. Interactions outside the target are simulated with the GCALOR model. Before we proceed with the more detailed description of the simulation, it is necessary to define a naming convention for the interactions and produced particles:

- primary particles - beam protons,
- primary interactions - an interaction of the primary beam protons with the target or the elements of the beam-line,
- secondary particles - particles produced in the primary interactions,
- secondary interactions - interactions between the secondary particles and the material in the beam-line (target, horns, etc...),
- tertiary particles - particles produced in the secondary interactions or the higher order interactions,
- tertiary interactions - interactions of the tertiary particles.

Fluka2011 simulation

In the first part of the simulation, hadron interactions inside the target are simulated with FLUKA2011. This model was chosen since it gave the best prediction for the available hadron production measurements. The geometry used in FLUKA2011 is rather simple, it consists of graphite baffle, helium gas in front of the target and the target itself (see Fig. 2.14). Beam protons are generated at the upstream end of the hole in the baffle with a kinetic energy of 30 GeV. Since position, where the beam proton hits the target can change the probability of re-interactions and the focusing efficiency, it is necessary to generate the same beam profile as the one obtained from the measurements.

The equation of motion for the particle beam inside a synchrotron is the Hill equation, and phase space of such system has four dimensions (two coordinates and two divergences). If we look only in the 2D phase space (let's say one coordinate and one divergence), the beam is represented by an ellipse. It is useful to introduce the so-called twiss parametrization of the ellipse which is also used to describe parameters of the J-PARC beam. There are four parameters: α, β, γ and ϵ which are shown in Fig. 2.15. Only three of these parameters are independent, and we can write an equation of the ellipse:

$$\gamma x^2 + 2\alpha x x' + \beta x'^2 = \epsilon. \tag{2.16}$$

The parameter ϵ is called the beam emittance, and it is an area of the ellipse divided by π. The emittance is an internal property of the beam, and it is constant (Liouville's theorem) if we neglect beam losses. In case of the Gaussian beam profile, the width of the beam is related to the twiss parameters:

$$2\sigma_x = \sqrt{\beta\epsilon}. \tag{2.17}$$

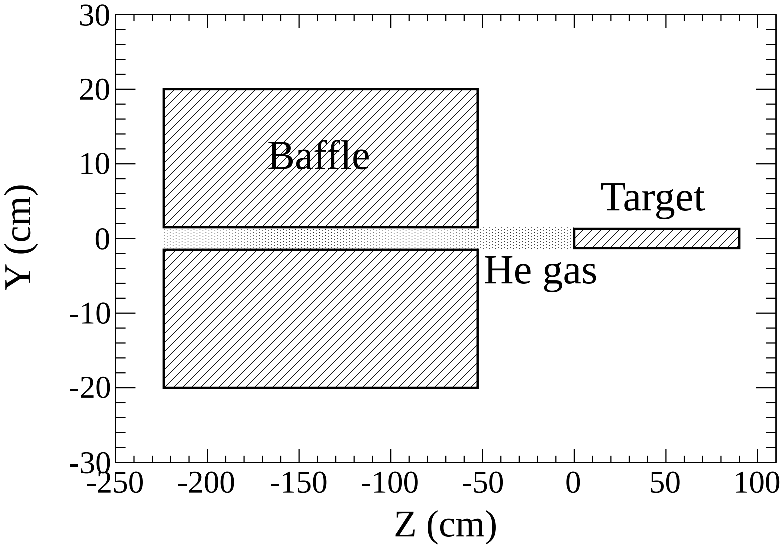

Figure 2.14: FLUKA2011 geometry used in the first step of the JNUBEAM simulation.

In T2K, the beam parameters σ_x, α and ϵ were chosen to be independent, while β and γ are calculated using Eq. 2.16 and Eq. 2.17. An example of the J-PARC proton beam profile and phase space for the T2K run 4 is shown in Fig. 2.16. To simulate the beam profile for one coordinate in the FLUKA2011 simulation we generate two normally distributed, non-biased random numbers r_1 and r_2 with variance equal to 1. The numbers are then used for the calculation of the beam position and divergence:

$$\begin{pmatrix} x \\ x' \end{pmatrix} = \begin{pmatrix} \cos\theta & -\sin\theta \\ \sin\theta & \cos\theta \end{pmatrix} \begin{pmatrix} ar_1 \\ br_2 \end{pmatrix} + \begin{pmatrix} \overline{x} \\ \overline{x'} \end{pmatrix}, \tag{2.18}$$

where a and b are semi-major and semi-minor axes of the ellipse respectively:

$$a = \frac{1}{2}\sqrt{\frac{\epsilon}{\gamma + \alpha\tan\theta}}, \tag{2.19a}$$

$$b = \frac{1}{2}\sqrt{\frac{\epsilon}{\beta - \alpha\tan\theta}}, \tag{2.19b}$$

$$\tag{2.19c}$$

and θ is an angle between the semi-major axis and $x-$axis:

$$\theta = \frac{1}{2}\arctan\frac{2\alpha}{\gamma - \beta}. \tag{2.19d}$$

Parameters $\overline{x}$ and $\overline{x'}$ are mean values of the beam position and divergence respectively. Naturally, the procedure described above must be repeated for the (y, y') phase space to get full beam profile. In total, six twiss parameters and four mean values are used to describe the proton beam fully.

When beam profile is generated, the interactions insides the baffle and the target are simulated in such a way that the history of all produced hadrons which exit the geometry shown in Fig. 2.14 are preserved.

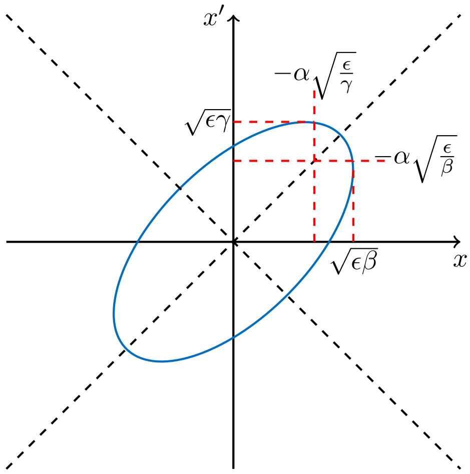

Figure 2.15: Twiss parametrization of the beam.

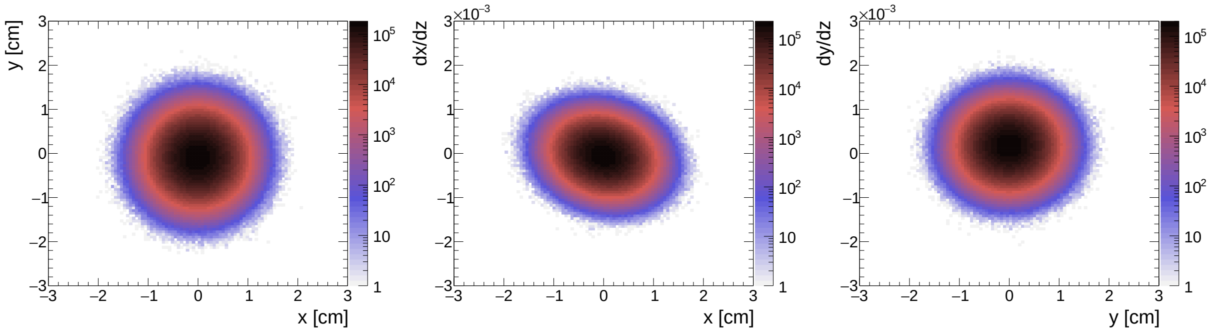

(a)

(b)

(c)

Figure 2.16: J-PARC proton beam profile for T2K run 4 (a), beam divergence div$x$ vs. x (b) and div$y$ vs. y (c).

Geant3 simulation

Hadrons from the Fluka2011 stage of the simulation are then propagated in JNUBEAM all the way to the beam dump if they don't decay in flight to neutrinos. There are several constraints imposed onto the tracking of the particles to speed up the simulation and reduce the output size. Tracking is stopped for hadrons and muons with momentum less than 0.1 GeV/c and their decays are simulated with appropriate branching ratios. The momentum threshold for tracking of electrons and gammas is set higher, at 1 GeV/c, since they do not contribute to the neutrino flux. If hadrons pass through the beam dump, the limit is also set to 1 GeV/c. In addition, neutrinos produced in the decays of particles with momentum less than 10 MeV/c are ignored since their energy is very low and the interaction rate they produce at the *ND280* or *Super-Kamiokande* is insignificant. All particles decaying to neutrinos are forced to produce neutrinos in the direction of the *ND280* and *Super-Kamiokande* to minimize computation time. However, additional weight is applied to the neutrinos to account for the probability that created neutrinos have direction towards the near and the far detectors. In case of *Super-Kamiokande*, this weight is straightforward to calculate, since distance is large enough so that the neutrino source can be considered point-like. In contrast to *Super-Kamiokande*, the neutrino source from the *ND280* is a line. Therefore, a position at the cross section of the detector is randomly chosen, and then the probability of neutrino production in this direction is calculated. A total of 14 different decays which are taken into account are summarized in Tab. 2.1. The history of all neutrinos (all parents and grandparents with interactions and decays) is saved to the output of the simulation.

Particle	Channel	BR [%]
$\pi^\pm$	$\mu^\pm\nu_\mu(\overline{\nu}_\mu)$	99.9877
	$e^\pm\nu_e(\overline{\nu}_e)$	0.0123
$\mu^\pm$	$e^\pm\nu_e(\overline{\nu}_e)\overline{\nu}_\mu(\overline{\nu}_\mu)$	100
$K^\pm$	$\mu^\pm\nu_\mu(\overline{\nu}_\mu)$	63.55
	$\pi^0 e^\pm\nu_e(\overline{\nu}_e)$	5.07
	$\pi^0\mu^\pm\nu_\mu(\overline{\nu}_\mu)$	3.35
K^0_L	$\pi^\pm e^\mp\nu_e(\overline{\nu}_e)$	40.55
	$\pi^\pm\mu^\mp\nu_\mu(\overline{\nu}_\mu)$	27.04

Table 2.1: Decay channels taken into account in JNUBEAM.

Neutrino spectra and neutrino parent particles

Since most of the produced hadrons are pions, it is obvious that neutrino flux is dominated by the flux coming from the pion decays. Therefore, it is expected to get a narrow peak in the neutrino spectra as explained in subsection 2.4.1. A small percentage of the produced particles are kaons, and because of their higher mass, they will contribute to the flux with much broader spectra and higher maximum. On the other hand, a small fraction of the neutrino flux also comes from the muon decays, but the typical energy of these neutrinos is slightly below the main peak. Contribution to the ν_μ flux in the positive focusing mode at the *ND280* and *Super-Kamiokande* is shown in Fig. 2.17. The flux is shown per unit area, per 10^{21} protons on target and normalized by the total branching ratio of the decay channels which produce neutrinos. Integrated fractions of neutrinos for energies less than 10 GeV coming from different parents are shown in Tab. 2.2.

	Neutrino flux [%]			
Parent	ν_μ	$\overline{\nu}_\mu$	ν_e	$\overline{\nu}_e$
pion	95.08	82.88	0.98	0.40
kaon	4.91	6.95	41.52	89.23
muon	0.01	10.17	57.50	10.37

(a)

	Neutrino flux [%]			
Parent	ν_μ	$\overline{\nu}_\mu$	ν_e	$\overline{\nu}_e$
pion	94.54	82.72	0.98	0.35
kaon	5.45	8.19	46.15	92.19
muon	0.01	9.09	52.87	7.46

(b)

Table 2.2: Proportion of the flux from different parent particles in positive focusing mode at the *ND280* (a) and *Super-Kamiokande* (b).

In general, fluxes in the positive and negative focusing mode show similar behavior at low energies. However, the ν_μ flux in the positive mode is around 15% higher at the peak energy with respect to the $\overline{\nu}_\mu$ flux in the negative focusing mode. The reason for this is related to the

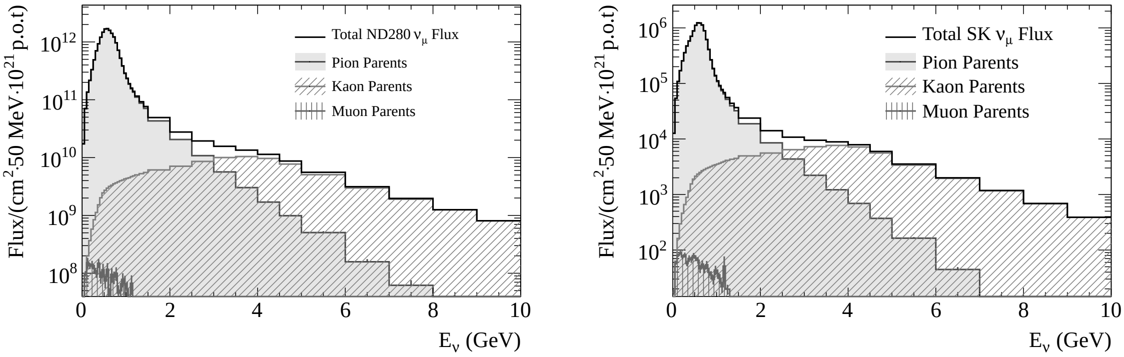

(a) (b)

Figure 2.17: Neutrino flux coming from different parent particles as a function of neutrino energy at the *ND280* (a) and *Super-Kamiokande* (b).

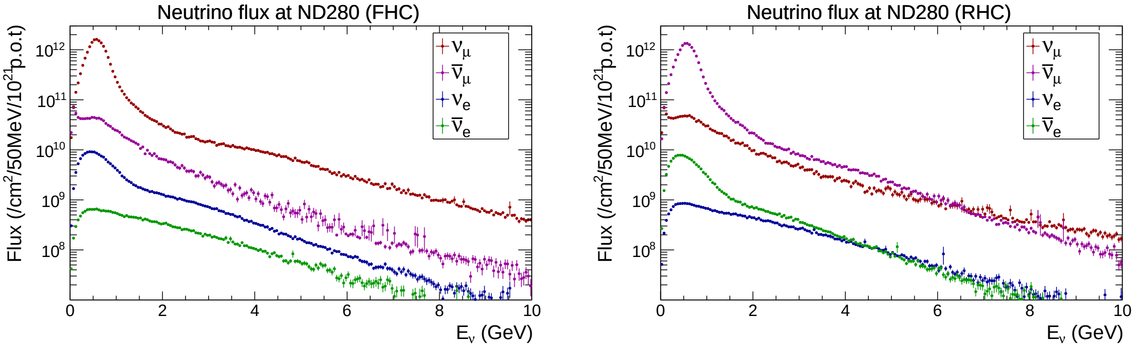

(a) (b)

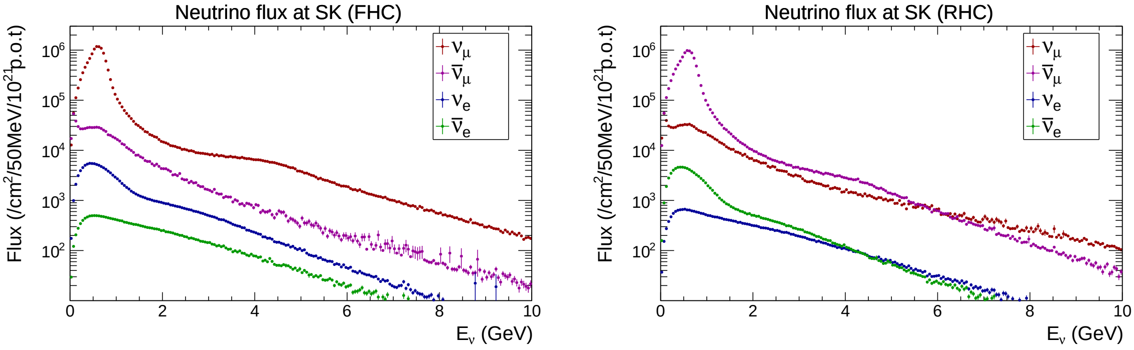

(c) (d)

Figure 2.18: Neutrino flux for T2K run 6 at the *ND280* for FHC (a) and RHC (b); neutrino flux at *Super-Kamiokande* for FHC (c) and RHC (d).

u-d quark asymmetry of the primary interactions (p + C). For the same reason contribution of the wrong-sign neutrinos in the negative focusing mode will be higher. Also, at higher neutrino energies, in the negative focusing mode, main contributions come from K^- and K_L^0. Neutrino fluxes at the *ND280* and *Super-Kamiokande* are shown in Fig. 2.18, both in the positive and negative focusing mode. Different colors represent contributions from different (anti)neutrinos.

2.4.3 Systematic uncertainties of the neutrino flux

Estimate of the flux uncertainties is of crucial importance for T2K since expected neutrino interaction rates in the detectors are proportional to the flux. There are several contributions to the flux uncertainty:

- proton beam profile and off-axis angle,
- number of P.O.T.,
- horn and target alignment,
- horn current and field,
- material modeling and,
- hadron interactions.

The neutrino flux is affected by the beam profile. In particular, a change in the position and the width of the beam affects the hadron production inside the target by changing amount of material through which the particles pass. Also, this changes how produced particles are focused by the horns and the neutrino beam direction. The off-axis angle is especially sensitive to the proton beam y position and width because the near and the far detectors are shifted from the beam direction in the vertical plane. The direction of the neutrino beam is measured by the muon monitor and *INGRID*. A typical uncertainty of the beam direction and thus uncertainty of the off-axis angle is around 0.4 mrad. The uncertainty of the proton beam intensity measured by CTs biases the neutrino flux. The total contribution of the beam profile and the beam intensity uncertainty to the neutrino flux uncertainty is from 2% to 10% for the ν_μ and $\overline{\nu}_\mu$ fluxes in the positive and negative focusing mode respectively.

The horn and the target alignment were changed in the simulation within their uncertainties. The most significant contribution to the neutrino flux uncertainty from the alignment comes from the overall alignment between the primary and secondary beam-line and the angular alignment of the first horn. The value of this uncertainty is around 3%. The uncertainty of the horn current is 2% which corresponds to the current variations within ±5 kA. Alongside with the contributions from the magnetic field asymmetry, this induces possible flux bias of 2%.

Materials used in the construction of the target and the elements in the beam-line are modeled by the simulation and have assigned nominal densities to them. However, the real densities are only known up to a certain precision and any bias will induce a bias in the interaction probability and therefore a bias in the neutrino flux prediction. The estimated systematic uncertainty of the flux coming from the modeling of the materials is estimated to be around 2% or below.

The major contribution to the systematic uncertainty of the neutrino flux comes from the modeling of the hadron interactions. Measurements of the hadron production in the T2K energy range and with the same materials are sparse and do not constrain Monte Carlo models very well. If only models were used without any external hadron production data, the uncertainty of the neutrino flux would increase to more than 25%. To illustrate this, a simulation of proton interactions and re-interactions inside the 90 cm graphite rod was made with three different models: FLUKA2011, NUBEAM and QGSP_BERT physics lists from GEANT4.10. A comparison of π^+ spectra in the phase space of polar angle (θ) and momentum (p) is presented in Fig. 2.19. Large differences can be seen between the models and without any external data to distinguish between them, those differences must be included as a systematic uncertainty of the flux. Therefore, hadron production measurements are necessary for providing the accurate prediction of the neutrino flux. A more detailed description of the usage of the external hadron production data is provided in the next section.

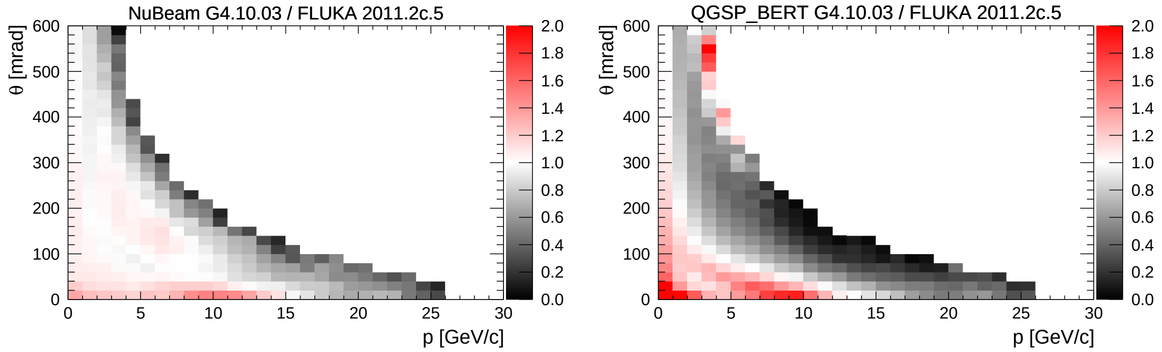

(a) (b)

Figure 2.19: Comparison of FLUKA2011 π^+ yields, emitted from the surface of 90 cm long graphite rod, with NUBEAM (a) and QGSP_BERT (b) physics lists from GEANT4.10. Proton beam of 31 GeV/c has been used, and a total number of $5 \cdot 10^6$ primary interactions have been simulated for all three models.

With the current knowledge of the hadron production, the uncertainty of the flux prediction is around 10%. The uncertainty of the ν_μ and $\overline{\nu}_\mu$ flux in *Super-Kamiokande* is shown in Fig. 2.20 with all previously described components. A detailed description of the uncertainties can be found in the Ref. [75].

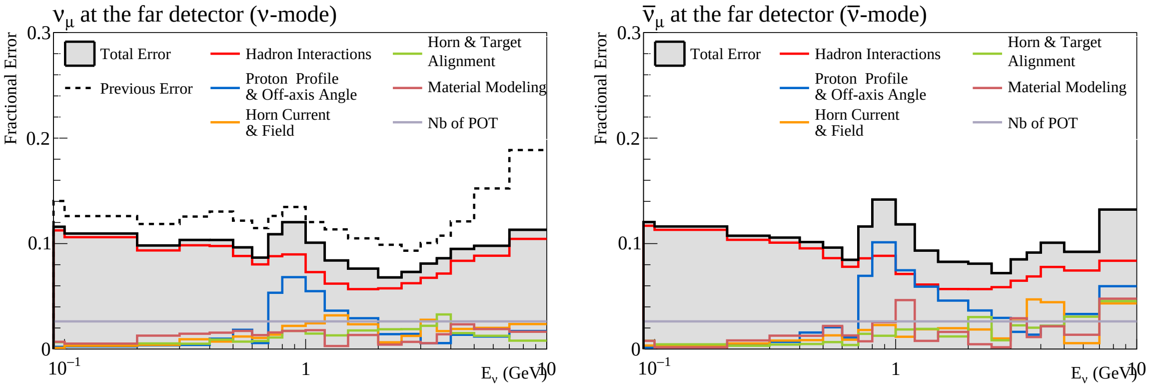

(a) (b)

Figure 2.20: Uncertainties of the ν_μ flux (a) and $\overline{\nu}_\mu$ flux (b) at *Super-Kamiokande* for positive and negative focusing mode respectively based on the NA61/SHINE thin-target measurements.

2.5 Re-weighting of the T2K neutrino flux with hadron production measurements

It was already shown that the prediction of the hadron yields from different Monte Carlo models could be radically different. In principle, it would be possible to simulate the interactions by the updated model, based on the hadron production measurements, but this would coast a lot of computation time. Therefore, a re-weighting procedure which scales the Monte Carlo prediction to the external hadron production data must be applied to the primary interactions and all re-interactions in the target and the elements of the beam-line. This includes interactions of different hadrons ($\pi^{\pm}$, $K^{\pm}$, K^0_L, p, and n) with different materials (mostly carbon, aluminum, and iron). For each interaction, it is necessary to re-weight both the interaction probability and differential production spectra of hadrons. The interaction probability defines a mean free path through the material before the hadron interacts. On the other hand, differential production of the hadrons gives the shape of the produced hadron spectra and a total number of hadrons produced in the interaction. The re-weighting procedure is done after the neutrino beam simulation, and the weights are applied to all interactions and re-interactions which produced neutrinos. Consequently, a product of all weights from a single neutrino history is applied to that neutrino. Although several different measurements are used for the re-weighting procedure, the main source of the hadron production measurements is from NA61/SHINE [76] experiment at CERN. It provided measurements of the primary p + carbon interaction at 31 GeV/c [77, 78, 79].

2.5.1 Interaction probability re-weighting

Before the re-weighting of the interaction probability is presented, it is necessary to define two different types of the interaction processes which differ in the energy transfer from the projectile to the target and the number of particles produced. First one is a nuclear elastic scattering (from now on called just the elastic scattering) where the energy of the projectile particle is nearly conserved. In this case, new particles cannot be produced or the nuclei fragmented because of the small momentum transfer. The probability of the elastic scattering is governed by elastic cross section (σ_{el}). The second process is an inelastic scattering in which target nucleus is fragmented, and new particles can be produced. It is governed by inelastic cross section (σ_{inel}). Such sample of the inelastic events in which no new hadrons are produced except nucleons coming from the fragmentation of the target nuclei are called quasi-elastic events, and the respective cross section is the quasi-elastic cross section (σ_{qel}). In this case, the fragments of the nuclei usually have low momentum and projectile retains most of its energy. Majority of the inelastic events are so-called production events where new hadrons are produced. The respective cross section for this process is production cross section (σ_{prod}).

The interaction probability re-weighting is applied to the production events since only they contribute to the neutrino flux. All other processes keep the primary proton intact with most of its energy. The re-weighting starts with the calculation of interaction probability (from now on, it represents the probability of production of the new hadrons) in the infinitesimal length Δx after traveling a distance x through the material of nuclear density ρ. The calculation of the probability is done both for the data and Monte Carlo:

$$P(x;\sigma_{\mathrm{prod}}) = \int_x^{x+\Delta x} \sigma_{\mathrm{prod}}\rho \exp(-x'\sigma_{\mathrm{prod}}\rho)dx' = \Delta x \sigma_{\mathrm{prod}}\rho \exp(-x\sigma_{\mathrm{prod}}\rho). \tag{2.20}$$

The calculated weight is a ratio of probabilities:

$$W = \frac{P(x;\sigma'_{\text{prod}})}{P(x;\sigma_{\text{prod}})} \cdot \exp(-x(\sigma'_{\text{prod}} - \sigma_{\text{prod}})\rho), \tag{2.21}$$

where σ'_{prod} and σ_{prod} are production cross sections for the data and Monte Carlo model respectively. The weight has two distinct contributions: the first one is the weight for the probability of interaction and the second one is for an attenuation of the particle flux after traveling distance x. If a particle exits the material or decays before interacting, only the second contribution is used, and the weight becomes:

$$W = \exp(-x(\sigma'_{\text{prod}} - \sigma_{\text{prod}})\rho) \tag{2.22}$$

Several different measurements have been used for the interaction probability re-weighting. Some of these experiments measured σ_{inel}. In that case, it is necessary to subtract σ_{qel} from the results. A list of all used measurements alongside with the explanation how σ_{qel} for different interactions was calculated is provided in Ref. [75].

2.5.2 Multiplicity re-weighting

Re-weighting of the differential hadron production is done by re-weighting differential multiplicities:

$$\frac{dn}{dp}(\theta, p_{in}, A) = \frac{1}{\sigma_{\text{prod}}(p_{in}, A)} \frac{d\sigma}{dp}(\theta, p_{in}, A), \tag{2.23}$$

where p_{in} is a momentum of the projectile, A is an atomic number, and θ is a polar angle between the produced particle and the initial particle. Similarly to the interaction probability re-weighting, the weight is calculated as a ratio between the data (usually NA61/SHINE) and Monte Carlo:

$$W = \frac{\left[\frac{dn}{dp}(\theta, p_{in}, A)\right]_{data}}{\left[\frac{dn}{dp}(\theta, p_{in}, A)\right]_{MC}}. \tag{2.24}$$

If the available data match Monte Carlo in the initial particle momentum and the target material, weights defined in Eq. 2.24 are applied directly. However, sometimes this is not the case. If the initial particle momentum is different, data measurements are scaled assuming the perfect Feynman scaling. The previously calculated weights are converted to the (x_F, p_t) phase space, where p_t is transverse momenta of the produced particles and x_F is a Feynman variable:

$$x_F = \frac{p_L}{p_L^{max}}. \tag{2.25}$$

The Feynman variable is a ratio of the longitudinal momentum of the produced particle and the maximum allowed longitudinal momentum this particle can have (momentum in the center of mass frame). If the target nuclei in the data are not the same to the simulation, additional scaling is applied which includes A-dependence of the multiplicities (see Ref. [80, 81, 82]):

$$E\frac{d^3\sigma(A_1)}{dp^3} = \left[\frac{A_1}{A_0}\right]^{\alpha(x_F, p_t)} E\frac{d^3\sigma(A_0)}{dp^3}, \tag{2.26}$$

where:

$$\alpha(x_F, p_t) = (a + bx_F + cx_F^2)(d + ep_t^2). \tag{2.27}$$

The scaling includes five parameters $(a-e)$ which are determined by fitting the data taken with different target nuclei. Measurements usually do not cover full phase space. For the missing regions data is extrapolated by using the so-called BMPT parametrization [80]:

$$E\frac{d^3\sigma(A_1)}{dp^3} = A(1-x_R)^\alpha(1+Bx_R)x_R^{-\beta}\left[1+\frac{a}{x_R^\gamma}p_t+\frac{a^2}{2x_R^\delta}p_t^2\right]e^{-\frac{ap_t}{x_R^\gamma}}, \tag{2.28}$$

where α, β, γ, δ, a, A, B are parameters to be determined, p_t is a transverse momentum, and x_R is a radial scaling variable:

$$x_R = \frac{E}{E_{cm}^{max}}, \tag{2.29}$$

is a ratio of the particle energy and maximum possible energy in the center of mass frame. More details about the re-weighting procedure can be found in Ref. [75, 83].

2.5.3 Hadron production uncertainties

Hadron production uncertainties can be divided into three main parts: uncertainties on the interaction probability re-weighting (related to production cross section σ_{prod}), uncertainties on the meson re-weighting and uncertainties on the baryon re-weighting. The dominant contributions come from the interaction probability re-weighting and the meson multiplicity tuning, depending on the neutrino energy, flavor and focusing mode. Uncertainties of the production cross section come mainly from the hadron production measurements themselves and are usually caused by the removal of the quasi-elastic contribution from the inelastic cross section. The quasi-elastic contribution is often not well constrained or it is model dependent.

Re-weighting of the mesons has two regimes: a low energy regime where uncertainties are dominated by pions re-weighting and a high energy regime where uncertainties are dominated by kaon re-weighting. Underlying cause for this is apparent: the low energy neutrinos are mostly produced in the pion decays, while high energy neutrinos are mostly produced in the kaon decays. Both pion and kaon re-weighting uncertainty can be divided into four components:

- the uncertainty of the hadron production measurements,
- the uncertainties of the scaling to different energies,
- the uncertainty of the target material re-weighting and
- the uncertainty of the extrapolation to the uncovered phase space.

The meson re-weighting uncertainty is dominated by the hadron production measurements errors, mostly from NA61/SHINE since they are mostly used for re-weighting. Secondary protons are also re-weighted with the NA61/SHINE data, but the secondary interactions of this protons outside of the target are not re-weighted since they contribute to less than 10% of the neutrino flux. However, uncertainties for these interactions are also estimated. Currently, the total hadron production uncertainty is around 9% and can be found in Ref. [75]

2.5.4 Hadron production measurements with the replica target

The total uncertainty of the neutrino flux is dominated by the hadron production uncertainty. Since produced hadrons have continuous energy spectra and can re-interact with various materials, scaling of the hadron production measurements to different energies and materials is necessary. However, around 90% of the flux is coming from the decays of hadrons created in the target. Thus, by measuring hadron spectra at the surface of the T2K replica target, it is possible to directly re-weight 90% of the neutrino flux. This kind of measurement does not require knowledge of the interaction probability, and all re-interactions inside the target are already included in the measurement. Re-interactions outside of the target must be treated in the same way as before. This greatly reduces the hadron production uncertainties of the neutrino flux. An estimate of the uncertainty after re-weighting the neutrino flux with the T2K replica target measurements is $4-5\%$. Consequently, the goal of the T2K collaboration is to reach this precision, since any future measurements of the δ_{CP} are predicated on the assumption that the flux uncertainty will be reduced. Because of the magnetic focusing and re-interactions, the interactions in the different parts of the target contribute differently to the neutrino flux as can be seen in Fig. 2.21. Any experiment capable of providing the measurements with the replica of the T2K target must also be able to reconstruct hadron position on the target surface in at least five longitudinal bins and the downstream target face. The only experiment, capable of installing the T2K replica target and measuring the hadron yields coming from its surface in the phase space of interest is the NA61/SHINE experiment at CERN.

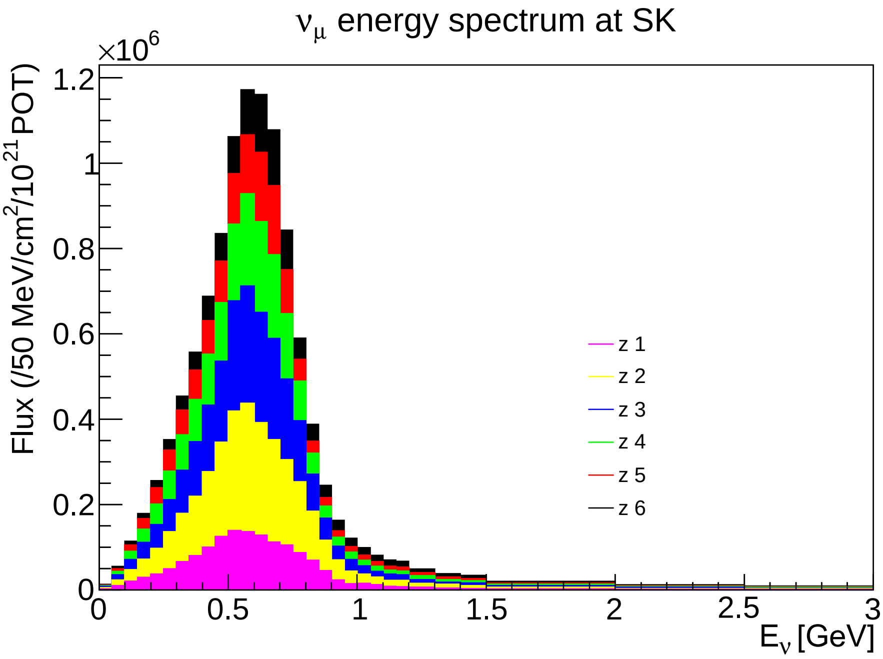

Figure 2.21: Contirbution of the different longitudinal bins to the flux at *Super-Kamiokande*.

Chapter 3

The NA61/SHINE experiment

Contents

The NA61/SHINE (SPS Heavy Ion and Neutrino Experiment) is a fixed-target, multi-purpose experiment located in the North Area of the CERN Super Proton Synchrotron (SPS). The experiment was proposed in 2006, while the pilot data-taking was performed in 2007. Main components of the experimental setup were inherited from the NA49 experiment [84]. A rich physics program of the NA61/SHINE can be divided into three main parts:

1. hadron production measurements for improving the neutrino flux prediction in the T2K and Fermilab-neutrino experiments,
2. hadron production measurements for improving the cosmic ray air-shower simulations, and
3. study of the onset of deconfinement and search for the critical point of strongly interacting matter in proton-proton, proton-nucleus, and nucleus-nucleus collisions.

The aim of this chapter is to present T2K-related measurements along with the experimental setup, reconstruction and calibration procedures used in these measurements.

3.1 Hadron production measurements for the T2K experiment

Hadron production measurements for the T2K experiment were performed by using 30.92 GeV/c secondary proton beam and two different targets: a thin carbon target and a T2K replica target. These measurements follow the ideas described in section 2.5. Measurements with the thin target were done to constrain primary interactions, while measurements with the T2K replica target were designed to constrain all interactions inside the T2K target. Dimensions and characteristics of the targets are described in subsection 3.2.2.

3.1.1 Data-taking periods

Data-taking for the T2K experiment started in 2007 and continued in 2009 and 2010. All data-taking periods are summarized in Tab. 3.1. Low statistics data-sets collected in 2007, both with the thin [77, 78] and replica targets [85] were used for development of the dedicated calibration and analysis procedures. Moreover, the thin target results from 2007 were also successfully incorporated in the T2K neutrino flux simulation and considerably reduced hadron production uncertainty. Measurements performed in 2009, again both with the thin [79] and replica targets [86] had ten times larger statistics, and they will be discussed in more details in the next two subsections. Finally, a large statistics data-set with the replica target was taken in 2010, and the analysis of this data-set is the main topic of this thesis.

Beam	Target	Year	Triggers [10^6]	Results
p at 31 GeV/c	thin	2007	0.7	π^+, π^-, K^+, K^0_s, Λ multiplicities and σ_{prod} [77, 78]
	replica	2007	0.2	proof of principle for replica target measurements [85]
	thin	2009	5.4	π^+, π^-, K^+, K^-, p, K^0_s, Λ multiplicities and σ_{prod} [79]
	replica	2009	2.8	π^+, π^- multiplicities on target surface [86]
	replica	2010	10.1	π^+, π^-, K^+, K^-, p multiplicities on target surface (this thesis)

Table 3.1: The NA61/SHINE data collected for the T2K experiment.

3.1.2 Thin target measurements with 2009 data-set

The purpose of the thin target measurements, as explained in section 2.5, is to constrain primary production of the neutrino parent particles. The aim of 2009 thin target measurements was to perform high-precision measurements of $\pi^{\pm}$, $K^{\pm}$, p, K^0_s and Λ production in proton-carbon interactions at 31 GeV/c. As a result, it allowed to reduce further statistical and systematic uncertainties of our results obtained in 2007 and to measure K^- spectra for the first time. Thin target measurements can be divided into two main parts: measurements of the production cross-section (σ_{prod}) and measurements of the hadron multiplicities. Measurements of the production cross-section are used to constrain interaction probability of protons at 31 GeV/c in carbon, while measurements of the hadron multiplicities constrain production of hadrons. In addition to the inelastic events, a small fraction of elastic and quasi-elastic events is selected because of the inefficiencies in the NA61/SHINE trigger system. For this reason, we cannot measure production cross-section directly. Rather we measure a so-called trigger cross-section (σ_{trig}). Those inefficiencies are corrected by applying Monte Carlo correction factors. By removing elastic events and correcting for any lost quasi-elastic and inelastic events, we obtain information about the inelastic cross section. On the other hand, if quasi-elastic events are also removed (i.e., fragmentation of the nuclei, ...), we obtain the production cross section. Usage of Monte Carlo models for correcting trigger inefficiencies creates a model dependence of our result. This was studied in great detail, and corresponding systematic uncertainty was assigned to the results [87]

$$\sigma_{\text{inel}} = (258.4 \pm 2.8(\text{stat}) \pm 1.2(\text{det})^{+5.0}_{-2.9}(\text{mod}))\,\text{mb}, \tag{3.1a}$$

$$\sigma_{\text{prod}} = (230.7 \pm 2.8(\text{stat}) \pm 1.2(\text{det})^{+6.3}_{-3.5}(\text{mod}))\,\text{mb}. \tag{3.1b}$$

Detector systematic uncertainty comes from uncertainty in the size of the scintillator counter which discards elastic events. The importance of 2009 measurement is in uncertainty which is reduced by a factor of two when compared to the 2007 result. Comparison of our results with previous measurements is shown in Fig. 3.1. The NA61/SHINE measurement from 2009 is consistent with our measurement from 2007.

Spectra of produced hadrons are measured in the momentum and polar angle (p,θ) phase space. It is important for the T2K experiment to measure hadron spectra in the regions of the phase space which contribute to the neutrino flux at *Super-Kamiokande* and *ND280*. T2K phase space is shown for the primary hadrons which contribute to the neutrino flux in *Super-Kamiokande* in Fig. 3.2 and 3.3. Black lines represent coverage of the phase space by NA61/-SHINE measurements. Our measurements cover most of the regions of interest except very forward high momentum protons. This is due to poor forward acceptance of the detector with the magnetic field configuration used for this data-taking. The results are presented in the form of the double differential multiplicities which are calculated as a double differential cross section normalized by the total production cross section:

$$\frac{d^2n}{dpd\theta} = \frac{1}{\sigma_{\text{prod}}}\frac{d^2\sigma_h}{dpd\theta}. \tag{3.2}$$

In this form, our measurements show a number of hadrons per number of beam protons in the given momentum and polar angle bin. Since we measured both spectra of charged and neutral hadrons, two distinct analysis types were used. Particle identification for charged hadrons by a single method is not possible in the whole (p,θ) phase space. Because of that, two different particle identification techniques were used: energy loss and time of flight. For the measurement of the π^- spectra, we also used analysis without particle identification in which contamination by other hadrons is corrected with Monte Carlo simulation. All of the methods give consistent results in the overlapping regions of the phase space. In the case of neutral hadrons, we select so-called V^0 decay candidates which are characterized by two oppositely charged tracks created at the same point outside of the target. By assuming the mass of the outgoing tracks, the invariant mass of the V^0 candidate is calculated. A number of neutral hadrons in each bin is obtained from the signal and background fits to the invariant mass spectra. More details about the analyses and systematic uncertainties can be found in [79]. Although the main reason for thin target measurements is in constraining T2K neutrino flux, our results can also be used for checking the validity of various Monte Carlo models. A comparison of $\pi^{\pm}$, $K^{\pm}$, p, K^0_s and Λ yields with several models was performed. In particular, we used: FTF_BIC physics list from GEANT4.9.5, GEANT4.9.6 and GEANT4.10 [88] [89], QGSP_BERT physics list from GEANT4.10, EPOS1.99 [90], VENUS4.12 [91] and GIBUU1.6 [92] [93] models. Only some of the comparisons are presented here in Fig. 3.4 - 3.10, while all comparison can be found in CERN preprint [94]. Hadron yields, total uncertainty, and comparison with two chosen models are

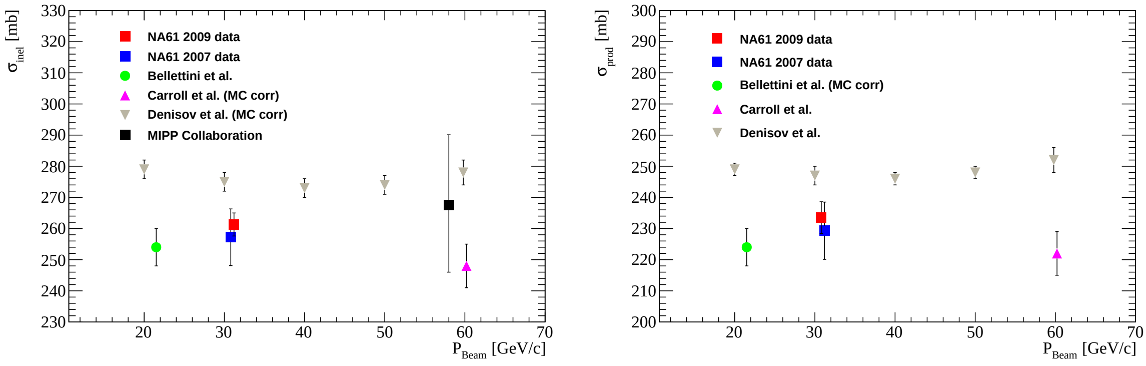

(a) (b)

Figure 3.1: Measurements of the inelastic cross-section (a) and production cross-section (b). The results are compared with other measurements, in particular with the NA61/SHINE measurement from 2007.

shown in each figure. In the case of $\pi^{\pm}$ spectra, FTF_BIC physics list gives the best prediction, while other models show larger inconsistencies. For kaons and more massive hadrons, none of the models give the accurate prediction of the hadron spectra. It is interesting to note that VENUS4.12 which is the oldest model used here gives best predictions for baryons (p and Λ), although some differences up to 40% can be observed.

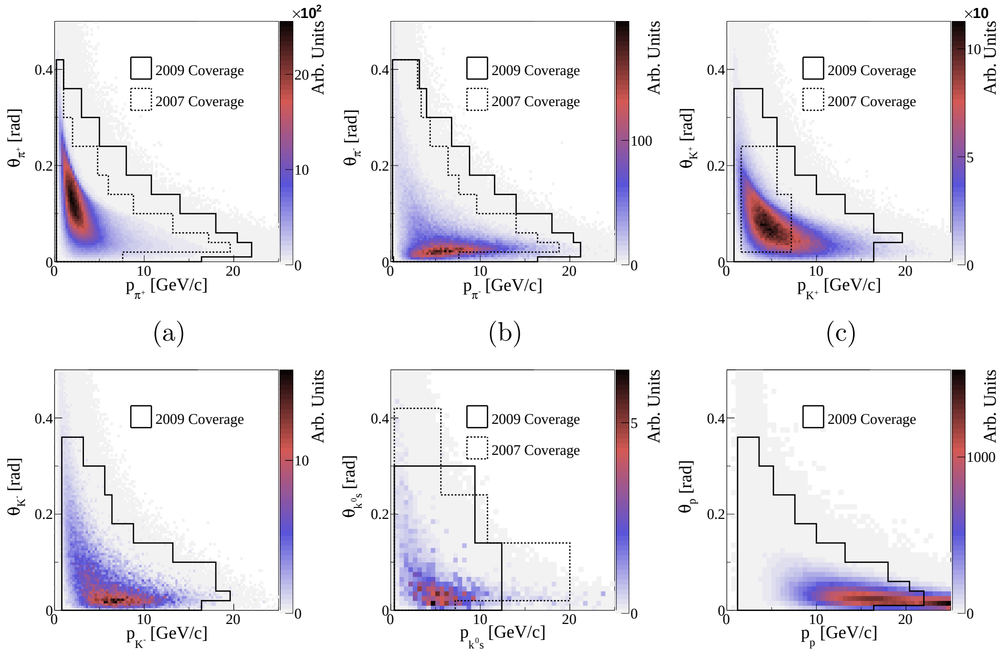

(a) (b) (c)

(d) (e) (f)

Figure 3.2: The phase space of $\pi^{\pm}$, $K^{\pm}$, K_s^0 and protons contributing to the neutrino flux at *Super-Kamiokande* in positive focusing configuration. Solid and dashed line represent coverage of the NA61/SHINE measurements from 2009 and 2007 respectively.

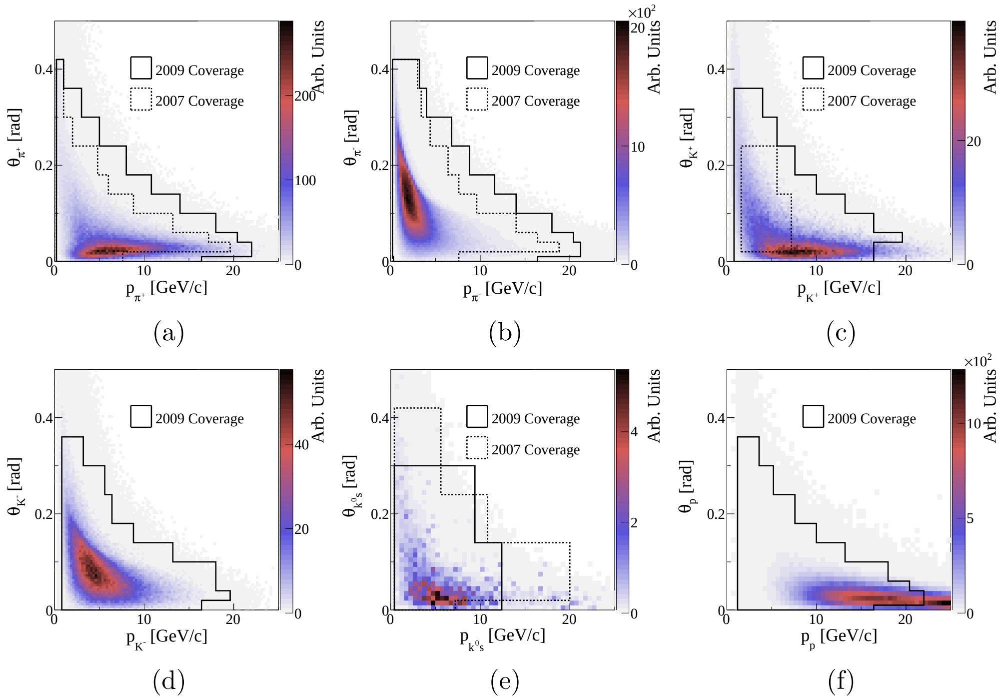

(a) (b) (c)

(d) (e) (f)

Figure 3.3: The phase space of $\pi^\pm$, $K^\pm$, K^0_s and protons contributing to the neutrino flux at *Super-Kamiokande* in negative focusing configuration. Solid and dashed line represent coverage of the NA61/SHINE measurements from 2009 and 2007 respectively.

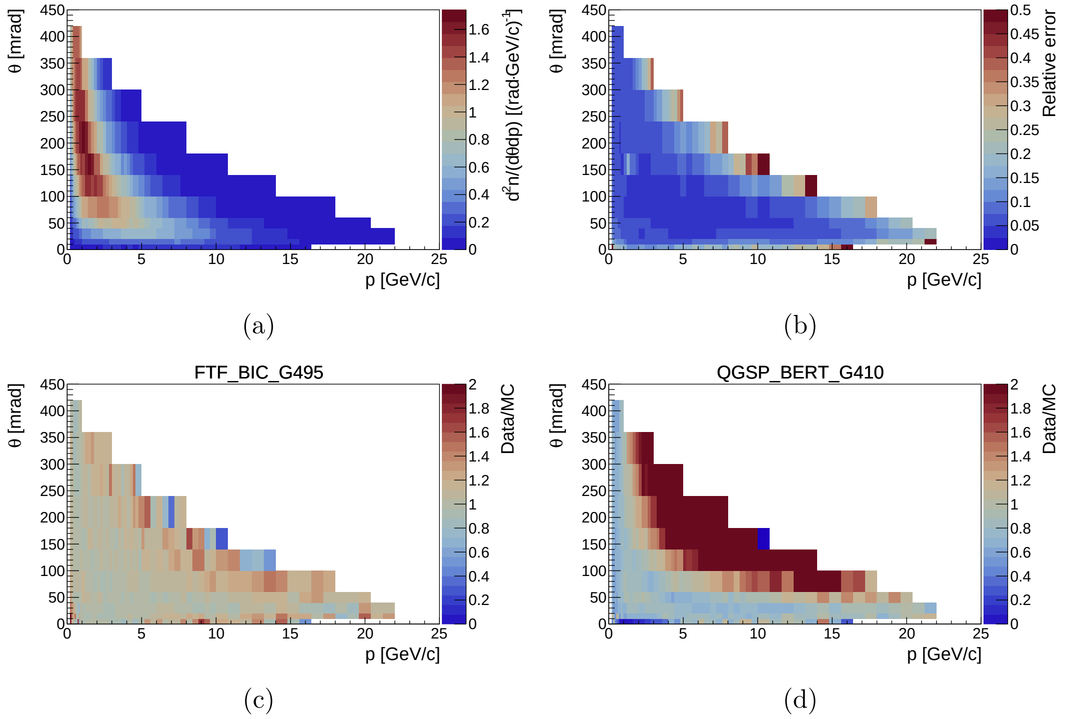

(a) (b)

(c) (d)

Figure 3.4: Double differential multiplicities of π^+ mesons (a), total fractional errors (b), comparison with FTF_BIC physics list from Geant4.9.5 (c) and comparison with QGSP_BERT physics list from Geant4.10 (d).

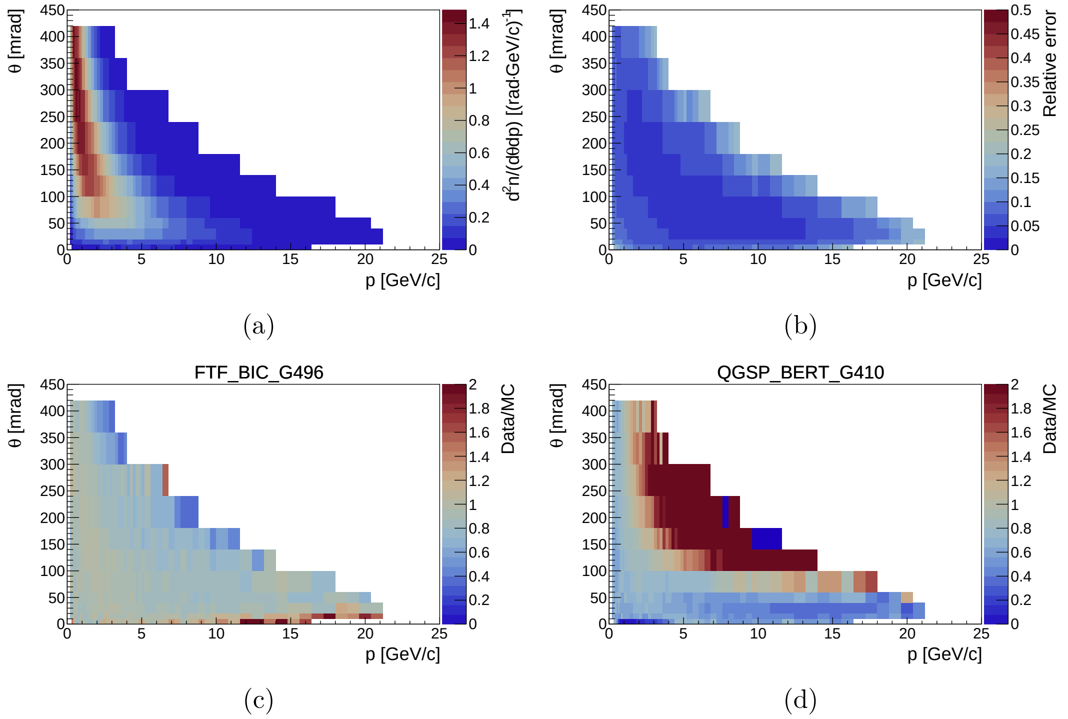

(a) (b)

(c) (d)

Figure 3.5: Double differential multiplicities of π^- mesons (a), total fractional errors (b), comparison with FTF_BIC physics list from GEANT4.9.6 (c) and comparison with QGSP_BERT physics list from GEANT4.10 (d).

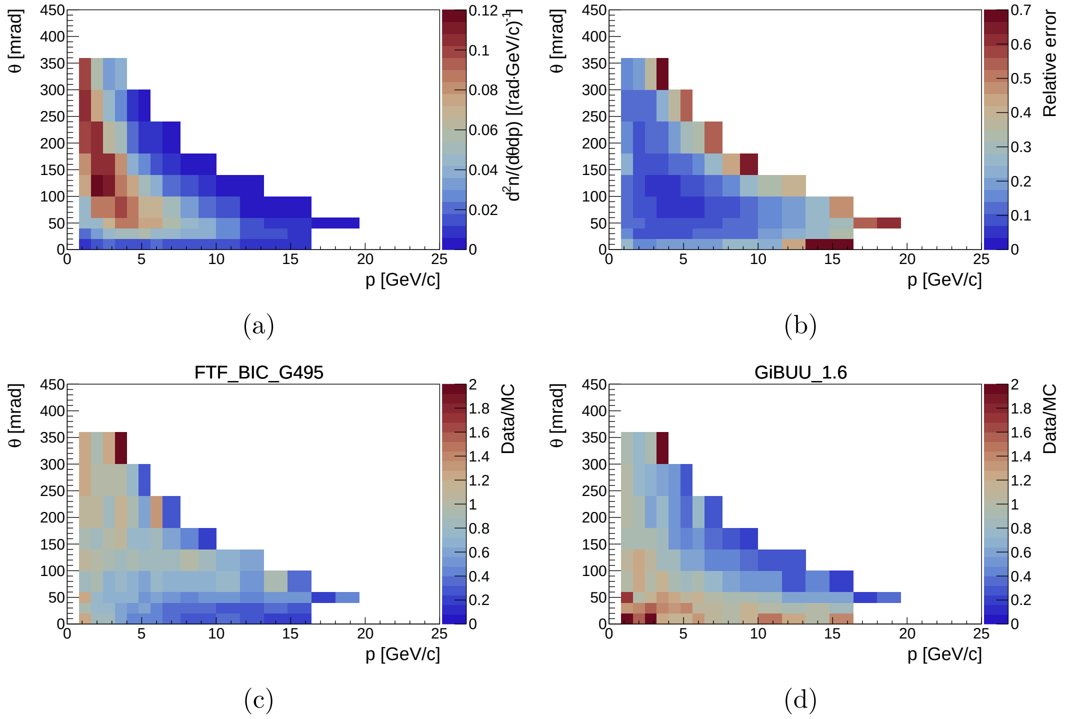

(a) (b)

(c) (d)

Figure 3.6: Double differential multiplicities of K^+ mesons (a), total fractional errors (b), comparison with FTF_BIC physics list from GEANT4.9.5 (c) and comparison with GIBUU1.6 model (d).

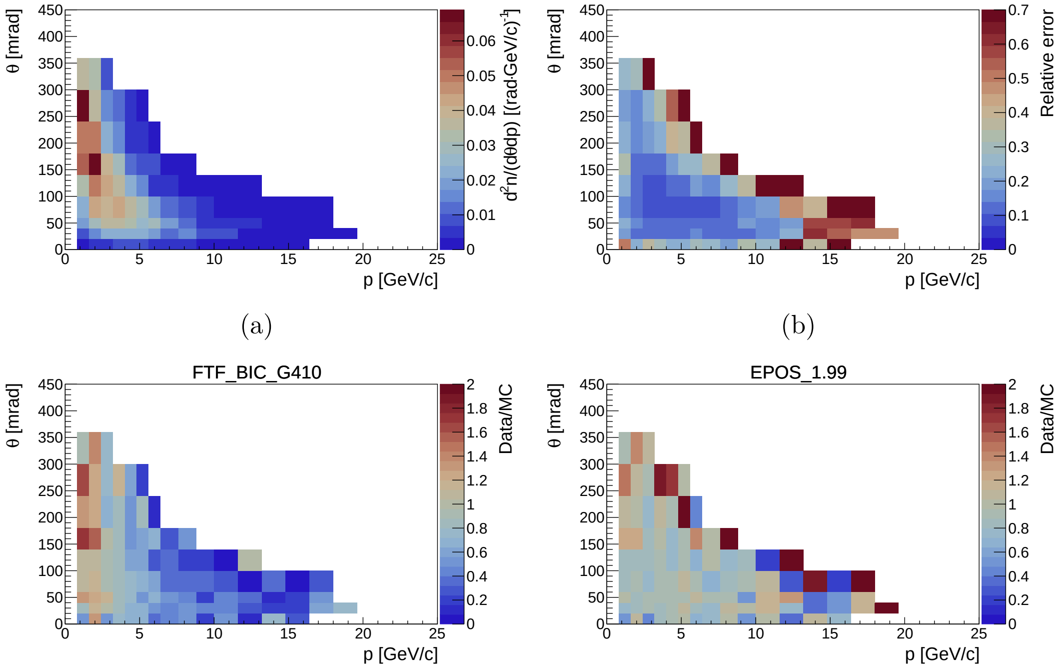

(a) (b) (c) (d)

Figure 3.7: Double differential multiplicities of K$^-$ mesons (a), total fractional errors (b), comparison with FTF_BIC physics list from GEANT4.10 (c) and comparison with EPOS1.99 model (d).

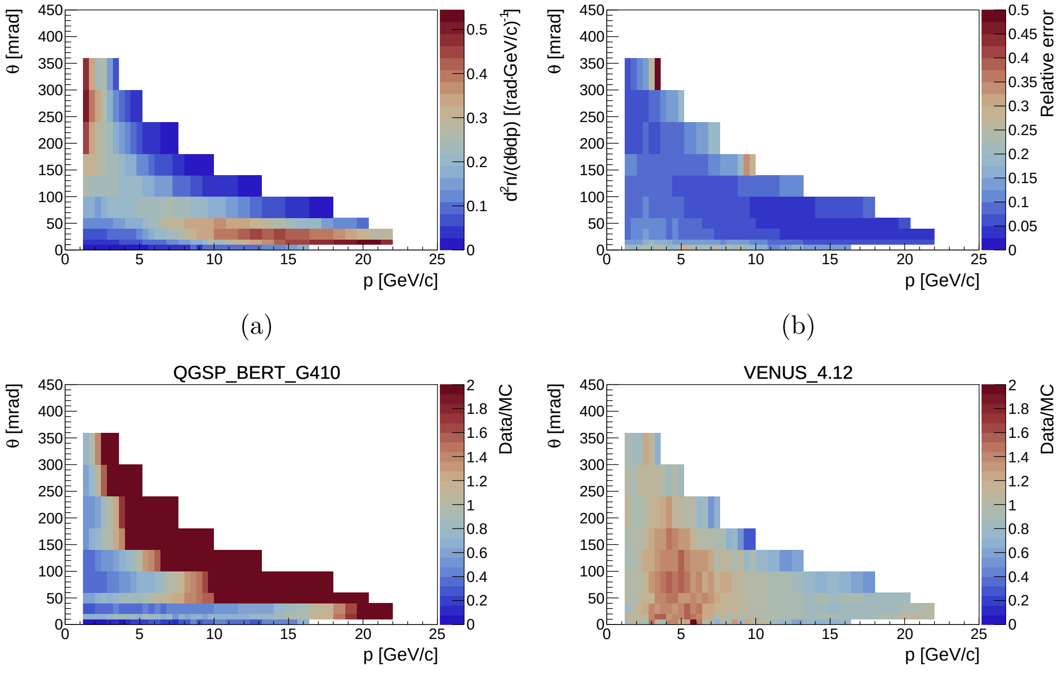

(a) (b) (c) (d)

Figure 3.8: Double differential multiplicities of p (a), total fractional errors (b), comparison with QGSP_BERT physics list from GEANT4.10 (c) and comparison with VENUS4.12 model (d).

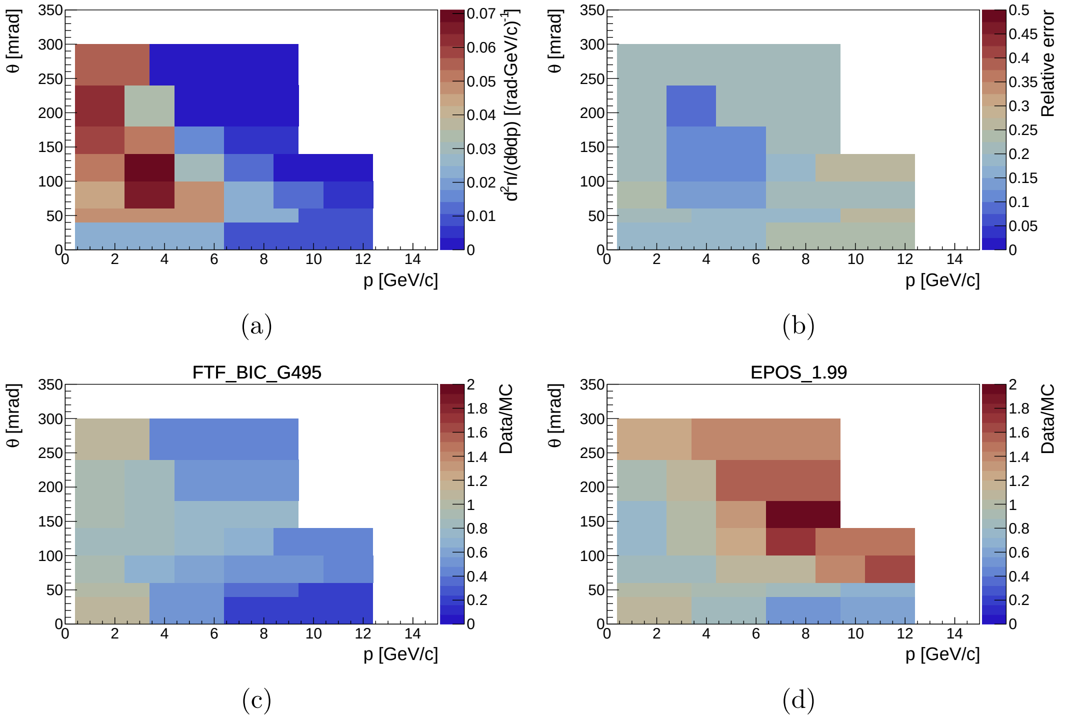

(a) (b)

(c) (d)

Figure 3.9: Double differential multiplicities of K_s^0 (a), total fractional errors (b), comparison with FTF_BIC physics list from GEANT4.9.5 (c) and comparison with EPOS1.99 model (d).

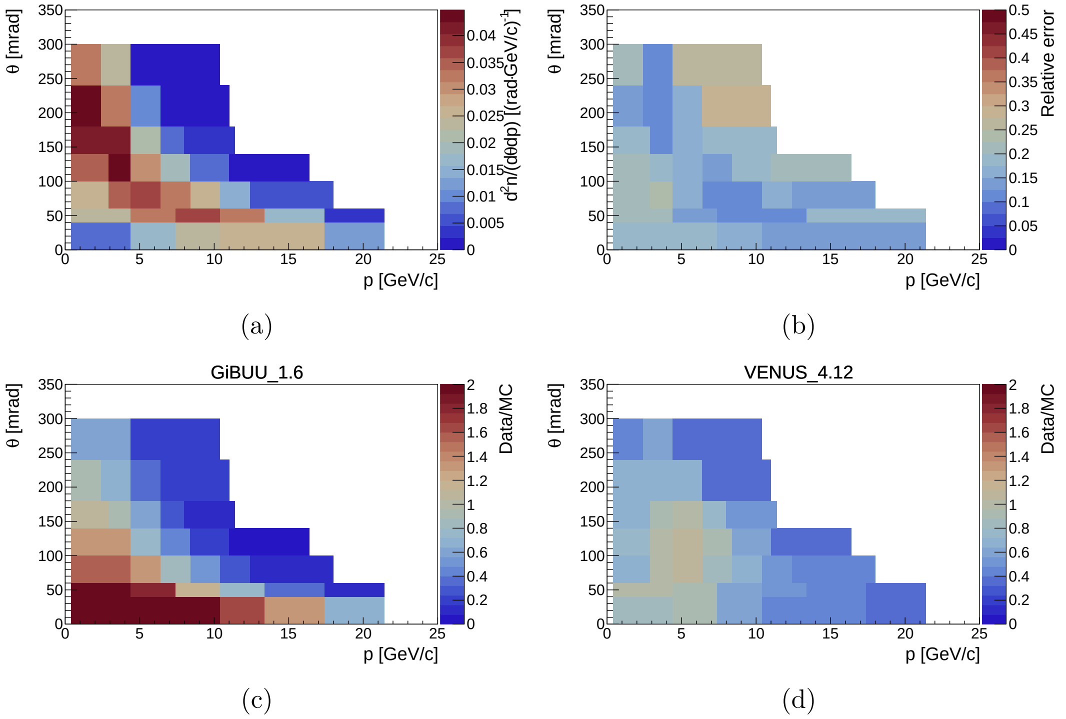

(a) (b)

(c) (d)

Figure 3.10: Double differential multiplicities of Λ (a), total fractional errors (b), comparison with GIBUU1.6 (c) and VENUS4.12 (d) models.

3.1.3 The T2K replica target measurements with 2009 data-set

The purpose of hadron production measurements with the T2K replica target is to measure the emission of hadrons from the 90 cm-long target. The measurement includes a contribution from the secondary and tertiary hadrons produced inside the target and, because of that, independent measurement of the p + C production cross-section is not necessary. In 2009, we measured only $\pi^{\pm}$ spectra [86] in the phase space of momentum, polar angle and longitudinal position at the target surface (p, θ, z). One of the requirements of the T2K collaboration is to use at least six longitudinal bins. Since the phase space has one more dimension, collected statistics were not enough to measure spectra of other hadrons like it was done in the case of the thin target measurements. The results are presented in the form of differential multiplicities which are in this case equal to the number of hadrons in a given bin normalized by the number of beam protons and momentum bin size. An example of the results for π^{+} and π^{-} is shown in Fig. 3.11 alongside with FLUKA2011 model [95] [96] prediction. FLUKA2011 was selected because it is used for simulation of interactions inside the target in the T2K neutrino beam simulation [75]. It gives consistent predictions of the $\pi^{\pm}$ yields when compared to our data. The figure 3.11 shows a small fraction of the angular range. Rest of the spectra will be shown and discussed at the later stage as a comparison with our new measurements.

3.2 Experimental setup

Experimental setup of the NA61/SHINE will be discussed in this section, but the discussion will be centered around the setup used during the 2010 run for the replica target measurements. The setup can be seen in Fig. 3.12 with the coordinate system definition located in the bottom right corner. The z-axis points in the direction of the beam, while the x-axis is directed to the left from the beam point of view and the y-axis points upwards. The NA61/SHINE experiment is a hadron spectrometer, and it consists of five Time Projection Chambers (TPCs). Two of the TPCs (VTPC-1, VTPC-2) are located inside the magnetic field of two superconducting magnets. Between the VTPCs there is a small TPC called GTPC which covers the very forward region. Downstream from the VTPCs, two large main TPCs (MTPC-L and MTPC-R) are positioned symmetrically to the beam-line. A scintillator wall for measuring particle time of flight is located behind the MTPCs. Beam position in front of the TPCs is measured by three Multi-Wire Proportional Chambers (MWPCs), called Beam Position Detectors (BPD1, BPD2, and BPD3), while beam identification is done by Cherenkov Differential Counter with Achromatic Ring Focus (CEDAR) [97] and Threshold Cherenkov Counter (THC). Several scintillator counters are used in coincidence and anti-coincidence for triggering event. More details about important detector subsystems and the beam-line will be presented in the following subsections.

3.2.1 Beam-line and triggers

Search for the critical point of strongly interacting matter requires scan through the phase space of energy and system size, which is only possible by changing beam and target composition as well as beam momentum. Furthermore, hadron production measurements also require different hadron beams. Consequently, the NA61/SHINE experiment uses secondary hadron (p, $\pi^{\pm}$, $K^{\pm}$) and ion beams (Be, Ar, Pb, ...) with the momentum range from 13 GeV/c to 400 GeV/c. To achieve this, primary protons or ions from the SPS are extracted and transported around 1 km towards the primary target. Primary target station consists of several beryllium plates which are located 11 m underground to contain radiation. Secondary particles produced

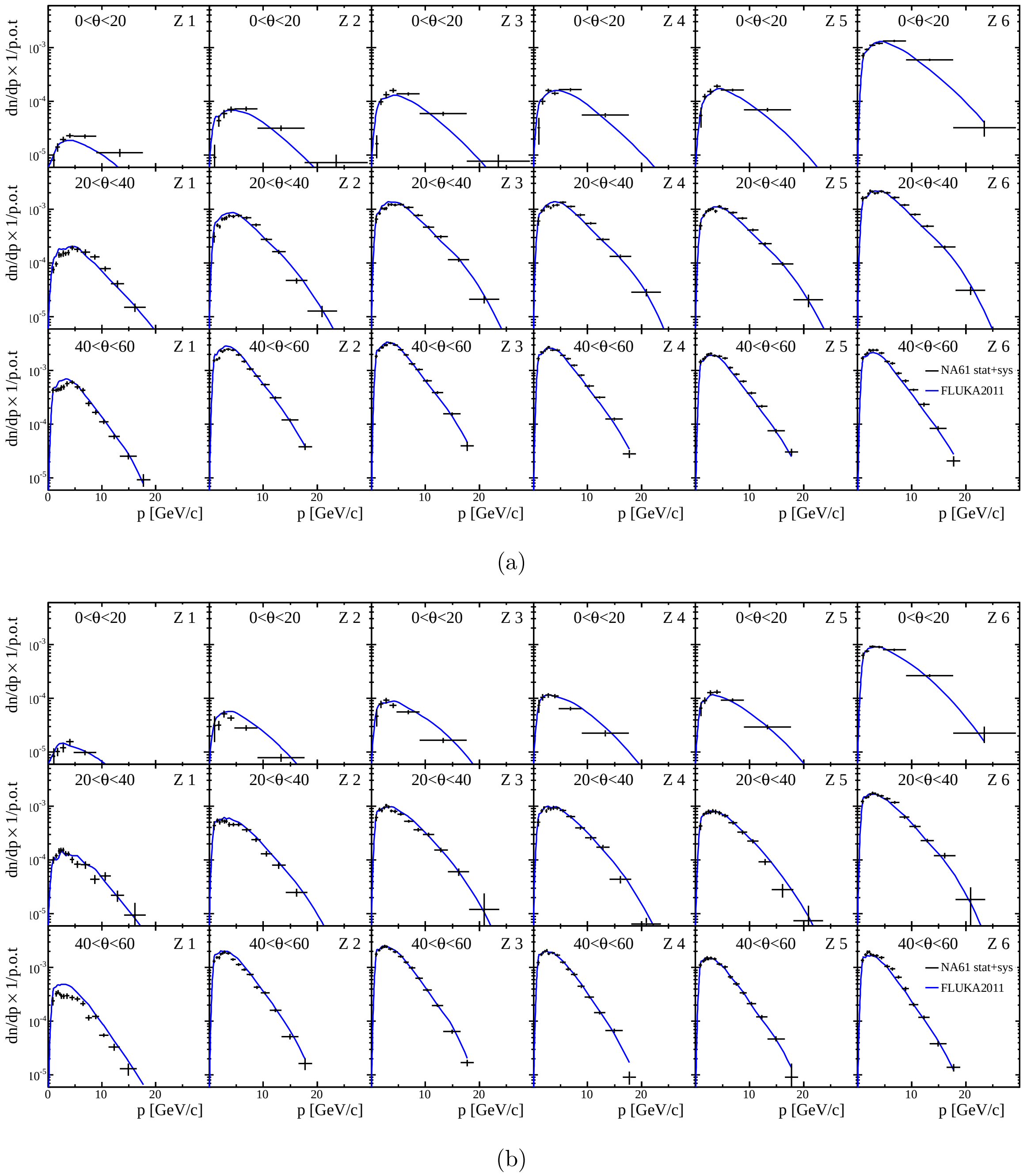

Figure 3.11: Differential multiplicities of π^+ (a), and π^- (b). Each column is a different z bin, while each row shows different polar angle intervals. The blue line is a FLUKA2011 prediction.

in the primary interactions are then used as a NA61/SHINE beam and transported towards the experiment by the so-called H2 beam-line. Beam particles are selected according to their rigidity (momentum to charge ratio) by two spectrometers and set of collimators downstream from the primary target. In addition, the incident angle of the primary beam can be changed to modify production angle of the desired secondary particles. Beam particles which are selected

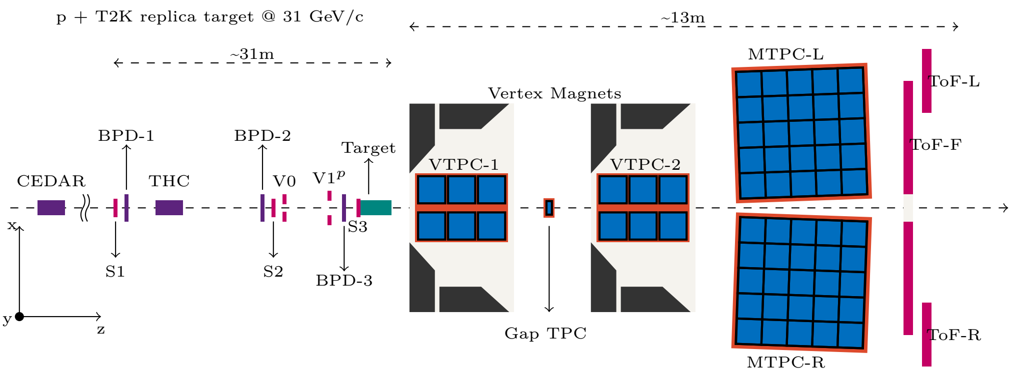

Figure 3.12: NA61/SHINE setup used for the T2K hadron production measurements.

by rigidity selection are usually mix of different hadrons and leptons with similar rigidity and therefore must be identified before hitting the NA61/SHINE target. This is done differently for hadrons and ions. Here, only selection of hadron beam particles will be discussed because it is used for hadron production measurements. More information on ion beams can be found in [76]. For the hadron beams, identification is done by the already mentioned CEDAR. This counter is filled with gas, usually with helium for beam momenta lower than 60 GeV/c and with nitrogen for higher momenta. If beam particle enters the counter, it radiates Cherenkov light cone which is in turn transported by the optical system onto a diaphragm. The diaphragm has a circular slit through which light passes towards eight photomultiplier tubes (PMTs). The pressure of the gas can be tuned so that only light coming from desired beam particles passes through the slit. Signals from at least six channels are used in coincidence for the beam identification. Furthermore, to increase the purity of the beam, THC is tuned so that desired beam particles have velocity below Cherenkov threshold and it is used in anti-coincidence. Total number of misidentified particles is below 0.8%.

Except for two Cherenkov counters, there are several scintillator counters in the beam-line which are used to ensure that the beam hits the NA61/SHINE target. The list of all scintillator counters used in the case of the T2K replica target measurements alongside with their dimensions is shown in Tab. 3.2. Counters with the hole are used in anti-coincidence. The counter S1 is providing the start signal for the whole trigger system and the reference time. It has four PMT channels, although only one of them is used in the trigger system. However, other channels are used during calibration to correct for the time jitter of the start signal.

Counter	Dimension [cm]
S_1	$6 \times 6 \times 0.5$
S_2	$\Phi = 2.8$, 0.2 thickness
S_3	$\Phi = 2.6$, 0.5 thickness
V_0	$\Phi = 8$, $\Phi_{hole} = 1$, 0.2 thickness
V_1'	$30 \times 30 \times 1$, $\Phi_{hole} = 4$

Table 3.2: List of the scintillator counters used in the trigger logic.

Different combinations of the counters are used for triggering the events. In the hadron production measurements in 2010, four different triggers were used. The triggers were named T1-T4 and their exact definitions listed in Tab. 3.3. Trigger T1 represents only events with a selected proton beam. Counter V_0 ensures that only a narrow beam is selected, around 0.7 cm in size at the upstream target face. It will be explained in the latter stages of this thesis why the beam profile is important. Although T2 trigger selects wider beam, the S3 counter which is glued to the upstream target face and has the same radius as the target, ensures that beam particles hit the target. Main trigger T3 is the same as the T2 trigger, but in contrast to the T2 trigger, it also selects narrower beam (same as T1). And finally, trigger T4 selects only wide beam without identification or requirement that beam hits the target. In addition, the main trigger was recorded each time, while other triggers were downscaled and only some fraction of them was recorded. To precisely determine trajectories of the beam particles, triggers are not enough. For this reason, we use measurements by already mentioned beam position detectors (BPDs). The detectors are proportional chambers filled with a mixture of Ar and CO_2. Each BPD consists of six planes: a central plane, two orthogonal wire planes, and two outer cathode readout planes. The readout planes are made of 24 aluminized mylar strips which are $48 \times 2 \times 0.025\,\mu$m in size. Usually, passing beam particles induce the signal on five strips, and this gives position resolution of about $200\,\mu$m. If the signals in all three detectors are good, this allows for precise determination of the beam position at the upstream surface of the T2K replica target.

Trigger	Definition
T1	$\mathrm{S1} \cdot \mathrm{S2} \cdot \overline{\mathrm{V}}_0 \cdot \overline{\mathrm{V'}}_1 \cdot \mathrm{CEDAR} \cdot \overline{\mathrm{THC}}$
T2	$\mathrm{S1} \cdot \mathrm{S2} \cdot \mathrm{S3} \cdot \overline{\mathrm{V'}}_1 \cdot \mathrm{CEDAR} \cdot \overline{\mathrm{THC}}$
T3	$\mathrm{S1} \cdot \mathrm{S2} \cdot \mathrm{S3} \cdot \overline{\mathrm{V}}_0 \cdot \overline{\mathrm{V'}}_1 \cdot \mathrm{CEDAR} \cdot \overline{\mathrm{THC}}$
T4	$\mathrm{S1} \cdot \mathrm{S2} \cdot \mathrm{S3} \cdot \overline{\mathrm{V'}}_1$

Table 3.3: List of the scintillator counters used in the trigger logic.

3.2.2 The T2K replica target

It was already shown in subsection 2.3.3 that the T2K target is a rather complex object and therefore, it is not straightforward to install it in the NA61/SHINE beam-line. For this reason, a simplified version of the target, which is named as the T2K replica target, is used for this purpose. It is made of the same graphite. However, it does not contain cooling and thin titanium casing on the surface. Besides these differences, T2K replica target has a flange at the upstream edge. The inner part of the flange is made of the graphite, while the outer shell is made of aluminum. The flange is used for the purpose of anchoring the target to the holder. On the outside layer of the flange, there is a hole which ensures that beam hits the graphite. Scintillator counter S3 is fitted into the hole, while BPD3 is mounted on top of that. Schematic view of the target alongside with the picture of the mounted target without BPD3 is shown in Fig. 3.13. Also, technical characteristics of the replica target are compared to the thin target in Tab. 3.4. Downstream target face is fixed by a thin plastic tread tied to the plastic ring to minimize material budget between produced particles and the TPCs. It is important to note that density of the T2K replica target is higher by around 1.5% when compared to the density of the T2K target. This difference is equal in size to the density measurement uncertainty (see table 3.4). Nominally, the same graphite was used as for the real T2K target (Toyo Tanso IG-43, see Ref. [98]), but there are possible fluctuations in the density from sample to sample as stated on the Toyo Tanso's web page. The uncertainty of the replica target density must be taken into account when hadron yields from the surface of T2K replica target are used for the re-weighting of the neutrino flux.

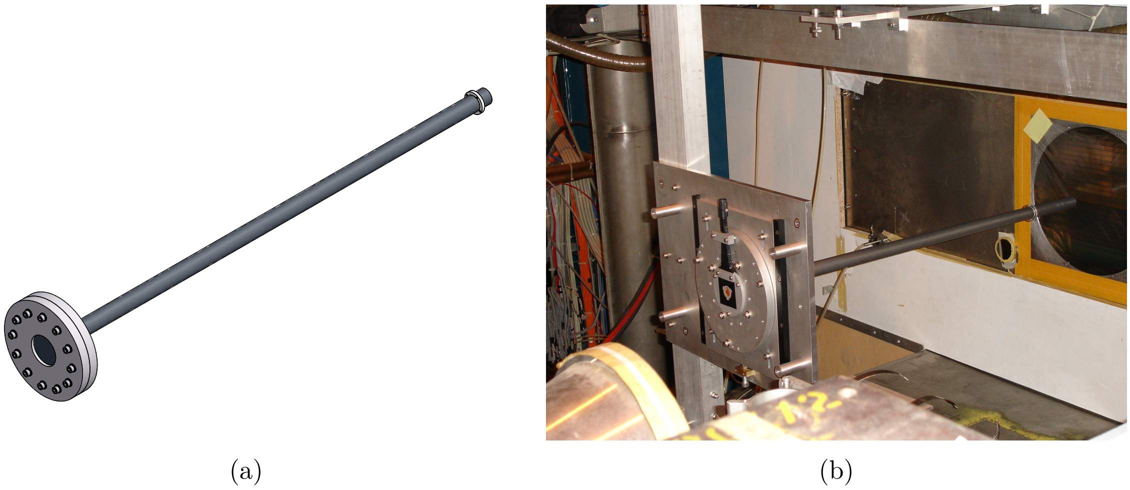
(a)

(b)

Figure 3.13: Schematic overview of the T2K replica target (a), mounted target without the BPD3 (b).

Target	Thin	T2K replica
Material	Graphite	Graphite
Density [g/cm^3]	1.84 ± 0.03	1.83 ± 0.03
Length [cm]	2	90
x-Section	2.5×2.5 cm^2	$\oslash = 2.6\,\mathrm{cm}$
Int. length [λ_I]	0.04	1.9

Table 3.4: Dimension and characteristics of the thin and the T2K replica target.

3.2.3 Time projection chambers

It was already stated in the introduction of this chapter that tracking system consists of five TPCs. Each TPC is made of gas chambers filled with a mixture of Ar and CO$_2$, support frame and readout chambers (MWPC). When a particle passes through the gas, it leaves a trail of ionized atoms and electrons. The high electric field is provided between the plates of the TPCs. The field must be uniform to get constant drift velocity for the electrons drifting towards the readout plane. This is achieved by 25 μm wide aluminized mylar strips which go around the surface of the chamber. The voltage is divided stepwise from the cathode at the bottom of the chamber. The composition of the VTPC and a signal generation mechanism are shown in Fig. 3.14. The readout planes work in the proportional range. Electrons drift through the gating grid and cathode plane towards the anode sense wires. There, electron signal is amplified by a factor of $5 \cdot 10^4$ because of the avalanche process in the strong electric field near the wires.

The signal is then induced in the segmented pad plane which provides measurements of the track's x and y position, while measurement of the drift time provides z position. The readout of the signal is performed by TPC Front End Electronics (FEE) which replaced electronics from the NA49 experiment to increase the readout speed. In total 32 channels are available per one FEE. The electronics cards pre-amplify the charge signal and store it in the capacitor array. Afterwards, it is digitized by Wilkinson Analog to Digital converter (ADC). Although all TPCs work on the same principle, there are differences in size (number of sectors), gas composition, pad size and alignment and drift voltage. These are summarized in Tab. 3.5.

	VTPC-1	VTPC-2	MTPC-L/R	GTPC
Size (L×H×W) [cm]	$250 \times 200 \times 98$	$250 \times 200 \times 98$	$390 \times 390 \times 180$	$30 \times 81.5 \times 70$
# of pads/TPC	26886	27648	63360	672
Pad size [mm]	$3.5 \times 28(16)$	3.5×28	3.6×40, 3.6×40	4×28
Drift length [cm]	66.60	66.60	111.74	58.97
Drift velocity [cm/μs]	1.4	1.4	2.3	1.3
Drift field [V/cm]	195	195	170	173
Drift voltage [kV]	13	13	19	10.2
Gas Mixture	Ar/CO_2 (90/10)	Ar/CO_2 (90/10)	Ar/CO_2 (95/5)	Ar/CO_2 (90/10)
# of sectors	2×3	2×3	5×5	1
# of padrows	72	72	90	7
# of pads/padrow	192	192	192, 128	96

Table 3.5: Parameters of the VTPCs, MTPCs and GTPC [76].

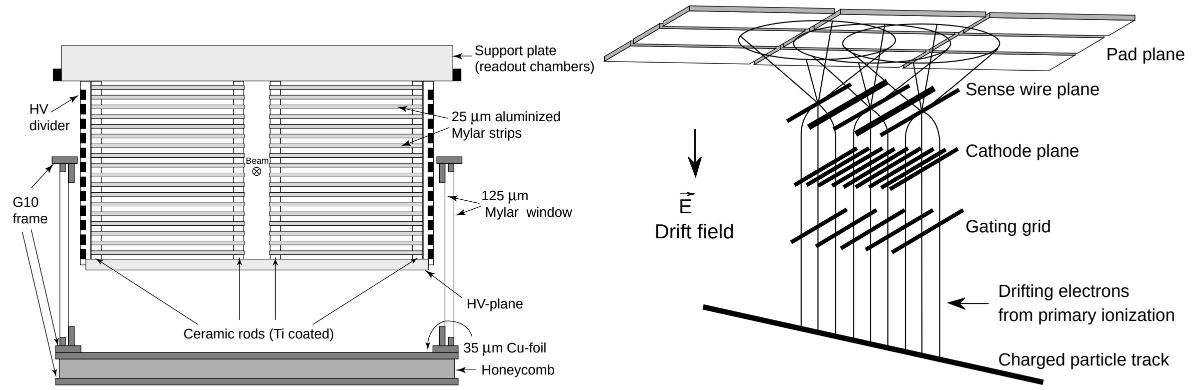

(a) (b)

Figure 3.14: Schematic drawing of the VTPC (a) and TPC readout scheme (b) [84].

While TPCs measure trajectory of the particle, additional pieces of information are needed for measuring particle yields. Therefore, VTPCs and GTPC are immersed into the field of two superconducting dipole magnets for measuring charge and momentum of the particles. The magnets have a total bending power of 9 Tm, and at the standard setting, the field is around 1.5 T in the first and 1.1 T in the second magnet. This setting is used for beam momenta larger than 150 GeV/c, and it is optimized to maximize spectrometer acceptance. For lower beam momenta, the magnetic field is scaled down. Otherwise, most of the low momentum tracks are bent out and never reach the MTPCs. Additional information about magnets, gas system and

the TPC electronics can be found in [84] and in [76].
Achieved momentum resolution is around 1% or better depending on the number of clusters in the VTPCs and GTPC. The NA61/SHINE experiment suffers from low coverage of the high-momentum forward going tracks whose momenta is usually measured just by GTPC. In this case, momentum resolution drops significantly. This issue has been addressed by developing and building two additional forward TPCs (FTPC-1 and FTPC-2). These TPCs have been used for the first time in July of 2017. The energy loss measurement has a resolution of around 4%, and it depends on the number of clusters in the TPCs. These measurements are not performed in the GTPC since its maximum of seven clusters would not improve dE/dx measurement in any significant way.

3.2.4 Forward time of flight wall

The forward time of flight wall (ToF-F wall) is a detector used for measuring particle time of flight (*tof*). The purpose of the *tof* measurement is particle identification, and it is complementary to the energy loss measurement. The ToF-F wall was built for the sole purpose of hadron production measurement for the T2K experiment. It was constructed in 2007, and originally it consisted of 8 modules. However, two additional modules were added in 2009. The modules were mounted on the frame just behind the MTPCs. Each module is an independent detector and consists of eight scintillator slats which are placed in two rows (zig-zag pattern) with 1 cm overlap between them. The slats are made of the plastic scintillator (Bicron BC-408) and have dimensions of $120 \times 10 \times 2.5\,\text{cm}^3$. Size and position of the ToF-F detector are shown in Fig. 3.15. A numbering of the slats is as follows: the first slat is located close to the corner of the MTPC-L at $x \approx 370\,\text{cm}$ (Jura side), while the last slat is close to the corner of MTPC-R at $x \approx -370\,\text{cm}$ (Saleve side). The light from each slat is read out by two Fast-Hamamatsu R1828 PMTs located on the top and bottom of the slat. For this reason, slats are wrapped with aluminum foil to reflect light towards the PMTs. On top of that, slats were covered with black plastic foil and tape. The signals from the 160 PMT channels are passed to the constant fraction discriminators (CFD). Each CFD has divider which divides signal for separate charge and time measurement. While CFDs provide stop signal, the start signal is provided by S1 counter which is part of the

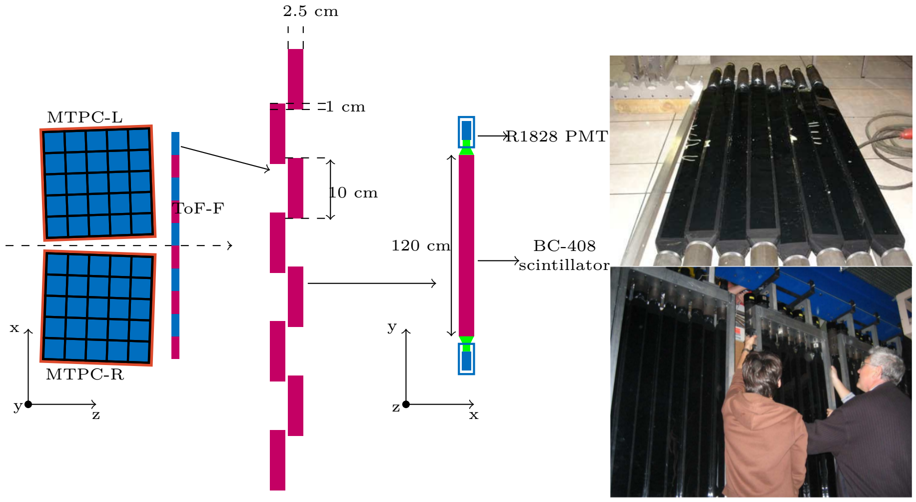

Figure 3.15: ToF-F wall

trigger system. The charge and time measurements were done by LeCroy Fastbus TDC and LeCroy ADC respectively. The TDC time window is 4000 channels in size with a sampling rate of 25 ps. Since the NA61/SHINE proton beam rate during the hadron production measurements for the T2K was around 100 kHz or less, it is possible to reject pile-up tracks by using only tracks with assigned *tof* hits. Measurements from a single slat are taken as a mean value from the top and bottom channels:

$$tof = \frac{tof_{top} + tof_{bottom}}{2} \tag{3.3}$$

Squared mass of each track is calculated by combining *tof*, momentum and track length:

$$m^2_{tof} = \left(\frac{p}{c}\right)^2 \left[\frac{c^2 tof^2}{l^2} - 1\right], \tag{3.4}$$

and it can be used for particle identification. Resolution of *tof* measurements and efficiency of the detector will be discussed in subsection 4.6.7. It is important to note that although the ToF-F wall has large phase space coverage, it is not useful in the nucleus-nucleus measurements for which track density drastically increases. If two or more tracks hit the same slat, it is impossible to distinguish between them. For the nucleus-nucleus collisions, a detector with finer granularity is needed.

3.2.5 Other detector systems

On top of the ToF-F wall, there are two additional *tof* walls (ToF-L and ToF-R) which are suitable for higher track density. They consist of scintillator pixels which vary in size (34 mm ×60(70)(80) mm). These detectors have much smaller coverage of the phase space, and usually, they are used during data-taking for heavy ion programme of the NA61/SHINE. In addition to the ToF-L and ToF-R, there are several other detectors used during heavy ion data-taking. The most important is the Projectile Spectator Detector (PSD) which is a modular lead hadron calorimeter containing 44 modules with a total area of $120 \times 120\,\mathrm{cm}^2$. It is used for measuring the energy of projectile spectators in nucleus-nucleus collisions. Spectators are nucleons which did not interact and by keeping their number low, we ensure centrality in the nucleus-nucleus collisions. This is important for measuring fluctuations of the physical quantities which are expected near the quark-gluon plasma transition. Trivial fluctuations caused by collision geometry are removed by the PSD. On the other hand, in hadron-nucleus collisions centrality of the collision can be inferred by measuring a number of low momentum protons (grey protons). This is done by the Low Momentum Particle Detector (LMPD), which consists of two small TPCs located in the transverse plane surrounding the target and measuring radially emitted particles. The detector is divided into several detection and plastic absorber layers. By measuring energy loss and range, it is possible to measure low momentum protons.

In addition to these detectors, there will be three additional detectors installed in the near future. Two of them are FTPC-1 and FTPC-2 which were already mentioned. They will improve acceptance for high momentum forward going particles. The design uses light materials to minimize material budget in the beam-line. Since FTPC-2 will be located downstream from the MTPCs, some changes will be introduced to the geometry of the ToF-F wall. Another feature of the NA61/SHINE spectrometer which will be improved is the determination of the vertex position in the target. For this reason, a vertex detector will be installed between target and VTPC-1. It will consist of four-pixel stations of increasing size featuring Mimosa-26 sensors. The Mimosa-26 sensor is CMOS Monolithic Active Pixel Sensor, and it has a very low material budget (thickness of $50\,\mu$m) and the pixel pitch of $18.4\,\mu$m. It includes pixel output discrimination for binary readout and zero suppression microcircuits (see Ref. [99]). Discussion about further upgrades and continuation of the measurements beyond 2020 are ongoing.

3.3 NA61/SHINE software

Since the configuration of the NA61/SHINE setup changes not just with hardware upgrades, but also depending on the data-taking, it is important to have the versatile software. The legacy software developed for the NA49 experiment has several serious limitations which limit changes in the detector description necessary for different data-taking periods. Among others, these are a usage of the mixed code (written in C, C++, and Fortran), outdated simulation and production tools, portability issues (cannot be used outside of CERN) and lack of support. For this reason, it was decided to migrate to the new framework, called SHINE framework [100]. It is based on the software from the Pierre Auger collaboration [101] and written in C++. The main parts of the framework are:

1. detector interface
2. SHINE Offline Event (SH⊛E) and
3. modules.

Detector interface provides geometry and all calibration constants of the detector. The data is stored in the XML files or the MySQL database. It is accessed by CentralConfig and users are not allowed to change it. SHINE Offline Event is a collection of stream-able classes stored in the ROOT file format. The legacy software uses several data structures, and the purpose of SH⊛E is to replace all of them by a single file format. The advantage of SH⊛E is scalability, it connects parent and child-object by indices, and it can store event information on several levels: from raw detector signals to fully reconstructed events. Modules are used as a user interface to the detector information and SH⊛E files. The XML configuration files are used to set-up the detector information and modules, which can be stacked together. The specific task of calibration, analysis or reconstruction are done by specialized modules. Recently, a lot of effort was put forward to migrate the reconstruction, simulation, and calibration entirely to the SHINE framework.

3.4 Reconstruction of the data

The main purpose of the reconstruction software is to convert signals measured by detectors to particle trajectories to calculate the event kinematics. Reconstruction based on the legacy software is done as follows:

1. BPD reconstruction
2. cluster finder in the TPCs,
3. track reconstruction,
4. momentum determination,
5. primary vertex reconstruction,
6. momentum determination with vertex constraint,

7. calculation of the maximum number of clusters which a given track can have (so-called potential points),
8. energy loss and time of flight, and
9. V^0 and Ξ finder.

Reconstruction of the beam position is independent of the TPC reconstruction, and it consists of cluster finder in the BPDs and track fitting. Moreover, this information is only necessary during the later stages of reconstruction for determination of the primary interaction vertex. Similarly, TPC track reconstruction starts with cluster finder. After the cluster reconstruction, corrections are applied to remove distortions which can come for example from $\mathbf{E} \times \mathbf{B}$ effect. Additional residual corrections can also be applied if they are calculated previously in the calibration procedure. From the reconstructed clusters in each TPC, it is possible to build local tracks. These tracks are then matched with their counterparts in other TPCs (if any exists) and global track parameters are fitted. In the case of measurements with the T2K replica target, the main vertex is determined by extrapolating global TPC tracks toward the beam track until the minimal distance of approach is reached. Once the primary vertex is determined, the TPC tracks are refitted with a vertex constraint. However, both global tracks with and without vertex constraint are kept on output. In the next step, potential points are counted by estimating how many pad rows track crossed. After this step, energy loss is calculated for each track, and *tof* hits are matched with the tracks. Some of the reconstructed tracks do not come from the primary vertex. Rather, they are created in weak decays or re-interactions outside of the target. Two finders (V^0 and Ξ) look for this kind of events. The first one looks for decays in which two oppositely charged particles are created (K^0_s or Λ decay), while the second one searches for Ξ decays. These can be recognized as a kink in the original track since for example, Ξ^- decays on π^- and Λ. Most of the calibration constants can be obtained only after reconstruction, several iterations of reconstruction are necessary. Most of the reconstructions steps are also used for the Monte Carlo simulation.

3.5 Monte Carlo simulation chain

Monte Carlo chain for p + T2K replica target interactions was developed for 2007 and 2009 data-taking. The same chain was used for analysis of the 2010 data with minor technical changes. It consists of several stages:

1. simulation of the proton interactions and re-interactions inside the T2K replica target,
2. propagation of the particles from target surface through the detector by Geant3 with a GCALOR model,
3. reconstruction of the simulated events and matching of the simulated particles with the reconstructed tracks,
4. conversion to the SHOE format.

Simulation of the interactions inside the target is done by the Fluka2011 model to match the T2K neutrino beam simulation. To study systematic uncertainties, Fluka2011 can be replaced by physics lists from Geant4. It is important to emphasize that beam profile used in the simulation is based on the data. Two histograms containing dependence of the divergence in x and y on the beam position are added to the Fluka2011 input. These histograms are used as templates for generating simulated beam profile. Scintillators in front of the target and BPDs are not simulated. Instead, protons are generated at the BPD3 position, and propagated towards the target. Since S3 scintillator is glued to the upstream target face, it is included in the FLUKA2011 simulation. Particles created inside the target are propagated to the target surface. The output of the FLUKA2011 is stored in the ROOT files as follows: each entry represents particle on the target surface with all necessary pieces of information (momentum, exit point, pid, ...). Also, the whole history of the particle including all interactions and parent particles is stored to the output. This is done to mimic the output of first part of the T2K neutrino beam simulation. All re-interactions and decays outside of the target are simulated with GCALOR model which is also used for interactions in the horns and other elements of the beam-line in the T2K experiment. Simulation of the induced signals in the TPCs is done by GEANT3 based simulation [102]. However, simulation of the ToF-F signals is not performed. Instead, *tof* mass is assigned to the particles which hit ToF-F wall with a resolution based on the data. For this reason, ToF-F efficiency cannot be corrected with Monte Carlo simulation. In the next step, simulated signals are reconstructed with the same procedure as in the data. Afterwards, reconstructed tracks are matched with simulated tracks and events are converted to the new SHOE format. During the simulation and reconstruction, various parameters, such as drift velocity, detector positions, and alignment are taken from the calibration of the data.

3.6 Calibration of the data

Calibration of the data can be roughly divided into several steps:

1. TPC T0 and gain calibration (pad by pad and global),
2. drift velocity and TPC alignment (smoothing of the measured drift velocity, scaling, time dependent residual corrections, GTPC drift velocity),
3. residual corrections for TPC clusters,
4. magnetic field,
5. BPD alignment,
6. BPD-TPC alignment,
7. energy loss, and
8. time-of-flight.

T0 and gain calibration

In the first calibration step, time delays are calculated for all pads in the TPCs. These delays come from two sources: cable length, which is the same for all pads connected to one chip and signal shaping time variations which are independent from pad to pad. The former contribution is usually much larger than the later one. Calibration is done by injecting a charge to the cathode wires, which in turn induces a signal in the pad plane. Time delays of the induced signals are then subtracted to get non-biased drift time measurement. Additionally, pad gains are calibrated by introducing an excited state of the ^{83}Kr nuclei to the TPCs. Introduced atoms decay to the ground state by releasing 41.5 keV photons which in turn convert and ionize TPC gas. The gains in the pads are then tuned so that signals match the energy of the peak. Proper gain calibration is important for precise energy loss measurement. A global time delay for the TPCs is calculated by extrapolating MTPC tracks to the ToF-L and ToF-R walls. The position of the tracks is compared with the positions of the active channels in the *tof* walls. Any difference in y positions shows the miscalibration of the global MTPC delay time.

Drift velocity calibration

Differences may also arise due to biased drift velocity. Obtained position offset Δy has a linear dependence on measured drift time with a drift velocity as a slope. The product of the drift velocity and the delay time is the intercept parameter. It is important to note that drift velocity is measured during data-taking for all TPCs except for GTPC. Obtained values usually vary due to fluctuations in temperature and pressure in the TPCs and need to be smoothed. Because of these measurements, any change in the drift velocity of the MTPC after calibration with TOF-L/R walls is expected to be small. After calibrating MTPCs, they are used as a reference for the VTPC calibration. Also, time-dependent residual corrections are applied to the drift time to reduce any fluctuations and distortions in the measurement. Finally, GTPC drift velocity is calibrated by checking y alignment with other TPCs.

Magnetic field calibration and residual corrections

Alignment of the TPCs can also be checked for x, and any difference is usually small and points to the miscalibration of the magnetic field or to the distortions in the TPCs. The former one is calibrated by finding K_s^0 and Λ decay candidates in the detectors. By fitting invariant mass distributions and comparing obtained masses with PDG values, it is possible to find bias in the momentum and therefore in the magnetic field. These corrections are usually very small. Distortions in the TPCs are usually larger close to the edges of the TPCs, and they are calculated by looking to the residuals between fitted global tracks and clusters. The detector is binned in the (x, y, z) space and residuals (cluster position − track position) are calculated for all the tracks in the data. These residuals are stored in the spatial bins, and an average value is calculated for each bin. If the average value in a given bin is different than zero, a correction is applied to the positions of clusters in this bin. The correction is equal to the negative average value.

BPD-TPC alignment

Similarly, how alignment between TPCs is important for the accurate determination of the track parameters, it is also important to determine alignment between BPDs. Large distances between BPDs especially between BPD1 and other BPDs prevents accurate measurement of the position before data-taking. Once this task is completed, it is also necessary to check alignment between TPCs and BPDs. This is done by extrapolating TPC tracks to the target plane and comparing position with BPD track. In the case of long target measurements (T2K replica target or liquid hydrogen target), alignment with this method is more complicated to achieve, since we do not know exact z position of the interaction vertex. Therefore, a modified method is used which will be explained in section 4.5.

Energy loss and time-of-light calibration

Last steps of the calibration procedure include energy loss and time of flight calibration. Energy loss depends on many parameters: gas mixture, gas pressure, drift losses and TPC gain. All of the effects are usually corrected once per data-taking. On top of that, time-dependent residual corrections are applied to account for the fluctuations (for example, fluctuations of the gas pressure).

Some of the calibration tasks were done as a part of this thesis work. They include the TPC alignment, the BPD-TPC alignment and the time of flight calibration. All of them are described in more detail in the next chapter, alongside with the corresponding software development.

Chapter 4

Software and calibration

Contents

Software for special calibration tasks and analysis of p + T2K replica target data was already developed for the data taken in 2007 and 2009. In the meantime, the NA61/SHINE collaboration is switching to the new software framework, and because of that a lot of previously developed code will soon become obsolete. For this reason, the whole analysis code alongside with some calibration procedures was re-written from scratch as a part of technical work done for this thesis. As a consequence, any similar future measurement will profit from this work. In the first section of this chapter, the discussion will be centered around the analysis tools and track extrapolation in the non-homogeneous magnetic field with error propagation. Later on, several calibration tasks will be reviewed. All of them profit from the developed track extrapolation in the magnetic field.

4.1 Analysis tools

As described in subsection 3.4, TPC tracks are used together with the beam track to determine a position of the primary interaction point (also known as the main vertex). In the case of p + T2K replica target measurements, we require positions of the created particles on the target surface. Reconstruction chain is not designed to extrapolate tracks to the target surface, and because of that, track extrapolation is done during the analysis. The analysis code is divided into several modules, and it is a part of the new SHINE framework. The scheme in Fig. 4.1 shows all analysis stages, where a single stage is done by one SHINE module. In the first stage, tracks are extrapolated to the target surface, and the simplest cuts are applied. These cuts remove bad events and tracks, for example, tracks without fitted momentum or complete events where the position of the beam track is not properly determined. All selected events and tracks are stored with only necessary information in the form of the ROOT TTrees. In this way, size of the data for analysis is reduced from a few TB to less than 1GB. Because of the track extrapolation and large size of the files, the first stage of the analysis is slow. Once the first stage is done, it does not need to be repeated unless some of the calibration constants (like target position) have changed. In the second stage, all other cuts are applied, and tracks are stored in the phase space bins chosen for analysis. The third module is a fitter based on RooFit, and it determines particle content in each bin. Afterwards, fit results for data and MC are combined in the particle yields. In the final step, systematic uncertainties are calculated, and the results are plotted. Several auxiliary modules were also written for optimizing the cuts, defining phase space binning and calculating, plotting the beam profile, etc... All of the auxiliary modules operate on the output from the first stage.

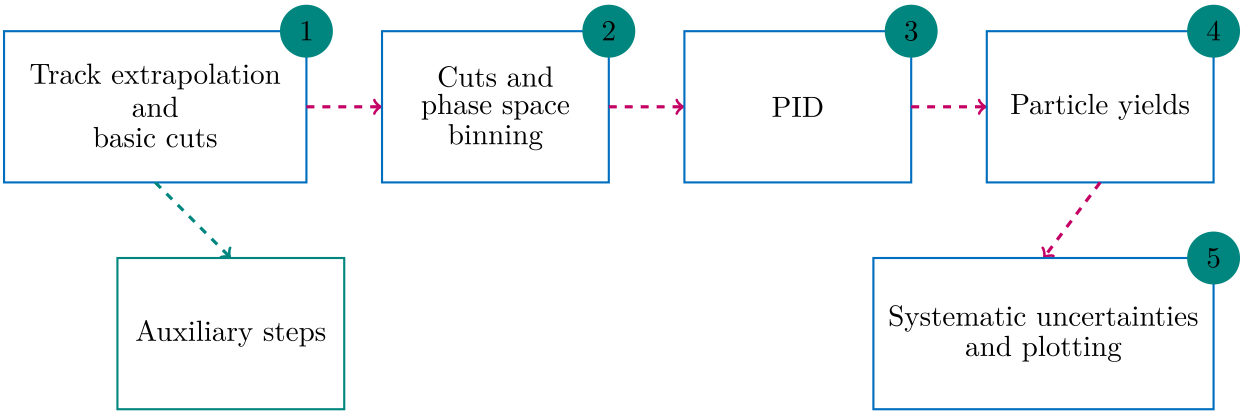

Figure 4.1: Analysis tasks

4.2 Track extrapolation in non-homogeneous magnetic field

4.2.1 Magnetic field

The magnetic field map of the NA61/SHINE spectrometer is read from the SHINE database. The only important component is the y component which is at least three orders of magnitude larger than other components of the field in the whole volume of interest. The field map covers VTPCs, GTPC, and parts of the magnet. Target is located inside the residual field of the first magnet, but only less than 30% of the target is covered by the field map. In Fig. 4.2, 2D slices of the map are plotted for the field component B_y. Rectangles are showing the size of the target, VTPCs and GTPC are superimposed to the plots (nonsensitive volume of the TPCs is included).

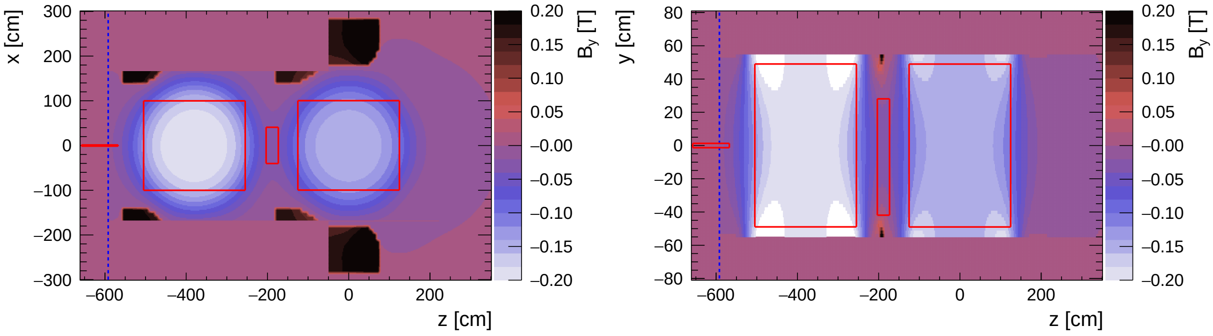

(a) (b)

Figure 4.2: Slices of the field map: B_y in $x-z$ slice for $y=0\,\mathrm{cm}$ (a) and B_y in $y-z$ slice for $x=0\,\mathrm{cm}$ (b). Red rectangles from left to right are: target, VTPC-1, GTPC and VTPC-2. Dashed blue line is the upstream border of the field map.

For this analysis, the magnetic field map was extended to the whole target region in z by fitting an exponential function to the tail of the magnetic field. The function is then used for calculating the field outside of the existing field map. An example is shown in Fig. 4.3. The dashed blue lines correspond to the target position. This figure shows the extrapolation of the filed for $x=0\,\mathrm{cm}$ and $y=0\,\mathrm{cm}$, but it was confirmed that the exponential function with the same rate parameter works for every x and y.

4.2.2 Equation of motion

The force acting on charged particles in the magnetic field is the Lorentz force, and a corresponding equation of motion is:

$$\frac{d\mathbf{p}}{dt} = \kappa \cdot q \cdot \mathbf{v} \times \mathbf{B}, \tag{4.1}$$

where $\mathbf{p}$ is a momentum, q is a charge, $\mathbf{v}$ is a particle velocity, and $\mathbf{B}$ is magnetic field. Since we want to use momentum in GeV/c, velocity in cm/s, charge in unit charge and field in kG, a constant κ is equal to $\kappa = 2.99792458 \cdot 10^{-4}\,(\mathrm{GeV}/c)\mathrm{kG}^{-1}\mathrm{cm}^{-1}$. If we ignore particle energy loss in materials, the value of the momentum and therefore particle speed will be conserved. The only change occurs in the direction of the momentum. This allows us to replace time with the path length s, so that $dt = ds/v$. Also, useful concept to introduce is the unit vector $\mathbf{e} = \frac{\mathbf{v}}{v} = \frac{\mathbf{p}}{p}$. In our analysis we want to get track z position on the target surface, so instead of the path length, we want to use z position as a parameter. A path length differential can be written as:

$$ds = \sqrt{1 + t_x^2 + t_y^2} \cdot dz, \tag{4.2}$$

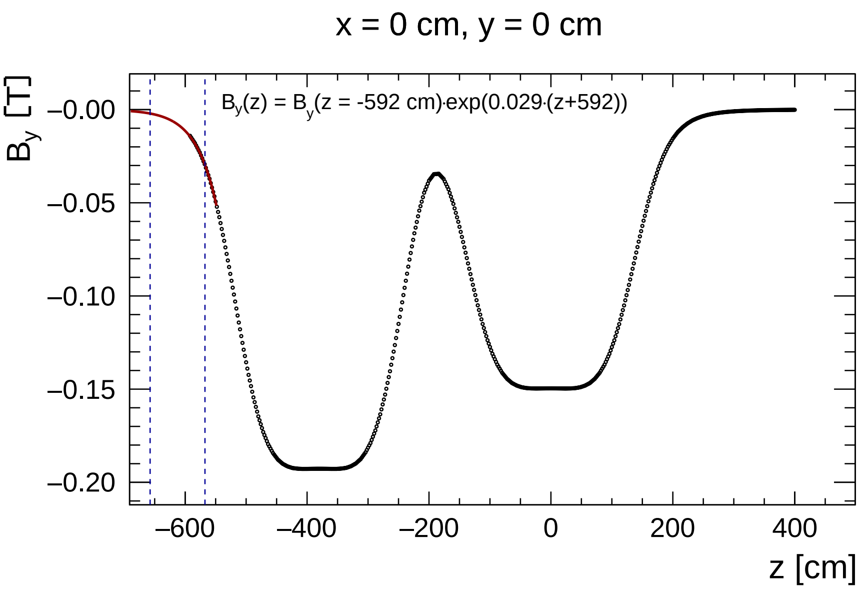

Figure 4.3: Extrapolation of the field component B_y outside of the field map. The dashed blue lines represent target position.

where $t_x = \frac{e_x}{e_z} = \frac{dx}{dz}$ and $t_y = \frac{e_y}{e_z} = \frac{dy}{dz}$ are track directions. From Eq. 4.1, it is possible to extract differential equations for particle directions and together with previously written definitions we get five differential equations of the first order:

$$\frac{dx}{dz} = t_x, \tag{4.3a}$$

$$\frac{dy}{dz} = t_y, \tag{4.3b}$$

$$\frac{dt_x}{dz} = \kappa \cdot \frac{q}{p} \cdot \sqrt{1+t_x^2+t_y^2} \cdot \Big(t_x t_y \cdot B_x - (1+t_x^2) \cdot B_y + t_y \cdot B_z\Big), \tag{4.3c}$$

$$\frac{dt_y}{dz} = \kappa \cdot \frac{q}{p} \cdot \sqrt{1+t_x^2+t_y^2} \cdot \Big((1+t_y^2) \cdot B_x - t_x t_y \cdot B_y - t_x \cdot B_z\Big), \tag{4.3d}$$

$$\frac{d}{dz}\left(\frac{q}{p}\right) = 0. \tag{4.3e}$$

From Eq. 4.3, it is evident that there exists a natural set of parameters which describe our tracks:

$$\mathbf{r} = (x, y, t_x, t_y, (q/p))^T, \tag{4.4}$$

where each component of the vector $\mathbf{r}$ is a function of z.

4.2.3 Track extrapolation in non-homogeneous magnetic field

Track extrapolation in a magnetic field is essentially solving the equations of motion 4.3a - 4.3e with given initial condition $\mathbf{r}_{z_0}$ and calculating the state vector for some value of z. Extrapolated x and y positions are just integrals of track directions, so the essential part in extrapolation is solving equations 4.3c and 4.3d. Speed and accuracy were both needed in this analysis. An analytical method developed by S. Gorbunov and I. Kisel [103] was used for this purpose. The method was developed for the CBM experiment. The basic principles of the method will be reviewed in this subsection. Derivatives of the directions t_x and t_y can be rewritten in the form:

$$\frac{dt_x}{dz} = \sum_{i_1=x,y,z} B_{i_1}(z) \cdot a_{i_1}(z), \tag{4.5a}$$

$$\frac{dt_y}{dz} = \sum_{i_1=x,y,z} B_{i_1}(z) \cdot b_{i_1}(z), \tag{4.5b}$$

where magnetic field components B_{i_1} can be written as functions of z. This is only possible because the field value is taken at track position and track x and y position are functions of z. The factors $a_{i_1}(z)$ and $b_{i_1}(z)$ do not depend on the magnetic field and can be written as components of the vectors:

$$\mathbf{a}(z) = \kappa \cdot \frac{q}{p} \cdot \sqrt{1+t_x^2+t_y^2} \cdot \Big(\quad t_x t_y, \; -(1+t_x^2), \quad t_y \Big), \tag{4.6a}$$

$$\mathbf{b}(z) = \kappa \cdot \frac{q}{p} \cdot \sqrt{1+t_x^2+t_y^2} \cdot \Big((1+t_y^2), \quad -t_x t_y, \; -t_x \Big). \tag{4.6b}$$

For a general function T which depends only on the track directions t_x and t_y, a derivative is equal to:

$$\frac{dT}{dz} = \frac{dT}{dt_x} \cdot \frac{dt_x}{dz} + \frac{dT}{dt_y} \cdot \frac{dt_y}{dz}. \tag{4.7}$$

If we replace direction derivatives with Eq. 4.5a and Eq. 4.5b, we get:

$$\frac{dT}{dz} = \sum_{i_1=x,y,z} B_{i_1}(z) \left(\frac{dT}{dt_x} a_{i_1}(z) + \frac{dT}{dt_y} b_{i_1}(z) \right) = \sum_{i_1=x,y,z} B_{i_1}(z) T_{i_1}. \tag{4.8}$$

Each factor $T_{i_1}(z)$ is also just a function of the track directions $t_x(z)$ and $t_y(z)$. Therefore we can use the same identity for calculation of the $\frac{dT_{i_1}}{dz}$ as in the previous equation. The procedure can be iteratively repeated, and in each step we get factors:

$$\frac{dT_{i_1 \dots i_k}}{dz} = \frac{dT_{i_1 \dots i_{k-1}}}{dt_x} a_{i_k} + \frac{dT_{i_1 \dots i_{k-1}}}{dt_y} b_{i_k}. \tag{4.9}$$

Now, we can rewrite function $T(z)$ as a sum of magnetic field path integrals:

$$
\begin{aligned}
T(z) &= T(z_0) + \int_{z_0}^{z} T'(z_1)dz_1 \\
&= T(z_0) + \sum_{i_1=x,y,z} \int_{z_0}^{z} B_{i_1}(z_1) T_{i_1}(z_1) dz_1 \\
&= T(z_0) + \sum_{i_1=x,y,z} \int_{z_0}^{z} B_{i_1}(z_1) \left(T_{i_1}(z_0) + \int_{z_0}^{z_1} B_{i_2}(z_2) T_{i_2}(z_2) dz_2 \right) dz_1 \\
&= ... \\
&= T(z_0) + \sum_{k=1}^{n} \sum_{i_1,...,i_k=x,y,z} T_{i_1...i_k}(z_0) \cdot \left(\int_{z_0}^{z} B_{i_1} ... \int_{z_0}^{z_{k-1}} B_{i_k} dz_k ... dz_1 \right) \\
&+ O\left(\frac{(\kappa(q/p)(z-z_0))^{n+1}}{(n+1)!} \right).
\end{aligned}
\tag{4.10}
$$

Relation 4.10 is valid for a generic function $T(t_x(z), t_y(z))$, but in the case of track extrapolation we have two simple functions: $T_1 = t_x$ and $T_2 = t_y$. For initial values $t_x(z_0)$ and $t_y(z_0)$ we can calculate $t_x(z)$ and $t_y(z)$ by using Eq. 4.10 with a desired precision. The only issue left is how to calculate path integrals of the magnetic field in Eq. 4.10, because we do not know the path before the extrapolation. For any non-homogeneous magnetic field we can do extrapolation in small steps so that the field is approximately constant. Because of this, field integrals become just integrals of the polynomial functions. All the details on how to implement these results into track extrapolation software are presented in the CBM technical note [104]. The extrapolated track parameters after one step Δz are equal to:

$$x(z_0 + \Delta z) = x(z_0) + t_x(z_0)\Delta z + \sum_{k=1}^{n} \sum_{i_1,...,i_k=x,y,z} h^k A_{i_1...i_k} S_{i_1...i_k}, \tag{4.11a}$$

$$y(z_0 + \Delta z) = y(z_0) + t_y(z_0)\Delta z + \sum_{k=1}^{n} \sum_{i_1,...,i_k=x,y,z} h^k B_{i_1...i_k} S_{i_1...i_k}, \tag{4.11b}$$

$$t_x(z_0 + \Delta z) = t_x(z_0) + \sum_{k=1}^{n} \sum_{i_1,...,i_k=x,y,z} h^k A_{i_1...i_k} s_{i_1...i_k}, \tag{4.11c}$$

$$t_y(z_0 + \Delta z) = t_y(z_0) + \sum_{k=1}^{n} \sum_{i_1,...,i_k=x,y,z} h^k B_{i_1...i_k} s_{i_1...i_k}, \tag{4.11d}$$

where $s_{i_1...i_k}$ and $S_{i_1...i_k}$ are integrals of the field:

$$s_{i_1...i_k} = \int_{z_0}^{z_0+\Delta z} B_{i_1}(z_1) ... \int_{z_0}^{z_{k-1}} B_{i_k}(z_k) dz_k ... dz_1, \tag{4.12a}$$

$$S_{i_1...i_k} = \int_{z_0}^{z_0+\Delta z} \int_{z_0}^{z'} B_{i_1}(z_1) ... \int_{z_0}^{z_{k-1}} B_{i_k}(z_k) dz_k ... dz_1 dz'. \tag{4.12b}$$

Parameters $A_{i_1 \dots i_k}$ and $B_{i_1 \dots i_k}$ are normalized parameters from Eq. 4.9 for $T = t_x$ and $T = t_y$ respectively:

$$A_{i_1 \dots i_k} = t_{x_{i_1 \dots i_k}} / h^k, \tag{4.13}$$

$$B_{i_1 \dots i_k} = t_{y_{i_1 \dots i_k}} / h^k, \tag{4.14}$$

where h is a constant for each track and it is equal to:

$$h = \kappa \frac{q}{p} \sqrt{1 + t_x^2(z_0) + t_y^2(z_0)}. \tag{4.15}$$

Depending on desired precision, parameters $A_{i_1 \dots i_k}$ and $B_{i_1 \dots i_k}$ can be calculated only till specific order n. For example, if we keep only first order, we will get very fast extrapolation code, but it will not be very precise. Authors of the method claim in [103] that using all coefficients below the fourth order will give the same precision as the fourth-order Runge-Kutta method with the same step size. The method used to calculate all the coefficients is described in [104]. Furthermore, in our case, some of the low-order coefficients can be discarded if they are multiplied with the path integral of the x or z field component. List of all coefficient is located in Appendix A. The extrapolation step size was chosen to be 0.5 mm.

4.2.4 Propagation of uncertainties

If a track has long TPC segments in the magnetic field, so that momentum is properly fitted, reconstruction software also calculates full covariance matrix. However, this matrix is only provided for the position at which track parameters are evaluated. To get covariance information at the extrapolated position, the covariance matrix needs to be transformed in a way similar to the transformation between different coordinate systems. After each extrapolation step, Jacobian matrix is calculated in the following manner:

$$J_{ij} = \frac{d\alpha_i}{d\alpha_{j,0}}, \tag{4.16}$$

where α_i is a component of the state vector from Eq. 4.4 after the extrapolation step, while $\alpha_{j,0}$ is a component of the initial state vector. Jacobian is then used for the covariance matrix transformation:

$$C(z_0 + \Delta z) = J C(z_0) J^T. \tag{4.17}$$

4.2.5 Treatment of multiple scattering

Propagated uncertainties from the previous subsection are underestimated because multiple Coulomb scattering is not taken into account. Multiple scattering represents a noise for the track extrapolation. During each extrapolation step, a correction must be added to the covariance matrix. Added contribution can be written in the form of noise covariance matrix. A good approximation of the multiple scattering can be found in work from G. R. Lynch and O. I. Dahl [105]. They present a simple formula for the width of the angular distribution:

$$\sigma(\theta_s) = \frac{13.6}{\beta c p} z \sqrt{\frac{L}{L_r}} \left[1 + 0.038 \log\left(\frac{L}{L_r}\right) \right], \tag{4.18}$$

where βc is a velocity of the particle, p is a momentum in MeV/c, L is a track length, and L_r is a radiation length of the medium. For air, the radiation length is equal to 304 m. The formula can be applied to all relativistic particles, including heavy ions, and the authors claim a precision of 11%. Implementation of the formula 4.18 for the track extrapolation was done by R.J. Wolin and L.L. Ho in [106]. They give covariance matrices of the noise for two different sets of track parameters, one of which correspond to our choice. It is assumed that momentum of the particle is conserved, therefore no noise is added to the q/p uncertainty. The covariance matrix of the multiple scattering is:

$$\mathbf{Q} = \begin{bmatrix} (\Delta z)^2\,\mathrm{Var}(t_x) & (\Delta z)^2\,\mathrm{Cov}(t_x,t_y) & -\Delta z\,\mathrm{Var}(t_x) & -\Delta z\,\mathrm{Cov}(t_x,t_y) & 0 \\ (\Delta z)^2\,\mathrm{Cov}(t_x,t_y) & (\Delta z)^2\,\mathrm{Var}(t_y) & -\Delta z\,\mathrm{Cov}(t_x,t_y) & -\Delta z\,\mathrm{Var}(t_y) & 0 \\ -\Delta z\,\mathrm{Var}(t_x) & -\Delta z\,\mathrm{Cov}(t_x,t_y) & \mathrm{Var}(t_x) & \mathrm{Cov}(t_x,t_y) & 0 \\ -\Delta z\,\mathrm{Cov}(t_x,t_y) & -\Delta z\,\mathrm{Var}(t_x) & \mathrm{Cov}(t_x,t_y) & \mathrm{Var}(t_y) & 0 \\ 0 & 0 & 0 & 0 & 0 \end{bmatrix} \tag{4.19}$$

where $\mathrm{Var}(t_x)$, $\mathrm{Var}(t_y)$ and $\mathrm{Cov}(t_x,t_y)$ are equal to:

$$\mathrm{Var}(t_x) = \sigma^2(\theta_s)\left(1+t_x^2\right)\left(1+t_x^2+t_y^2\right), \tag{4.20a}$$

$$\mathrm{Var}(t_y) = \sigma^2(\theta_s)\left(1+t_y^2\right)\left(1+t_x^2+t_y^2\right), \tag{4.20b}$$

$$\mathrm{Cov}(t_x,t_y) = \sigma^2(\theta_s)t_x t_y\left(1+t_x^2+t_y^2\right). \tag{4.20c}$$

4.2.6 Extrapolation to the target surface and validation

In the analysis, TPC tracks are extrapolated towards the target surface. Extrapolation is done until track hits the target or distance of closest approach is found. Because of that, any uncertainty of the target position will limit our extrapolation precision. This will be discussed in section 4.5. Although the analytical method for track extrapolation was proven to work in [103], basic sanity checks were done to avoid any bugs in the code. Monte Carlo chain described in section 3.5 was used to check for any extrapolation biases. Tracks from the Monte Carlo simulation were extrapolated backward towards the target and extrapolated track parameters were compared to the simulated parameters. Comparison of all important track parameters can be seen in Fig. 4.4 to check for a possible bias or a mistake in the extrapolation code. Momentum comparison is not shown because momentum is conserved during the extrapolation and by definition, there is no bias. Tracks can start in different TPCs and they can have crucially different momentum resolutions and different distances from the target. Because of this reason, all distributions in Fig. 4.4 have long tails.

4.3 Kalman filter

Kalman filter is an iterative method for estimating a future state of the system by using measurements observed in the past. The method was developed in 1960 by R. E. Kalman [107], and it is widely used in navigation, aircraft control, signal processing and particle physics. It took more than 25 years for the Kalman filter to be introduced into the particle physics, and now it is used for vertex fitting, track fitting, and merging. Only a brief review of Kalman filtering will be provided here on the example of the NA61/SHINE experiment, while a more detailed explanation is provided in work done by R. Fruhwirth [108]. The idea behind Kalman

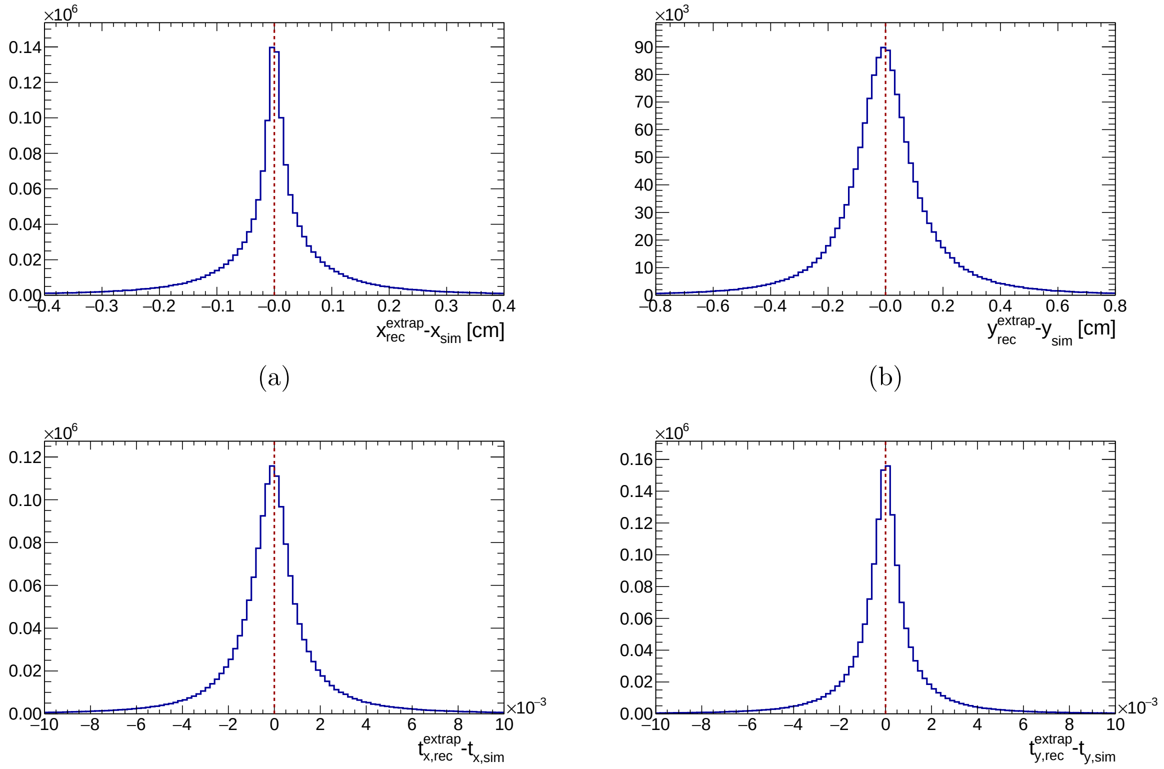

(a) (b)

(c) (d)

Figure 4.4: Comparison of the extrapolated and simulated track parameters: x (a), y (b), t_x (c) and t_y (d).

filter is to predict the system state after step Δt (time or some other parameter) and compare prediction with measurement. Both, measurement and prediction have covariance matrices assigned to them. New prediction for the same point, called filtered prediction is calculated as a most probable value of the state parameters given the two covariance matrices. Graphical representation of the Kalman filter algorithm is shown in Fig. 4.5. For a better clarity, let's briefly examine 1D case. Both, prediction and measurement are described by a Gaussian. In this case, filtered value is a mean value of the product of two Gaussians which is actually the weighted mean.

When tracks are fitted in the detector such as TPC, we only look at discrete intersections of the tracks and detector which are called clusters or points. Therefore, our system to which we want to apply the Kalman filter is a discrete system. If a track state at point $k-1$ is known, state at point k is given by:

$$\mathbf{r}(z_k) \equiv \mathbf{r}_k = \mathbf{F}_{k-1}\mathbf{r}_{k-1} + \mathbf{w}_{k-1}, \tag{4.21}$$

where $\mathbf{r}_{k-1}$ and $\mathbf{r}_k$ are track states at points $k-1$ and k respectively, $\mathbf{F}_{k-1}$ is a track propagator, while $\mathbf{w}_{k-1}$ is a process noise. Track state is defined in Eq. 4.4 and the track propagator is defined by the extrapolation procedure and it is given by Eq. 4.11. Noise of the system comes from multiple Coulomb scattering and it is expected to be independent for all $\mathbf{w}_k$, unbiased and with a finite variance. Furthermore, covariance matrix of the noise was already defined in Eq. 4.19. Although, track state contains five parameters, usually only some of them are

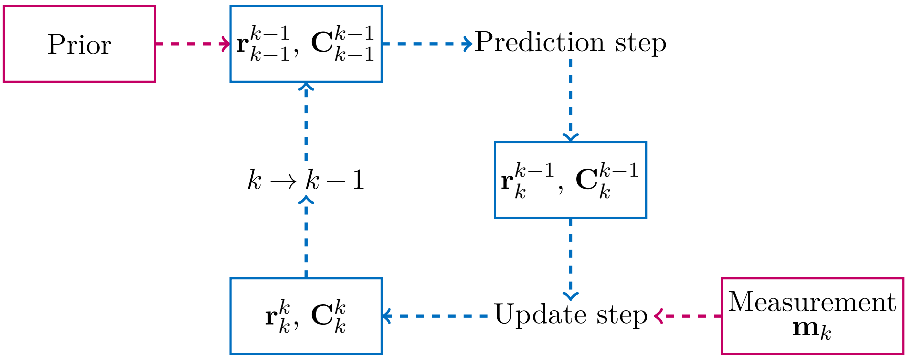

Figure 4.5: Schematic view of the Kalman filter algorithm.

measured or some combination of them is measured. We define measured state at point k as:

$$\mathbf{m}_k = \mathbf{H}_k \mathbf{x_k} + \boldsymbol{\epsilon}_k, \tag{4.22}$$

where $\boldsymbol{\epsilon}_k$ is the noise of the measurement, while $\mathbf{H}_k$ in the NA61/SHINE case is defined as:

$$\mathbf{H}_k = \begin{bmatrix} 1 & 0 & 0 & 0 & 0 \\ 0 & 1 & 0 & 0 & 0 \end{bmatrix} \tag{4.23}$$

The matrix $\mathbf{H}_k$ extracts only parameters x and y which represent cluster positions in the TPCs. Measurement noise is also unbiased, independent and has a covariance matrix $\mathbf{V}_k$. From these definition it is possible to calculate filtered value of the track state:

$$\mathbf{r}_k^k = \mathbf{r}_k^{k-1} + \mathbf{K}_k \left(\mathbf{m}_k - \mathbf{H}_k \mathbf{r}_k^{k-1} \right), \tag{4.24}$$

where $\mathbf{r}_k^k$ is filtered value, $\mathbf{r}_k^{k-1}$ is predicted value and $\mathbf{K}_k$ is a Kalman gain matrix which is defined as:

$$\mathbf{K}_k = \mathbf{C}_k^{k-1} \mathbf{H}_k^T \left(\mathbf{V}_k + \mathbf{H}_k \mathbf{C}_k^{k-1} \mathbf{H}_k^T \right)^{-1}. \tag{4.25}$$

Filtered covariance matrix is equal to:

$$\mathbf{C}_k^k = \left(\mathbf{I} - \mathbf{K}_k \mathbf{H}_k \right) \mathbf{C}_k^{k-1}. \tag{4.26}$$

To better understand the role of the Kalman gain matrix, we can return to the 1D example in which Kalman gain is a number:

$$r_k^k = \frac{\frac{r_k^{k-1}}{(\sigma_k^{k-1})^2} + \frac{m_k}{(\sigma_m^k)^2}}{\frac{1}{(\sigma_k^{k-1})^2} + \frac{1}{(\sigma_m^k)^2}} = r_k^{k-1} + \frac{(\sigma_k^{k-1})^2}{(\sigma_k^{k-1})^2 + (\sigma_m^k)^2} \left(r_k^{k-1} + m_k \right) = r_k^{k-1} + K_k \left(m_k - r_k^{k-1} \right). \tag{4.27}$$

Now it is easy to understand that if uncertainty of the prediction is much larger than uncertainty of the measurement, Kalman gain goes to 1 and update of the prediction is maximal. If opposite is true, Kalaman gain goes to 0 and therefore prediction is not changed. If track was not previously fitted by some other method it is important to select proper prior value for the track state. Initial values of the parameters are not important, only if initial variances of the parameters are large compared to the variances of the measurement. If too small initial variances are selected, it would take very long time (a lot of measurements) for track parameters to converge. Track fitting during the track reconstruction in NA61/SHINE is done by a global method which estimates track parameters at first point of track which is not suitable for some of the calibration tasks. This was the main motivation for developing Kalman filter as a part of the analysis code. Developed code can be used for the calibration purposes in any dataset within the NA61/SHINE experiment. It is a part of *TrackExtrapolation* class and, in particular, *DoKalmanStep* function which extrapolates a track towards provided cluster and calculates filtered track parameters and its covariance matrix.

4.4 TPC alignment

When track segments from different TPCs are merged, any misalignment between the TPCs will cause bias in the global track parameters. In turn, this will bias our hadron yields since misalignment does not exist in Monte Carlo simulation. By using Kalman filter it is possible to estimate track parameters for each track segment separately. Track segments are then extrapolated to the common z position, while x and y positions are compared. To check alignment quality we compare segments from VTPC-2 to the segments from other TPCs since VTPC-2 is in the center of the experimental setup. Alignment check for x and y can be seen in Fig. 4.6. There are no significant systematic shifts between the TPCs. Small distortions can be found close to the beam-line or close to the edges of the TPCs. These do not come from the overall shift in the position of a TPC. Rather they are caused by various edge effects. If some of these regions are not present in the Monte Carlo simulation, it is possible to remove such tracks by carefully choosing quality cuts during the analysis. The TPC alignment is implemented in the form of S<u>HINE</u> module *GeoAlign*.

4.5 Target position calibration

A systematic shift of the target creates bias in the backward track extrapolation in the data. For the tracks with a small polar angle (~5 mrad) even a small shift of 0.05 cm in target x position can induce migration in z which is $5-10$ cm in size. Therefore, it is important to precisely determine target position and its uncertainty with respect to the TPCs. Target position is parametrized by five parameters: (x, y, z) position of the center of upstream target face, target tilt in $x-z$ plane and target tilt in $y-z$ plane.

4.5.1 Upstream target position

The position of the target upstream face with respect to the beam can be determined easily because of the existing feature of the T2 trigger. It was explained in subsection 3.2.1 that T2 trigger was used for selection of the beam tracks which hit the target at upstream target face. By plotting beam (x, y) position at target z position, it is possible to get a sharp circle which represents upstream target face. It must be noted that measurement of the target z position was performed before the data-taking along with the position of the BPDs. The z position is equal to:

$$z_t = (-657.41 \pm 0.05)\,\text{cm}. \tag{4.28}$$

However, there were some doubts in the conversion from surveyor's measurement coordinate system to the NA61/SHINE system, and this will be checked later on. Even variation in z of 1 cm induces negligible changes in the beam (x, y) distribution. Once we obtain (x, y) position of

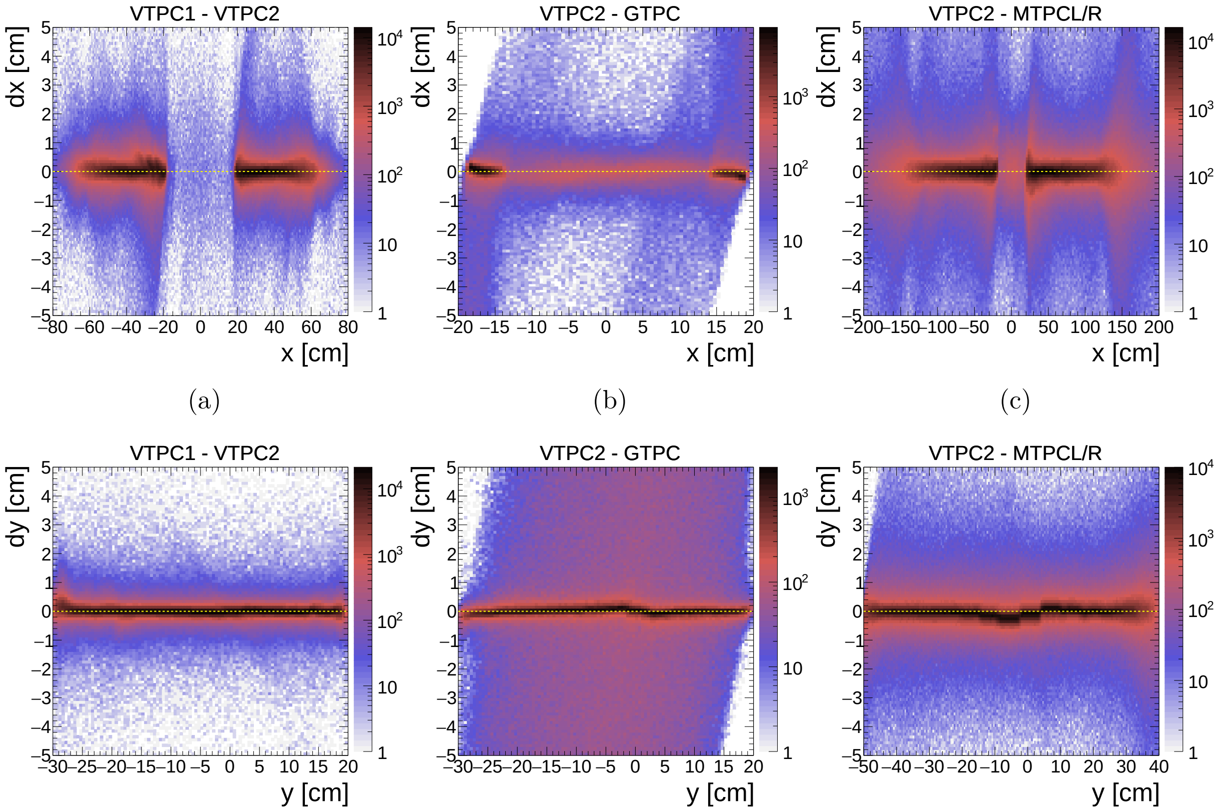

(a) (b) (c)

(d) (e) (f)

Figure 4.6: Alingment in x (a)-(c) and alignment in y (d)-(f).

the target with respect to the BPDs, it must be corrected for any misalignment between TPCs and BPDs. During the data-taking in 2010, around 10% of the data was recorded with the maximal magnetic field in the TPCs. In these data, beam protons which did not interact were bent to the GTPC, VTPC-2, and MTPC-L. Measured TPC tracks can be extrapolated towards the target and compared with the beam tracks. Any difference in position is due to $BPD - TPC$ misalignment. Quality cuts have been applied to the TPC proton tracks: the number of clusters in the TPCs must be larger than 30 and the difference between extrapolated polar angle and beam track polar angle must be less than 2 mrad. The position of the upstream target face and BPD-TPC misalignment are shown in Fig. 4.7. Several sources of the systematic biases were checked for the BPD-TPC alignment: variation of the quality cuts, alignment of the TPCs and variations of the drift velocity in the TPCs. The total systematic uncertainty is presented in Tab. 4.1. The uncertainty of the x position is slightly larger (around 0.03 cm), and this is mostly due to TPC alignment.

Target z position is checked by extrapolating all TPC tracks in an event towards the respective beam track. When the minimal distance from the beam track is reached, the value of the z position is stored. Tracks with momentum lower than 1 GeV/c were removed to remove tertiary particles (produced in decays and re-interactions). Obtained distribution is shown in Fig. 4.8. A step function is fitted to the rising edge of the distribution, and z value of the half-maximum is taken as the target z position. Dependence of this result on the BPD-TPC alignment and the

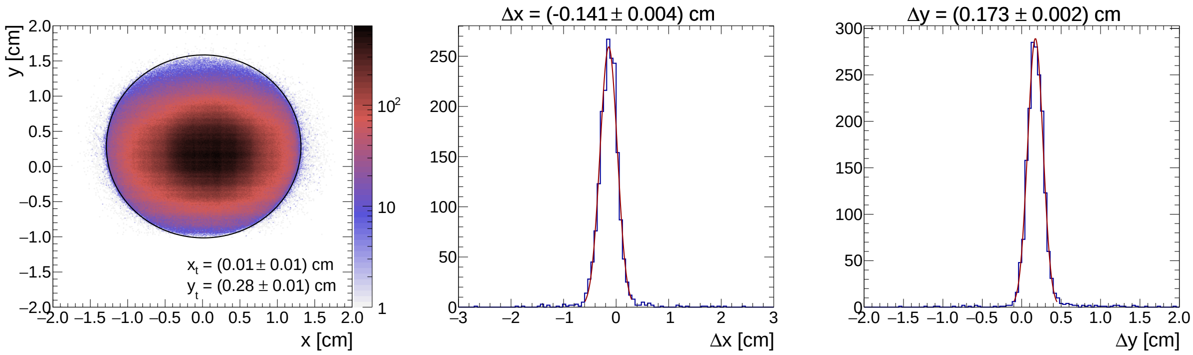

(a) (b) (c)

Figure 4.7: Target position with respect to the BPDs (a), x BPD-TPC alignment (b) and y BPD-TPC alignment (c).

function choice is taken as systematic uncertainty. The result is summarized in Tab. 4.1 and it is consistent with the result in Eq. 4.28.

4.5.2 Target tilt

In the case of the NA61/SHINE experiment, target tilt can only be determined by looking at vertex x and y distributions along the target. If distribution shifts with z position, the target is tilted with respect to the beam-line. However, if the beam width is smaller than the target radius, tilt will not influence vertex positions. For this reason, T2 triggers need to be used in the tilt determination. Moreover, change in the mean x and y vertex position along z can be due to beam divergence since beam tracks close to target surface can exit the target before downstream target face. The mean proton beam divergence is around 0.3 mrad and cannot be neglected. Vertex distributions were determined by extrapolating TPC tracks toward the beam tracks until the minimal distance is reached. Similarly, same quality cuts were applied as for the check of the target z position. No appreciable tilt was found, either in the $x-z$ or $y-z$ plane. The mean value of the divergence was taken as a systematic uncertainty of the tilt.

	x [cm]	y [cm]	z [cm]	t_x [mrad]	t_y [mrad]
Value	0.15	0.12	−657.5	0.0	0.0
Uncertainty	0.03	0.02	0.1	0.3	0.3

Table 4.1: Position of the T2K replica target and its uncertainty.

4.6 Forward time of flight wall calibration

It has already been stated in subsection 3.2.4 that the time of flight measurement is complementary to the energy loss measurement. Particle identification in the momentum regions where energy loss distributions cross is not possible without the time of flight measurement. It also reduces the systematic uncertainty of the proton and kaon yields since proton and kaon energy loss distributions overlap in the whole momentum region of interest. Therefore, a precise

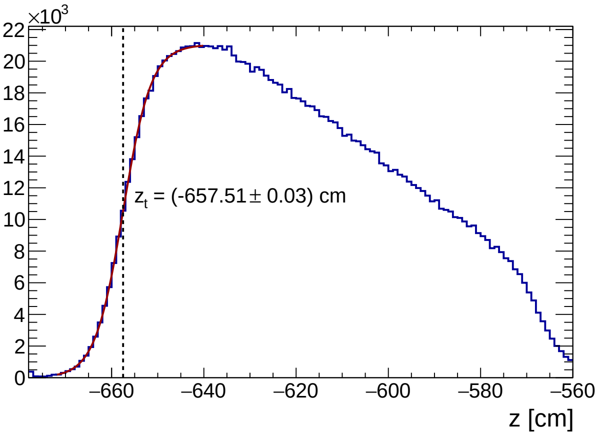

Figure 4.8: Target z position.

calibration of the forward time of flight wall is necessary, and it was done as a part of this thesis. This calibration is implemented in the S$\underline{\text{HINE}}$ module called *FTOFCalib*. Times measured by top and bottom channels in each slat contain several sources of biases, and they are equal to:

$$\begin{aligned} T_{top} &= tof + \Delta t_{S1} + \underbrace{t_{beam} + t_{cable}^{top}}_{t_0^{top}} + \frac{\frac{l}{2} - y}{v_{slat}}, \\ T_{bottom} &= tof + \Delta t_{S1} + \underbrace{t_{beam} + t_{cable}^{bottom}}_{t_0^{bottom}} + \frac{\frac{l}{2} + y}{v_{slat}}, \end{aligned} \tag{4.29}$$

where tof is a true value of the time of flight, Δt_{S1} is a time jitter of the start signal, t_{beam} is a time needed for a beam proton to travel from the S1 counter to the interaction point, t_{cable} is time delay caused by cables and CFDs, and the last term is a signal delay caused by finite speed of the signal inside a slat. The time jitter of the start signal does not create any systematic bias in the mean value of the squared mass measurement, however, it can degrade the resolution. Correction on the event by event basis is necessary to improve the resolution. Interaction point can be anywhere in the target, so t_{beam} also varies on the event basis. Since the target is not inside the tracking system and the percentage of tertiary tracks is not negligible, it is nearly impossible to determine the position of interaction point with great precision. For this reason t_{beam} is taken as the time needed for a beam proton to reach the target center. This does not introduce any bias in the overall squared mass distributions, but it will degrade squared mass resolution mostly for protons, and it will be discussed later. Beam track length change due to divergence is negligible, and for any practical purpose t_{beam} was a constant during the data-taking period. The sum $(t_{beam} + t_{cable})$ is constant named t_0 and it is different for each channel. The speed of signal propagation inside the slat (v_{slat}) depends on 2 contributions: a speed of light and geometry which defines path length for the light. The speed of light is a function of the scintillator refraction index, and it can change due to aging effects, while geometry depends on dimensions of the slat and quality of the aluminum foil wrapping, i.e., wrinkles in the foil can change reflection angle. When we use mean time measured by top and bottom channels, signal delay in the slat cancels out except for a constant term. This constant term can be included into t_0. However it will be clear later why we keep it separate and apply signal delay correction for each channel separately. Before correcting the measured time for all biases, it is necessary to determine the exact position of each slat in relation to the tracking system.

4.6.1 ToF-F slat positions and track-hit matching

In the first step, only slats with the good signal are selected in each event. This was done by looping over all events and selecting only slats which had good QDC and TDC values for both PMTs. QDC values need to be above the certain threshold, and TDC values must be inside the TDC time window defined in subsection 3.2.4. After the reconstruction, hits from four slats were missing. The reason for this was found to be the problem with electronics for one of the PMTs in these slats. Afterwards, hits in these 4 slats were reconstructed by using only one PMT. However, this affects the efficiency of the ToF-F wall and *tof* resolution and, it will be discussed later on. In the second step, *tof* hits were matched with TPC tracks. Matching depends in particular on the precise knowledge of the slat x position. For example, if we want to determine the x position of the slat m, we select events which contain hit in the slat m and extrapolate all tracks from these events to the z position of the ToF-F wall. In the process of the TPC track reconstruction, track parameters (momentum, position, and covariance matrix) are calculated and stored only for the first point on track which is usually inside the VTPC-1, more than 10 m away from the ToF-F wall. This greatly reduces the extrapolation precision. To overcome this issue, Kalman filter with track extrapolation procedure described in subsection 4.2 was used. This allows us to get track parameters at the last point on the track. Afterwards, the track is extrapolated from the last point to the ToF-F wall. Extrapolated track length from the target center to the ToF-F wall and the extrapolation uncertainty are shown in Fig. 4.9. The track length vs. x distribution has a comb-like structure which is due to the zig-zag positioning of the slats as explained in subsection 3.2.4. The extrapolation uncertainty in x is less than 0.5 mm for a typical track. Without Kalman filter, these uncertainties would be an order of magnitude larger. The center of slat m is determined by fitting a superposition of two error functions and a constant to the extrapolated x distribution. An example of this procedure can be seen in Fig. 4.10. The shape of the slat is visible in the $y-x$ distribution. Background in these distributions comes from the tracks which never actually hit the ToF-F wall (because of the decays, etc...), but they passed the cuts and were extrapolated to the ToF-F wall position. Most of them can be removed by applying stricter cuts and selecting only tracks which reach the last sector in the MTPCs. After obtaining slat positions, tracks are matched with the ToF-F hits if they are extrapolated within 1 cm from the edge of the active slat, which is equal to the width of the overlapping region.

4.6.2 Signal propagation speed in the ToF-F slats

From Eq. 4.29 we expect to have a linear dependence of the measured time in each channel on the y position of the hit. The slope is equal to the inverse signal propagation speed in the slat. To extract slope value, for a given slat, measured times for both channels were plotted vs. y position of the hit. Distributions are divided into slices in y, and Gaussian is fitted to each slice. Lines are then fitted to the mean values of the slices for both channels. Mean value of the two slopes is taken as an inverse signal propagation speed in a given slat. An example of the procedure described above is shown in Fig. 4.11. There are some nonlinearities at the edges of the slat, and they are probably due to imperfections in the foil wrapping and attenuation of the light for the hits which are created far away (near the opposite PMT). Mean inverse signal propagation speed in the whole ToF-F wall is 70.3 ps/cm and it can be seen in Fig. 4.12. This value is quite different from the value obtained in 2007, which is equal to 64.2 ps/cm. It was

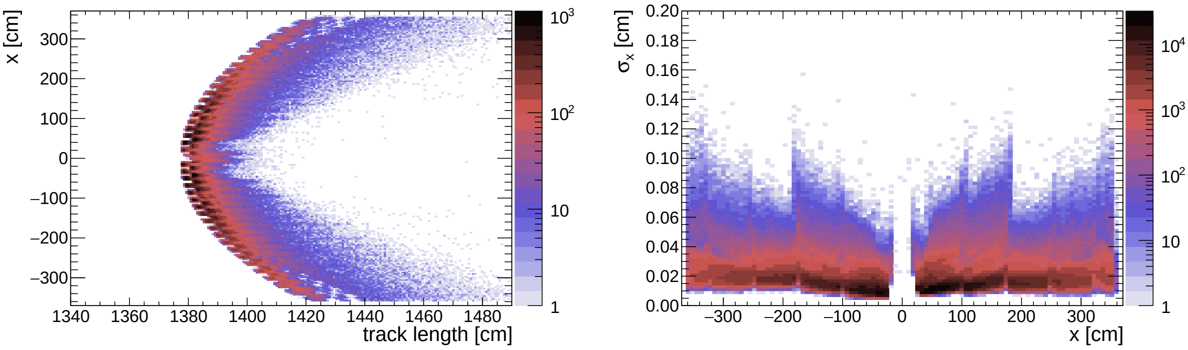

(a) (b)

Figure 4.9: Extrapolated track x position at ToF-F wall vs. extrapolated track length from the target center to the ToF-F wall (a) and extrapolated x uncertainty vs. x (b).

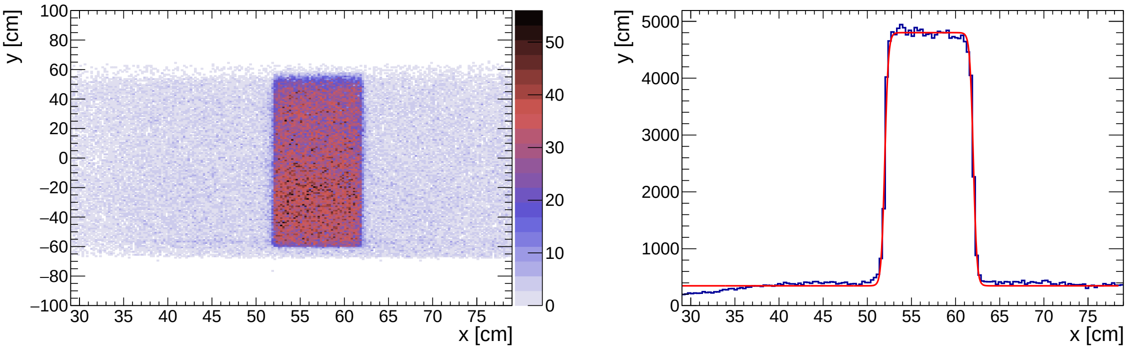

(a) (b)

Figure 4.10: Extrapolated position of tracks coming from the events with hit in scintillator 34: y-x distribution (a) and x distribution with fitted scintillator x position (b).

assumed that this is due to aging effects. However, there is no significant difference between central and edge slats where track density is higher and lower respectively.

4.6.3 Subtraction of t_0 values

In the next calibration step, a measured time in each channel is corrected for a t_0 constant. Calculation of t_0 constants is done under the assumption that produced hadrons below 2 GeV/c are mostly pions. Energy loss distribution for electrons and positrons is well separated from the pion energy loss distribution, so they can be removed from the hadron sample. Selected TPC tracks are extrapolated towards the center of the target and the ToF-F wall. Under the assumption that the track is a pion and with a known momentum and a track length it is possible to calculate a prediction for the time of flight. Calculated time is subtracted from the measured time of flight for both PMTs in the active slat. Obtained distributions are Gaussians with a background which comes from the other hadrons identified as pions. Mean of the Gaussian is the t_0 constant for a given PMT. An example of t_0 distribution can be seen in Fig. 4.13. In the next iteration, the raw time of flight with subtracted t_0 is used for calculating the squared mass of the particles. Now, it is possible to apply cut on the mass and select only pions. With pure

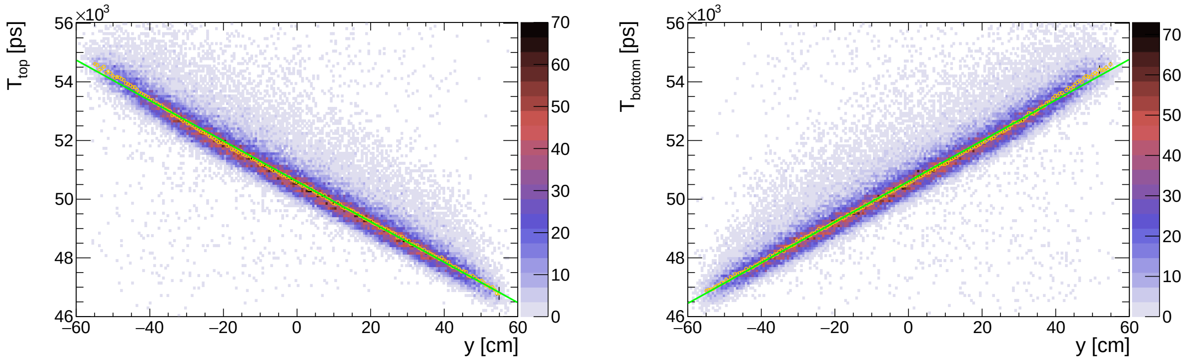

(a)

(b)

Figure 4.11: Time of flight dependence on the y coordinate of the hit for the top PMT (a) and bottom PMT (b) in the slat 25. Superimposed orange points are mean values of each slice. Superimposed dashed green lines are linear fits. Absolute value if the slope is equal to the estimate of inverse signal propagation speed in the slat.

pion sample, the whole procedure is repeated to get small corrections for the t_0 values. These corrections are usually in the range $0-2$ ps in size. Final t_0 values are shown in Fig. 4.14. The distinction is made for the top and bottom PMTs in each ToF-F slat. It is visible that the values are grouped in groups of 8 which shows a correlation between PMTs in the same ToF-F module.

4.6.4 Calibration of the start signal

A signal from the PMT1 connected to the S1 counter is used as a start signal for the whole trigger system. However, the beam has a non-negligible width, and beam particles can hit S1 at different regions, thus generated light will need different time to reach the PMT1. The time needed for light to reach PMT1 from the beam center is part of the t_{beam} and is included into t_0 constant. Fluctuations around beam center will cause fluctuations in the measured tof. In the end, this only affects the resolution of the squared mass, but not the mean value. As explained in subsection 3.2.1, the S1 counter has four PMTs, connected on 4 different sides. By using the mean time from all 4 PMTs it is possible to remove the dependence on the beam position and to get correct start signal. The correction is equal to:

$$T^{corr}_{start} = T_{start} + \Delta t = t_1 + \frac{1}{4}\left(\Delta t_{21} + \Delta t_{31} + \Delta t_{41}\right), \tag{4.30}$$

where t_1 is the start time used for the trigger, and it is defined as 0 and Δt_{j1} is the measured time difference between the signal in other PMTs and the first one. To improve the tof resolution, T^{corr}_{start} is subtracted from the measured tof. In previous measurements in 2007 and 2009, a typical start signal jitter correction is from -50 to 50 ps in size, depending on the event. It was clear that to reach tof measurement precision from 2007 and 2009, the jitter corrections need to have an order of magnitude larger range. This large increase suggests that there was another, not well-understood effect. Also, the information about TDC sampling rate for the S1 time difference measurement was lost, and the S1 counter was completely replaced before the start of this work. For these two reasons, a special procedure for calculating the time jitter correction was developed. Pions below 1 GeV/c were selected by applying energy loss and squared mass cuts. Energy loss was used to remove electrons and positrons, while squared mass resolution without

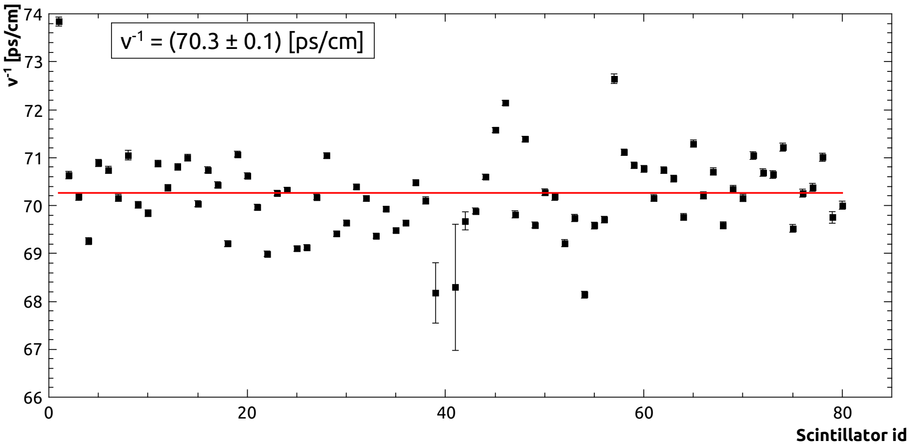

Figure 4.12: Inverse speed of light inside the ToF-F scintillator slats as a function of the slat number.

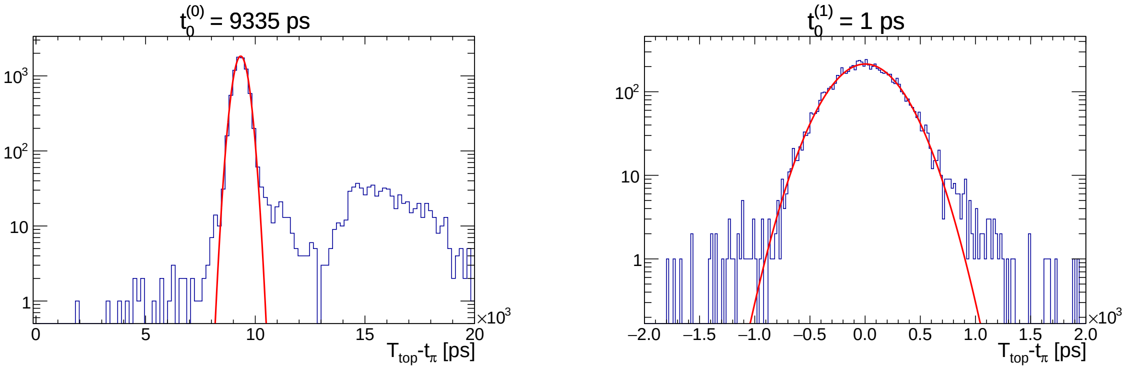

(a) (b)

Figure 4.13: Gaussian fit to the T0 distribution for top PMT in the slat 69: first iteration (a) and second iteration (b).

jitter corrections was good enough to remove protons and kaons. True *tof* was parametrized as:

$$tof_{true} = tof_{meas.} - \frac{1}{4}\left[k_{21}\Delta T_{31} + k_{31}\Delta T_{21} + k_{41}\Delta T_{41}\right], \tag{4.31}$$

where tof_{true} and $tof_{meas.}$ are the true and measured *tof* respectively, ΔT_{j1} is the measured TDC value with subtracted mean and k_{j1} parameters are to be determined. For selected pions, variance of squared mass was calculated as a function of k_{j1} parameters. Values of these parameters for which squared mass variance is minimal were determined by using Newton's method:

$$k_{21} = 6.55\,\text{ps}, \quad k_{31} = 1.63\,\text{ps}, \quad k_{41} = 9.25\,\text{ps} \tag{4.32}$$

Before applying the correction, the large correlations were found between the difference of measured and calculated *tof* for pions and TDC values measured by 3 additional PMTs connected to S1. After correcting for the jitter, these correlations vanish. This can be clearly seen in figure 4.15.

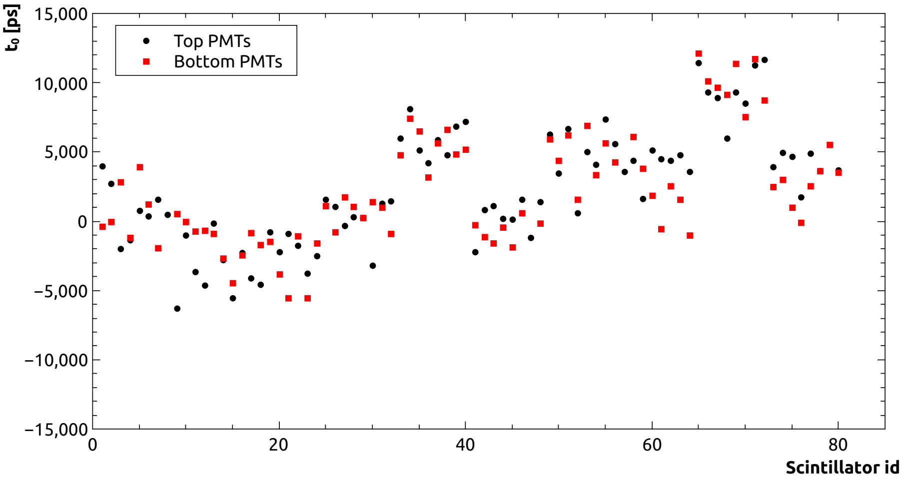

Figure 4.14: t_0 constants for top and bottom PMTs.

4.6.5 Intrinsic ToF-F resolution

After the calibration, the *tof* resolution was calculated to check the performance of the detector. It is possible to calculate the *tof* resolution for a single slat by comparing the measured time from the top and bottom channels. We expect to get Gaussian centered around 0, and a half width of the Gaussian is equal to the resolution of the *tof* measurement. The obtained resolution is equal to 113 ps, which is in agreement with the value of 110 ps reported in [109]. It is important to note that this value is not valid for all slats since we have four slats with only one channel working. Resolution of *tof* measurements for these slats is around 160 ps. This approach is shown in Fig. 4.16a. Low-quality hits, which are located in the tails of the same distribution can be discarded by applying quality cut, but this can be done only for slats with both channels working. Value of $|tof_{top} - tof_{bottom}| < 2000$ ps was used. This reduces the efficiency of the detector, but it improves separation between particles. If track hits the ToF-F wall in the region where two slats overlap it is possible to estimate the *tof* measurement resolution between 2 slats. Because centers of the two neighboring slats are 3 cm apart in z, we expect to get Gaussian centered roughly around 100 ps. As can be seen in Fig. 4.16b, the width of the Gaussian divided by $\sqrt{2}$ is equal to the *tof* resolution. The extracted value is equal to 123 ps which is comparable with the resolution obtained from the single slat measurements.

4.6.6 Squared mass resolution

Except for the intrinsic TOF-F resolution, effects like jitter of the start signal reduce the precision of the *tof* measurement. In turn, this affects the precisions of the $\mathrm{m}^2_{\mathrm{tof}}$. A realistic estimate of the $\mathrm{m}^2_{\mathrm{tof}}$ resolution is important for particle identification used in the analysis. The $\mathrm{m}^2_{\mathrm{tof}}$ vs. p distribution is plotted in Fig. 4.17a. To determine the resolution for hadrons, electrons and positrons were removed by using the energy loss cut. All tracks with energy loss larger than 1.35 mip are assumed to be electrons or positrons. Hadrons were separated by using a simple $\mathrm{m}^2_{\mathrm{tof}}$ cut. This can be done up to 4 GeV/c for protons and pions and up to 2 GeV/c for kaons. In the next step, $\mathrm{m}^2_{\mathrm{tof}}$ distributions for hadrons were binned in momentum and Gaussians were fitted to each bin. The width of the Gaussian was taken as an estimate of the $\mathrm{m}^2_{\mathrm{tof}}$ resolution for a given momentum slice. A parabola was then fitted to the obtained widths to get momentum

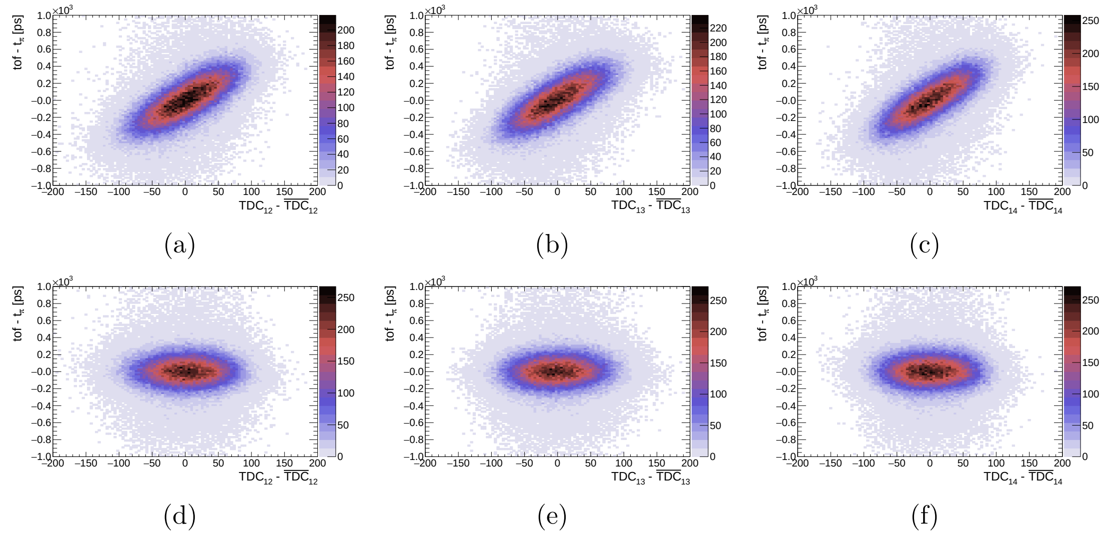

(a) (b) (c)

(d) (e) (f)

Figure 4.15: Difference between the measured and predicted *tof* vs. mean subtracted TDC value for PMT 2, 3, 4 in S1 counter, before (a, b and c) and after (d, e, f) jitter correction.

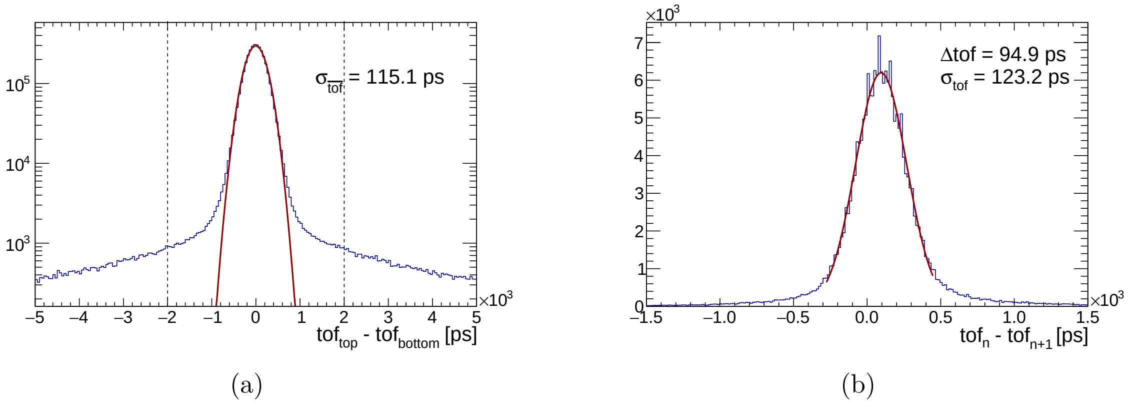

(a) (b)

Figure 4.16: Difference between the *tof* measured by top and bottom channels (a). The dark red line is fitted Gaussian, while dashed black lines are quality cuts. Resolution of the *tof* measurement by single slat is equal to the half width of the fitted Gaussian. Time resolution between two overlapping slats (b). Resolution of the *tof* measurement between two slats is equal to the width of the fitted Gaussian divided by $\sqrt{2}$.

dependence. This is shown in Fig. 4.17b. It can be seen that m^2_{tof} resolution is a bit better for pions than for more massive hadrons. The reason for this can be found in our choice that t_{beam} is constant for all events and tracks. Imagine, for example, that beam proton interacts at upstream target face and creates another proton with much lower momentum. Since we measure t_{beam} from S1 to the target center, bias in the measured *tof* is equal to:

$$\Delta tof = \frac{l}{2}\left(\frac{1}{v_{beam}} - \frac{1}{v}\right), \tag{4.33}$$

where l is the target length, v_{beam} is the beam proton speed which for this purpose can be equal to c and v is a speed of produced proton. For 1 GeV/c proton the bias is around 500 ps, but for a pion with the same momentum it is only 14 ps.

4.6.7 ToF-F efficiency

Signals in the TOF-F wall were not digitized in the Monte Carlo simulation, and therefore the efficiency of the hit detection with proper $\mathrm{m}^2_{\mathrm{tof}}$ measurement cannot be corrected with the Monte Carlo. There are two contributions to the inefficiency:

1. quality cut $|tof_{top} - tof_{bottom}| < 2000\,\mathrm{ps}$ and
2. multiple tracks hitting the same slat.

The first contribution depends mostly on the slat electronics and can vary independently from slat to slat. Slats with only one active channel do not suffer from this inefficiency. The second contribution depends on track density, and it is higher near the beam-line. The efficiency is determined by selecting only long tracks with good momentum measurement and a segment in the last sector of the MTPCs. This is done to avoid decays before the ToF-F wall and artificially reducing efficiency. A number of selected tracks with proper $\mathrm{m}^2_{\mathrm{tof}}$ measurement divided by the total number of selected tracks gives the efficiency as shown in Fig. 4.18. The efficiency of the first slat from the right is a bit lower. The reason for this is noisy electronics. It is hard to determine the efficiency of the central slats because this area is not instrumented by the TPCs. Also, this region is not very important, because the number of selected tracks is very low. It can be seen in the sub-figure 4.18b around −60 cm and −160 cm that two slats have a bit higher efficiency than neighboring slats. These two slats had only one active channel and, therefore, the quality cut on the *tof* measurement was not applied. Overall, mean efficiency is slightly lower than 97%. This information will be used for correcting the hadron yields during the analysis.

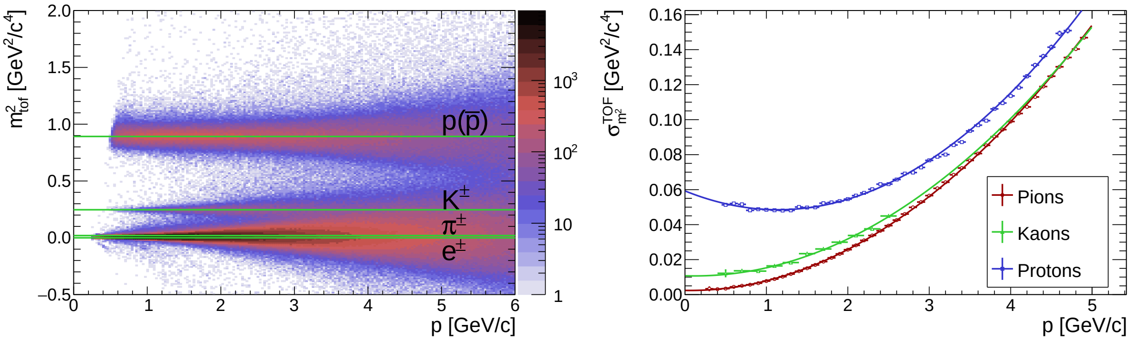

(a) (b)

Figure 4.17: Squared mass vs. momentum after the calibration procedure (left) and squared mass resolution vs. momentum for pions, kaons and protons (right).

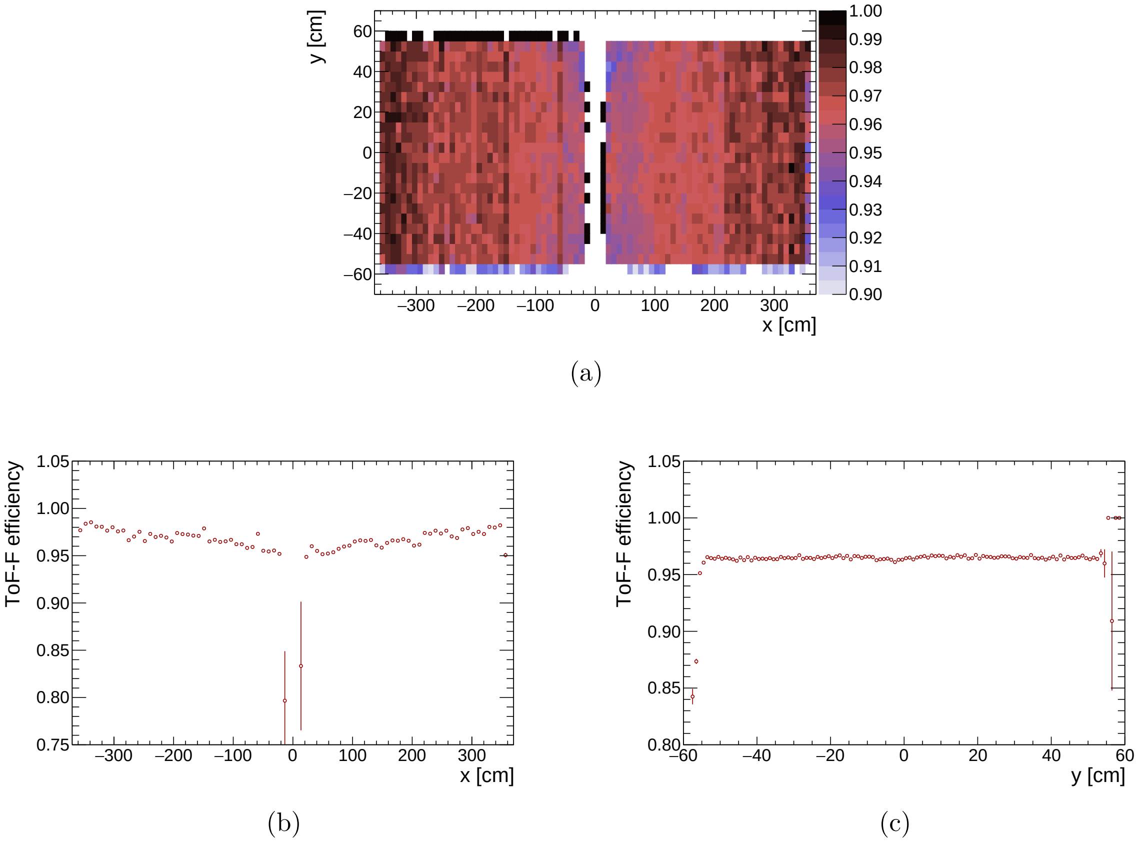

(a)

(b)

(c)

Figure 4.18: ToF-F efficiency: y vs. x (a), mean efficiency per slab (b) and mean efficiency of all slabs vs. y coordinate of the hit (c).

Chapter 5

Analysis of p + T2K replica target data

Contents

The analysis of the p + T2K replica target data will be presented in this chapter. The aim of this analysis is to extract hadron yields (π^+, π^-, K$^+$, K$^-$ and p) at the surface of the T2K replica target. Data were taken during the summer of 2010 and a total number of collected triggers is around 10.2×10^6. Additionally, it is important to note that around 11.7% of these events were recorded with the maximal magnetic field in the TPCs. This gives a possibility to measure a fraction of the non-interacting beam protons which are bent to the TPCs because of the high magnetic field. This subset of the data was previously used to improve calibration of the target position. The data taken with the maximum magnetic field will be denoted as high magnetic field data-set (HMF dataset), while data taken with the optimized magnetic field (to maximize total acceptance of the detector for these interactions) will be called low magnetic field dataset (LMF dataset). The analysis will be presented as follows: first, selection of the events and tracks will be explained. Afterwards, selected track for both the data and the Monte Carlo simulation will be binned in the phase space of momentum, polar angle and longitudinal position at the target surface (p, θ, z). A particle identification will be performed to distinguish between different hadron species and to remove any $e^{\pm}$ contamination. The results will be corrected for various inefficiencies by using Monte Caro simulation and data-based time of flight efficiencies. Finally, possible systematic biases will be discussed.

5.1 Beam and triggers

The secondary proton beam at 30.92 GeV/c used in 2010 data-taking was created by scattering primary SPS proton beam on the beryllium target. When selecting good events, it is necessary to ensure that:

1. beam hits the target,
2. pile-up events are removed and
3. number of misidentified beam particles is minimal.

5.1.1 Beam profile

As explained in subsection 3.2.1, the beam position is measured by three BPD detectors. After finding clusters in x and y BPD planes, two lines are fitted to the cluster positions and extrapolated towards the upstream target face. An example of reconstructed beam profile is shown in Fig. 5.1, both for T2 and T3 triggers. It is important to note that beam position in Fig. 5.1 is not corrected for the BPD-TPC alignment. A mesh structure can be seen on both of the beam profiles. The origin of the structure is unphysical and comes from the biased description of induced charge distribution on the cathode strip planes in the BPDs. During the reconstruction, clusters are determined by checking if there is a signal in one or more strips which is higher than a predefined threshold. Afterwards, a cluster is extended to include all surrounding strips which have signal larger or equal to 15% of the maximum. Gaussian is then fitted to the cluster to obtain cluster position. It was shown by Endo et al. [110] that using centroid methods for finding clusters in MWPCs yield biased cluster positions and cause the appearance of comb-like structures. These biases are possible to correct by calculating proper charge distributions. However, an attempt was made to improve beam profiles by tunning the signal thresholds used in cluster finding. The best result was obtained by using the threshold of 10% of the maximum. The improved beam profiles are shown in Fig. 5.2.

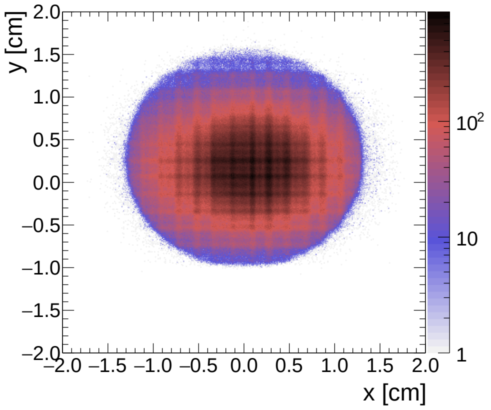

(a) (b)

Figure 5.1: T2 beam profile (a) and T3 beam profile (b).

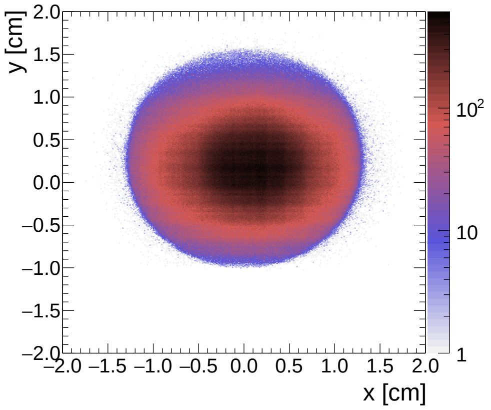

(a) (b)

Figure 5.2: T2 beam profile (a) and T3 beam profile (b) after adjustment of the signal threshold.

There is a clear correlation between the beam profile and position of the track exit point on the target surface. This will be explained in great detail in the final chapter. For this reason, it is important to use the same beam profile in Monte Carlo simulation as explained in the section 3.5. Any bias in the Monte Carlo beam profile will induce bias in the Monte Carlo correction factors. It is also necessary to account for the beam divergence which is taken as a slope from the linear fits. The beam divergence is shown in Fig. 5.3.

Several cuts are introduced to select beam tracks which hit the target. First, only beam tracks with three good clusters both in $x-z$ and $y-z$ planes are selected. This cut is denoted as BPD cut and it is applied by selecting only events with BPD reconstruction flag equal to 0. It removes beam tracks in which one or more clusters hit the BPD edge, or they are created by two beam particles which passed in quick succession. In next step, each beam track is extrapolated towards the downstream target face. If the beam track can exit from the target before the downstream target face (because of the divergence or target tilt), it is discarded (R cut). Since the error of the BPD measurement is around 200 μm, all tracks coming to the target mantle within this distance are discarded. Reason for this comes from the T2K experiment. Proton beam at J-PARC is narrow and proton track cannot exit through the target mantle without scattering.

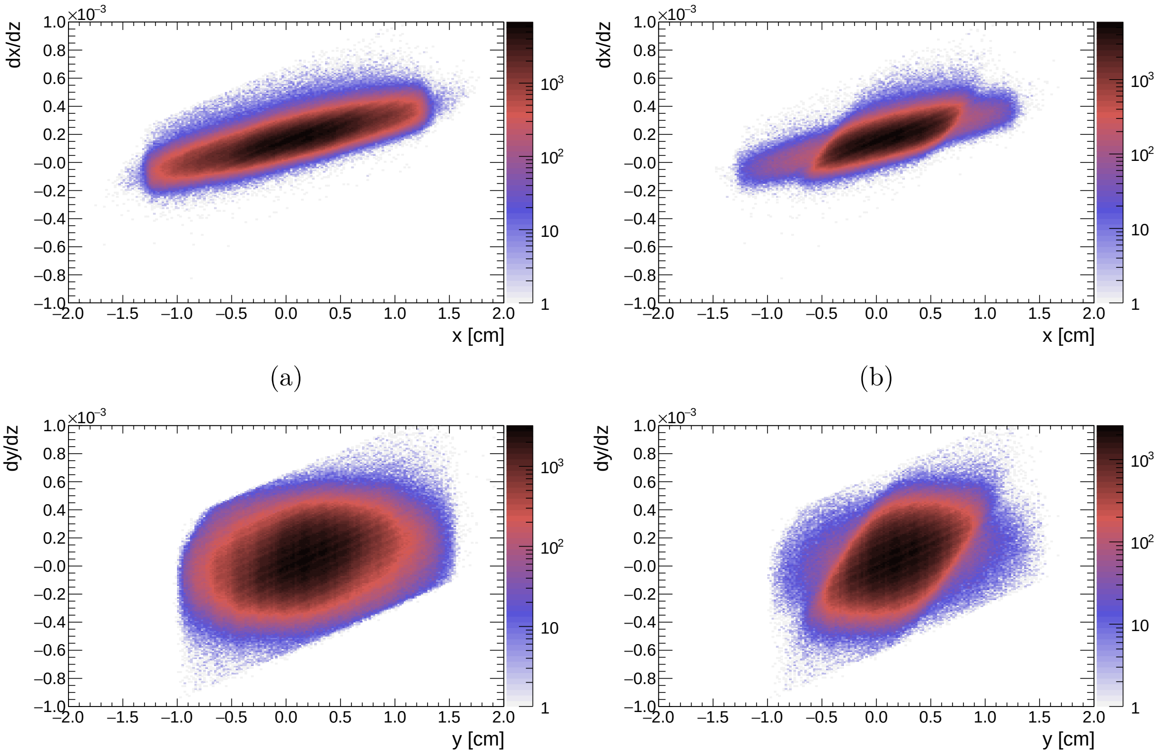

(a) (b)

(c) (d)

Figure 5.3: Beam divergence: dx/dz vs. x for T2 beam profile (a) and T3 beam profile (b); dy/dz vs. y for T2 beam profile (c) and T3 beam profile (d).

5.1.2 Beam composition and purity

Since proton beam used in the NA61/SHINE experiment is the secondary beam, it is obligatory to check the purity of the selected beam particles. If there is an admixture of other particles present in the beam, this will bias the hadron spectra. Beam identification is done by CEDAR in coincidence and the THC in anti-coincidence. The gas pressure in CEDAR is set so that only protons produce Cherenkov radiation with a specific angle so that CEDAR optical system can transport it to the PMTs. This also depends on the beam momentum, for higher momentum, separation is harder to achieve. In the case of 30.92 GeV/c protons, pressure for protons is around 3.3 bar, and it is shown in figure 5.4a. This measurement (so-called pressure scan) is done by changing gas pressure and measuring detection probability of Cherenkov radiation with six PMTs. The beam contains around 76.3% of π^+, 1.6% of K^+ and 12% of protons. Separation of protons and other hadrons is nearly perfect. Only possible misidentification comes from a small background caused by multiple scattering inside the CEDAR gas and beam divergence. From the CEDAR measurement, the purity of the beam is higher than 99.9%.

On the other hand, THC pressure scan gives gas pressure threshold below which protons do not radiate Cherenkov radiation. Percentage of protons found in THC pressure scan is consistent with CEDAR measurement, and it can be seen in Fig. 5.4a. Purity of the beam if selected only with THC would be around 91.2%, while combined CEDAR and THC measurements give purity very close to 100%. This ensures that it is not necessary to correct measured hadron yields for the beam purity effect. A conservative estimation of the low limit on the beam purity was done for 2009 beam and the reported value in [79] is 99.8%.

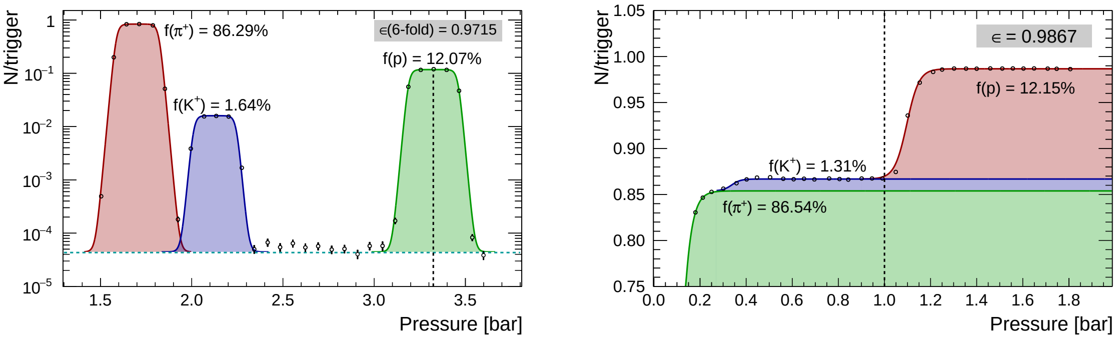

(a)

(b)

Figure 5.4: CEDAR pressure scan (a) and THC scan (b). Beam composition measured by both detectors is superimposed on the figures alongised with detector efficiencies. Vertical lines represent pressure settings used during 2010 data-taking.

5.1.3 Removal of off-time events

The acquisition time of the TPCs is quite long (around 50 μs) because of the long drift time needed for electrons to drift from the bottom to the top of the gas chamber. Off-time events, also called pile-up, are created when additional beam particles hit and interact with the target inside the acquisition time of the detector. Any particle produced in off-time interaction will be wrongly assigned to the triggered event. Since production of this particles is shifted in time with respect to the triggered event, the y position of these tracks in the TPCs will also be shifted. Secondary proton beam intensity measured by the S1 counter in 2010 was around 75000 particles per spill. Each spill had a duration of approximately 9 s. This gives beam intensity of around 8.3 kHz. By using Poisson distribution, it is straightforward to calculate the probability that there is at least one additional beam particle within $\pm 25\,\mu$s around the trigger. The obtained value is 34.1%. Usually, off time particles are measured by the Wave-Form Analyzer (WFA), but there was a problem with cabling during the data-taking, and this measurement was rendered wrong. In any case, removing whole events which possibly contain off-time tracks is not an optimal solution. The solution lies within the properties of the ToF-F wall. Its acquisition time is only 100 ns. The probability that off-time track hits the ToF-F wall inside of acquisition time window is less than 0.1%. Besides this, measurement of *tof* are used for particle identification, so practically all off-time tracks are removed without additionally loosing any statistics.

5.1.4 Beam and trigger selection

From the discussion in previous three subsections, it is clear that the only cuts which must be applied to the events are BPD and R cut. Additional quality selection will be performed on the individual tracks in the detector. Table 5.1 shows fractions of the events which passed the selection for both the LMF and the HMF datasets. Beam position detectors and triggers are not simulated in the Monte Carlo, so by default, the MC events have good beam track, and there is no pile-up or contamination of the beam. Furthermore, the HMF data does not have the T2 triggers recorded, because of a problem with the S3 counter during the HMF data-taking. For this reason, the S3 signal was removed from the T3 triggers in the HMF data. However, this did not change the beam profile since T3 beam is very narrow because of the V1' counter. In the LMF dataset, both, the T2 and the T3 triggers are not independent subsets of the data. In the 80% of the data, the T3 triggers make a subset within the T2 triggers. In the remaining data, information that event is a T2 was not stored for all events (it was prescaled by a factor of two). This is usual practice in the NA61/SHINE experiment in which often only main triggers are recorded every time (in this case T3), while others are prescaled by a predefined factor.

The hadron yields can be measured for both beam profiles. However, it is necessary to decide which one is more convenient for T2K. From the previous work by Alexis Haesler [83], it is already known that hadron yields at the upstream part of the target strongly depend on the beam width and position on the upstream target face. A Monte Carlo study was done by using Fluka2011.2c.5, π^+ yields were simulated on the surface of the T2K replica target with both of the NA61/SHINE beam profiles and compared with the π^+ yields simulated with the T2K run 4 beam profile. Ratios of the simulated yields are shown in Fig. B.1 and B.2. Yields are binned in momentum, polar angle and the six longitudinal bins on the target surface, sixth bin being downstream target face. It is clear that simulation with both of the NA61/SHINE beam profiles does not generate same π^+ yields at the low polar angle and upstream longitudinal bins as the simulation with the T2K beam profile. Ratios for T2 beam profile in the problematic region are larger than two, while for the T3 beam profile, they are around one half or less. It is important to note that the T2 beam profile is wider, while the T3 beam profile is narrower than the T2K beam profile. In the first order approximation, these differences can be explained purely by geometry (see discussion in section 6.2). Since both of the beam profiles do not accurately recreate conditions like in the T2K experiment, the final results must be re-weighted for these differences or it must be proven that these differences do not change the neutrino flux. Consequently, the only criteria or choosing the beam profile is statistics and for this reason, T2 has been chosen.

	Total	T2		T3		BPD		R	
	$[10^6]$	$[10^6]$	[%]	$[10^6]$	[%]	$[10^6]$	[%]	$[10^6]$	[%]
LMF data	8.970	8.239	91.85	-	-	6.762	75.39	6.726	74.98
		-	-	4.982	55.53	4.110	45.81	4.106	45.77
HMF data	1.235	-	-	0.686	55.55	0.566	45.82	0.566	45.82

Table 5.1: Event selection in data and MC.

5.2 Track selection

After selection of the events, additional selection criteria have been applied to the TPC tracks. In most of the NA61/SHINE analyses, this is done at the level of so-called vertex tracks which are regular TPC tracks re-fitted with the vertex constraint. However, in the case of this analysis, as it was stressed several times already, it is necessary to match TPC tracks with the point on the target surface. Therefore, the selection is applied directly to the TPC tracks before and after the backward extrapolation to the target surface. Tracks in the TPCs differ from each other in the two major ways. First, track parameters (for example momentum resolution) strongly depend on the number of points in the TPCs and in which of the TPCs the track has been reconstructed. So, we can divide tracks into several topologies, depending on which TPC inside the magnetic field they are passing. Different TPC topologies cover different areas of the (p, θ, z) phase space. Additionally, each track can be a right side track (RST) or a wrong side track (WST). Right side tracks are defined by the relation:

$$q \cdot p_x > 0, \tag{5.1}$$

where q is a measured charge and p_x is a x component of the momentum. The magnetic field is in $-y$ direction, so right side tracks will always be bent in the direction of p_x and therefore away from the beamline. In contrast to the right side tracks, the wrong side tracks are bent towards the beamline and often enter the opposite MTPC. They can be distinguished from the RSTs by the relation:

$$q \cdot p_x < 0. \tag{5.2}$$

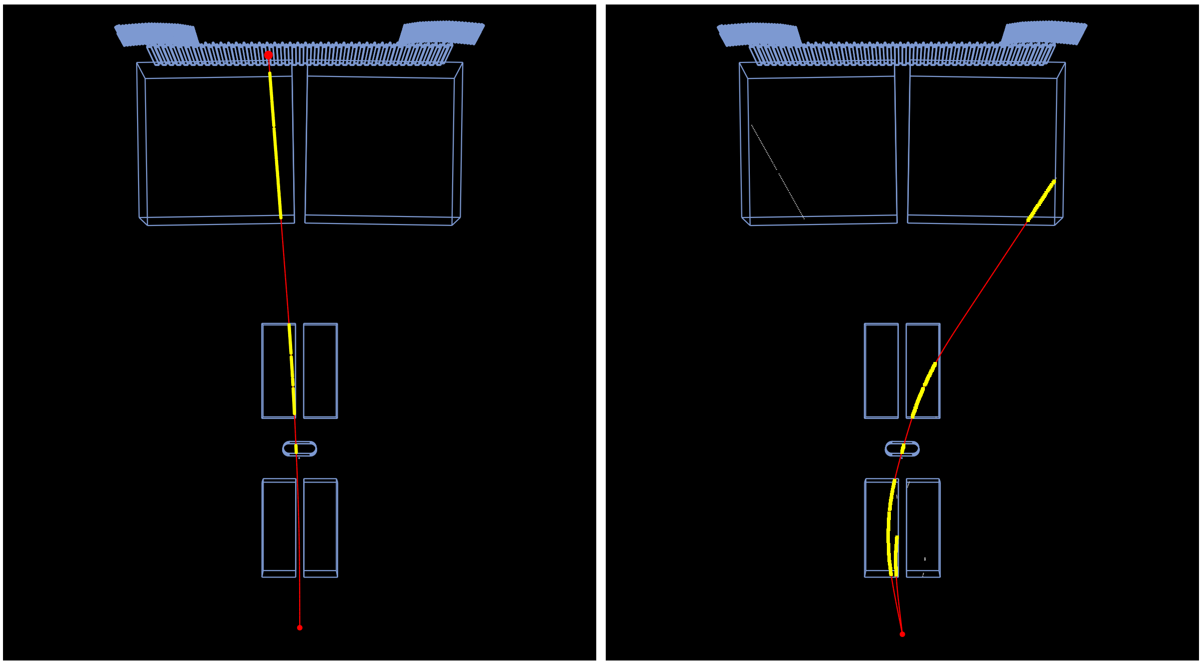
(a) (b)

Figure 5.5: Example of the right side track (a) and the wrong side track (b).

An example of the RST and the WST is shown in Fig. 5.5. Momentum and polar angle phase space coverages are rather different for the RSTs and the WSTs, and it will be shown later on. For this reason, momentum resolution will also be affected even though tracks from both categories can pass through the same TPCs. Momentum resolution for the different TPC topologies, RSTs, and WSTs is plotted in Fig. 5.6. It is achieved from the track fits directly. The worst resolution is obtained for the wrong side tracks for which the momentum was determined only by the GTPC. This is obvious since tracks can only have the maximum of seven clusters in the GTPC. This limits the precision of the backward extrapolation of the tracks. Average resolution for the majority of the tracks is below 1%. Some of the tracks with bad topologies can be removed by applying quality cuts.

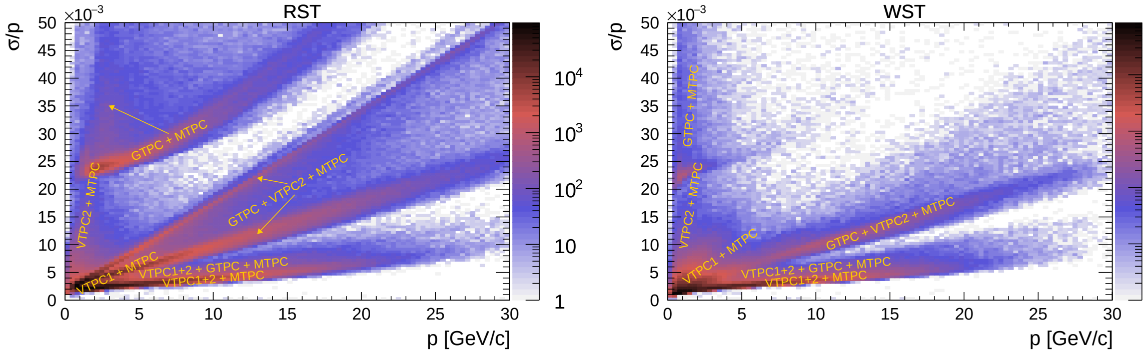

(a) (b)

Figure 5.6: Momentum resolution of the RSTs (a) and WSTs (b) for different TPC topologies.

5.2.1 Quality selection of the TPC tracks

The selection criteria were adopted and modified from the previous analyses done by N. Abgrall [111] and by A. Haesler [83]. In the "proof of concept" analysis done by N.Abgrall on the low statistics data taken in 2007, very strict selection criteria were used. Although these cuts minimized correction factors and systematic uncertainties of the measurements, they also removed tracks in the low polar angle regions of the phase space. However, pions in this region contribute greatly to the wrong sign flux in T2K (for example, contamination with the $\overline{\nu}_\mu$ in the ν_μ beam). For this reason, strict cuts were abandoned in favor of the more loose cuts which did not completely remove tracks in the low polar angle region. A Similar idea was followed by A. Hasler who analyzed data taken in 2009. The selection of the tracks can be roughly divided into five steps:

1. track has properly fitted momentum which is larger than 0.2 GeV,

2. track has energy loss and time of flight measurement,

3. track has a certain number of clusters:

   - if track momentum has been measured only by the GTPC, track needs to have at least 30 clusters in the MTPCs and 5 clusters in the GTPC,

   - if track momentum has been measured by one TPC (other than the GTPC), track needs to have at least 25 clusters in the VTPCs,

   - if track momentum has been measured by more than one TPC, track needs to have more than 20 clusters combined in VTPC1, VTPC2 and GTPC,

4. track is inside the defined azimuthal region of the acceptance, and
5. the point of closest approach to the target surface is within $3\sigma_R$, where σ_R is extrapolated radial position uncertainty.

Momentum selection

The requirement that TPC tracks have fitted momentum is trivial to understand since we want to measure hadron yields as a function of the momentum. Cut on the momentum value ($p > 0.2\,\mathrm{GeV}/c$) is not necessary, but it was applied to decrease computation time and remove tracks which would be removed by other cuts. There are several reasons why we can remove these tracks. Low-momentum tracks are bent away from the MTPCs and the TOF-F wall because of the too strong magnetic field. Only high polar angle ($> 260\,\mathrm{mrad}$) wrong side tracks with the momentum of $0.2\,\mathrm{GeV}/c$ can hit the TOF-F wall. This limit goes up for lower angles and becomes $0.4\,\mathrm{GeV}/c$. Additionally, pions with momenta below $0.07\,\mathrm{GeV}/c$ do not reach the TOF-F wall inside the time acquisition window. A similar limit for kaons is around $0.25\,\mathrm{GeV}/c$ and for protons is around $0.5\,\mathrm{GeV}/c$. Since one of the goals of this analysis is the measurement of the pions yields, the cut value was set to $0.2\,\mathrm{GeV}/c$.

Particle identification cuts

It is necessary for a track to have measurements of the energy loss and the time of flight. These two pieces of information are used for particle identification. Energy loss can be used in most of the cases alone, except when the energy loss distributions for different particle species cross. In that case, time of flight is used to distinguish between the particles.

Selection of the track quality

Momentum and position resolution depend on the number of clusters in the TPCs. The cut on the number of clusters changes with track topology. If the track momentum was measured by more than one TPC in the magnetic field, tracks with less than 21 clusters in those TPCs (VTPC1 + VTPC2 + GTPC) are discarded. This is sufficient to get momentum resolution of 2% or better (depending on momentum). When the track momentum has been measured by one of the VTPCs, only tracks with more than 25 clusters in the VTPCs are selected. Near the edges of the TPCs, there can exist a distortion in the electric and the magnetic fields. Such distortions can bias track parameters and reduce the efficiency of the matching of the track segments between the VTPCs and the MTPCs. Selected tracks with more than 25 clusters ensure that this bias is minimal. Track passing through the GTPC can have a maximum of 7 clusters, while a minimum number of 4 clusters is required for the reconstruction software to reconstruct a GTPC track. In cases when momentum has been measured only by GTPC, tracks must have at least 5 clusters in the GTPC. Also, these tracks need to have at least 30 clusters in the MTPCs. This condition removes GTPC tracks with momentum resolution worse than 5%. Additionally, all high momentum tracks ($> 10\,\mathrm{GeV}$) passing nearly parallel and close to the edges of the MTPCs are removed by this cut. In this region, interactions with the material in the MTPCs are not negligible, and the secondary track density is high, thus decreasing the efficiency of the matching between the track segments. In contrast to the previous analyses, no requirement on the number of clusters in the MTPCs is applied to other track topologies. Possible systematic biases regarding this choice of the cuts will be discussed in more details in sections 5.3 and 5.5.

Azimuthal selection

The efficiency of the detector changes depending on the azimuthal angle (ϕ) of the tracks. After TPC tracks have been extrapolated towards the target surface, it is straightforward to calculate the azimuthal angle:

$$\phi = \tan^{-1}\left(\frac{p_y}{p_x}\right), \tag{5.3}$$

where p_x and p_y are x and y components of the momentum respectively. One reconstructed event in the $x-y$ plane of the NA61/SHINE coordinate system is shown in Fig. 5.7. Coordinate axes and naming scheme for the azimuthal angle are overlaid on top of the figure. It is clear that tracks with a higher polar angle (θ) will be reconstructed only for azimuthal angles around 0° and 180°. The goal of applying the azimuthal angle selection is to select only regions in $\theta-\phi$ space in which acceptance is constant.

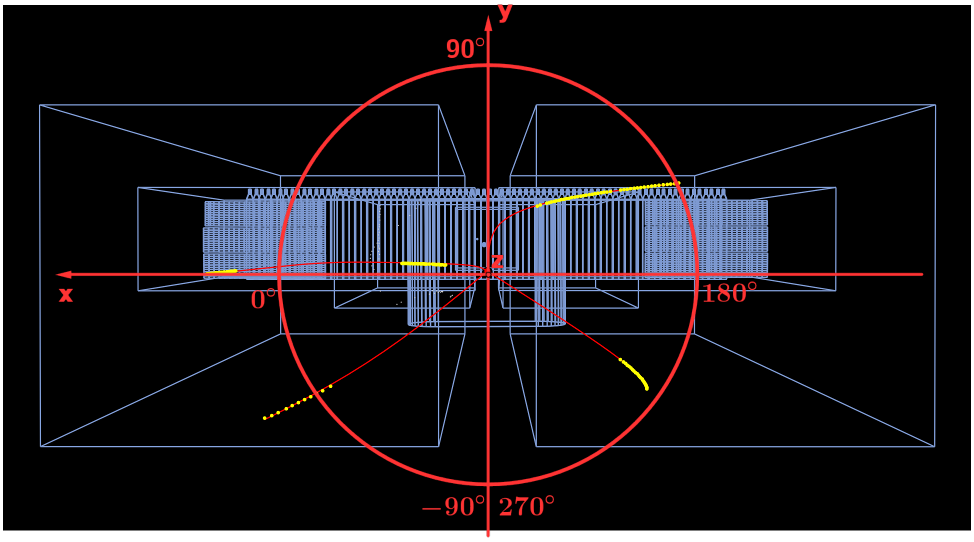

Figure 5.7: Azimuthal angle definition in the NA61/SHINE coordinate system.

The purpose of this cut is to reduce the model dependence of the particle yields. As mentioned before, measured yields will be presented in the bins of momentum, polar angle and longitudinal position along the target surface. Inefficiencies for all bins are corrected with Monte Carlo simulation. Momentum and polar angle distributions of the hadrons in the simulation may significantly differ from the data distributions. If this is the case and acceptance varies significantly in a given bin, this could bias the correction factor. For this reason, the polar angle has been divided into eleven intervals, and for each interval, only tracks within following

ϕ ranges are selected:

$$0 \le \theta < 20\,\mathrm{mrad} \quad \phi \in [-70°, 70°] \cup [110°, 250°], \tag{5.4a}$$
$$20 \le \theta < 40\,\mathrm{mrad} \quad \phi \in [-60°, 60°] \cup [140°, 220°], \tag{5.4b}$$
$$40 \le \theta < 60\,\mathrm{mrad} \quad \phi \in [-45°, 35°] \cup [145°, 225°], \tag{5.4c}$$
$$60 \le \theta < 80\,\mathrm{mrad} \quad \phi \in [-30°, 30°] \cup [150°, 210°], \tag{5.4d}$$
$$80 \le \theta < 100\,\mathrm{mrad} \quad \phi \in [-20°, 20°] \cup [160°, 200°], \tag{5.4e}$$
$$100 \le \theta < 120\,\mathrm{mrad} \quad \phi \in [-17°, 17°] \cup [163°, 197°], \tag{5.4f}$$
$$120 \le \theta < 140\,\mathrm{mrad} \quad \phi \in [-15°, 15°] \cup [165°, 195°], \tag{5.4g}$$
$$140 \le \theta < 160\,\mathrm{mrad} \quad \phi \in [-13°, 13°] \cup [167°, 193°], \tag{5.4h}$$
$$160 \le \theta < 200\,\mathrm{mrad} \quad \phi \in [-12°, 12°] \cup [168°, 192°], \tag{5.4i}$$
$$200 \le \theta < 240\,\mathrm{mrad} \quad \phi \in [-11°, 11°] \cup [169°, 191°], \tag{5.4j}$$
$$\theta \ge 240\,\mathrm{mrad} \quad \phi \in [-10°, 10°] \cup [170°, 190°]. \tag{5.4k}$$

Additionally, such cuts remove not just regions with rapidly changing acceptance, but also regions where simulation behaves differently than data (for example regions where the percentage of the selected tracks drops slower in the simulation than in the real data). Selected $\theta-\phi$ regions are shown in Fig. 5.8a, while the projection of the $2D$ distribution to the ϕ axis normalized to one is shown both for the data (black points) and for Monte Carlo (red line) in Fig. 5.8b. Monte Carlo distribution is in good agreement with the data.

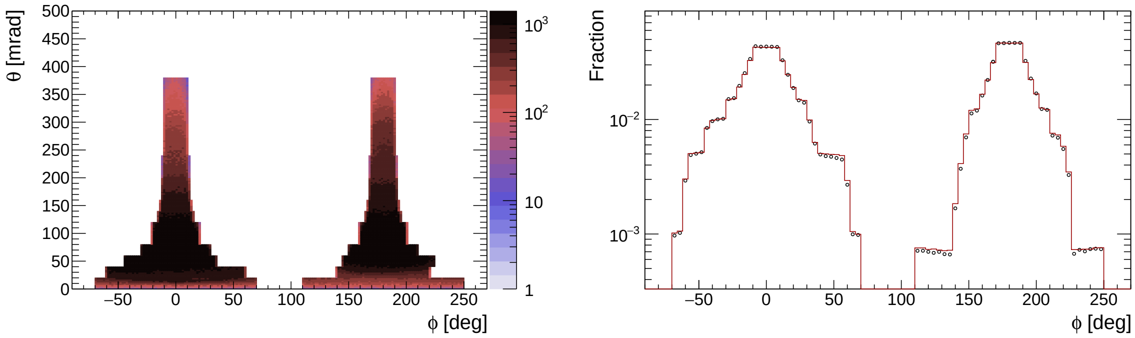

(a)

(b)

Figure 5.8: Selected region in the $\theta-\phi$ phase space for the data (a) and comparison of the selected ϕ angles between the data and the MC (b).

Point of closest approach

Some of the selected and extrapolated tracks were created outside of the target in the re-interactions with the material in the detector or in the weak decays. An additional cut was applied to the distance of approach with respect to the target surface, to minimize the number of these tracks. Extrapolation is stopped when track reaches minimal distance from the target surface. If a track does not hit the target, it is selected only if the distance from the target surface is less than three radial position uncertainties. The uncertainty of the extrapolated position depends strongly on the distance between the first cluster in the TPCs and the target.

Additionally, it depends on the target topology (quality of the reconstruction). Distance from the target surface, together with the radial position uncertainty are shown in Fig. 5.9. Different track topologies have different uncertainty distributions which reflect already mentioned causes (distance from the target and reconstruction quality). Around 93% of the tracks passes this cut, and this number is somewhat lower for tracks which do not start in the VTPC1 (around 88%) and somewhat higher for other tracks (95%).

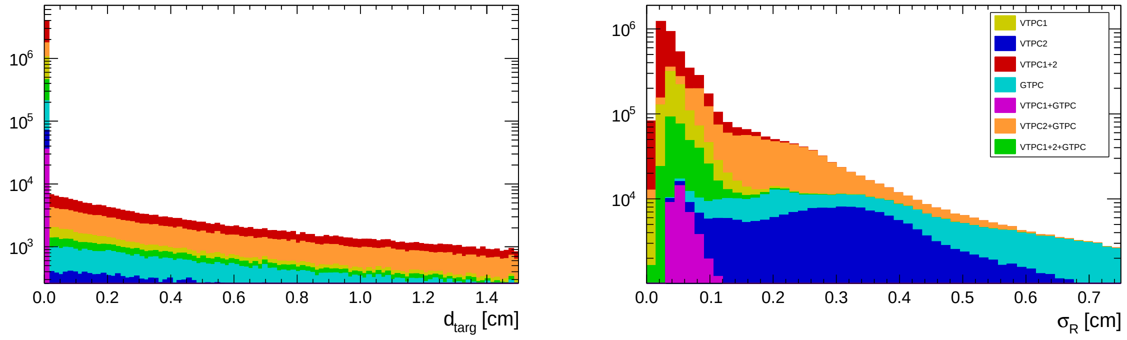

(a)

(b)

Figure 5.9: Track distance from the target surface (a) and radial position uncertainty (b).

A total number of the selected tracks, both for the data and the Monte Carlo is presented in the appendix C (see table C.1). Fractions of tracks which belong to different track topologies are also written in the table after each cut. Numbers of selected tracks for the data and the Monte Carlo simulation are expected to be different since we do not expect to have the same momentum and polar angle distribution in the Monte Carlo simulation. A number of selected tracks per event can point out how large are differences between FLUKA2011.2c.5 and the data:

$$R = \left(\frac{N_{tr}}{N_{ev}}\right)_{MC} : \left(\frac{N_{tr}}{N_{ev}}\right)_{data} = 1.08, \tag{5.5}$$

where N_{tr} and N_{ev} are numbers of selected tracks and event respectively. The average number of the selected tracks per event is around 8% higher in the data compared to the simulation. However, one needs to keep in mind that reconstruction of the *tof* signals was not done in the Monte Carlo simulation (hits are just assigned to the tracks which hit the TOF-F wall). Some of these differences come from the TOF-F measurement efficiency which is on average between 96% and 97%. Also, as it was described before, protons below $0.5\,\mathrm{GeV}/c$ do not reach the TOF-F wall during the acquisition time. If additional cut on momentum is applied ($p > 0.5\,\mathrm{GeV}/c$) and the number of selected tracks is corrected for the TOF-F inefficiency ratio becomes:

$$R = 1.02. \tag{5.6}$$

5.2.2 Phase space

Selected tracks have been divided into the bins of momentum (p), polar angle (θ) and longitudinal position along the target surface (z). Reason for measuring hadron yields in the bins of the longitudinal position is explained in subsection 2.5.4. Target has been partitioned into five longitudinal bins covering whole target length and downstream target face as a sixth bin. Then number of selected tracks per number of events as a function of the longitudinal position on the target surface is shown in Fig. 5.10. Monte Carlo distribution is scaled down by a factor of 0.965 To account for the TOF-F efficiency. It is clear that the number of selected tracks in the simulation is lower with respect to the data at the downstream part of the target (last two bins) and a bit higher at the upstream side. This gives a hint that the best agreement between measured hadron yields and the FLUKA2011.2c.5 will be obtained for the central z bin. Selected tracks in each z bin are further divided into $\theta - p$ bins. Polar angle vs. momentum phase space is shown in Fig. 5.11 and 5.12 for the right side tracks and the wrong side tracks respectively. It is clear that RSTs and WSTs do not cover same areas in the phase space. Right side tracks cover low polar angle regions and higher momenta, while for the higher angles and low momenta, they are bent out from the TPCs before hitting the TOF-F wall. In contrast to the right side tracks, the wrong side tracks cover higher polar angles since they are bent back to the beam-line. For this reason, wrong side high momentum forward going tracks stay in the beam-line and they are not detected in the TPCs. A total number of $\theta - p$ bins depends on which hadron yields we want to measure. It is obvious that the pion statistics will be much higher than the kaon statistics (order of magnitude difference), so the number of bins for pions can be proportionally larger. Pion binning for all z bins includes in total 884 $\theta - p$ bins, while for the kaons number is equal to 144. In case of protons, there is a limitation in the momentum space. As already mentioned, protons below 0.5 GeV/c cannot hit the TOF-F wall in the acquisition time window, while this is not the case in the Monte Carlo simulation. For this reason, momentum bins for protons below 0.5 GeV/c are not allowed. Total number of $\theta - p$ bins for protons is 580. Binning has been optimized so that statistical uncertainty in each bin is roughly equal, except for some bins at the edge of the phase space.

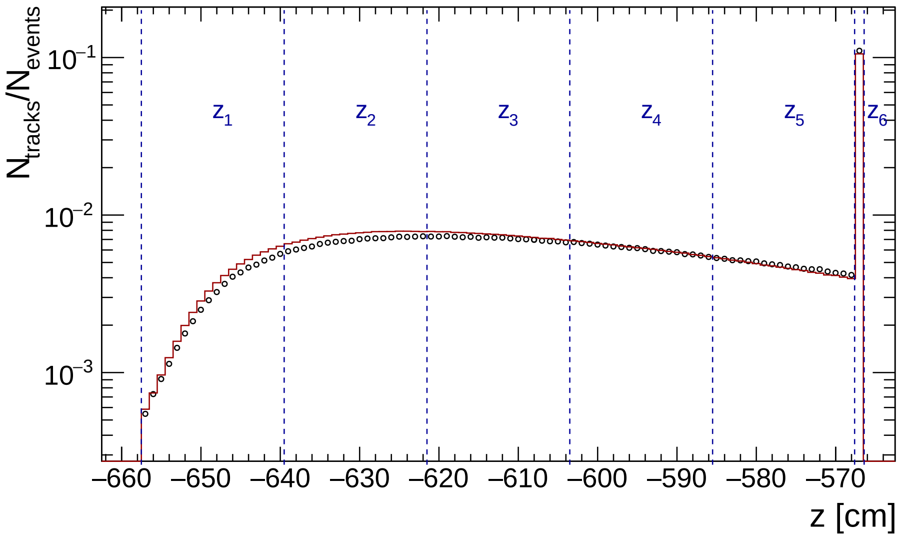

Figure 5.10: Extrapolated z distribution for the data (black points) and for the Monte Carlo simulation (red line). Longitudinal bin borders are overlaid on the top of the distribution.

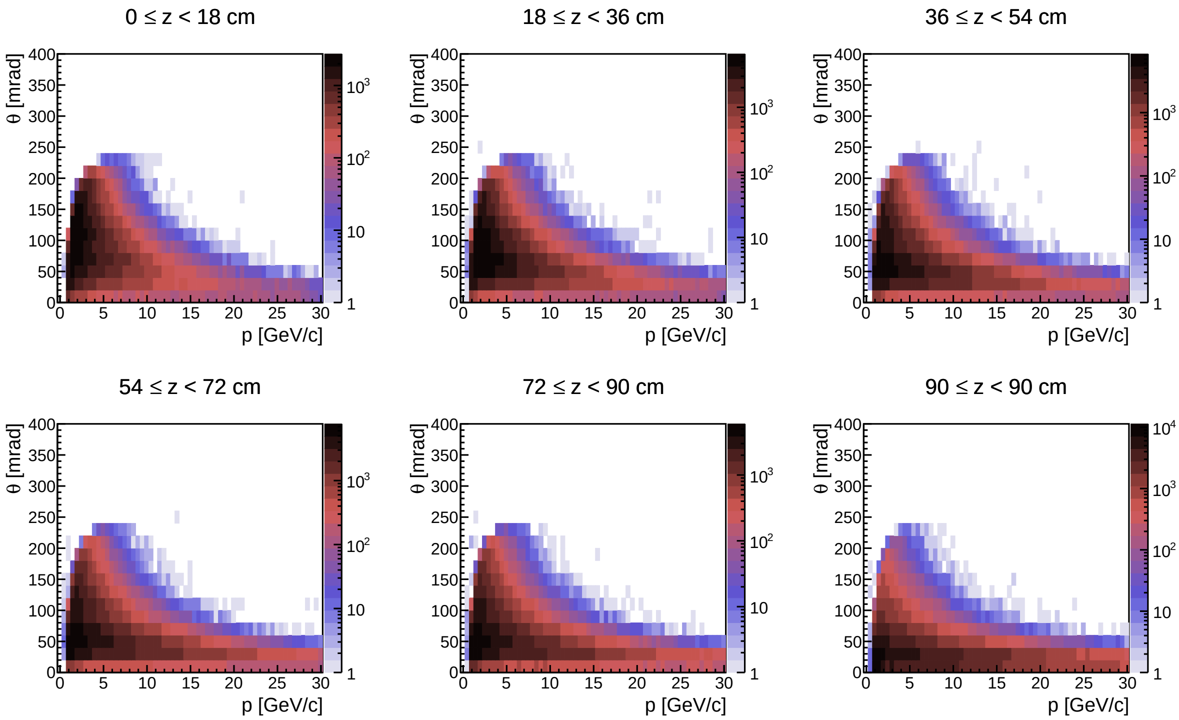

Figure 5.11: Polar angle vs. momentum ($\theta - p$) phase space for the right side tracks. Each panel represent different z bin.

5.3 Particle identification

Particle identification is applied to the positive and negatively charged tracks separately. Method for particle identification is the so-called joint energy loss and time of flight identification. Both, energy loss (dE/dx) and time of flight (tof) have limitations when used separately, which are avoided when used together. Energy loss suffers from ambiguity in the region around few GeV/c. The reason for this is crossing of the energy loss distributions for protons and kaons over the distributions for the lower mass particles (pions and electrons/positrons). In this region, time of flight measurement has the sufficient resolution to distinguish between kaons, protons, and pions, while above 8 GeV/c resolution becomes insufficient for any discrimination between the particles.

The reconstructed tracks are mostly: $e^{\pm}$, $\pi^{\pm}$, $K^{\pm}$, and p. There is also a non-negligible number of $\bar{\text{p}}$, which is not enough to measure yields with good precision but must be taken into account. Contamination with deuterons is mostly negligible and can be taken into account by applying a cut on the tof mass squared (deuterons are well separated from all other tracks below 4 GeV/c). Muons created in decays of pions and kaons cannot be distinguished from pions because of the similar mass. Nevertheless, a number of the muons is kept well below 1% in all bins simply by applying cut on the distance of approach to the target surface. Any remaining muons are removed by a Monte Carlo based correction factor. Any possible biases coming from the correction are studied as a part of the systematic uncertainties. As a consequence, four positive (e^+, π^+, K^+, p) and four negative (e^-, π^-, K^-, $\bar{\text{p}}$) particle species are taken into account. For each of the particle species, it is necessary to build joint $dE/dx - m^2_{tof}$ distribution.

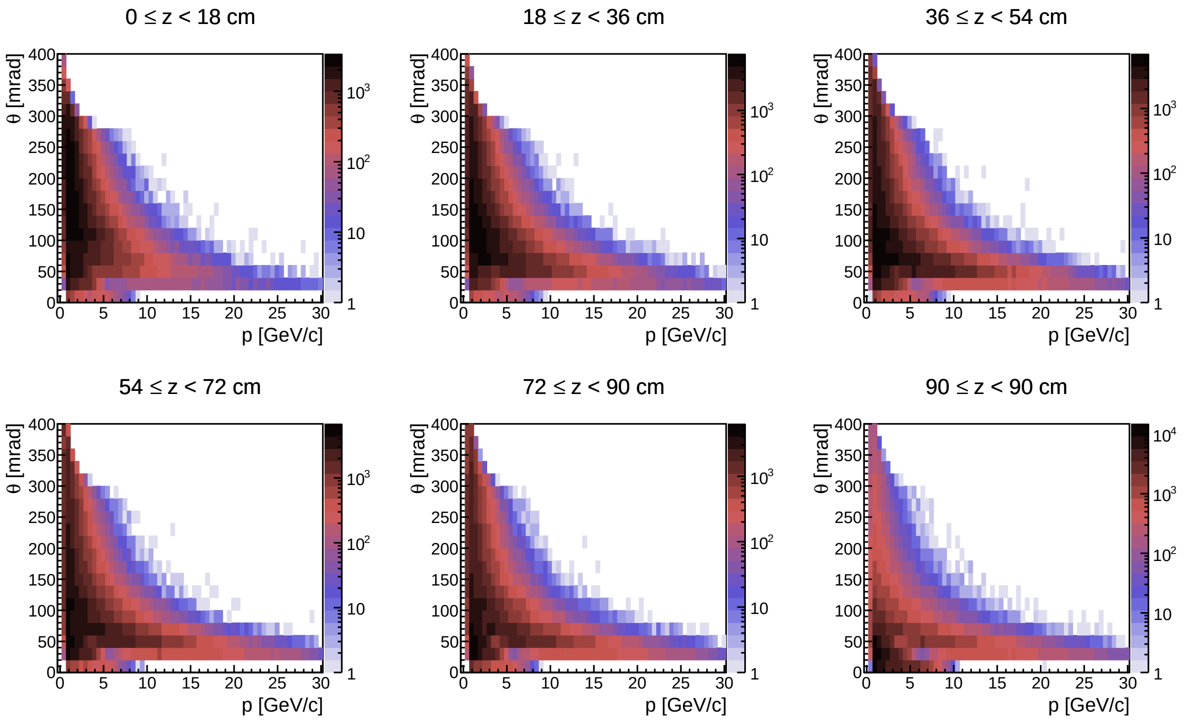

Figure 5.12: Polar angle vs. momentum ($\theta - p$) phase space for the wrong side tracks. Each panel represent different z bin.

5.3.1 Energy loss

Energy loss measurement is done in all TPCs except in the small GTPC. Therefore, resolution of the energy loss measurement will depend on the total number of clusters in those TPCs. The measured energy loss can be seen in Fig. 5.13 as a function of log$p$, alongside with the parametrized mean values for different particles.

If we take a slice in momentum, the obtained dE/dx distribution is expected to be Gaussian-like. In each phase space bin there are tracks with different number of clusters, therefore energy loss distribution for particle species α should be a sum of Gaussians:

$$f_i^\alpha(dE/dx;\mu_\alpha,\sigma_1,...,\sigma_n) = \sum_{j=1}^{n} \frac{A_{ij}^\alpha}{\sigma_j\sqrt{2\pi}} \exp\left(-\frac{(dE/dx-\mu_i^\alpha)^2}{2\sigma_j^2}\right), \tag{5.7}$$

where i is a phase space bin number (which determines momentum range), μ_i^α is a dE/dx mean value, which depends on the particle species and the momentum, σ_j is a width of the dE/dx distribution for tracks with j number of clusters and $A_{\alpha j}$ is a number of tracks with j clusters. It is assumed that widths of the dE/dx distribution do not depend on the momentum. A maximum number of clusters (n) for which energy loss has been measured is 234. Cluster distribution is shown in Fig. 5.14a, while dependence of the dE/dx resolution as a function of the number of clusters is shown in Fig. 5.14b. Above 60 clusters per track, the resolution changes slowly from 5% to 3%. For the lower number of clusters, the resolution changes rapidly from 15% to 5%. Around 98.5% of the selected tracks have more than 60 clusters, so it is possible to simplify

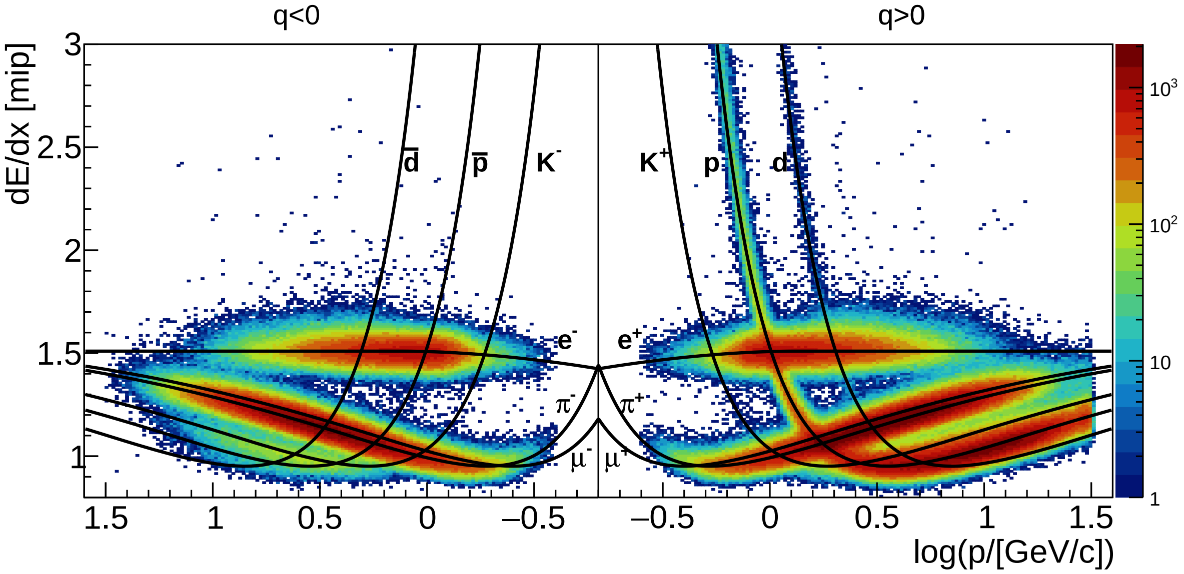

Figure 5.13: Energy loss distribution vs. $\log(p)$ for the data. The left panel shows the distribution of the negatively charged tracks and the right panel shows the distribution of the positively charged tracks. Energy loss parameterization is overlaid on top of the distributions.

relation 5.7 by assuming that a single Gaussian is sufficient for describing the dE/dx distribution in a single phase space bin:

$$f_i^\alpha(dE/dx;\mu_\alpha,\sigma_i^\alpha) = \frac{A_i^\alpha}{\sigma_i^\alpha\sqrt{2\pi}}\exp\left(-\frac{(dE/dx-\mu_i^\alpha)^2}{2(\sigma_i^\alpha)^2}\right). \tag{5.8}$$

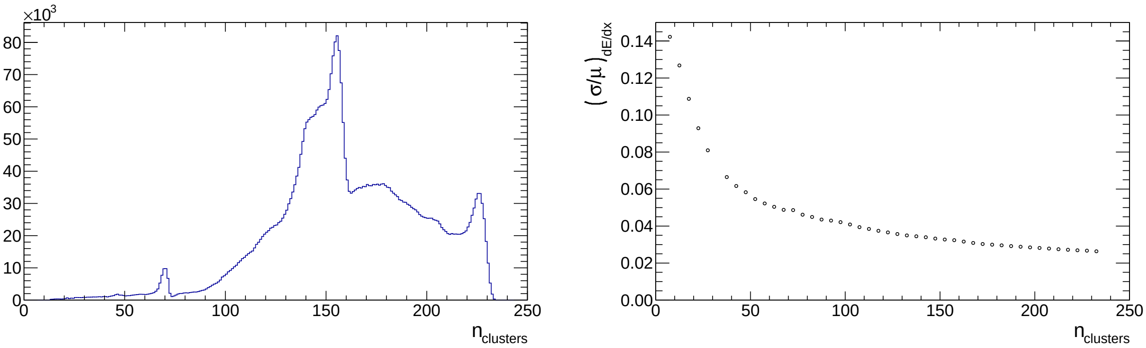

(a)

(b)

Figure 5.14: Distribution of a number of clusters for selected tracks (a) and energy loss resolution with respect to the number of clusters. Resolution saturates around 0.03 for tracks with the large number of clusters. Clusters in the GTPC are not included since energy loss measurement is not performed in the GTPC.

Tracks with the low number of clusters may create tails in the dE/dx distribution for a given phase space bin. The possibility of the bias is investigated in subsection 5.5.6.

5.3.2 Time of flight

Particle identification with the time of flight is done by using the *tof* mass squared measurement as explained in detail in section 4.6. Similarly to the energy loss, *tof* mass squared distribution in a given phase space bin should be normally distributed. From the calibration, it has been already shown that width of the distribution is proportional to the momentum squared ($\sigma \propto p^2$). If we divide one phase space bin (which can be for example 1 GeV/c in size) to several momentum slices (let's say 0.2 GeV/c in size), *tof* mass squared distributions can have radically different widths in each slice. Furthermore, different track topologies have different momentum resolution which can result in different *tof* mass squared resolution. It was found that best description of the *tof* mass squared distribution is given by a double Gaussian:

$$f_i^\alpha(m_{tof}^2; m_{\alpha i}^2, \sigma_{\alpha 1,2}^{tof}, \eta) = \frac{A_i^\alpha}{\sqrt{2\pi}}\left[\frac{\eta}{\sigma_{\alpha 1 i}^{tof}}\exp\left(-\frac{(m_{tof}^2 - m_{\alpha i}^2)^2}{2(\sigma_{\alpha 1 i}^{tof})^2}\right) + \frac{(1-\eta)}{\sigma_{\alpha 2 i}^{tof}}\exp\left(-\frac{(m_{tof}^2 - m_{\alpha i}^2)^2}{2(\sigma_{\alpha 2 i}^{tof})^2}\right)\right], \tag{5.9}$$

where A_i^α is a number of particles α in a given phase space bin i, $m_{\alpha i}^2$ is a mean value of the mass squared distribution for the particle species α, $\sigma_{\alpha 1,2 i}^{tof}$ are widths of the mass squared distribution, and η is a fraction of the first Gaussian in the total distribution. The fraction is assumed to be the same for all particle species. Above 8 GeV/c where *tof* measurements lose their discriminatory power, η is fixed to one, in other words, single Gaussian is used. Single Gaussian can also be used for lower momenta without creating any significant bias, but double Gaussian gives better fits especially for momenta below 3 GeV/c.

5.3.3 Joint energy loss and *tof* mass squared fit

When dE/dx and *tof* are used together, each particle species is represented by the normally distributed structure in the two-dimensional $m_{tof}^2 - dE/dx$ space. Joint $m_{tof}^2 - dE/dx$ parametrization for the two-dimensional distribution is:

$$f_i^\alpha(dE/dx, m_{tof}^2; A_i^\alpha, \mu_i^\alpha, \sigma_{\alpha i}^{dE/dx}, m_{\alpha i}^2, \sigma_{\alpha 1 i}^{tof}, \sigma_{\alpha 1 i}^{tof}, \eta) = \frac{A_i^\alpha}{2\pi\sigma_i^{dE/dx}}\exp\left(-\frac{(dE/dx - \mu_i^\alpha)^2}{2(\sigma_i^{dE/dx})^2}\right)\times \left[\frac{\eta}{\sigma_{\alpha 1 i}^{tof}}\exp\left(-\frac{(m_{tof}^2 - m_{\alpha i}^2)^2}{2(\sigma_{\alpha 1 i}^{tof})^2}\right) + \frac{(1-\eta)}{\sigma_{\alpha 2 i}^{tof}}\exp\left(-\frac{(m_{tof}^2 - m_{\alpha i}^2)^2}{2(\sigma_{\alpha 2 i}^{tof})^2}\right)\right], \tag{5.10}$$

where all parameter have been previously defined in Eq. 5.8 and 5.9. In total, there are 25 parameters for the positively charged tracks and the same number for the negatively charged tracks, while for momenta above 8 GeV/c number of parameters decreases to 20. Extended log likelihood fits were performed within the RooFit framework. Parameters A_i^α represent raw particle yields in a given phase space bin (not corrected for any inefficiency effects). An example of the fit for a single phase space bin is shown in Fig. 5.15. The figure shows two-dimensional distribution and projection to the dE/dx and m_{tof}^2 axes with corresponding residuals. Bins are usually optimized for one particle species, for example, pions. Selected tracks are re-binned, and the fits are repeated to extract other particle species with low statistical uncertainty.

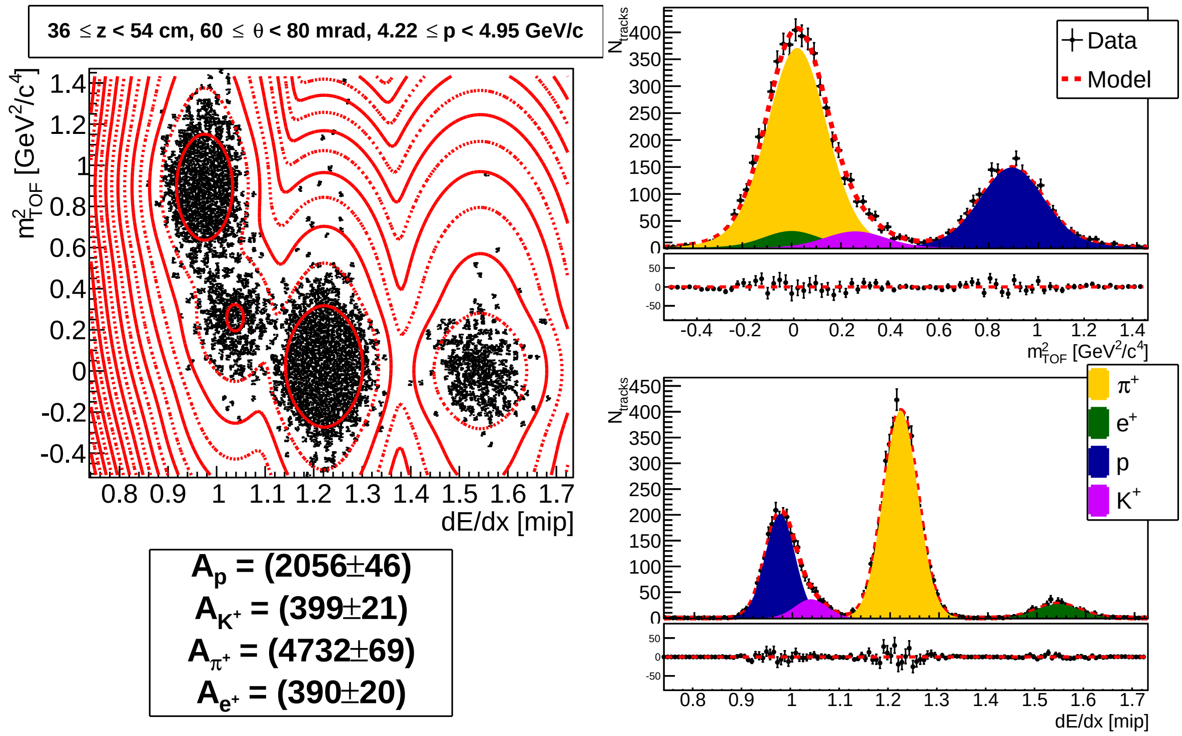

Figure 5.15: Example of the particle identification fit for the positively charged tracks. The top left panel shows $m^2_{tof} - dE/dx$ distribution, the top right panel shows a projection to the m^2_{tof} axis, the bottom right panel shows a projection to the dE/dx axis and the bottom left panel shows a number of extracted particles.

5.3.3.1 Initialization of the parameters

Because of a large number of parameters, it is important to set the initial values and ranges of the parameters properly. The mean value of the energy loss is taken from the calibrated dE/dx parametrization (see figure 5.13). The allowed range for the mean value of the energy loss varies depending on the particle species. For pions, it is set to ±10%, while for the protons and electrons/positrons it is ±8%. In case of kaons, the range is set to only ±5%. This is because kaons are under the proton peak in the energy loss distribution and under the pion peak in the *tof* mass squared distribution for the momenta larger than 2 GeV/*c*. This makes K^+ yields difficult to extract with great precision. The width of the dE/dx distribution is estimated to be $0.04\mu_i^\alpha$ for all particle species, and the range is set to ±35% of the value, to account for the possible variations in the number of clusters per track.

Mean values for the squared *tof* mass are taken from the figure 4.17a. Ranges for electrons/positrons and pions are set to ±100% because of the very small absolute values of the masses (for example, $m_\pi^2 = 0.019\,\text{GeV}^2/\text{c}^4$). Ranges for kaons and protons are set to ±50% and ±30% respectively. Widths of the *tof* mass squared distributions which are momentum dependent are also taken from the calibration (see figure 4.17b), while the ranges are set to ±35% for all particle species. Since there are two *tof* widths for each particle species, first one is evaluated at the low momentum border of the phase space bin, while the second one is evaluated at the high momentum border. Fraction η is set to value 0.7 and allowed to change from zero to one for momenta below 8 GeV/*c* and fixed to one above the defined threshold.

After initial values for the energy loss and the *tof* parameters have been determined, initial values for the multiplicity yields are calculated by counting the number of tracks 2.5σ around the mean values for dE/dx and m^2_{tof}. Allowed ranges are set to ±50% for electrons/positrons, pions, and protons, while for kaons range is set to ±100%. This is because kaon distribution mostly overlaps with the proton or the pion distribution.

5.4 Correction factors

Raw yields extracted from the particle identification fits need to be corrected for various effects like geometrical acceptance, detector efficiency, bin migration, etc. This follows the procedure developed in [111] and in [83] which proved that multiplicative corrections properly corrected the data and more complicated procedures like unfolding are not necessary. Two separate corrections are applied to the raw yields. First one is a Monte Carlo based correction, while the second one is a data-based *tof* efficiency correction. The total correction factor is a product of the Monte Carlo correction factor and the *tof* correction factor. The standard convention in the NA61/SHINE collaboration is to use inverse correction factors which can be represented as efficiencies:

$$C^{-1}_{ijk} = \epsilon^{MC}_{ijk} \epsilon^{tof}_{ijk}, \tag{5.11}$$

where C^{-1}_{ijk} is an inverse total correction factor in a $i-$th z bin, $j-$th θ bin and $k-$th p bin, ϵ^{MC}_{ijk} is a Monte Carlo efficiency in the same bin and ϵ^{tof}_{ijk} is a *tof* efficiency.

5.4.1 Monte Carlo correction factors

Monte Carlo efficiency is defined as:

$$\epsilon^{MC}_{ijk} = \frac{n^{sel}_{ijk}}{N^{sim}_{ijk}}, \tag{5.12}$$

where n^{sel}_{ijk} is a number of particles (for example π^+), reconstructed, selected and extracted from the Monte Carlo fits. Parameter N^{sim}_{ijk} is a total number of simulated particles in the same phase space bin. The efficiency from the previous equation can be expanded into several different factors:

$$\epsilon^{MC}_{ijk} = \epsilon^{feed-down}_{ijk} \cdot \epsilon^{mig}_{ijk} \cdot \epsilon^{sel}_{ijk} \cdot \epsilon^{rec}_{ijk} \cdot \epsilon^{loss}_{ijk} \cdot \epsilon^{\phi}_{ijk}, \tag{5.13}$$

where:

- ϵ^{ϕ}_{ijk} is a geometrical efficiency,
- ϵ^{loss}_{ijk} is a hadron loss efficiency,
- ϵ^{rec}_{ijk} is a reconstruction efficiency,
- ϵ^{mig}_{ijk} is an extrapolation migration efficiency, and

- $\epsilon_{ijk}^{feed-down}$ is a feed-down efficiency.

Geometrical efficiency is a pure geometrical factor. It is a ratio of the simulated number of tracks in the defined azimuthal angle region and the total number of the simulated tracks in a given bin. Hadron loss efficiency accounts for the hadrons which decayed or re-interacted before hitting the TOF-F wall. Reconstruction efficiency can be divided into two factors: an efficiency of the detector ($\epsilon_{ijk}^{TPC\,rec}$) and an efficiency of the extrapolation (ϵ_{ijk}^{ext}). The former one is essentially the probability that track is reconstructed in the TPCs after passing through the TPCs, while latter one gives the probability that the reconstructed Monte Carlo track is extrapolated to the same phase space bin in which it was simulated. Migration efficiency is a ratio of the number of reconstructed tracks which originated from the target surface and were extrapolated to a given bin and the number of the reconstructed tracks which originated from the same bin. In some cases, it can be larger than one. Finally, feed-down efficiency is a ratio of the total number of particles reconstructed, selected and extracted from the Monte Carlo fits and the number of reconstructed and selected tracks which originated from the target surface. This efficiency is also larger than one since there are additional tracks created outside of the target which can be extrapolated to the target surface and pass all cuts. These tracks usually come from the weak decays outside of the target, for example, decays of K_s^0 and Λ.

Although Monte Carlo correction is applied in its global form, the factorization of the Monte Carlo efficiency is useful since it is necessary to check for possible systematic biases for all factors.

5.4.2 Time-of-flight efficiency correction

Since the time of flight efficiency cannot be corrected with the Monte Carlo correction factor, the *tof* efficiency correction is based on the data. The efficiency of each slat in the TOF-F wall and its uncertainty have been evaluated during the calibration procedure and presented in subsection 4.6.7. These results can be used for calculating *tof* efficiency in a given phase space bin:

$$\epsilon_{ijk}^{tof} = \frac{n_{ijk}}{\sum_{s=1}^{80} n_{ijk}^{s}/\epsilon_s}, \tag{5.14}$$

where n_{ijk} is a total number of data tracks in a given phase space bin, n_{ijk}^s is a number of tracks in a given bin with a *tof* hit in the *tof* slat s and ϵ_s is an efficiency of the slat s. Usually, tracks from a single phase space bin have hits only in a few neighboring *tof* slats. Very small bins contain tracks with hits in a single *tof* slat. It is clear that uncertainty of the *tof* efficiency correction depends on the statistics contained in the phase space bin and the size of the bin itself. Therefore, the *tof* efficiency and the uncertainty are re-calculated for different particles species when different binning is used. As mentioned before, phase space bins were produced so that obtained statistical uncertainty is roughly constant. This also creates stable *tof* efficiency factors. Overall, the *tof* efficiency is close to 97%, but it can go down to 90% for the wrong side tracks crossing the beam-line and hitting one of the central TOF-F slats.

5.4.3 Ad hoc correction factor

Monte Carlo correction factor, alongside with the data based *tof* correction factors are usually sufficient to fully correct any of the NA61/SHINE data. However, it was noticed that for the first three upstream bins and the polar angles larger than 260 mrad, there is a sudden decrease in the hadron yields. This sharp decrease was caused by the large decrease in the selection efficiency in the data which was in some cases more than 50% lower than in the simulation. The missing tracks have been found only as segments in the VTPC1 (with more than 15 clusters), while in the Monte Carlo these tracks were also reconstructed in the MTPCs and have the *tof* hit assigned to them. High polar angle tracks coming from the upstream part of the target, enter the VTPC1 close to its outer wall (far away from the beamline). Afterwards, these tracks partially pass through the magnet yoke and close to the edge of the magnetic field map. In Monte Carlo, the field outside of the coverage of the magnetic field map is zero, while this is not the case in reality. Additionally, there is a strong possibility that the field at the edges of the field map is not adequately described, and tracks passing through this region could be bent differently than in the simulation. To correct for this effect an ad hoc correction was applied to the hadron yields:

$$C_{ijk}^{adhoc} = \left(\frac{n_{sel,tof}^{MC}}{n_{sel}^{MC}}\right)_{ijk} / \left(\frac{n_{sel,tof}^{data}}{n_{sel}^{data}}\right)_{ijk}, \tag{5.15}$$

where $n_{sel,tof}^{MC(data)}$ is a number of selected tracks with *tof* hit in the Monte Carlo (data) and $n_{sel}^{MC(data)}$ is a number of selected tracks in the Monte Carlo(data) without the *tof* requirement. In total, only around 1.5% of the phase space bins for pions and protons are affected by this problem. Phase space bins for kaons are large and cover large polar angle regions (last polar angle bin is $180\,\text{mrad} - 280\,\text{mrad}$) so this bias is negligible. It is important to note that pion yields in [83] are probably biased in the same region.

5.5 Systematic uncertainties

Before estimating the systematic uncertainties, it is necessary to define the hadron yields. The results will be presented in the form of double differential multiplicities:

$$\left(\frac{dn_\alpha}{d\theta dp}\right)_{ijk} = \frac{1}{N_{ev}} \cdot \frac{n_{ijk}^{\alpha}}{\Delta\theta_{ijk} \cdot \Delta p_{ijk}} \cdot C_{ijk}^{MC} \cdot C_{ijk}^{tof}, \tag{5.16}$$

where:

- ijk are indexes representing i-th z bin, $j-$th polar angle bin and $k-$th momentum bin,
- N_{ev} is a number of selected events,
- n_{ijk}^{α} is a number of measured particles of species $\alpha = \pi^+, \pi^-, \mathrm{K}^+, \mathrm{K}^-, \mathrm{p}$,
- $\Delta\theta_{ijk}$ is a polar angle bin size,
- Δp_{ijk} is a momentum bin size,
- C_{ijk}^{MC} is a Monte Carlo correction factor, and
- C_{ijk}^{tof} is a data based *tof* correction factor.

Correcting the data with the Monte Carlo or data based correction factors induces possible systematic biases. Such biases are estimated by changing various parameters in the analysis like cuts or target position. After changing one or more selection criteria or some other parameter, the analysis is repeated, and ratios of the new hadron yields and the nominal hadron yields are computed. In many cases, most of the factors defined in Eq. 5.16 cancel out. Systematic uncertainties are taken as deviations of the ratio from one. There are several possible systematic biases which need to be estimated:

- hadron loss,
- reconstruction algorithm,
- backward extrapolation uncertainty,
- feed-down correction,
- particle identification,
- *tof* efficiency, and
- ad-hoc correction for high polar angles ($> 300\,\mathrm{mrad}$)

5.5.1 Hadron loss

Produced hadrons can re-interact with the material in the detector or in the case of pions and kaons, they can decay before reaching the TOF-F wall. Since all selected tracks have reconstructed TOF-F hits, it is expected that additional cut on the distance of the last measured cluster from the TOF-F wall will not change the hadron yields. In other words:

$$n^{\alpha}_{ijk} \cdot C^{MC}_{ijk} = \mathrm{const.} \tag{5.17}$$

This assumption has been examined by selecting tracks with the z position of the last cluster equal to $z = 620\,\mathrm{cm}$, which is equivalent to the maximum distance of approximately $150\,\mathrm{cm}$ from the TOF-F wall. No limitation on this distance has been applied in the standard selection. Hadron loss systematic uncertainties are presented in Fig. 5.16 till the figure 5.20 for π^+, π^-, K^+, K^-, p (in that order). In the majority of the phase space bins, there is no difference before and after applying the additional selection criteria. However, in the regions where wrong side tracks cross beamline and remain close to the opposite MTPC wall, there can be large differences. Example for this is region can be seen in the region between $20\,\mathrm{mrad}$ and $60\,\mathrm{mrad}$ and from $5\,\mathrm{GeV}/c$ to $10\,\mathrm{GeV}/c$ in the first z bin. For positively charged pions and protons, the additional cut seems to increase the yields in this regions up to 40%. For negatively charged pions, bias goes in the opposite direction. In the same polar angle and momentum regions, in other z bins, a similar effect is present, but it is much smaller in size ($< 15\%$). Such behavior may be explained if the sensitive areas in the MTPCs are slightly shifted in the Monte Carlo to

$-x$ side with respect to the data. These TPCs were built in the 1990s and inherited from the NA49 experiment. Technical documentation is mostly lost, and there is a strong possibility that description of the MTPCs in the Monte Carlo (close to the beamline) was not done properly. In case of kaons, observed bias is much smaller, and this is a consequence of the bin sizes. Much larger bin sizes ensure that number of the problematic tracks in a given bin is dominated by the number of tracks passing through the well-described regions of the detector.

5.5.2 Reconstruction bias

Reconstruction bias related to the choice of the track merging algorithms was investigated for the 2009 $p+C$ measurements. Since reconstruction software remained the same till now, the estimated value of 2% from 2009 analysis has been assigned to the whole phase space.

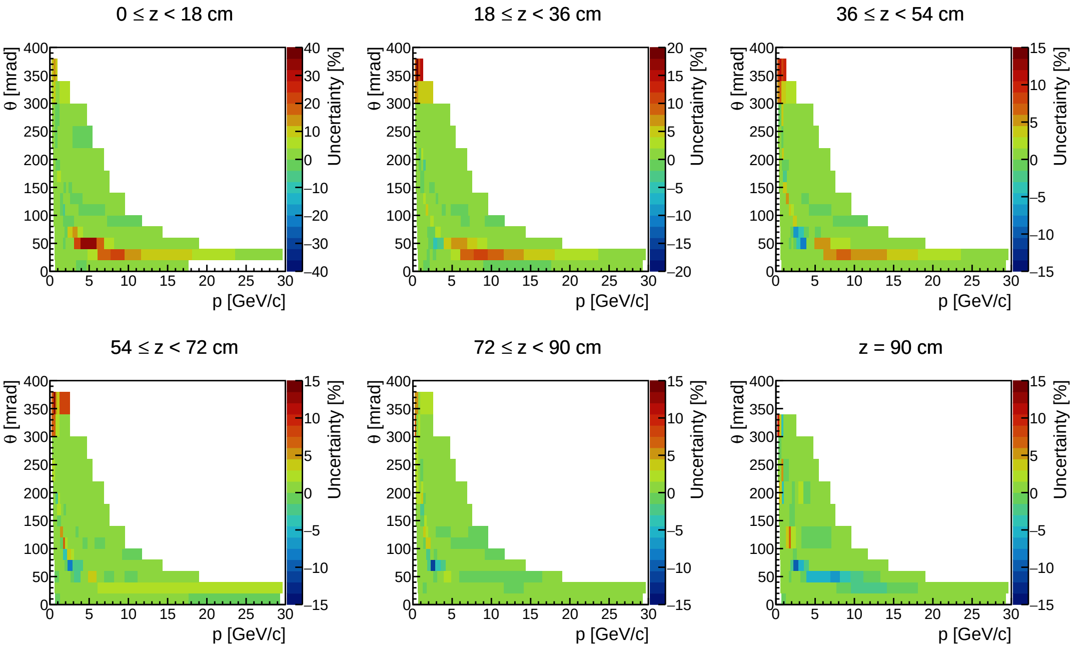

Figure 5.16: Hadron loss systematic uncertainty for positively charged pions. Each panel shows different z bin. Uncertainty ranges for the first two z bins are different. Errors presented here show negative value which underlines the fact that these errors are asymmetric and go only in one direction.

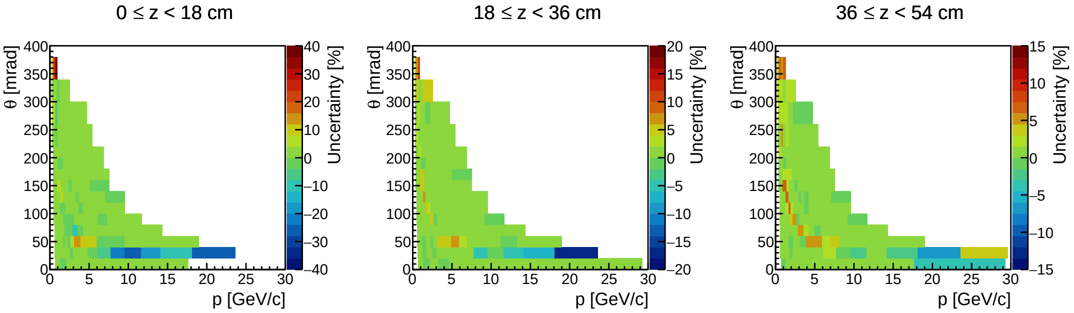

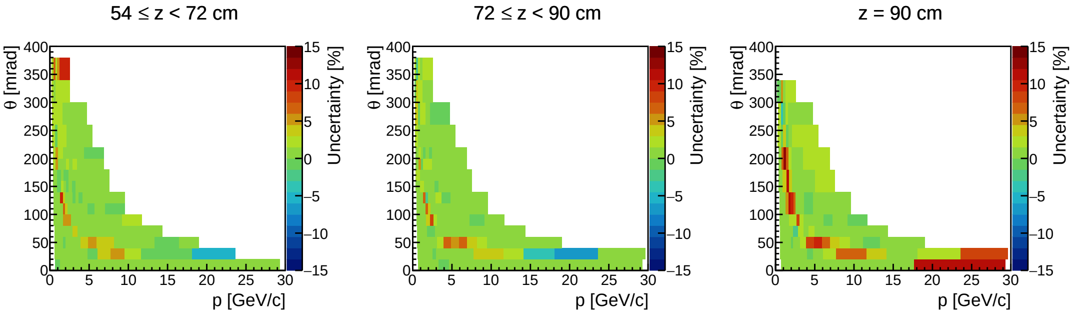

Figure 5.17: Hadron loss systematic uncertainty for negatively charged pions. Each panel shows different z bin. Uncertaintys range for the first two z bins are different.

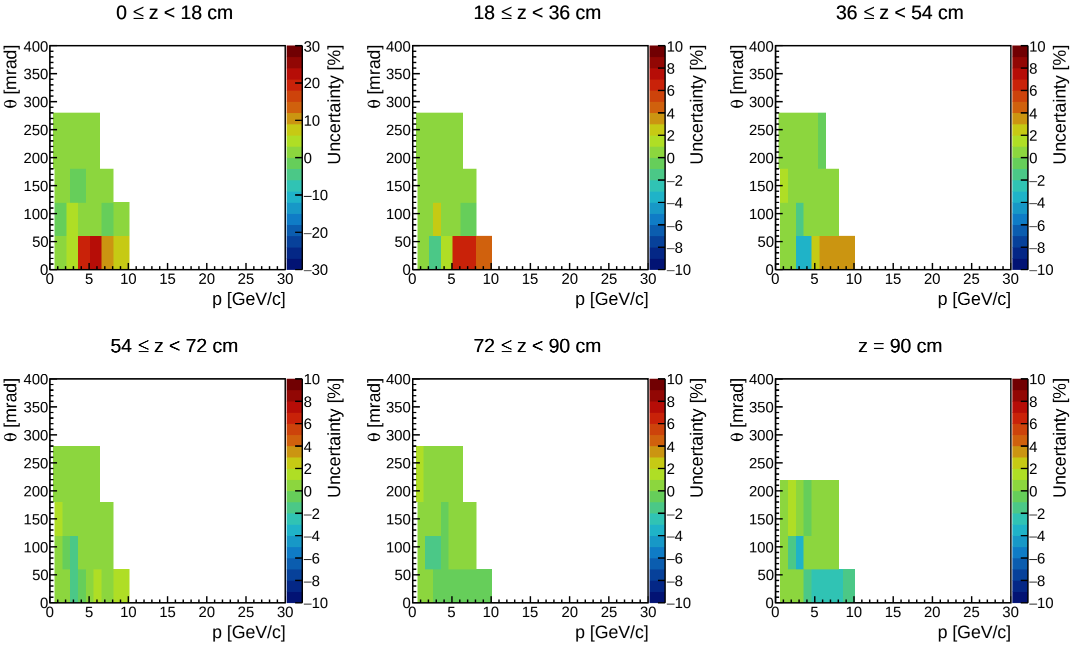

Figure 5.18: Hadron loss systematic uncertainty for positively charged kaons. Each panel shows different z bin. Uncertainty ranges for the first z bin is different.

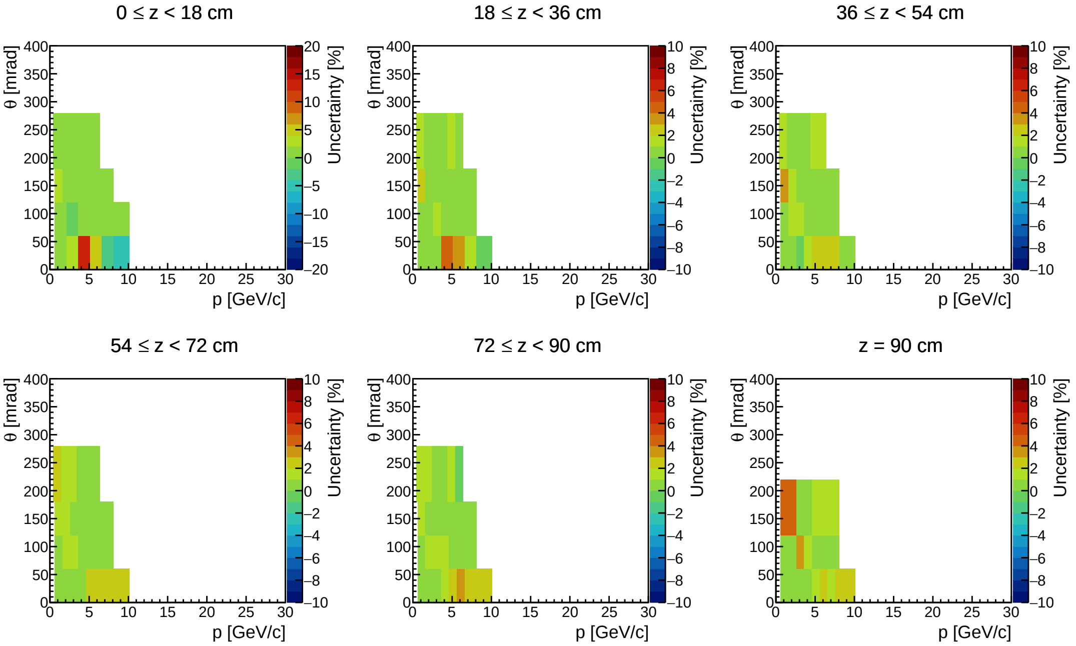

Figure 5.19: Hadron loss systematic uncertainty for negatively charged kaons. Each panel shows different z bin. Uncertainty range for the first z bis is different.

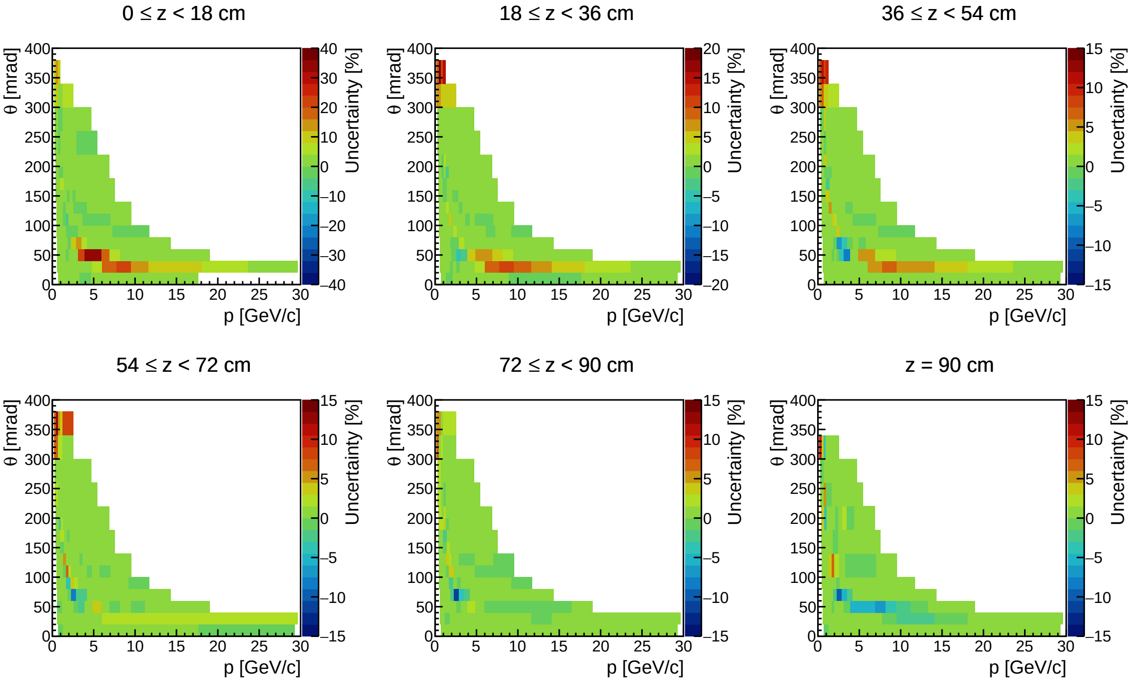

Figure 5.20: Hadron loss systematic uncertainty for protons. Each panel shows different z bin. Uncertainty ranges for the first two z bins are different.

5.5.3 Backward track extrapolation

The accuracy of the backward extrapolation to the target surface is greatly affected by the track topology and the distance of the first track cluster from the target. For this reason, the worst precision is achieved for very low polar angle tracks ($< 20\,\mathrm{mrad}$) and $GTPC + MTPC$ topology. Migration of the low polar angle tracks to different z bins can be larger than 50%. Polar angle and longitudinal position migration are shown in Fig. 5.21, while momentum dependence is not presented. For higher polar angles, migration is from 5% to 15%. As previously described in section 4.5, the target position is known within calibration uncertainties, and this can induce potential bias in the backward extrapolation.

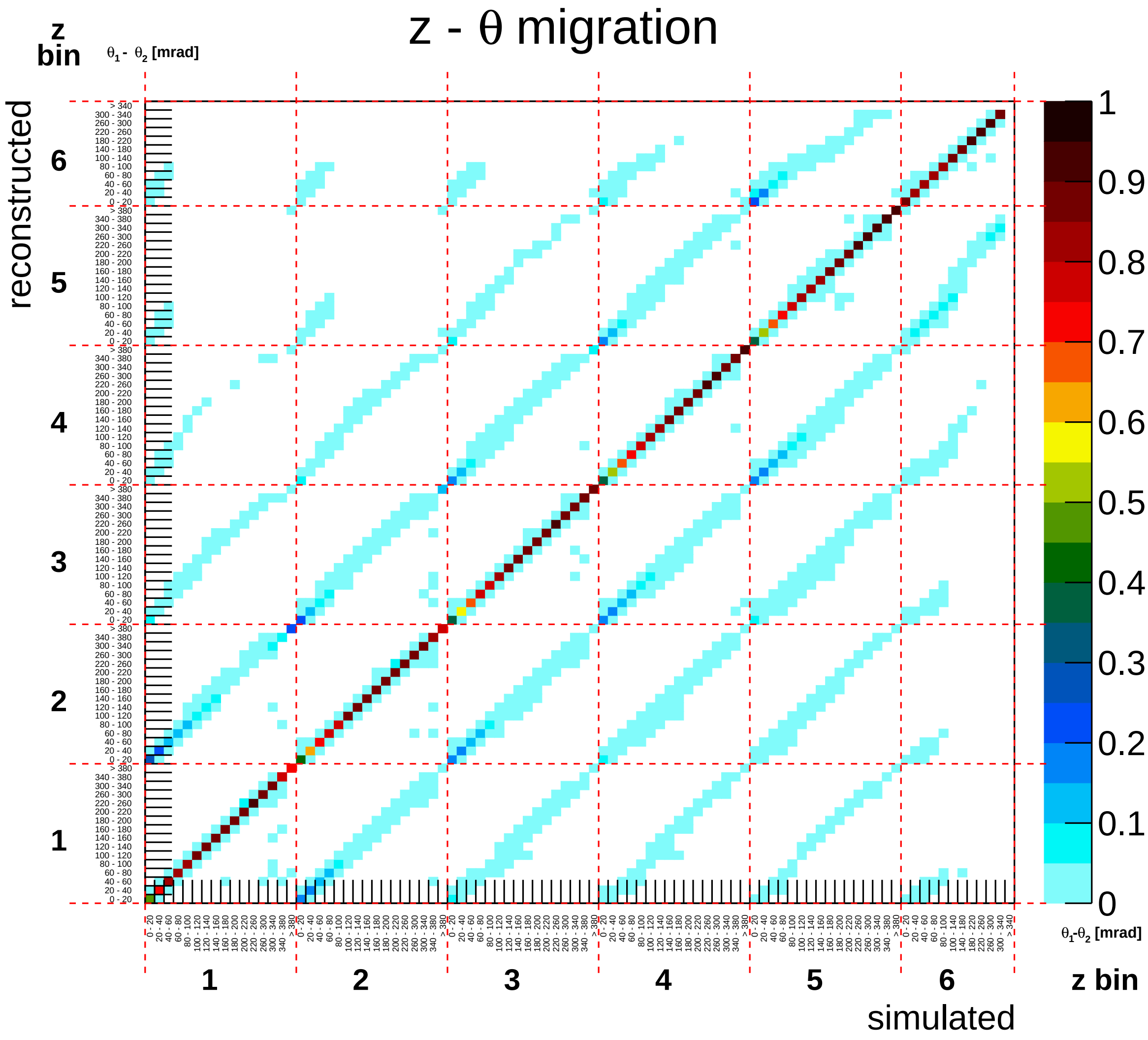

Figure 5.21: Migration matrix shows percentages of tracks extrapolated to different $z - \theta$ bins. Each column is normalized to one.

For this reason, data has been reanalyzed after moving the target position and tilt within the calibration uncertainties. The change has been applied only to the data since target position in the simulation is perfectly known. Each target parameter has been changed in positive and negative direction. For example, systematic changes of π^+ yields after changing each parameter separately are shown in figures D.1 - D.30. Total systematic uncertainties coming from the uncertainties of the different target parameters are calculated by adding individual components in quadrature. Afterwards, line segments have been fitted to get smoother distributions (see figures D.31 - D.36). Total backward extrapolation systematic uncertainties for all particle species are shown in Fig. 5.22 - 5.26. As expected, largest uncertainties can be found in the first longitudinal bin and low polar angles ($5\% - 10\%$). In low polar angle regions, distributions do not look smooth, and this is due to transitions between different track topologies (in particular, GTPC+VTPC2+MTPC $\rightarrow$ GTPC+MTPC) which are affected differently by the change in the target position. At downstream target face, for higher angles, systematic uncertainties are around 3%. This is because of the higher polar angle tracks which exit closer to the outer rim of the downstream target face, and therefore, they are sensitive to the target shifts in x and y. For all other regions, backward extrapolation uncertainties are below 1%.

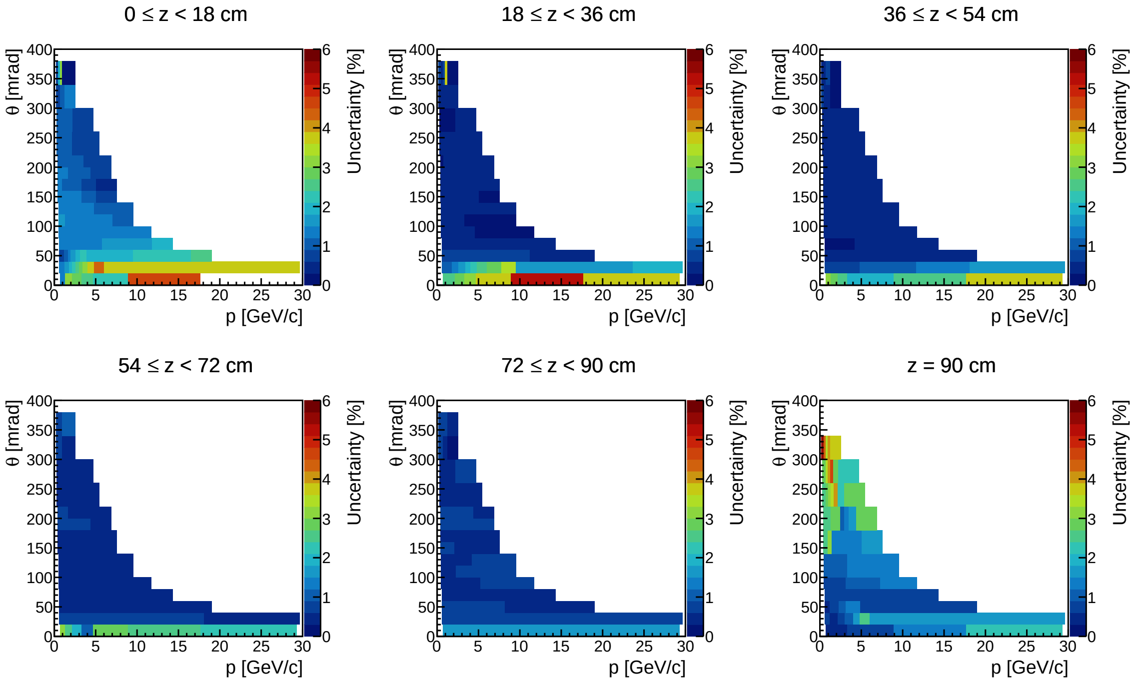

Figure 5.22: Backward extrapolation systematic uncertainty for positively charged pions. Each panel shows different z bin.

5.5.4 Feed-down correction

Selected tracks which do not come from the interactions in the target are removed with the Monte Carlo based feed-down correction. These hadrons come from two different sources: re-interactions in the detector and weak decays. All hadron species can be created in re-interactions. However, only pions and protons can be created in the weak decays of K^0_s and Λ. Kaons are also created in the decays of ϕ mesons. But ϕ mesons decay via strong interaction and therefore do not have enough time to exit from the target surface. Feed-down correction for protons and pions produced from the weak decays outside of the target surface is model dependent because it depends on the K^0_s and Λ spectra. From the previous experiences in the analysis of the

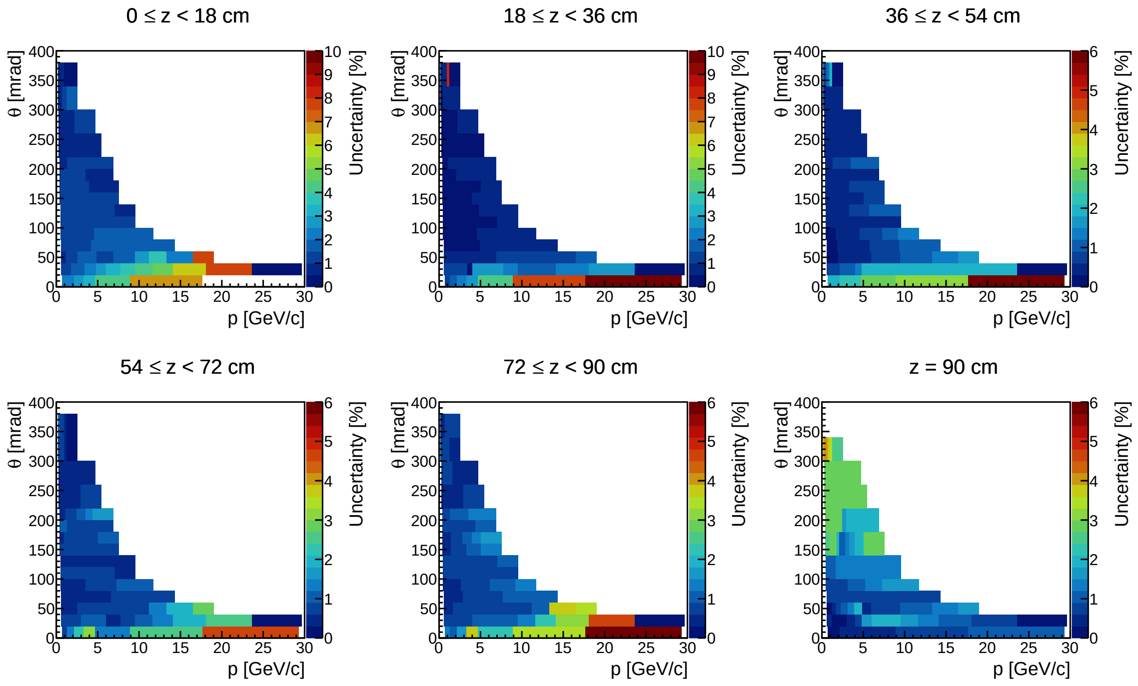

Figure 5.23: Backward extrapolation systematic uncertainty for negatively charged pions. Each panel shows different z bin. Scales in the first two z bins are different.

2009 data, it was found that it is sufficient to take one-third of the feed down correction as a systematic uncertainty. Feed-down uncertainty for positively charged pions (mostly coming from the K^0_s decays) is the largest in the low momentum region at the upstream part of the target and downstream target face, but it never goes above 1.5% (see figure 5.27). In case of the negatively charged pions, the correction factor is larger (it goes above 2%) since there is a contribution coming from the Λ decays. However, the same regions of the phase space are affected (see figure 5.28). The feed-down uncertainty of the proton yields comes purely from the Λ decays, and it can be larger than 3% for the first z bin and momenta between 5 GeV/c and 10 GeV/c (see figure 5.29).

5.5.5 Time-of-flight efficiency

Time of flight correction factor has an uncertainty which comes from the efficiency uncertainties of the TOF-F slats and statistics in a given phase space bin. Usually, efficiency uncertainties for the TOF-F slats are below 0.5%. To estimate possible bias, the *tof* correction factor has been varied within its uncertainties for all particle species separately. Obtained systematic uncertainties, although mostly below 1%, are slightly larger for negatively charged particles because of the lower statistics (see figures 5.30 - 5.34).

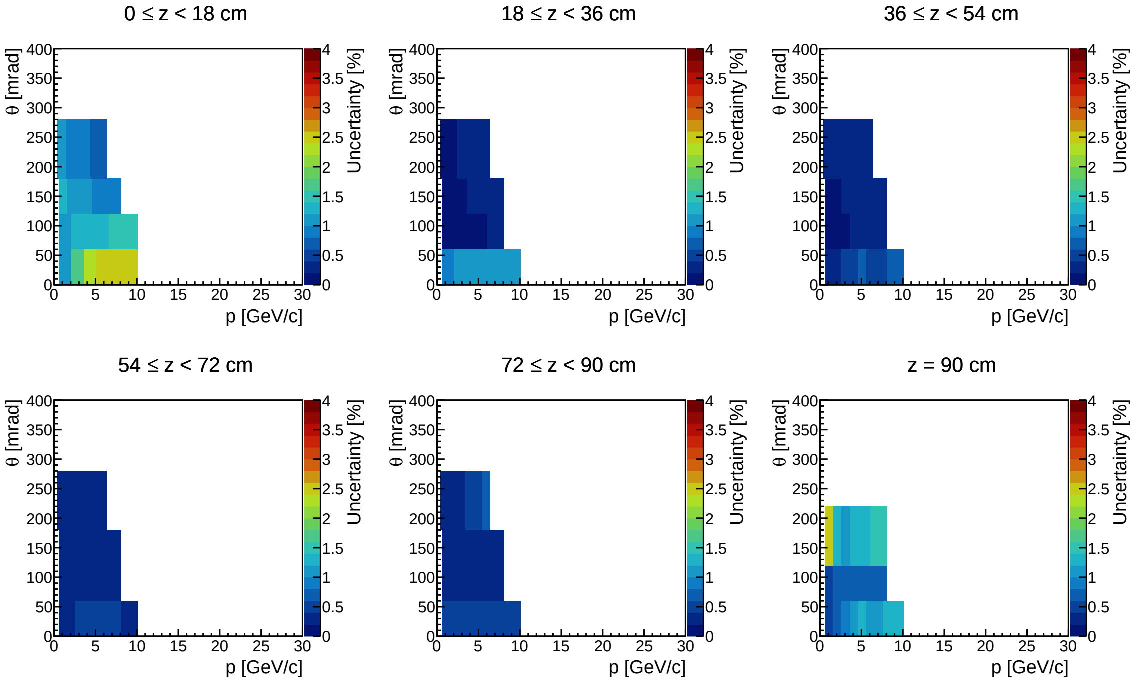

Figure 5.24: Backward extrapolation systematic uncertainty for positively charged kaons. Each panel shows different z bin.

5.5.6 Particle identification

It was already mentioned before that choice of the fitting function for $dE/dx - m^2_{tof}$ spectra can potentially bias the hadron yields. In particular, description of the energy loss distribution with a single Gaussian is possibly not sufficient because of the tails caused by the tracks with the small number of clusters. However, after trying a combination of two Gaussians with the same and different mean values, no significant bias in the hadron yields was found (differences are well below 0.5%). Only problematic regions are high momentum bins for the polar angle between 20 mrad and 40 mrad in which difference of 2% was observed. However, this may be explained purely by fluctuations in the fits since statistical uncertainties, in this case, are above 10%. Another possible bias in the particle identification is tied for positively charged kaons. As explained before, they are located under the proton peak in the energy loss distribution and under the pion peak in the *tof* mass squared distribution. If the shape of the $dE/dx - m^2_{tof}$ spectra is not properly described by the fitting function, there can be migration between K^+ and p in both directions, especially for momenta above 4 GeV/c. The same effect is possible both in data and Monte Carlo, but proton spectra in the simulation are not the same as in data, so mentioned migration might be different and this induces possible bias. To estimate this effect, Monte Carlo K^+ yields extracted from the fits have been compared to the true number of positively charged kaons in each bin. In some cases, for higher momentum a difference around 30% can be found. However, in the most cases, it is below 10% (see figure 5.35).

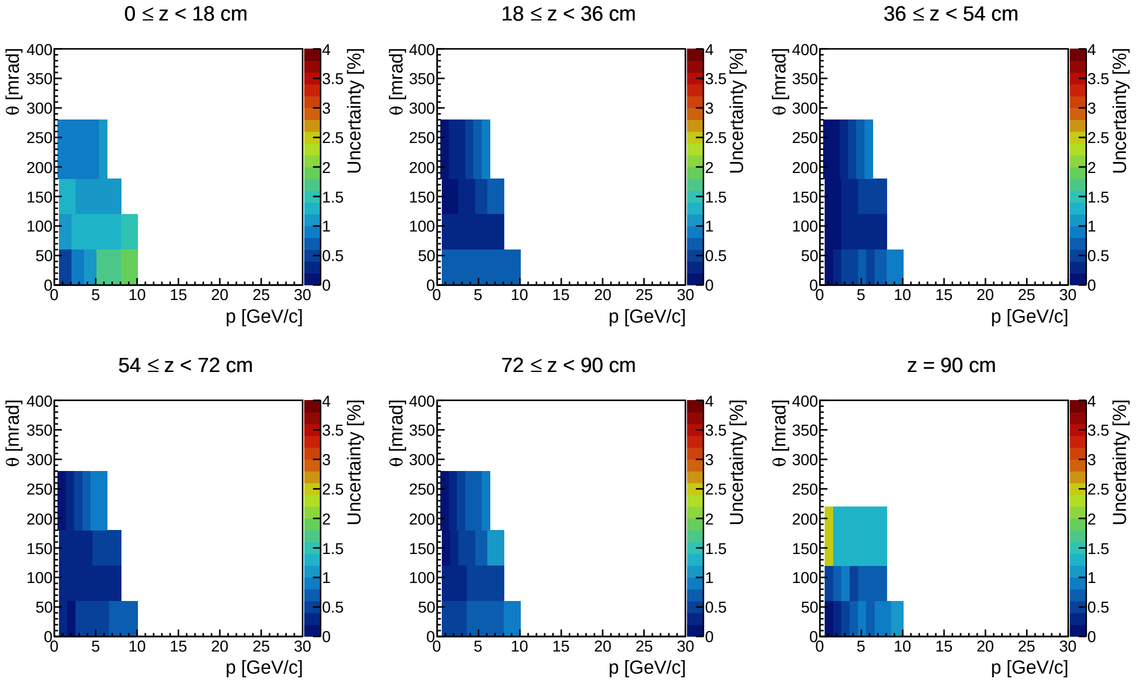

Figure 5.25: Backward extrapolation systematic uncertainty for negatively charged kaons. Each panel shows different z bin.

5.5.7 Ad hoc correction

An ad hoc correction factor was applied only to a small number of bins for protons and pions. Systematic uncertainties have been estimated by varying the correction factor within 50% of it value, which gives 50% uncertainty. As it was mention before, only around 1.5% of the bins are affected, and they are not of particular importance for the re-weighting of the T2K neutrino flux.

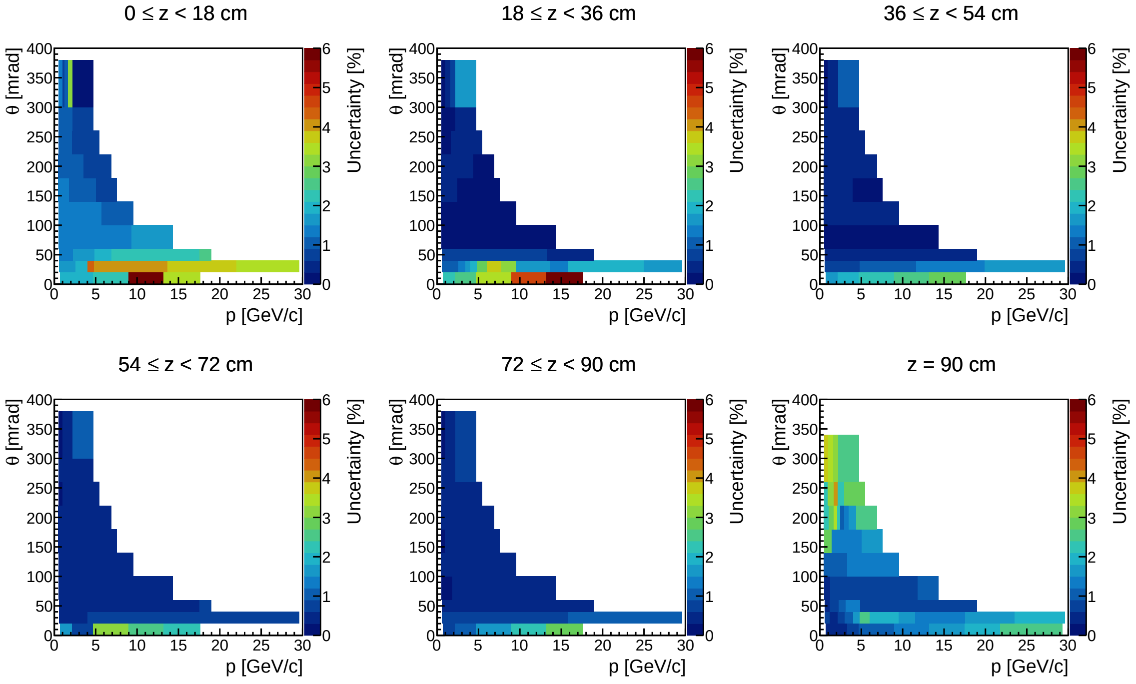

Figure 5.26: Backward extrapolation systematic uncertainty for protons. Each panel shows different z bin.

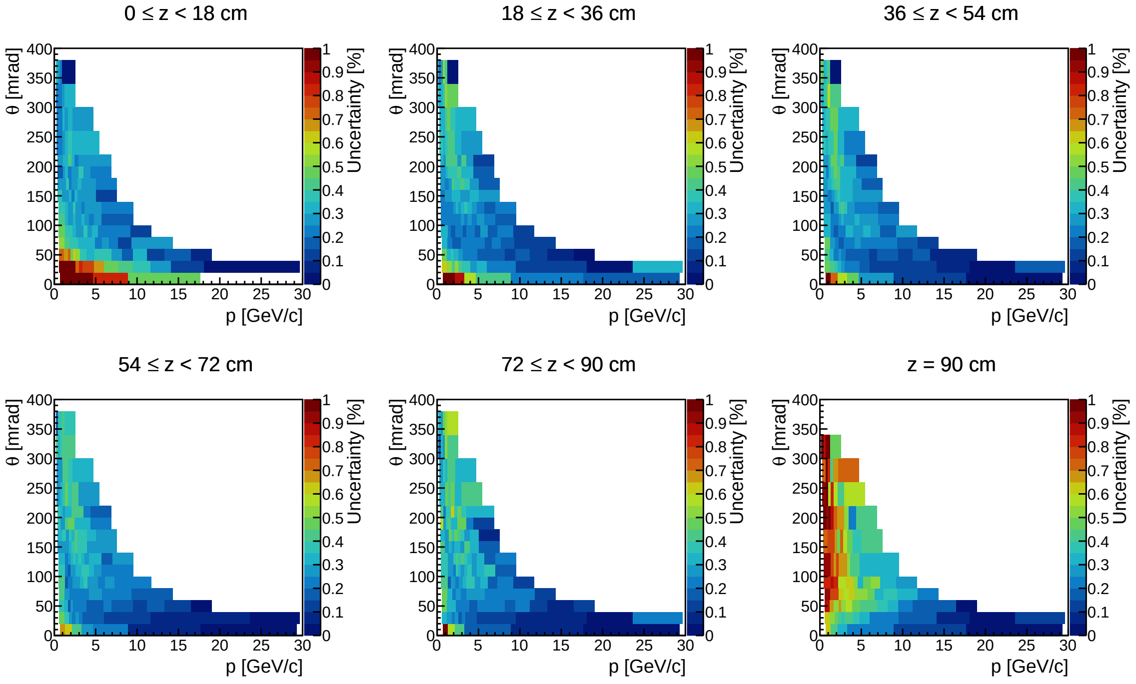

Figure 5.27: Feed-down systematic uncertainty for positively charged pions. Each panel shows different z bin.

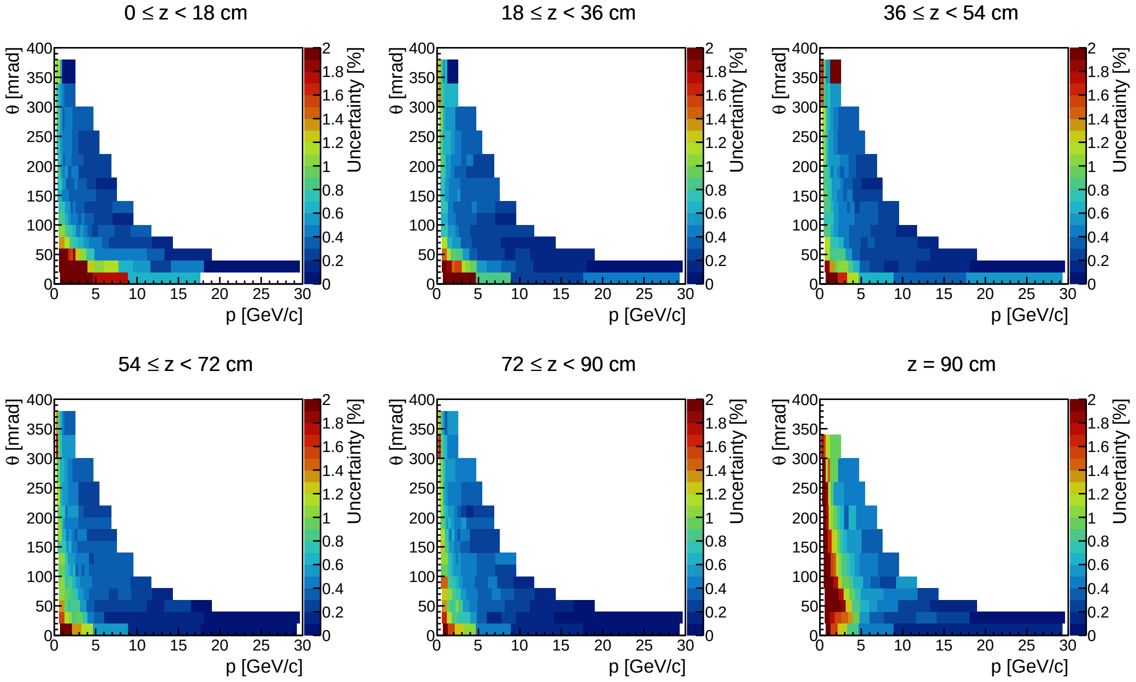

Figure 5.28: Feed-down systematic uncertainty for negatively charged pions. Each panel shows different z bin.

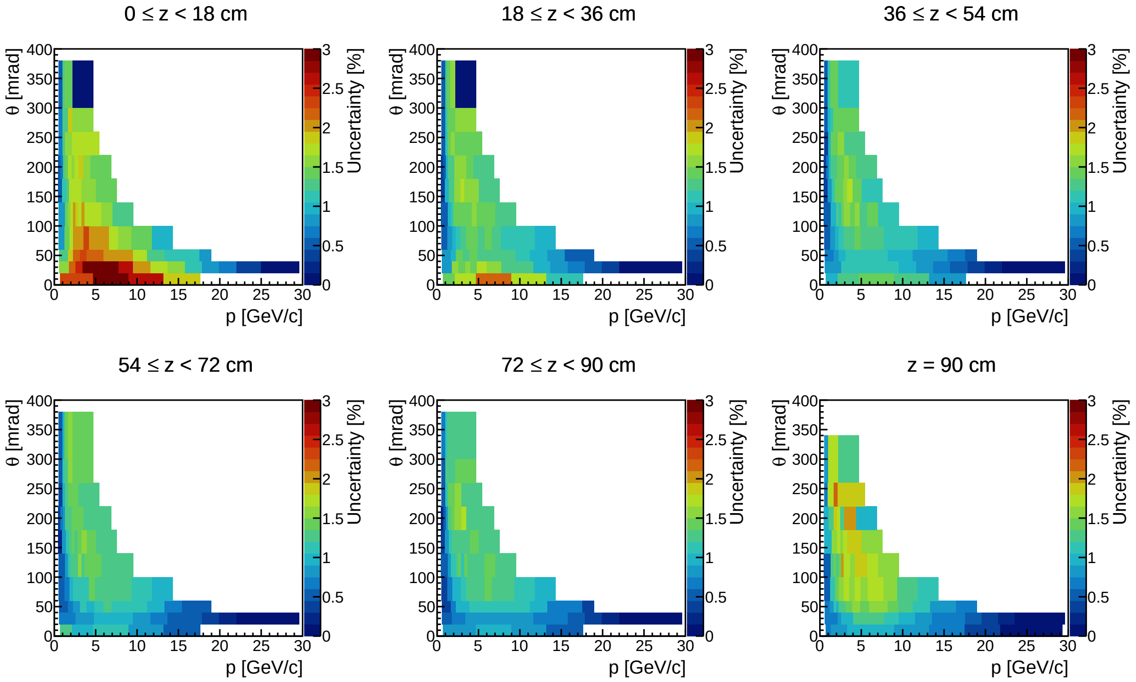

Figure 5.29: Feed-down systematic uncertainty for protons. Each panel shows different z bin.

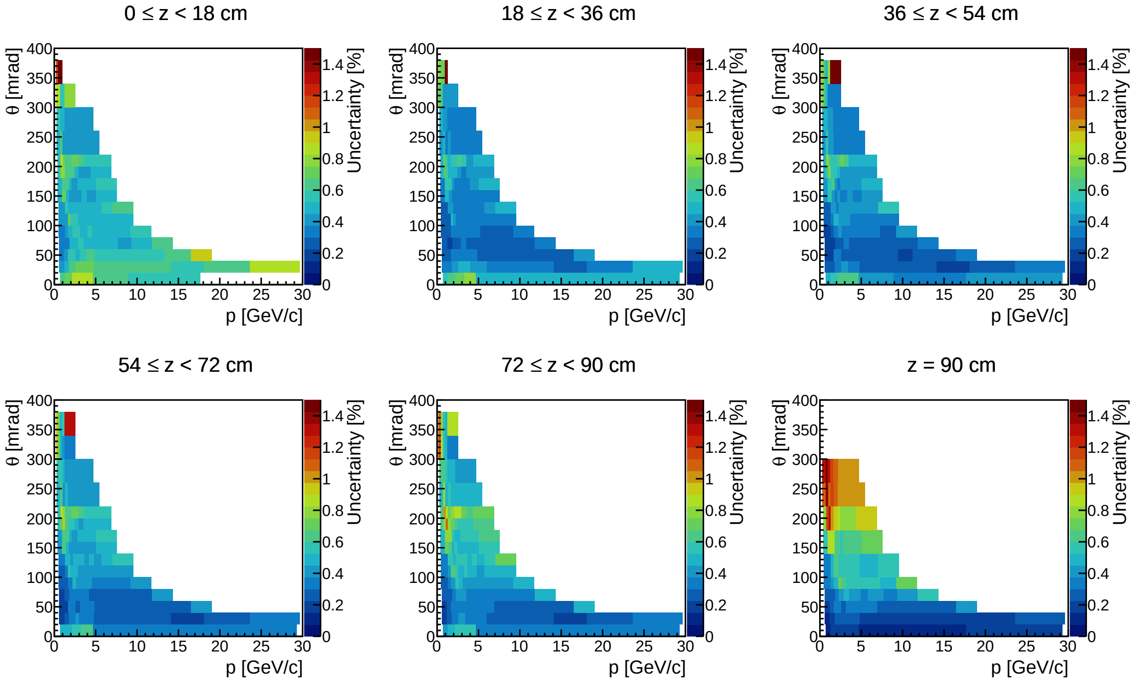

Figure 5.30: Time of flight systematic uncertainty for positively charged pions. Each panel shows different z bin.

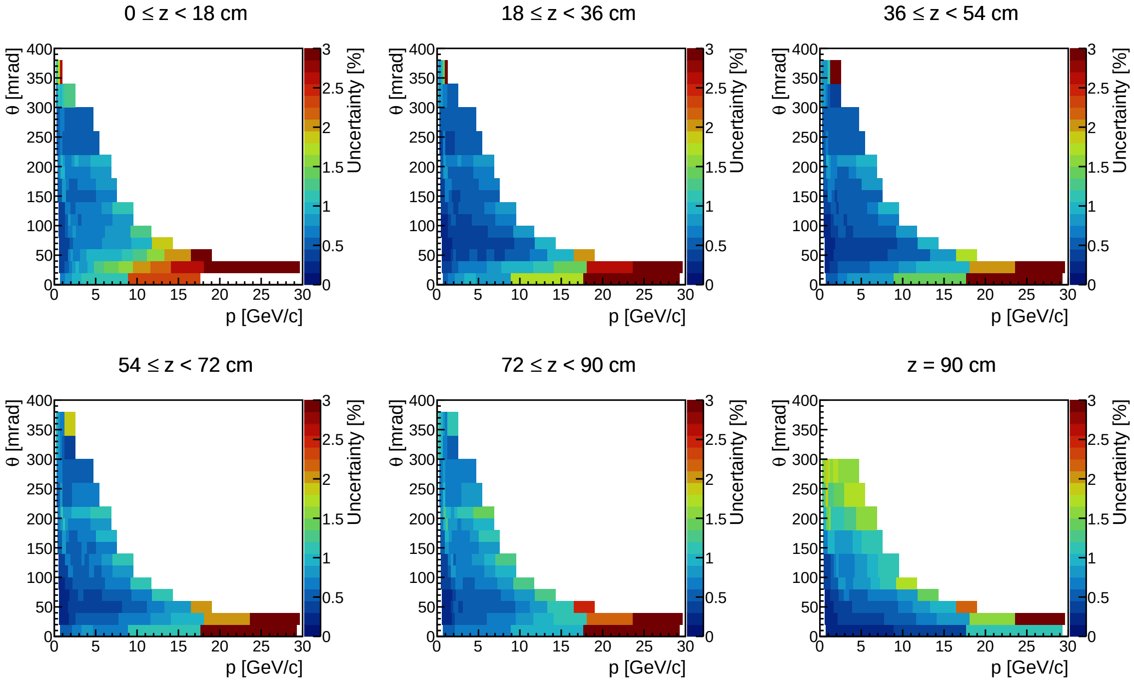

Figure 5.31: Time of flight systematic uncertainty for negatively charged pions. Each panel shows different z bin.

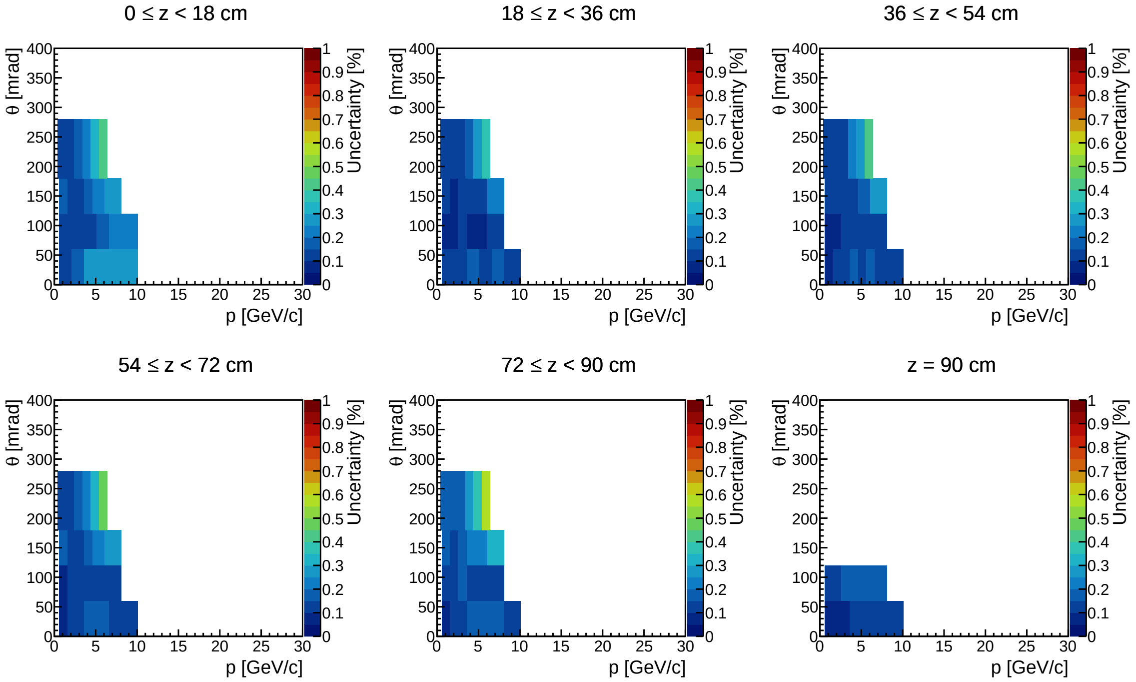

Figure 5.32: Time of flight systematic uncertainty for positively charged kaons. Each panel shows different z bin.

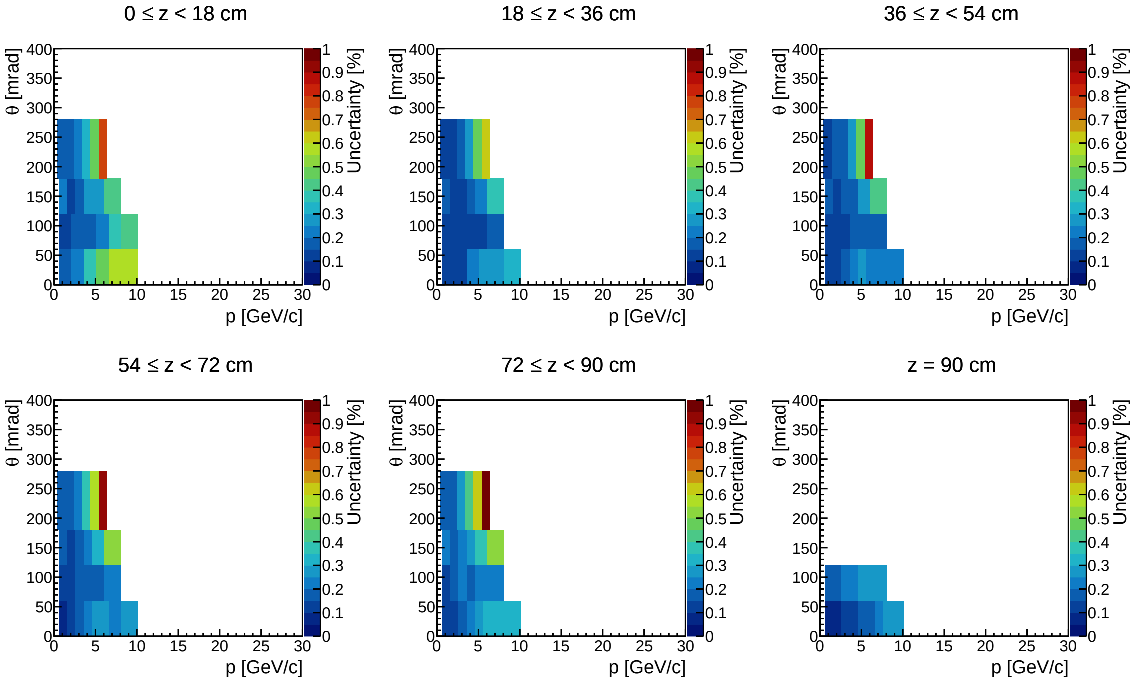

Figure 5.33: Time of flight systematic uncertainty for negatively charged kaons. Each panel shows different z bin.

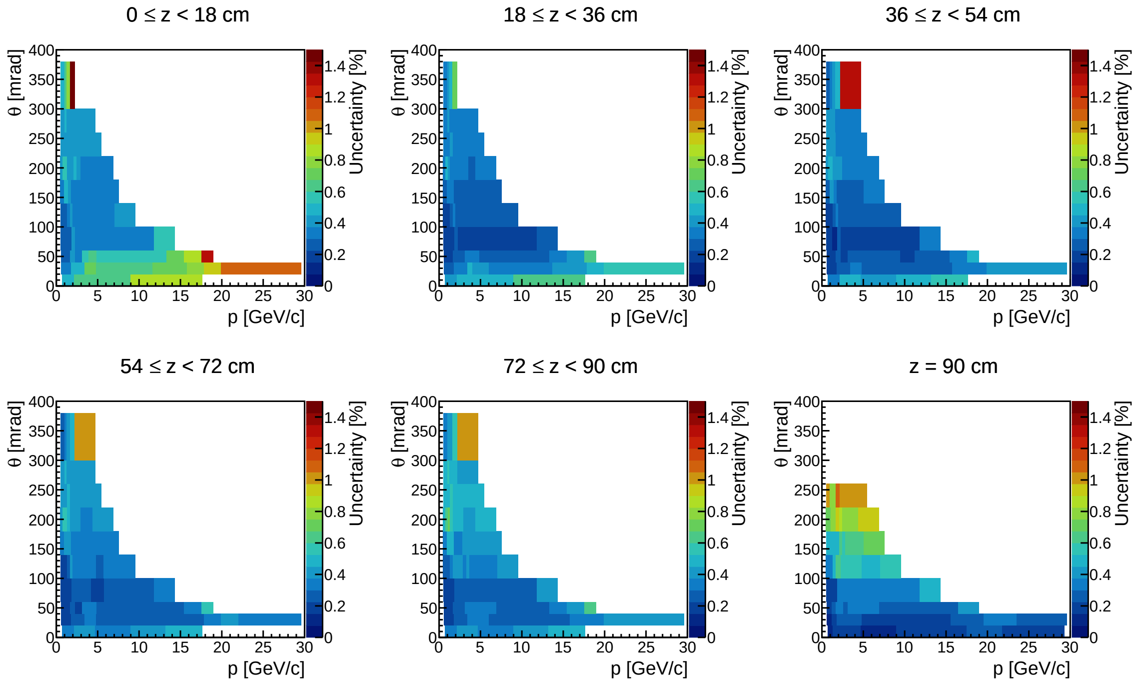

Figure 5.34: Time of flight systematic uncertainty for protons. Each panel shows different z bin.

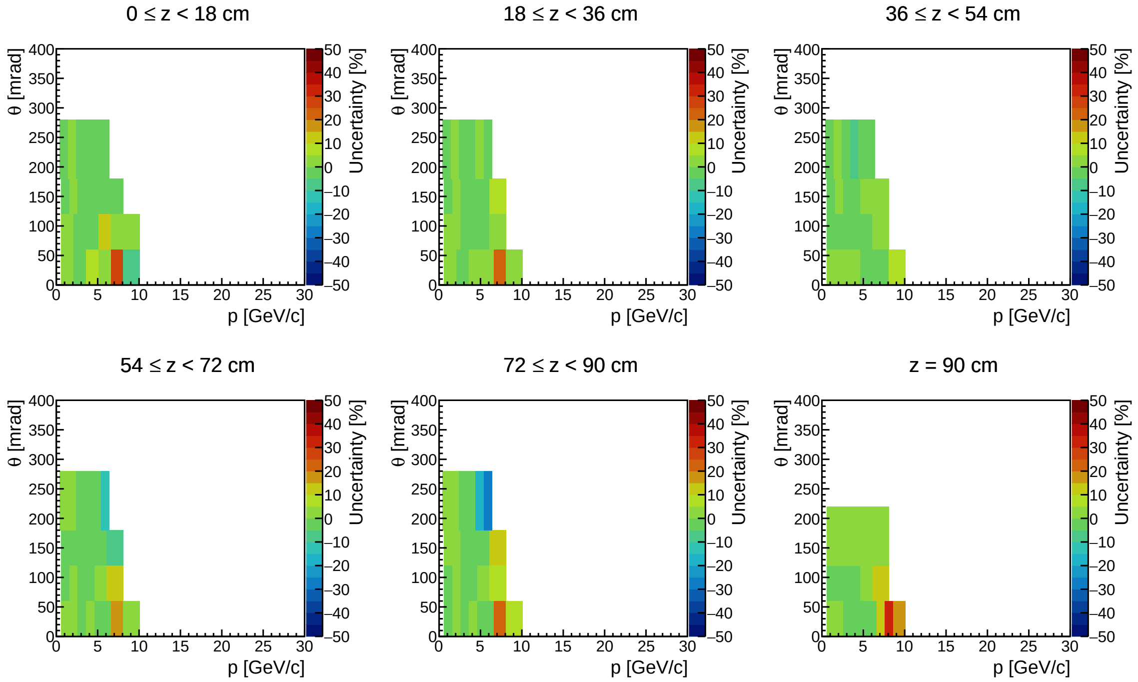

Figure 5.35: Particle identification systematic uncertainty for positively charged kaons. Each panel shows different z bin.

Chapter 6

Hadron yields in p + T2K replica target interactions

Contents

6.1 Comparison with Monte Carlo models

Fully corrected π^+, π^-, K^+, K^- and p double differential yields will be presented in this chapter as a function of the hadron momentum. Tables with results can be found in Ref. [112]. While the primary use of the hadron yields will be re-weighting of the neutrino flux, it is important to compare the results to different Monte Carlo models. The results will be compared with:

- FLUKA2011.2c.5 Monte Carlo model,
- NUBEAM physics list from GEANT4.10.03, and
- QGSP_BERT physics list from GEANT4.10.03.

The choice of FLUKA2011.2c.5 is obvious since it is used in the T2K neutrino beam simulation. An attempt was made by the GEANT team to introduce NUBEAM physics list which can be used for purposes of the neutrino beam simulations. In other words, it uses a combination of models whose transitions have been tuned so that it gives the best prediction of the hadron yields in the largest region of the phase space possible. NUBEAM physics list uses Bertini cascade model (BERT) for energies lower than 3 GeV, for intermediate energies (≈ 10 GeV) it uses FRITIOF (FTF) model, and for high energies it uses a variance of Quark Gluon String model (QGSP). Hadron yields presented in this thesis are for momenta lower than 30 GeV, so that comparisson will be actually for FTF and BERT models. Among others, NA61/SHINE measurements of charged pion spectra in proton-carbon interaction at 31 GeV/c [77] have been used for tuning of the NuBeam physics list. These data were taken in 2007, and they have limited statistics. The second physics list from Geant4.10.03 (QGSP_BERT) was chosen to be entirely different from the NuBeam. It is known from the previous measurements that it gives rather a different prediction for the hadron yields in proton-carbon interactions. It uses the same model (BERT) for low energy part of the spectra. However, its usage has been extended up to 9 GeV. In the intermediate region ($9-25$ GeV), QGSP_BERT uses Low Energy Parameterized (LEP) models which are a re-engineered version of the Gheisha. At high energies, QGSP is used to simulate hadron interactions.

In the following subsections, comparisons of the measured hadron yields are shown. Yields for different z bins are plotted in separate figures, while polar angle bins are represented by separate panels within the same figure. Data is always drawn with black hollow markers, the Fluka2011.2c.5 prediction is always a red line, NuBeam is a blue line, and QGSP_BERT is a green line. Total errors for the data are shown in the form of vertical error bars, while systematical errors are grey rectangles. In some cases, systematic errors are highly asymmetrical. This is because of the hadron loss contribution (cut on the z position of the last cluster) as previously explained.

Yields of positively charged pions are shown in Fig. 6.1-6.6. Total uncertainties are around 5% for most of the bins. Exceptions can be found at the edges of the phase space (high momenta) where statistical uncertainties dominate. This is also the case, between 20 mrad and 60 mrad in the first z bin where the total systematic uncertainties can go up to 30% because of the backward extrapolation and the hadron loss. In addition, for the upstream z bins and very high polar angle, systematic uncertainties can go up to 25% because of the ad hoc correction factor. Overall, best prediction is given by Fluka2011.2c.5 with differences being in the most cases smaller than 20%. The largest difference is for very low angles and high momenta, for upstream z bins (more than 50%). Fluka2011.2c.5 predicts higher maxima and lower tails of the distributions (the differences are within 20%). NuBeam physics list gives prediction very similar to Fluka2011.2c.5, except for the very low momenta where it is slightly higher.

Similarly, yields of negatively charged pions are shown in Fig. 6.7-6.12. These yields are around 25% lower than the π^+ yields because of the u-d quark asymmetry in the primary interactions. Consequently, this increases slightly statistical uncertainties, especially for the high momenta, but in the most cases, they are still around 5%. Systematics uncertainties remain mostly the same, except for the ad hoc correction which affects a slightly larger number of high polar angle bins. Again, all models have the same behavior as for the π^+ yields and Fluka2011.2c.5 being one with the most accurate predictions.

Positively charged kaon yields are shown in Fig. 6.13-6.18 while negatively charged kaons are shown in Fig. 6.19-6.24. Statistical uncertainties are around 10% and 15% for positively charged kaons and negatively charged hadrons respectively. Systematic errors are similar in size (around 10%) and are mostly dominated by the particle identification systematic uncertainty. On average NuBeam and QGSP_BERT give a slightly better prediction for positively charged kaons, while for negatively charged kaons, Fluka2011.2c.5 and NuBeam are better. It is hard to choose a single model because of the size of total errors.

In case of proton yields (see figures 6.25-6.30), statistical errors are around 5% to 10% and for the majority of the phase space bins, dominate the total uncertainties. All models fail to reproduce the proton yields, and the differences can be more than a factor of two in size. One cannot improve the predictions by scaling them with a constant factor since the shape of the spectra is different. The Fluka2011.2c.5 prediction improves for more downstream z bins.

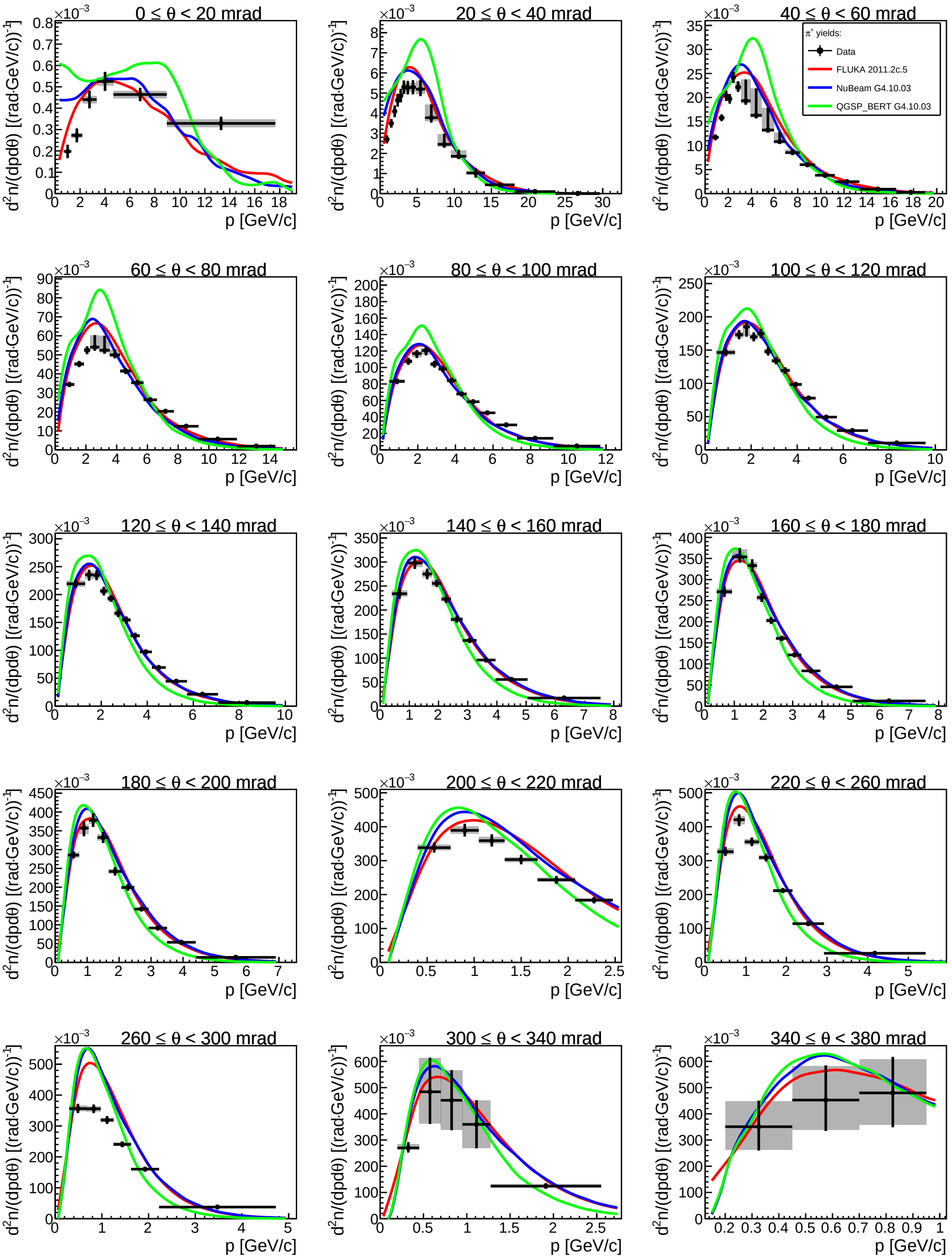

Figure 6.1: Comparison of fully corrected π^+ yields for the first longitudinal z bin with Monte Carlo models: Fluka2011.2c.5 (red line), NuBeam physics list from Geant4.10.03 (green line) and QGSP_BERT physics list from Geant 4.10.03 (green line). Vertical error bars are total uncertainties, while grey rectangles are systematic uncertainties. Each panel shows different polar angle region.

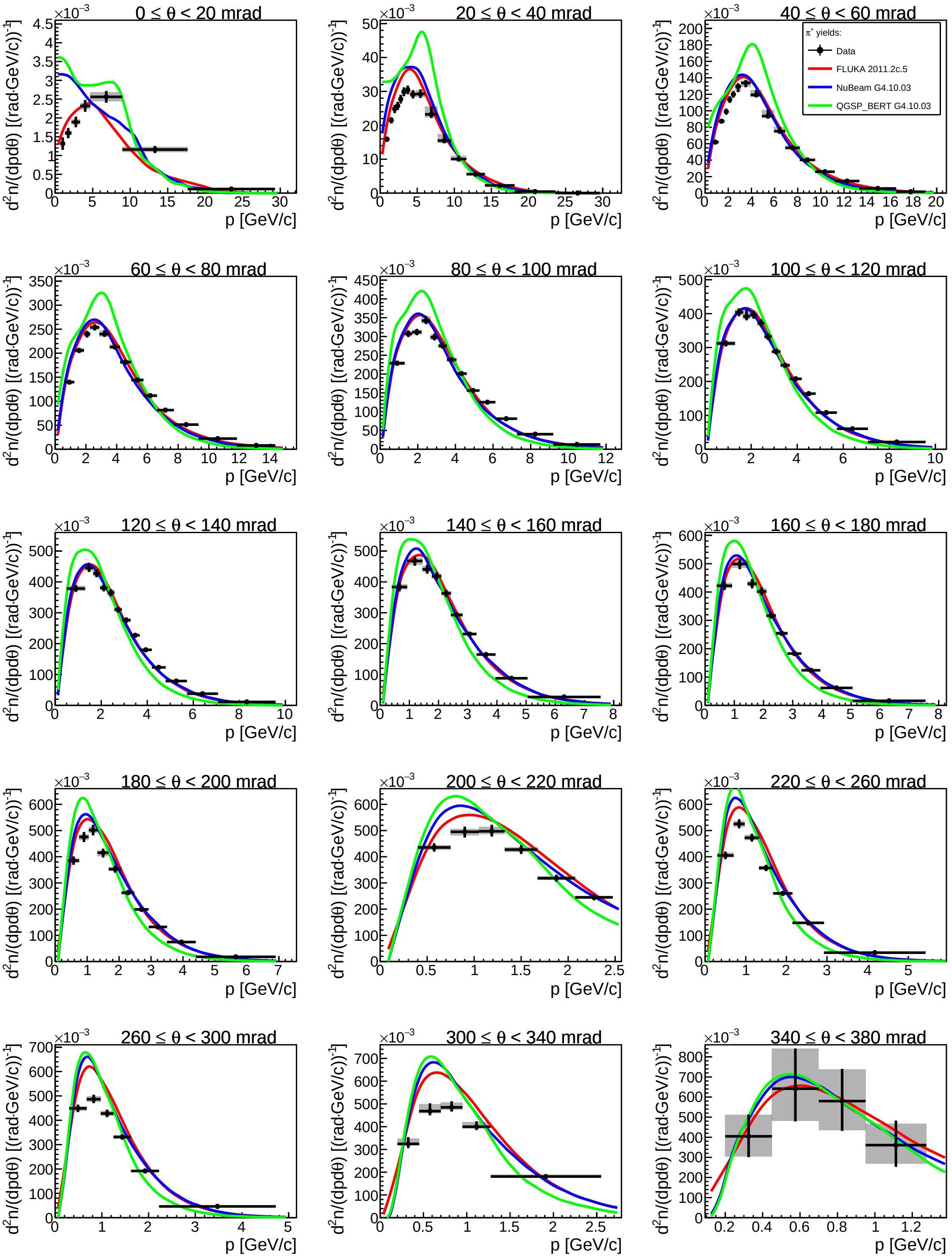

Figure 6.2: Comparison of fully corrected π^+ yields for the second longitudinal z bin with Monte Carlo models: Fluka2011.2c.5 (red line), NuBeam physics list from Geant 4.10.03 (blue line) and QGSP_BERT physics list from Geant 4.10.03 (green line). Vertical error bars are total uncertainties, while grey rectangles are systematic uncertainties. Each panel shows different polar angle region.

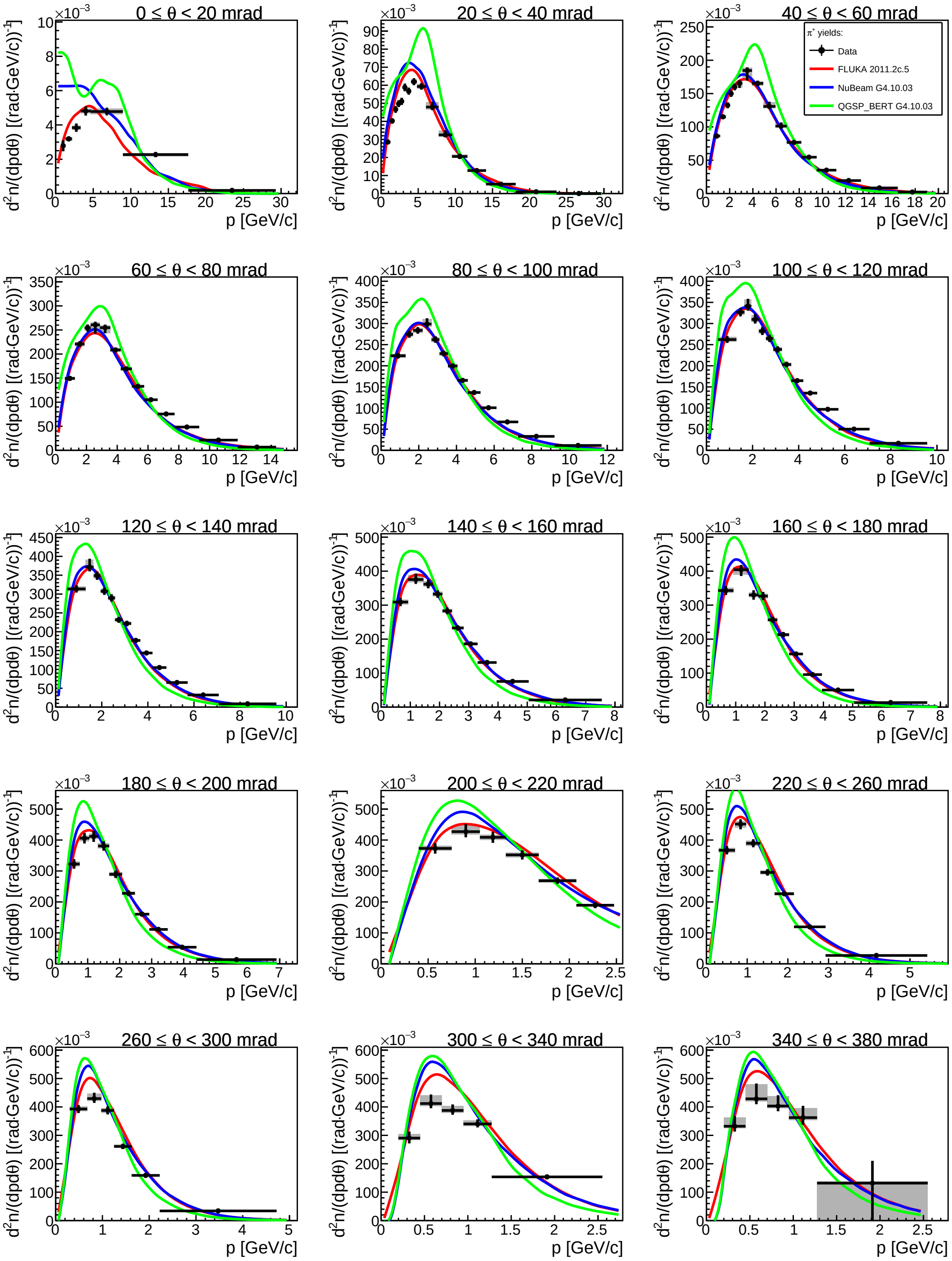

Figure 6.3: Comparison of fully corrected π^+ yields for the third longitudinal z bin with Monte Carlo models: FLUKA2011.2c.5 (red line), NUBEAM physics list from GEANT 4.10.03 (blue line) and QGSP_BERT physics list from GEANT 4.10.03 (green line). Vertical error bars are total uncertainties, while grey rectangles are systematic uncertainties. Each panel shows different polar angle region.

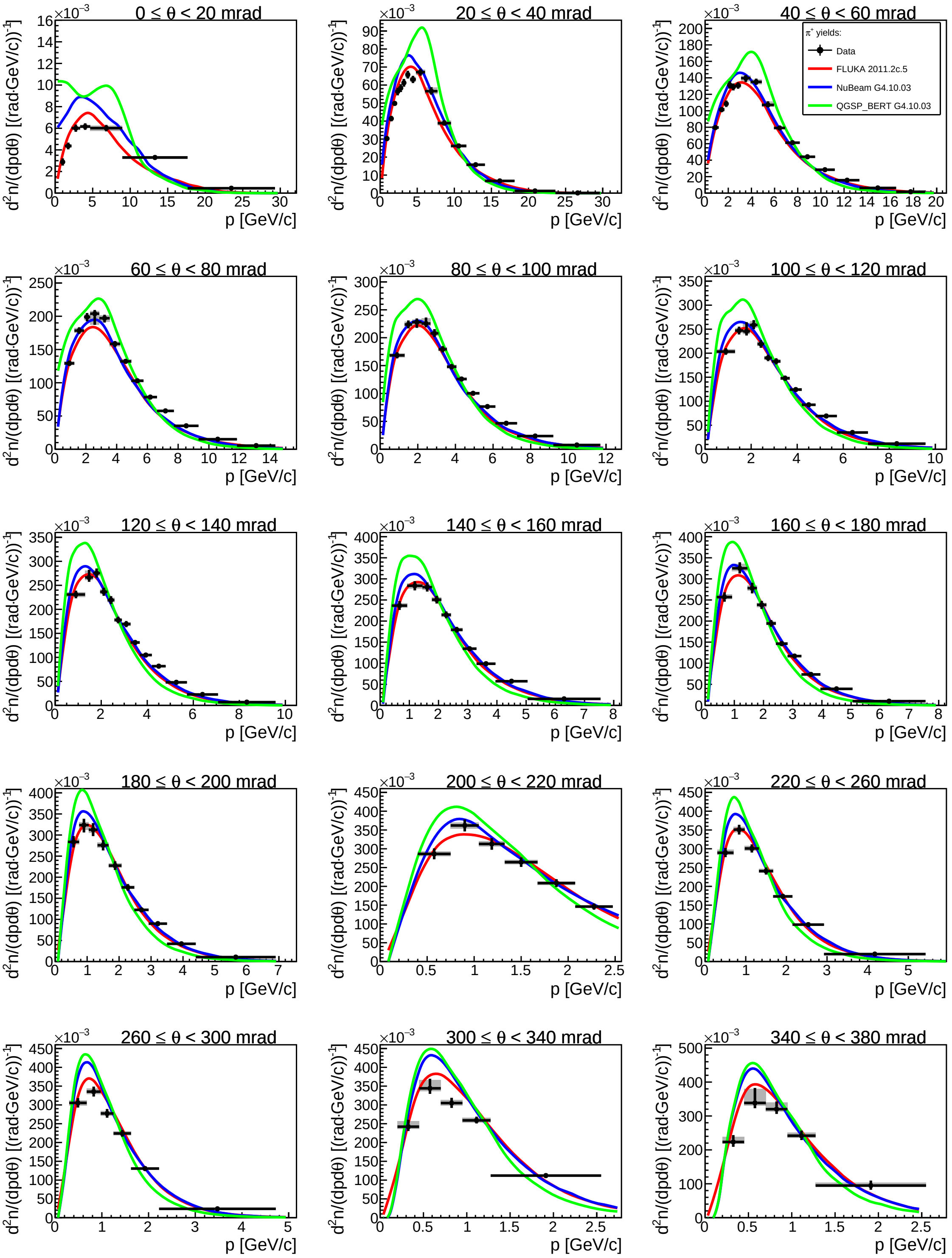

Figure 6.4: Comparison of fully corrected π^+ yields for the fourth longitudinal z bin with Monte Carlo models: Fluka2011.2c.5 (red line), NuBeam physics list from Geant 4.10.03 (blue line) and QGSP_BERT physics list from Geant 4.10.03 (green line). Vertical error bars are total uncertainties, while grey rectangles are systematic uncertainties. Each panel shows different polar angle region.

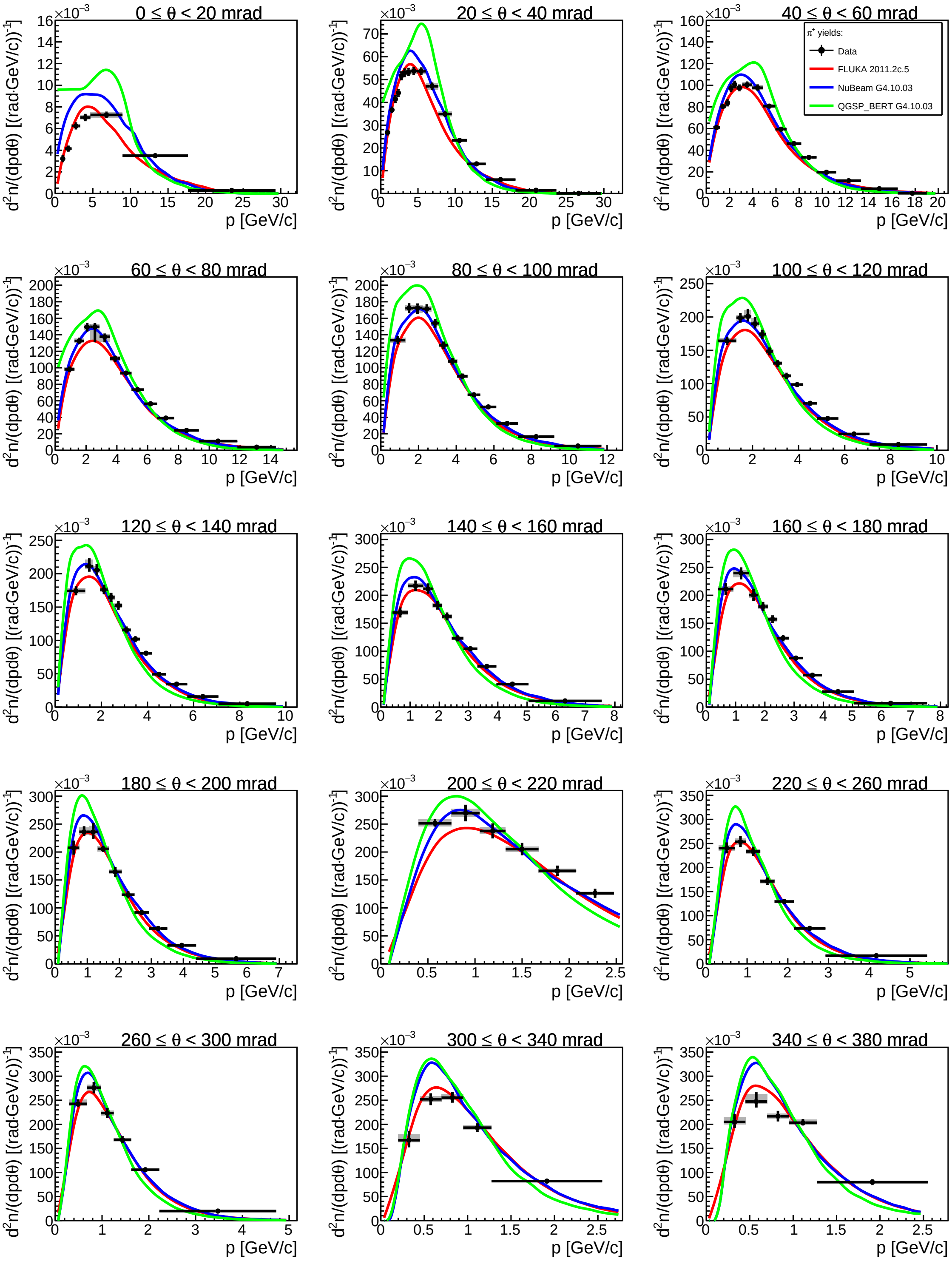

Figure 6.5: Comparison of fully corrected π^+ yields for the fifth longitudinal z bin with Monte Carlo models: FLUKA2011.2c.5 (red line), NUBEAM physics list from GEANT 4.10.03 (blue line) and QGSP_BERT physics list from GEANT 4.10.03 (green line). Vertical error bars are total uncertainties, while grey rectangles are systematic uncertainties. Each panel shows different polar angle region.

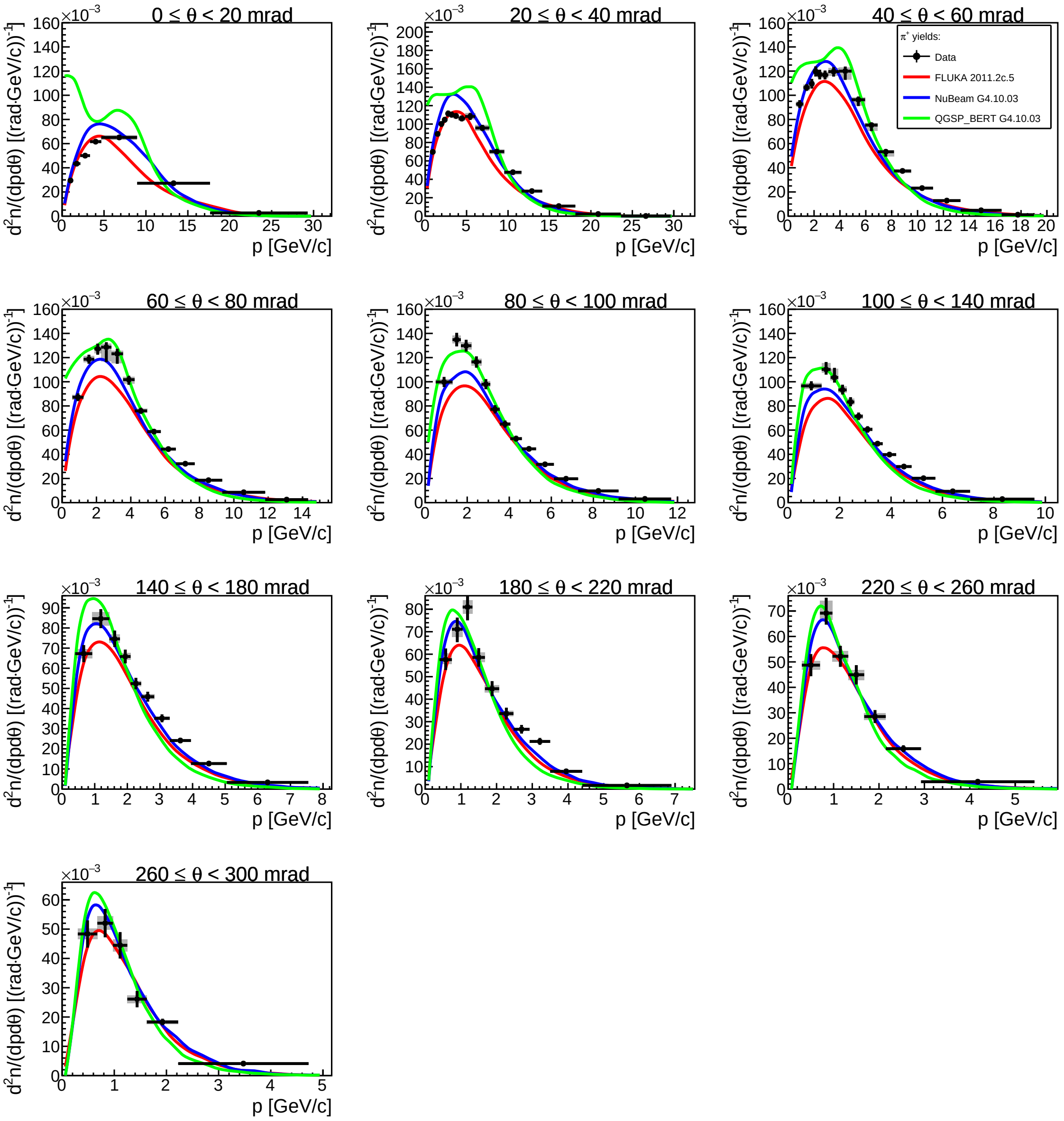

Figure 6.6: Comparison of fully corrected π^+ yields for the downstream target face with Monte Carlo models: FLUKA2011.2c.5 (red line), NuBeam physics list from Geant 4.10.03 (blue line) and QGSP_BERT physics list from Geant 4.10.03 (green line). Vertical error bars are total uncertainties, while grey rectangles are systematic uncertainties. Each panel shows different polar angle region.

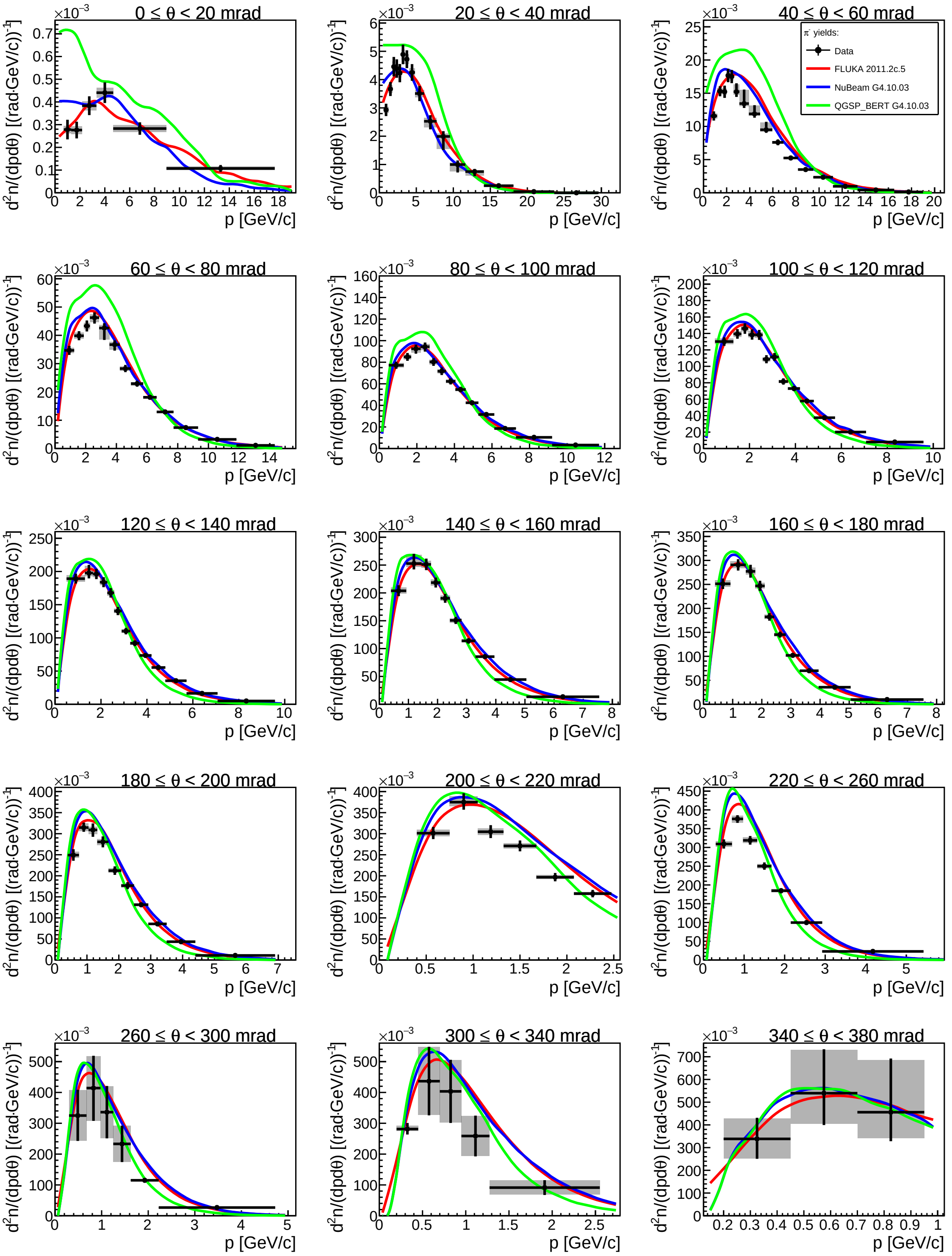

Figure 6.7: Comparison of fully corrected π^- yields for the first longitudinal z bin with Monte Carlo models: FLUKA2011.2c.5 (red line), NUBEAM physics list from GEANT 4.10.03 (blue line) and QGSP_BERT physics list from GEANT 4.10.03 (green line). Vertical error bars are total uncertainties, while grey rectangles are systematic uncertainties. Each panel shows different polar angle region.

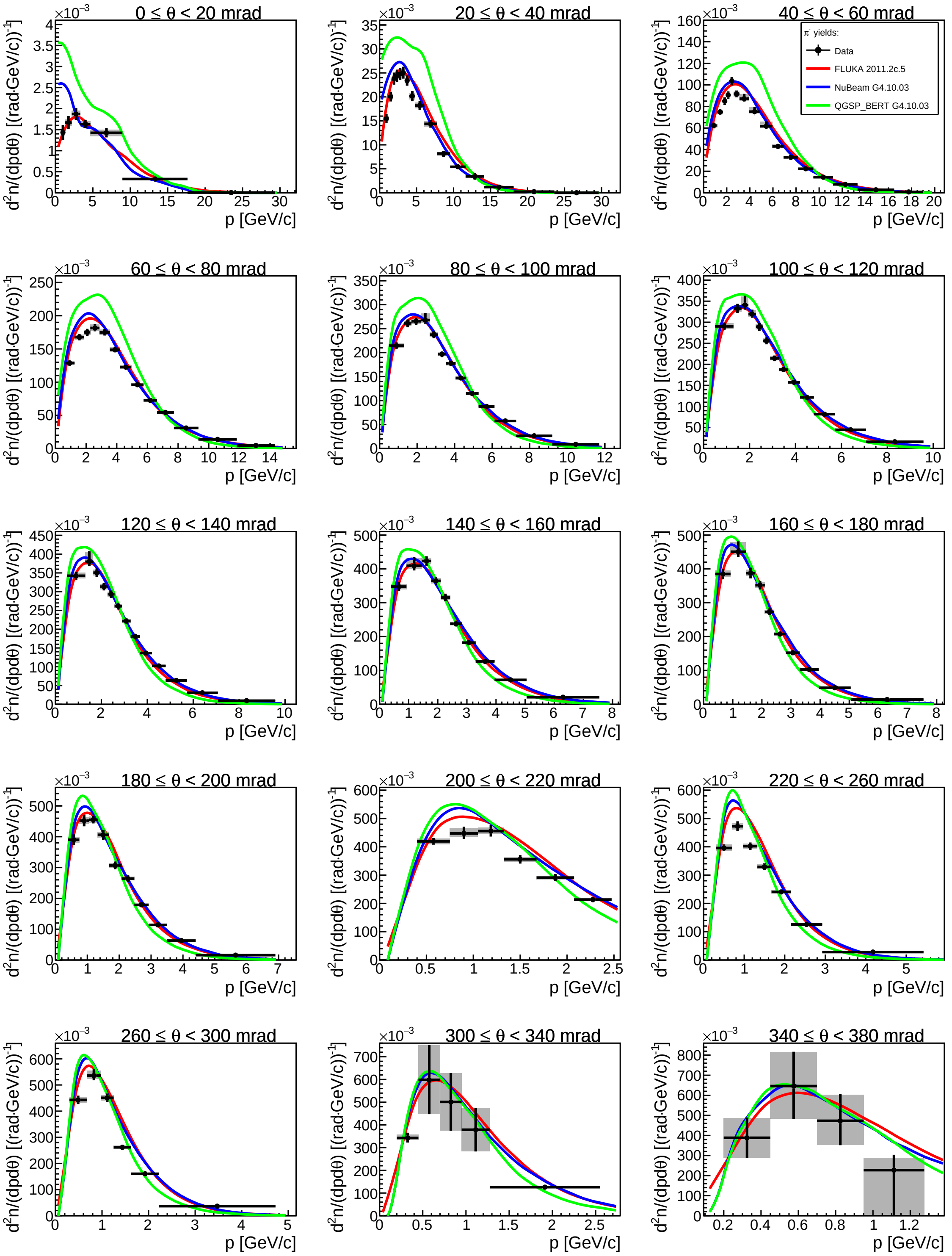

Figure 6.8: Comparison of fully corrected π^- yields for the second longitudinal z bin with Monte Carlo models: Fluka2011.2c.5 (red line), NuBeam physics list from Geant 4.10.03 (blue line) and QGSP_BERT physics list from Geant 4.10.03 (green line). Vertical error bars are total uncertainties, while grey rectangles are systematic uncertainties. Each panel shows different polar angle region.

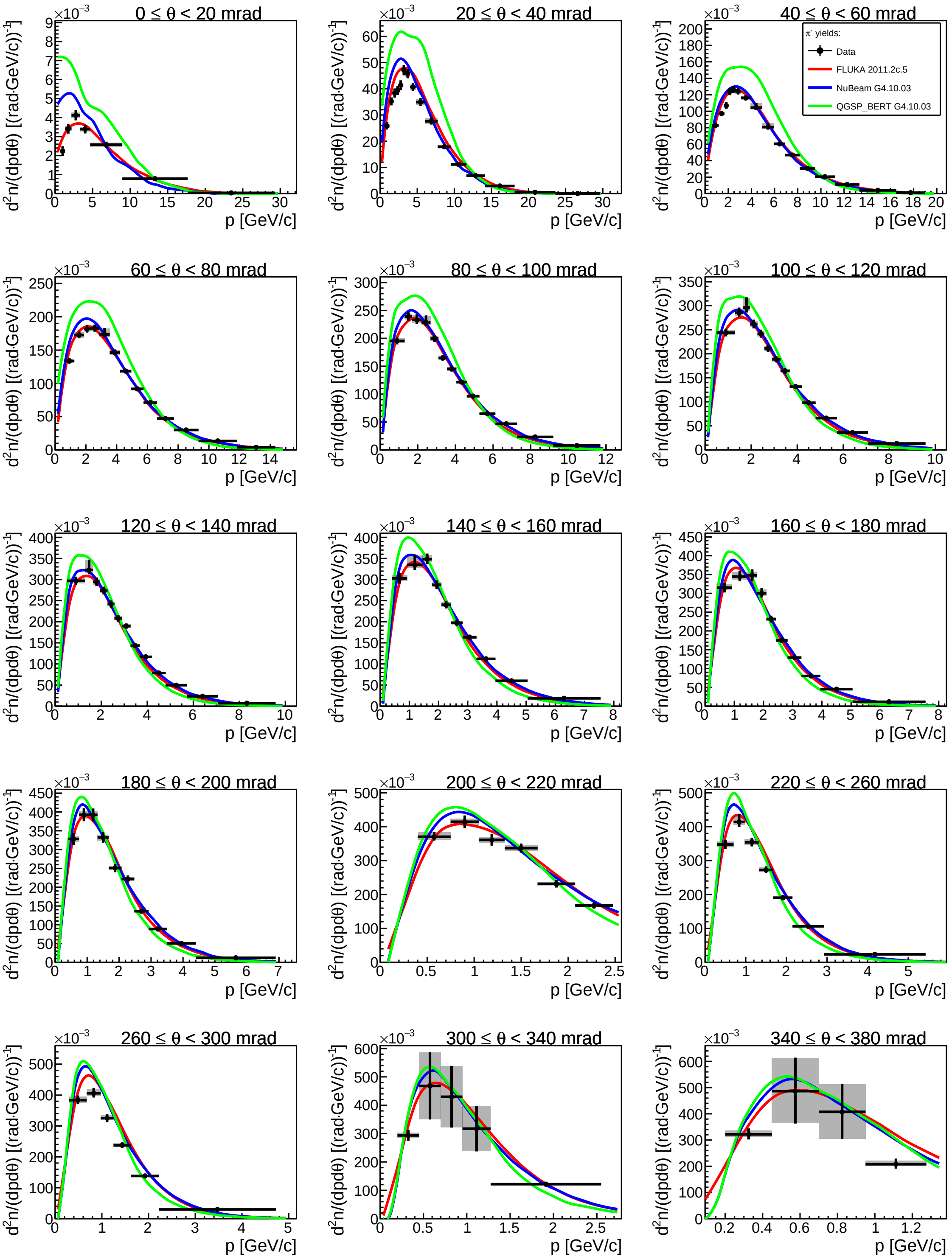

Figure 6.9: Comparison of fully corrected π^- yields for the third longitudinal z bin with Monte Carlo models: Fluka2011.2c.5 (red line), NuBeam physics list from Geant 4.10.03 (blue line) and QGSP_BERT physics list from Geant 4.10.03 (green line). Vertical error bars are total uncertainties, while grey rectangles are systematic uncertainties. Each panel shows different polar angle region.

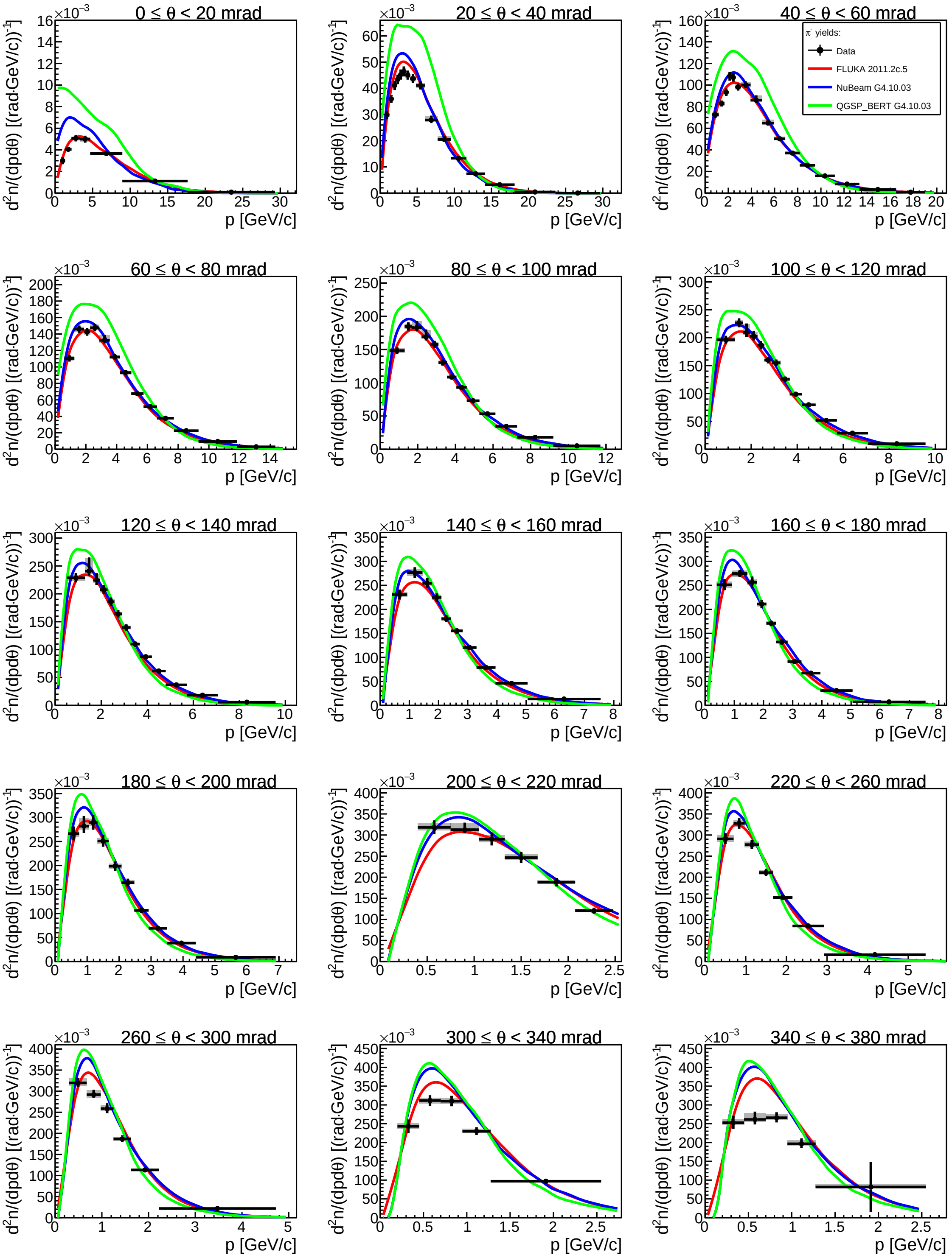

Figure 6.10: Comparison of fully corrected π^- yields for the fourth longitudinal z bin with Monte Carlo models: Fluka2011.2c.5 (red line), NuBeam physics list from Geant 4.10.03 (blue line) and QGSP_BERT physics list from Geant 4.10.03 (green line). Vertical error bars are total uncertainties, while grey rectangles are systematic uncertainties. Each panel shows different polar angle region.

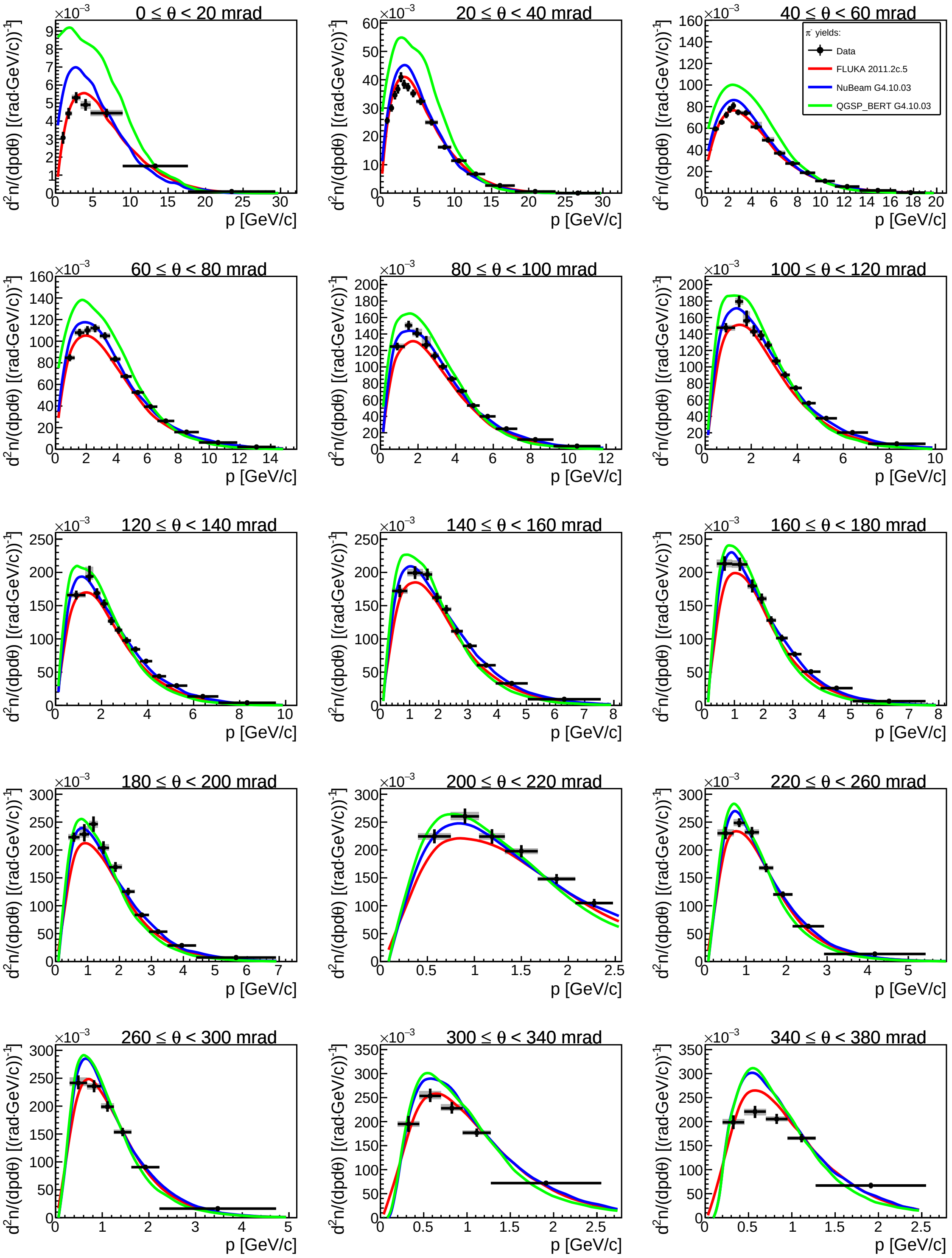

Figure 6.11: Comparison of fully corrected π^- yields for the fifth longitudinal z bin with Monte Carlo models: FLUKA2011.2c.5 (red line), NUBEAM physics list from GEANT 4.10.03 (blue line) and QGSP_BERT physics list from GEANT 4.10.03 (green line). Vertical error bars are total uncertainties, while grey rectangles are systematic uncertainties. Each panel shows different polar angle region.

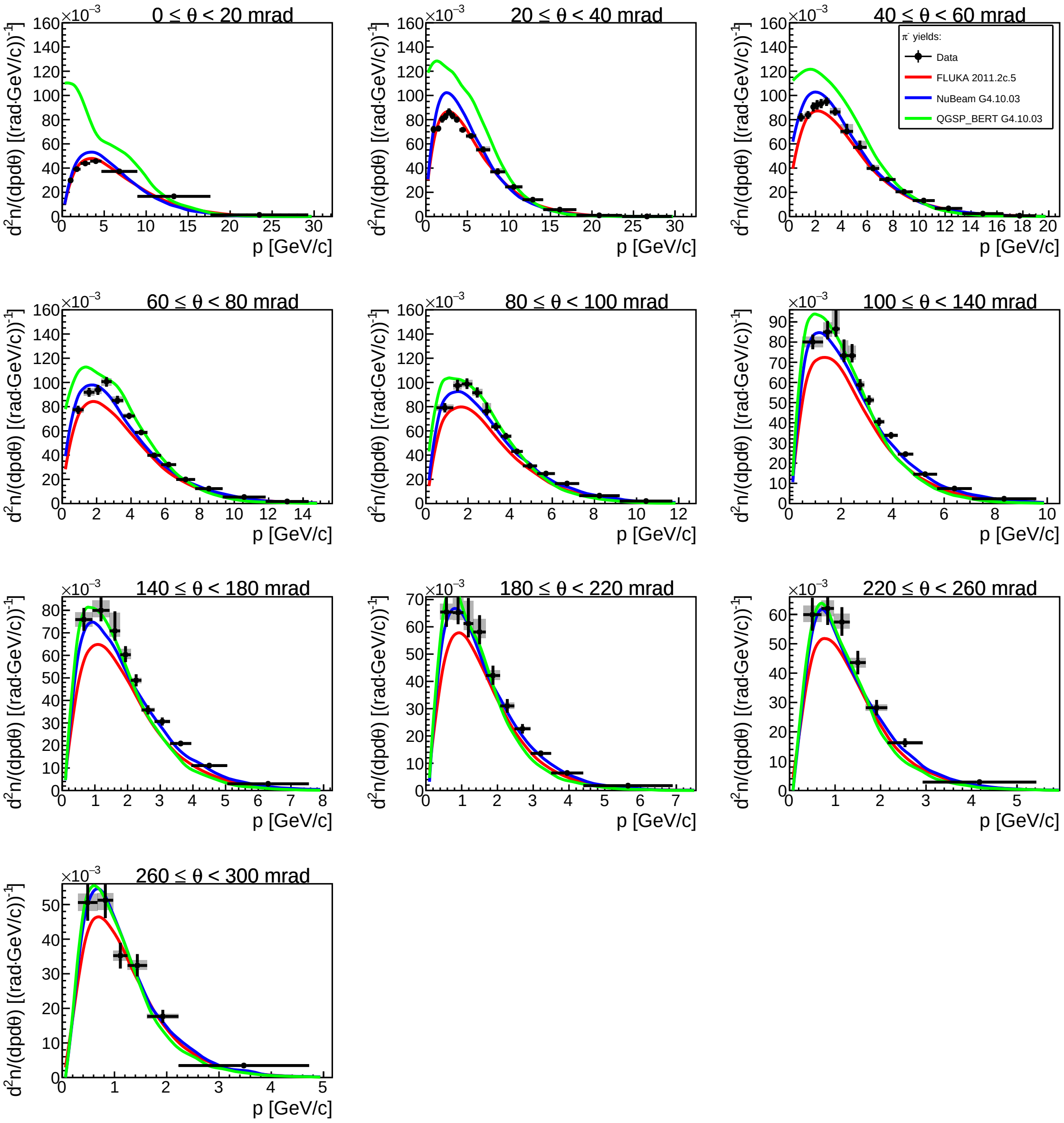

Figure 6.12: Comparison of fully corrected π^- yields for the downstream target face with Monte Carlo models: Fluka2011.2c.5 (red line), NuBeam physics list from Geant 4.10.03 (blue line) and QGSP_BERT physics list from Geant 4.10.03 (green line). Vertical error bars are total uncertainties, while grey rectangles are systematic uncertainties. Each panel shows different polar angle region.

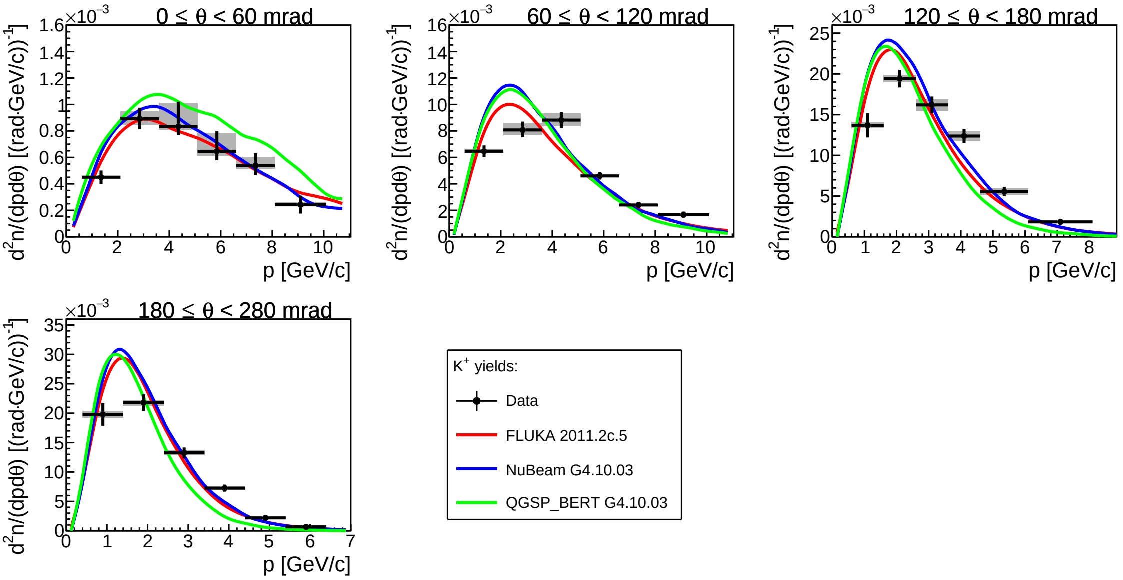

Figure 6.13: Comparison of fully corrected K$^+$ yields for the first longitudinal z bin with Monte Carlo models: Fluka2011.2c.5 (red line), NuBeam physics list from Geant 4.10.03 (blue line) and QGSP_BERT physics list from Geant 4.10.03 (green line). Vertical error bars are total uncertainties, while grey rectangles are systematic uncertainties. Each panel shows different polar angle region.

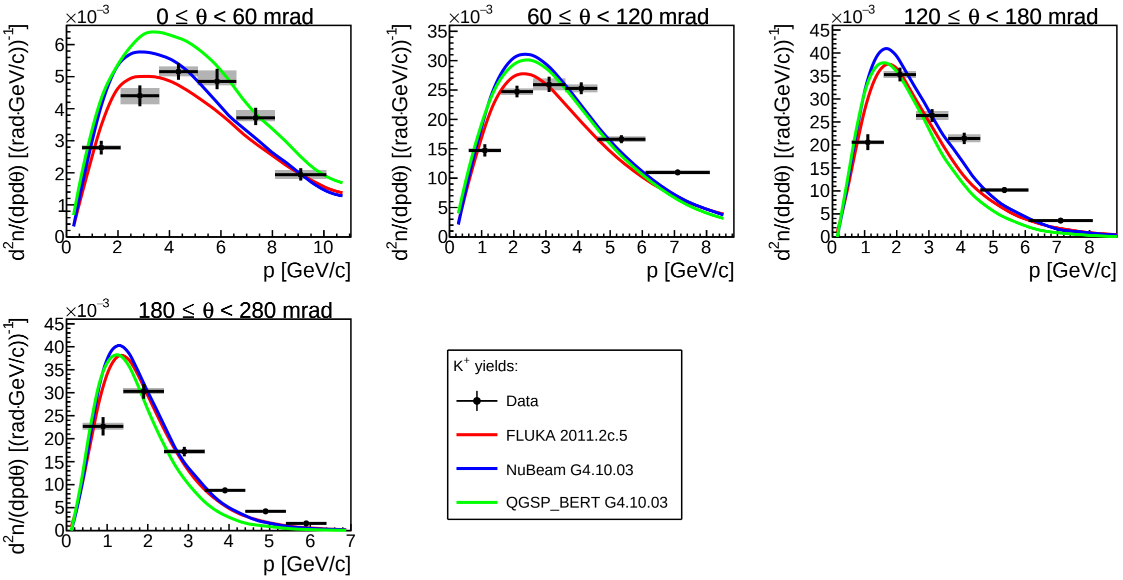

Figure 6.14: Comparison of fully corrected K$^+$ yields for the second longitudinal z bin with Monte Carlo models: Fluka2011.2c.5 (red line), NuBeam physics list from Geant 4.10.03 (blue line) and QGSP_BERT physics list from Geant 4.10.03 (green line). Vertical error bars are total uncertainties, while grey rectangles are systematic uncertainties. Each panel shows different polar angle region.

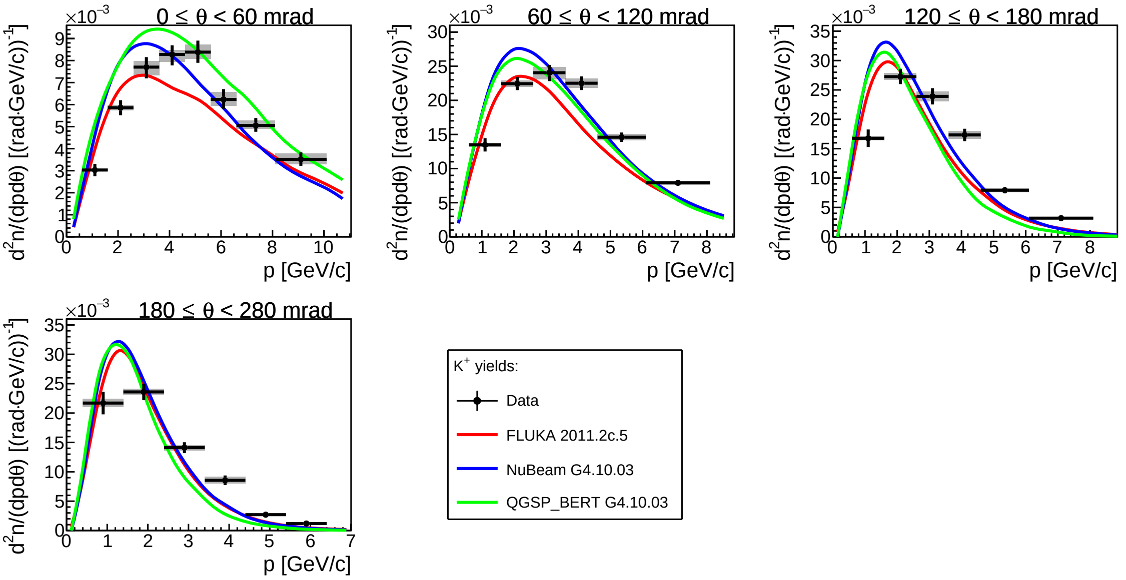

Figure 6.15: Comparison of fully corrected K$^+$ yields for the third longitudinal z bin with Monte Carlo models: FLUKA2011.2c.5 (red line), NuBeam physics list from Geant 4.10.03 (blue line) and QGSP_BERT physics list from Geant 4.10.03 (green line). Vertical error bars are total uncertainties, while grey rectangles are systematic uncertainties. Each panel shows different polar angle region.

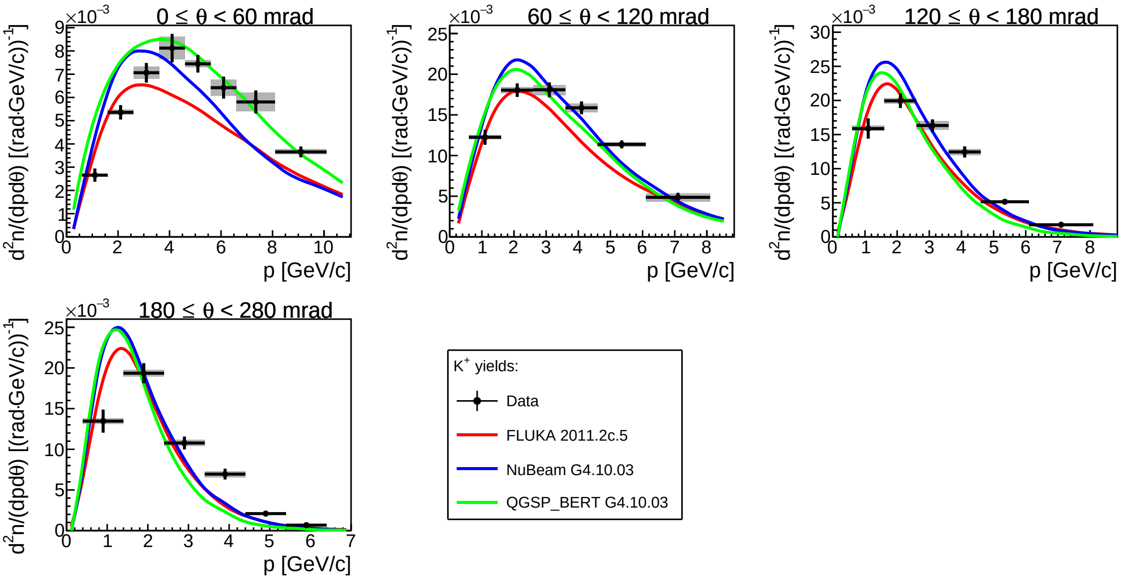

Figure 6.16: Comparison of fully corrected K$^+$ yields for the fourth longitudinal z bin with Monte Carlo models: FLUKA2011.2c.5 (red line), NuBeam physics list from Geant 4.10.03 (blue line) and QGSP_BERT physics list from Geant 4.10.03 (green line). Vertical error bars are total uncertainties, while grey rectangles are systematic uncertainties. Each panel shows different polar angle region.

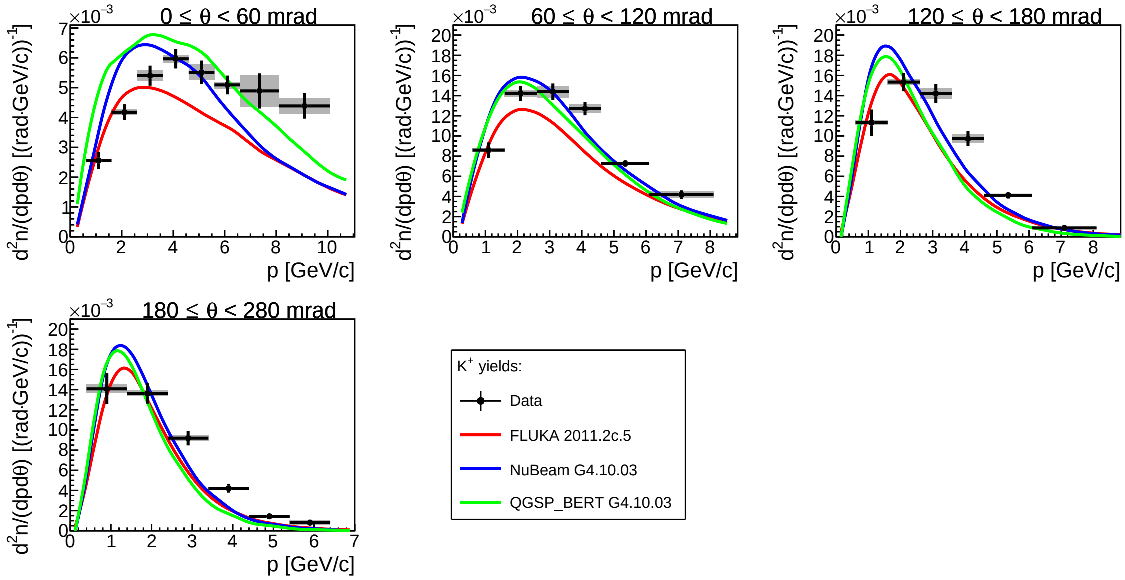

Figure 6.17: Comparison of fully corrected K^+ yields for the fifth longitudinal z bin with Monte Carlo models: FLUKA2011.2c.5 (red line), NuBeam physics list from Geant 4.10.03 (blue line) and QGSP_BERT physics list from Geant 4.10.03 (green line). Vertical error bars are total uncertainties, while grey rectangles are systematic uncertainties. Each panel shows different polar angle region.

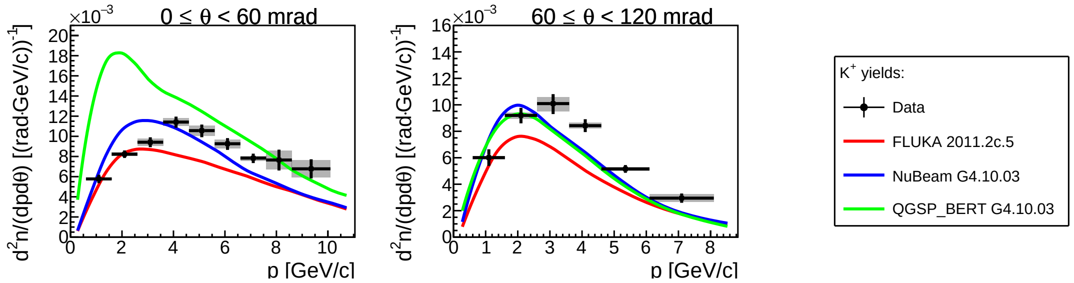

Figure 6.18: Comparison of fully corrected K^+ yields for the downstream target face with Monte Carlo models: FLUKA2011.2c.5 (red line), NuBeam physics list from Geant 4.10.03 (blue line) and QGSP_BERT physics list from Geant 4.10.03 (green line). Vertical error bars are total uncertainties, while grey rectangles are systematic uncertainties. Each panel shows different polar angle region.

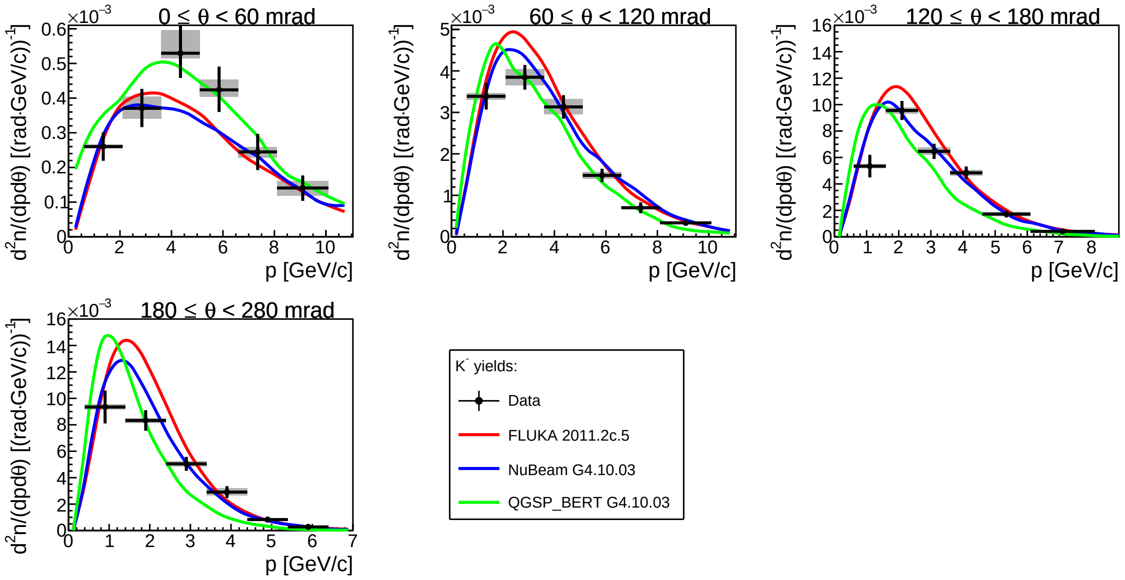

Figure 6.19: Comparison of fully corrected K$^-$ yields for the first longitudinal z bin with Monte Carlo models: Fluka2011.2c.5 (red line), NuBeam physics list from Geant 4.10.03 (blue line) and QGSP_BERT physics list from Geant 4.10.03 (green line). Vertical error bars are total uncertainties, while grey rectangles are systematic uncertainties. Each panel shows different polar angle region.

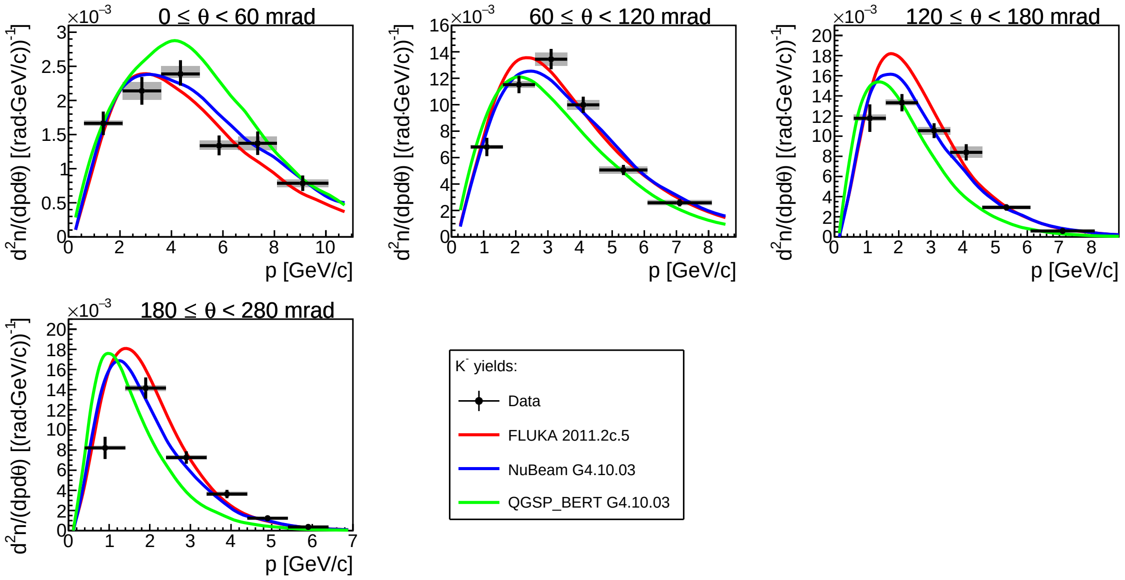

Figure 6.20: Comparison of fully corrected K$^-$ yields for the second longitudinal z bin with Monte Carlo models: Fluka2011.2c.5 (red line), NuBeam physics list from Geant 4.10.03 (blue line) and QGSP_BERT physics list from Geant 4.10.03 (green line). Vertical error bars are total uncertainties, while grey rectangles are systematic uncertainties. Each panel shows different polar angle region.

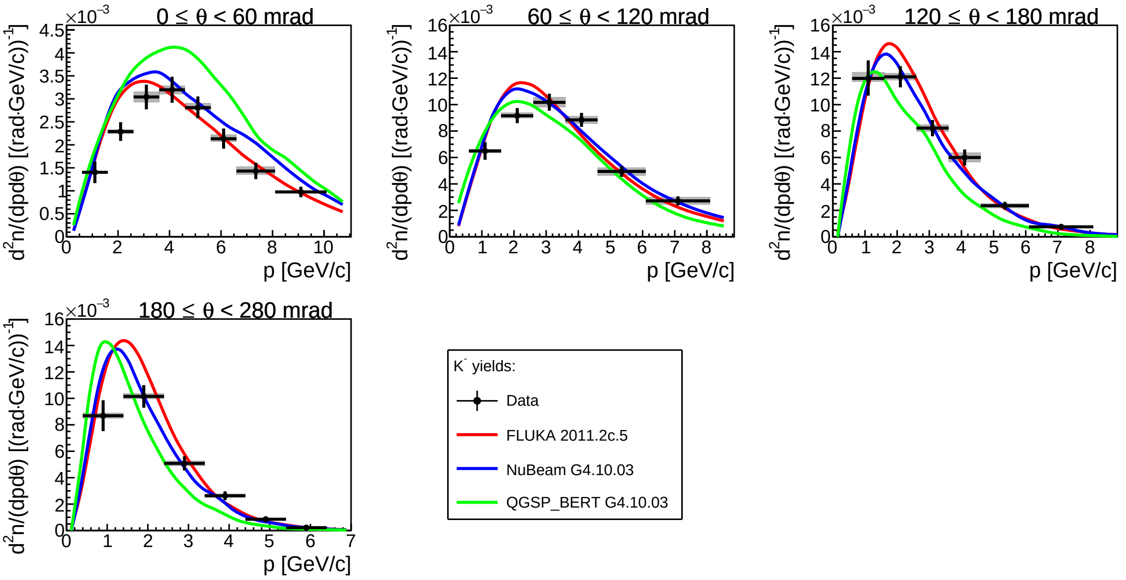

Figure 6.21: Comparison of fully corrected K$^-$ yields for the third longitudinal z bin with Monte Carlo models: FLUKA2011.2c.5 (red line), NuBeam physics list from Geant 4.10.03 (blue line) and QGSP_BERT physics list from Geant 4.10.03 (green line). Vertical error bars are total uncertainties, while grey rectangles are systematic uncertainties. Each panel shows different polar angle region.

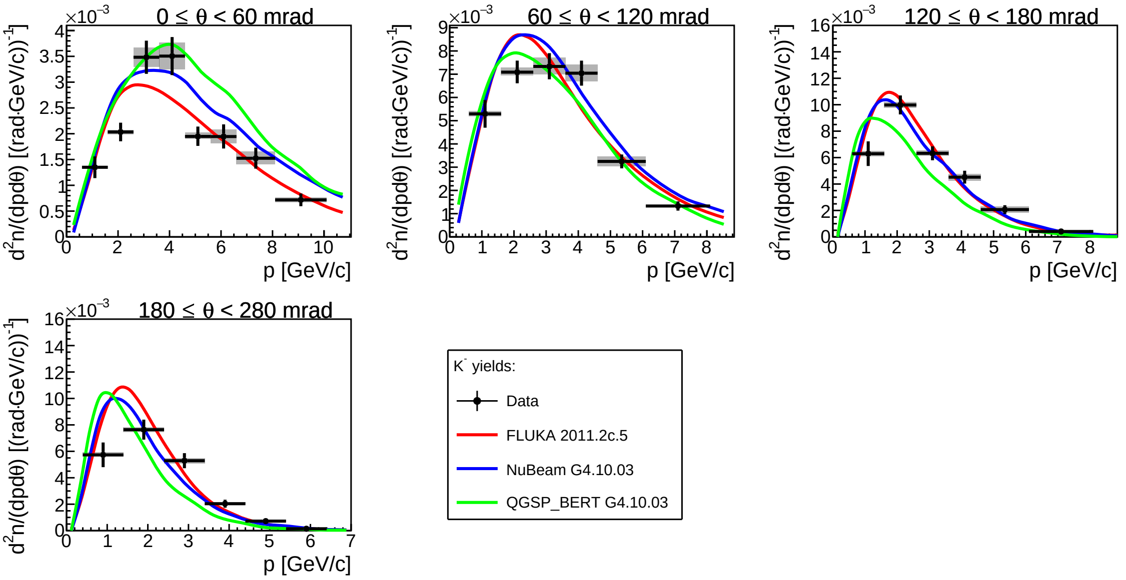

Figure 6.22: Comparison of fully corrected K$^-$ yields for the fourth longitudinal z bin with Monte Carlo models: FLUKA2011.2c.5 (red line), NuBeam physics list from Geant 4.10.03 (blue line) and QGSP_BERT physics list from Geant 4.10.03 (green line). Vertical error bars are total uncertainties, while grey rectangles are systematic uncertainties. Each panel shows different polar angle region.

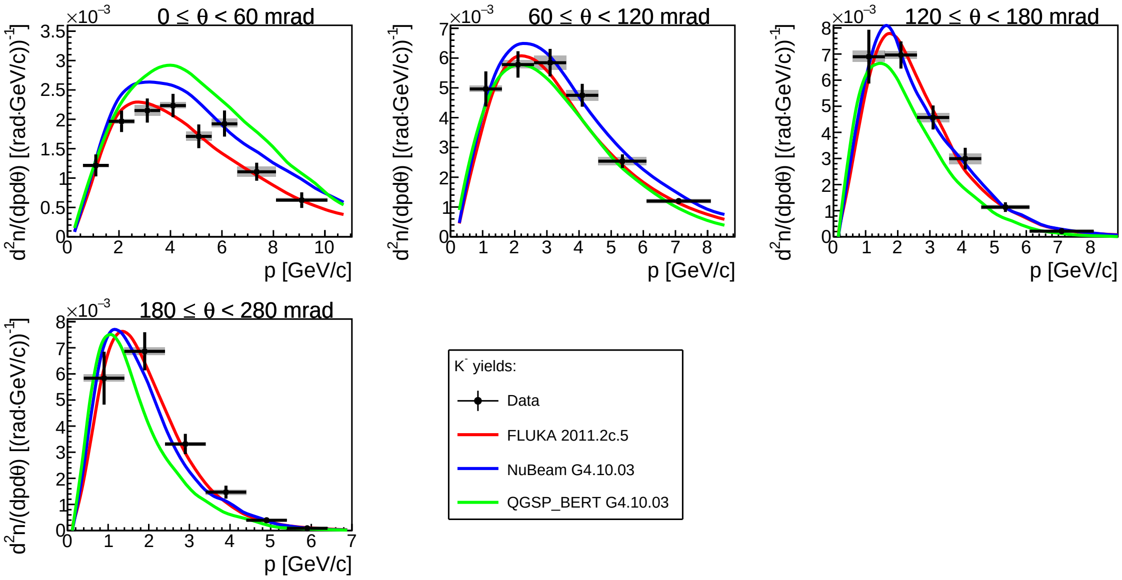

Figure 6.23: Comparison of fully corrected K$^-$ yields for the fifth longitudinal z bin with Monte Carlo models: FLUKA2011.2c.5 (red line), NUBEAM physics list from GEANT 4.10.03 (blue line) and QGSP_BERT physics list from GEANT 4.10.03 (green line). Vertical error bars are total uncertainties, while grey rectangles are systematic uncertainties. Each panel shows different polar angle region.

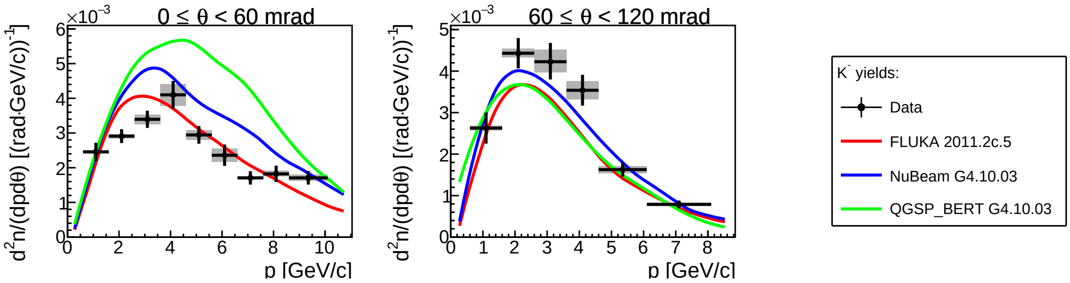

Figure 6.24: Comparison of fully corrected K$^-$ yields for the downstream target face with Monte Carlo models: FLUKA2011.2c.5 (red line), NUBEAM physics list from GEANT 4.10.03 (blue line) and QGSP_BERT physics list from GEANT 4.10.03 (green line). Vertical error bars are total uncertainties, while grey rectangles are systematic uncertainties. Each panel shows different polar angle region.

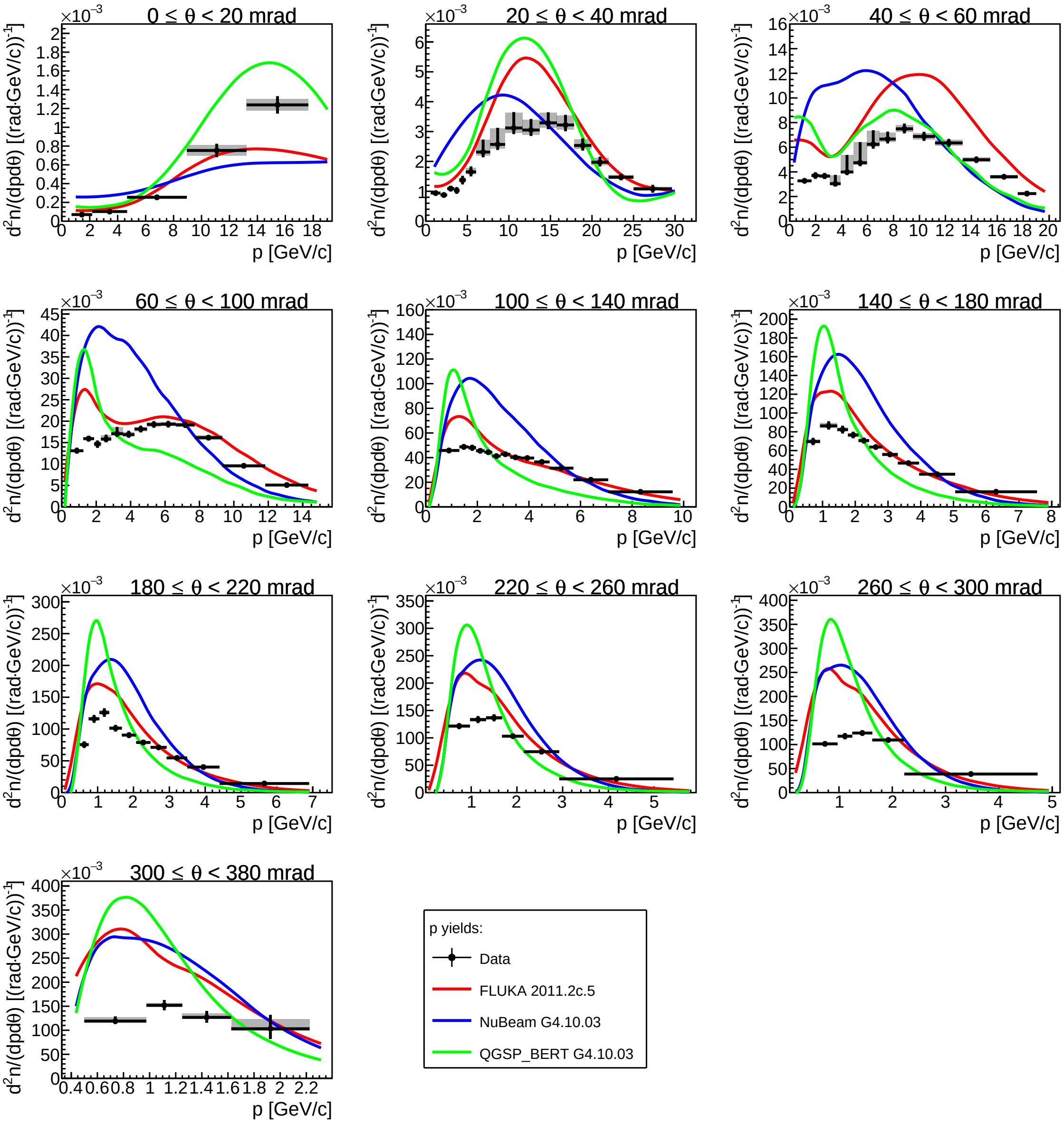

Figure 6.25: Comparison of fully corrected p yields for the first longitudinal z bin with Monte Carlo models: Fluka2011.2c.5 (red line), NuBeam physics list from Geant 4.10.03 (blue line) and QGSP_BERT physics list from Geant 4.10.03 (green line). Vertical error bars are total uncertainties, while grey rectangles are systematic uncertainties. Each panel shows different polar angle region.

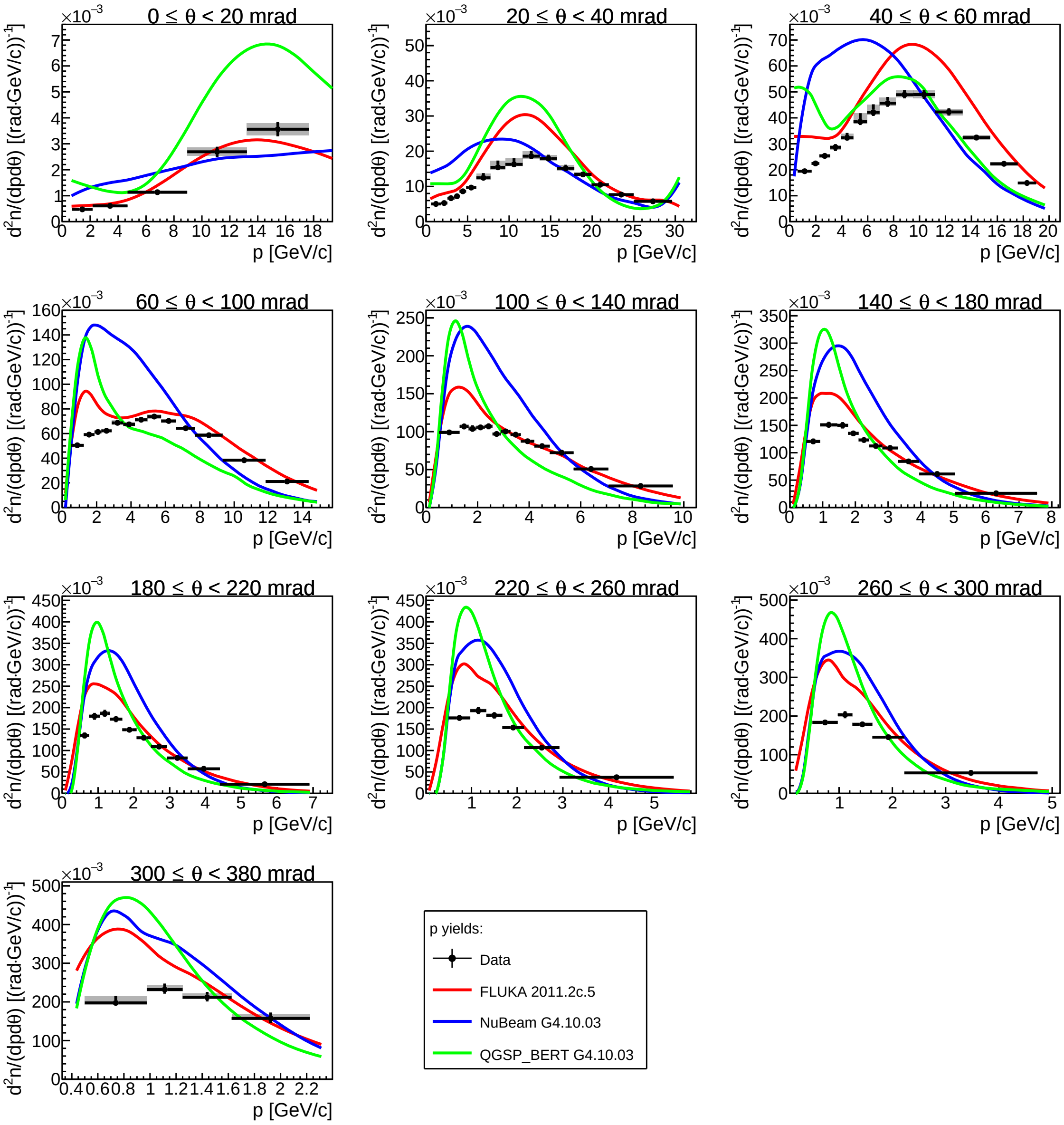

Figure 6.26: Comparison of fully corrected p yields for the second longitudinal z bin with Monte Carlo models: FLUKA2011.2c.5 (red line), NuBeam physics list from Geant 4.10.03 (blue line) and QGSP_BERT physics list from Geant 4.10.03 (green line). Vertical error bars are total uncertainties, while grey rectangles are systematic uncertainties. Each panel shows different polar angle region.

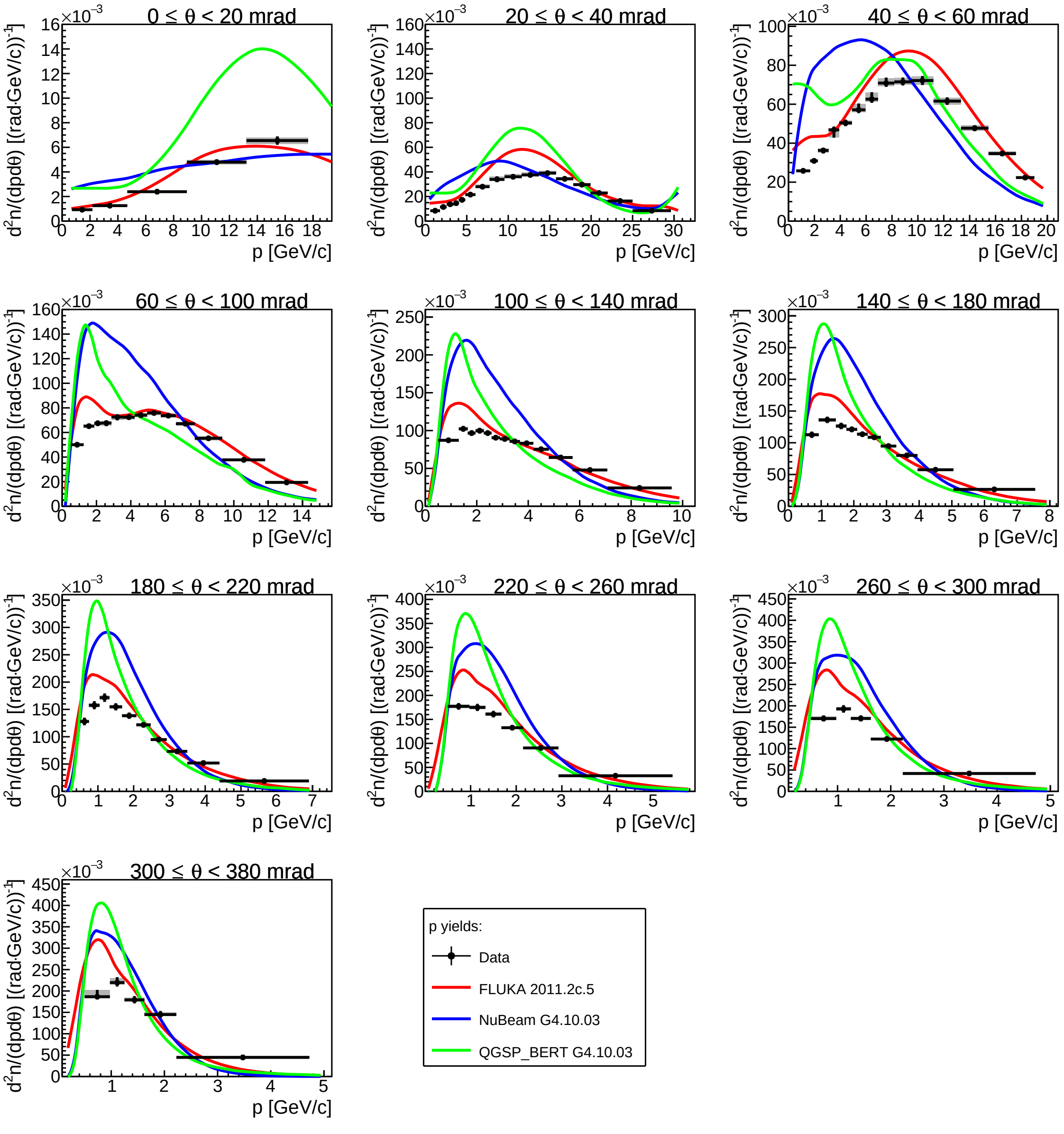

Figure 6.27: Comparison of fully corrected p yields for the third longitudinal z bin with Monte Carlo models: FLUKA2011.2c.5 (red line), NuBeam physics list from Geant 4.10.03 (blue line) and QGSP_BERT physics list from Geant 4.10.03 (green line). Vertical error bars are total uncertainties, while grey rectangles are systematic uncertainties. Each panel shows different polar angle region.

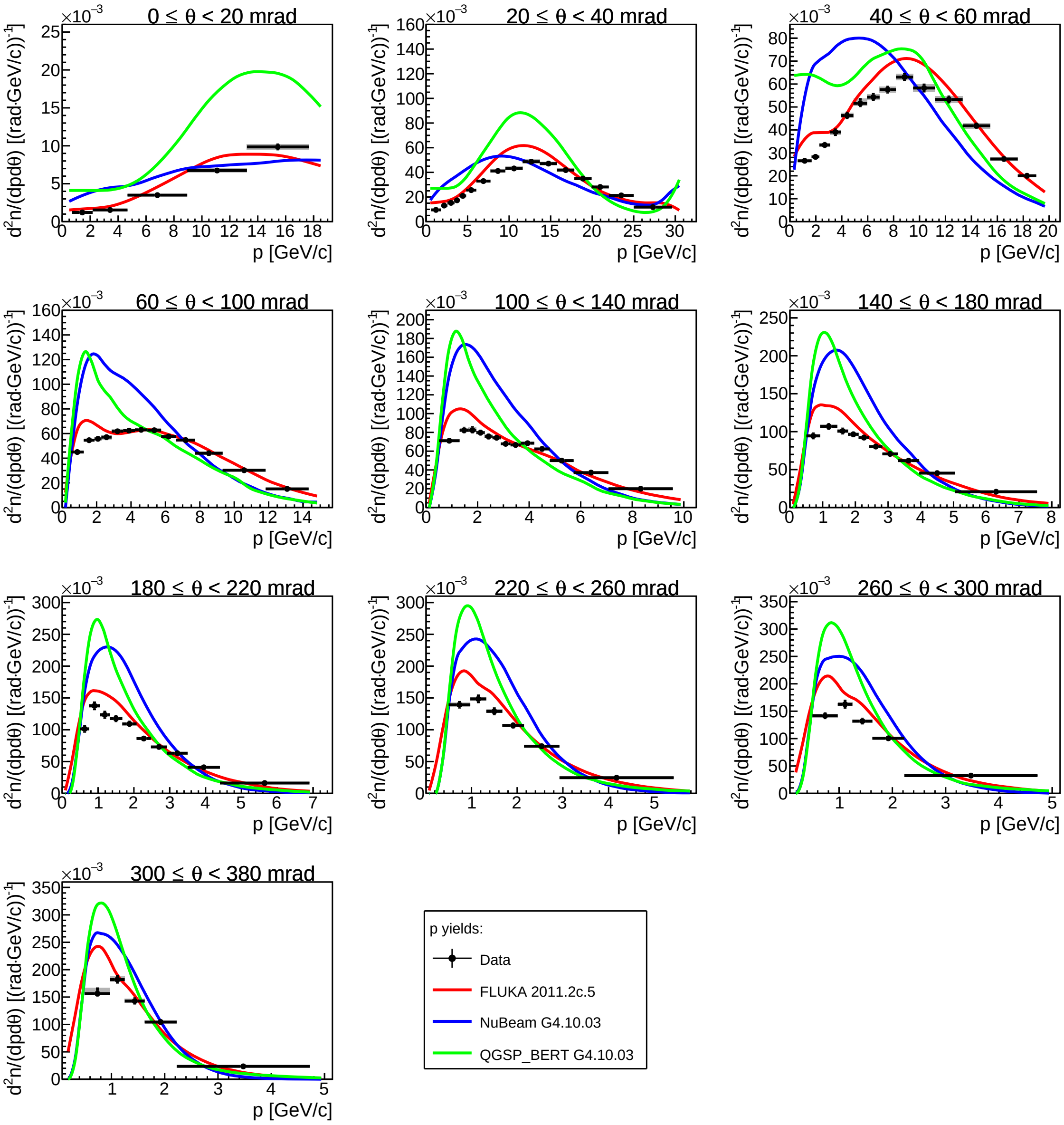

Figure 6.28: Comparison of fully corrected p yields for the fourth longitudinal z bin with Monte Carlo models: Fluka2011.2c.5 (red line), NuBeam physics list from Geant 4.10.03 (blue line) and QGSP_BERT physics list from Geant 4.10.03 (green line). Vertical error bars are total uncertainties, while grey rectangles are systematic uncertainties. Each panel shows different polar angle region.

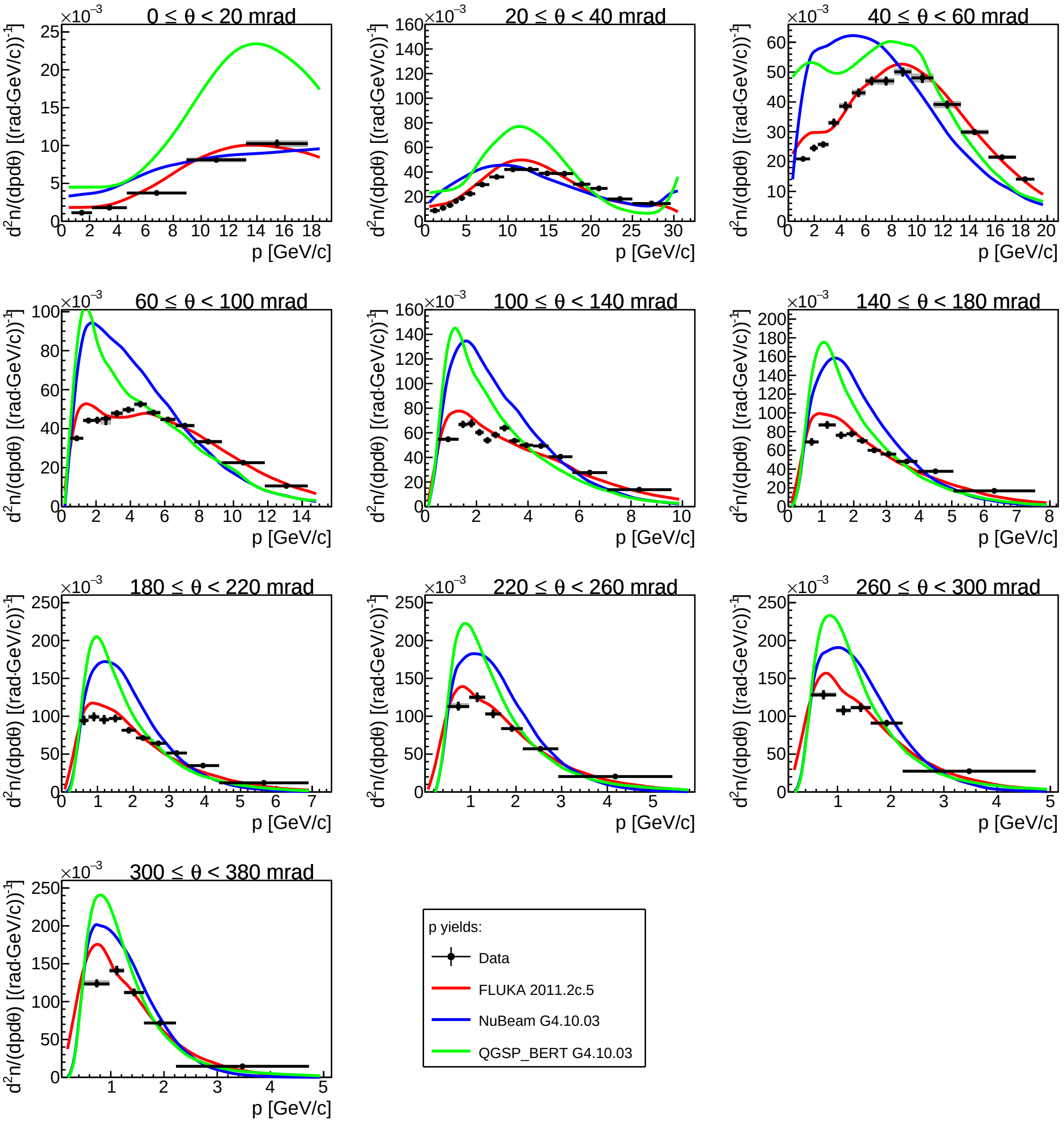

Figure 6.29: Comparison of fully corrected p yields for the fifth longitudinal z bin with Monte Carlo models: Fluka2011.2c.5 (red line), NuBeam physics list from Geant 4.10.03 (blue line) and QGSP_BERT physics list from Geant 4.10.03 (green line). Vertical error bars are total uncertainties, while grey rectangles are systematic uncertainties. Each panel shows different polar angle region.

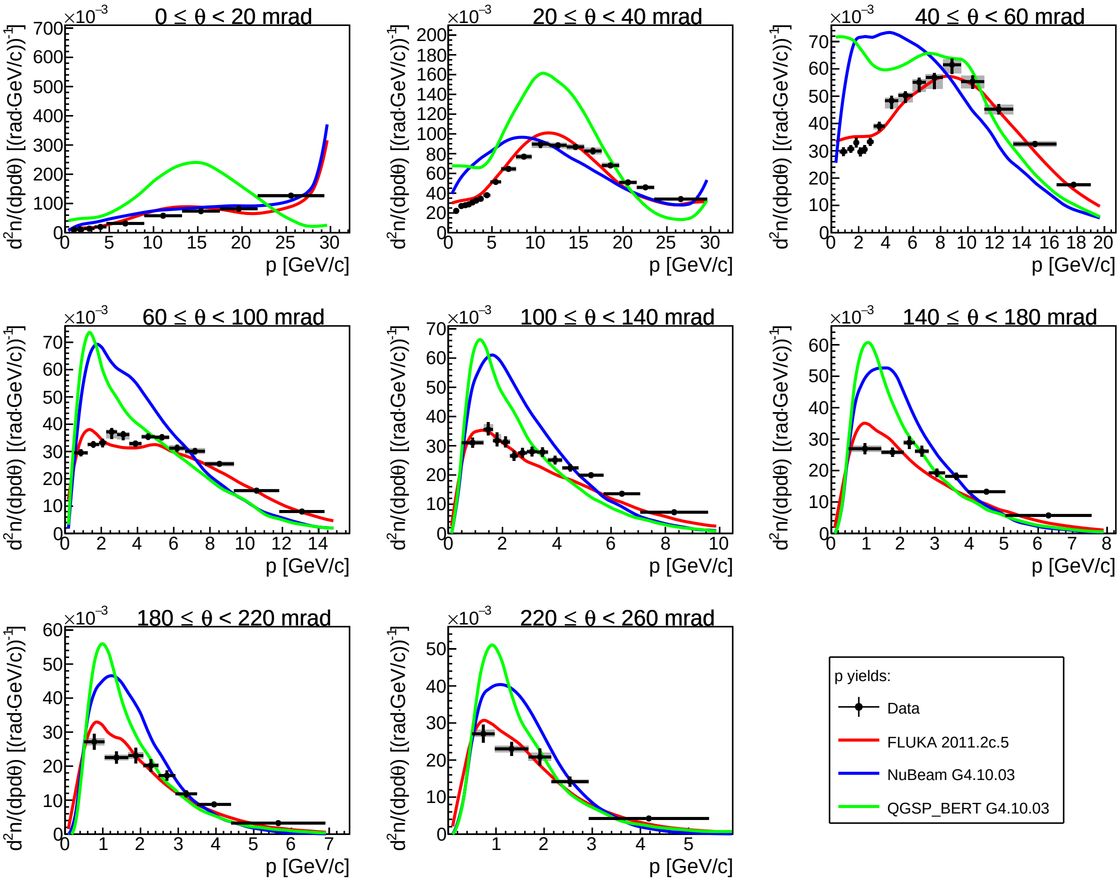

Figure 6.30: Comparison of fully corrected p yields for the downstream target face with Monte Carlo models: FLUKA2011.2c.5 (red line), NUBEAM physics list from GEANT 4.10.03 (blue line) and QGSP_BERT physics list from GEANT 4.10.03 (green line). Vertical error bars are total uncertainties, while grey rectangles are systematic uncertainties. Each panel shows different polar angle region.

6.2 Beam profile dependence

It is essential to ensure that previously presented results are used correctly in the T2K neutrino flux simulation. One of the greatest concerns is to quantify how different beam profiles used in T2K and NA61/SHINE may bias the neutrino flux prediction. On top of that, the possible bias may change per T2K run due to changing beam characteristics. To illustrate the dependence of hadron yields on beam profile, pion yields obtained in this analysis have been re-binned and compared to the measurements performed using 2009 data. Such comparisons can be found in the appendix E. Beam profile in 2009 was around 10% wider compared to the beam profile used during data-taking in 2010. For this reason, there is a suppression of hadron yields in new measurements for upstream z bins and low polar angle.

Such suppression can be understood easily if we imagine two beam particles hitting different spots on the target upstream face and both of them producing a pion with a polar angle equal to 40 mrad. If the first proton hits the target center and if we imagine that pion does not re-interact with carbon, it will exit the target at the z position which is around 32.5 cm away from the interaction point. In contrast, if the second proton hits, for example, a distance of 1 cm away from the target center, a minimum possible z distance which pion will traverse before exiting the target depending on the momentum direction is 7.5 cm. This simple observation shows that for certain beam positions, secondary hadrons with low polar angle cannot exit the target at upstream z bins. Therefore, the only contribution to this region of the phase space for narrow beam can come from the tertiary hadrons. Such contribution is limited in momentum due to conservation laws and should be negligible for the first z bin because of small amounts of material available for re-interactions. For NA61/SHINE beams, there is always a tail in radial beam distribution, so there will always be a non-vanishing contribution of secondary hadrons in the suppressed bins.

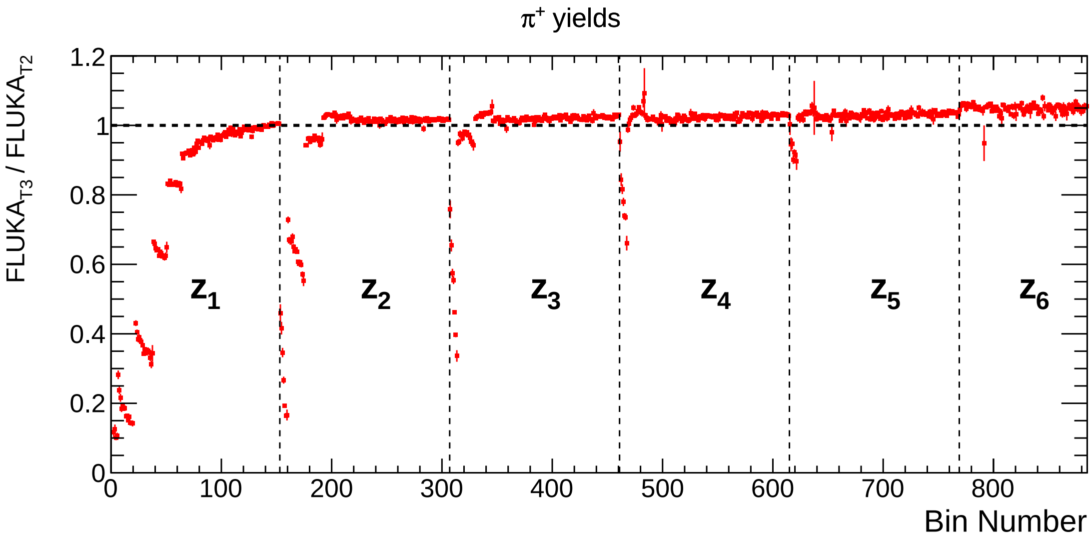

Figure 6.31: Ratio of FLUKA2011.2c.5 π^+ yields vs. bin number simulated with T2 and T3 beam profiles.

A Monte Carlo study was done to assess the dependence of the hadron yields on the beam profile. For this study, T2 and T3 beam profiles were used. Ratios of FLUKA2011.2c.5 π^+ yields vs. bin number, simulated with T2 and T3 beam profiles are shown in Fig. 6.31. Bin counting starts in the first longitudinal region, $(0-18\,\mathrm{cm})$, for the lowest polar angle and momentum bins and rises with momentum and polar angle. In this case, bin 154 is the last bin in the first longitudinal region and next one is the first bin in the second longitudinal region. It is clear that π^+ yields simulated with T3 beam profile are suppressed, mostly in the first longitudinal bin. Bins which seem grouped, span over the same polar angle region, however, they have different momenta. Bins with higher bin number in the same group have higher momenta. It is obvious that the suppression is higher for them. For high momentum, tertiary pions cannot be produced. We can conclude that overall effect of using narrower beam is a shift of the hadron exit position on the target surface towards the downstream target face. There is an increase in the number of high polar angle pions. Such increase seems to be partially caused by re-interactions of low polar angle hadrons. One idea of using measured hadron yields in the T2K neutrino beam simulation is to calculate weights on the target surface for each bin $(n_z, n_\theta, n_p) = (i, j, k)$:

$$W_{ijk} = \left(\frac{1}{N_{pot}}\frac{n_{ijk}}{\Delta p_{ijk}\Delta\theta_{ij}}\right)_{data} \Big/ \left(\frac{1}{N_{pot}}\frac{n_{ijk}}{\Delta p_{ijk}\Delta\theta_{ij}}\right)_{MC} \tag{6.1}$$

and apply these weights to each hadron exiting the target surface. If both, data and Monte Carlo have the same beam profile, some of the effects coming from the change of the beam profile may cancel out in these ratios. In fact, this would be exactly the case if the differences are purely geometrical (changes in re-interactions are negligible). Invariance of the ratios with respect to the beam profile change would mean that ratios calculated with one beam profile could be applied to the Monte Carlo created with another beam profile. This hypothesis is straightforward to test by taking two different Monte Carlo models. For this purpose, Fluka2011.2c.5 is used as a data and NuBeam from Geant4.10.p2 is used as a Monte Carlo. This choice seems ideal since differences between those two models are similar in size to the differences between Fluka and the data. Ratios have been compared for two hadrons: π^+ and protons. Protons have been chosen since there are large differences in the Monte Carlo prediction (see figure 6.32) and this allows us to test if invariance of the weights is valid only if the differences between the Monte Carlo predictions (or between data and MC) are large.

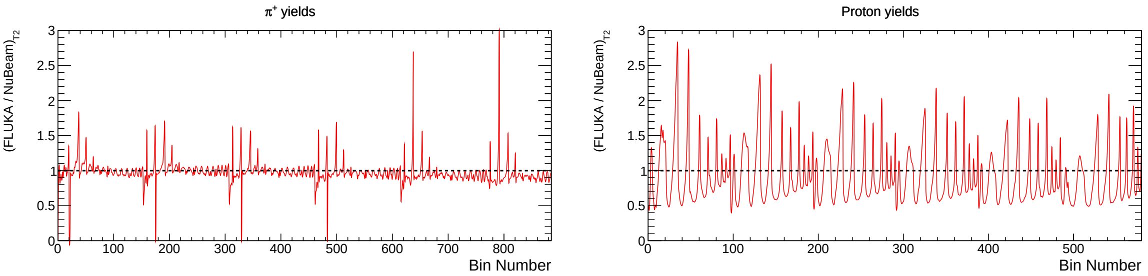

(a) (b)

Figure 6.32: Ratio of Fluka2011.2c.5 model prediction over NuBeamGeant4.10.02 for pions (a) and protons (b) as a function of bin number.

Re-weighting factors simulated for T2 and T3 beam profiles are compared in Fig. 6.33. For the majority of the bins, any potential bias is less than 2%. Only exceptions are the low polar angle and upstream z bins which are heavily affected. However, most differences in this region are below 8%. Total uncertainties of the measured pion yields in the problematic bins is between 7% and 15%, so the precision of the re-weighting factors in T2K will not be greatly affected.

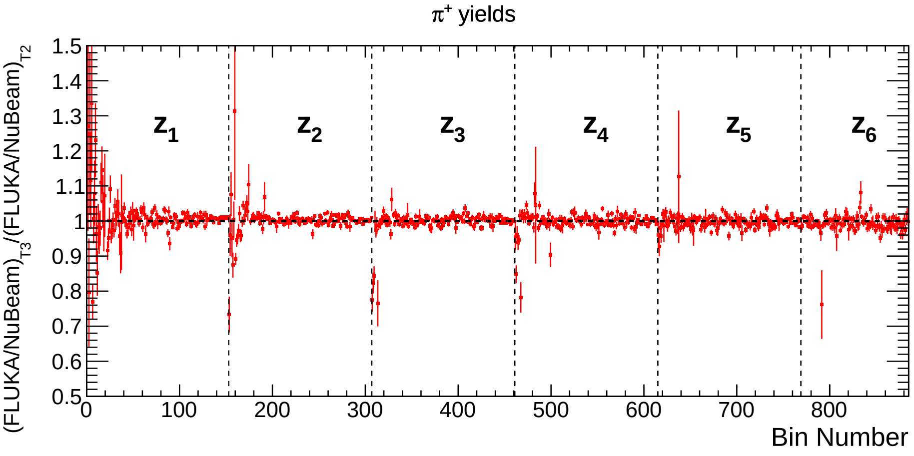

(a)

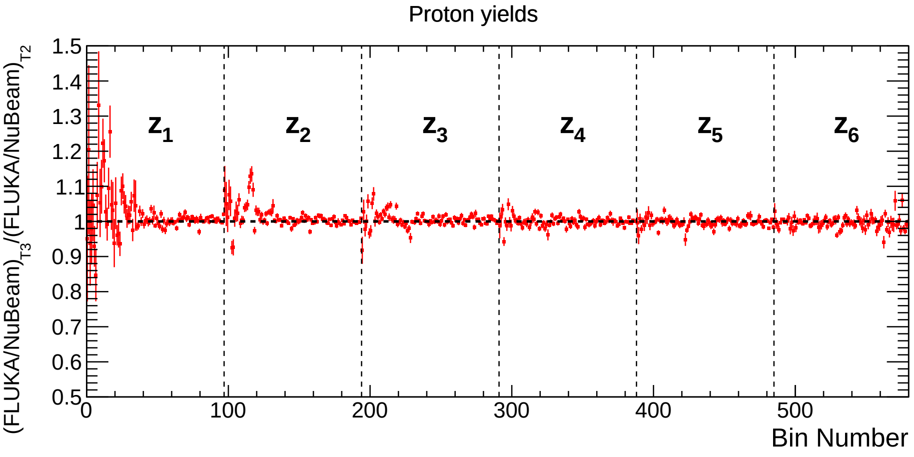

(b)

Figure 6.33: Ratio of the simulated re-weighting factors produced with T2 and T3 beam profiles for π^+ (a) and protons (b).

Beam profiles used in this study represent an extreme case. In reality, the width of the T2K beam profile is in-between the two studied NA61/SHINE beam profiles (T2 and T3). For this reason, suppression of hadron yields in T2K compared to the results presented in this thesis will be smaller. Therefore, any possible bias will also be reduced. A simple solution for dealing with different beam profiles in the T2K neutrino beam simulation is proposed:

1. simulate Fluka yields for NA61/SHINE T2 beam profile,
2. calculate weights of data and simulated Fluka with T2 beam profile,
3. apply weights to the Fluka yields simulated with T2K beam parameters, and
4. assign additional systematics for the low polar angle and upstream z bins.

The last step should be done by using a correct T2K beam profile for a given T2K run and dedicated a Monte Carlo study. However, since this study was done for extreme beam differences, it is expected that this error is smaller than 5%.

6.3 Possible reduction of the T2K neutrino flux uncertainty

Although the results from this thesis have not been used for the re-weighting of the T2K neutrino flux, some indications about the impact of these results can be inferred. Preliminary implementation of the pion yields measured in 2009 has been done by Tomislav Vladisavljević (see Ref. [113]) Resulting hadron production uncertainty of the neutrino flux can be seen in Fig. 6.34.

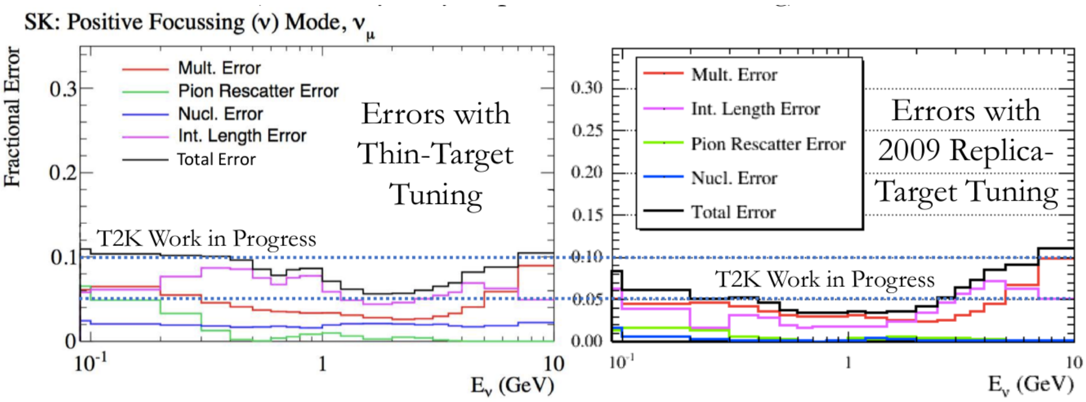

Figure 6.34: Comparison of the hadron production component of ν_μ flux uncertainty at *Super-Kamiokande* after thin target re-weighting (left) and after replica target re-weigihting (right). Only pions have been re-weigheted with the replica target measurements.

In case of the thin target re-weighting, the dominant contribution to the hadron production uncertainty at peak flux energy (0.6 GeV) comes from the interaction length error. This contribution is greatly reduced since re-weighting with the replica target does not require knowledge of the cross-section. However, the interaction length error is still present, since pions in the regions which are not covered by the replica target measurements are re-weighted with the thin target measurements. Also, all hadrons produced in re-interactions outside of the target must be re-weighted by using the thin target re-weighting procedure. Furthermore, for higher neutrino energies, neutrinos are produced in kaon decays. In our previous replica target measurement we did not measure kaon yields, and for this reason, hadron production uncertainty in this region was not reduced. Uncertainties of pion yields measured in 2009 are dominated by statistical component. For the results presented in this thesis, statistical uncertainties are reduced by a factor $1.4-2$, since some bins are split in two. This improvement will further reduce hadron production uncertainty of the neutrino flux. Without taking any additional uncertainty for the beam profile differences, the expected hadron production uncertainty around the peak energy should be 3%. This number was estimated simply by comparing total uncertainties in the new pion yields with the total uncertainties in the old pion yields. Implementation of these results in the T2K neutrino beam simulation is necessary to obtain accurate estimates. Reduction of the flux uncertainties is also expected for higher energies because of the kaon yields measured on the replica target surface.

Conclusion

Accelerator-based neutrino experiments such as T2K suffer from large neutrino flux uncertainties which are caused by a poor knowledge of the hadron production. Neutrino beam in T2K is created mostly from the decays of pions and kaons which are produced in interactions of the proton beam with a 90 cm-long graphite target. To tackle this problem, NA61/SHINE collaboration performed hadron-production measurements for T2K by using a 31 GeV/c proton beam and graphite targets. Two types of measurements had been performed: with the thin carbon target and with the 90 cm long T2K replica target. The latter measurement are the main topic of this thesis. The analyzed data were taken in 2010 with three physics goals in mind:

1. to measure positively and negatively charged pion yields coming from the surface of the T2K replica target with greater precision than in measurements performed in 2009,
2. to measure for the first time positively and negatively charged kaon yields coming from the surface of the T2K replica target and
3. to measure for the first time proton yields coming from the surface of the T2K replica target.

For these measurements and because NA61/SHINE collaboration started using a new SHINE framework, several tools for analysis and calibration were developed. All three of physics goals have been achieved in this thesis, and the results were presented in the form of double differential yields in the phase space of outgoing particle momentum, polar angle and longitudinal position on the target surface (p, θ, z).

In measurement performed with the data collected in 2009, total uncertainty of the pion yields was dominated by the statistical uncertainty, while in the results presented in this thesis, this was not the case. The total mean uncertainty across all phase space bins, dropped from around 8% to around 5%, while the total number of bins is increased by 25%. Pion yields in the region between 340 mrad and 380 mrad in polar angle are covered for the first time. Kaon yields are measured with the statistical and systematical uncertainty of around 10%. Kaons have limited coverage of the phase space (limited to below 10 GeV/c) because of the limitations coming from energy loss and time of flight measurements. In addition, proton yields are also measured for the first time, however with much better phase space coverage.

Yields for all five measured particle species ($\pi^{\pm}$, $K^{\pm}$, p) are compared to FLUKA2011.2c.5 Monte Carlo, NUBEAM and QGSP_BERT physics lists from GEANT4.10.03. In case of pions, FLUKA2011.2c.5 gives the best prediction, while QGSP_BERT fails to describe the data. NUBEAM physics list which was specially tuned for the usage in the neutrino beam simulations gives a slightly worse prediction for low momenta when compared to FLUKA2011.2c.5. Similarly to pion yields, FLUKA2011.2c.5 and NUBEAM give a more accurate prediction of the kaons yields with differences being up to 30%. None of the models give the accurate prediction of the proton yields. The predictions are in some cases different by a factor of two or three compared to the data. FLUKA2011.2c.5 prediction improves for downstream z bins, while GEANT4.10.03 physics lists fail to reproduce even the shape of the spectra.

The hadron yields presented here will be used for the calculation of neutrino and antineutrino fluxes in the T2K experiment. The expected impact of these new measurements is a reduction of (anti)neutrino flux uncertainties from 10% down to about 4%.

Appendix A

Track extrapolation coefficients

A.1 A - coefficients

x	**y**	**z**
$t_x t_y$	$-(1+t_x^2)$	t_y

Table A.1: First order coefficients A_i.

	x	**y**	**z**
x	$t_x(3t_y^2+1)$	$-t_y(3t_x^2+1)$	$t_y^2-t_x^2$
y	$-t_y(3t_x^2+1)$	$3t_x(t_x^2+1)$	$-2t_x t_y$
z	$2t_y^2+1$	$-2t_x t_y$	$-t_x$

Table A.2: Second order coefficients A_{ij}.

	x	**y**	**z**
x	$3t_x t_y(5t_y^2+3)$	$-3(t_x^2+t_y^2+5t_x^2 t_y^2)-1$	$t_y(-6t_x^2+3t_y^2+1)$
y	$-3(t_x^2+t_y^2+5t_x^2 t_y^2)-1$	$3t_x t_y(5t_x^2+3)$	$t_x(3t_x^2-6t_y^2+1)$
z	$2t_y(-2t_x^2+2t_y^2+1)$	$2t_x(2t_x^2-2t_y^2+1)$	$-4t_x t_y$

Table A.3: Third order coefficients A_{xij}.

	x	**y**	**z**
x	$-3(t_x^2+t_y^2+5t_x^2t_y^2)-1$	$3t_xt_y(5t_x^2+3)$	$t_x(3t_x^2-6t_y^2+1)$
y	$3t_xt_y(5t_x^2+3)$	$-3(t_x^2+1)(5t_x^2+1)$	$3t_y(3t_x^2+1)$
z	$-2t_x(4t_y^2+1)$	$2t_y(4t_x^2+1)$	$2(t_x^2-t_y^2)$

Table A.4: Third order coefficients A_{yij}.

	x	**y**	**z**
x	$2t_y(4t_y^2+3)$	$-2t_x(4t_y^2+1)$	$-4t_xt_y$
y	$-2t_x(4t_y^2+1)$	$2t_y(4t_x^2+1)$	$2(t_x^2-t_y^2)$
z	$-3t_xt_y$	$3t_x^2+1$	$-t_y$

Table A.5: Third order coefficients A_{zij}.

A.2 B - coefficients

x	**y**	**z**
$(1+t_y^2)$	$-t_xt_y$	$-t_x$

Table A.6: First order coefficients B_i.

	x	**y**	**z**
x	$3t_y(t_y^2+1)$	$-t_x(3t_y^2+1)$	$-2t_xt_y$
y	$-t_x(3t_y^2+1)$	$t_y(3t_x^2+1)$	$t_x^2-t_y^2$
z	$-2t_xt_y$	$2t_x^2+1$	$-t_y$

Table A.7: Second order coefficients B_{ij}.

	x	**y**	**z**
x	$3(t_y^2+1)(5t_y^2+1)$	$-3t_xt_y(5t_y^2+3)$	$-3t_x(3t_y^2+1)$
y	$-3t_xt_y(5t_y^2+3)$	$3(t_x^2+t_y^2+5t_x^2t_y^2)+1$	$-t_y(-6t_x^2+3t_y^2+1)$
z	$-2t_x(4t_y^2+1)$	$2t_y(4t_x^2+1)$	$2(t_x^2-t_y^2)$

Table A.8: Third order coefficients B_{xij}.

	x	**y**	**z**
x	$-3t_xt_y(5t_y^2+3)$	$3(t_x^2+t_y^2+5t_x^2t_y^2)+1$	$-t_y(-6t_x^2+3t_y^2+1)$
y	$3(t_x^2+t_y^2+5t_x^2t_y^2)+1$	$-3t_xt_y(5t_x^2+3)$	$-t_x(3t_x^2-6t_y^2+1)$
z	$2t_y(2t_x^2-2t_y^2-1)$	$-2t_x(2t_x^2-2t_y^2+1)$	$4t_xt_y$

Table A.9: Third order coefficients B_{yij}.

	x	**y**	**z**
x	$-2t_x(4t_y^2+1)$	$2t_y(4t_x^2+1)$	$2(t_x^2-t_y^2)$
y	$2t_y(4t_x^2+1)$	$-2t_x(4t_x^2+3)$	$4t_xt_y$
z	$-(3t_y^2+1)$	$3t_xt_y$	t_x

Table A.10: Third order coefficients B_{zij}.

Appendix B

Comparison of FLUKA 2011.2c.5 π^+ yields

Monte Carlo simulation of p + T2K replica target interactions was repeated three times with three different beam profiles: a NA61 T2 beam profile, a NA61 T3 beam profile and a T2K run 4 beam profile. Yields of π^+ on the target surface were compared in the figures B.1 and B.2.

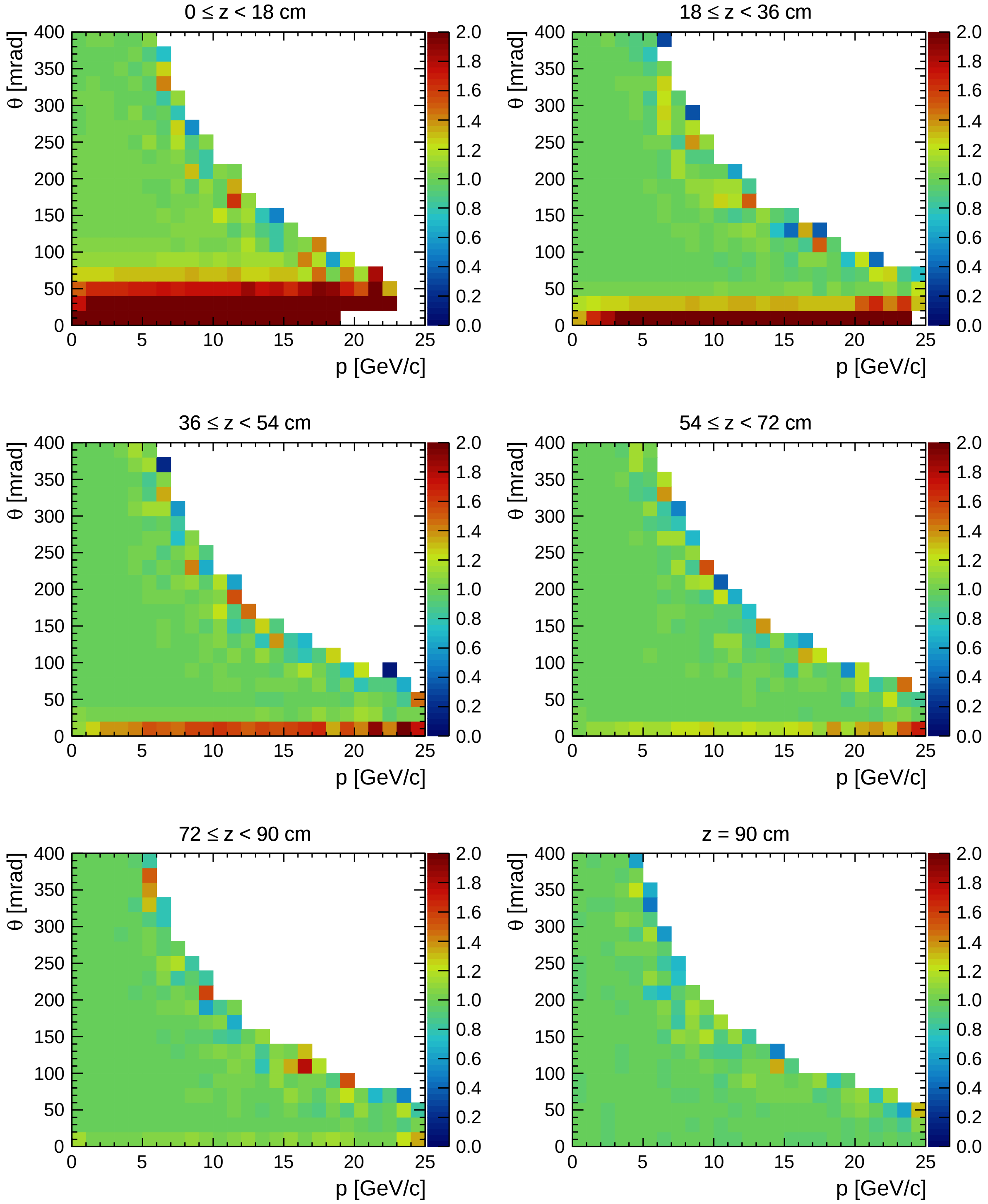

Figure B.1: Ratio of the FLUKA 2011.2c.5 π^+ yields on the T2K replica targer surface simulated with the T2 beam profile and the π^+ yields simulated with the T2K (run 4) beam profile. First five panels show five longitudinal bins (18 cm in size), while last panel shows downstream target face.

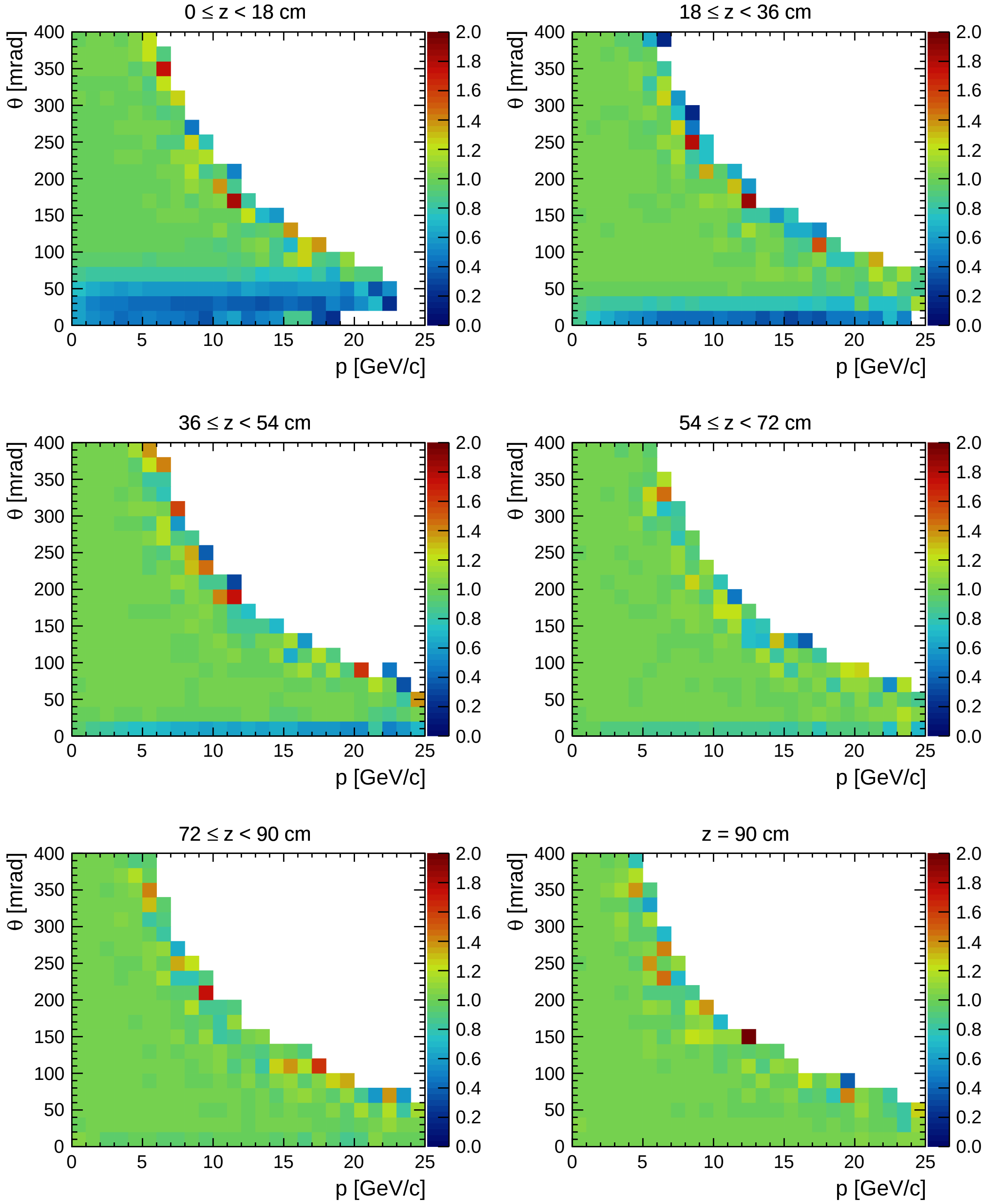

Figure B.2: Ratio of the FLUKA 2011.2c.5 π^+ yields on the T2K replica targer surface simulated with the T3 beam profile and the π^+ yields simulated with the T2K (run 4) beam profile. First five panels show five longitudinal bins (18 cm in size), while last panel shows downstream target face.

Appendix C

Track selection efficiencies

Topology		Total	p fit	dE/dx-tof	Clusters	ϕ	d/σ_R
	$[10^6]$	83.081	38.188	6.353	6.166	4.677	4.118
	[%]		100	16.64	16.15	12.25	10.78
VTPC1	$[10^6]$		25.324	0.761	0.744	0.637	0.604
	[%]		66.32	11.98	12.07	13.61	14.67
VTPC2	$[10^6]$		4.089	0.490	0.385	0.248	0.049
	[%]		10.71	7.72	6.24	5.31	1.19
VTPC1+2	$[10^6]$		5.567	2.946	2.945	2.376	2.258
	[%]		14.58	46.37	47.77	50.80	54.82
GTPC	$[10^6]$		0.527	0.395	0.355	0.204	0.165
	[%]		1.38	6.22	5.76	4.37	4.00
VTPC1+GTPC	$[10^6]$		0.156	0.053	0.052	0.041	0.037
	[%]		0.41	0.84	0.85	0.87	0.89
VTPC2+GTPC	$[10^6]$		1.976	1.388	1.364	0.908	0.757
	[%]		5.17	21.85	22.13	19.40	18.38
VTPC1+2+GTPC	$[10^6]$		0.549	0.319	0.319	0.264	0.249
	[%]		1.44	5.03	5.18	5.64	6.04

(a)

Topology		Total	p fit	dE/dx-tof	Clusters	ϕ	d/σ_R
	$[10^6]$	253.751	166.237	36.876	36.200	26.484	25.187
	[%]		100	22.18	21.77	15.93	15.15
VTPC1	$[10^6]$		108.757	4.808	4.711	3.764	3.649
	[%]		65.42	13.04	13.02	14.21	14.49
VTPC2	$[10^6]$		10.609	1.332	1.009	0.697	0.327
	[%]		6.38	3.61	2.79	2.63	1.30
VTPC1+2	$[10^6]$		28.322	17.511	17.510	13.632	13.360
	[%]		17.04	47.49	48.37	51.47	53.04
GTPC	$[10^6]$		2.655	2.297	2.147	1.164	1.058
	[%]		1.60	6.23	5.93	4.40	4.20
VTPC1+GTPC	$[10^6]$		0.724	0.293	0.287	0.218	0.209
	[%]		0.44	0.79	0.79	0.82	0.83
VTPC2+GTPC	$[10^6]$		11.661	8.456	8.355	5.263	4.881
	[%]		7.01	22.93	23.08	19.87	19.38
VTPC1+2+GTPC	$[10^6]$		3.509	2.180	2.180	1.746	1.704
	[%]		2.11	5.91	6.02	6.59	6.76

(b)

Table C.1: Track selection for the data (a) and for MC (b).

Appendix D

Systematic uncertainties

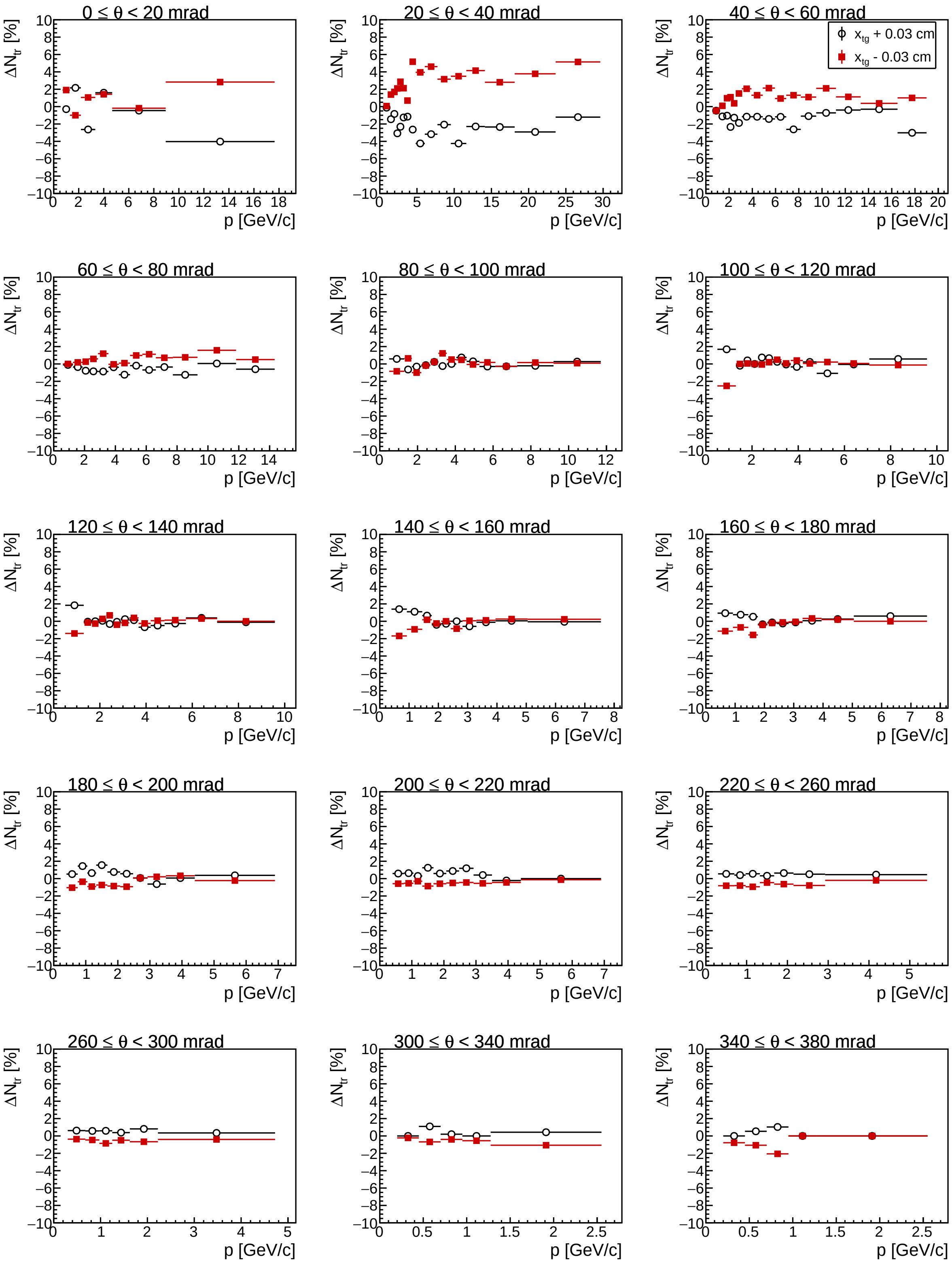

Figure D.1: Change in the number of selected positive tracks in the first z bin after changing target x position within measured uncertainty. Black points are for $x_{tg} + 0.03\,\mathrm{cm}$ change and red points are for $x_{tg} - 0.03\,\mathrm{cm}$ change). Phase space has been optimized for pions.

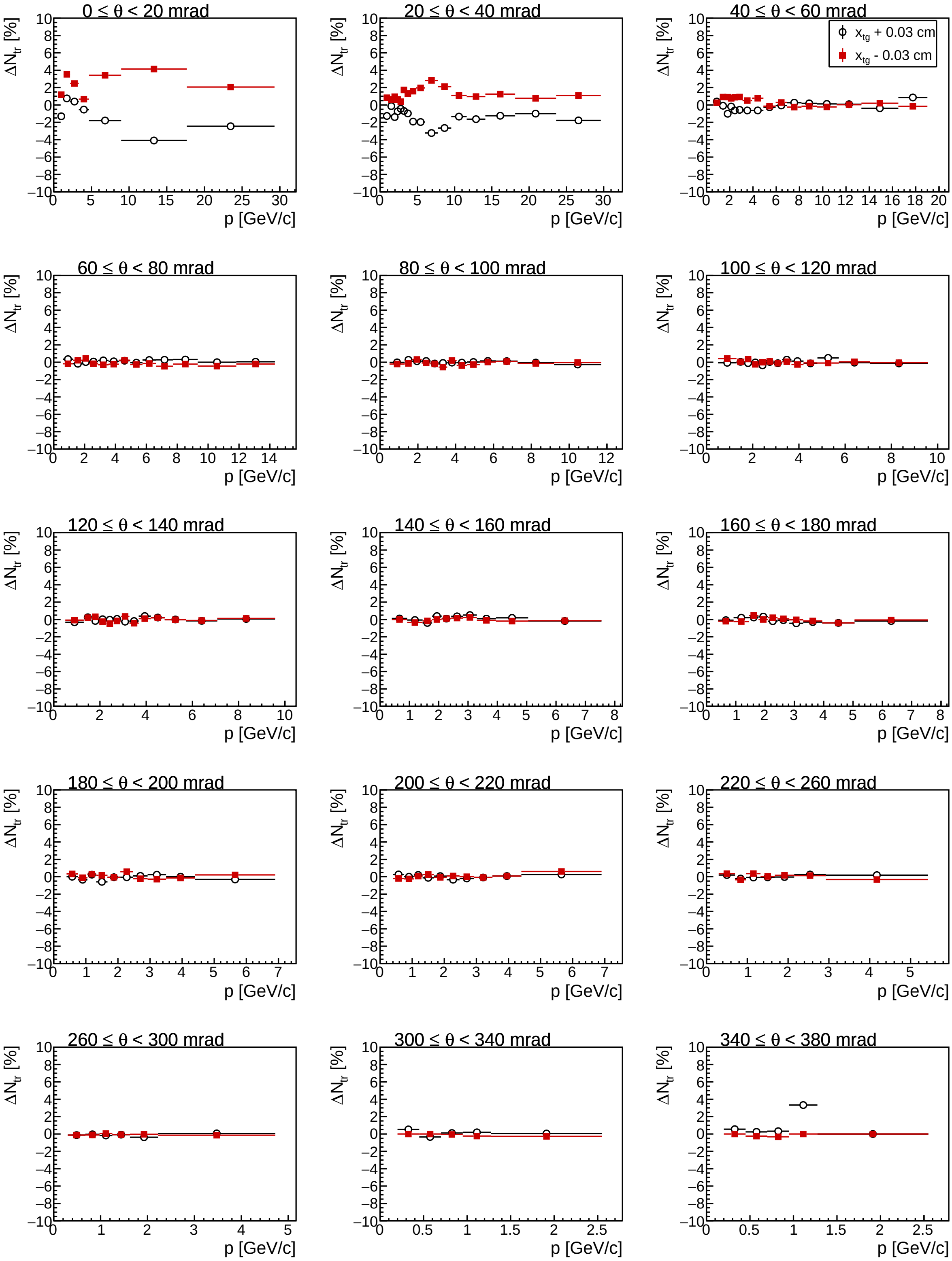

Figure D.2: Change in the number of selected positive tracks in the second z bin after changing target x position within measured uncertainty. Black points are for $x_{tg} + 0.03\,\mathrm{cm}$ change and red points are for $x_{tg} - 0.03\,\mathrm{cm}$ change). Phase space has been optimized for pions.

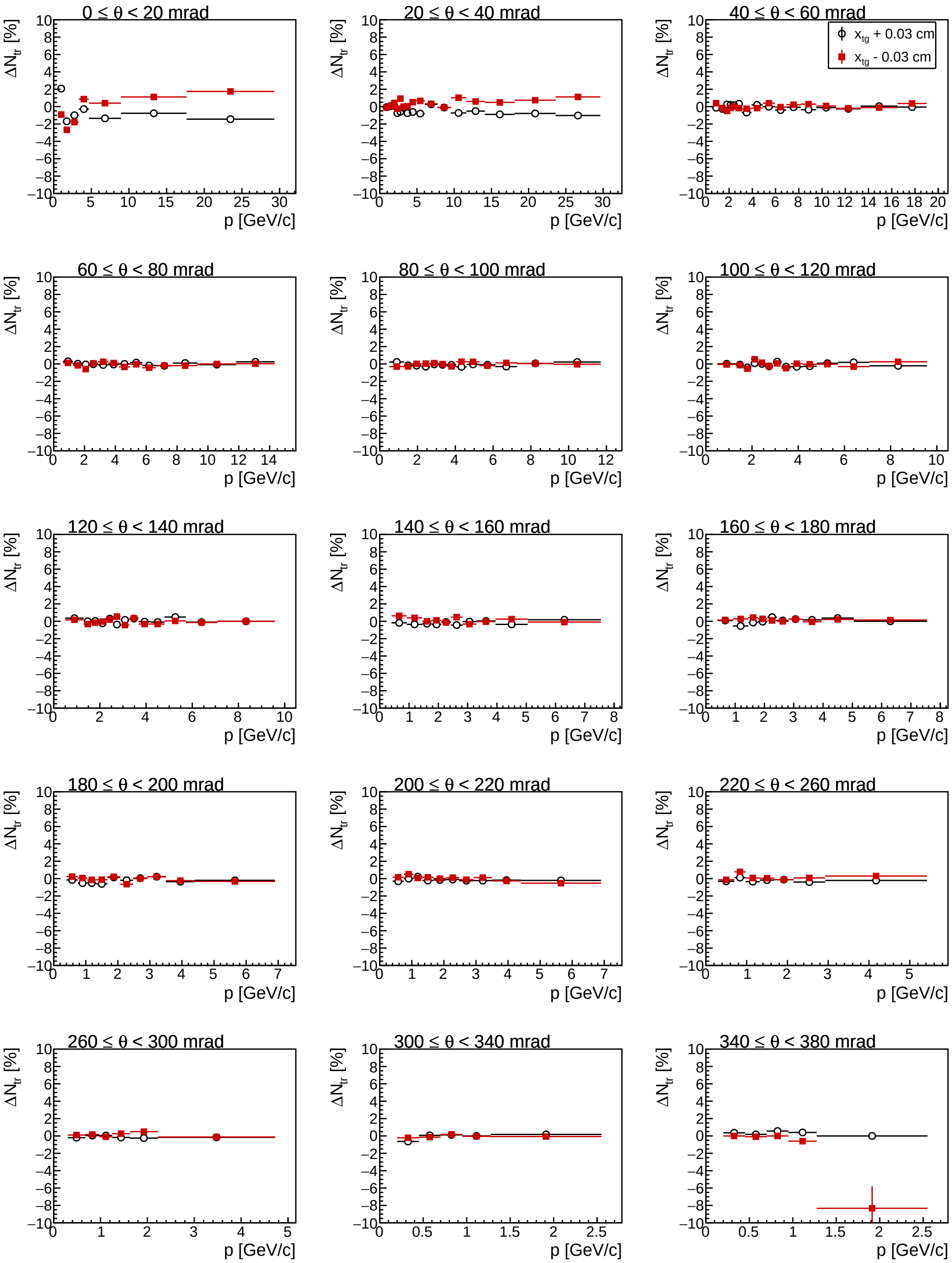

Figure D.3: Change in the number of selected positive tracks in the third z bin after changing target x position within measured uncertainty. Black points are for $x_{tg} + 0.03\,\mathrm{cm}$ change and red points are for $x_{tg} - 0.03\,\mathrm{cm}$ change). Phase space has been optimized for pions.

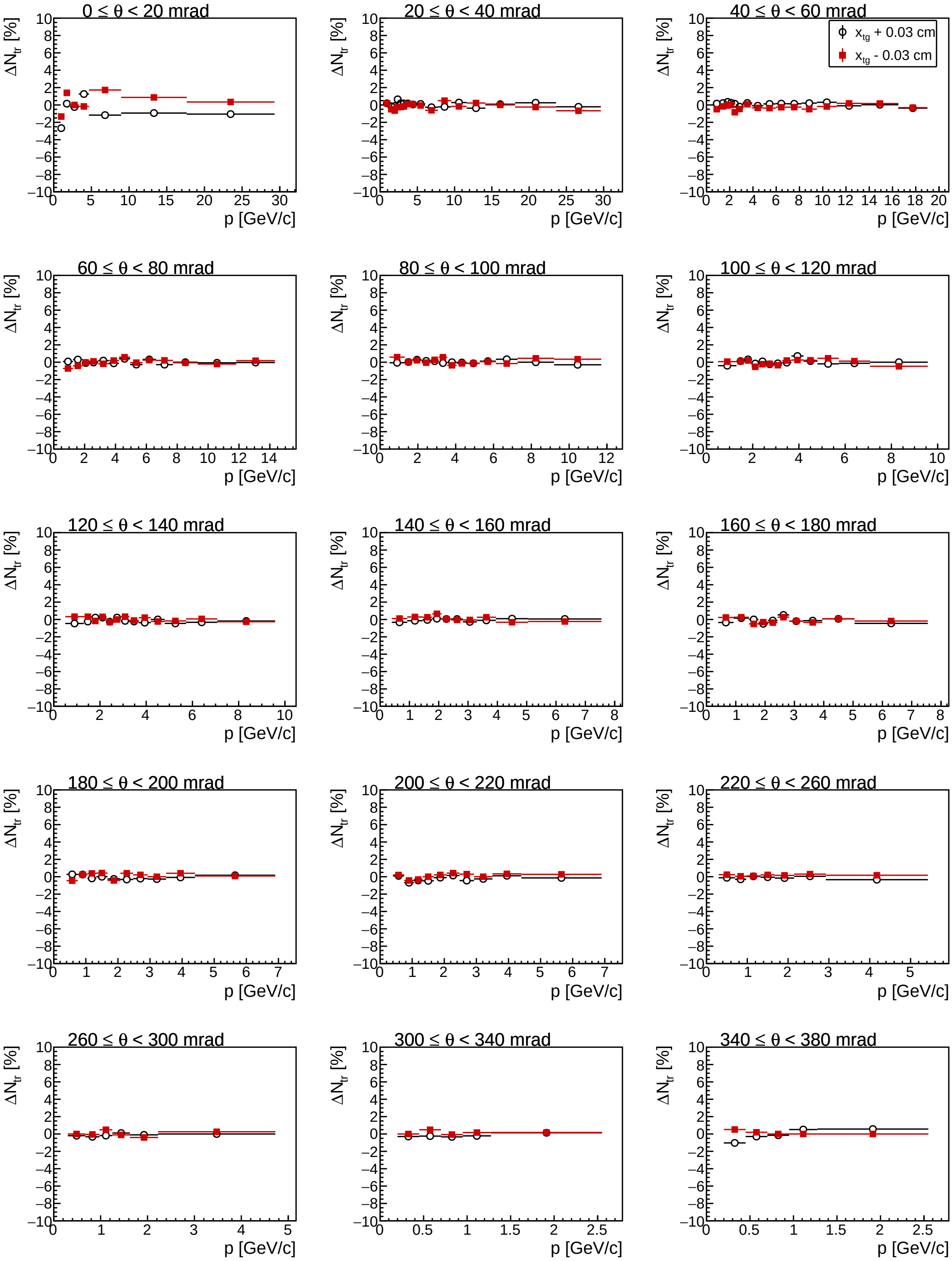

Figure D.4: Change in the number of selected positive tracks in the fourth z bin after changing target x position within measured uncertainty. Black points are for $x_{tg} + 0.03\,\text{cm}$ change and red points are for $x_{tg} - 0.03\,\text{cm}$ change). Phase space has been optimized for pions.

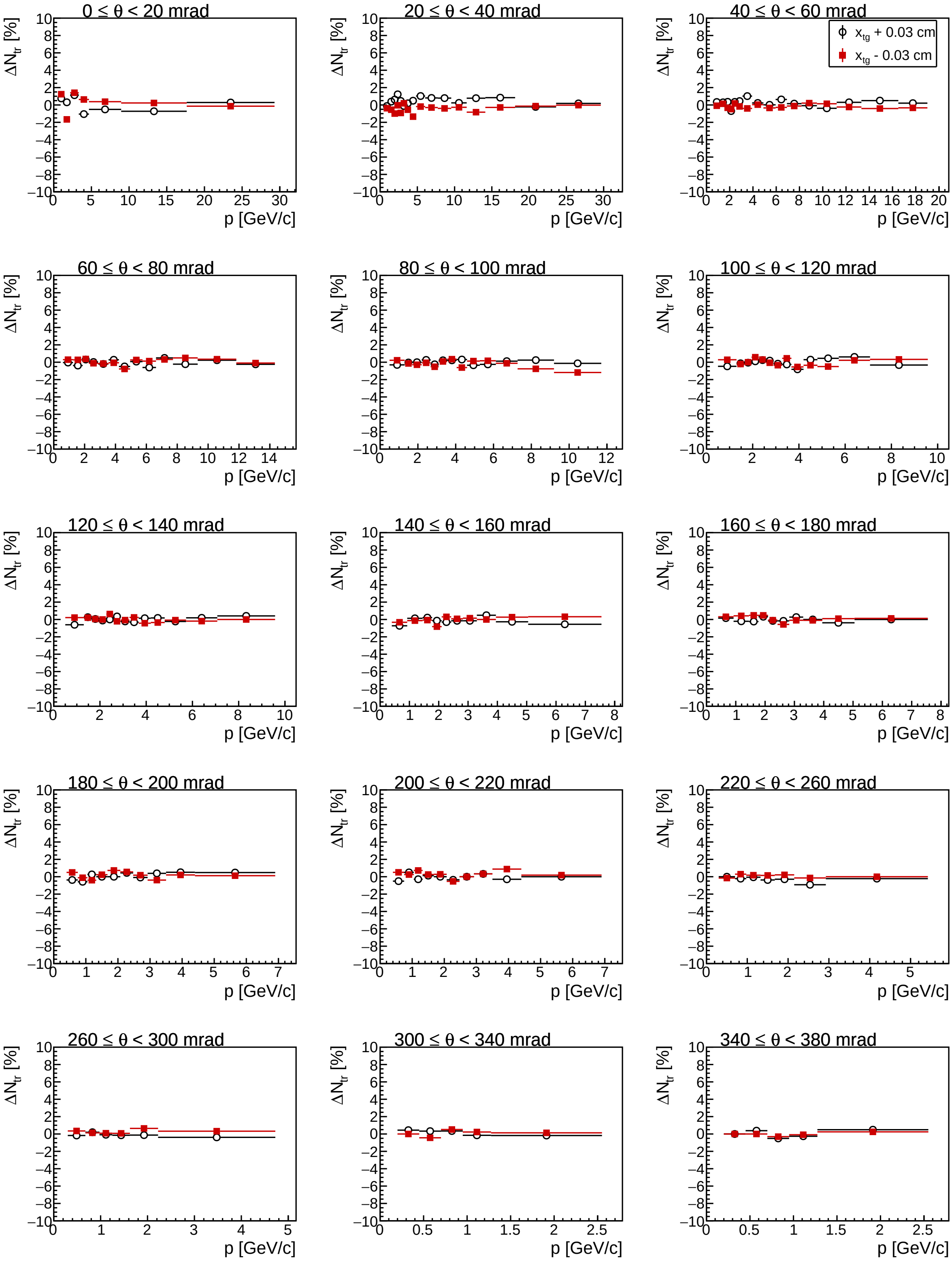

Figure D.5: Change in the number of selected positive tracks in the fifth z bin after changing target x position within measured uncertainty. Black points are for $x_{tg} + 0.03\,\mathrm{cm}$ change and red points are for $x_{tg} - 0.03\,\mathrm{cm}$ change). Phase space has been optimized for pions.

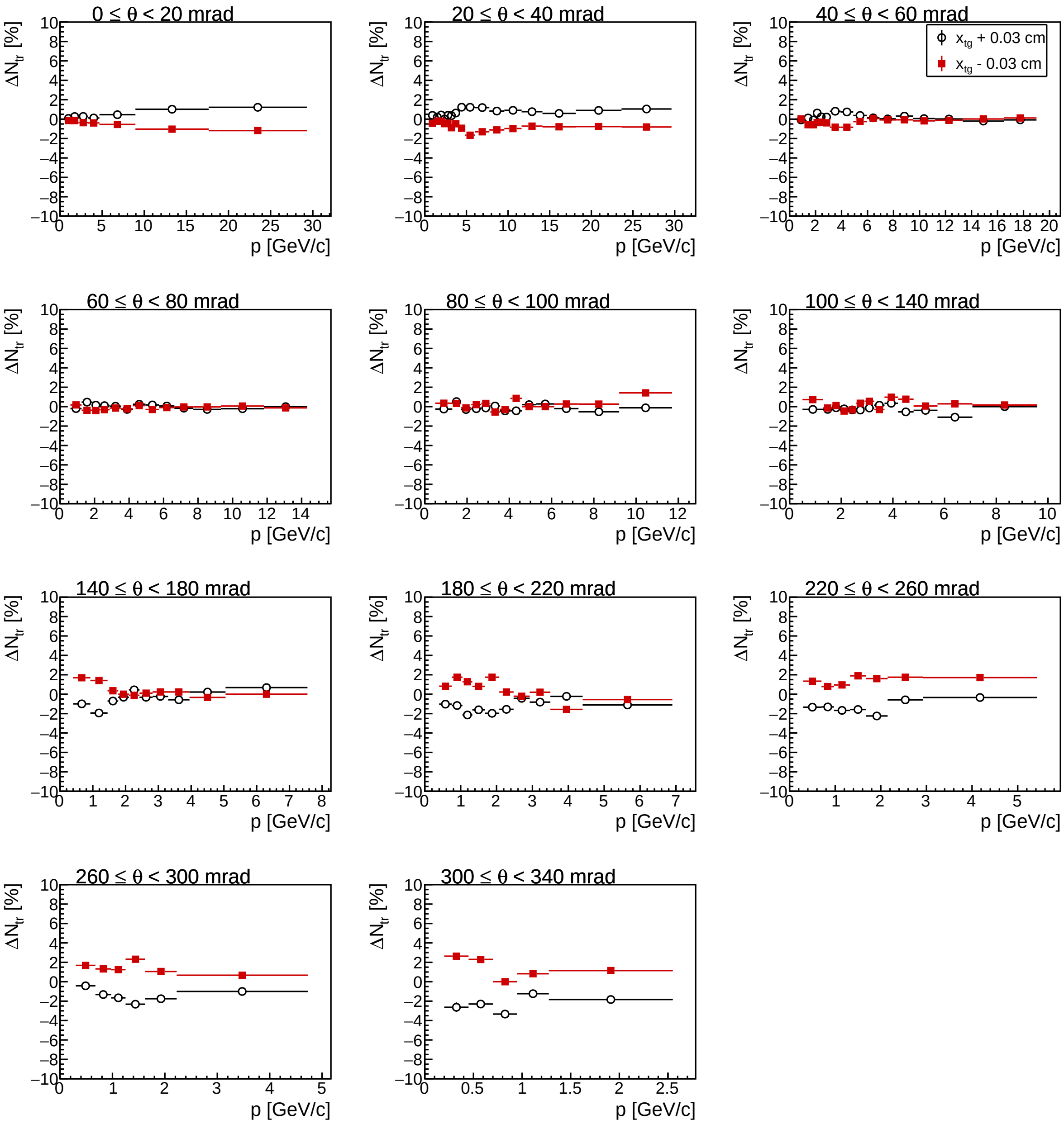

Figure D.6: Change in the number of selected positive tracks in the sixth z bin after changing target x position within measured uncertainty. Black points are for $x_{tg} + 0.03\,\text{cm}$ change and red points are for $x_{tg} - 0.03\,\text{cm}$ change). Phase space has been optimized for pions.

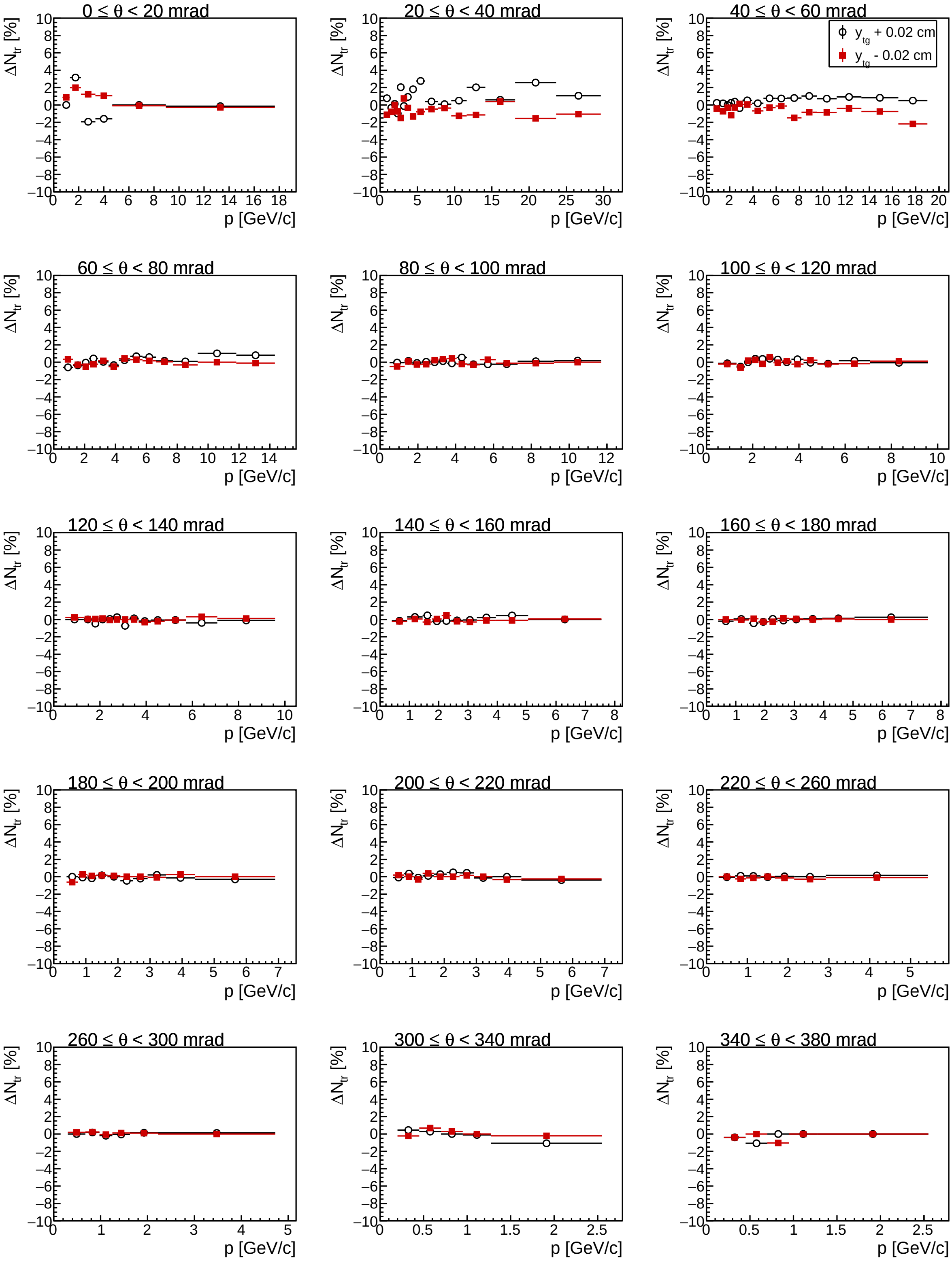

Figure D.7: Change in the number of selected positive tracks in the first z bin after changing target y position within measured uncertainty. Black points are for $y_{tg} + 0.02\,\text{cm}$ change and red points are for $y_{tg} - 0.02\,\text{cm}$ change). Phase space has been optimized for pions.

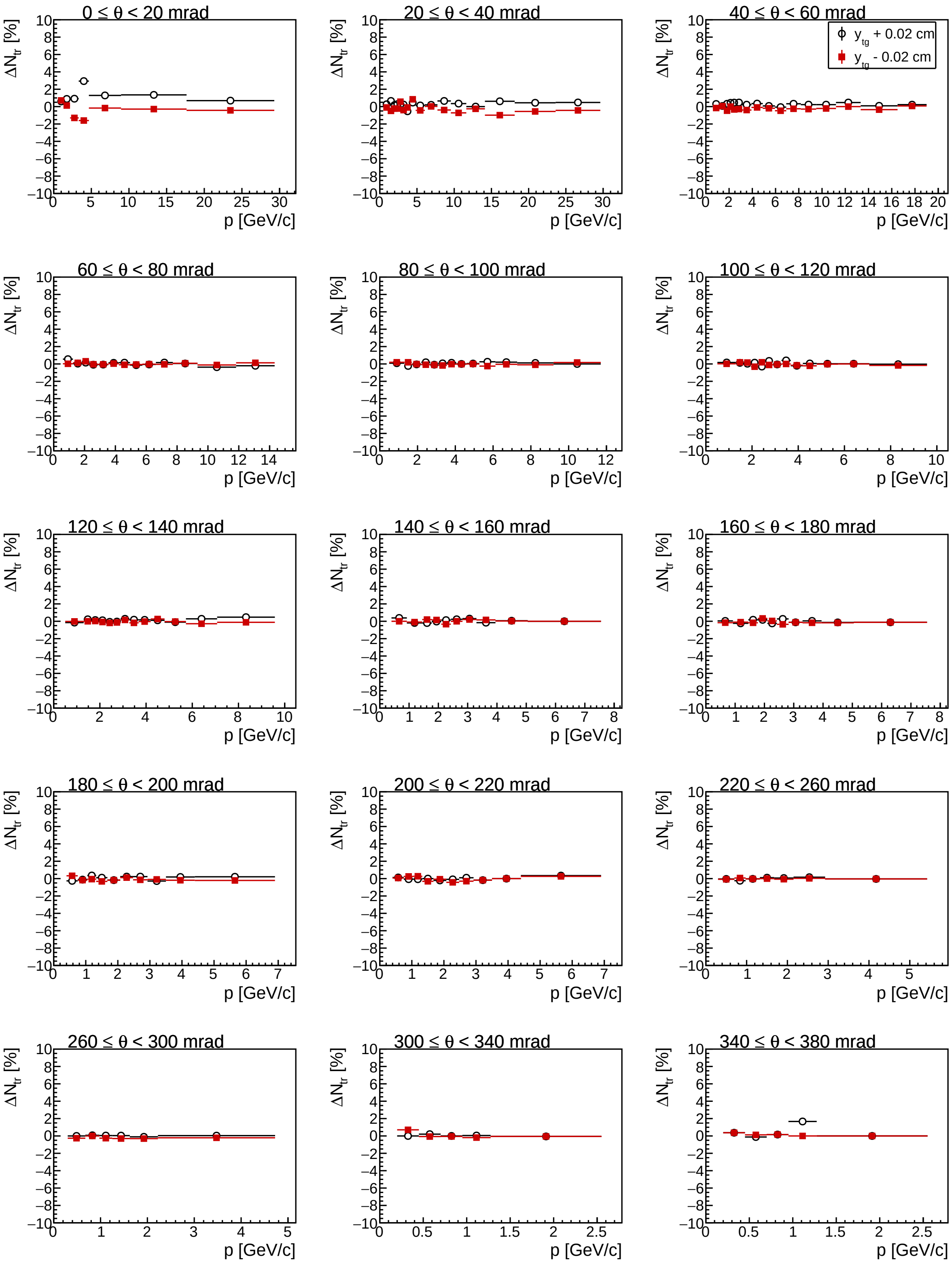

Figure D.8: Change in the number of selected positive tracks in the second z bin after changing target y position within measured uncertainty. Black points are for $y_{tg} + 0.02\,\mathrm{cm}$ change and red points are for $y_{tg} - 0.02\,\mathrm{cm}$ change). Phase space has been optimized for pions.

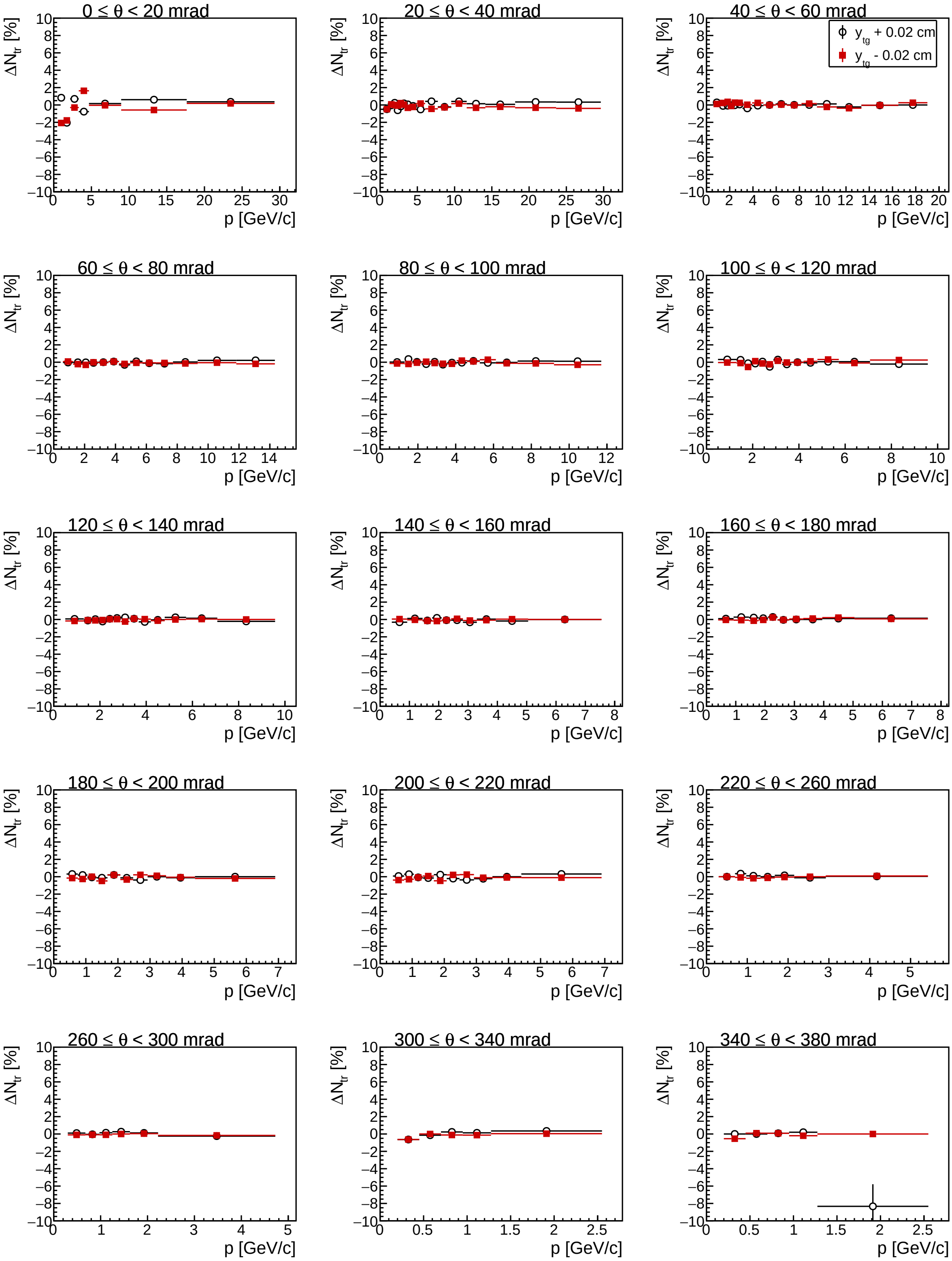

Figure D.9: Change in the number of selected positive tracks in the third z bin after changing target y position within measured uncertainty. Black points are for $y_{tg} + 0.02\,\text{cm}$ change and red points are for $y_{tg} - 0.02\,\text{cm}$ change). Phase space has been optimized for pions.

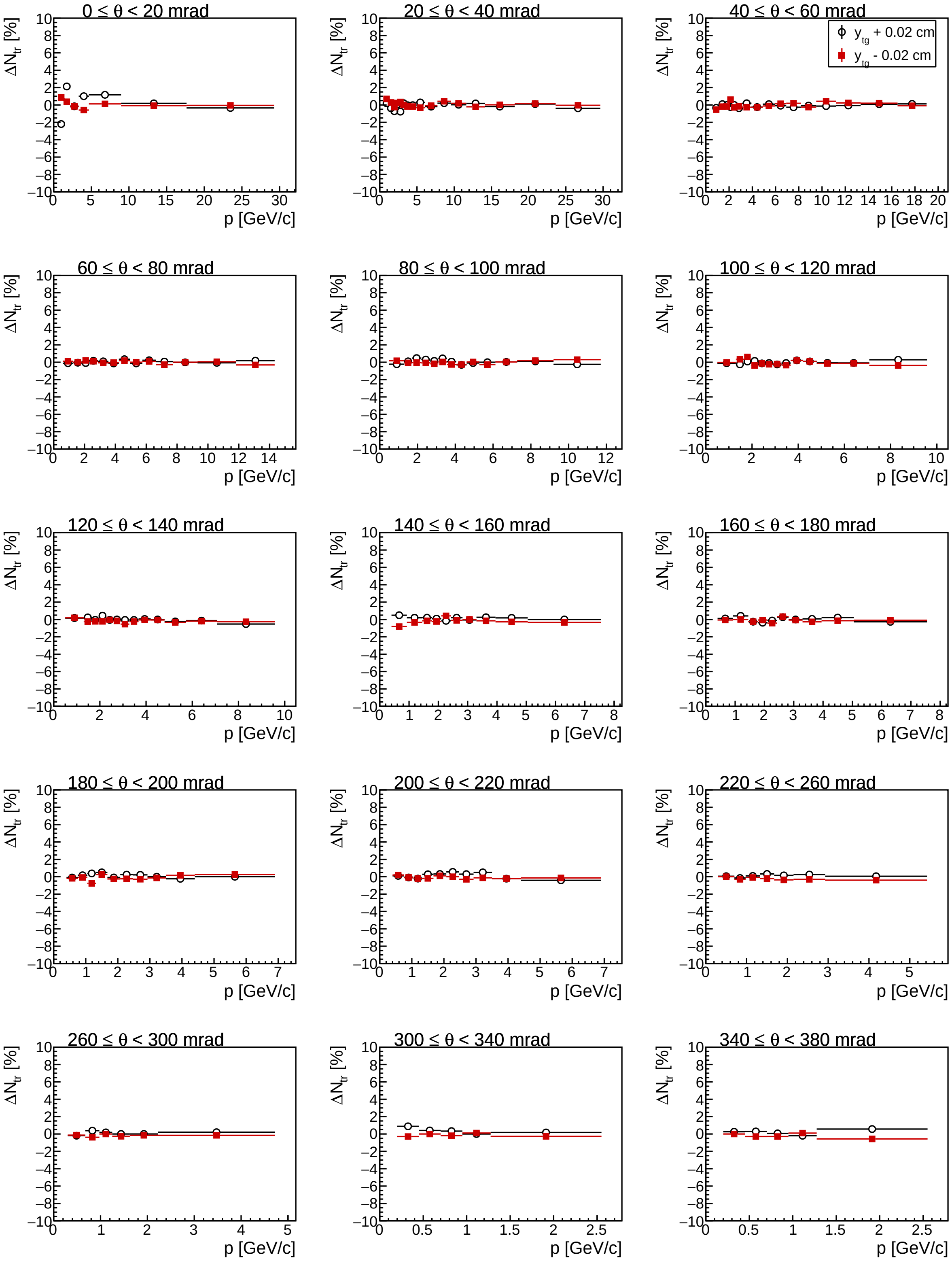

Figure D.10: Change in the number of selected positive tracks in the fourth z bin after changing target y position within measured uncertainty. Black points are for $y_{tg} + 0.02\,\mathrm{cm}$ change and red points are for $y_{tg} - 0.02\,\mathrm{cm}$ change). Phase space has been optimized for pions.

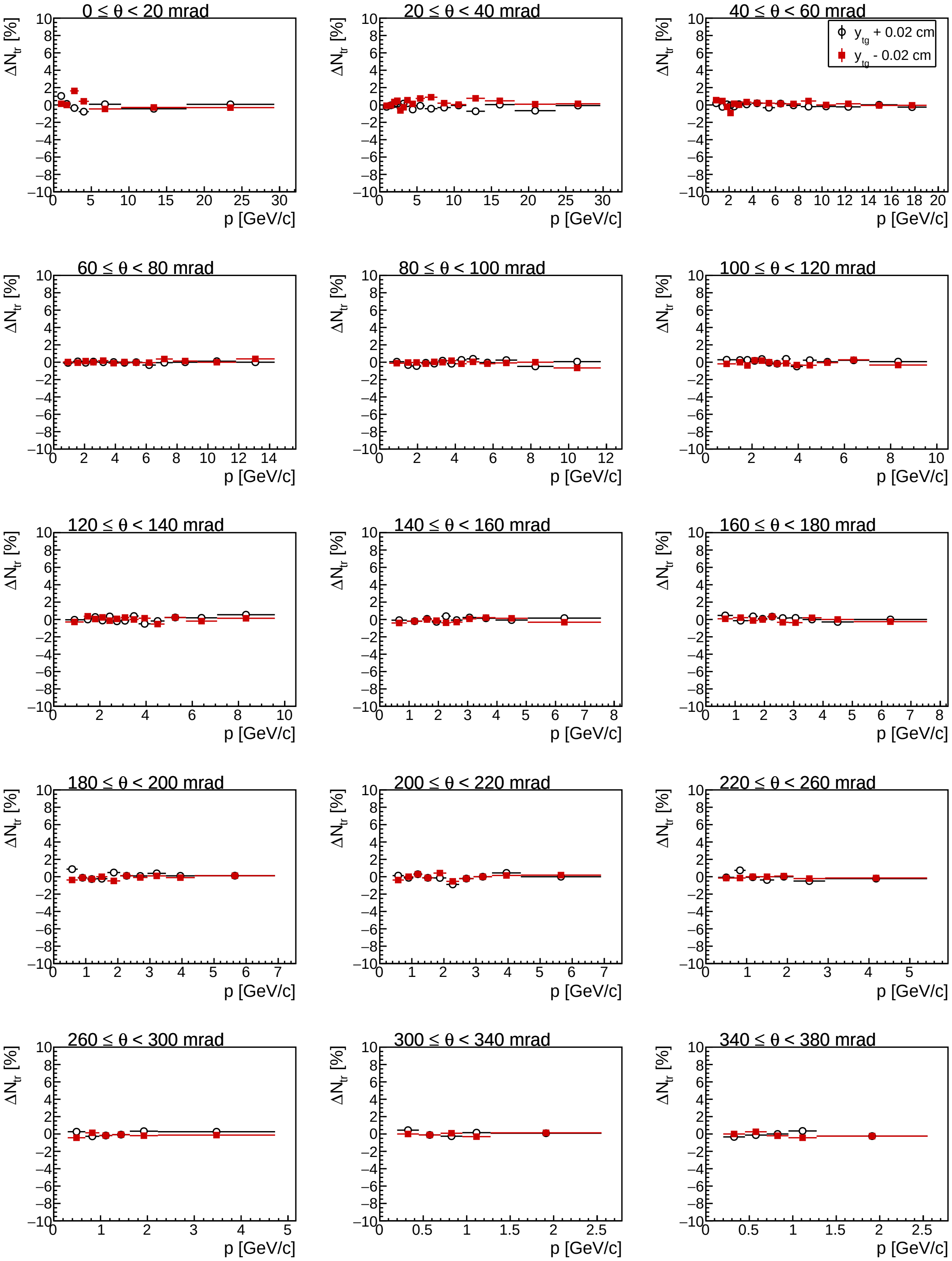

Figure D.11: Change in the number of selected positive tracks in the fifth z bin after changing target y position within measured uncertainty. Black points are for $y_{tg} + 0.02\,\mathrm{cm}$ change and red points are for $y_{tg} - 0.02\,\mathrm{cm}$ change). Phase space has been optimized for pions.

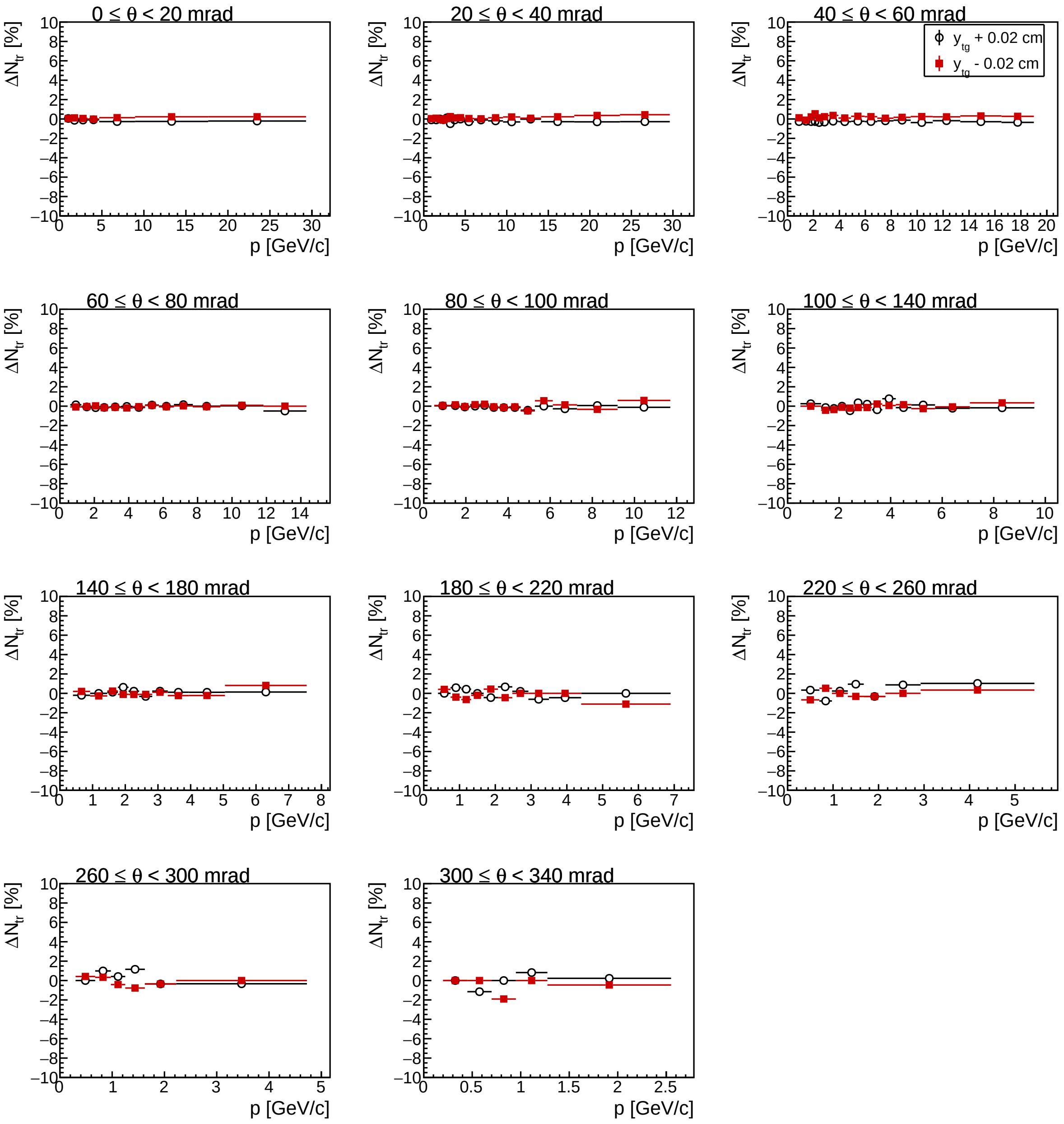

Figure D.12: Change in the number of selected positive tracks in the sixth z bin after changing target y position within measured uncertainty. Black points are for $y_{tg} + 0.02\,\text{cm}$ change and red points are for $y_{tg} - 0.02\,\text{cm}$ change). Phase space has been optimized for pions.

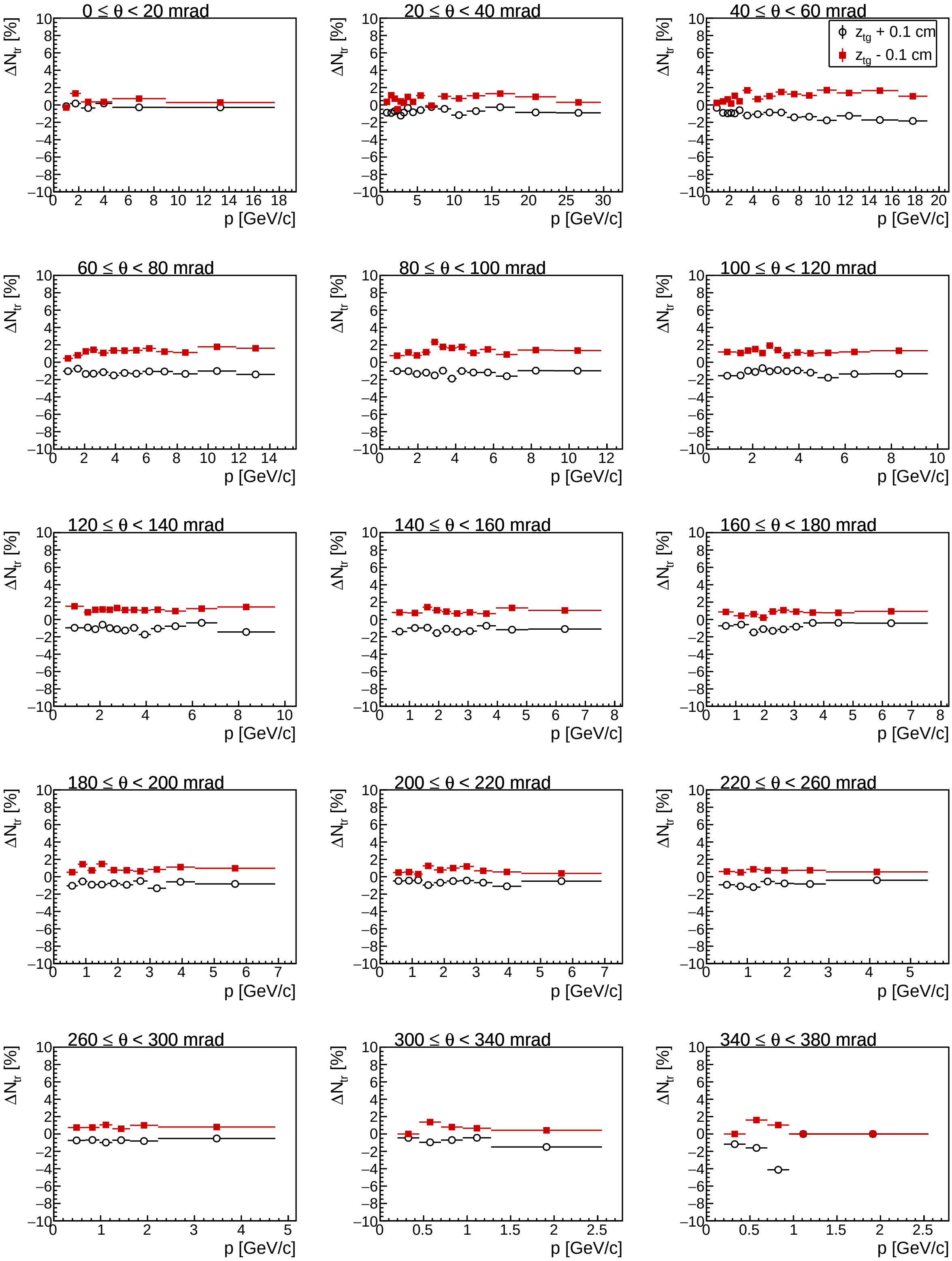

Figure D.13: Change in the number of selected positive tracks in the first z bin after changing target z position within measured uncertainty. Black points are for $z_{tg} + 0.1\,\mathrm{cm}$ change and red points are for $z_{tg} - 0.1\,\mathrm{cm}$ change). Phase space has been optimized for pions.

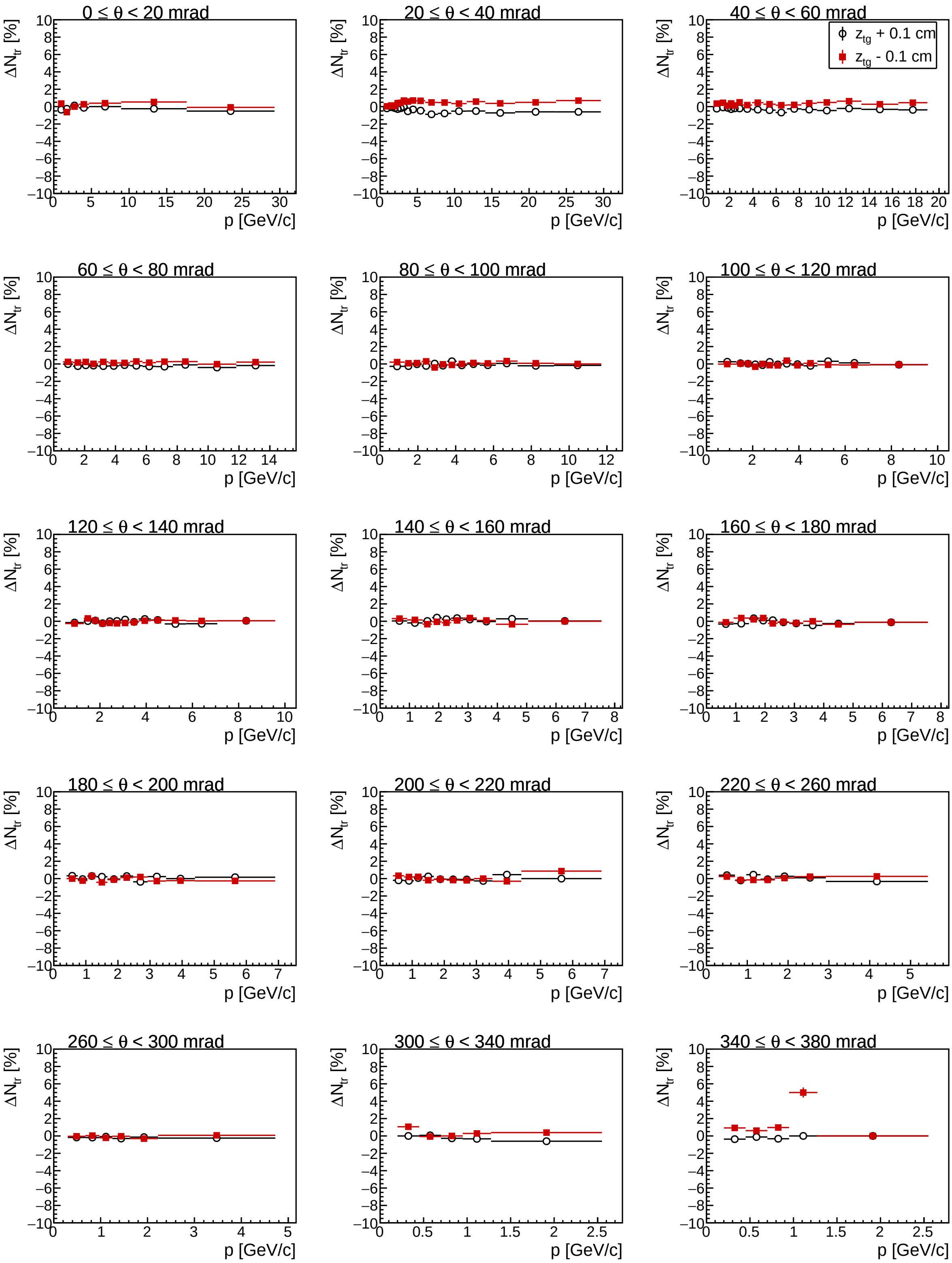

Figure D.14: Change in the number of selected positive tracks in the second z bin after changing target z position within measured uncertainty. Black points are for $z_{tg} + 0.1\,\mathrm{cm}$ change and red points are for $z_{tg} - 0.1\,\mathrm{cm}$ change). Phase space has been optimized for pions.

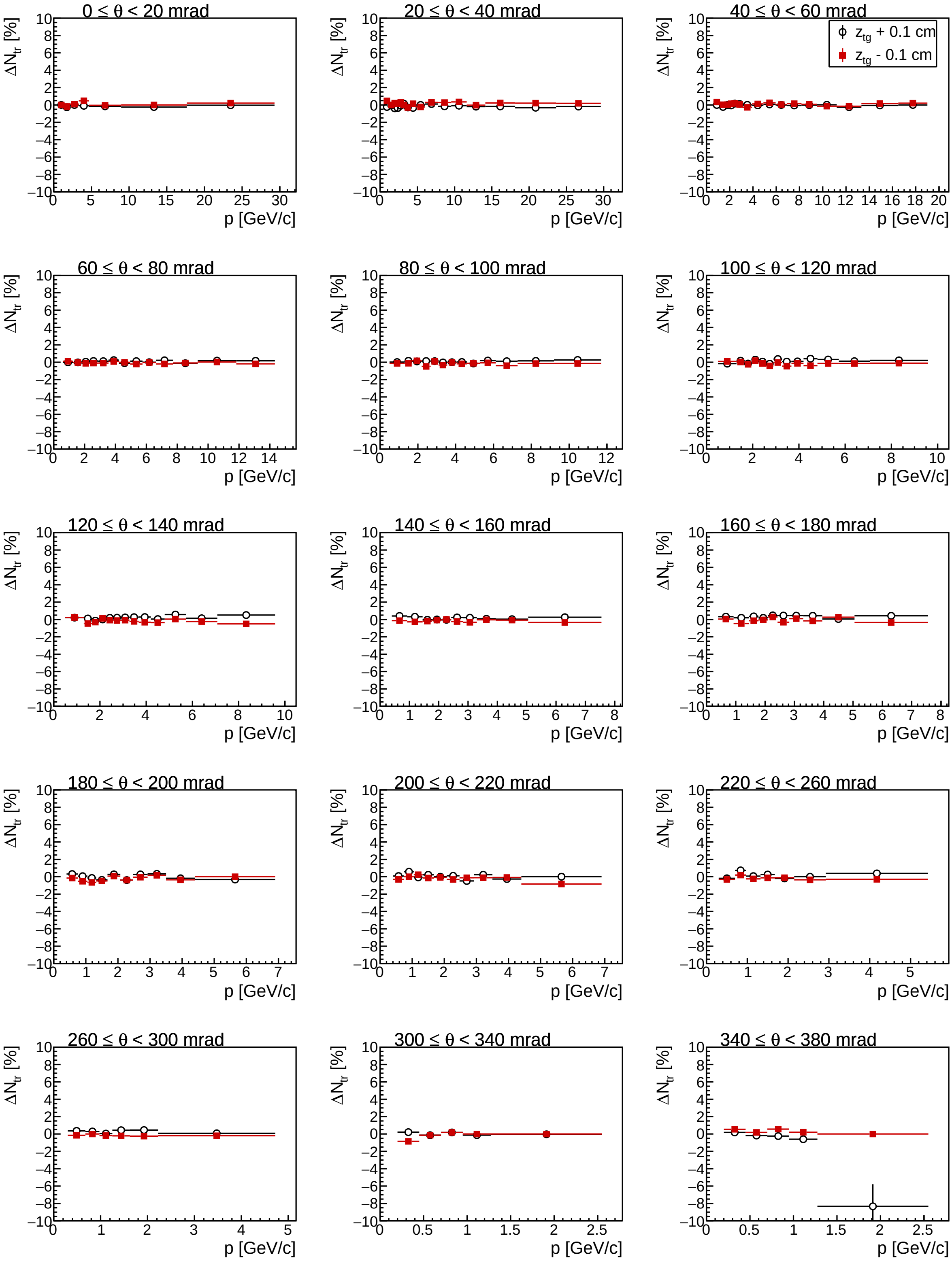

Figure D.15: Change in the number of selected positive tracks in the third z bin after changing target z position within measured uncertainty. Black points are for $z_{tg} + 0.1\,\mathrm{cm}$ change and red points are for $z_{tg} - 0.1\,\mathrm{cm}$ change). Phase space has been optimized for pions.

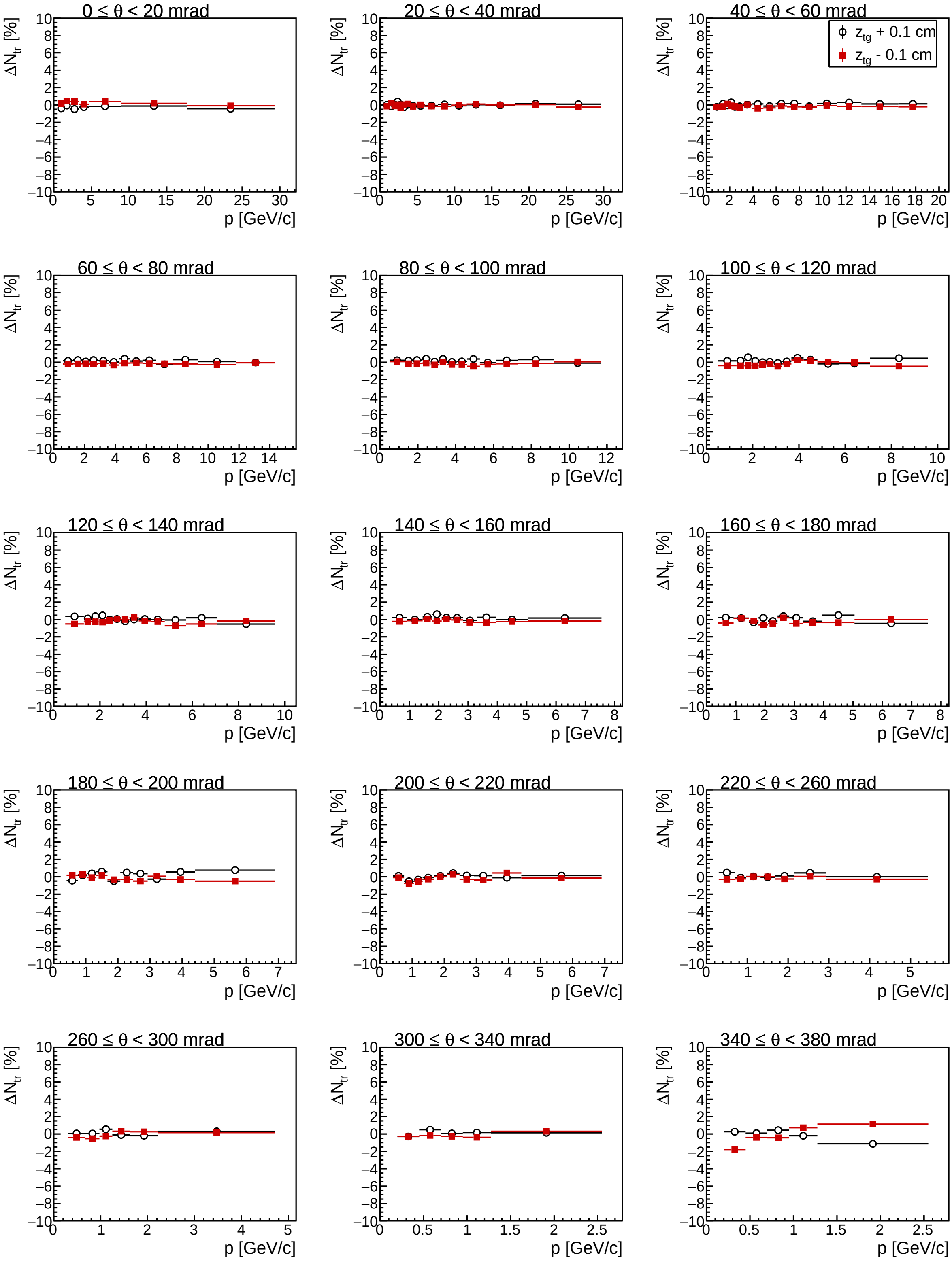

Figure D.16: Change in the number of selected positive tracks in the fourth z bin after changing target z position within measured uncertainty. Black points are for $z_{tg} + 0.1\,\text{cm}$ change and red points are for $z_{tg} - 0.1\,\text{cm}$ change). Phase space has been optimized for pions.

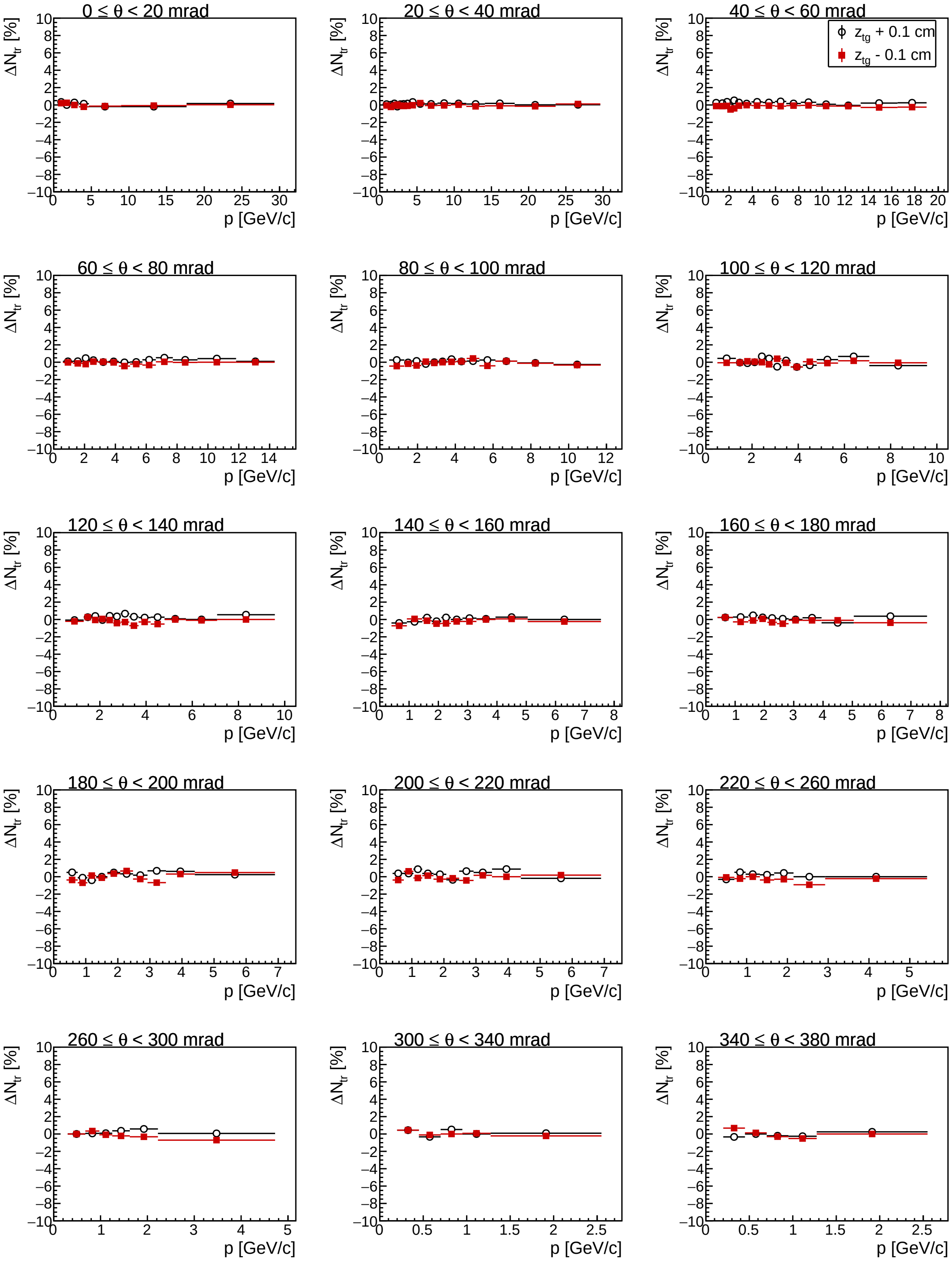

Figure D.17: Change in the number of selected positive tracks in the fifth z bin after changing target z position within measured uncertainty. Black points are for $z_{tg} + 0.1\,\mathrm{cm}$ change and red points are for $z_{tg} - 0.1\,\mathrm{cm}$ change). Phase space has been optimized for pions.

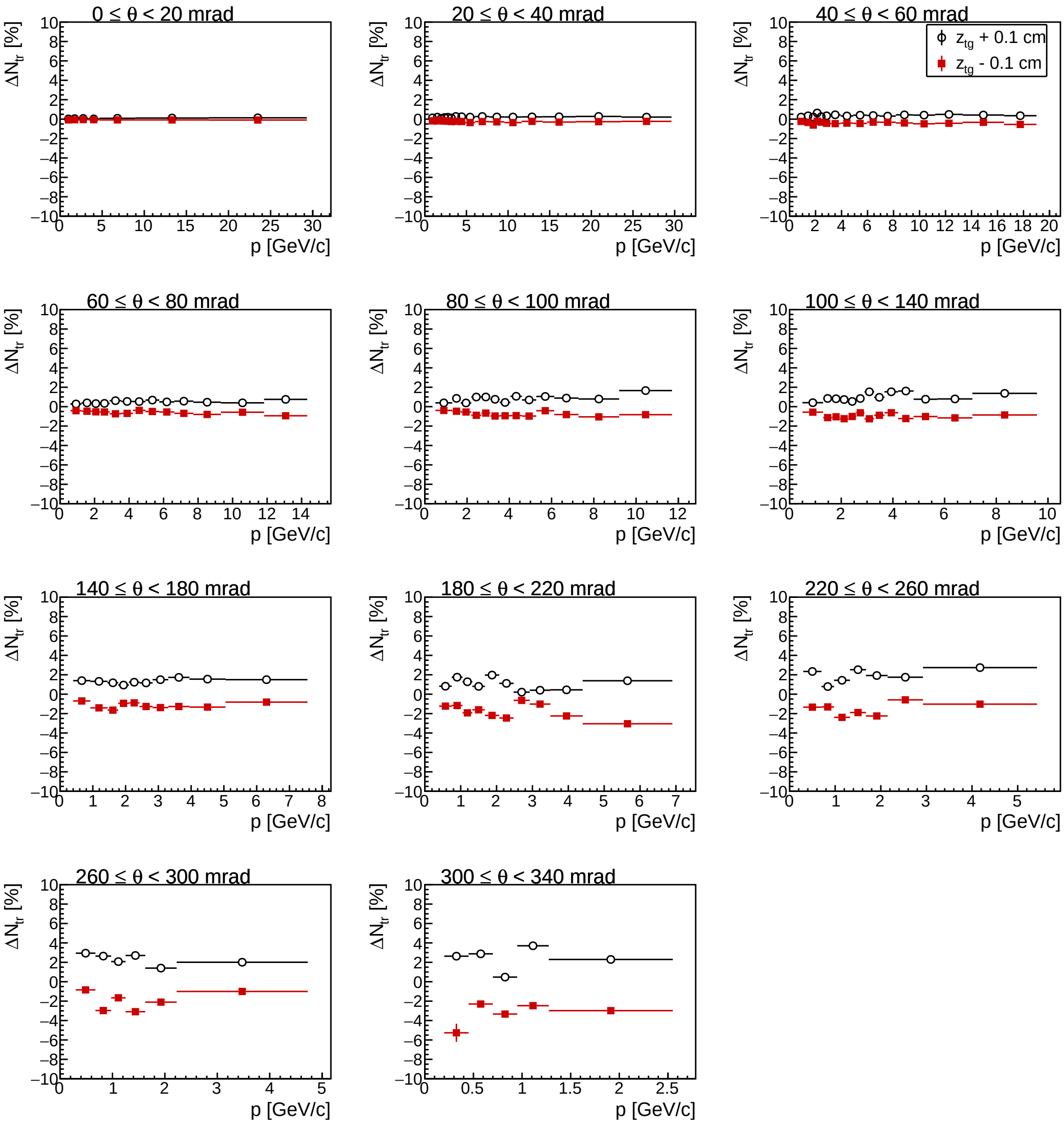

Figure D.18: Change in the number of selected positive tracks in the sixth z bin after changing target z position within measured uncertainty. Black points are for $z_{tg} + 0.1\,\text{cm}$ change and red points are for $z_{tg} - 0.1\,\text{cm}$ change). Phase space has been optimized for pions.

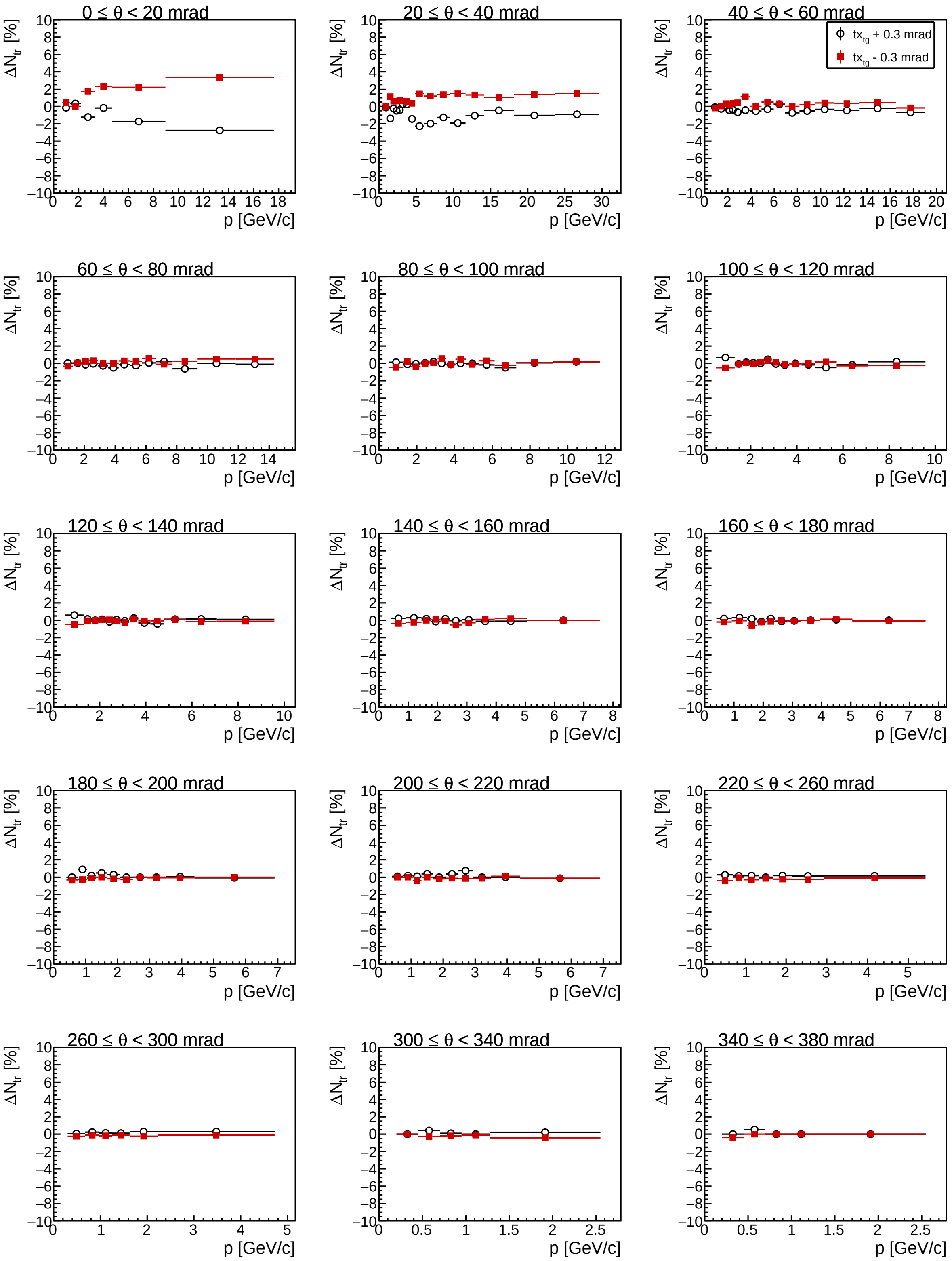

Figure D.19: Change in the number of selected positive tracks in the first z bin after changing target x tilt within measured uncertainty. Black points are for $tx_{tg} + 0.3\,\text{mrad}$ change and red points are for $tx_{tg} - 0.3\,\text{mrad}$ change). Phase space has been optimized for pions.

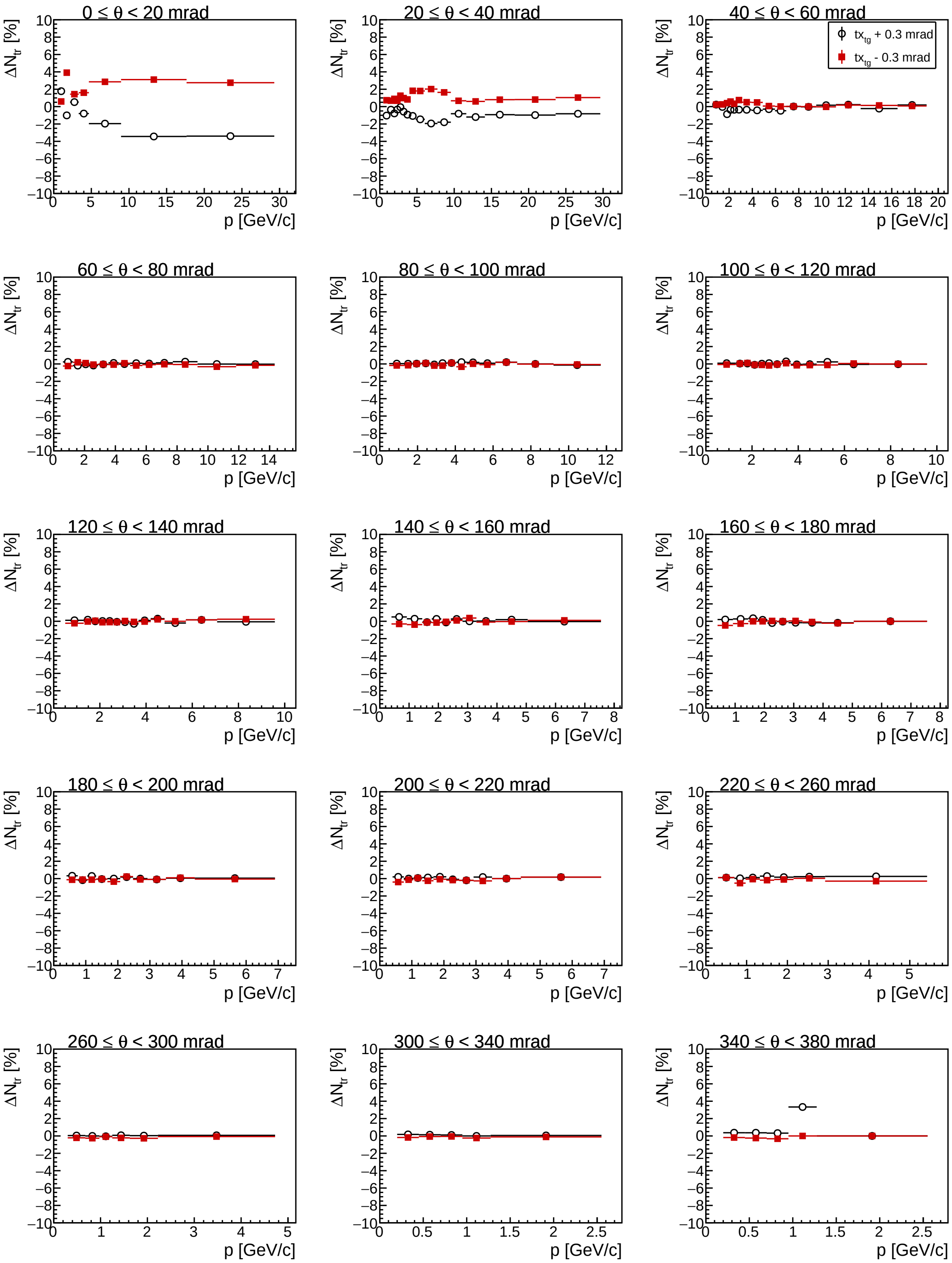

Figure D.20: Change in the number of selected positive tracks in the second z bin after changing target x tilt within measured uncertainty. Black points are for $tx_{tg} + 0.3\,\mathrm{mrad}$ change and red points are for $tx_{tg} - 0.3\,\mathrm{mrad}$ change). Phase space has been optimized for pions.

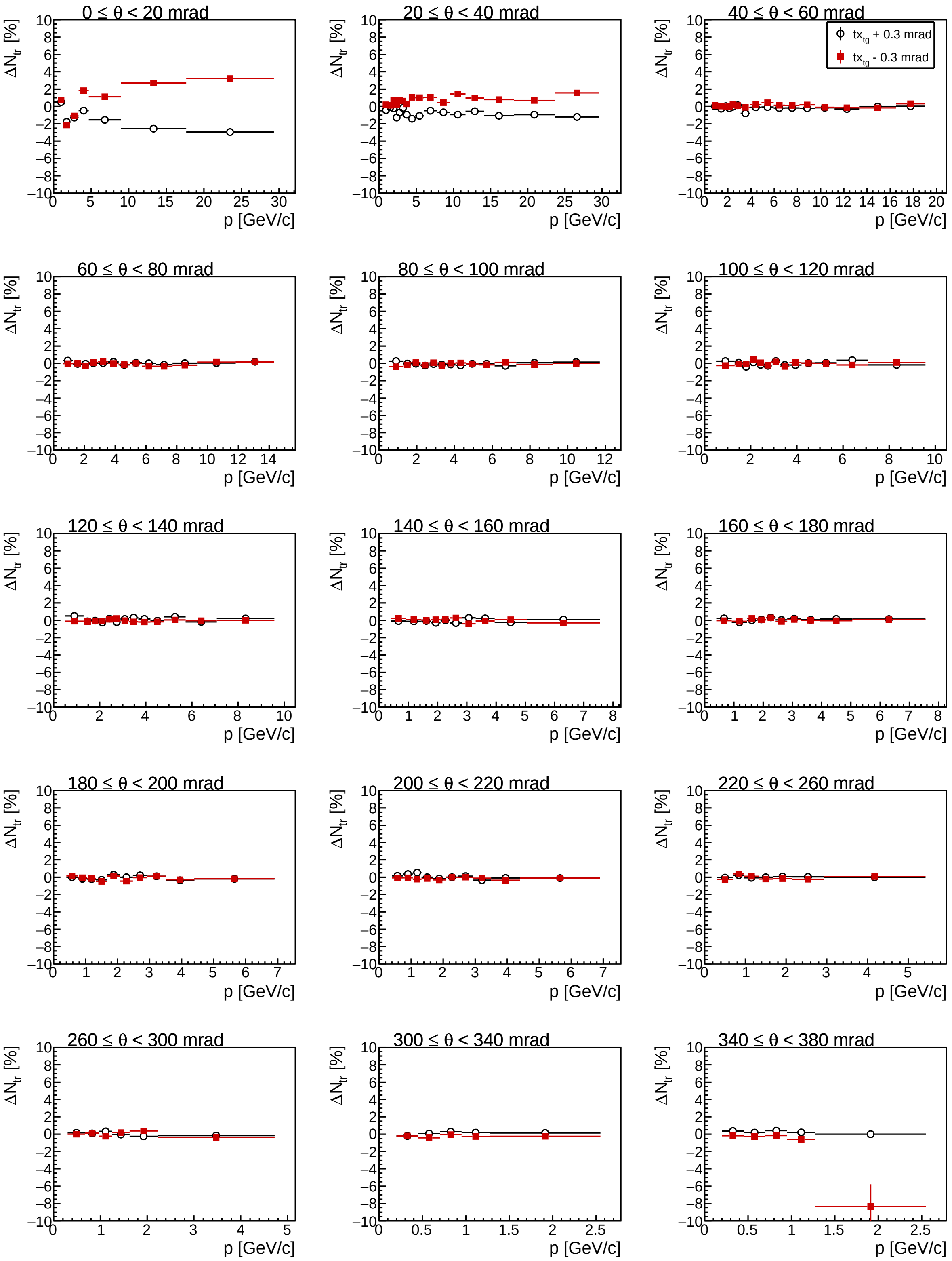

Figure D.21: Change in the number of selected positive tracks in the third z bin after changing target x tilt within measured uncertainty. Black points are for $tx_{tg} + 0.3\,\mathrm{mrad}$ change and red points are for $tx_{tg} - 0.3\,\mathrm{mrad}$ change). Phase space has been optimized for pions.

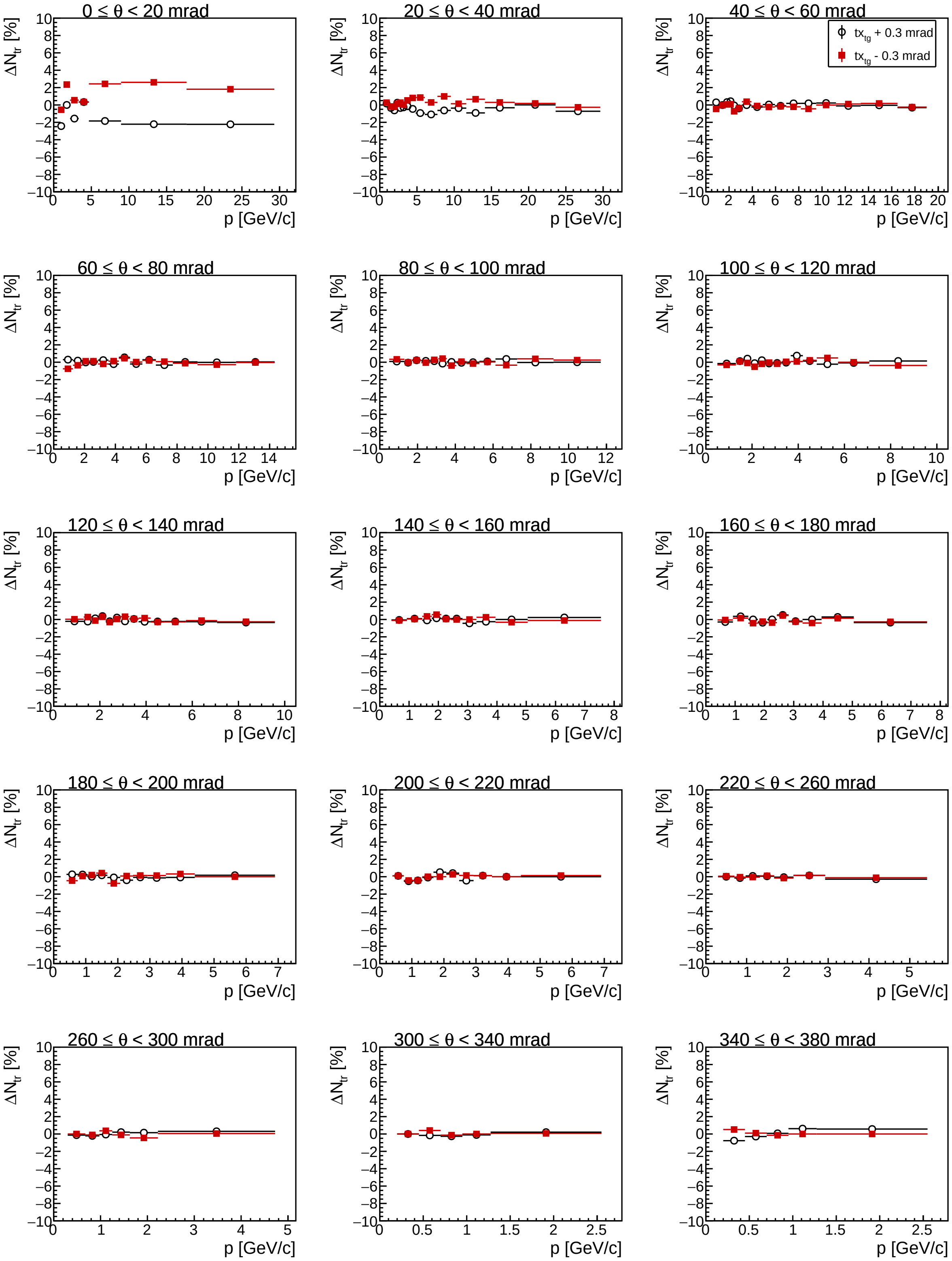

Figure D.22: Change in the number of selected positive tracks in the fourth z bin after changing target x tilt within measured uncertainty. Black points are for $tx_{tg} + 0.3\,\text{mrad}$ change and red points are for $tx_{tg} - 0.3\,\text{mrad}$ change). Phase space has been optimized for pions.

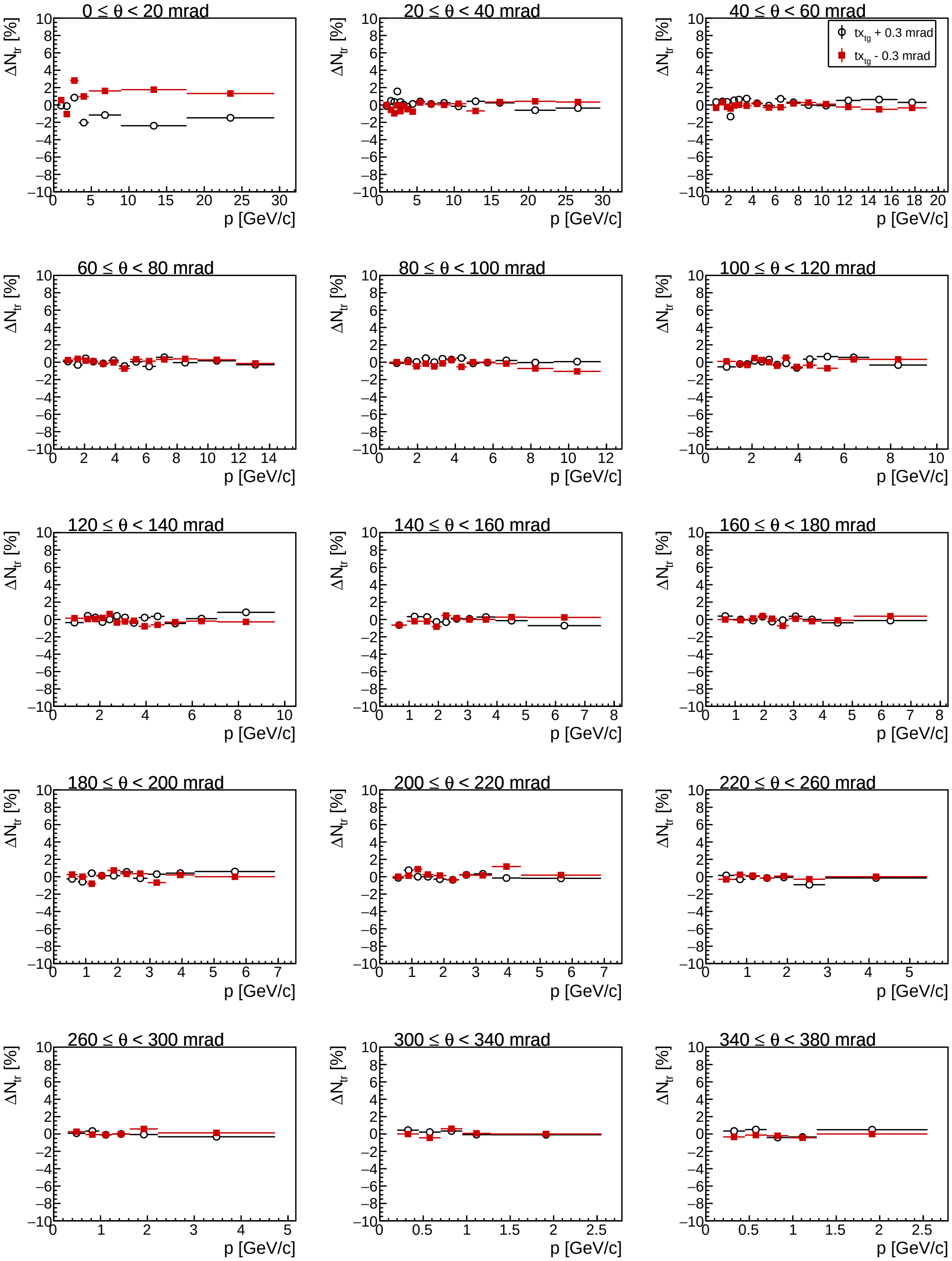

Figure D.23: Change in the number of selected positive tracks in the fifth z bin after changing target x tilt within measured uncertainty. Black points are for $tx_{tg} + 0.3\,\text{mrad}$ change and red points are for $tx_{tg} - 0.3\,\text{mrad}$ change). Phase space has been optimized for pions.

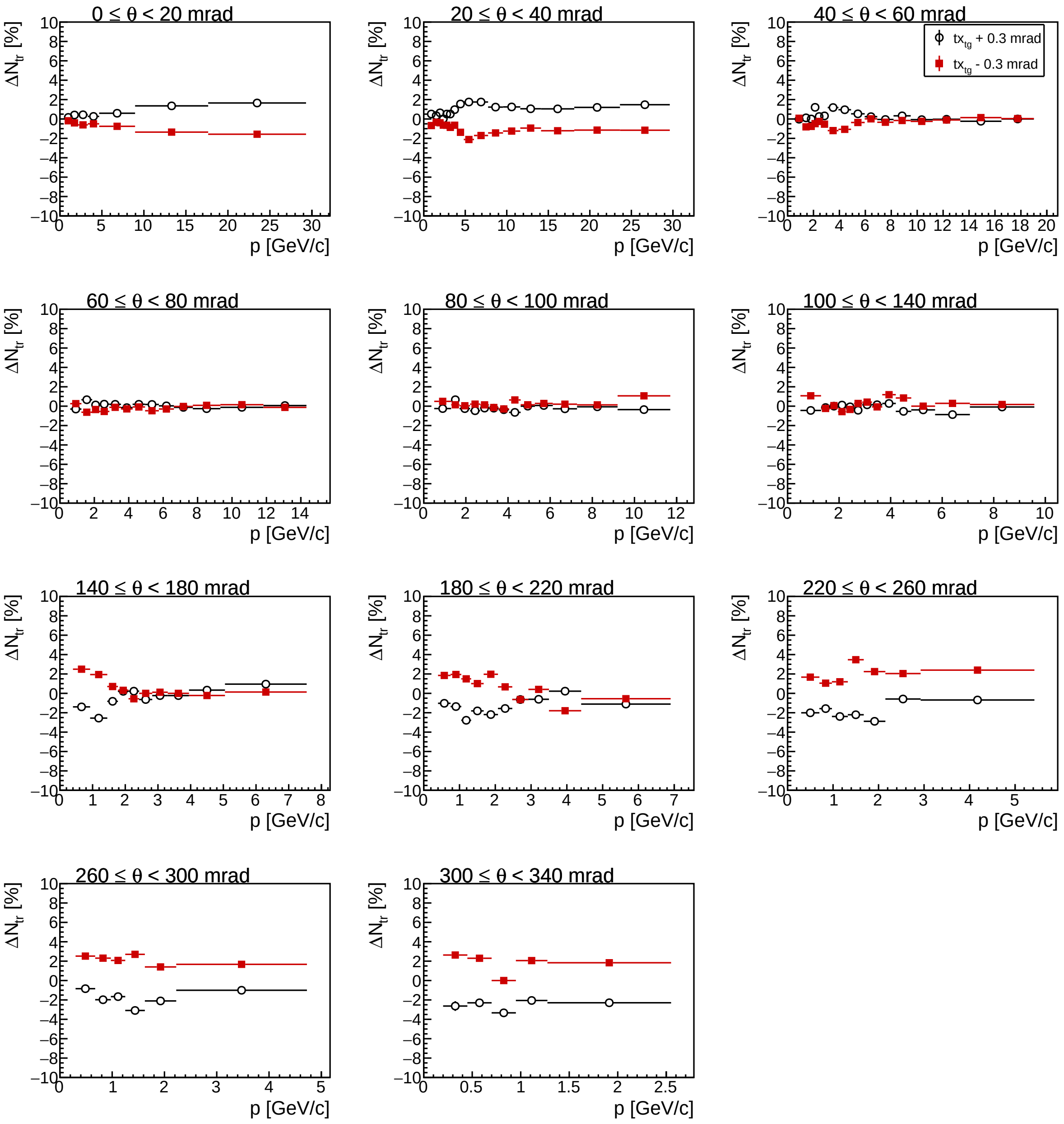
0 ≤ θ < 20 mrad; 20 ≤ θ < 40 mrad; 40 ≤ θ < 60 mrad; 60 ≤ θ < 80 mrad; 80 ≤ θ < 100 mrad; 100 ≤ θ < 140 mrad; 140 ≤ θ < 180 mrad; 180 ≤ θ < 220 mrad; 220 ≤ θ < 260 mrad; 260 ≤ θ < 300 mrad; 300 ≤ θ < 340 mrad

Figure D.24: Change in the number of selected positive tracks in the sixth z bin after changing target x tilt within measured uncertainty. Black points are for $tx_{tg} + 0.3\,\mathrm{mrad}$ change and red points are for $tx_{tg} - 0.3\,\mathrm{mrad}$ change). Phase space has been optimized for pions.

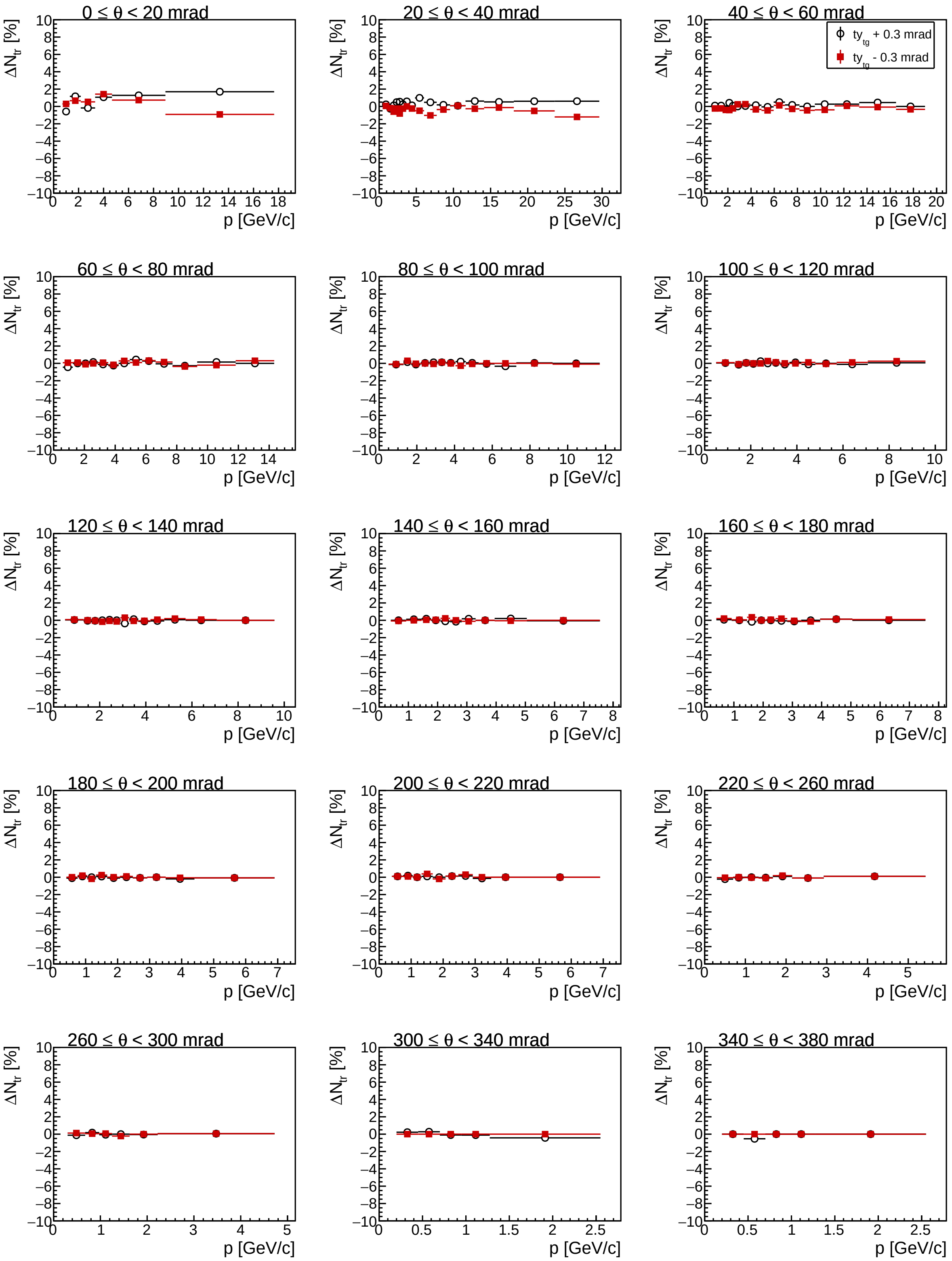

Figure D.25: Change in the number of selected positive tracks in the first z bin after changing target y tilt within measured uncertainty. Black points are for $ty_{tg} + 0.3\,\text{mrad}$ change and red points are for $ty_{tg} - 0.3\,\text{mrad}$ change). Phase space has been optimized for pions.

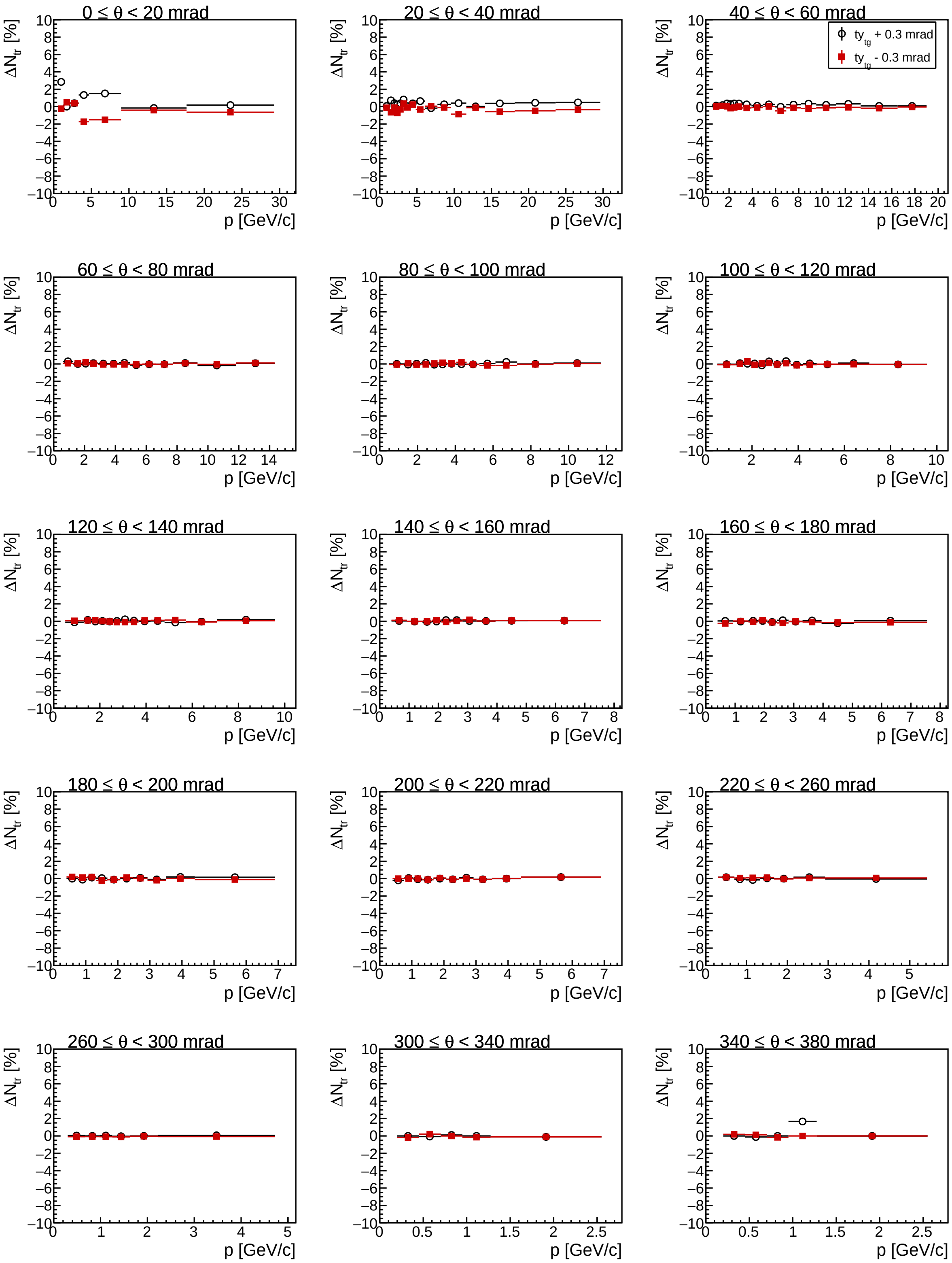

Figure D.26: Change in the number of selected positive tracks in the second z bin after changing target y tilt within measured uncertainty. Black points are for $ty_{tg} + 0.3\,\text{mrad}$ change and red points are for $ty_{tg} - 0.3\,\text{mrad}$ change). Phase space has been optimized for pions.

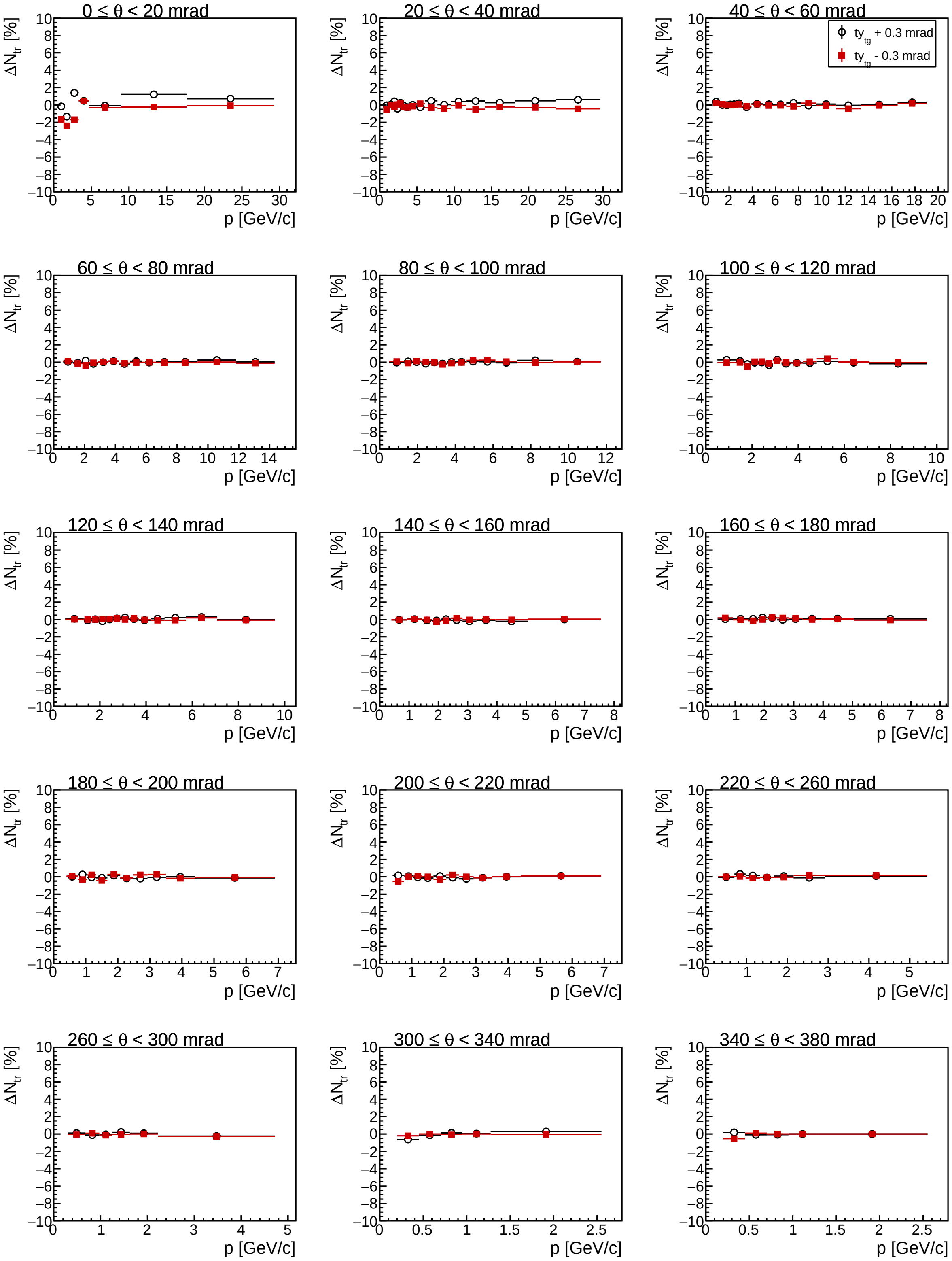

Figure D.27: Change in the number of selected positive tracks in the third z bin after changing target y tilt within measured uncertainty. Black points are for $ty_{tg} + 0.3\,\mathrm{mrad}$ change and red points are for $ty_{tg} - 0.3\,\mathrm{mrad}$ change). Phase space has been optimized for pions.

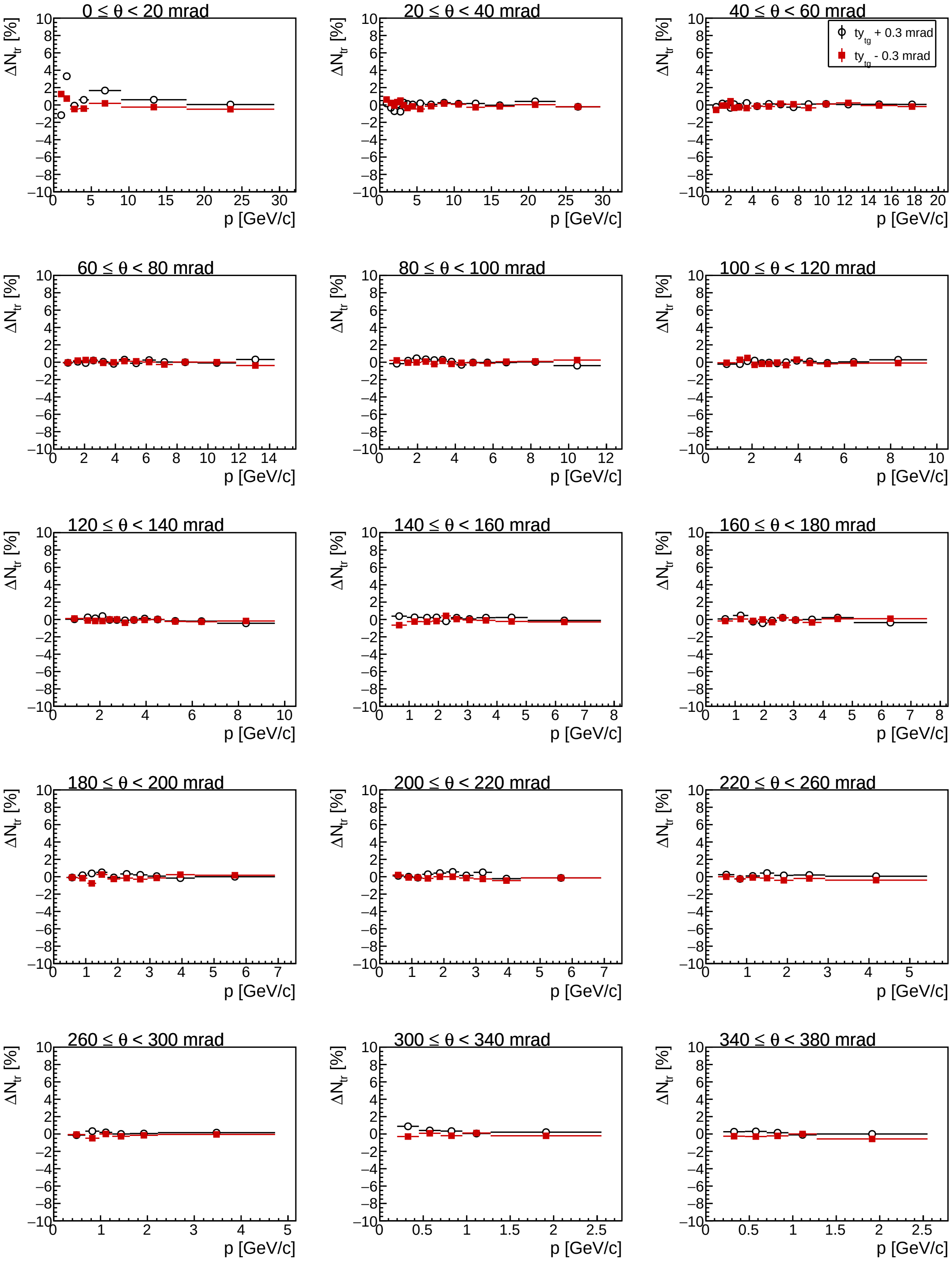

Figure D.28: Change in the number of selected positive tracks in the fourth z bin after changing target y tilt within measured uncertainty. Black points are for $ty_{tg} + 0.3\,\text{mrad}$ change and red points are for $ty_{tg} - 0.3\,\text{mrad}$ change). Phase space has been optimized for pions.

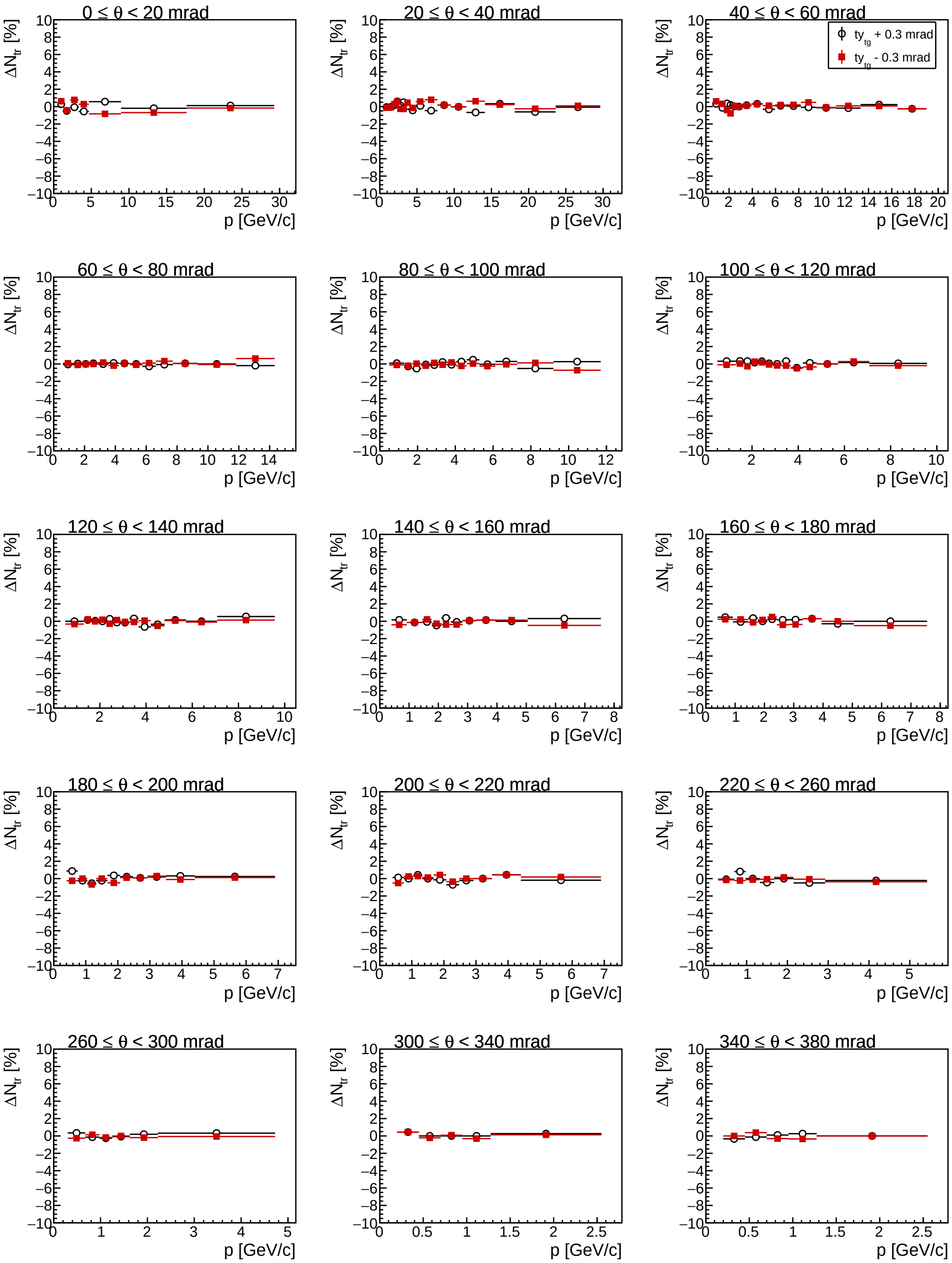

Figure D.29: Change in the number of selected positive tracks in the fifth z bin after changing target y tilt within measured uncertainty. Black points are for $ty_{tg} + 0.3\,\mathrm{mrad}$ change and red points are for $ty_{tg} - 0.3\,\mathrm{mrad}$ change). Phase space has been optimized for pions.

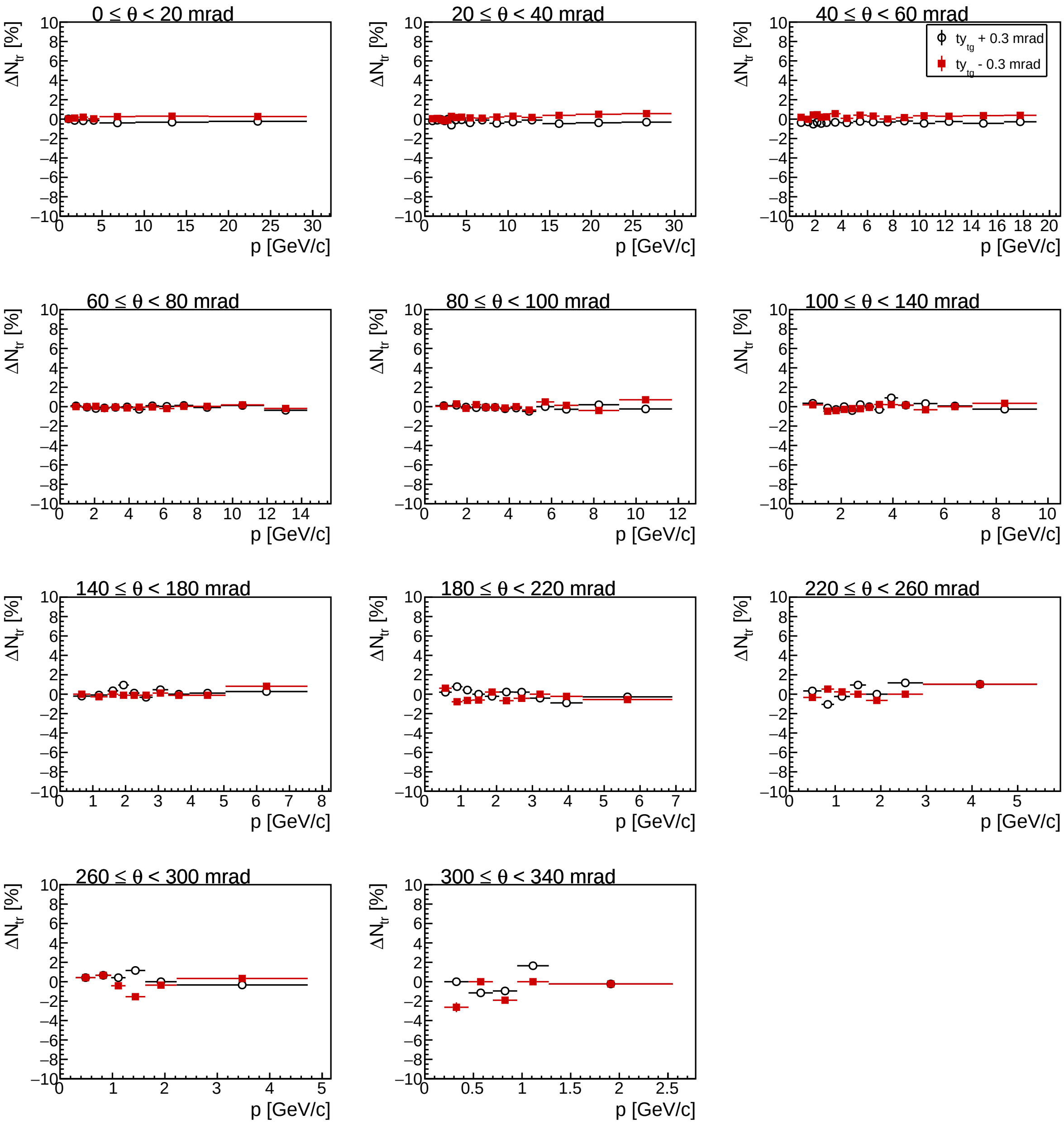

Figure D.30: Change in the number of selected positive tracks in the sixth z bin after changing target y tilt within measured uncertainty. Black points are for $ty_{tg} + 0.3$ mrad change and red points are for $ty_{tg} - 0.3$ mrad change). Phase space has been optimized for pions.

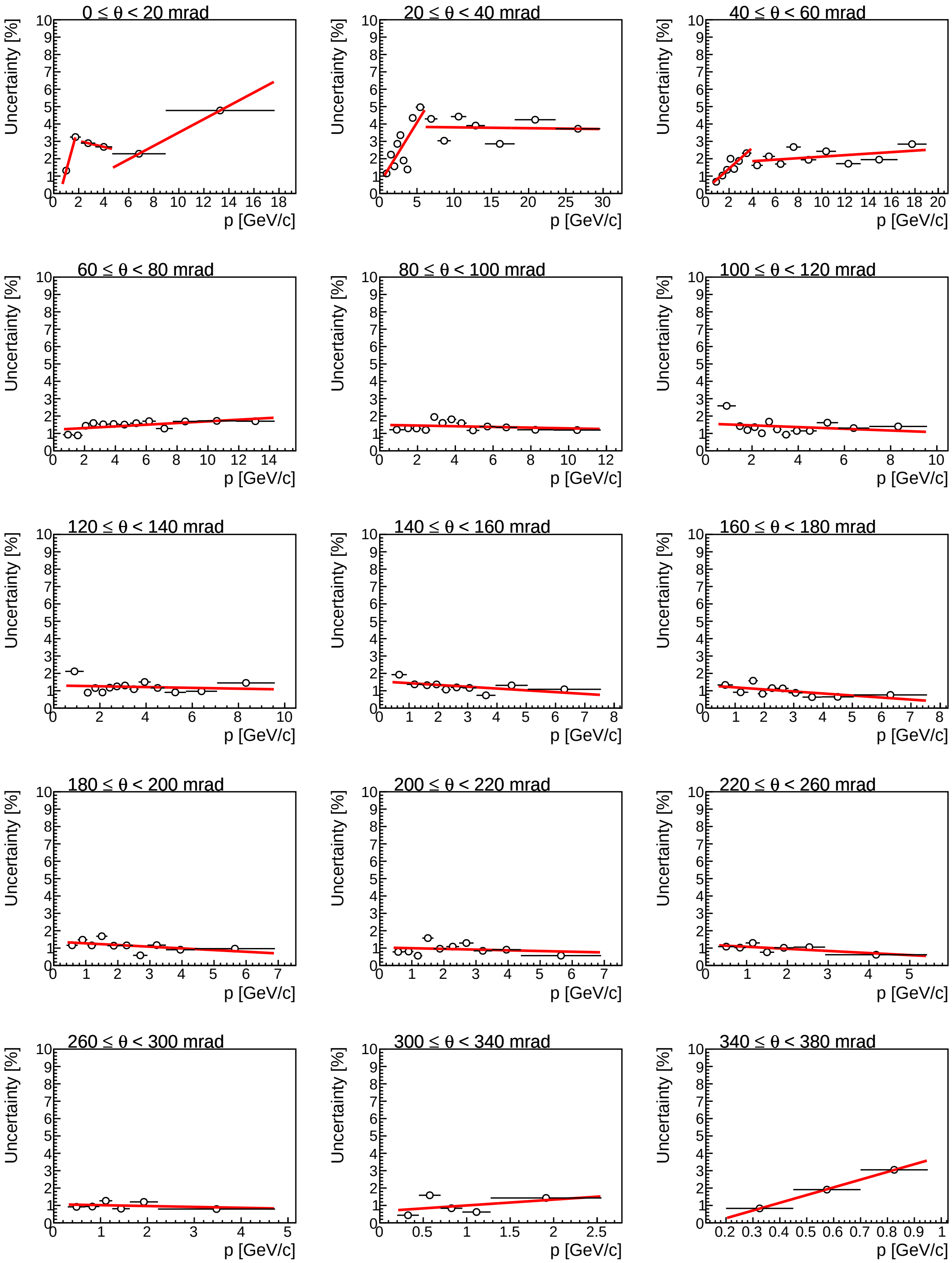

Figure D.31: Systematic uncertainties of the π^+ yields for the first z bin, coming from the uncertainty of the target position. Line segments are fitted to the distributions. Each panel represents different polar angle bin.

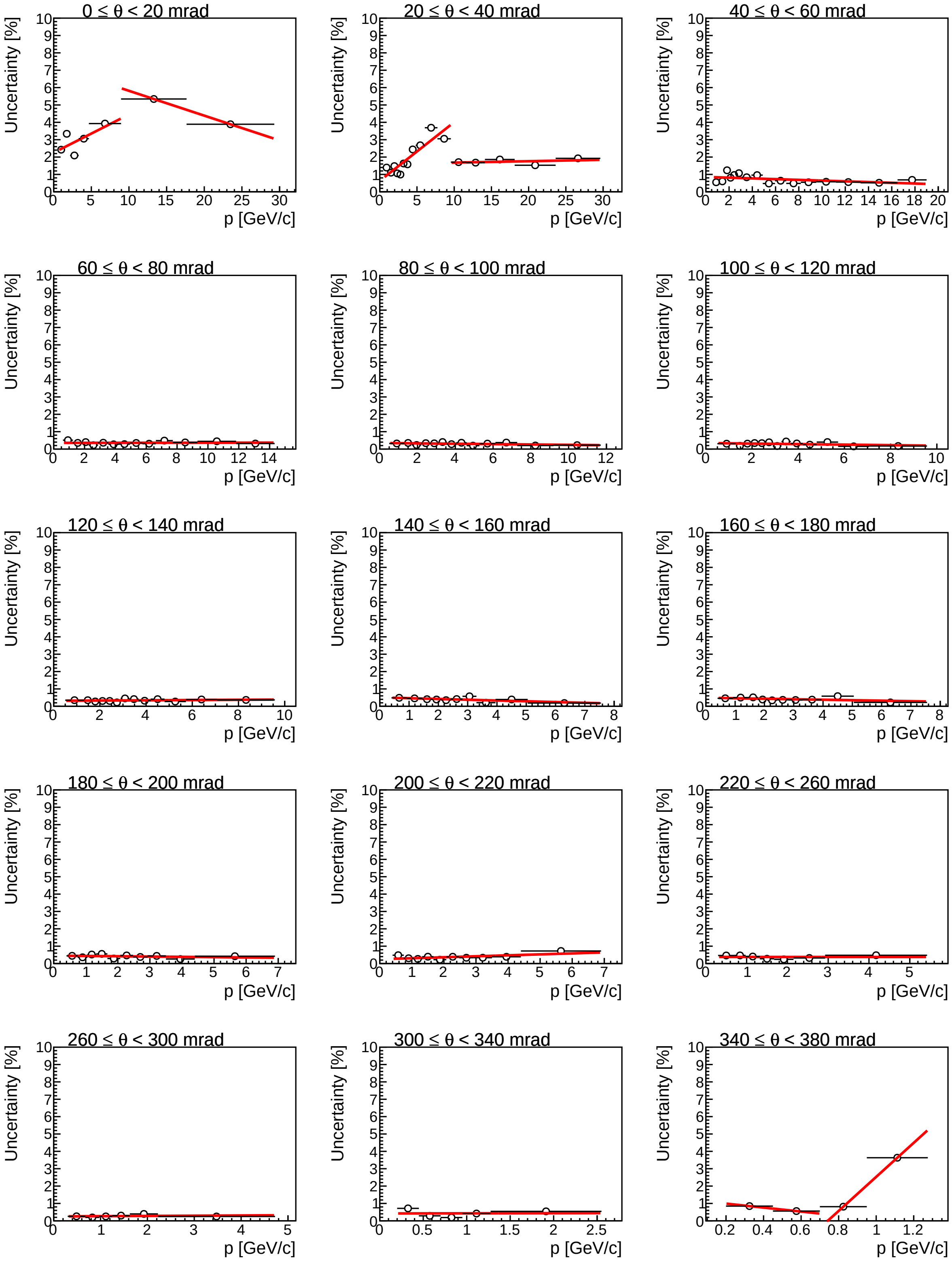

$0 \leq \theta < 20$ mrad

$20 \leq \theta < 40$ mrad

$40 \leq \theta < 60$ mrad

$60 \leq \theta < 80$ mrad

$80 \leq \theta < 100$ mrad

$100 \leq \theta < 120$ mrad

$120 \leq \theta < 140$ mrad

$140 \leq \theta < 160$ mrad

$160 \leq \theta < 180$ mrad

$180 \leq \theta < 200$ mrad

$200 \leq \theta < 220$ mrad

$220 \leq \theta < 260$ mrad

$260 \leq \theta < 300$ mrad

$300 \leq \theta < 340$ mrad

$340 \leq \theta < 380$ mrad

Figure D.32: Systematic uncertainties of the π^+ yields for the second z bin, coming from the uncertainty of the target position. Line segments are fitted to the distributions. Each panel represents different polar angle bin.

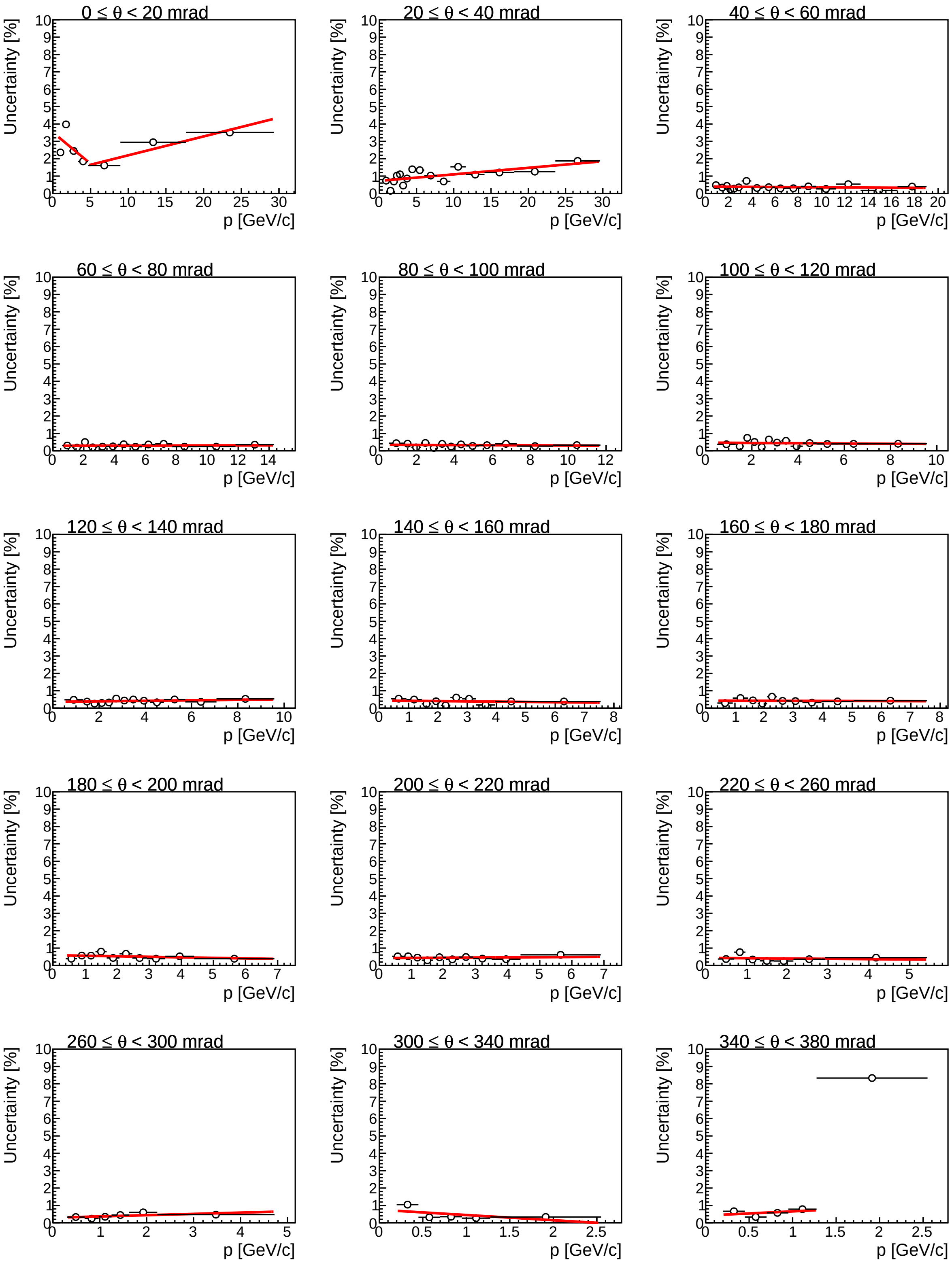

Figure D.33: Systematic uncertainties of the π^+ yields for the third z bin, coming from the uncertainty of the target position. Line segments are fitted to the distributions. Each panel represents different polar angle bin.

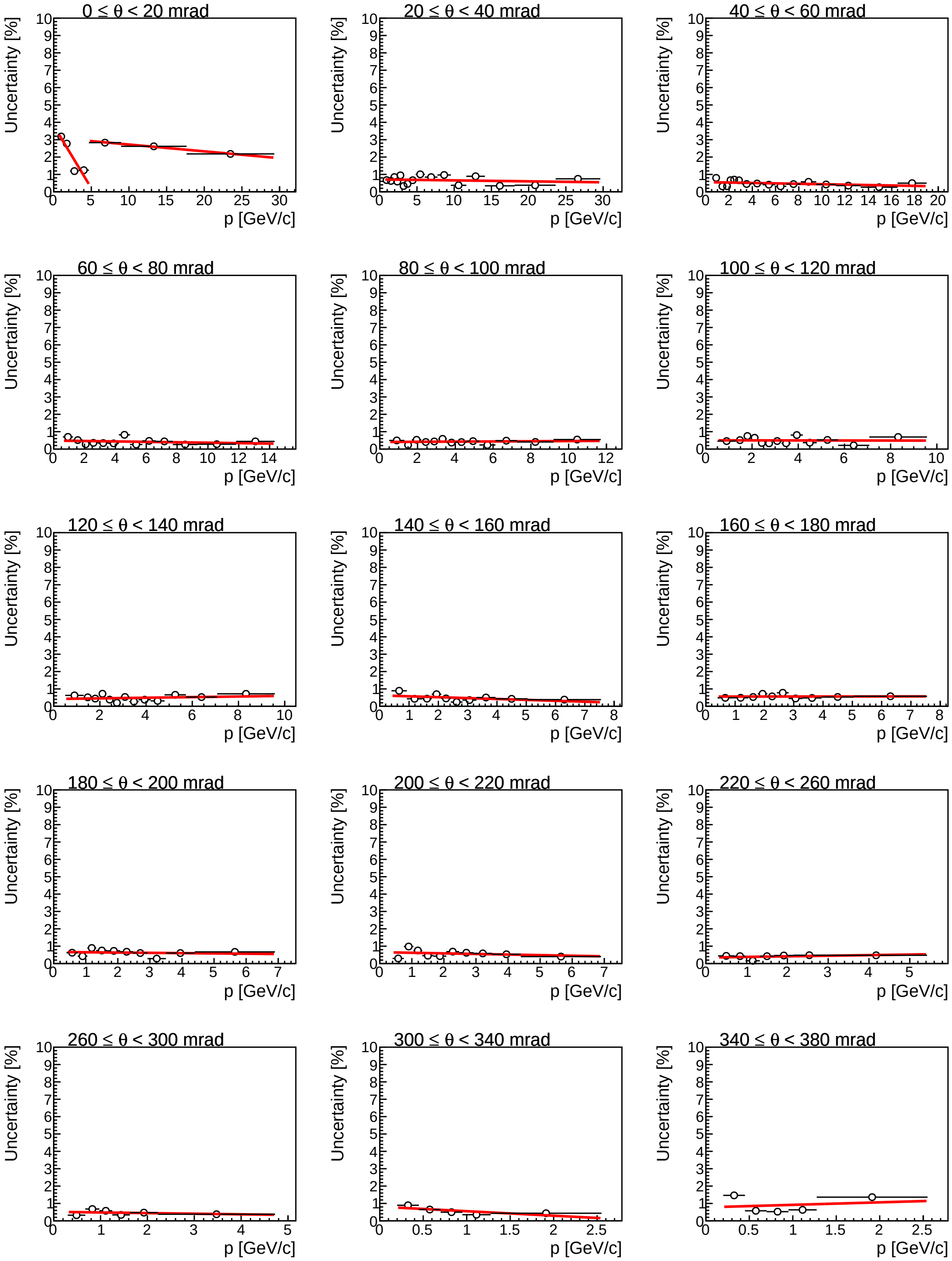

Figure D.34: Systematic uncertainties of the π^+ yields for the fourth z bin, coming from the uncertainty of the target position. Line segments are fitted to the distributions. Each panel represents different polar angle bin.

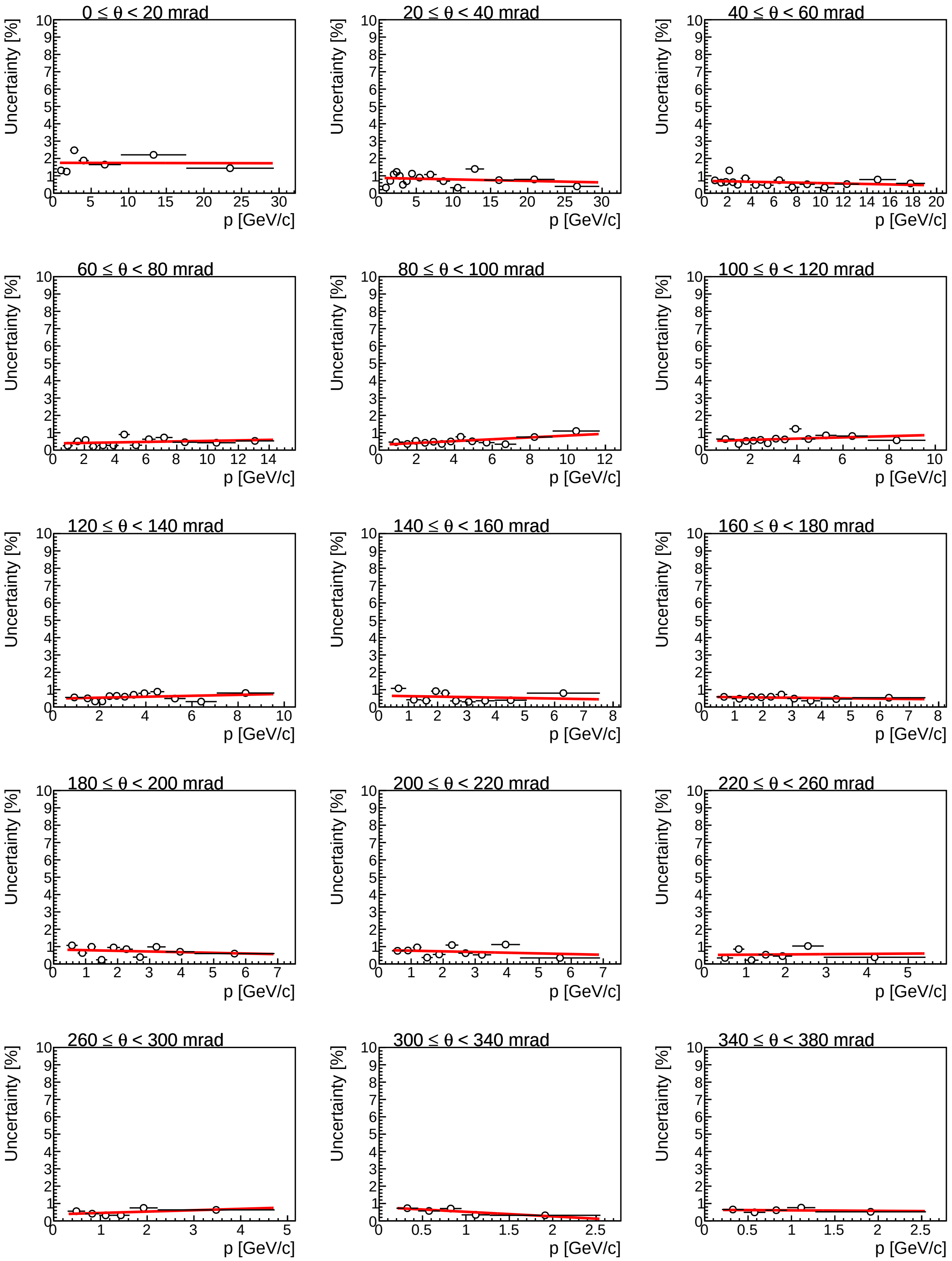
0 ≤ θ < 20 mrad
20 ≤ θ < 40 mrad
40 ≤ θ < 60 mrad
60 ≤ θ < 80 mrad
80 ≤ θ < 100 mrad
100 ≤ θ < 120 mrad
120 ≤ θ < 140 mrad
140 ≤ θ < 160 mrad
160 ≤ θ < 180 mrad
180 ≤ θ < 200 mrad
200 ≤ θ < 220 mrad
220 ≤ θ < 260 mrad
260 ≤ θ < 300 mrad
300 ≤ θ < 340 mrad
340 ≤ θ < 380 mrad

Figure D.35: Systematic uncertainties of the π^+ yields for the fifth z bin, coming from the uncertainty of the target position. Line segments are fitted to the distributions. Each panel represents different polar angle bin.

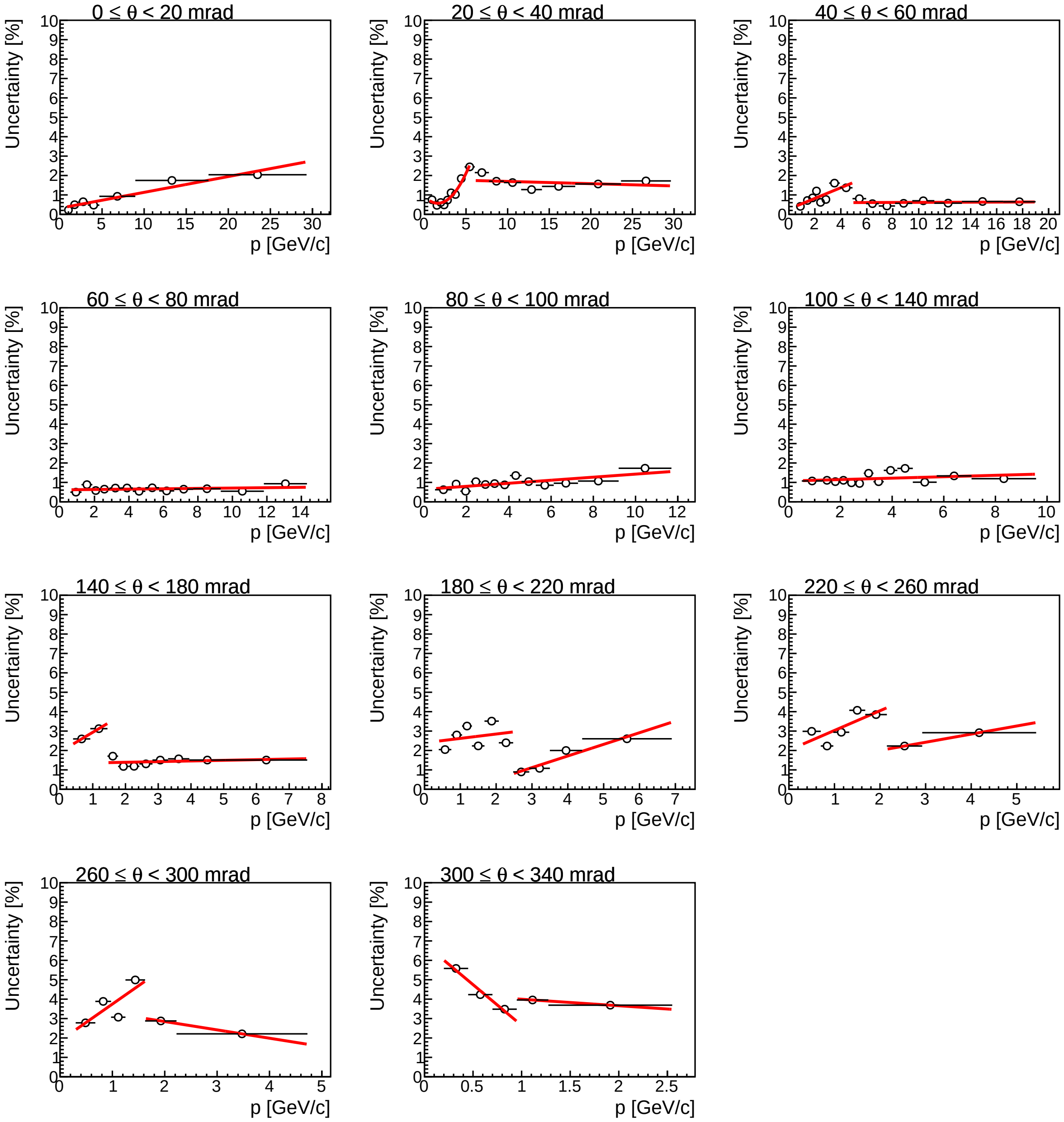

Figure D.36: Systematic uncertainties of the π^+ yields for the sixth z bin, coming from the uncertainty of the target position. Line segments are fitted to the distributions. Each panel represents different polar angle bin.

Appendix E

Monte Carlo comparisons

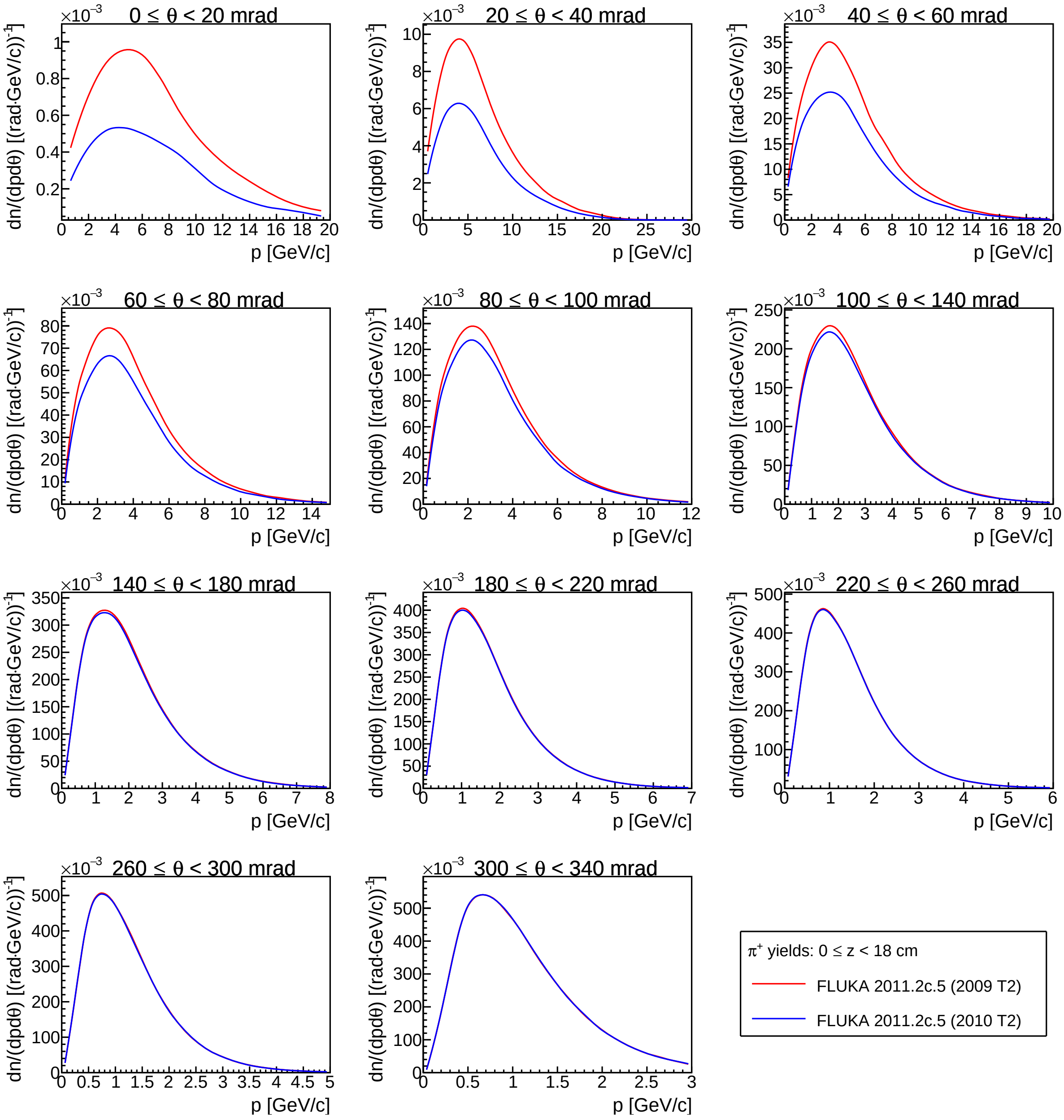

Figure E.1: Yields of positively charged pions for the first z bin, simulated with FLUKA2011.2c.5 by using 2009 T2 beam profile (red line) and 2010 T2 beam profile (blue line).

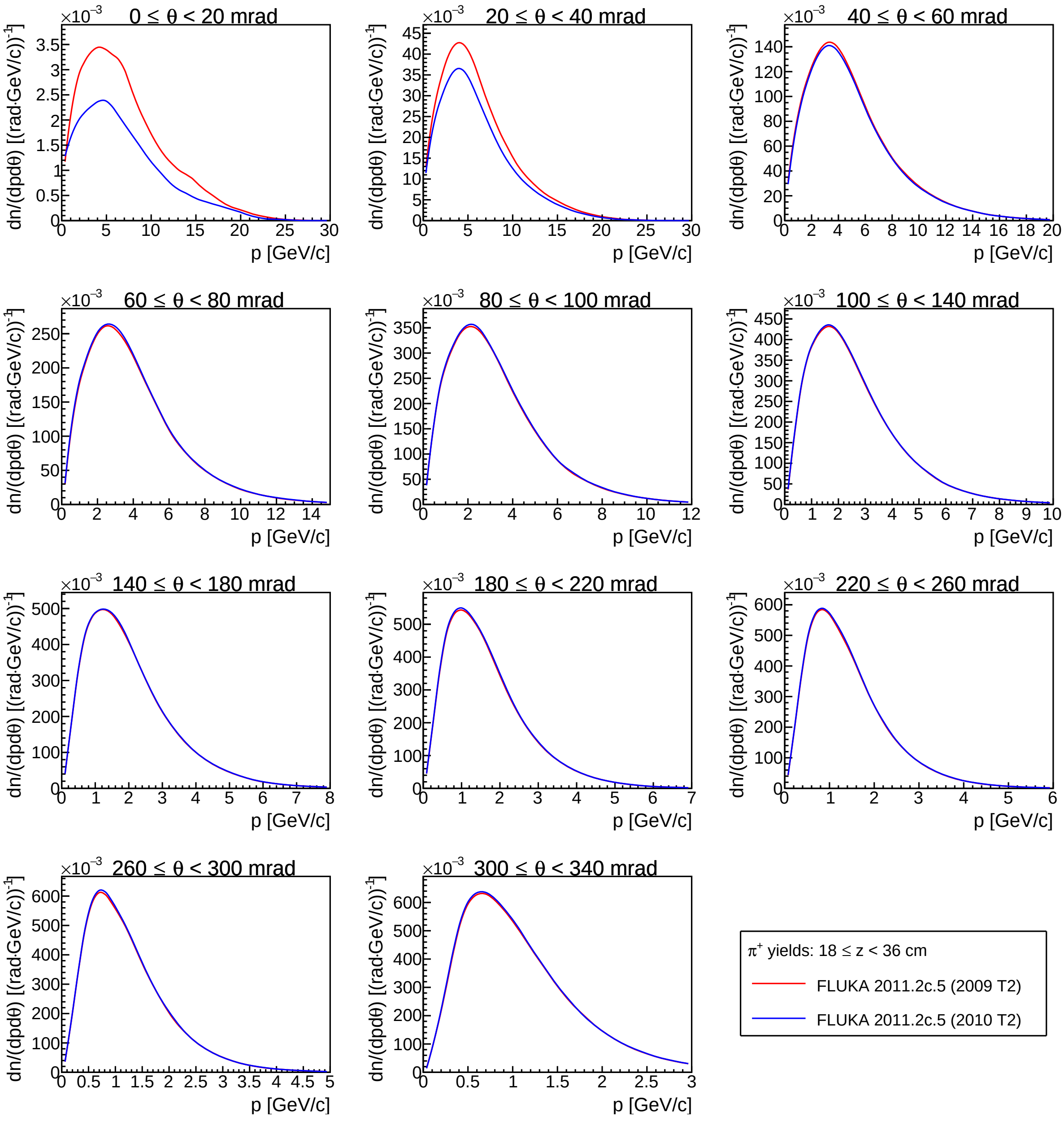

Figure E.2: Yields of positively charged pions for the second z bin, simulated with Fluka2011.2c.5 by using 2009 T2 beam profile (red line) and 2010 T2 beam profile (blue line).

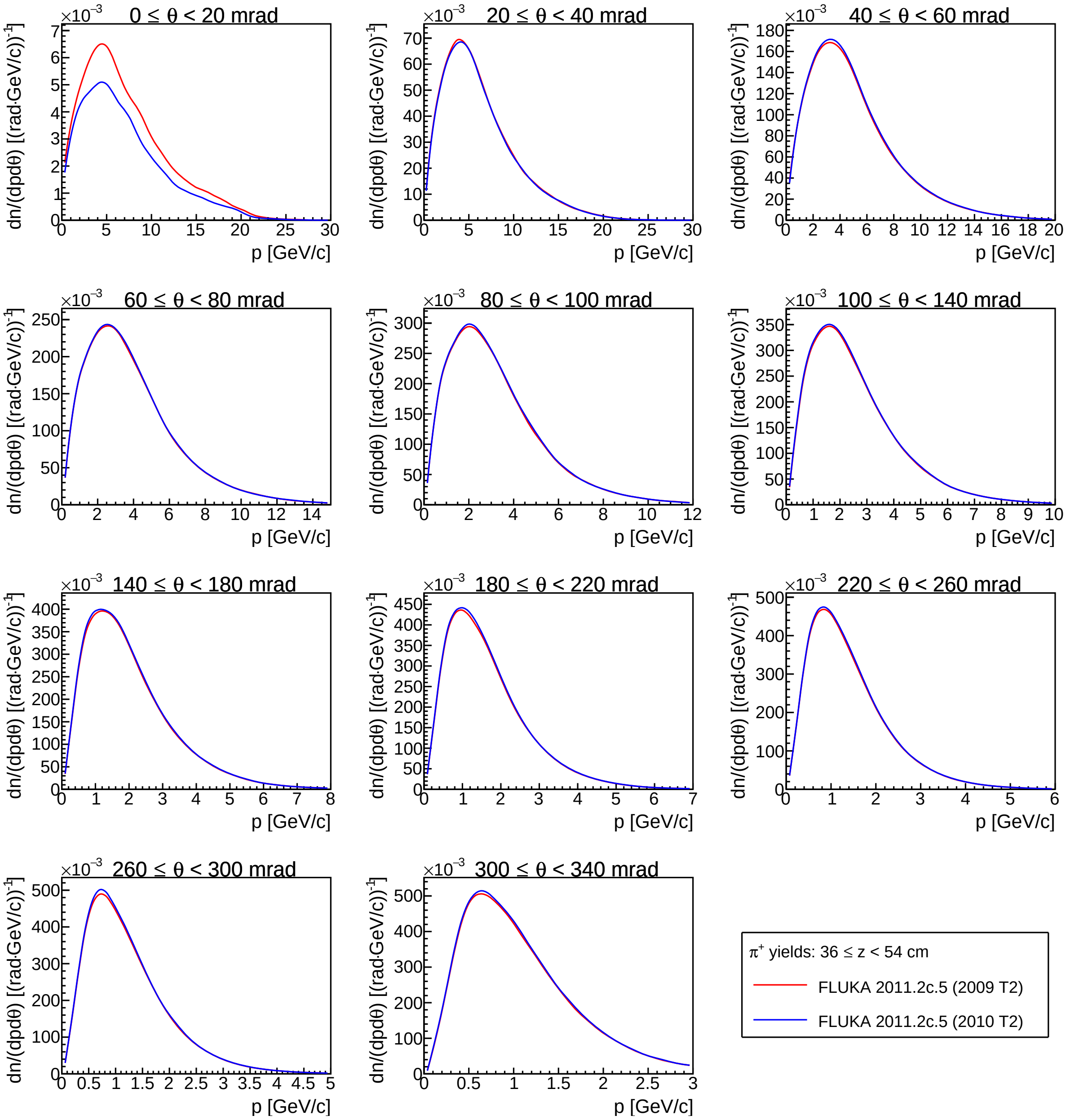

Figure E.3: Yields of positively charged pions for the third z bin, simulated with FLUKA2011.2c.5 by using 2009 T2 beam profile (red line) and 2010 T2 beam profile (blue line).

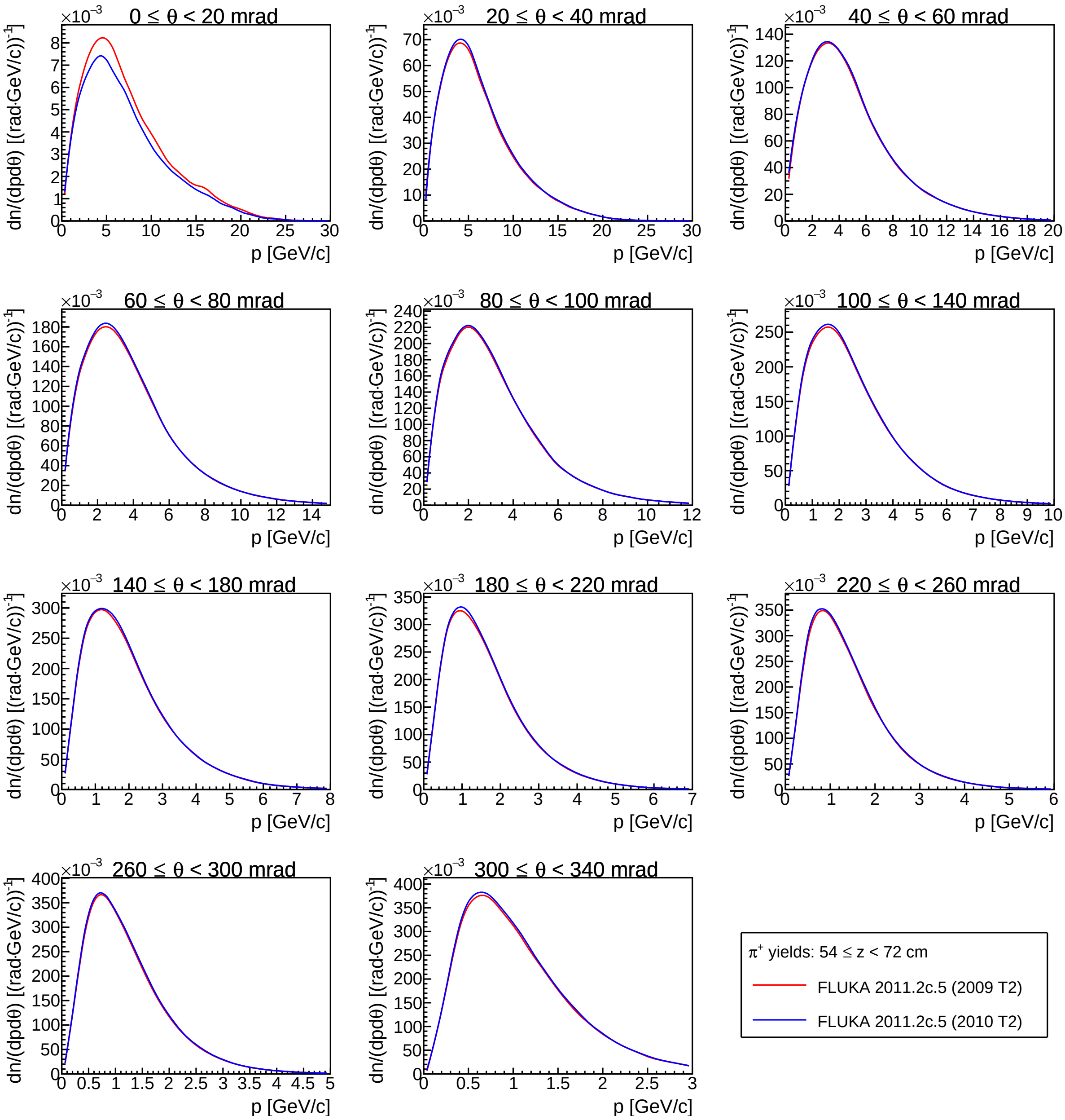

Figure E.4: Yields of positively charged pions for the fourth z bin, simulated with FLUKA2011.2c.5 by using 2009 T2 beam profile (red line) and 2010 T2 beam profile (blue line).

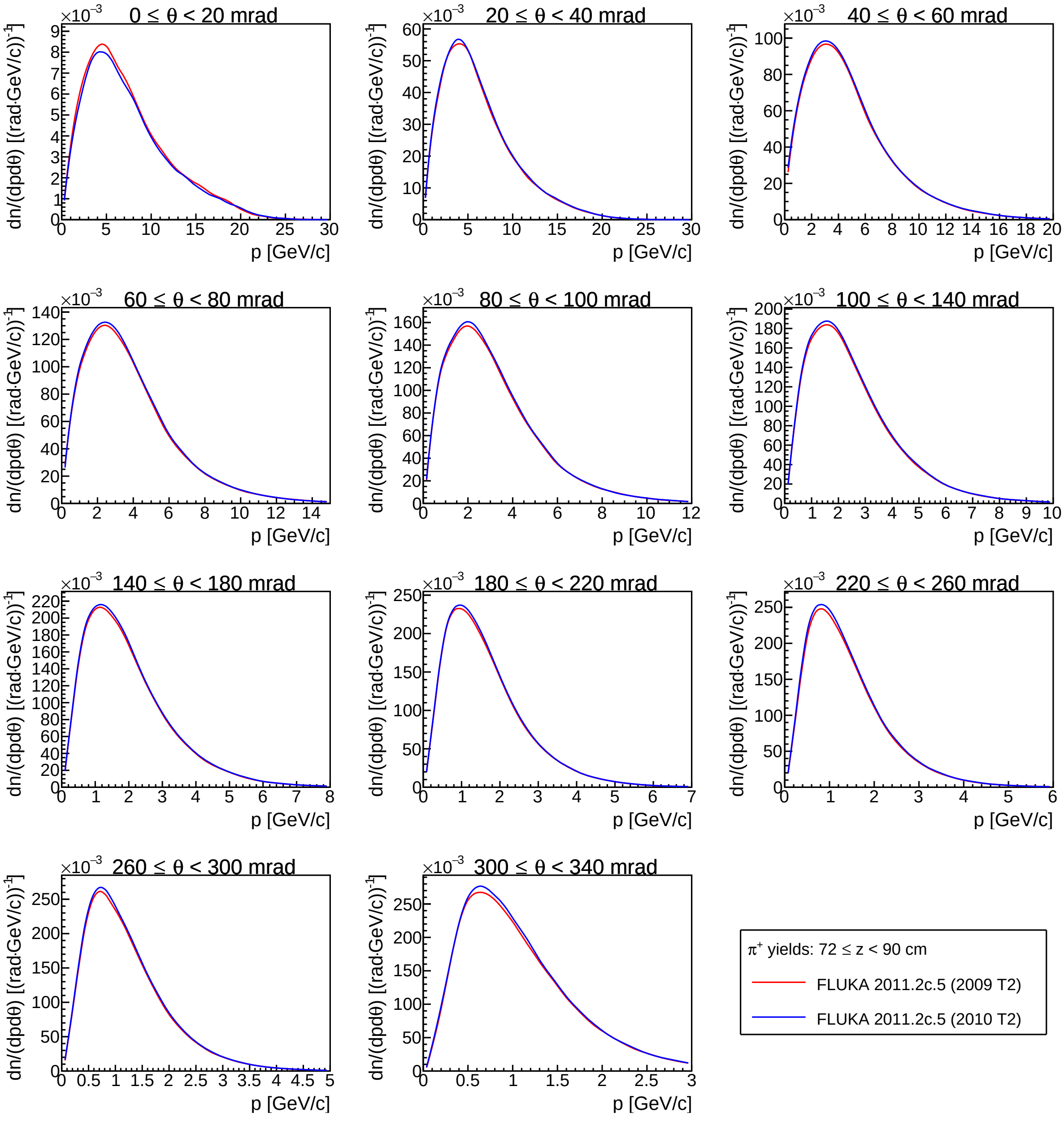

Figure E.5: Yields of positively charged pions for the fifth z bin, simulated with FLUKA2011.2c.5 by using 2009 T2 beam profile (red line) and 2010 T2 beam profile (blue line).

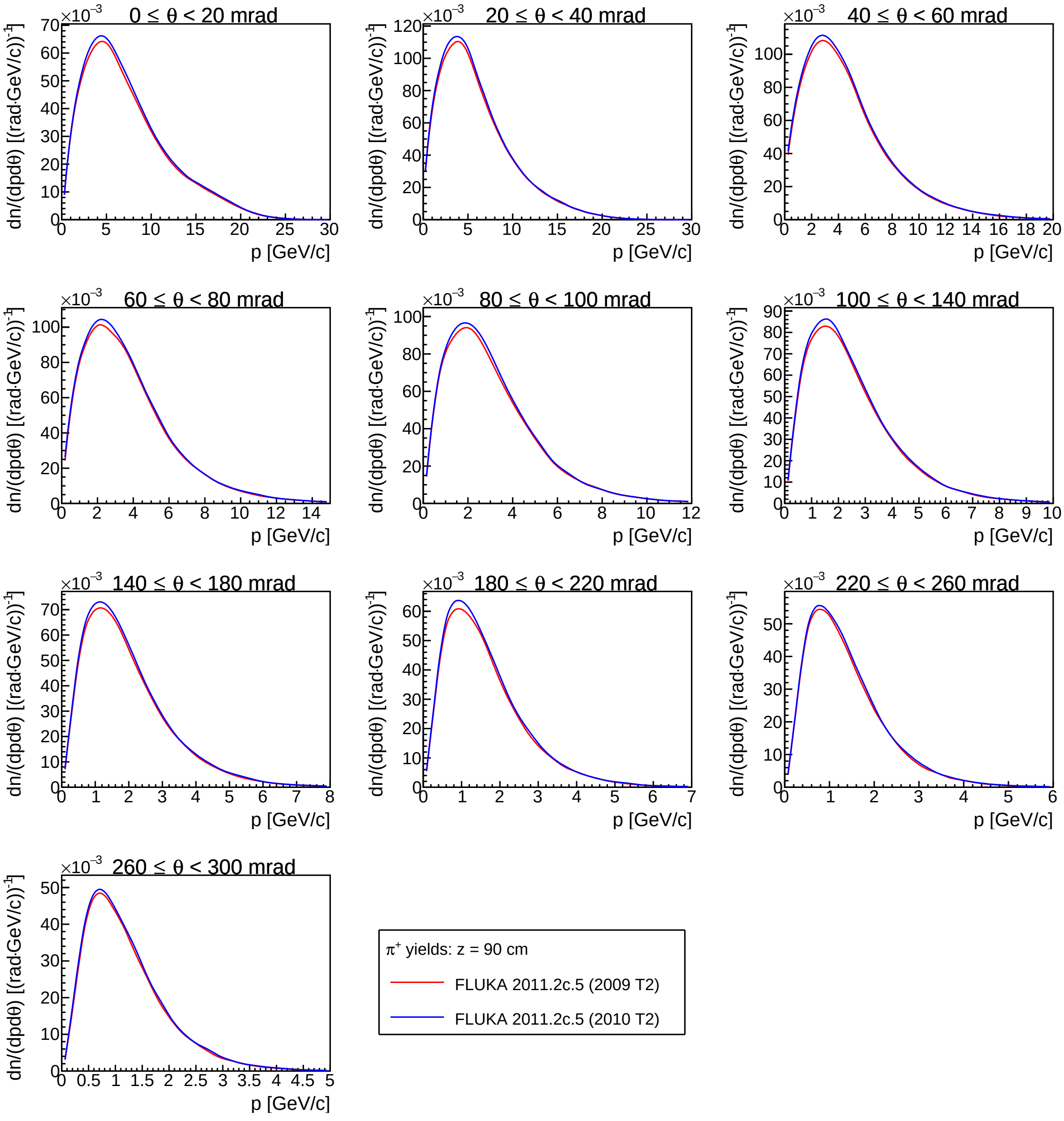

Figure E.6: Yields of positively charged pions for the downstream target face, simulated with FLUKA2011.2c.5 by using 2009 T2 beam profile (red line) and 2010 T2 beam profile (blue line).

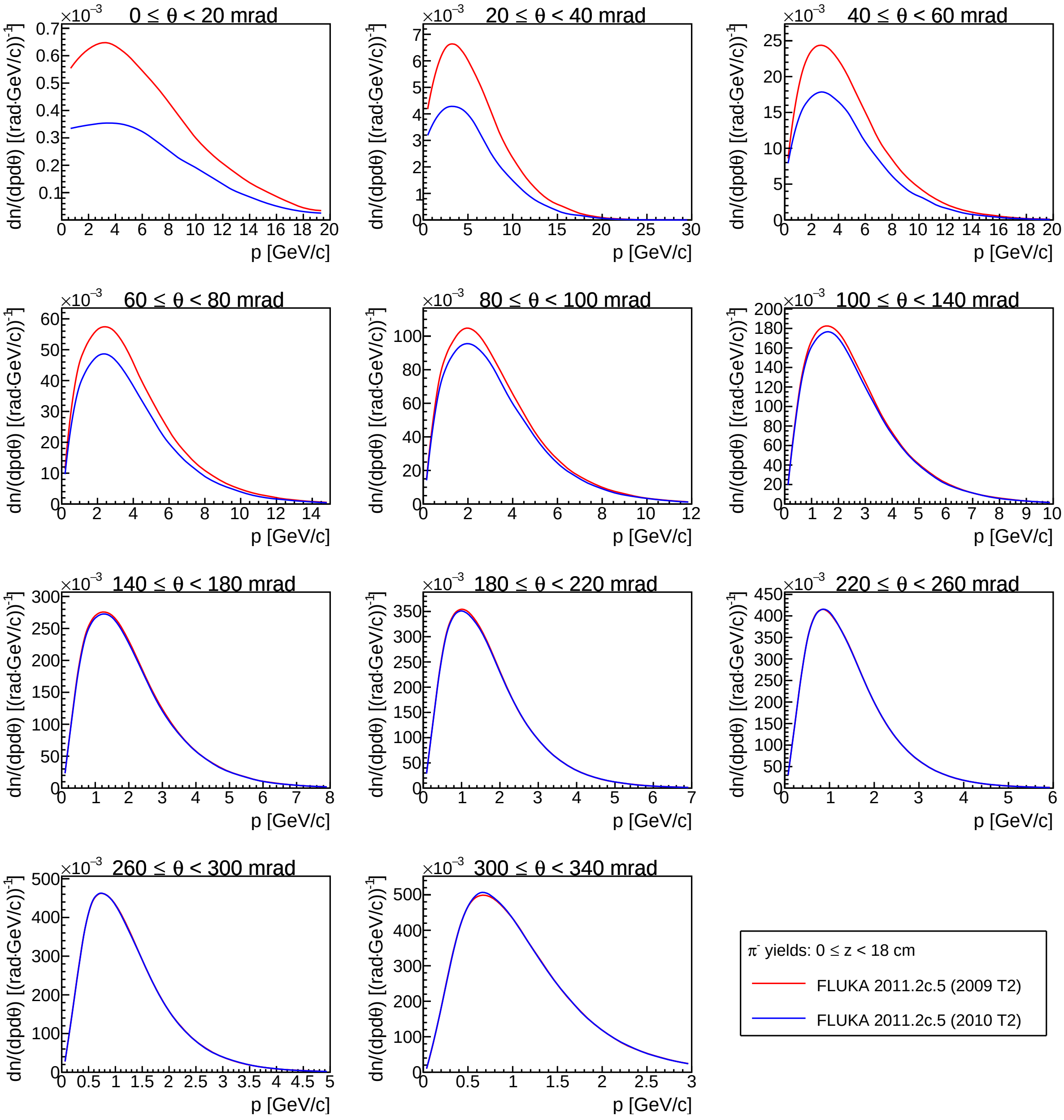

Figure E.7: Yields of negatively charged pions for the first z bin, simulated with FLUKA2011.2c.5 by using 2009 T2 beam profile (red line) and 2010 T2 beam profile (blue line).

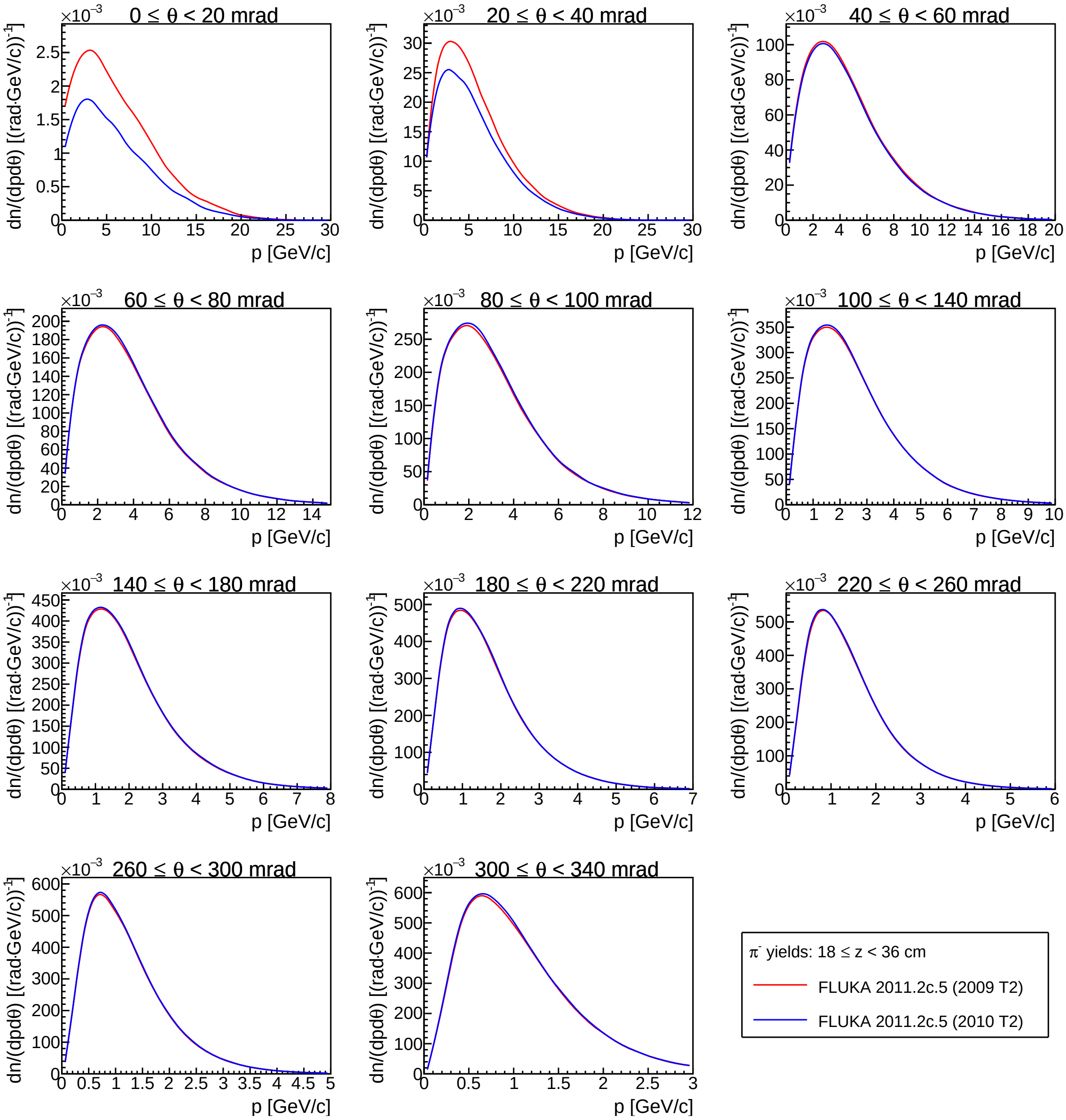

Figure E.8: Yields of negatively charged pions for the second z bin, simulated with FLUKA2011.2c.5 by using 2009 T2 beam profile (red line) and 2010 T2 beam profile (blue line).

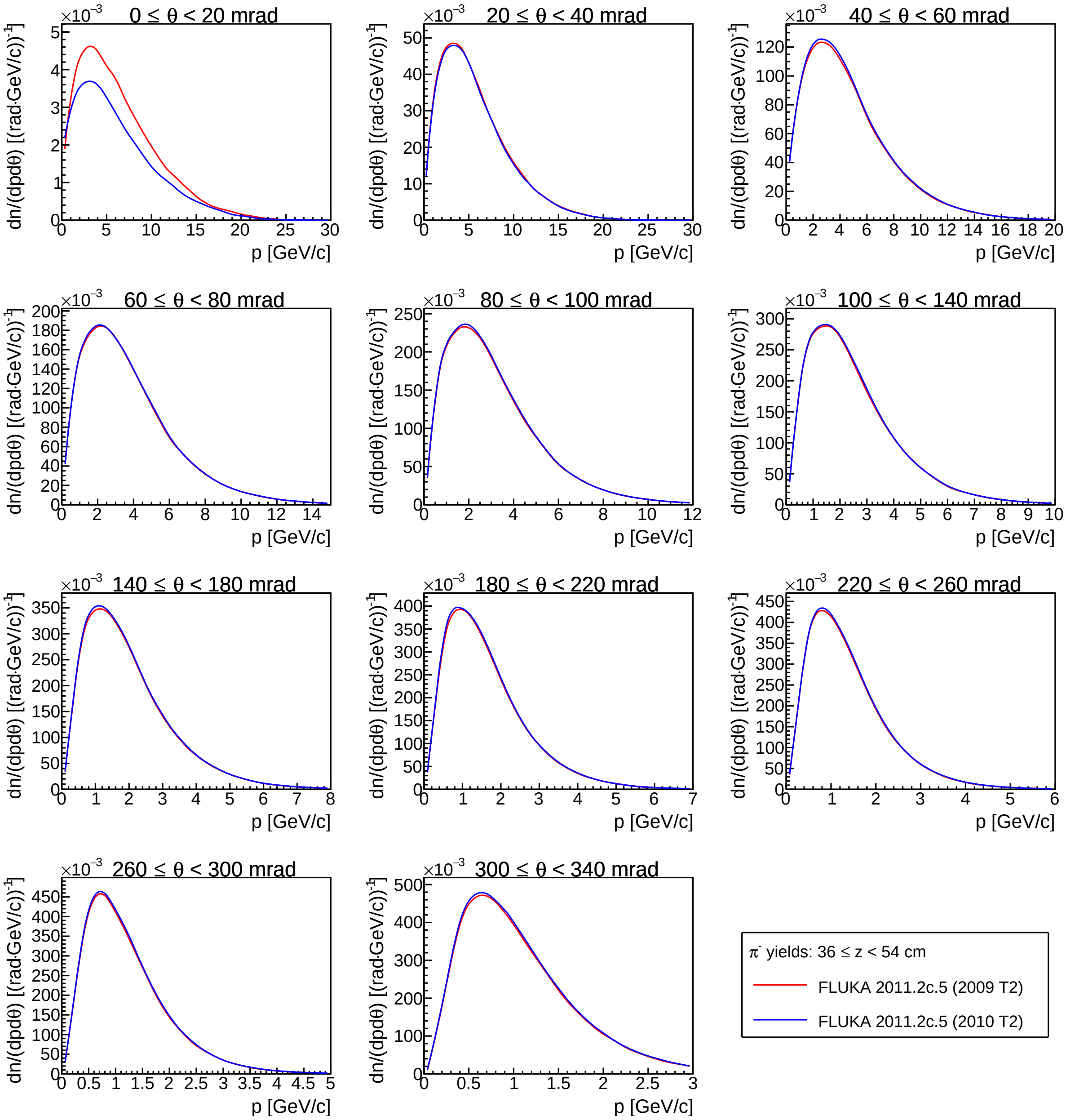

Figure E.9: Yields of negatively charged pions for the third z bin, simulated with FLUKA2011.2c.5 by using 2009 T2 beam profile (red line) and 2010 T2 beam profile (blue line).

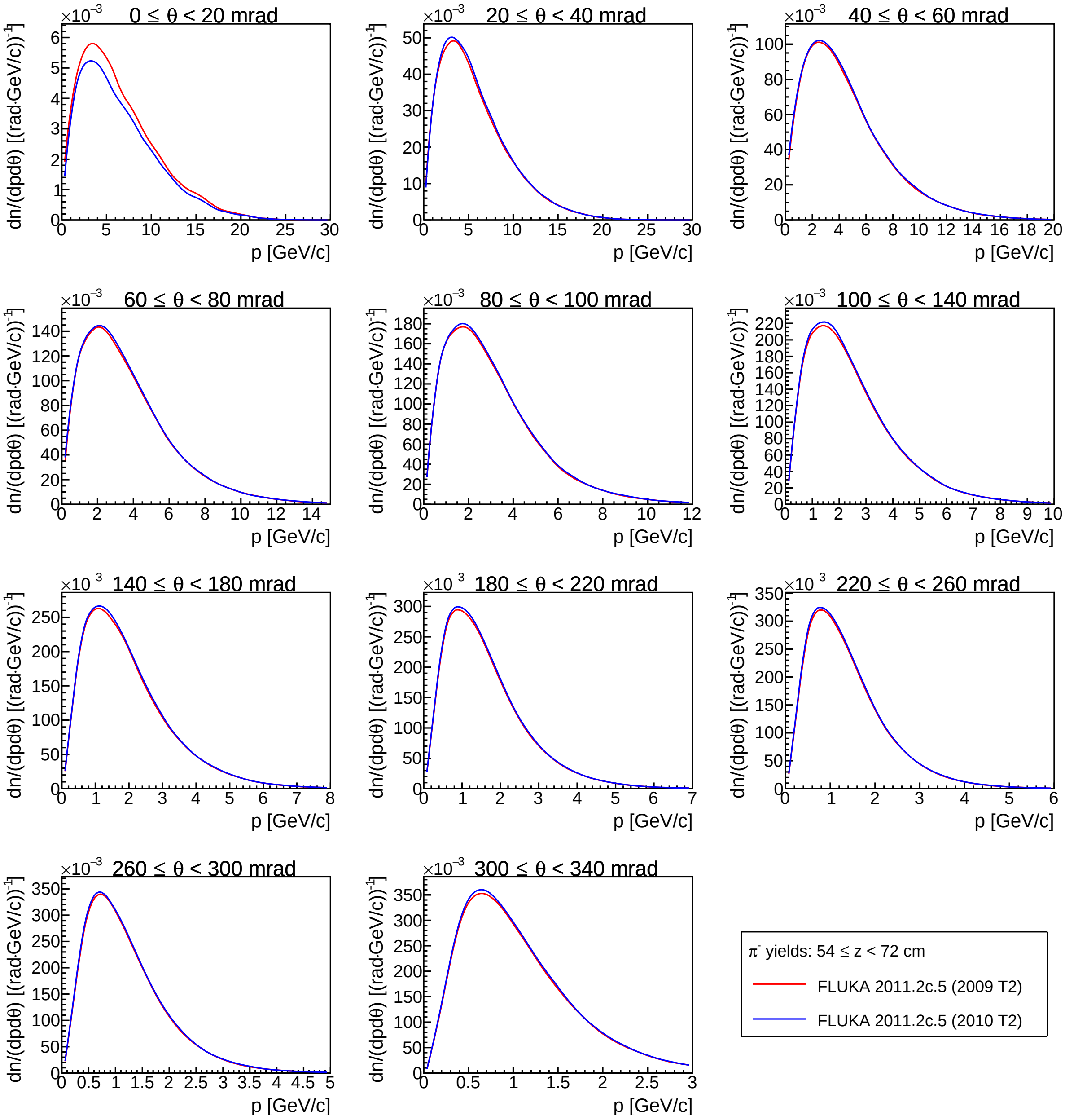

Figure E.10: Yields of negatively charged pions for the fourth z bin, simulated with FLUKA2011.2c.5 by using 2009 T2 beam profile (red line) and 2010 T2 beam profile (blue line).

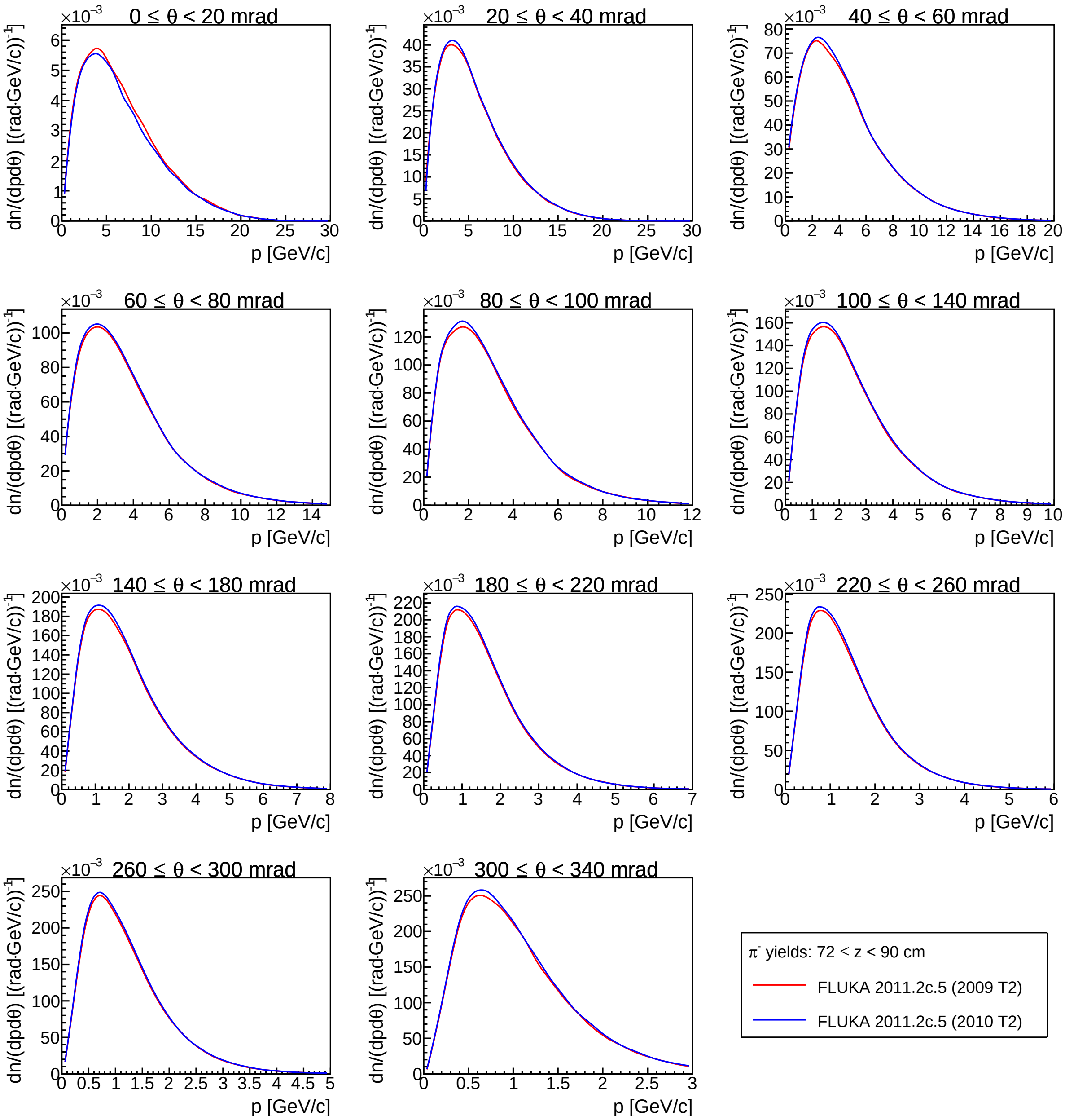

Figure E.11: Yields of negatively charged pions for the fifth z bin, simulated with FLUKA2011.2c.5 by using 2009 T2 beam profile (red line) and 2010 T2 beam profile (blue line).

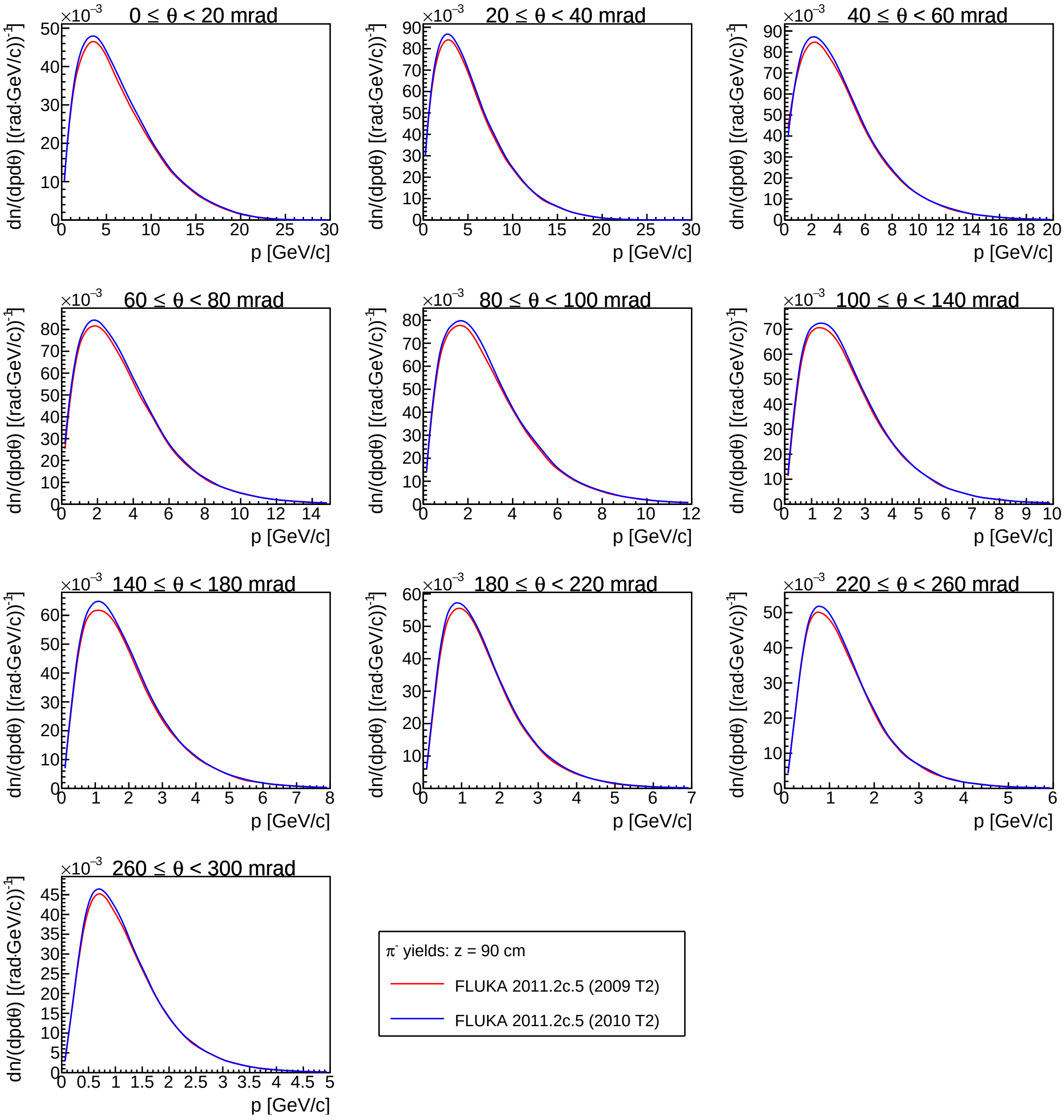

Figure E.12: Yields of negatively charged pions for the downstream target face, simulated with FLUKA2011.2c.5 by using 2009 T2 beam profile (red line) and 2010 T2 beam profile (blue line).

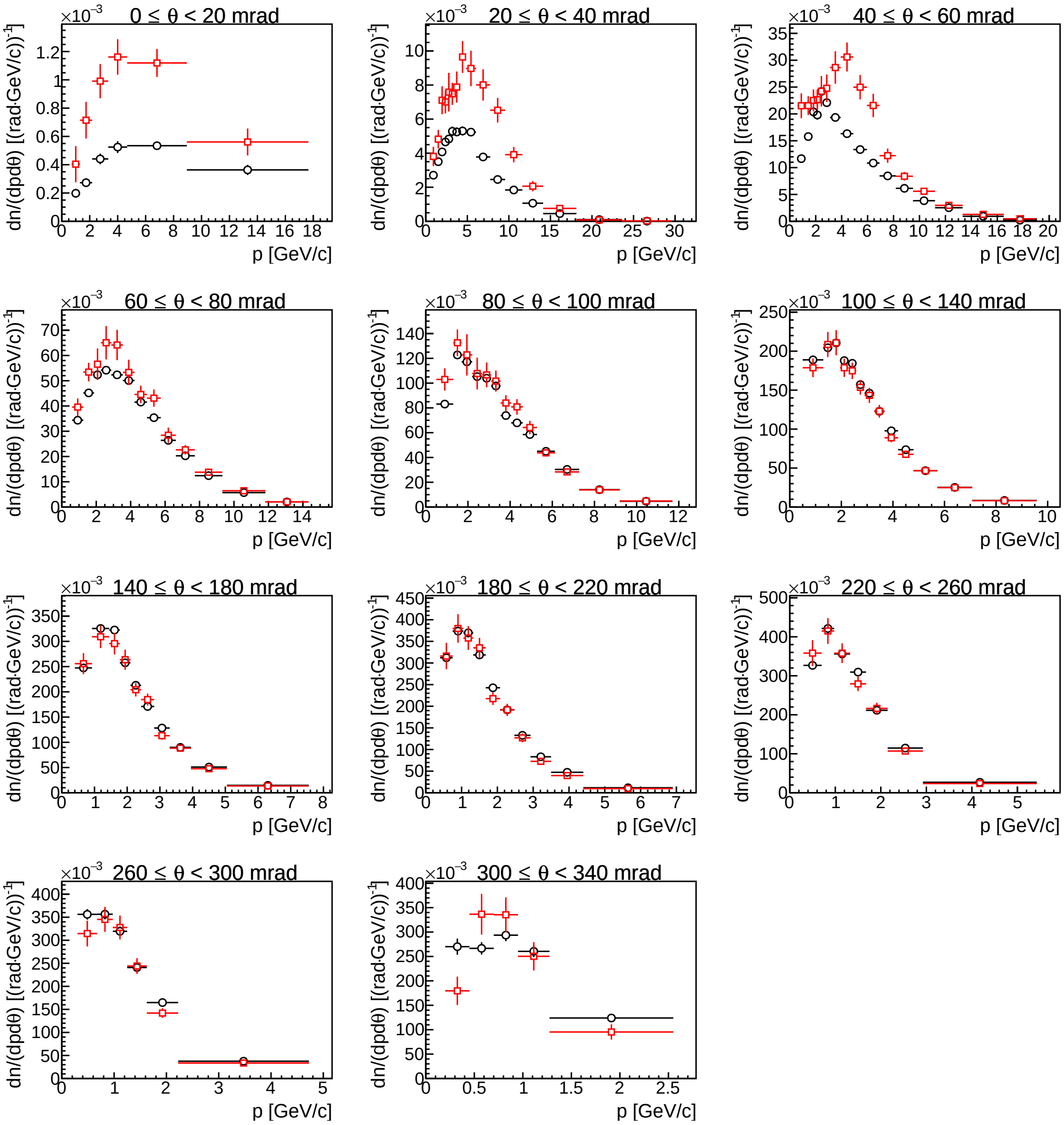

Figure E.13: Comparison of fully corrected π^+ yields (black points) with previous NA61/SHINE measurements [86] (red points) for the first longitudinal z bin.

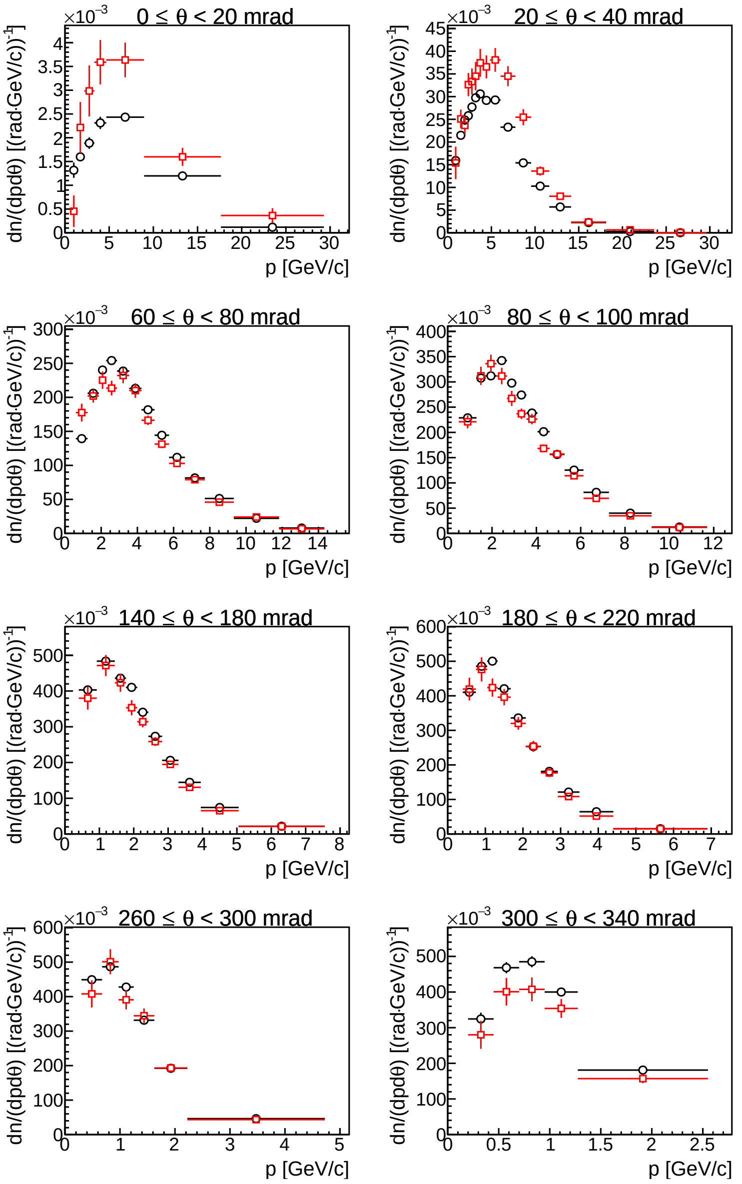

Figure E.14: Comparison of fully corrected π^+ yields (black points) with previous NA61/SHINE measurements [86] (red points) for the second longitudinal z bin.

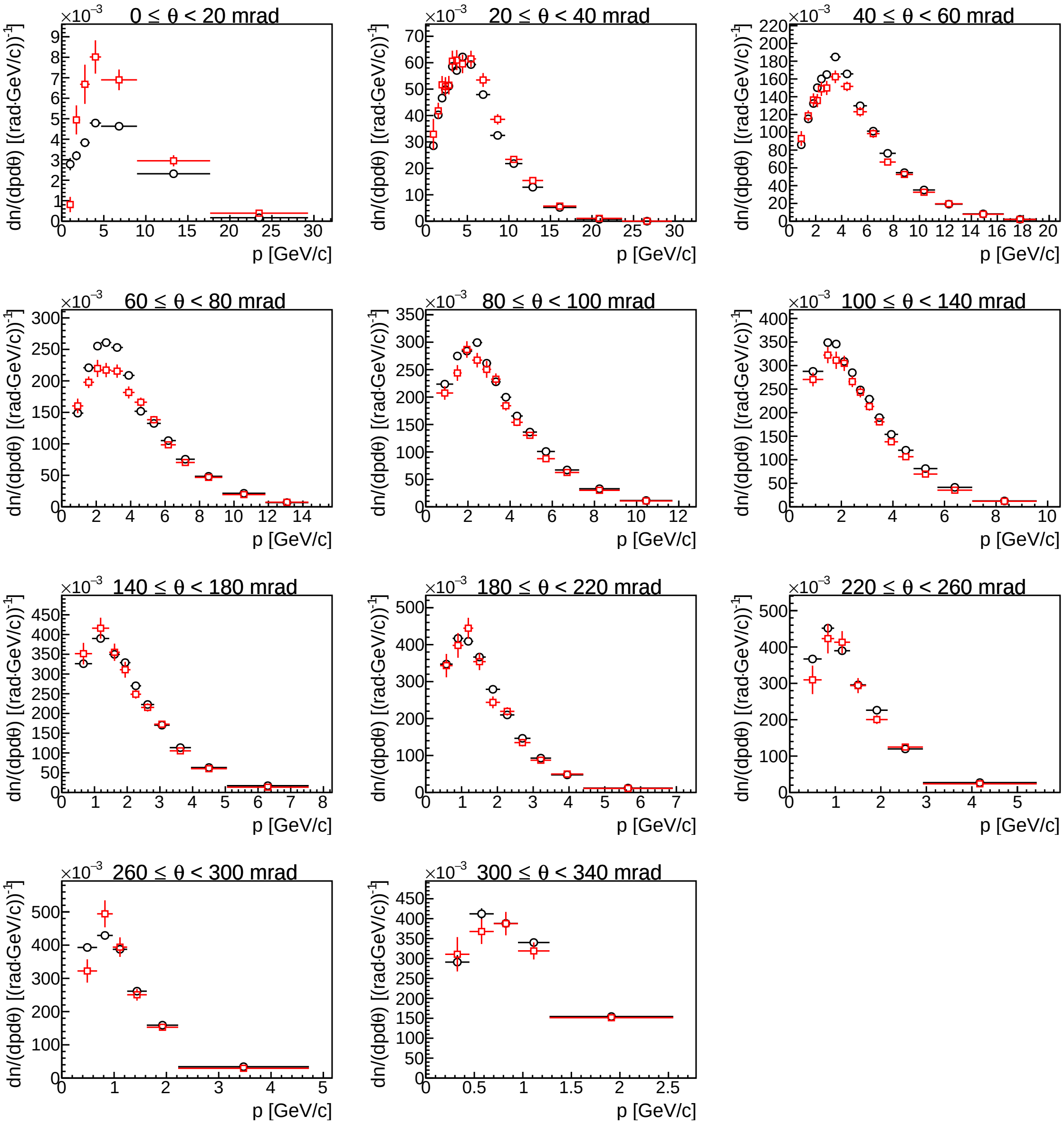

Figure E.15: Comparison of fully corrected π^+ yields (black points) with previous NA61/SHINE measurements [86] (red points) for the third longitudinal z bin.

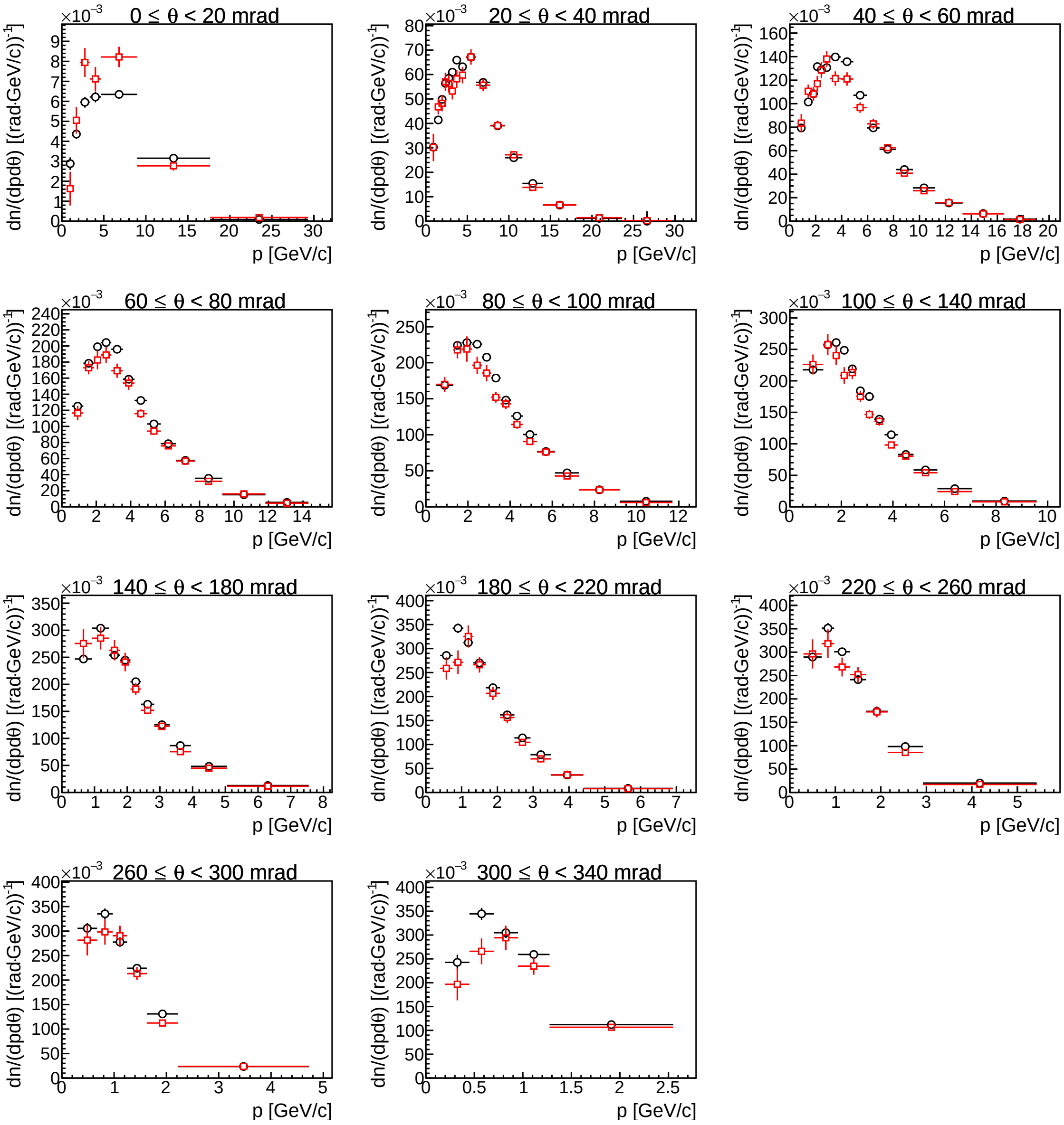

Figure E.16: Comparison of fully corrected π^+ yields (black points) with previous NA61/SHINE measurements [86] (red points) for the fourth longitudinal z bin.

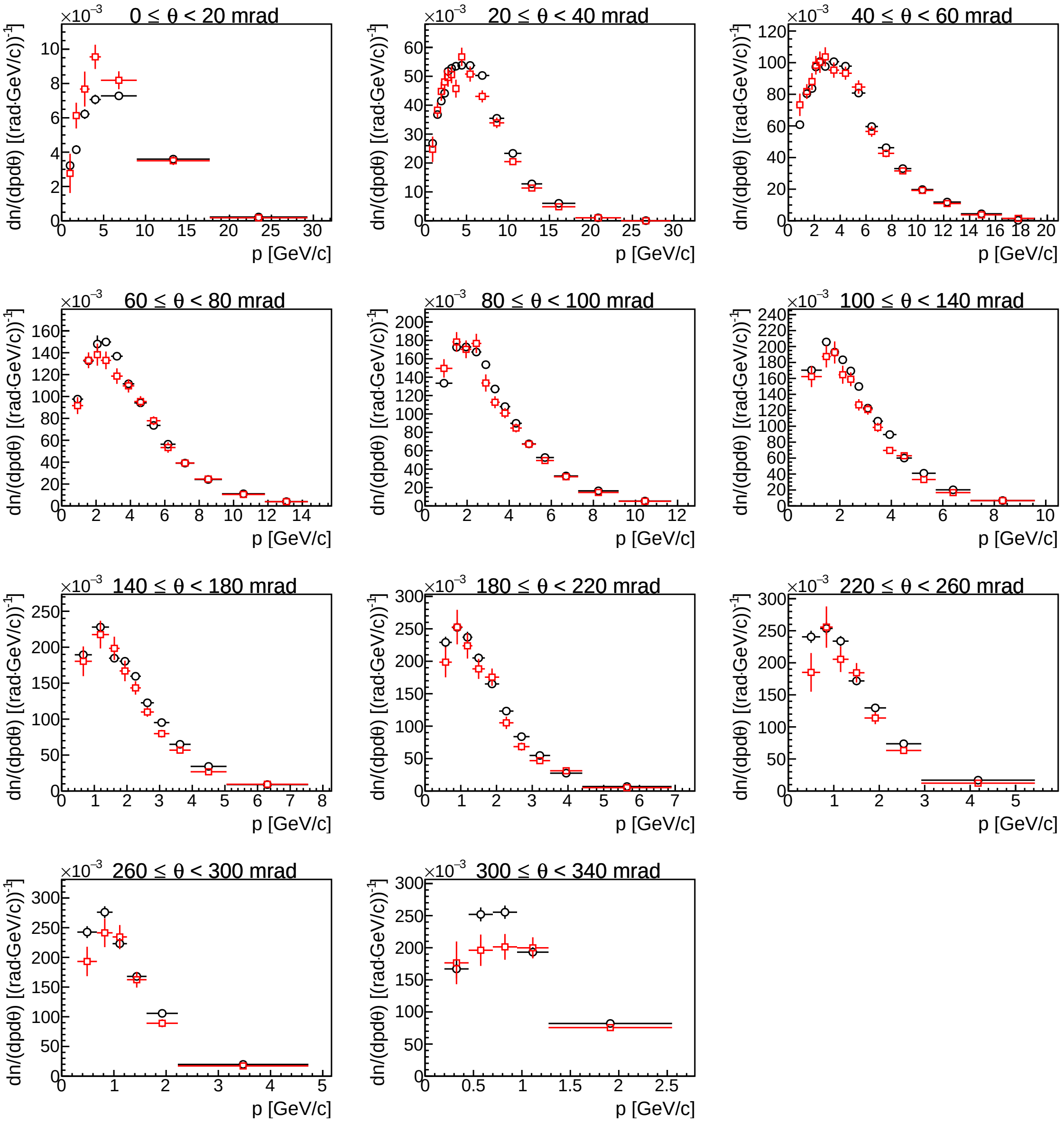

Figure E.17: Comparison of fully corrected π^+ yields (black points) with previous NA61/SHINE measurements [86] (red points) for the fith longitudinal z bin.

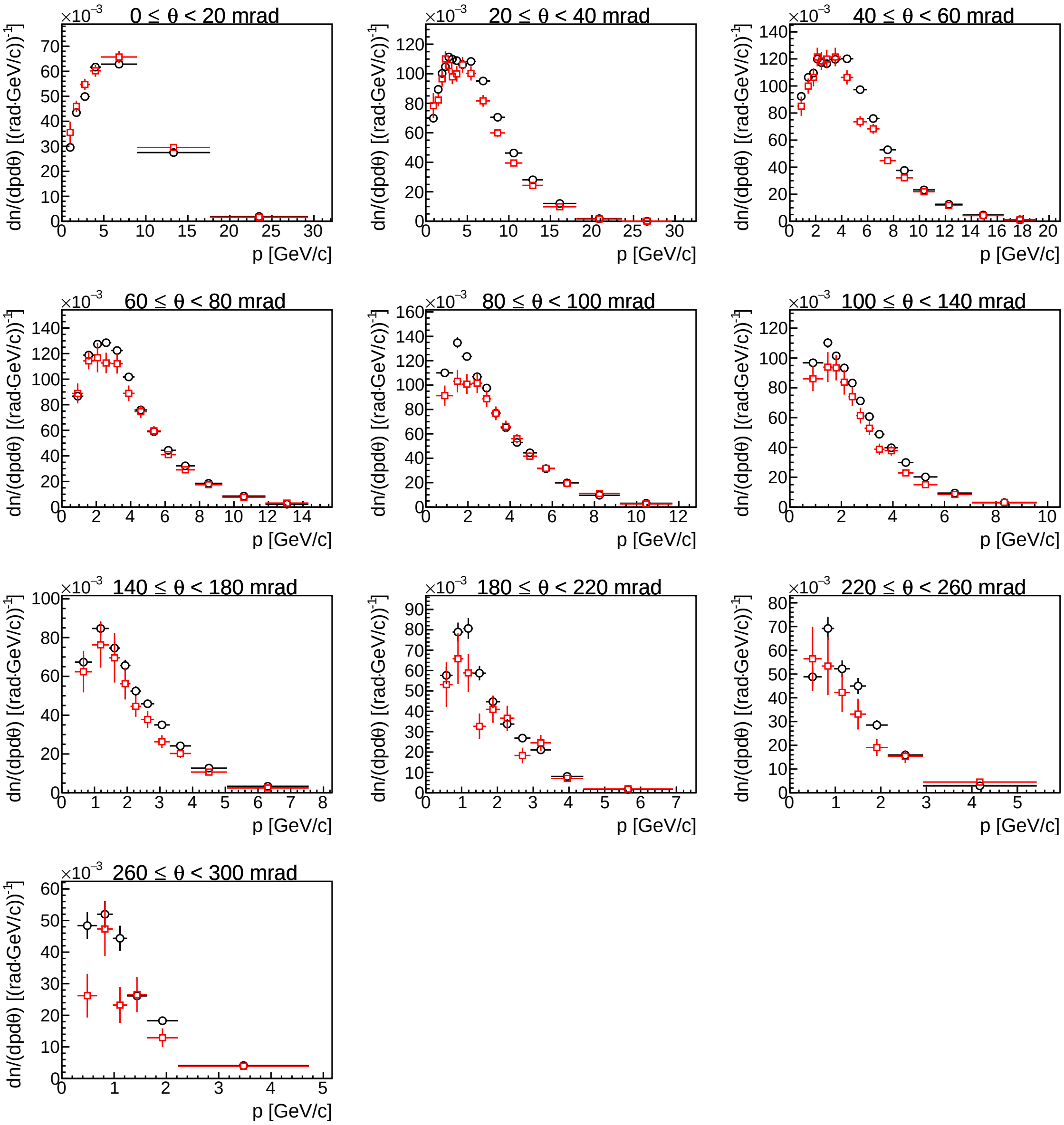

Figure E.18: Comparison of fully corrected π^+ yields (black points) with previous NA61/SHINE measurements [86] (red points) for the downstream target face.

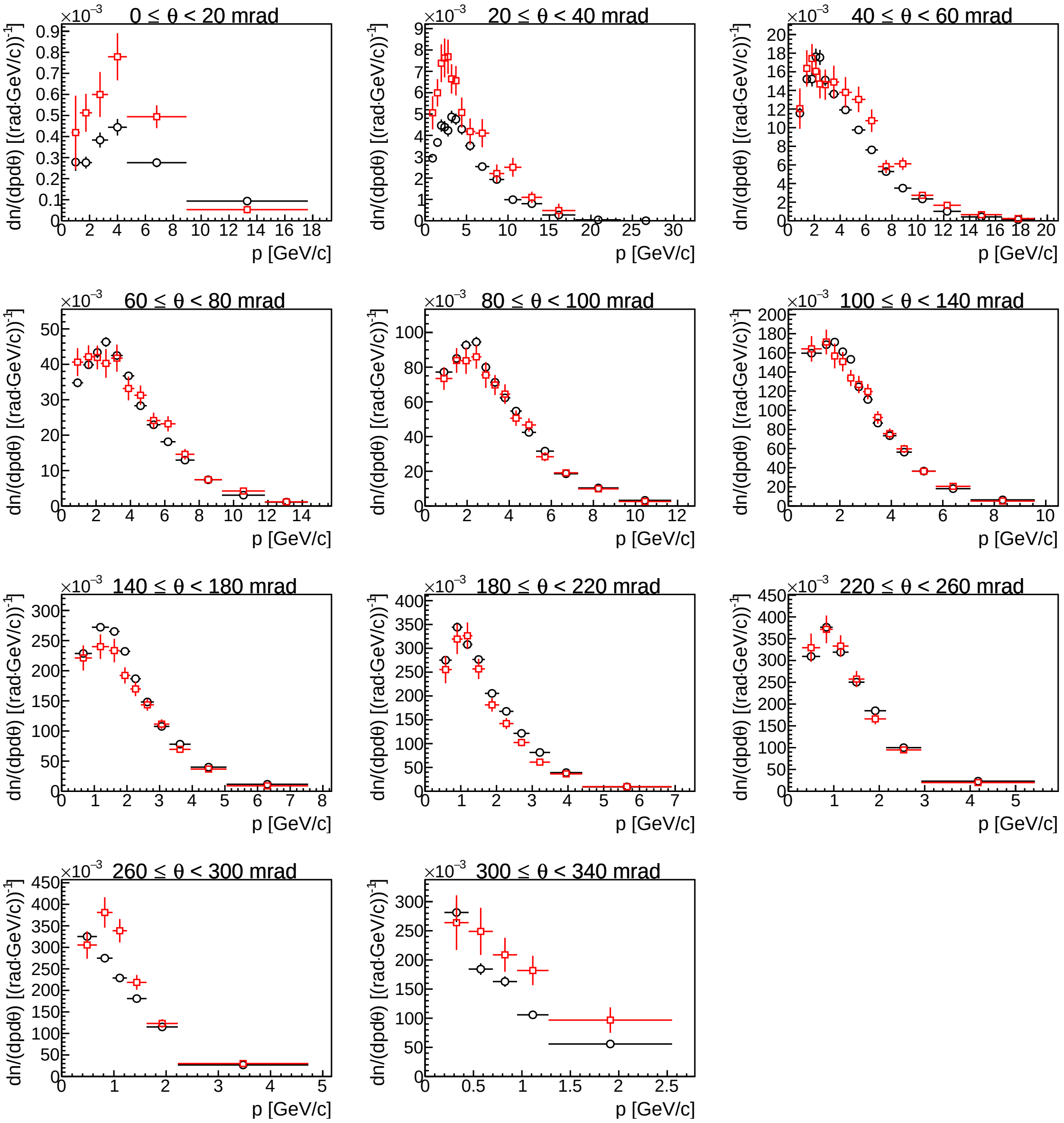

Figure E.19: Comparison of fully corrected π^- yields (black points) with previous NA61/SHINE measurements [86] (red points) for the first longitudinal z bin.

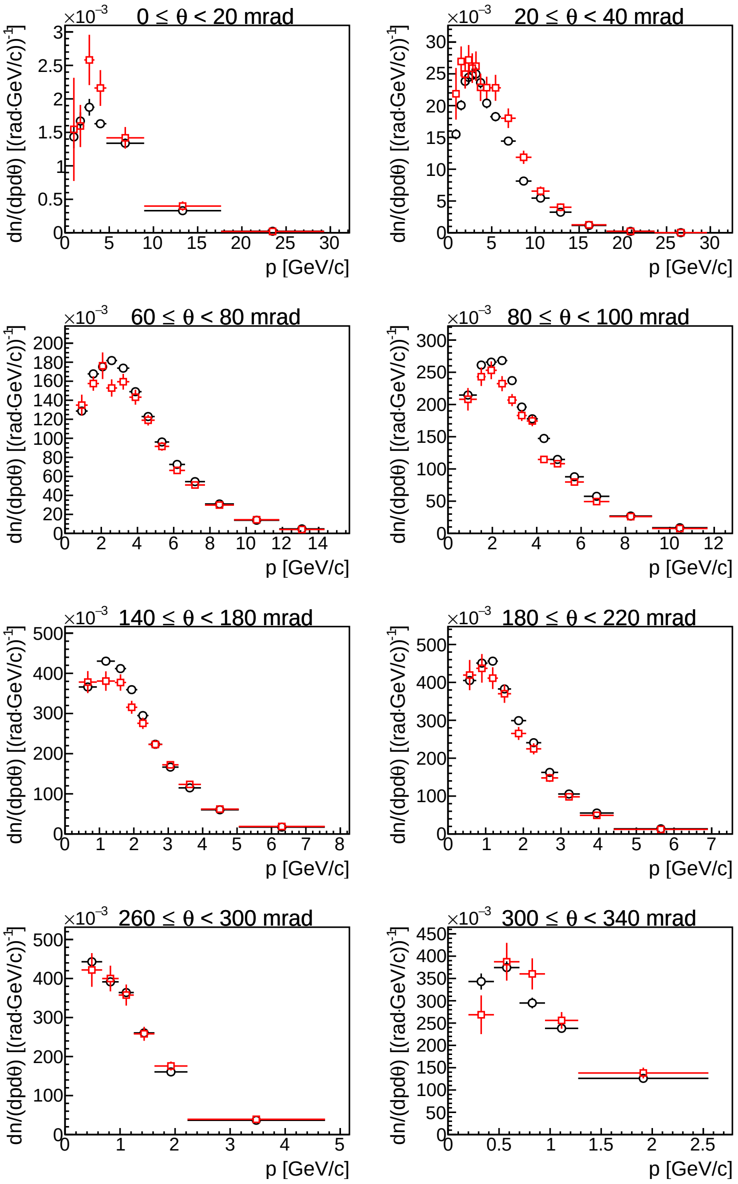

Figure E.20: Comparison of fully corrected π^- yields (black points) with previous NA61/SHINE measurements [86] (red points) for the second longitudinal z bin.

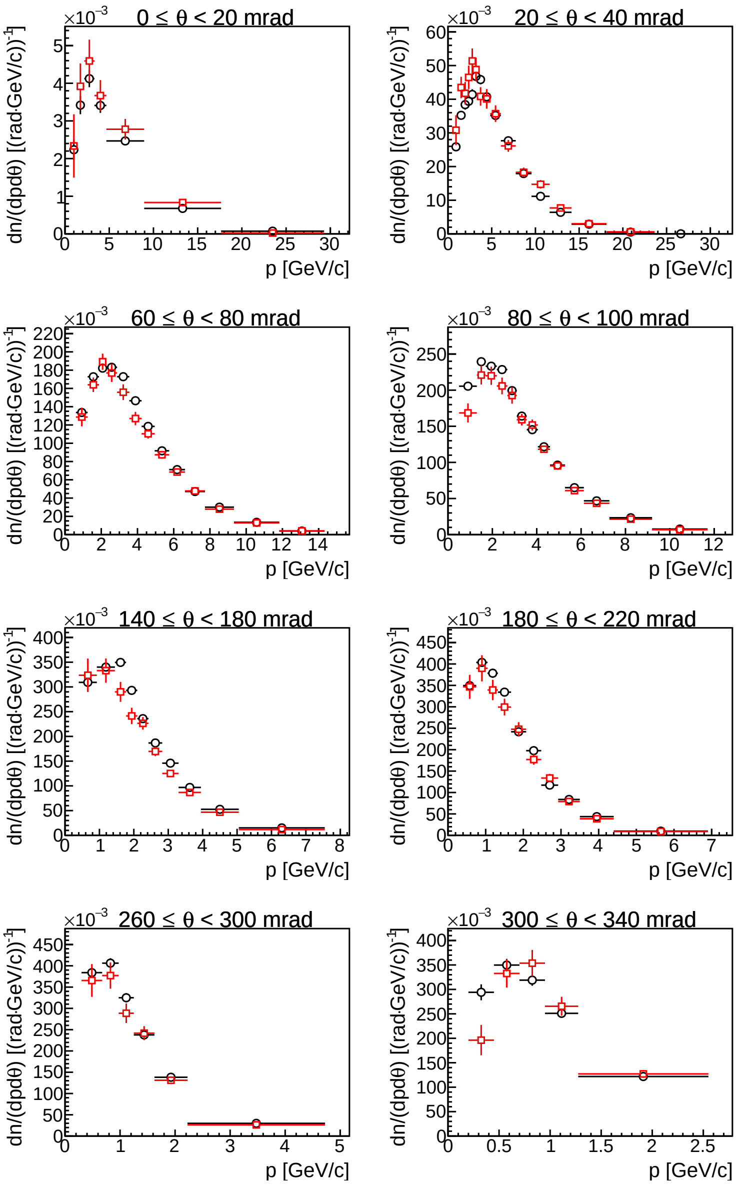

Figure E.21: Comparison of fully corrected π^- yields (black points) with previous NA61/SHINE measurements [86] (red points) for the third longitudinal z bin.

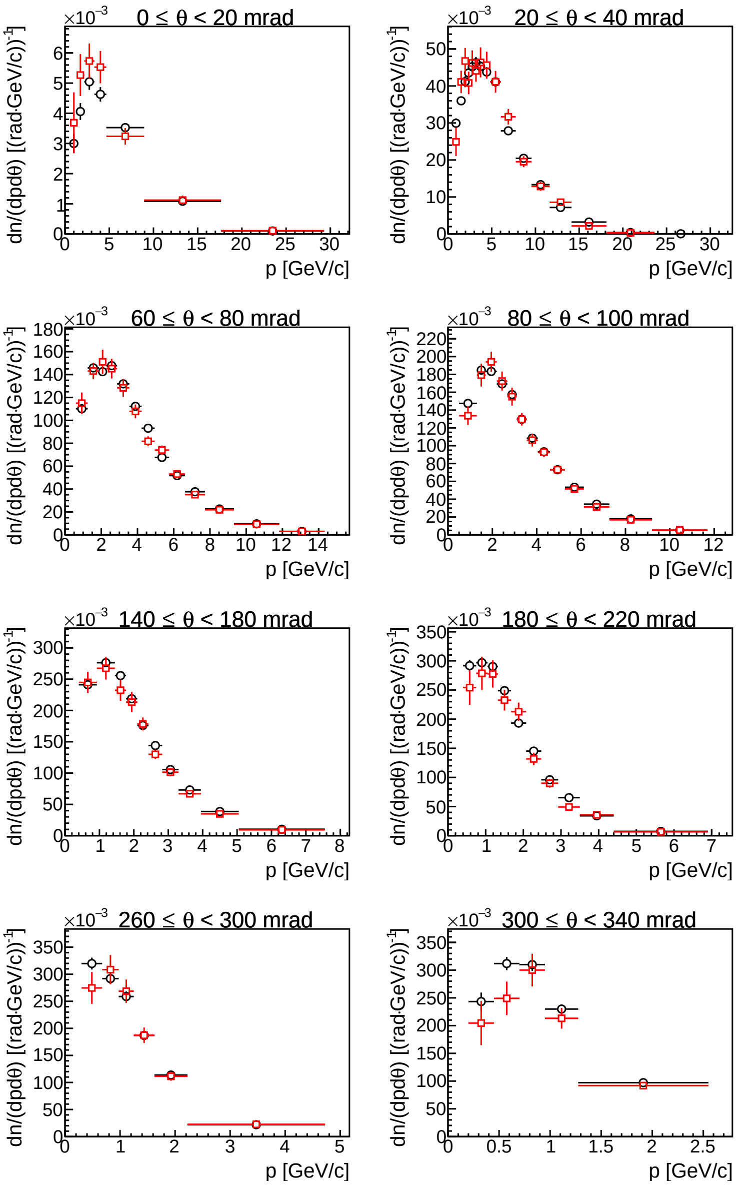

Figure E.22: Comparison of fully corrected π^- yields (black points) with previous NA61/SHINE measurements [86] (red points) for the fourth longitudinal z bin.

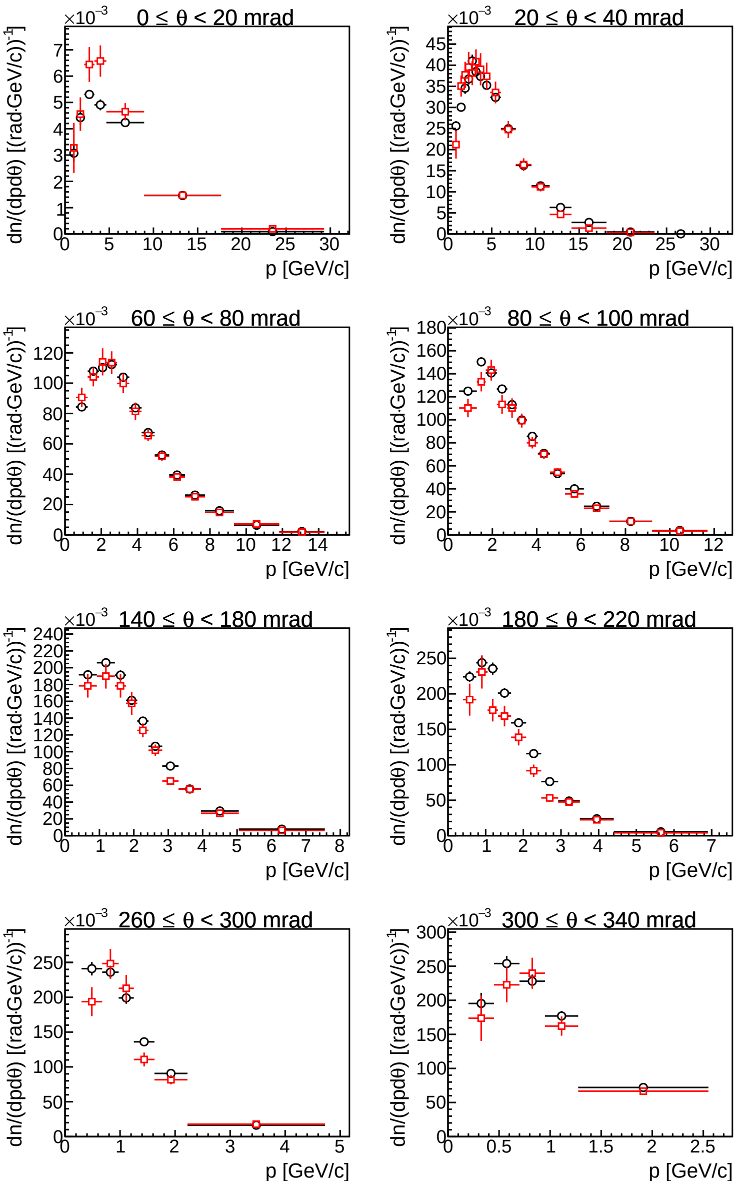

Figure E.23: Comparison of fully corrected π^- yields (black points) with previous NA61/SHINE measurements [86] (red points) for the fith longitudinal z bin.

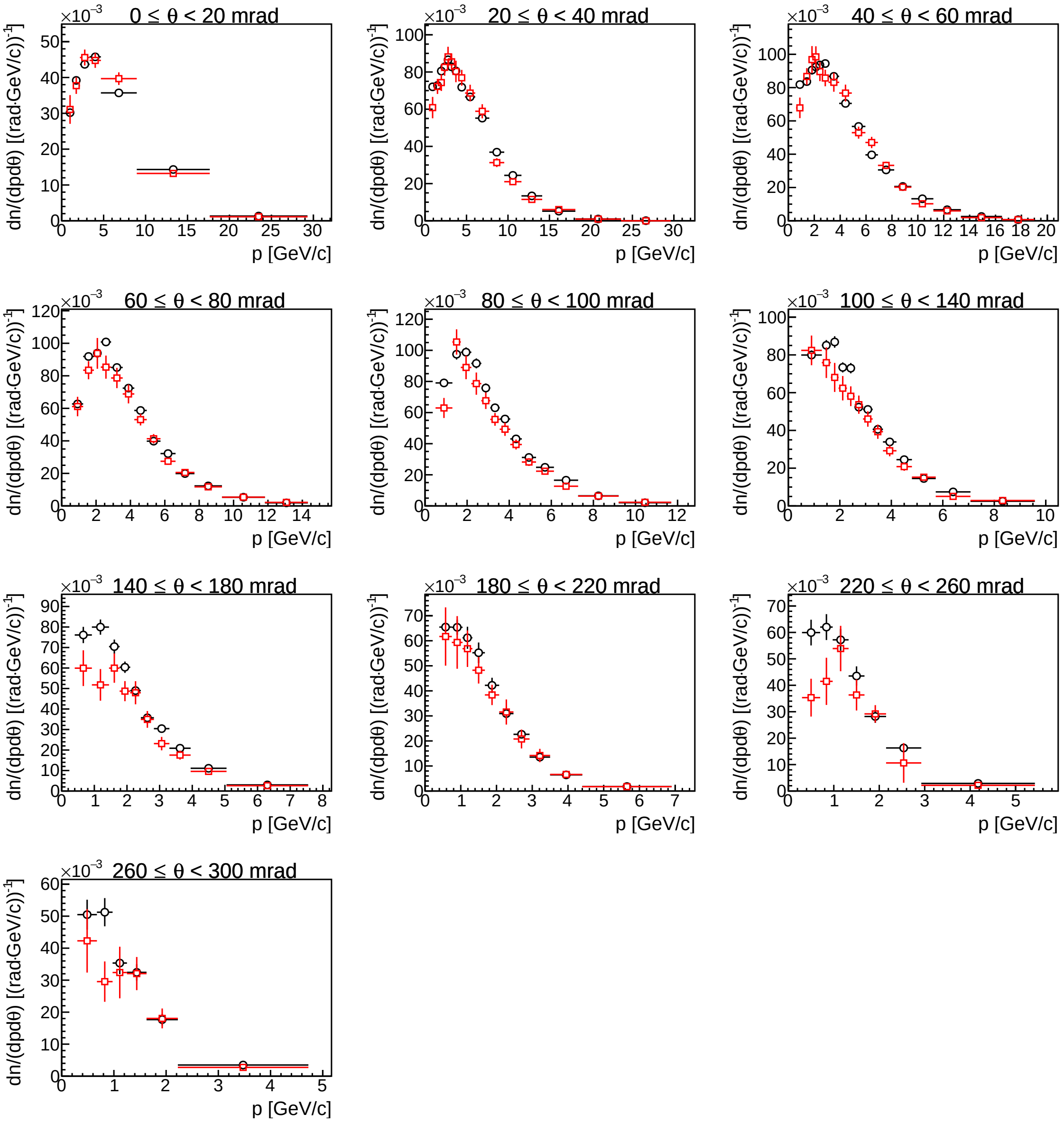

Figure E.24: Comparison of fully corrected π^- yields (black points) with previous NA61/SHINE measurements [86] (red points) for the downstream target face.

List of Figures

List of Tables

Bibliography

[1] F. Englert and R. Brout. Broken Symmetry and the Mass of Gauge Vector Mesons. *Phys. Rev. Lett.*, 13:321–323, 1964.

[2] Peter W. Higgs. Broken Symmetries and the Masses of Gauge Bosons. *Phys. Rev. Lett.*, 13:508–509, 1964.

[3] Georges Aad et al. Observation of a new particle in the search for the Standard Model Higgs boson with the ATLAS detector at the LHC. *Phys. Lett.*, B716:1–29, 2012.

[4] Serguei Chatrchyan et al. Observation of a new boson at a mass of 125 GeV with the CMS experiment at the LHC. *Phys. Lett.*, B716:30–61, 2012.

[5] P. A. R. Ade et al. Planck 2015 results. XIII. Cosmological parameters. *Astron. Astrophys.*, 594:A13, 2016.

[6] Y. Fukuda et al. Evidence for oscillation of atmospheric neutrinos. *Phys. Rev. Lett.*, 81:1562–1567, 1998.

[7] Q. R. Ahmad et al. Direct evidence for neutrino flavor transformation from neutral current interactions in the Sudbury Neutrino Observatory. *Phys. Rev. Lett.*, 89:011301, 2002.

[8] David J Griffiths. *Introduction to elementary particles; 2nd rev. version.* Physics textbook. Wiley, New York, NY, 2008.

[9] F. Reines, C. L. Cowan, F. B. Harrison, A. D. McGuire, and H. W. Kruse. Detection of the free anti-neutrino. *Phys. Rev.*, 117:159–173, 1960.

[10] G. Danby, J. M. Gaillard, Konstantin A. Goulianos, L. M. Lederman, Nari B. Mistry, M. Schwartz, and J. Steinberger. Observation of High-Energy Neutrino Reactions and the Existence of Two Kinds of Neutrinos. *Phys. Rev. Lett.*, 9:36–44, 1962.

[11] K. Kodama et al. Observation of tau neutrino interactions. *Phys. Lett.*, B504:218–224, 2001.

[12] John N. Bahcall, Aldo M. Serenelli, and Sarbani Basu. New solar opacities, abundances, helioseismology, and neutrino fluxes. *Astrophys. J.*, 621:L85–L88, 2005.

[13] Raymond Davis, Jr., Don S. Harmer, and Kenneth C. Hoffman. Search for neutrinos from the sun. *Phys. Rev. Lett.*, 20:1205–1209, 1968.

[14] K. S. Hirata et al. Observation of a small atmospheric muon-neutrino / electron-neutrino ratio in Kamiokande. *Phys. Lett.*, B280:146–152, 1992.

[15] C. Patrignani et al. Review of Particle Physics. *Chin. Phys.*, C40(10):100001, 2016.

[16] B. Aharmim et al. Electron energy spectra, fluxes, and day-night asymmetries of B-8 solar neutrinos from measurements with NaCl dissolved in the heavy-water detector at the Sudbury Neutrino Observatory. *Phys. Rev.*, C72:055502, 2005.

[17] Y. Ashie et al. A Measurement of atmospheric neutrino oscillation parameters by SUPER-KAMIOKANDE I. *Phys. Rev.*, D71:112005, 2005.

[18] Walter Greiner. *Relativistic quantum mechanics : wave equations.* Springer-Verlag, Berlin New York, 1990.

[19] Walter Greiner. *Quantum electrodynamics.* Springer, Frankfurt am Main, 2009.

[20] F Halzen. *Quarks and leptons : an introductory course in modern particle physics.* Wiley, New York, 1984.

[21] C. S. Wu, E. Ambler, R. W. Hayward, D. D. Hoppes, and R. P. Hudson. Experimental Test of Parity Conservation in Beta Decay. *Phys. Rev.*, 105:1413–1414, 1957.

[22] G. Arnison et al. Experimental Observation of Isolated Large Transverse Energy Electrons with Associated Missing Energy at s**(1/2) = 540-GeV. *Phys. Lett.*, 122B:103–116, 1983. [,611(1983)].

[23] G. Arnison et al. Experimental Observation of Lepton Pairs of Invariant Mass Around 95-GeV/c**2 at the CERN SPS Collider. *Phys. Lett.*, 126B:398–410, 1983.

[24] M. Banner et al. Observation of Single Isolated Electrons of High Transverse Momentum in Events with Missing Transverse Energy at the CERN anti-p p Collider. *Phys. Lett.*, 122B:476–485, 1983.

[25] P. Bagnaia et al. Evidence for Z0 —> e+ e- at the CERN anti-p p Collider. *Phys. Lett.*, B129:130–140, 1983.

[26] V. N. Aseev et al. An upper limit on electron antineutrino mass from Troitsk experiment. *Phys. Rev.*, D84:112003, 2011.

[27] S. Yasumi et al. The Mass of the electron-neutrino from electron capture in Ho-163. *Phys. Lett.*, B334:229–233, 1994.

[28] Eleonora Di Valentino, Elena Giusarma, Olga Mena, Alessandro Melchiorri, and Joseph Silk. Cosmological limits on neutrino unknowns versus low redshift priors. *Phys. Rev.*, D93(8):083527, 2016.

[29] S. Schael et al. Precision electroweak measurements on the Z resonance. *Phys. Rept.*, 427:257–454, 2006.

[30] Boris Kayser. Neutrino Mass, Mixing, and Flavor Change. 2008.

[31] C. Alduino et al. Analysis techniques for the evaluation of the neutrinoless double-β decay lifetime in ^{130}Te with the CUORE-0 detector. *Phys. Rev.*, C93(4):045503, 2016.

[32] B. Pontecorvo. Mesonium and anti-mesonium. *Sov. Phys. JETP*, 6:429, 1957. [Zh. Eksp. Teor. Fiz.33,549(1957)].

[33] K. Abe et al. Combined Analysis of Neutrino and Antineutrino Oscillations at T2K. *Phys. Rev. Lett.*, 118(15):151801, 2017.

[34] X. Qian and P. Vogel. Neutrino Mass Hierarchy. *Prog. Part. Nucl. Phys.*, 83:1–30, 2015.

[35] Boris Kayser. Neutrino physics. *eConf*, C040802:L004, 2004.

[36] Atsuto Suzuki. Results from KamLAND reactor neutrino detection. *Phys. Scripta*, T121:33–38, 2005.

[37] K. Abe et al. Solar Neutrino Measurements in Super-Kamiokande-IV. *Phys. Rev.*, D94(5):052010, 2016.

[38] M. H. Ahn et al. Measurement of Neutrino Oscillation by the K2K Experiment. *Phys. Rev.*, D74:072003, 2006.

[39] P. Adamson et al. Measurement of Neutrino and Antineutrino Oscillations Using Beam and Atmospheric Data in MINOS. *Phys. Rev. Lett.*, 110(25):251801, 2013.

[40] P. Adamson et al. First measurement of muon-neutrino disappearance in NOvA. *Phys. Rev.*, D93(5):051104, 2016.

[41] Roger Wendell. Atmospheric Neutrino Oscillations at Super-Kamiokande. *PoS*, ICRC2015:1062, 2016.

[42] M. G. Aartsen et al. Neutrino oscillation studies with IceCube-DeepCore. *Nucl. Phys.*, B908:161–177, 2016.

[43] Liang Zhan. Recent Results from Daya Bay. *PoS*, NEUTEL2015:017, 2015.

[44] S. B. Kim. New results from RENO and future RENO-50 project. *Nuovo Cim.*, C39(4):317, 2017.

[45] A. Minotti. Latest results from Double Chooz. *Phys. Part. Nucl.*, 48(1):47–54, 2017.

[46] K. Abe et al. Updated T2K measurements of muon neutrino and antineutrino disappearance using 1.5×10^{21} protons on target. *Phys. Rev.*, D96(1):011102, 2017.

[47] P. Adamson et al. Combined analysis of ν_μ disappearance and $\nu_\mu \to \nu_e$ appearance in MINOS using accelerator and atmospheric neutrinos. *Phys. Rev. Lett.*, 112:191801, 2014.

[48] K. Abe et al. Precise Measurement of the Neutrino Mixing Parameter θ_{23} from Muon Neutrino Disappearance in an Off-Axis Beam. *Phys. Rev. Lett.*, 112(18):181801, 2014.

[49] C. Athanassopoulos et al. Evidence for anti-muon-neutrino —> anti-electron-neutrino oscillations from the LSND experiment at LAMPF. *Phys. Rev. Lett.*, 77:3082–3085, 1996.

[50] A. A. Aguilar-Arevalo et al. A Search for electron neutrino appearance at the $\Delta m^2 \sim 1\text{eV}^2$ scale. *Phys. Rev. Lett.*, 98:231801, 2007.

[51] Ivan Esteban, M. C. Gonzalez-Garcia, Michele Maltoni, Ivan Martinez-Soler, and Thomas Schwetz. Updated fit to three neutrino mixing: exploring the accelerator-reactor complementarity. *JHEP*, 01:087, 2017.

[52] R. Acciarri et al. Long-Baseline Neutrino Facility (LBNF) and Deep Underground Neutrino Experiment (DUNE). 2016.

[53] K. Abe et al. Letter of Intent: The Hyper-Kamiokande Experiment — Detector Design and Physics Potential —. 2011.

[54] K. Abe et al. A Long Baseline Neutrino Oscillation Experiment Using J-PARC Neutrino Beam and Hyper-Kamiokande. 2014.

[55] Ko Abe et al. Sensitivity of the T2K accelerator-based neutrino experiment with an Extended run to 20×10^{21} POT. 2016.

[56] J-parc tdr, kek-report 2002-13 and jaeri-tech 2003-044, 2003. http://hadron.kek.jp/ accelerator/TDA/tdr2003/index2.html.

[57] K. Abe et al. Indication of Electron Neutrino Appearance from an Accelerator-produced Off-axis Muon Neutrino Beam. *Phys. Rev. Lett.*, 107:041801, 2011.

[58] K. Abe et al. Observation of Electron Neutrino Appearance in a Muon Neutrino Beam. *Phys. Rev. Lett.*, 112:061802, 2014.

[59] S. Assylbekov et al. The T2K ND280 Off-Axis Pi-Zero Detector. *Nucl. Instrum. Meth.*, A686:48–63, 2012.

[60] I. Giomataris, R. De Oliveira, S. Andriamonje, S. Aune, G. Charpak, P. Colas, A. Giganon, Ph. Rebourgeard, and P. Salin. Micromegas in a bulk. *Nucl. Instrum. Meth.*, A560:405–408, 2006.

[61] N. Abgrall et al. Time Projection Chambers for the T2K Near Detectors. *Nucl. Instrum. Meth.*, A637:25–46, 2011.

[62] P. A. Amaudruz et al. The T2K Fine-Grained Detectors. *Nucl. Instrum. Meth.*, A696:1–31, 2012.

[63] D. Allan et al. The Electromagnetic Calorimeter for the T2K Near Detector ND280. *JINST*, 8:P10019, 2013.

[64] S. Aoki et al. The T2K Side Muon Range Detector (SMRD). *Nucl. Instrum. Meth.*, A698:135–146, 2013.

[65] K. Abe et al. Measurements of the T2K neutrino beam properties using the INGRID on-axis near detector. *Nucl. Instrum. Meth.*, A694:211–223, 2012.

[66] J. Hosaka et al. Three flavor neutrino oscillation analysis of atmospheric neutrinos in Super-Kamiokande. *Phys. Rev.*, D74:032002, 2006.

[67] H. Nishino et al. Search for Proton Decay via p —> e+ pi0 and p —> mu+ pi0 in a Large Water Cherenkov Detector. *Phys. Rev. Lett.*, 102:141801, 2009.

[68] Y. Fukuda et al. The Super-Kamiokande detector. *Nucl. Instrum. Meth.*, A501:418–462, 2003.

[69] K. Abe et al. The T2K Experiment. *Nucl. Instrum. Meth.*, A659:106, 2011.

[70] T. Sekiguchi et al. Development and operational experience of magnetic horn system for T2K experiment. *Nucl. Instrum. Meth.*, A789:57–80, 2015.

[71] A. K. Ichikawa. Design concept of the magnetic horn system for the T2K neutrino beam. *Nucl. Instrum. Meth.*, A690:27–33, 2012.

[72] K. Matsuoka et al. Design and Performance of the Muon Monitor for the T2K Neutrino Oscillation Experiment. *Nucl. Instrum. Meth.*, A624:591–600, 2010.

[73] K. Matsuoka, A. Ichikawa, H. Kubo, T. Maruyama, A. Murakami, T. Nakaya, and M. Yokoyama. Development and production of the ionization chamber for the T2K muon monitor. *Nucl. Instrum. Meth.*, A623:385–387, 2010.

[74] Jean-Michel Levy. Kinematics of an off axis neutrino beam. 2010.

[75] K. Abe et al. T2K neutrino flux prediction. *Phys. Rev.*, D87(1):012001, 2013. [Addendum: Phys. Rev.D87,no.1,019902(2013)].

[76] N. Abgrall et al. NA61/SHINE facility at the CERN SPS: beams and detector system. *JINST*, 9:P06005, 2014.

[77] N. Abgrall et al. Measurements of Cross Sections and Charged Pion Spectra in Proton-Carbon Interactions at 31 GeV/*c*. *Phys. Rev.*, C84:034604, 2011.

[78] N. Abgrall et al. Measurement of Production Properties of Positively Charged Kaons in Proton-Carbon Interactions at 31 GeV/*c*. *Phys. Rev.*, C85:035210, 2012.

[79] N. Abgrall et al. Measurements of $\pi^{\pm}$, $K^{\pm}$, K^0_S , Λ and proton production in proton–carbon interactions at 31 GeV/c with the NA61/SHINE spectrometer at the CERN SPS. *Eur. Phys. J.*, C76(2):84, 2016.

[80] M. Bonesini, A. Marchionni, F. Pietropaolo, and T. Tabarelli de Fatis. On Particle production for high-energy neutrino beams. *Eur. Phys. J.*, C20:13–27, 2001.

[81] D. S. Barton et al. Experimental Study of the a-Dependence of Inclusive Hadron Fragmentation. *Phys. Rev.*, D27:2580, 1983.

[82] P. Skubic et al. Neutral Strange Particle Production by 300-GeV Protons. *Phys. Rev.*, D18:3115–3144, 1978.

[83] Alexis Hasler and Alain Blondel. T2K Replica Target Hadron Production Measurements in NA61/SHINE and T2K Neutrino Flux Predictions, 2015. Presented 22 Jun 2015.

[84] S. Afanasev et al. The NA49 large acceptance hadron detector. *Nucl.Instrum.Meth.*, A430:210–244, 1999.

[85] N. Abgrall et al. Pion emission from the T2K replica target: method, results and application. *Nucl. Instrum. Meth.*, A701:99, 2013.

[86] N. Abgrall et al. Measurements of $\pi^{\pm}$ differential yields from the surface of the T2K replica target for incoming 31 GeV/c protons with the NA61/SHINE spectrometer at the CERN SPS. *Eur. Phys. J.*, C76(11):617, 2016.

[87] D. Sgalaberna. *Study of ν and ν flavor oscillations at the T2K experiment and impact on the δCP phase determination within the 3-ν paradigm.* PhD thesis, ETH Zurich, Diss. ETHZ No. 23350, 2016.

[88] S. Agostinelli et al. GEANT4: A Simulation toolkit. *Nucl. Instrum. Meth.*, A506:250, 2003.

[89] J. Allison et al. Geant4 developments and applications. *IEEE Trans.Nucl.Sci.*, 53:270, 2006.

[90] K. Werner. The hadronic interaction model EPOS. *Nucl. Phys. Proc. Suppl.*, 175-176:81–87, 2008.

[91] K. Werner. Strings, pomerons, and the venus model of hadronic interactions at ultrarelativistic energies. *Phys. Rept.*, 232:87–299, 1993.

[92] O. Buss, T. Gaitanos, K. Gallmeister, H. van Hees, M. Kaskulov, O. Lalakulich, A. B. Larionov, T. Leitner, J. Weil, and U. Mosel. Transport-theoretical Description of Nuclear Reactions. *Phys. Rept.*, 512:1–124, 2012.

[93] K. Gallmeister and U. Mosel. Production of charged pions off nuclei with 3...30 GeV incident protons and pions. *Nucl. Phys.*, A826:151–160, 2009.

[94] N. Abgrall et al. CERN-PH-EP-2015-278.

[95] Alfredo Ferrari, Paola R. Sala, Alberto Fasso, and Johannes Ranft. FLUKA: A multi-particle transport code (Program version 2005). 2005.

[96] T.T. Böhlen, F. Cerutti, M.P.W. Chin, A. Fassò, A. Ferrari, P.G. Ortega, A. Mairani, P.R. Sala, G. Smirnov, and V. Vlachoudis. The {FLUKA} code: Developments and challenges for high energy and medical applications. *Nuclear Data Sheets*, 120(0):211 – 214, 2014.

[97] C. Bovet, R. Maleyran, L. Piemontese, A. Placci, and M. Placidi. The Cedar Counters for Particle Identification in the SPS Secondary Beams: A Description and an Operation Manual. 1982.

[98] Toyotanso graphite. http://www.toyotanso.co.jp/Products/Special_graphite/data_en.html.

[99] J. Baudot et al. First test results Of MIMOSA-26, a fast CMOS sensor with integrated zero suppression and digitized output. In *Proceedings, 2009 IEEE Nuclear Science Symposium and Medical Imaging Conference (NSS/MIC 2009): Orlando, Florida, October 25-31, 2009*, pages 1169–1173, 2009.

[100] R. Sipos et al. The offline software framework of the NA61/SHINE experiment. *J.Phys.Conf.Ser.*, 396:022045, 2012.

[101] S. Argiro, S. L. C. Barroso, J. Gonzalez, L. Nellen, Thomas Cantzon Paul, T. A. Porter, L. Prado, Jr., M. Roth, R. Ulrich, and D. Veberic. The Offline Software Framework of the Pierre Auger Observatory. *Nucl. Instrum. Meth.*, A580:1485–1496, 2007.

[102] René Brun, F. Bruyant, Federico Carminati, Simone Giani, M. Maire, A. McPherson, G. Patrick, and L. Urban. GEANT Detector Description and Simulation Tool, 1994.

[103] S. Gorbunov and I. Kisel. Analytic formula for track extrapolation in non-homogeneous magnetic field. *Nucl. Instrum. Meth.*, A559:148–152, 2006.

[104] S. Gorbunov and I. Kisel. *An analytic formula for track extrapolation in an inhomogeneous magnetic field*, 2005. CBM-SOFT-note-2005-001.

[105] Gerald R. Lynch and Orin I. Dahl. Approximations to multiple Coulomb scattering. *Nucl. Instrum. Meth.*, B58:6–10, 1991.

[106] E. J. Wolin and L. L. Ho. Covariance matrices for track fitting with the Kalman filter. *Nucl. Instrum. Meth.*, A329:493–500, 1993.

[107] R.E. Kalman. A New Approach to Linear Filtering and Prediction Problems. *J. Basic. Eng.*, 82:35–45, 1960.

[108] R. Fruhwirth. Application of Kalman filtering to track and vertex fitting. *Nucl. Instrum. Meth.*, A262:444–450, 1987.

[109] Sebastien Murphy. *Measurement of charged Pion and Kaon production cross sections with NA61/SHINE for T2K.* PhD thesis, Geneva U., 2012-04-13.

[110] Ichita Endo, Tatsuo Kawamoto, Yoshinari Mizuno, Takashi Ohsugi, and Tohru Takeshita. Charge Centroid Finding for the Cathode Readout Multiwire Proportional Chamber. *Nucl. Instrum. Meth.*, 188:51, 1981.

[111] N. Abgrall, 2011. PhD. Thesis, University of Geneva, Switzerland, `https://edms.cern.ch/document/1172455/1`.

[112] Pavin M. Tables with numerical results for the t2k replica target 2010 paper. https://edms.cern.ch/document/1828979/1.

[113] Tomislav Vladisavljevic. Estimating the T2K Neutrino Flux with NA61/SHINE 2009 Replica-Target Data, 2017. Poster at the NuInt workshop, 25-30 June 2017, Toronto, Ontario, Canada.